NBS SPECIAL PUBLICATION 525

U.S. DEPARTMENT OF COMMERCE/National Bureau of Standards

Ultrasonic Tissue Characterization II

NATIONAL BUREAU OF STANDARDS

The National Bureau of Standards[1] was established by an act of Congress March 3, 1901. The Bureau's overall goal is to strengthen and advance the Nation's science and technology and facilitate their effective application for public benefit. To this end, the Bureau conducts research and provides: (1) a basis for the Nation's physical measurement system, (2) scientific and technological services for industry and government, (3) a technical basis for equity in trade, and (4) technical services to promote public safety. The Bureau's technical work is performed by the National Measurement Laboratory, the National Engineering Laboratory, and the Institute for Computer Sciences and Technology.

THE NATIONAL MEASUREMENT LABORATORY provides the national system of physical and chemical and materials measurement; coordinates the system with measurement systems of other nations and furnishes essential services leading to accurate and uniform physical and chemical measurement throughout the Nation's scientific community, industry, and commerce; conducts materials research leading to improved methods of measurement, standards, and data on the properties of materials needed by industry, commerce, educational institutions, and Government; provides advisory and research services to other Government Agencies; develops, produces, and distributes Standard Reference Materials; and provides calibration services. The Laboratory consists of the following centers:

Absolute Physical Quantities[2] — Radiation Research — Thermodynamics and Molecular Science — Analytical Chemistry — Materials Science.

THE NATIONAL ENGINEERING LABORATORY provides technology and technical services to users in the public and private sectors to address national needs and to solve national problems in the public interest; conducts research in engineering and applied science in support of objectives in these efforts; builds and maintains competence in the necessary disciplines required to carry out this research and technical service; develops engineering data and measurement capabilities; provides engineering measurement traceability services; develops test methods and proposes engineering standards and code changes; develops and proposes new engineering practices; and develops and improves mechanisms to transfer results of its research to the utlimate user. The Laboratory consists of the following centers:

Applied Mathematics — Electronics and Electrical Engineering[2] — Mechanical Engineering and Process Technology[2] — Building Technology — Fire Research — Consumer Product Technology — Field Methods.

THE INSTITUTE FOR COMPUTER SCIENCES AND TECHNOLOGY conducts research and provides scientific and technical services to aid Federal Agencies in the selection, acquisition, application, and use of computer technology to improve effectiveness and economy in Government operations in accordance with Public Law 89-306 (40 U.S.C. 759), relevant Executive Orders, and other directives; carries out this mission by managing the Federal Information Processing Standards Program, developing Federal ADP standards guidelines, and managing Federal participation in ADP voluntary standardization activities; provides scientific and technological advisory services and assistance to Federal Agencies; and provides the technical foundation for computer-related policies of the Federal Government. The Institute consists of the following divisions:

Systems and Software — Computer Systems Engineering — Information Technology.

[1]Headquarters and Laboratories at Gaithersburg, Maryland, unless otherwise noted; mailing address Washington,D.C. 20234.
[2]Some divisions within the center are located at Boulder, Colorado, 80303.

The National Bureau of Standards was reorganized, effective April 9, 1978.

Ultrasonic Tissue Characterization II

A collection of reviewed papers based on talks presented at the
Second International Symposium on Ultrasonic Tissue Characterization
held at the National Bureau of Standards, Gaithersburg, Maryland
June 13-15, 1977

Edited by

Melvin Linzer

National Measurement Laboratory
National Bureau of Standards
Washington, DC 20234

Cosponsors of Symposium on Ultrasonic Tissue Characterization:

National Bureau of Standards
(National Measurement Laboratory)

National Science Foundation
(Research Applied to National Needs, RANN)

National Institutes of Health
(Diagnostic Radiology Department, Clinical Center)

U.S. DEPARTMENT OF COMMERCE, Juanita M. Kreps, Secretary
Jordan J. Baruch, Assistant Secretary for Science and Technology

NATIONAL BUREAU OF STANDARDS, Ernest Ambler, Director

Issued April 1979

Library of Congress Catalog Card Number: 79-600026

National Bureau of Standards Special Publication 525
Nat. Bur. Stand. (U.S.), Spec. Publ. 525, 339 pages (Apr. 1979)
CODEN: XNBSAV

U.S. GOVERNMENT PRINTING OFFICE
WASHINGTON: 1979

For sale by the Superintendent of Documents, U.S. Government Printing Office, Washington, D.C. 20402
Stock No. 003–003–02058–3 Price $5.50
(Add 25 percent additional for other than U.S. mailing)


NEW

FOREWORD

The Second International Symposium on Ultrasonic Tissue Characterization set the stage for establishing this series of meetings as the world's leading forums for the dissemination of the most recent and advanced research in the field. Undoubtedly, the Symposium contributed significantly to the contemporary improvement in medical diagnosis. This improvement has resulted from the application to instrumentation design of the results of measurements of the interactions of ultrasound with tissue and from the deeper understanding of the physical principles underlying these interactions.

The interdiciplinary approach of engineers, physical scientists, physicians, and mathematicians made the Symposium a unique and fertile occasion. This collection of reviewed papers which describes the research results presented at the meeting makes it possible for the benefits of this work to be shared by the whole community of those dedicated to the advancement of biomedical ultrasonics and its application to health care.

The National Bureau of Standards is pleased to be responsible for this publication and to have joined the National Science Foundation and the National Institutes of Health as cosponsors of the Symposium.

John D. Hoffman

Director
National Measurement Laboratory
National Bureau of Standards

PREFACE

This volume forms a comparison with Ultrasonic Tissue Characterization, NBS Special Publication 453 (1976). It contains extended versions of 43 of the 54 papers presented at the Second International Symposium on Ultrasonic Tissue Characterization which was held at the National Bureau of Standards on June 13-15, 1977. In a departure from the normal practice for conference proceedings, these papers were critically reviewed by experts in the field.

In the pages preceding the scientific papers, an overview of the meeting is presented. The first article in this chapter is a resumé of the proceedings of the entire Symposium and it serves to put the presentations and discussions into perspective. This is folowed by a report summarizing the Panel Discussion on Breast Cancer, which was one of the highlights of the meeting, and finally, by the introductory talk given by Dr. A. J. Eggers, Jr., who at the time of the meeting was Assistant Director for Research Application, National Science Foundation. The scientific papers presented at the meeting are grouped into chapters devoted to: attenuation and velocity I: mechanisms; attenuation and velocity II: methodology and measurements; scattering and attenuation; scattering; tumor Doppler signatures; propagation through bone and skull; image reconstruction; signal processing and pattern recognition; and tissue viability and tissue phantoms. A survey of velocity and attenuation data in mammalian tissue is included in an appendix.

The success of the Symposium was due to the dedicated efforts of many individuals. Acknowledgment is given to the members of the Program committee (F. Dunn, A. C. Kak, J. F. Greenleaf, J. G. Miller, R. C. Waag and P. N. T. Wells) and to the other individuals who served as reviewers for this volume. Special appreciation is due to Peter Wells for his contributions as cochairperson of the Panel Discussion on Breast Cancer and for his valuable collaboration in preparing the summaries of the Symposium and of the Panel Discussion. The efforts of Ronald B. Johnson and Sara Torrence and their conference staffs in the organization and management of the Symposium are gratefully acknowledged. Special thanks is given to Rosemary S. Maddock who has provided the coordination and the editorial assistance in the many phases of the preparation of this volume.

Melvin Linzer

Editor and
Symposium Chairperson

ABSTRACT

The Second International Symposium on Ultrasonic Imaging and Tissue Characterization was held at the National Bureau of Standards on June 13-15, 1977. The meeting was cosponsored by the National Bureau of Standards, the National Science Foundation, and the National Institutes of Health. This volume contains extended and reviewed papers based on 43 of the 54 talks presented at the Symposium. Topics covered include techniques for measurement of ultrasonic tissue parameters, the dependence of tissue properties on physical and biological variables (e.g., ultrasonic frequency, temperature), mechanisms of ultrasonic tissue interactions, propagation through bone and skull, tumor Doppler signatures, computerized tomography, signal processing and pattern recognition, and tissue phantoms. A survey of velocity and attenuation data in mammalian tissue is included in an appendix.

Key words: Absorption; attenuation; computerized tomography; Doppler; impedance; medical diagnosis; microscopy; pattern recognition; scattering; signal processing; tissue characterization; tissue parameters; ultrasound; velocity.

In order to describe experiments adequately, it has been necessary to identify commercial materials and equipment in this book. In no case does such identification imply recommendation or endorsement by the National Bureau of Standards, nor does it imply that the material or equipment is necessarily the best available for the purpose.

CONTENTS

Chapter 1

OVERVIEW

The Second International Symposium on Ultrasonic Tissue Characterization had six principal objectives:

- to review the progress which had been made in the past two years since the first Symposium
- to provide a forum for the exchange of ideas among researchers, manufacturers, and clinicians
- to identify clinical problems which might be solved by ultrasonic tissue characterization
- to identify research opportunities
- to promote the transfer of new technological advances in medical ultrasound to commercial application
- to explore the potential for using ultrasonic tissue characterization as a mass screening technique for breast cancer.

The Symposium, which extended over three days, was cosponsored by the National Bureau of Standards (NBS), the National Science Foundation (NSF), and the National Institutes of Health (NIH). The Introductory Session opened with a welcoming address by Dr. E. Ambler, Director of NBS. He spoke of the rapid growth in the application of ultrasonic diagnosis. The U.S. market was estimated to be $64M in 1977, increasing at 31 percent per year. Ultrasonic diagnosis was apparently safe. Quantitative methods were being developed, accelerated by the work of the Tissue Signature Project supported by NSF. One of the most exciting possibilities was that ultrasound might be useful in mass screening for breast cancer. The interest and involvement of NBS in these medical applications was increasing. Dr. A. J. Eggers, Jr., Assistant Director for Research Applications, NSF, emphasized the importance of interagency collaboration. He pointed out the dramatic decline in the cost of microelectronic systems; forecasts indicated that tasks requiring microelectronics presently costing $1M would cost (1977 money) $100K in five years, and only $10K in ten years. He predicted the imminent end of the "visible" computer age, anticipating the development of displays with integrated microelectronics for operator interaction. He referred to the 1973 findings of the study group sponsored by NSF, and to the resulting initiation of Experiment No. 5, which was designed to test the acceleration of technology transfer to industry through the vehicle of diagnostic ultrasound. This had been followed by the preparation by the Alliance for Engineering in Medicine and Biology (AEMB), with NSF support, of a five-year research and development agendum; 23 research categories had been identified. Finally, in addition to many project grants, NSF was supporting the Tissue Signature Project of the Carnegie-Mellon Institute of Research. Dr. Eggers was followed by Dr. M. B. Lipsett, Director, Clinical Center, NIH. Dr. Lipsett outlined the NIH program of support for diagnostic ultrasonic research, presently running at about $5M per year. The National Cancer Institute (NCI) was funding projects concerned with breast pathology imaging and with endoscopy. The National Heart and Lung Institute (NHLI) was involved with real-time imaging and with Doppler studies of blood flow. The National Institute of General Medical Sciences (NIGMS) was supporting research in imaging systems and the biological effects of ultrasound. The Clinical Center was developing a real-time scanner, and was collaborating with NBS in the construction of a comprehensive tissue analysis system. Dr. Lipsett stated that NBS expected to continue to be concerned with the advancing horizon of ultrasonic diagnostics.

The Symposium Chairperson, Dr. M. Linzer (NBS, Gaithersburg, Maryland) discussed the present knowledge of the ultrasonic properties of tissues. He reviewed the advantages of ultrasonic diagnosis, particularly in comparison with x-ray imaging. He demonstrated these by state-of-the-art illustrations of ultrasonic data obtained in several leading laboratories -- Ultrasonics Institute, Sydney, Australia, Duke University, Durham, North Carolina, and Horizons Research Laboratories, Fort Lauderdale, Florida. Comparably impressive results were beginning to be obtainable with commercial instruments. Dr. Linzer went on to discuss basic data necessary for further development of ultrasonic diagnostics and he spoke of new methods of display. He then recalled the First International Symposium on Ultrasonic Tissue Characterization which had been held two years previously at NBS in Gaithersburg. That meeting had been attended by more than 200 people and the proceedings were recorded in NBS Special Publication 453. As a result of the meeting, NSF had supported the Ultrasonic Tissue Signature Working Group and the Advisory Council of Users. Data on tissue parameters were being updated, and libraries of algorithms and scans were to be collected. In the present Symposium, there were to be more than 50 papers, both from within the United States and by 15 speakers from nine countries outside the United States. It was evident that measurements were more difficult to make in the clinic than in the laboratory. Dr. Linzer outlined the conference program which was designed to focus sharply on measurement of tissue characteristics. He emphasized that other considerations were also vital for clinical success, and that consequently the program for the Third Symposium, which would be held in June 1978, would have an expanded scope and would include imaging and Doppler techniques.

The first scientific session, Velocity and Attenuation I: Mechanisms, began with R. L. Johnston, S. A. Goss, V. Maynard, J. K. Brady, L. A. Frizzell, W. D. O'Brien, Jr., and F. Dunn (University of Illinois, Urbana, Illinois) reviewing ultrasonic

propagation properties. Different materials were considered in order of increasing complexity. In water, attenuation was proportional to the square of the frequency, although the absolute value of attenuation was rather greater than that which would be expected to be due to viscosity. Solutions of amino acids had similar properties to those of water; while those of polypeptides exhibited greater absorption probably due to such interactions as helix-coil rearrangements and proton transfers. Proteins were made up of large molecules, with relaxational absorption. Tissues had characteristic attenuation dependency on temperature and frequency. In general, both increasing attenuation and velocity seemed to be associated with decreasing water content and with increasing protein and collagen content. Bone and lung exhibited more complicated relationships. For non-gas-containing soft tissues, however, tissues with similar physiological functions had similar attenuation, and this property might be used to characterize tissues. In discussion, the authors stated that the strong frequency dependence of velocity in lung might be due to changing ultrasonic pathways, and they agreed that the role of collagen deserved further study. E. A. Carstensen (University of Rochester, Rochester, New York) then reviewed the absorption of ultrasound in tissue. He considered first the relatively small contribution to total absorption due to the cellular structural components of tissue. The linear frequency dependence of absorption suggested a spectrum of relaxation processes. The temperature coefficient of attenuation had been measured for few tissues, and data on dispersion were sparse. Experimental results, however, were consistent with the theory. Mechanisms of ultrasonic attenuation in soft tissue were further discussed by M. O'Donnell and J. G. Miller (Washington University, St. Louis, Missouri). They presented a theoretical analysis of losses due to cellular motion, and showed that in the limit for small scatterers there was a linear frequency dependence of attenuation. They concluded that losses due to microscopic inhomogeneities accounted for a substantial fraction of the total observed attenuation in soft tissues. The authors were questioned about the effects of concentration, which they said they had taken into account, and about the existence of dispersion, which they believed to be due to relaxation.

Session 2, Scattering and Attenuation, dealt with techniques for estimating attenuation from measurements of scattering. F. L. Lizzi and M. Elbaum (Riverside Research Institute, New York, New York) described clinical spectrum analysis techniques for tissue characterization. They had measured the echo amplitude decrement from within a narrow gated sample tracked increasingly deeply into homogeneous tissue layers. Moreover, spectral analysis revealed characteristic periodicities for different histologies. Within the eye and orbit, retina, hemorrhage, fat, melanoma and glioma could be distinguished. Using a model embodying scattering (from a fixed interface) and attenuation, S. Lévi and J. Keuwez (Hôpital Universitaire Brugmann, Brussels, Belgium) reported an attempt to characterize tissues in vivo by differential attenuation measurements on the basis of observations made at two frequencies (2 and 4 MHz). Results obtained in vivo with leiomyoma and cyst were encouraging. R. Kuc and M. Schwartz (Columbia University, New York, New York) and N. Finby and F. Dain (St. Luke's Hospital Center, New York, New York), in a joint paper on statistical estimation of the acoustic attenuation coefficient slope for liver tissue from reflected ultrasonic signals, discussed the separation of fixed and refrigerated liver tissue on the basis of spectral differences in the backscattered signals. The liver was treated as a random linear filter.

This Session was closely related to Session 3, Scattering. The surface of the lung was considered by T. L. Rhyne (Massachusetts Institute of Technology, Cambridge, Massachusetts) to have an ultrasonic tissue signature which could be represented by a stochastic model. Dr. Rhyne took special care to measure the characteristics of the ultrasonic transmitter, transducer, and receiver which he used. Recent developments in research into angle-scan and frequency-swept ultrasonic scattering characterization of tissue were reported by R. C. Waag, P. P. K. Lee, R. M. Lerner, L. P. Hunter, R. Gramiak, and E. A. Schenk (University of Rochester, Rochester, New York). Using an experimental arrangement giving a true analog of Bragg scattering, they demonstrated distinctive correlations for normal, cirrhotic, and fatty liver. Measurements of tissue in vitro were related to models and measurements of known suspensions. Some of the difficulties of measuring scattering had been solved by F. E. Barber (Harvard Medical School, Boston, Massachusetts), who described ultrasonic microprobe methods for tissue characterization. Dr. Barber's microprobe operated at 10 MHz, and had an almost Gaussian focus with a diameter of about 0.2 mm. Where large interfaces existed, they dominated the scattering. The relationships between interface dimensions and scattering directivity were elegantly demonstrated by reference to a micrograph of the experimental tissue. J. M. Reid and K. K. Shung (Providence Medical Center and Institute of Applied Physiology and Medicine, Seattle, Washington) presented quantitative measurements of scattering by heart and liver. They had plotted the scattering cross-sections of 12-20 cm^3 samples of tissue for many orientations, and they discussed these in relation to scattering equations for isotropic, plane, and lossy scatterers. In particular, they considered the effects of attenuation, both within the sample and in the region between the transducer and the sample. The dependence of ultrasound backscatter from human liver tissue on frequency and protein/lipid composition was discussed by M. Freese and E. A. Lyons (Radionics Limited, Montreal, Quebec, Canada). They had used a system with a bandwidth equal to 25 percent of the center frequency, and found that a frequency of 2.25 MHz gave the best separation between normal and fatty liver. Significant correlations of the backscatter with protein content were observed in normal liver and with both protein and lipid content in abnormal fatty liver. Finally in this Session, M. Hanss and M. Boynard, (Faculté de Medécine et de Biologie, Bobigny, France) reported data on ultrasound backscattering from blood and its hematocrit and erythrocyte aggregation dependence. They stated that fluctuations in backscattered amptitude were increased in frequency with higher sedimentation rates during the sedimentation process, and explained this by a theory involving the existence of rouleaux in High sedimentation rate blood, and the occupancy

of potential scattering sites. They suggested that eventually a noninvasive ultrasonic measurement might supersede the contemporary pathology test.

Session 4, Tumor Doppler Signatures, consisted of two papers describing measurements of blood flow changes due to malignancy. P. N. T. Wells, M. Halliwell, R. A. Montford, R. Skidmore, A. J. Webb, and J. P. Woodcock, (Bristol General Hospital and Bristol Royal Infirmary, Bristol, United Kingdom) explained the hypothesis that an in situ carcinoma only becomes a rapidly proliferating tumor after initiation of vascularization. They showed that asymmetrical arterial blood flow patterns might be found with two breasts, one containing a malignant tumor. This was confirmed in the following paper on Doppler echography by G. Dale, Ch. M. Gros, M. Gautherie, and B. Gairard (Senolgie-Hospices Civils, Strasbourg, France). These authors had used a pulsed 8 MHz Doppler system to study arterial flow patterns, and they explained the complementary nature of thermography in imaging venous flow. Returning to the paper by Wells and his colleagues, these authors had gone on to describe the discovery with an 8 MHz continuous wave system of abnormal flow signals, apparently associated with malignant tumor neovascularization, arising from within the breast lesions themselves. Such signals are not found in normal breasts, or associated with benign tumors. They reported that they had also detected similarly augmented blood flow signals, using a 2 MHz pulsed Doppler instrument, from within a malignant pancreatic tumor. In discussion, it was explained that the breast tumor signals were sometimes strongest at the edge of the lesion, perhaps because of necrosis at the center.

Three papers reporting studies of cardiac muscle were presented in Session 5, Attenuation and Velocity II: Myocardium. T. D. Franklin, Jr., N. T. Sanghvi, F. J. Fry, K. M. Egenes, and A. E. Weyman (Indiana School of Medicine and Indianapolis Center for Advanced Research, Indianapolis, Indiana) described ultrasonic tissue characterization studies of ischemic and infarcted myocardium. The impetus for this research came from the non-specificity of conventional echocardiography in evaluating infarction. Their preliminary results showed that attenuation fell immediately after infarct. A more extensive study by J. G. Miller, M. O'Donnell, J. W. Mimbs, and B. E. Sobel (Washington University, St. Louis, Missouri) of ultrasonic attenuation in normal and ischemic myocardium, involved measurements made with a cadmium sulfide phase-insensitive receiving transducer. The range of attenuation variation in normal myocardium was about 12 to 15 percent, and attenuation fell by about 20 percent when the temperature of the sample was increased from 20° to 37 °C. The slope of a least-squares line fitted to the attenuation coefficient versus frequency data served as a convenient ultrasonic index. In dogs with experimentally-induced ischemia, this slope was less than the normal value if sacrifice was within about 1 day after occlusion, but with later killing it became greater. This may reflect an increase in collagen content in necrotic scar tissue. Acoustic microscopic analysis of myocardium by D. E. Yuhas and L. W. Kessler (Sonoscan Inc., Bensenville, Illinois) had yielded 100 MHz data on attenuation and velocity in formalin-fixed tissue. In kidney, it had previously been shown that the effect on attenuation of formalin fixing may not be significant. In normal myocardium, the attenuation was about 3.5 to 5.7 dB cm^{-1} MHz^{-1}. Moreover, the detailed demonstration at high frequency of structures which were of wavelength-order dimensions at low megahertz frequencies was directly relevant to the study of scattering in conventional echography.

The second day of the Symposium began with Session 6, Image Reconstruction. G. H. Glover (General Electric Co., Milwaukee, Wisconsin) discussed in vivo measurement of ultrasonic refractive index distributions in human breasts by time-of-flight tomography. His laboratory instrument was a 5 MHz transmission computerized tomograph. The patient lay prone on a canvas sling with one of her breasts immersed in water at 32° to 36 °C. Nine minutes were required to scan a slice of 5 mm thickness. Reconstructed two-dimensional images revealed cysts and fibroadenomas (having velocities around 2 percent higher than water) and malignant tumors (having velocities about 4 to 5.5 percent lower). Young normals (age range 24 to 29 years) had quite wide velocity variations, but they might not need to be scanned in a mass screening program. Histograms of pixel velocity distributions, and cumulative pixel velocity plots, might provide accurate separation of normals from patients with breasts made asymmetrical by the presence of malignancy. Dr. Glover stated that he was developing a fan beam detector array with 127 elements, designed to reduce the examination time to 10 seconds per breast. Questions were raised by the audience concerning path straightness (Dr. Glover had ray plots), resolution (which was 1 ns, although 10 ns would have been adequate), point spread function (MTF ≃ 1 mm), and accessibility (slices could be within 20 mm of the chest wall in the experimental system). Using a synthetic "fan beam," R. Balasubramanian, J. F. Greenleaf, P. J. Thomas, and S. A. Johnson (Mayo Clinic, Rochester, Minnesota) reported measurements of temperature coefficients of ultrasonic speed in various human tissue. Apart from that of fat, the temperature coefficients of liver, kidney, and other tissues were all about 2 m $s^{-1}K^{-1}$. The possibility that tumors might be identifiable because of their elevated temperatures was mentioned during the discussion, but the authors had not investigated velocity changes with temperature in tumor tissue. Results obtained with computed tomographic reconstruction of attenuation images had previously been disappointing, but new approaches were suggested by A. C. Kak and K. A. Dines (Purdue University, West Lafayette, Indiana) in their paper on signal processing for the measurement of attenuation of soft tissue. They pointed out that reflection contributed a loss of about 4 percent at each major interface, making algebraic reconstruction techniques unsatisfactory. Other frequency and time domain methods, such as polynomial fitting, frequency averaging and energy analysis, might prove to be good candidates for attenuation measurements. For example, a reconstruction of a section through a dog's heart by the energy method demonstrated immunity to reflection artifacts. In discussion, members of the audience emphasized the importance of clinical practicability. S. A. Johnson, J. F.

Greenleaf, and B. Rajagopalan (Mayo Clinic, Rochester, Minnesota) and R. C. Bahn and B. Baxter (University of Utah, Salt Lake City, Utah), in a joint paper on the future role of high spatial resolution ultrasonic measurement techniques for characterization of static and moving tissue, discussed the determination by computerized tomography of three-dimensional fluid flow and temperature. They proposed the use of seismological approaches for high-resolution imaging. Another new method, possibly leading to mapping true ultrasonic backscatter and attenuation distributions in tissue -- a digital reconstruction approach -- was suggested by F. A. Duck and C. R. Hill (Institute of Cancer Research, Sutton, United Kingdom). By assuming that attenuation and scattering were constant and isotropic within each volume element of the object, they showed that the corresponding pixel values in the image could be calculated by algebraic reconstruction techniques (ART) in about six iterations. Discussion revealed that isotropic assumptions might not be satisfied in clinical practice.

Sessions 7 and 8, Signal Processing and Pattern Recognition I and II, contained a total of twelve papers. Region-of-interest analysis methods were used in feature extraction techniques designed to improve recognition of patterns in ultrasonic pictures of the prostate for tumor diagnosis, by W. V. Seelen (Johannes Gutenberg Universität, Mainz), E. G. Lock and G. Wessels (Deutsche Klinik für Diagnostik, Wiesbaden), U. Scheiding (Battelle Institut, Frankfurt), and A. Gaca (Deutsche Klinik für Diagnostik, Wiesbaden, Federal Republic of Germany). J. C. Birnholz (Harvard University, Boston, Massachusetts) then reviewed the elements of visual pattern recognition in ultrasonography. He showed some remarkably excellent grey-scale pictures. The influence of signal processing, and particularly of the detection method, on the quality of echograms was discussed by I. Beretsky, D. Arnold, and J. Cason (Searle Ultrasound Research and Advanced Development, Spring Valley, New York), in their paper on impulse detection in pulse echo ultrasound -- recent in vitro experiments with a human aorta. This was followed by a theoretical analysis of instantaneous power spectra as applied to spectra-color ultrasonography, by W. D. Jennings, E. Holasek, and E. W. Purnell (Case Western Reserve University, Cleveland, Ohio). The method was based on the separate display in the primary colors on the same image of three frequency bands constituting the echo signals. Session 7 ended with a paper by C. K. Kuni (University of Colorado Medical Center, Denver, Colorado) on tissue identification by spectral analysis of scattered ultrasound. Dr. Kuni discussed some of the problems of obtaining and interpreting backscattered spectra.

The following Session 8 began with a description of a comprehensive ultrasonic tissue analysis system by M. Linzer, S. I. Parks, R. W. Shideler, S. J. Norton, F. P. Higgins, and D. R. Dietz (National Bureau of Standards, Washington, D.C.) and J. L. Doppman and T. H. Shawker (National Institutes of Health, Bethesda, Maryland). Dr. Linzer described a dynamically-focused system using an expanding-aperture annular array with an approximately constant F-number, and an rf subsystem capable of operating with impulses, gated continuous wave, and chirp pulses. Chirp operation with 8:1 compression had been achieved. An ultrafast signal averager was developed for improvement of the signal-to-noise ratio of A-scans. This instrument had a sampling rate of 50 MHz and a 4-bit analog-to-digital converter, and had potential applications in the examination of obese patients, the use of higher frequencies, and the use of inefficient transducers. Next, an instrument called the "SonoChromascope" was described. Interfaced to a commercial two-dimensional B-scanner, this device formed a versatile digital real-time acquisition, signal processing, and display system. The 250 kbyte memory allowed operation in normalized averaging, maximum, minimum, and parameter comparison modes. Gray-scale, color, and window displays, as well as digital readout of area and average echo amplitude in regions-of-interest were possible. Finally, Dr. Linzer stated that other methods, including CT scanning, were being investigated at NBS. There was discussion about the rather low digitization accuracy of commercial transient recorders which do not contain sample-and-hold circuits. The subject of spectrum analysis was again considered in the following paper by L. Joynt, D. Boyle, H. Rakowski, and W. Beaver (Stanford University, Stanford, California), on the identification of tissue parameters by digital processing of real-time ultrasonic clinical data. Data obtained with a real-time phased array sector scanner from selected regions within the myocardium in various clinical conditions were subjected to spectral analysis. Although there was substantial overlap between groups, spectra from patients with myocardial infarcts had much less fluctuation in their means and variances as a function of time. J. C. Gore and S. Leeman (Royal Postgraduate Medical School, London, United Kingdom) presented two short papers. The first, on the theoretical evaluation of backscatter of ultrasonic pulses from human tissue and its implications for tissue characterization, dealt with the effects of the characteristics of pulser, transducer, and receiver. The second paper, on autocorrelation analysis of A-scans in vivo and the possible clinical application of temporal changes in echo characteristics, revealed similarities between the echoes from different specimens of the same types of tissue, while different types of tissue had dissimilar autocorrelation functions. With the goal of implementing computer spectral analysis of ultrasonic A-mode echoes, D. E. Robinson (Ultrasonics Institute, Sydney, Australia) had developed an on-line data acquisition system based on a clinical scanner, 10 MHz sample rate transient recorder, and Interdata 85 computer. Special consideration had been given by K. Preston, Jr. (Carnegie-Mellon University, Pittsburgh, Pennsylvania) and M. L. Skolnik (University of Pittsburgh, Pittsburgh, Pennsylvania) to the application of pattern recognition techniques to the separation of ultrasonic echoes from different types of tissue. Digitized A-scans had been converted to sound patterns as a preliminary to testing the feasibility of using the ear to distinquish the sound patterns from different types of tissue. The A-scans had been analyzed in terms of skew, kurtosis, and other statistical parameters. Initial results had been obtained from normal and neoplastic kidney. In order to determine the correlation function of echoes from a region-of-interest identified on a two-dimensional B-scan, J. Fraser and G. S. Kino (Stanford University,

Stanford, California) and J. Birnholz (Harvard Medical School, Boston, Massachusetts) reported the use of cepstrum processing for tissue analysis. The transducer response appeared mainly centered at the cepstrum origin, and it was gated out so that the inverted cepstrum allowed the well-deconvoluted autocorrelation response of the tissue alone to be observed. Finally in this lengthy pair of sessions, R. D. Lepper, R. Reuter, and H. G. Trier (Universität Bonn, Bonn, Federal Republic of Germany) pointed out the advantage of asychronous writing and reading on a storage tube in time-stretching ophthalmic A-scans in order to improve the precision of digitization.

Session 9 was a Panel Discussion on Ultrasonic Diagnosis of Breast Cancer. The cochairperson, P. N. T. Wells (Bristol General Hospital, Bristol, United Kingdom) in his introductory remarks pointed out that mortality from breast cancer had not improved over the last 20 years. He explained that in the Western World, breast cancer, which had many different pathological types, killed 1 in 50 women, was the main cause of death in females in the age range 40 to 44, and in the U.S. had an annual economic cost of $200M. Existing diagnostic methods were inadequate for mass screening. Interest in ultrasonic techniques hinged around the possibility that earlier detection by screening might improve prognosis. Cochairperson W. Pomerance (National Institutes of Health, Bethesda, Maryland), defined screening as the application of known methods to an asymptomatic population to detect early cancer. He considered that a successful method for breast screening would need to detect tumors of less than 5 mm diameter, and that it should be free from hazard and have at least a 90 percent success rate. Encouraging results with high-resolution scanning led L. Weiss (Roswell Park Memorial Institute, Buffalo, New York) to suggest that ultrasound might be capable of detecting lesions of 2 mm diameter. This would be an important although numerically modest improvement over the present ability to detect 5 mm lesions by manual palpation. He explained that it had been estimated that screening the whole adult female population with an effective ultrasonic method, if one should be developed, would have cost $620M per year in 1971, and he felt that it would therefore be necessary to restrict screening to women known to be at risk, or over 50 years old. J. L. Doppman (National Institutes of Health, Bethesda, Maryland) described the role of mammography, and stated that the x-ray exposure was presently less than 0.01 Gy. Mammography could ensure that the lesion was removed by the surgeon. Five years of experience of ultrasonic visualization of the breast in Japan were reviewed by T. Kobayashi (National Cancer Center Hospital, Tokyo, Japan). Ultrasonic screening was being made available by means of mobile units. G. Dale (Senologie-Hospices Civils, Strasbourg, France) described the complementary use of ultrasonic scanning, both pulse-echo and Doppler, together with thermography and mammography, to decrease the overall error rate. The results of research into high resolution pulse-echo imaging of the breast, and the problems of analyzing the scans, were presented by G. Baum (Albert Einstein College of Medicine, New York, New York). Elizabeth K. Fry (Indiana University School of Medicine and Indiana University Hospital, Indianapolis, Indiana) described a versatile ultrasonic breast scanning research instrument. She presented some scans, and discussed their interpretation, emphasized the importance of shadows, and the different patterns obtained with different transducers and frequencies. Cautious optimism was expressed by D. E. Robinson (Ultrasonics Institute, Sydney, Australia). He demonstrated some excellent scans, obtained with a 4 MHz focused beam in a water bath scanner, and spoke of eight features for which the scans required to be examined in reaching a diagnosis. J. F. Greenleaf (Mayo Clinic, Rochester, Minnesota) described the role of ultrasonic computed tomography in obtaining data on tissue properties and in correcting two-dimensional B-scans. G. H. Glover (General Electric Company, Milwaukee, Wisconsin) had previously talked about his work on ultrasonic computed tomography in a paper presented during Session 6. As time was short, Dr. Glover did not add to the information which he had already given concerning the increase in velocity associated with malignancy in breast tissue. For the same reason, Dr. Wells did not elaborate on the potential of neovascularization blood flow Doppler detection, as he had mentioned this in Session 4. M. Linzer (National Bureau of Standards, Washington, D.C.) emphasized the vast quantity of data which would be obtained in scanning only one patient, and of the refinements in methodology which would be necessary to make ultrasonic breast screening feasible. Members of the Panel and the audience then began an open discussion, and several points were made. The demonstration of microcalcification in ultrasonic scans was possible if sufficiently extensive. Ultrasonic scanning was beneficial in young women with "lumpy" breasts. Mammography did not contribute further when ultrasound had already detected a lesion. Present commercial equipment was unsuitable for starting a mass screening program. Mammography would in principle never be an acceptable mass screening method, as it would always involve exposure to some radiation. Dr. Wells closed the discussion with a short summary. Mass screening of selected groups of the female population would be worthwhile if a suitable technique could be developed. Such a technique might well be based on ultrasound but it would need to be accurate and economical. The present lines of research were promising; more resources should be devoted to solving the fundamental and technological problems, so that earlier clinical application would be possible.

Propagation Through Bone and Skull was the subject of Session 10, which opened the final day of the Symposium. A theory relating sonic velocity to mineral content in bone was presented by S. Lees (Forsyth Dental Center, Boston, Massachusetts). Bone had a higher velocity than that predicted on the basis of its longitudinal elastic modulus. Dr. Lees suggested that this was due to the bone consisting of mineral hydroxyapatite crystallites embedded in a matrix of collagen, behaving in the same way as a plastic filled with powdered mineral. H. S. Yoon and J. L. Katz (Rensselaer Polytechnic Institute, Troy, New York) considered the ultrasonic properties and microtexture of human cortical bone, and showed that bone could be treated as an elastic dielectric. The attenuation of ultrasound in cancellous bone was the subject of a paper by J. E. Barger (Bolt Beranek and Newman, Cambridge, Massachusetts). He distinguished between phase

and group velocities, and showed that scattering in the dipole made an important contribution to losses at frequencies in the range 0.5 to 2 MHz. The results of measurements of transmission through skull were presented, in a discussion of the acoustic characteristics of the skull, by D. N. White (Queens University, Kingston, Ontario, Canada). Dr. White explained that propagating ultrasonic energy appeared to be distributed between the bony and the soft tissue elements of cancellous bone resulting in substantial attenuation, although it was transmitted with relatively low loss through ivory bone. Inhomogeneities led to marked distortion of megahertz frequency beams transmitted through the skull. Because of this difficulty, F. J. Fry (Indianapolis Center for Advanced Research, Indianapolis, Indiana) had investigated the transkull transmission of axisymmetric focused ultrasonic beams in the 0.5 to 1 MHz frequency range, and its implications for brain tissue visualization, interrogation, and therapy. Beams at the relatively low frequency of 0.5 MHz were not greatly distorted in travelling through skull, and there seemed to be quite good correlation between transkull ultrasonic two-dimensional brain scans and x-ray computed tomographs. The potential for therapy resulting from the relatively low attenuation in the skull was demonstrated by a lesion induced in lucite by a beam of ultrasound which had passed through part of a cadaver skull. The feasibility of visualizing the brain was further demonstrated by some advances in acoustic imaging through the skull which were reported in a joint paper by S. W. Smith (Bureau of Radiological Health, Rockville, Maryland), D. J. Phillips (University of Washington, Seattle, Washington), and O. T. von Ramm and F. L. Thurstone (Duke University, Durham, North Carolina). Remarkable real-time pictures, showing brain structures and pulsating arteries, had been made with a phased-array sector scanner. Treating the skull as a random acoustic lens, optimal results were theoretically obtained at a frequency of about 1 MHz and an aperture width of about 35 to 40 mm. The ultrasonic images were well correlated with pictures from a brain atlas. The possibility was pointed out that phase correction for the effect of the skull could be obtained element-by-element across the array, if a suitable intracranial source of uniform wavefronts could be devised.

The following Sessions 11 and 12, Attenuation and Velocity III and IV had ten papers. S. A. Goss, R. L. Johnston, V. Maynard, L. Nider, L. A. Frizzell, W. D. O'Brien, Jr., and F. Dunn (University of Illinois, Urbana, Illinois) reviewed ultrasonic propagation parameter measurements. They discussed the advantages, disadvantages, and accuracies of resonant cavities, interferometers, and thermocouple probes, and techniques based on velocity difference measurement, pulse superposition, radiation pressure, and time-of-flight measurement. The temperature dependence of the velocity of sound in soft tissues, a parameter of great importance in hyperthermia therapy for control of cancer, was reported by T. Bowen, W. G. Connor, R. L. Nasoni, A. E. Pifer, and R. R. Sholes (University of Arizona, Tucson, Arizona). With the exception of fat, vegetable oil, and water, which had negative temperature coefficients of velocity, all the other tissues investigated -- spleen, muscle, liver, and kidney -- had positive temperature coefficients over the range 36° to 44 °C. A simple but effective device for measuring ultrasonic propagation velocity in tissue, both in vitro and, with suitable anatomy, in vivo, was described by B. D. Sollish (Weismann Institute of Science, Rehovat, Israel). The following three papers were concerned with ultrasonic studies of the breast. T. Kobayashi (National Cancer Center Hospital, Tokyo, Japan) spoke about the correlation of attenuation in breast cancers with connective tissue content. He showed that stronger shadowing, associated with greater attenuation, was correlated with higher connective tissue content. Thus, strong shadows were produced by scirrhous carcinoma (rich in connective tissue), average shadows by papillary carcinoma, and weak shadows by medullary carcinoma (poor in connective tissue). The comments of the audience substantiated the conclusion that increasing attenuation was correlated with increase in collagen, as in operative scars and older breasts. Next, G. Dale, Ch. M. Gros, M. Gautherie, and B. Gairard (Senologie-Hospices Civils, Strasbourg, France) carefully reviewed diagnostic image features, in their paper on echographic syndromes of breast cancer. This was followed by a multi-discipline approach to the detection of breast cancer by ultrasonic techniques, with intercomparison of signal-processed ultrasound transmission data, ultrasound pulse-echo information, and whole breast pathology, by E. K. Fry, N. T. Sanghvi, and F. J. Fry (Indiana University School of Medicine and Indianapolis Center for Advanced Research, Indianapolis, Indiana) and H. S. Gallager (University of Texas, Houston, Texas). Experiments with an excised, formalin-fixed breast revealed non-uniform attenuation particularly in and near the nipple. The audience asked about the contributions of reflections (which were felt not to be large), the possibility of the existence of bubbles and the effect of formalin, and, for in vivo measurements, the effects of lactation and the taking of the contraceptive pill. F. W. Kremkau, C. P. McGraw, and R. W. Barnes (Bowman Gray School of Medicine, Winston-Salem, North Carolina) reported the results of some careful measurements of the acoustic properties of human brain. The infant brain had about 60 percent lower attenuation than the adult. In adult brain, fixing with formalin increased velocity by about 30 percent. Fixed brain had a dispersion of about 1.6 m $s^{-1}MHz^{-1}$, and fresh brain about 2 m $s^{-1}MHz^{-1}$. The temperature coefficient of attenuation was negative, and attenuation was 1.4 times greater in white matter than in gray. Tissue characterization using acoustic transmission and scattering parameters was further discussed in a joint paper by M. P. Kadaba, W. P. Cockerill, and P. K. Bhagat (University of Kentucky, Lexington, Kentucky), and R. W. Ware (Veterans Administration Hospital, Lexington, Kentucky). In tissues such as kidney, liver, and cardiac muscle, over the frequency range to 1 to 10 MHz, attenuation increased from about 2 to 16 dB cm^{-1}, and velocity, from 1520 to 1580 m s^{-1} (i.e., by about 4 percent). In another joint paper, D. H. Le Croissette, R. C. Heyser, P. M. Gammell, and J. A. Roseboro (California Institute of Technology, Pasadena, California), and R. L. Wilson (University of Southern California, Los Angeles, California) reported values of the attenuation of selected tissue as a function of frequency. Using time-delay spectrometry, involving the measurement of the frequency difference between the received signal

and a transmitted frequency-modulated wavetrain, they studied attenuation over the range 1 to 8 MHz in liver, pancreas, muscle, and fat. In liver, for example, attenuation decreased after death but increased as a result of fixing. Apparently similar tissues often had very different attenuations. Finally in Session 12, D. Hughes, L. A. Geddes, and V. Newhouse (Purdue University, West Lafayette, Indiana) discussed the velocity and attenuation of ultrasound in blood at 37 °C. These data were required in order to estimate Young's modulus of the aortic wall. Besides presenting accurate values, Hughes reported that attenuation increased with packed cell volume (up to at least 60 percent packing), and velocity had a minimum value with a packed cell volume of about 10 percent.

The final session, Session 13, Tissue Viability and Tissue Phantoms, began with a paper by L. Weiss (Roswell Park Memorial Institute, Buffalo, New York) on tissue signatures -- a matter of life and death. Dr. Weiss discussed the changes which took place in in vitro tissues, and the precautions which needed to be taken to minimize consequential changes in tissue signature interactions. For example, poor oxygenation might result in death within 5 minutes. Even in life, many tumors had dead or dying cells, and these differences probably affect ultrasonic imaging. Mechanically-induced cell separation measurements were related to degenerative changes in tissue, and might possibly be used to standardize interactions with ultrasound. The remaining three papers in this Session were concerned with tissue equivalent materials for ultrasonic imaging. In a joint paper, P. Edmonds, Z. Reye, and D. Parkinson (Stanford Research Institute, Menlo Park, California), R. Filly (University of California Medical Center, San Francisco, California), and H. Busey (Picker Corporation, Northford, Connecticut) described a human tissue phantom for testing conventional ultrasonic scanners. After experimenting with several rubber and plastic materials, it was found that gelatin-water gels, loaded with glass microspheres or cellulose fillers as scatterers, gave satisfactory results. Questions from the audience were answered by statements that the gel had an acceptable dependence of attenuation on frequency, and that the plastic materials had attenuations which were too high to permit the addition of scatterers. R. C. Eggleton (Indiana University School of Medicine and Indianapolis Center for Advanced Research, Indianapolis, Indiana) mentioned the application of tissue simulators for ultrasonic diagnosis, in teaching and training, evaluation of scanner performance, and as models for basic research. He presented results obtained with a plastisol, and showed the effects of adding scatterers. A joint paper by P. L. Carson, L. Shabason, and D. E. Dick (University of Colorado Medical Center, Denver, Colorado) and W. Clayman (Alderson Research Laboratories, Inc., Denver, Colorado) on tissue equivalent test objects for comparison of ultrasound transmission tomography by reconstruction and pulse echo imaging, also discussed special plastic materials. Although these materials did have rather high attenuation (about 2 dB $cm^{-1}MHz^{-1}$), scatterers could be added and phantoms satisfactory for testing systems could be constructed. Finally, Dr. Carson showed an ultrasonic CT scan of an in vivo breast indicating an attenuation coefficient of about 15 dB cm^{-1} at 3.5 MHz.

In summary, the Second International Symposium on Ultrasonic Tissue Characterization brought the subject into focus and perspective. The 286 participants, including many of the leaders in the field, spent three days exchanging ideas and learning from each other. Mass screening for breast cancer in particular was identified as one of several clinical problems which might be solved by ultrasonic tissue characterization. Research opportunities were evident in the development of fundamental theories, the acquisition of data on velocity, attenuation and scattering, and in clinical validation. Image reconstruction, signal processing, pattern recognition, and Doppler blood flow signals, emerged as fruitful areas for investigation. New technological advances, for example, in tissue phantom materials, were identified as already being ready for transfer to commercial application.

M. Linzer
P. N. T. Wells

July, 1977

REPORT ON PANEL DISCUSSION

ULTRASONIC DIAGNOSIS OF BREAST CANCER

PANEL

Cochairpersons

William Pomerance
Diagnosis Branch
Division of Cancer Biology and Diagnosis
National Institutes of Health
Bethesda, Maryland

P. N. T. Wells
Department of Medical Physics
Bristol General Hospital
Bristol, United Kingdom

Panel Members

Gilbert Baum
Albert Einstein College of Medicine
Bronx, New York

John L. Doppman
Department of Diagnostic Radiology
Clinical Center
National Institutes of Health
Bethesda, Maryland

G. H. Glover
General Electric Company
Medical Systems Division
Milwaukee, Wisconsin

Toshiji Kobayashi
Department of Internal Medicine
National Cancer Center Hospital
Tokyo, Japan

D. E. Robinson
Ultrasonics Institute
Sydney, Australia

G. J. Dale
Senologie-Hospices Civils
Strasbourg, France

Elizabeth K. Fry
Indiana University School of Medicine and
Indiana University Hospital
Indianapolis, Indiana

J. F. Greenleaf
Mayo Clinic
Rochester, Minnesota

Melvin Linzer
National Measurement Laboratory
National Bureau of Standards
Washington, D.C.

Leonard Weiss
Roswell Park Memorial Institute
Buffalo, New York

In his introductory remarks, P. N. T. Wells pointed out that the overall mortality from breast cancer was the main cause of death in Western women between the ages of 40 and 44 years, and the annual economic cost of the disease in the U.S. was around $200M. Consequently, it was timely to review the contribution which ultrasonic diagnostics might make to the solution of the breast cancer problem. There were many different malignant tumors of the breast -- scirrhous, mammary duct, papillary, medullary, colloid, lobular, intracystic, apocrine and adenoid cystic carcinoma, Paget's disease, lymphoma, and sarcoma. The earlier that breast cancer was treated, the better was the prognosis. A patient treated with in situ carcinoma was cured. If the tumor was localized, the five-year survival was 85 percent; but this fell to 53 percent if there was lymph node involvement. A patient with distant metastases was incurable, although the survival time varied from patient to patient. Interest in screening hinged around the possibility that earlier detection might improve prognosis. Unfortunately, thermography was unsatisfactory as a screening method for breast cancer: in one series, for example, only 25 percent of those who developed cancer within 18 months were detected, and the false positive rate was approaching 15 percent. When combined with clinical examination, in another trial, only about 20 percent of cancers in women under 50 years of age would not have been detected without mammography. Moreover, mammography, whilst having a negligible risk as far as the individual patient was concerned, would itself induce by radiation a large number of cancers if every member of a large population were to be exposed to it.

William Pomerance said that it had to be admitted that contemporary methods of treating advanced breast cancer were ineffective, and that progress might depend on earlier detection. He defined screening as the application of known methods to an asymptomatic population to detect early cancer. He considered that an acceptable method for breast cancer screening would need to detect tumors of less than 5 mm diameter, and that it should be free from hazard and have at least a 90 percent success rate. The assessment of the value of breast cancer screening would take a long time, since the mortality of patients surviving treatment only coincided with that of the normal population after about 17 years. He thought that screening might have its biggest impact in detecting slowly growing asymptomatic tumors.

The fact that screening for cancer of the uterine cervix had resulted in a reduction in mortality led Leonard Weiss to hope that breast cancer screening might also be effective. Moreover, he was encouraged by results which he had obtained using a high-resolution ultrasonic scanner, that it might soon become possible to detect lesions of less than 2 mm diameter, although it might be difficult to distinguish histologically between different types of lesion. The detection of 2 mm diameter lesions would be an important but numerically modest advance from the present ability to detect 5 mm lesions by manual palpation; an improvement of 10 percent in effectively treated patients might result. Weiss stressed the importance of growth rate in determining prognosis. He then referred to a study of the feasibility of breast cancer screening, which had been carried out in 1971. If the 38 million women in the U.S. who might have benefited from screening were to have been given this advantage, it had been estimated that the annual cost then would have been around $620M. He felt that it would therefore be necessary to restrict screening to women known to be at risk, or over 50 years old.

The role of mammography was discussed by J. L. Doppman. He showed some typical mammograms, and explained that the method was best for visualizing microcalcification. Three-dimensional display was needed. A great advantage of mammography was that it could be used by the surgeon to ensure that he removed the entire lesion. Recent developments had resulted in a reduction in the x-ray exposure, which presently was generally less than 0.01 Gy (1 rad).

Next, experience with pulse-echo ultrasonic methods was reviewed. Toshiji Kobayashi had worked for five years in Japan on the ultrasonic visualization of the breast. For Japanese women, scanning through a flexible membrane at the bottom of a water-bath was satisfactory. Kobayashi described the distinctive echographic features of lesions of differing histologies, and he emphasized the importance of retrotumorous shadowing in deducing information about the attenuation by the lesion. Such was the confidence which was felt in the method in Japan that specially equipped minibuses were being used in mass screening trials. In the breast cancer clinic, both pulse-echo and Doppler investigations were complementary to thermography and mammography, according to G. J. Dale. He discussed the ultrasonic scans of two typical patients, and concluded that in breast cancer diagnosis the false positive rate was 0.6 percent; the false negative rate was 11 percent, but this fell to 5 percent when combined with clinical examination. Using pulsed Doppler, he had traced breast arteries of greater than 1 to 2 mm in diameter, and he explained that Doppler information related more to function than to structure. He had not studied the capillary system of malignant tumors by the Doppler method. Gilbert Baum described the interpretation of breast echograms. Not only was textural analysis of breast tissue patterns difficult because of their wide variations, but also the skin of different individuals seemed often to transmit ultrasound differently. He felt that it was necessary to scan through water, particularly because lesions might otherwise be displaced by the pressure of the ultrasonic probe. Coupling through a water bath also allowed a large aperture transducer to be used, and the scanning motion could be automatic. Apart from the need to develop instrumentation capable of yielding reproducible results, the main problem was not to obtain the scans, but to find the time to analyze them. Furthermore, it was subjectively apparent that image degradation occurred when digitized either to fewer than 360 x 360 pixels, or to less than 32 gray levels. Sixty scans were obtained for each patient, and to reduce the analysis time he had tried color-coding, and the superimposition of seven serial scans on a three-dimensional optical hologram. Even with such techniques, it was obvious that screening could only be offered to selected groups of patients. Elizabeth K. Fry had constructed a versatile scanner for research into breast disease. This was important, because the modification of instruments primarily designed for the examination of other structures was unsatisfactory. The patient lay prone, her breasts immersed in water. A variety of transducers, operating at different frequencies, had been used to make many scans, producing a great range of patterns for analytical study. Cautious optimism was expressed by D. E. Robinson because of his experience with a water-immersion breast scanner using a 4 MHz transducer, with an aperture of 40 mm diameter and a focal length of 100 mm. Both simple and compound scans had been made with this instrument. The ultrasonic breast scan pattern depended on the age of the patient. Cysts could easily be demonstrated, and so could some parts of the ductal system. Robinson mentioned eight features, such as the degree of shadowing, for which scans of solid lesions required to be examined in reaching a diagnosis. It was easier to see skin dimpling associated with malignancy in immersed breasts, because of the extra support provided by the water.

The possible role of ultrasonic computed tomography in obtaining data on tissue properties was emphasized by J. F. Greenleaf. In any particular breast, it should be possible to measure the attenuation and velocity in the constituent image pixels, and these data could be used to correct conventional two-dimensional pulse-echo scans. G. H. Glover had previously talked about his work on ultrasonic computed tomography in a paper presented during Session 6. As time was short, Glover did not add to the information which he had already given concerning the increase in velocity associated with malignancy in breast tissue. For the same reason, Wells did not elaborate on the potential of neovascularization blood flow Doppler detection, as he had mentioned this in the paper which he had already presented in Session 4.

Melvin Linzer emphasized that computed reflection and transmission tomography coupled with ray tracing and frequency-dependent time-gain-compensation techniques would be needed to make ultrasonic breast screening feasible. Because of the complexity of these calculations and the vast quantities of data which would be obtained in scanning only one patient, ultrafast processers with large memory are required. He felt that the potential advantages of ultrasonic investigation, and especially the possibility of safe serial surveys, justified the expenditure of substantial resources on research.

Members of the Panel and the audience then began an open discussion. M. L. Skolnik asked whether it was possible to demonstrate microcalcification on ultrasonic scans, and Dale replied that this was so if the calcification was sufficiently extensive. Fry pointed out that the echography was very helpful in monitoring young women with "lumpy" breasts, because a suggestion of the development of malignancy could be discovered early on; Robinson agreed with this. Pomerance asked Fry whether she felt that mammography had anything to contribute where a lesion had been detected by ultrasound, and although she thought that this might occasionally be the case, Weiss did not. C. R. Hill returned to the value of echography in managing patients with benign lesions, but he felt that the method was not helpful if the lesions were very small. Greenleaf stressed the importance of data obtained from time-of-flight computed tomography. Fry considered that past progress more than justified continued efforts to develop an ultrasonic breast screening method; but there was general agreement with Baum when he said that the presently available commercial equipment ought not to be used in a trial of ultrasonic breast cancer screening as this would inevitably bring the method into disrepute. F. E. Barber enquired about the potential of low-dose mammography, and Doppman replied that the accuracies of such techniques had not been assessed; he thought that it would be better to wait for a viable ultrasonic method, than to extend the use of mammography. According to Pomerance, even if the x-ray exposure were to be reduced to 2 mGy, mammography would be unacceptable for mass screening. A member of the audience asked whether it was the tumor which was demonstrated by echography, or the reaction of the surrounding tissue. Robinson replied that both features might be seen; for example, besides the echoes from the tumor, there might be skin thickening and shadowing. In this connection, Fry mentioned the change in the collagen content of the entire breast, which might be due to a malignant tumor. Wells closed the discussion with a short summary.

He said that it seemed to have been established that mass screening of selected groups of the female population for breast cancer -- those specially at risk, and those more than 50 years old -- would be worthwhile, if a suitable technique could be developed. Such a technique might well be based on ultrasound but it would not necessarily be a simple pulse-echo method. It would need to be accurate and economic. The present lines of research were promising; more resources should be devoted to solving the fundamental and technological problems, so that earlier clinical application would be possible.

P. N. T. Wells

July, 1977

INTRODUCTORY ADDRESS

THE RELATIONSHIP OF TISSUE SIGNATURE RESEARCH TO IMPROVED HEALTH CARE

Alfred J. Eggers, Jr.

Assistant Director for Research Applications
National Science Foundation
Washington, DC 20550

It is a pleasure to be here today before such a distinguished audience. It has been only two years since the first conference devoted to ultrasonic tissue characterization. Much has been accomplished in those two years. Even more will be done in the future. You should be proud to be part of such a vigorous research effort, and I know you share my pleasure at the prospects for the improved medical devices that should derive from the efforts of all of you.

It is because of these prospects that the applications side of the National Science Foundation is so interested in your efforts. In addition, there is the revolution in microelectronics which has provided an order of magnitude reduction in cost and improved performance every five years for well over 25 years. Our technologists confidently expect another decade of the same. What does this mean? Suppose a highly sophisticated piece of equipment using the current tissue signature technology would cost $1,000,000 on the market today. I'm told that this is a reasonable ball park estimate. Five years from now the cost could plummet to $100,000--still a bit rich for the average physician. But in another five, we find that $100,000 may drop to $10,000--much closer to what can be afforded.

Reflect for a moment on what the implications of these changes could be. We may be approaching the end of the "visible" computer because microelectronics can make a computer so small and inexpensive that it will disappear behind the imaging screen. One question is how will we exploit this capability? This is why efforts such as this conference are so important. It is one crucial step in preparing wisely for the future.

Of course, we must be aware that extrapolation is sometimes a hazardous experience. There is no assurance that wanting or expecting a major cost--performance breakthrough will make that change happen. Still, we would all be derelict in discharging our responsibilities if we were not ready. After all, the sums being devoted to research are not trivial, but they are really a low cost insurance payment if the predicted gains from electronics are realized. The real waste would be to have all this great technology available and not be ready to apply it for improved health care. You might be interested in the background for the Research Applied to National Needs (RANN) participation with the National Bureau of Standards and the National Institutes of Health in support of this conference. Early in the history of the applications directorate, we set up a series of experiments to investigate ways of accelerating the use of technology. One is of particular interest to you. The first step was to set up a study group in 1973 which evaluated the state of development of medical ultrasonic diagnostic instruments. This survey team found that existing technology could be marshalled into improved systems. Our group of R&D incentives experiments, therefore, included an Experiment No. 5 to encourage the industrial community to create these new systems. As in most experiments, we have learned and did not do everything to perfection. Overall, however, it was a useful investigation. Today there is new equipment on the market and clinical ultrasound is rapidly becoming an important part of diagnostic services.

That same report of 1973 also had another major finding. To make a major step forward beyond the experiment five objectives would take far more research across a broad front of activity. Later, we had the Alliance for Engineering in Medicine and Biology suggest in their report entitled, "A Five Year Research and Development Agendum for Ultrasonic Imaging Diagnostic Instrumentation," that a complete system look across 23 research categories was needed. In broad terms, the report pointed out the need to balance the total program and consider it as a system of interrelated parts. Funds for research on biohazard were described as needed. Still, it is silly to not avail oneself of the opportunity to acquire information at lower powers which are intuitively less risky. Both types of efforts were recommended. Included in this list was research on tissue characterization--the subject of this conference.

A direct outgrowth of the last tissue signature conference was a recognition that ultrasound tissue signature research was not yet a coherent body of knowledge. The RANN program provided grant funds to establish and disseminate a preliminary data base for ultrasound tissue characterization research. I understand that a newsletter is being published and that several of you in this conference will meet on June 16 to continue the task of systematically collating research results. I also understand that the first meeting will take the place of an advisory committee under the leadership of Dr. McKinney, past

president of the AIUM and professor of neurology at the Bowman Gray Medical School. Both of these groups are part of a major effort whose objective is clear. We want improved patient care. Moving from the present to the future is difficult, and we must be sure that all opinions are brought to focus on this objective.

Now, let me point out that we have three basic objectives in the RANN program. These are to:

Increase the effective use of science and technology in dealing with national problems;
Shorten the lead time between basic scientific discoveries and relevant practical applications; and
provide early warning of potential national problems and initiative assessments and research useful in avoiding or solving such problems.

It is clear that your research efforts satisfy these criteria. You will note that we emphasize national needs. I believe that each country shares our concerns about improved health care. It is a pleasure to join with all of you from many nations to present, hear, and discuss common research interests in this area. I wish you all the best in your efforts today, tomorrow, and in the future to use science and technology more effectively to make this world a healthier place in which to live and thrive.

CHAPTER 2

ATTENUATION AND VELOCITY I: MECHANISMS

Reprinted from *Ultrasonic Tissue Characterization II*, M. Linzer, ed., National Bureau of Standards, Spec. Publ. 525 (U.S. Government Printing Office, Washington, D.C., 1979).

ELEMENTS OF TISSUE CHARACTERIZATION

Part I. Ultrasonic Propagation Properties

R. L. Johnston, S. A. Goss, V. Maynard, J. K. Brady,
L. A. Frizzell, W. D. O'Brien, Jr., and F. Dunn

Bioacoustics Research Laboratory
University of Illinois
Urbana, Illinois 61801, U.S.A.

Tissues can be characterized ultrasonically by their attenuation, absorption, and velocity, all of which correlate well with the presence of the major tissue components of water, and protein, particularly, collagen. This correlation is examined in solutions of biologically important molecules and in a number of tissues and organs. It is shown that tissues can be grouped according to similar ultrasonic propagation properties, physiological functions, and concentration of elementary constituents. The role of collagen in determining ultrasonic properties of normal and pathological tissues is discussed.

Key words: Absorption; amino acids; attenuation; frequency; mammalian tissues; polypeptides; proteins; tissue characterization; ultrasonics; velocity.

1. Introduction

The ultrasonic propagation properties of biological materials include the behavior of those measurable acoustic parameters, as functions of the state and acoustic variables, which characterize the fate of acoustic signals propagating within the biological environment. The ultrasonic attenuation includes not only the absorption of the ultrasonic signal, which is degraded to heat, but also losses due to other mechanisms by which energy is extracted from the propagating wave or is redirected by virtue of the inhomogeneous nature of the media. The ultrasonic velocity and the characteristic acoustic impedance, which can be determined with the addition of density information, embody within them both the inertial and restoring parameters of the particular materials. Thus, knowledge of the ultrasonic velocity and loss terms may provide a basis for developing tissue signatures for various biological materials.

The paper will deal with the ultrasonic propagation properties of tissues beginning with the elemental constituents. As water, soft tissues, and organs have very much the same densities and compressibilities, it is instructive to begin a review with properties of aqueous media.

2. Biological Molecules in Solution

A. Water

The measured ultrasonic absorption in water is proportional to the square of the frequency, over the range 10^{-2} to 10^{-3} MHz, with the frequency-free absorption coefficient, α/f^2, having a constant value of 15.7×10^{-17} s^2/cm at 37 °C. The magnitude of this absorption is greater than one would expect from consideration of the so-called classical absorption due to viscosity and thermal conductivity. This absorption in excess of the classical value has been attributed by Hall [1][1] to a structural relaxation mechanism involving a transition between two possible quasi-crystalline states for water. More recent experimental results [2] are consistent with the hypothesis that water undergoes a structural relaxation characterized by a time constant of 10^{-12} seconds, and supports the idea that water is a mixture of two or more states and that the relaxation processes consist of the independent jumping of molecules from one state to another.

The velocity of sound propagation in pure water exhibits a maximum at 75 °C due to the existence of a minimum in the product of density and adiabatic compressibility at that temperature [3]. Similar behavior is exhibited by dilute aqueous solutions, although the temperature of maximum velocity may be decreased since the solutes modify the structural arrangements of water. The velocity in water has been measured most precisely by McSkimin [4], Greenspan and Tschiegg [5], and DelGrosso and Mader [6].

B. Amino Acids

Since it has been observed that proteins play a dominant role in the absorption properties of tis-

[1]Figures in brackets indicate literature references at the end of this paper.

sues, aqueous solutions of amino acids and polypeptides require attention, for completeness. When dissolved in water without additional ionic constituents to influence the state of charge of the amino acid, the solution exhibits a magnitude of the frequency-free absorption parameter, α/f^2, which varies little with frequency in the megahertz range, and differs only slightly from that of the solvent, water [7-12]. Amino acids in aqueous solution at neutral pH may be considered according to their action of structure making or structure breaking in the solvent. Herein, the amino acids are present as doubly charged molecules (zwitterions) and are susceptible to dissociation and recombination reactions upon a change of their environment. Hydrogen-bonding sites are located on both the amino and carboxyl groups, while the side chain may be acidic, nonpolar, or basic. Thus, the potential for breaking or making structure, in the vicinity of the solute molecules are considerable. Hammes and Pace [7] suggested that the predominate ultrasonic absorption mechanism in aqueous solutions of glycine, diglycine, and triglycine is that which involves solute-solvent (water) interaction. When the pH of an amino acid aqueous solution is within the range of 2 to 4 or 11 to 13, the relaxational behavior can be described by a single relaxation frequency. A number of amino acids have been investigated as a function of pH, viz., glycine [9,13-16], serine and threonine [8], glutamic acid, aspartic acid and alanine [14], and arginine and lysine [10,15]. Absorption maxima have been observed within the pH ranges 2 to 4, and 11 to 13, with such peaks being described quantitatively by assuming that the proton-transfer reaction dominates the absorption.

C. Polypeptides

When the amino acids are formed into polypeptide chains, the absorption increases dramatically, and the mechanisms believed to be responsible for the absorption in tissues may begin to appear. In general, aqueous solutions of polypeptides at neutral pH exhibit an ultrasonic absorption behavior greatly increased over those of amino acids in solution or of water, and with a somewhat lesser than the square-of-frequency dependence. The absorption in aqueous polypeptide solutions may involve any or all of the following four possible mechanisms, viz., proton transfer, helix-coil transition, solvation, and relaxation of the shear viscosity. Major interest has tended to be focused on the proton-transfer reactions [17-20] and helix-coil transitions [21-24].

D. Proteins

Continuing with increasing complexity of the biological media, the polypeptides may be considered to be arranged in a particular, ubiquitous way to form the globular proteinaceous state. Hemoglobin and serum albumin solutions have received considerable attention, partly because of the availabilities of the materials. Special consideration is given to other macromolecular species such as nucleic acids and polysaccharides.

When biological macromolecules, such as the globular protein hemoglobin are in aqueous solution, a certain amount of the solvent becomes an inherent part of the molecule since the polymer possesses ionic and polar groups which associate with water molecules. In addition, proteins contain a number of nonpolar side chains such that, within the vicinity of the macromolecules, some water structuring occurs. Thus, it is possible that the structure of liquid water, the hydration layer, increases in the neighborhood of the biological macromolecule. It is considered, therefore, that as an acoustic wave propagates through an aqueous solution of biopolymers, it perturbs the hydration layer manifesting absorption of energy by a structural relaxation process. The role of molecular conformation of the biopolymer has also been considered as the origin of the observed ultrasonic absorption. Figure 1 shows the excess frequency-free absorption per unit concentration for several biomacromolecules and supports the view that structuring contributes to the ultrasonic absorption spectra [25]. Both dextran [26], a carbohydrate, and polyethylene glycol [27], a synthetic polymer, assume random coil configurations in aqueous solution and exhibit absorption magnitudes similar to that of gelatin. Hemoglobin has a quaternary structure, bovine serum albumin and ovalbumin have tertiary structure, polyglutamic acid [28], a synthetic polyamino acid, has secondary structure, and the double helix, DNA, has a rigid rod conformation [29]. However, hemoglobin in 5 molar aqueous guanidine hydrochloride solution exists as a random coil [30] and yet exhibits ultrasonic absorption spectra similar to that of hemoglobin in aqueous solutions [31]. The importance of molecular spatial arrangement is thus an unsettled question, though the polypeptide structure appears to be of considerable significance.

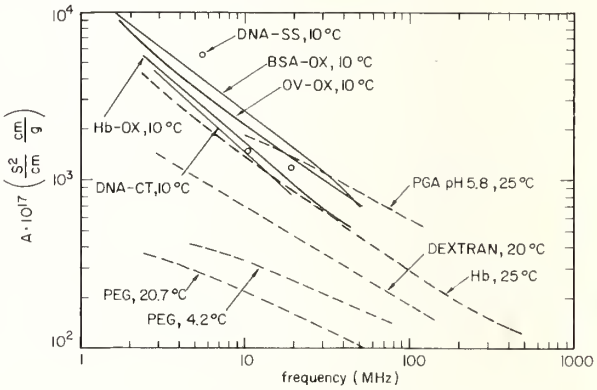

Fig. 1. Excess frequency-free ultrasonic absorption per unit concentration [25].

Within figure 1, bovine serum albumin and hemoglobin have a molecular weight of 68,000 while that of ovalbumin is 46,000. β-lactoglobin [32] (not on graph) with a molecular weight of 35,000, would fall in the range determined by hemoglobin, bovine serum albumin, and ovalbumin, while lysozyme [32] (not on graph) with a molecular weight of 14,600, would appear between hemoglobin at 25 °C and dextran. Two random coil polymers, dextran and polyethylene glycol, have been studied as a function of molecular weight. For dextran solutions, the frequency-free absorption per unit concentration increases with increasing molecular weight to a molecular weight of about 10,000, which corresponds to approximately 100 monomer units, beyond which it is independent of molecular

weight [33]. Aqueous polyethylene glycol solutions show similar absorption behavior in that beyond a molecular weight of about 4500, which also corresponds to a chain length of about 100 monomer units, the absorption is independent of molecular weight [27]. Thus, ultrasonic absorption depends to some degree upon molecular weight. Possibly beyond about 100 monomer units, the macromolecule assumes random coil characteristics.

It is uncertain whether the absorption mechanism(s) responsible for energy loss in biological polymer solutions (usually of concentrations less than 10 percent by weight) are the same as those responsible for the absorption properties of tissue [34]. Kremkau and Carstensen [11] have suggested that more highly concentrated macromolecular solutions, promoting solute-solute (intermolecular) interactions, may better approximate the tissue environment, and from the point of view of biological effects, may be the most important level at which the ultrasound interacts. In the case of dilute solutions, where the absorption is considered to vary linearly with polymer concentration, the mechanism of absorption is attributed to processes involving the interaction between the solvent (usually water) and the solute. In other than dilute solutions, the absorption is found to increase nonlinearly, and it has been suggested that this phenomenon is due to intermolecular interaction processes [34-36]. It has recently been shown [37], from absorption measurements of bovine serum albumin, to concentrations of 40 g/100 ml, over the frequency range 3.4 to 15 MHz, and at 20 °C, that the absorption dependence upon concentration does not possess a linear region. Here, the excess ultrasonic absorption can be described adequately by a concentration dependence to the 1.2 power. It thus appears essential to consider intermolecular interaction over the entire range.

3. Tissues

The nearly linear frequency dependence of attenuation in liver, kidney, brain, muscle, fat, and other parenchyma, are considered in the approximate frequency range of 100 kHz to 100 MHz, and the recent findings with regard to the temperature dependence are discussed. Several tissues and organs, such as bone, lung, refractive media of the eye, and collagenous tissues, are singled out for special detailed consideration. It is shown that classification of tissues according to certain ultrasonic propagation properties can be carried out with regard to water and collagen content, and with regard to certain teleological considerations. Pulmonary tissue is an exception here.

A. Frequency Dependence

The dependence of the ultrasonic absorption coefficient upon the acoustic frequency has been studied by numerous investigators. Goldman and Hueter [38] prepared an early compilation of ultrasonic velocity and absorption data in mammalian soft tissues. Therein it is seen that the velocity, excluding lung, is very nearly that of dilute salt solutions and varies only slightly among those tissues. Fatty tissues are exceptions in having a velocity about 10 percent less than the others. Figure 2, taken from their paper, is a graphical representation of the acoustic amplitude absorption coefficient per wavelength for several mammalian tissues in the frequency range of approximately 200 kHz to 10 MHz. As they attempted to include all measurements available at that time, by numerous investigators employing different experimental techniques, the scatter of the data exhibited by the bands, or broad shaded regions is thus not wholly surprising since many neglect to give either complete specifications of their experimental procedure or a description of the state of the specimen used. For example, it is not possible, in many cases, to determine from the literature the temperatures employed by the investigators reporting the data. It is, however, possible to discern several relatively simple relationships. For example, the absorption per cycle, α/f, is generally constant over the frequency range considered. For fat, α/f increases slightly in the frequency range from 1 to 10 MHz. The experimental results for striated muscle and liver appear to exhibit a minimum in the neighborhood of 2 MHz. Kessler [39] has shown that for kidney the linear dependence of the attenuation on frequency exists to about 100 MHz, after which a square law (or greater) dependence exists. Fry [40] has considered a viscous mechanism for the absorption of ultrasound in tissue, in which it is shown that the viscous forces acting between a suitably chosen distribution of suspended particles (or structural elements) and a suspending liquid can account for the experimentally observed linear relationship be-

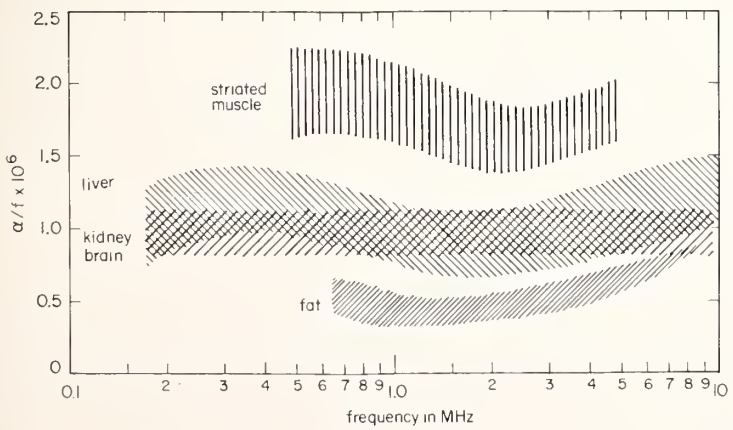

Fig. 2. Acoustic amplitude absorption coefficient (in dB/cm) per wavelength versus frequency for several mammalian tissues [38].

tween acoustic absorption coefficient and ultrasonic frequency. The frequency band over which linearity obtains (in the model) is determined by the limits of the distribution of values for the parameters chosen to describe the structural elements. Below the linear range the theory predicts a quadratic dependence, in agreement with experiment.

Figure 3 is another way of presenting the data which may be suggestive for determination of mechanisms of absorption [41]. Here, the logarithm of the absorption coefficient is plotted as a function of the logarithm of the ultrasonic frequency, and the slopes of the resulting curves are examined (the slope is the exponent of frequency upon which the magnitude of the absorption coefficient depends). Figure 3 shows data for several materials of increasing biological complexity, exhibiting correspondingly increasing complexity in absorptive behavior. The urea solution exhibits a slope of 2, indicative of classical viscous absorption for which α/f^2 is a constant. Homogenized milk, a suspension of fat particles and hydrated casein complexes, exhibits a slope of nearly unity from approximately 1 to 40 MHz. Behavior of this type cannot be explained in terms of simple viscosity or scattering theories. The curves of the absorption coefficients of egg albumin, brain tissue, liver, and striated muscle (not shown in fig. 3) exhibit slopes between 1 and 2 in the neighborhood of 1 MHz and approach a slope of 2 at higher frequencies. Hueter [41] has suggested that this type of frequency dependence can be described for specific muscle preparations by a double relaxation process in which the bulk (volume) viscosity of the tissue possesses a relaxation frequency near 40 kHz, and the shear viscosity possesses a relaxation near 400 kHz. Although it is conceded that this is an oversimplification of a complicated process, it will be shown below that the temperature dependence of the acoustic absorption coefficient lends support to this view.

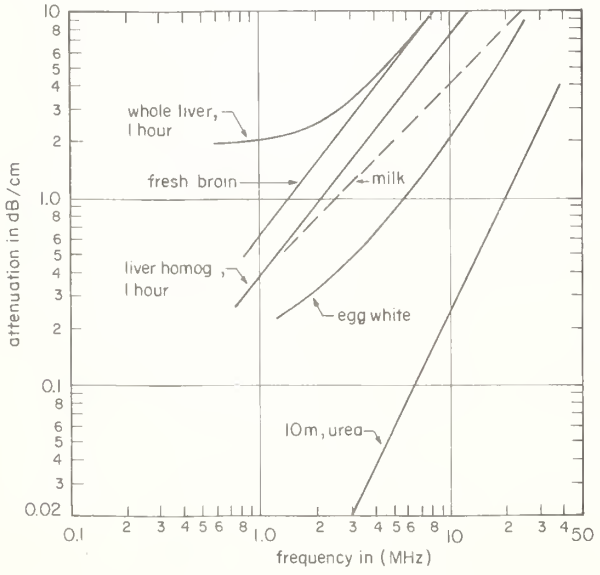

Fig. 3. Acoustic amplitude absorption coefficient versus frequency for materials of different biological complexity [41].

B. Temperature Dependence

Details of the absorption coefficient as a function of temperature and frequency have recently become available. Figure 4 shows observations on mammalian central nervous system, the only tissue for which such data are available.

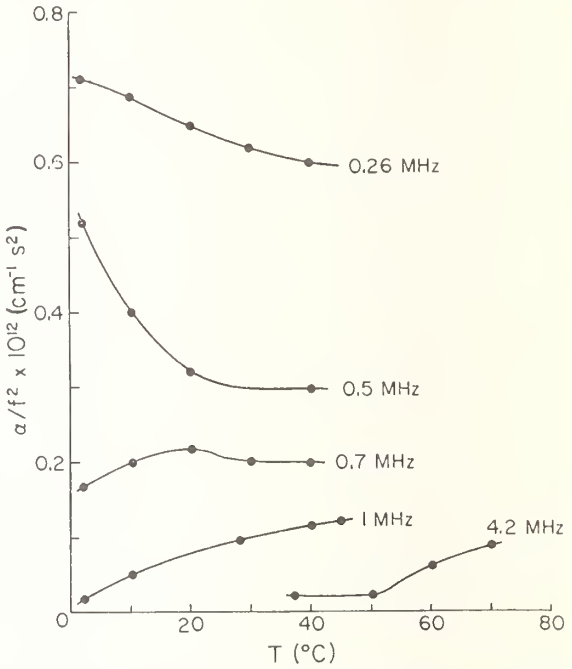

Fig. 4. Frequency and temperature dependence of ultrasonic absorption in mammalian central nervous tissue [43].

The curves for 0.26, 0.5, 0.7, and 1 MHz represent in vivo measurements in the spinal cords of neonatal mice (essential poikilotherms) [42-44] and those for 4.2 MHz are in vitro measurements in brains of adult cats (homeotherms) [45]. The relatively complex behavior of the frequency-free absorption coefficient with frequency and temperature suggests a family of curves whose maxima decrease in magnitude, and occur at ever higher temperatures, as frequency increases, supporting the suggestion mentioned above. It is not known whether other soft tissues exhibit similar behavior but Kishimoto [46] has observed a positive temperature coefficient for the absorption coefficient of bone in the frequency range 1.4 to 4.5 MHz. These data illustrate the necessity for complete specification of the state of specimens when reporting experimental results.

C. Absorption and Velocity in Bone

Bone is a tissue possessing acoustic propagation properties greatly different from those of the soft tissues discussed previously. An early study of specially prepared skull bone, in the frequency range 0.6 to 3.5 MHz (25 to 35 °C), yielded a quadratic dependence of the absorption coefficient upon frequency with a transition to a linear dependence beyond about 2 MHz [47]. An average value found for the acoustic amplitude

absorption coefficient per unit path length in skull bone, in the neighborhood of 1 MHz, was of the order of 1 cm^{-1}, approximately an order of magnitude greater than that of soft tissues of the same temperature. However, recent observations have called these values into question, and Adler and Cook [48] have obtained absorption measurements of 1.5 cm^{-1} and 2.2 cm^{-1} in freshly frozen dog tibia at room temperature at, respectively, 3 and 5 MHz. Reports of measurements of the longitudinal speed of sound in bone are largely in agreement that it is approximately twice that of soft tissues [46,48-50]. Anisotropy of elastic properties and variations in density of bone present special problems for measurement and for interpretation of results [48-50].

D. Refractive Media of the Eye

Begui [51] has studied the acoustic properties of the refractive media of the eye *in vitro*. He determined the ultrasonic absorption coefficient of the aqueous and vitreous humors at 30 MHz and that of the lens at 3 MHz. The specimens were obtained from excised fresh calf eyes. At 30 MHz and 27.5 °C, the aqueous and vitreous humors both exhibit an acoustic amplitude absorption coefficient of 0.35 cm^{-1}. Since this is approximately 50 percent greater than the absorption coefficient of dilute salt solutions, it suggests that the absorption coefficients of the humoral media of the calf eye possess a viscous-type dependence upon frequency; that is, the absorption coefficient probably increases as the square of the frequency. The lens of the calf eye exhibits a value of 0.7 cm^{-1} for the acoustic amplitude absorption coefficient at 3 MHz and 28 °C. Since the lens contains a relatively high concentration of protein, it is reasonable to assume, in the absence of further information, that the frequency dependence of the absorption coefficient of the lens resembles that of other soft tissue for which the absorption appears to be dominated by the protein content, *i.e.*, it is probable that the absorption coefficient per unit path length of the lens varies approximately with the first power of the frequency. Some investigators currently using ultrasonic methods for diagnosing disorders of the human eye feel that the lens absorption value given by Begui is larger than that for the human lens *in vivo*. The possible discrepancy may result because of species differences. Indeed, Begui observed that the viscosity of the intraocular fluid of calf eyes is greater than the values normally stated for the fluid media of human eyes. Further, the specimens used by Begui were first stored (at temperatures in the neighborhood of 0 to 5 °C) and were used for measurement purposes within a time interval of 10 days. Begui obtained for the speed of sound in refractive media of the eye 1497 m/s for the aqueous humor, 1516 for the vitreous humor, and 1616 for the lens.

E. Pulmonary Tissue

Two earlier studies [52,53] showed that ultrasonic attenuation in freshly excised dog lung was unusually high, that the speed of sound was considerably less than that of water, and that both of these quantities had a strong dependence on pulmonary inflation and acoustic frequency. It was also shown that a pathological condition involving an accumulation of liquid-like matter within the pulmonary architecture, had the effect of appreciably reducing both the attenuation and the velocity. Two recent studies have provided details of the frequency and inflation dependencies. Dunn [54] has shown that for excised dog lung of inflation to a fraction of residual air, such that the specimen density is 0.4 g/cm^3, the attenuation increases exponentially from 4 cm^{-1} at 1 MHz to 12 cm^{-1} at 5 MHz. In this same frequency range, the speed of sound increased linearly from 0.66×10^5 cm/s to 1.2×10^5 cm/s. These findings are in general agreement with those of Bauld and Schwan [55] who also showed that, for fixed inflated specimens, the energy reflected at the lung-liquid interface ever increases the gaseous inflation allowing for lesser amounts of energy to enter the lung.

4. Role of Collagen

Collagen is the most abundant single protein in the human body and the most common protein in the animal kingdom. It is closely associated in connective tissue of vertebrates and comprises between one-quarter and one-third of the total protein in the human body, being about six percent of the total body weight [56]. However, more than the prevalence of collage in the body, there is some evidence to suggest that its contribution to the elastic properties of most soft tissues, together with other structural proteins, determines acoustic contrast during echographic visualization [57,58]. This hypothesis is based on the fact that the static or low-frequency elastic modulus of collagenous fibers is at least 1000 times greater than those of soft tissues. Since the ultrasonic velocity is proportional to the square root of the elastic modulus, collagenous tissues are thought to introduce a greater impedance mismatch than would be the case for a soft tissue interface, thereby increasing the acoustic reflectivity. The increased deposition of collagen and the concomitant increase in attenuation seen in many pathological conditions is a basis for ultrasonic differential diagnosis.

Table 1 contains ultrasonic attenutation, velocity, water content, total protein content, and collagen content for various tissues [59]. It is apparent that the greater the collagen content, the greater the attenuation. Dependence of attenuation and velocity upon water content are also apparent. These data allow empirical relations to be formed for more quantitative assessment of the role of collagen content of tissues upon their ultrasonic propagation properties. For example, figure 5 represents a summary of table 1 of the ultrasonic attenuation at 1 MHz as a function of the wet weight percentage of collagen for ten tissues. Using linear regression by the method of least squares, a reasonable fit to the data is provided by the relation

$$A = 0.17\ C^{0.3}, \qquad (1)$$

where A is the ultrasonic attenuation in cm^{-1} and C is the wet weight percentage of collagen. The best fit parameter, the coefficient of determination, r^2, yields a value of 0.71 (unity represents a perfect fit). Equation 1 is represented on figure 5 by the solid straight line. Logarithmic, exponential, and linear functions were also analyz-

Table 1. Ultrasonic attenuation and velocity for tissues of various water, protein and collagen content.

Tissue	Attenuation at 1 MHz (cm^{-1})	Velocity (m/s)	Water (%)	Protein (%)	Collagen (%)
Water (20 °C)	0.0003	1483	100		
Amniotic fluid	0.0008	1510	97	0.27	
Aqueous humor	0.10 - 0.017	1497	99	0.005 - 1	
Vitreous humor	0.10 - 0.017	1516	99 - 99.9	0.02 - 0.25	0.014 - 0.067
CSF	0.0012	1499 - 1515	99	0.03	
Plasma	0.01	1571	90 - 95	7	
Testis	0.019 (absorption)		84	12	trace
Blood	0.02	1571	74 - 83		
Milk	0.04	1485	87	3 - 4	
Fat	0.04 - 0.09	1410 - 1479	10 - 19	5 - 7	yes
Spleen	0.06	1520 - 1591	76 - 80	17 - 18	0.5 - 1.2
Liver	0.07 0.13	1550 - 1607	68 - 78	20 - 21	0.1 - 1.3
Kidney	0.09 - 0.13	1558 - 1568	76-83	15 - 17	0.5 - 1.5
Brain	0.09 - 0.13	1510 - 1565	75 - 79	10 10	0.04 - 0.3
Spinal cord	0.09 - 0.12		64 - 80		
Striated muscle against grain with grain	0.18 - 0.25 0.08 - 0.12 0.16	1568 - 1603 1592 - 1603 1576 - 1587	66 - 80	20 - 21	0.7 - 1.2
Heart	0.25 - 0.38	1572	77 - 78	17	0.4 - 1.6
Tongue against grain with grain	 0.58 0.28	 1575 1585	62 - 68	14 - 17	
Lens	0.10 - 0.20	1616	63 - 69	30 - 36	
Articular capsule	0.38				
Integument	0.40	1498	60 - 72		7 - 30
Cartilage	0.58	1665	23 - 34 70	49 - 63	10 - 20
Tendon against grain with grain	 0.54 0.58	 1750	63	35	32

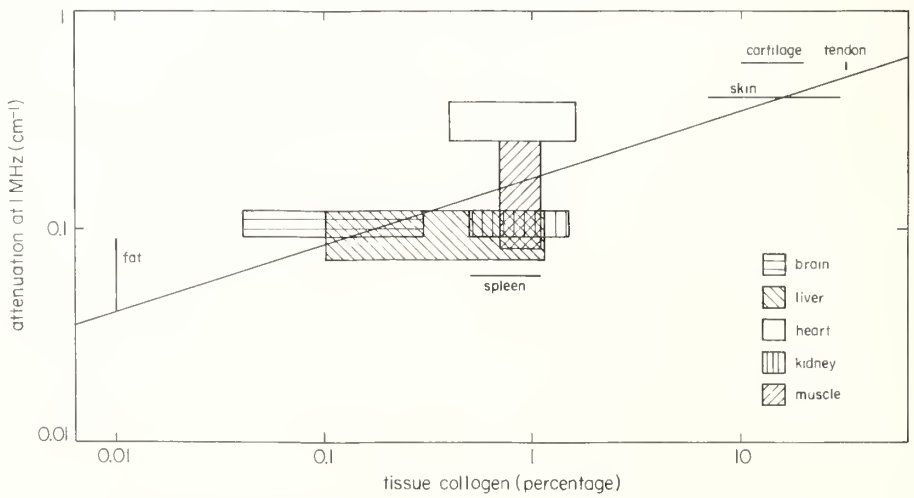

Fig. 5. Attenuation at 1 MHz as a function of the percentage of tissue collagen for 10 tissue types [59].

ed but yielded worse fits than equation 1. Similarly, to a first approximation, the ultrasonic velocity was examined as a function of collagen content for 8 tissues, excluding integument, and yielded the expression

$$C = -1700 + 230 \ln v, \qquad (2)$$

where v is the ultrasonic velocity in meters/second and $r^2 = 0.91$. Again, first approximations for wet weight percentage of total protein, P, yielded

$$A = 0.004\ P^{1.26},\ r^2 = 0.77, \qquad (3)$$

for 16 biological materials excluding integument. Thus to a first approximation there appear to be mathematical relationships which can be developed to relate the amount of tissue constituents to the ultrasonic propagation properties. There are some tissues, such as fat and integument, which may have to be treated separately but, otherwise, this approach suggests that such relationships may aid in developing ultrasonic tissue signatures which can be incorporated into clinical instrumentation.

5. Concluding Remarks

What emerges from all this is summarized in table 2, following Dussik and Dunn [60,61], which is an attempt to characterize tissues according to their ultrasonic propagation properties and biological function. It is seen that tissues can be grouped according to apparent teleology fashion with relatively narrow ranges of attenuation values within each group. The attenuation approximately doubles from group to group in the direction of increasing attenuation, and the speed of sound increases in the same direction. Further, proceeding from group to group in the same direction, tissues of ever-decreasing water content and ever-increasing structural protein content become included. Thus, it is seen that ultrasonic attenuation and velocity may be invoked to characterize tissues according to functional, structural, and teleological criteria. Possibly detailed measurements will allow assignment of resolvably unique values to each tissue structure, including usefully differentiable values for pathological states. Should this be the case, ultrasonic attenuation and impedance values, as functions of state and acoustic parameters, media, etc., should specify uniquely tissues for diagnostic purposes.

Acknowledgment

The authors acknowledge gratefully the partial support for portions of the activities described herein by grants from the National Institutes of Health.

Table 2. Average attenuation of tissues by categories.

	Tissue attenuation categories	Attenuation at 1 MHz (cm^{-1})	Tissue	Assumed teleology	General trends
1.	Very low	0.03	serum	ion, metabolic, etc., transport convection	↑ Increasing H_2O content; Increasing structural protein content; Increasing speed of sound
		0.01	blood		
2.	Low	0.06-0.07	adipose tissue	energy and (water) storage	
3.	Medium	0.08-0.11	nervous tissue	physiological function	
		0.11	liver		
		0.08-0.16	muscle	parenchymal tissue	
		0.23	heart		
		0.3	kidney		
4.	High	0.4	integument	structural integration	
		0.5	tendon		
		0.6	cartilage	stromal tissues	
5.	Very high	1 or more	bone (mineralized)	skeletal framework	
		> 4	pulmonary tissue	gaseous exchange	

References

[1] Hall, L., The origin of ultrasonic absorption in water, Phys. Rev. 73, 775 (1948).

[2] Davis, C. and Jarzynsky, J., Liquid Water-Acoustic Properties: Absorption and Relaxation, Chapter 12 in The Physics and Physical Chemistry of Water, Vol. I of Water: A Comprehensive Treatise, F. Franks, ed., (Plenum Press, New York, 1972).

[3] Willard, G. W., Temperature coefficient of ultrasonic velocity in solutions, J. Acoust. Soc. Am. 19, 235 (1947).

[4] McSkimin, H. J., Velocity of sound in distilled water for the temperature range 20 °C - 75 °C, J. Acoust. Soc. Am. 37, 325 (1965).

[5] Greenspan, M. and Tschiegg, C. E., Speed of sound in water by a direct method, J. Res. Natl. Bur. Std. 59 249-254 (1957).

[6] DelGrosso, V. A. and Mader, C. W., Speed of sound in pure water, J. Acoust. Soc. Am. 52,

1442-1446 (1972).

[7] Hammes, G. G. and Pace, C. N., Ultrasonic absorption measurements in aqueous solutions of glycine, diglycine, and triglycine, J. Phys. Chem. 72, 2227 (1968).

[8] White, R. D., Slutsky, L. J., and Pattison, S., Kinetics of the proton transfer reactions of serine and theronine, J. Phys. Chem. 75, 161 (1971).

[9] Hussey, M. and Edmonds, P. D., Ultrasonic examination of proton-transfer reactions in aqueous solutions of glycine, J. Acoust. Soc. Am. 49, 1309 (1971).

[10] Hussey, M. and Edmonds, P. D., Ultrasonic examination of proton-transfer reactions at the α-amino and side-chain groups of arginine and lysine in aqueous solution, J. Acoust. Soc. Am. 49, 1907 (1971).

[11] Kremkau, F. W. and Carstensen, E. L., Macromolecular Interaction in Sound Absorption, in Interaction of Ultrasound and Biological Tissues--Workshop Proceedings, J. M. Reid and M. R. Sikov, eds., DHEW Publication (FDA) 73-8008 BRH/DBE 73-1, p. 37 (U.S. Government Printing Office, Washington, D.C. 1972).

[12] Kremkau, F. W., Macromolecular Interaction in the Absorption of Ultrasound in Biological Material, Ph.D. Thesis, University of Rochester (1972).

[13] Maass, G., Ph.D. Thesis, University of Göttingen (1962).

[14] Applegate, K., Slutsky, L. J., and Parker, R. C., Kinetics of proton-transfer reactions of amino acids and simple polypeptides, J. Am. Chem. Soc. 90, 6909 (1968).

[15] Hussey, M., Proton Transfer at Side Chain Groups: A Mechanism for the Absorption of Ultrasound in Protein Solutions, Ph.D. Thesis, University of Pennsylvania (1970).

[16] Hussey, M., Proton Transfer Processes: One of the Modes of Interaction of Ultrasound with Proteins and DNA, in Interaction of Ultrasound and Biological Tissues, J. M. Reid and M. R. Sikov, eds., DHEW Publication (FDA), 73-8008 BRH/DBE 73-1, p. 31 (U.S. Government Printing Office, Washington, D.C. 1972).

[17] Zana, R. and Tondre, C., Ultrasonic studies of proton transfers in solutions of poly-(lysine) and poly(ornithine). Implications for the kinetics of the helix-cord transition of polypeptides and for the ultrasonic absorption of proteins, J. Phys. Chem. 76 1737 (1972).

[18] Lang, J., Tondre, C., and Zana, R., Effect of urea and other organic substances on the ultrasonic absorption of protein solutions, J. Phys. Chem. 75, 374 (1971).

[19] Zana, R. and Lang, J., Effect of pH on the ultrasonic absorption of aqueous solutions of proteins, J. Phys. Chem. 74, 2734 (1970).

[20] Applegate, K., Slutsky, L. J., and Parker, R. C., Kinetics of proton-transfer reactions of amino acids and simple polypeptides, J. Am. Chem. Soc. 90, 6909 (1968).

[21] Doty, P., Wada, A., Yang, J. T., and Blout, E. R., Polypeptides: VIII, molecular configurations of poly-L-glutamic acid in water-dioxane solution, J. Polymer Sci. 23, 851 (1957).

[22] Barksdale, A. D. and Stuehr, J. E., The kinetics of the helix-coil transition in aqueous poly-L-glutamic acid, J. Am. Chem. Soc. 94, 3334 (1972).

[23] Schwarz, G., On the kinetics of helix-coil transition of polypeptides in solution, J. Mol. Biol. 11, 64 (1965).

[24] Wada, Y., Sasabe, H., and Tomono, M., Viscoelastic relaxations in solutions of poly-(glutamic acid) and gelatin at ultrasonic frequencies, Biopolymers 5, 887 (1967).

[25] Dunn, F., Acoustic Properties of Biological Materials, in Fundamental and Applied Aspects of Nonionizing Radiation, S. M. Michaelson and M. W. Miller, eds., p. 21 (Plenum Publishing Corporation, New York, 1975).

[26] Hawley, A. S., Kessler, L. W., and Dunn, F., Ultrasonic absorption in aqueous solutions of high-molecular-weight polysaccharides, J. Acoust. Soc. Am. 38, 521 (1965).

[27] Kessler, L. W., O'Brien, W. D., Jr., and Dunn, F., Ultrasonic absorption in aqueous solutions of polyethylene glycol, J. Phys. Chem. 74, 4096 (1970).

[28] Burke, J. J., Hammes, G. G., and Lewis, T. B., Ultrasonic attenuation measurements in poly-L-glutamic acid solutions, J. Phys. Chem. 42, 3520 (1965).

[29] O'Brien, W. D., Christman, C. L., and Dunn, F., Ultrasonic investigation of aqueous solutions of deoxyribose nucleic acid, J. Acoust. Soc. Am. 52, 1251-1255 (1972).

[30] Kawahara, K., Kirscher, A. G., and Tanford, C., Dissociation of human co-hemoglobin by urea, guanidine hydrochloride and other reagent, Biochemistry 4, 1203 (1965).

[31] O'Brien, W. D., Jr. and Dunn, F., Ultrasonic examination of the hemoglobin dissociation process in aqueous solutions of guanidine hydrochloride, J. Acoust. Soc. Am. 50, 1213-1215 (1971).

[32] Lang, J., Tondre, G., and Zana, R., Effects of urea and other organic substances on the ultrasonic absorption of protein solutions, J. Phys. Chem. 75, 374 (1971).

[33] Hawley, S. A. and Dunn, F., Ultrasonic absorption in aqueous solutions of dextran, J. Chem. Phys. 50, 3523 (1969).

[34] O'Brien, W. D., Jr. and Dunn, F., Ultrasonic Absorption by Biomacromolecules, in Interaction of Ultrasound and Biological Tissues--Workshop Proceedings, J. M. Reid and M. R. Sikov, eds., p. 13, DHEW Publication (FDA) 73-8008 BRH/DBE 73-1 (U.S. Government Printing Office, Washington, D.C. 1972).

[35] Kessler, L. W. and Dunn, F., Ultrasonic investigation of the conformal changes of bovine serum albumin in aqueous solution, J. Phys. Chem. 73, 4256 (1969).

[36] O'Brien, W. D., Jr. and Dunn, F., Ultrasonic absorption mechanisms in aqueous solutions of bovine hemoglobin, J. Phys. Chem. 76, 528 (1972).

[37] Goss, S. A. and Dunn, F., Concentration Dependence of Ultrasonic Absorption in Aqueous Solutions of Bovine Serum Albumin, in IEEE Ultrasonics Symposium Proceedings, p. 65 (1974).

[38] Goldman, D. E. and Hueter, T. F., Tablar data of the velocity and absorption of high-frequency sound in mammalian tissues, J. Acoust. Soc. Am. 28, 35 (1956); 29, 655 (1957).

[39] Kessler, L. W., VHF ultrasonic attenuation in mammalian tissue, J. Acoust. Soc. Am. 53 1759 (1973).

[40] Fry, W. J., Mechanism of acoustic absorption in tissue, J. Acoust. Soc. Am. 24, 412-415 (1952).

[41] Hueter, T. F., Viscoelastic Losses in Tissues in the Ultrasonic Range, WADC Technical Report 57-706 (1958).

[42] Dunn, F., Temperature and amplitude dependence of acoustic absorption in tissue, J. Acoust. Soc. Am. 34, 1545 (1962).

[43] Dunn, F. and Brady, J. K., Pogloshchenie ul'trazvyeka v biologicheskikh sredakh, Biofizika 18, 1063 (1973). Translation, Ultrasonic absorption in biological materials, Biophysics 18, 1128 (1974).

[44] Dunn, F. and Brady, J. K., Temperature and Frequency Dependence of Ultrasonic Absorption in Tissue, in Proceedings 8th International Congress on Acoustics, Vol. I, p. 366c (Goldcrest Press, Trowbridge, Wilts., 1974).

[45] Robinson, T. C. and Lele, P. P., An analysis of lesion development in the brain and in plastics high intensity focused ultrasound at low megahertz frequencies, J. Acoust. Soc. Am. 51, 133 (1972).

[46] Kishimoto, T., Ultrasonic absorption in bones, Acustica 8, 179 (1958).

[47] Hueter, T. F., Messung der Ultraschallabsorption in menschlichen Schädelknochen und ihre Abhängigkeit von der Frequenz, Naturwissenschaften 39, 21 (1952).

[48] Adler, L. and Cook, K. V., Ultrasonic parameters of freshly frozen dog tibia, J. Acoust. Soc. Am. 58, 1107-1108 (1975).

[49] Thiesmann, H. and Pfander, F., Über die Durchlässigkeit des Knochens für Ultraschall, Strahlentherapie 80, 607 (1949).

[50] Lang, S. B., Ultrasonic Method for Measuring Elastic Coefficients of Bone and Results on Fresh and Dried Bovine Bones, IEEE Trans. Biomed. Eng. BME-17, 101 (1970).

[51] Begui, Z. E., Acoustic properties of the refractive media of the eye, J. Acoust. Soc. Am. 26, 365 (1954).

[52] Dunn, F. and Fry, W. J., Ultrasonic absorption and reflection by lung tissue, Phys. Med. Biol. 5, 401 (1961).

[53] Reid, J. M., Ultrasonic Diagnostic Methods in Cardiology, Ph.D. Thesis, University of Pennsylvania, 1965.

[54] Dunn, F., Attenuation and speed of sound in lung, J. Acoust. Soc. Am. 56, 1638 (1974).

[55] Bauld, T. J. and Schwan, H. P., Attenuation and reflection of ultrasound in canine lung tissue, J. Acoust. Soc. Am. 56, 1630 (1974).

[56] White, A., Handler, P., and Smith E. L., Principles of Biochemistry (McGraw Hill Book Co., New York, 1968).

[57] Fields, S. and Dunn, F., Correlation of echographic visualizability of tissue with biological composition and physiological state, J. Acoust. Soc. Am. 54, 809-812 (1973).

[58] Kessler, L. W., Fields, S. I., and Dunn, F., Acoustic microscopy of mammalian kidney, J. Clinical Ultrasound 2, 317-320 (1974).

[59] O'Brien, W. D., The Role of Collagen in Determining Ultrasonic Propagation Properties in Tissue, in Acoustical Holography, L. W. Kessler, ed., Vol. 7 (Plenum Press, New York, 1977).

[60] Dussik, K. T., Kyriazidov, M., Fritch, D. J., and Srear, R. S., Measurement of articular tissues with ultrasound, Amer. J. Phys. Med. 37, 160-165 (1958).

[61] Dunn, F., Ultrasonic Attenuation, Absorption, and Velocity in Tissues and Organs, in Ultrasonic Tissue Characterization, M. Linzer, ed., National Bureau of Standards Special Publication 453, pp. 21-28 (U.S. Government Printing Office, Washington, D.C. 1976).

Reprinted from *Ultrasonic Tissue Characterization II*, M. Linzer, ed., National Bureau of Standards, Spec. Publ. 525 (U.S. Government Printing Office, Washington, D.C., 1979).

ABSORPTION OF SOUND IN TISSUES

Edwin L. Carstensen

Department of Electrical Engineering
University of Rochester
Rochester, New York 14627, U.S.A.

In spite of extensive applications of ultrasound in diagnosis, therapy and even surgery, there are still many problems to be solved in the basic physics of sound propagation in tissues. Absorption of longitudinal ultrasonic waves occurs primarily at the macromolecular level. There is evidence to indicate that this absorption can be profoundly modified by macromolecular interaction. The specific structural or chemical relaxation mechanisms responsible for the absorption are unknown. Microscopic inhomogeneities may lead to certain forms of relative motion viscous losses or thermal absorption. Macroscopic inhomogeneities in tissue affect sound propagation and can lead to artifacts in certain methods of measurement of tissue absorption. Shear waves are not important in the soft tissues of the body.

Key words: Absorption of ultrasound; macromolecular relaxation; relaxation phenomenon; ultrasonic tissue absorption.

Although acoustic absorption phenomena play an important role in every medical application of ultrasound, we still have only a rudimentary understanding of the responsible physical mechanisms forty years after the first work in this field [1][1]. This review of basic concepts attempts to outline what we know about these processes and to identify problems to be solved.

1. Absorption Data

Information on absorption of sound in tissues, as it is available to us today, is outlined in figure 1. (A more complete summary of absorption data is included in the paper by Johnston et al. [2].) Data for packed red cells are included because we can think of this preparation as a kind of simple model tissue and because it has been studied over a wide range of frequencies. The absorption of sound in fatty tissue is significantly lower than the other soft tissues. Bone is much lossier than other tissues of the body. Water makes a negligible contribution to the absorption of tissues at low frequencies. Only a few measurements have been carried out above 10 MHz. We can guess that values of $(\alpha\lambda)$ for soft tissues will follow the pattern set by hemoglobin [3] and approach but remain significantly above that of water at frequencies of the order of 1000 MHz. From acoustic microscopy it is clear that sharp differences in absorption among components of cells exist at frequencies above 1000 MHz [4].

The range of values which have been reported for a given tissue type is large. This results in part from normal biological variability. In addition, there is a potential for error in measurement with inhomogeneous tissue samples.

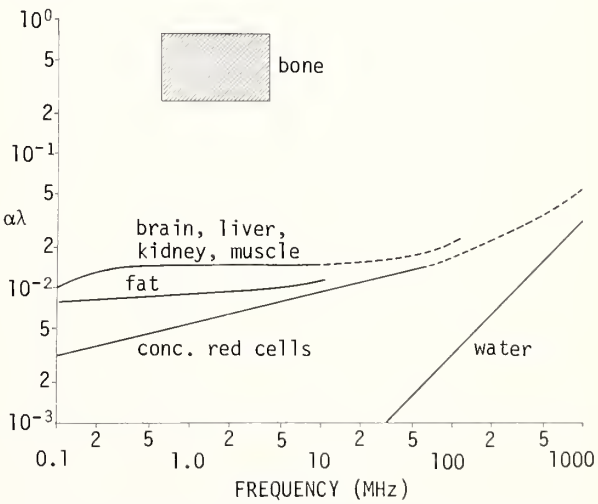

Fig. 1. Absorption of sound in biological materials. Solid lines are estimates of mean absorption coefficients from many investigators. The range of reported values is large particularly for bone. The high frequency extrapolation (dashed line) for concentrated red cells is based on measurements of hemoglobin solutions [3]. Ex Exprapolation of the data for soft tissues (dashed line) to 100 MHz is based on measurements of kidney at 100 and 200 MHz [35].

[1]Figures in brackets indicate literature references at the end of this paper.

For example, we found that in measuring sample attenuation with a phase sensitive receiver the apparent absorption for muscle could be as much as four times its true value [5]. It is interesting that the radiation force method used by Pohlman [1] in the first tissue absorption studies is still perhaps the most reliable technique available. Acoustoelectric receivers show great promise for this kind of investigation [6].

Almost all of the absorption studies have used excised tissue samples. Very few in vivo tissue absorption measurements have been made; but those few are in rough agreement with values for excised tissue. It was reported that freshly excised liver had a much higher absorption than aged tissue samples at frequencies near 1 MHz [7,8]. We have recently attempted to duplicate these observations without success [9]. Other aging studies have shown very little change in absorption of tissues with time after excision [10]. From the information available, it appears reasonable to assume that the data in figure 1 are valid for living tissues, but we should realize that this is an assumption which has not been thoroughly tested.

It is a surprising admission that after forty years of study we do not know the temperature dependence of the absorption coefficient for all of the tissues of the body. The absorption coefficients for blood [11], brain [12], and myocardial muscle [10] decrease slightly with temperature in the range 0 to 40 °C. One study reports a positive temperature coefficient for bone between 0 to 60 °C [13]. As discussed below, mouse spinal cord is reported to have a complex temperature dependence [14].

This discussion, of course, concerns longitudinal ultrasonic waves in tissue. The propagation constants for shear waves in tissues are not known in detail. However, recent rough measurements indicate that transverse waves will not be generated in any of the soft tissues of the body with any current medical application of ultrasound [9,15].

2. Macromolecular Absorption

The primary absorption of ultrasound in tissue appears to take place at the macromolecular level. This was demonstrated directly by Pauly and Schwan through a comparison in the absorption of sound in liver tissue and a subcellular homogenate of the tissue [16]. The near identity of the two values suggests that tissue structure had little influence on the absorption process.

A simpler biological system yields more detailed information. The absorption coefficients for packed red cells and for a solution of hemoglobin at the same concentration in which it is found in the erythrocyte (~ 30 g/100 ml) are essentially identical. This is shown as the upper curves in figure 2. Now, if a 26 percent suspension of red cells in physiological saline is prepared, the volumes of cells are the same as in the packed preparation. Thus, the local concentration and environment of the hemoglobin in the cell remains the same, and hence the contribution to the absorption from the hemoglobin should be in direct proportion to amount of protein present as shown by the dashed line in the figure 2 [17]. Saline contributes little to the absorption

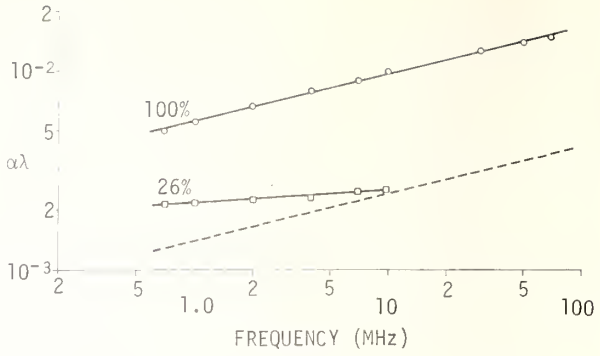

Fig. 2. Absorption of sound in a suspension of bovine erythrocyte in physiological saline [17,18]. Dashed curve is the macromolecular contribution to the absorption of the suspension (26% cells).

especially at low frequencies. Actual absorption measurements on such a suspension show that the contributions of the hemoglobin solution in the cell accounts for most, but not all, of the observed loss. The excess absorption which arises from the inhomogeneous property of the medium will be discussed later.

Since none of the smaller molecules or ions in the red cell makes a significant contribution to the absorption, it appears that the primary loss comes from the presence of the protein itself. Even the amino acid building blocks of hemoglobin have much smaller specific absorptions (i.e., absorption per gram solute) than the intact protein as shown in figure 3. In fact, the absorption of a 10 percent solution of amino acids in the proportions found in hemoglobin is barely distinguishable from water itself, where-

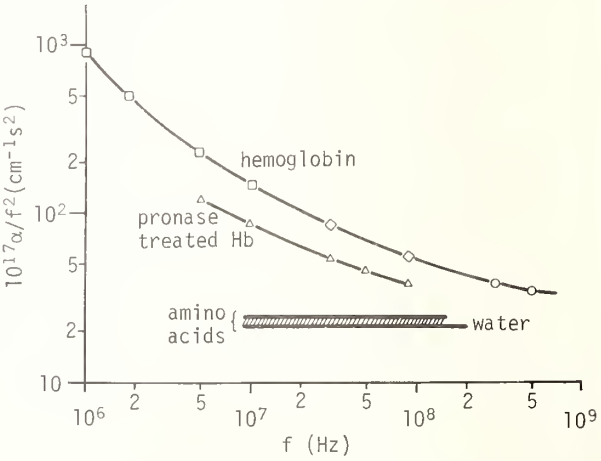

Fig. 3. Absorption of sound in a 10 percent hemoglobin solution at 25 °C [18]. Treatment with the enzyme pronase fragmented the protein yielding components with molecular weight less than 10,000 and resulting in a decreased absorption. A preparation of amino acids in concentrations equivalent to that in the hemoglobin solution give absorption values which are hardly different than water alone.

as the absorption of a 10 percent solution of hemoglobin is ten times that of water at 10 MHz [18]. A pronase-treated hemoglobin solution yielding subunits with molecular weight less than 10,000 showed a somewhat smaller specific absorption than that of the intact protein. A more subtle dissection of hemoglobin using quanidine hydrochloride produced specific absorptions which were both larger and smaller than that of intact hemoglobin as the fractionation proceeded [19].

The "whole much greater than the sum of its parts" is not limited to hemoglobin or, for that matter, to proteins. Figure 4 shows a very similar relationship among polysaccharides. The absorption for dextran is much greater than for simple sugars. It is interesting that the specific absorption of dextran and Ficoll molecules of the same molecular weight are roughly equal. Dextran is a long chain polymer whereas Ficoll is globular. As a result, the macroscopic viscosity of equivalent concentrations of the two molecules is dramatically different. This is just one of many observations that virtually eliminate classical viscous processes from consideration in tissue absorption.

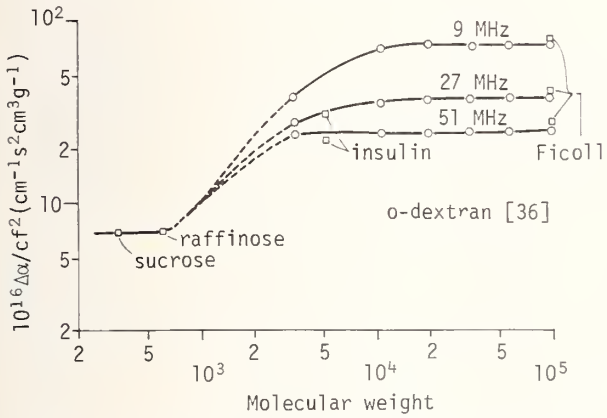

Fig. 4. Specific absorption of polysaccharides vs. molecular weight [18]. Data for dextran are taken from reference [36]. Another polysaccharide, Ficoll, which is nearly spherical and thus has a much lower intrinsic viscosity than dextran, has approximately the same specific absorption as dextran.

A number of proteins, nucleic acids and polysaccharides have now been studied [2]. The specific absorption values for the macromolecules are uniformly greater than those associated with the small molecules and ions which make up tissue.

3. Macromolecular Interaction

The increase in specific absorption with molecular complexity does not appear to stop at the macromolecular level. Association among macromolecules in some cases results in increased values for the absorption per molecule. This is a vague loosely defined concept and is not based on any specific, postulated mechanism. However, there are a number of observations which seem to fit this generic heading. The specific absorption of hemoglobin increases dramatically with

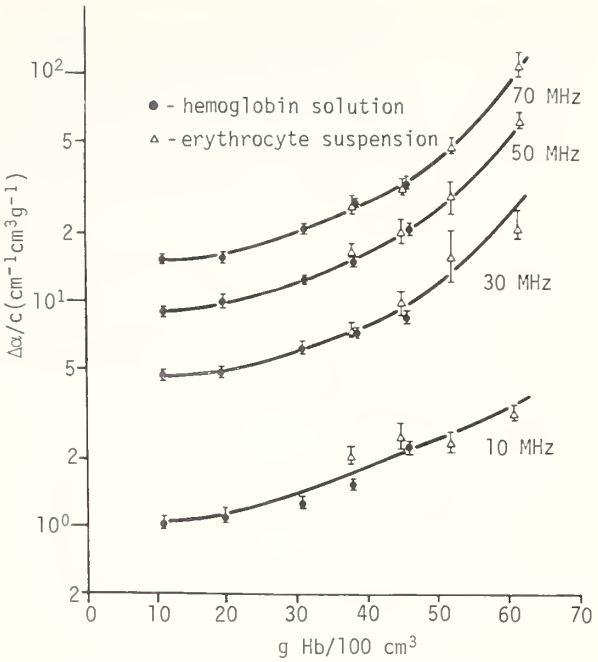

Fig. 5. Absorption of hemoglobin as a function of concentration at 25 °C [18]. For frequencies greater than 10 MHz the absorption coefficients of suspensions of red cells are determined almost entirely by the hemoglobin which they contain [11].

concentration as shown in figure 5 [18]. At a concentration of 60 grams hemoglobin per 100 ml solution, where the mean spacing of molecules is very nearly equal to the molecular diameter, the absorption per molecule is five times greater than its value in a dilute solution. Whether by introducing a new mechanism or modifying an existing process, the interaction between macromolecules as the concentration increases causes a marked increase in the specific absorption.

There are many other clear examples where macromolecular interaction is associated with increased absorption. The hemoglobin in rat erythrocytes, when stored in sodium citrate at 4 °C for several days, becomes paracrystalline (fig. 6) [20]. The specific absorption of paracrystalline cells is at least twice that of normal rat erythrocytes [18]. Treatment of red cells with acrolein cross links the hemoglobin and leads to specific absorption values which are four times greater than the values for normal erythrocytes as shown in figure 7 [21]. Other examples may be found in figure 8. It is interesting that the sediment from homogenized liver has a specific absorption three times greater than the "supernatant" from that preparation [16]. Presumably the supernatant is a dilute solution of macromolecules; whereas the sediment consists of highly organized subcellular particles.

Perhaps these observations are no more than a series of coincidences. However, the information available today suggests that the trend toward increasing absorption with increasing interaction extends beyond the macromolecular level to interactions among macromolecules.

Fig. 6. Electron micrographic comparison of normal and paracrystalline rat erythrocytes.

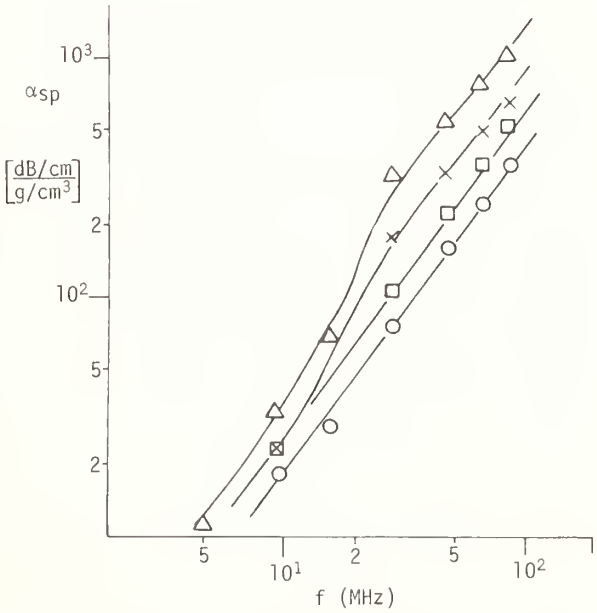

Fig. 7. Specific absorption for normal (o) and fixed (□,×,△) bovine erythrocytes in aqueous suspension at 25 °C. Acrolein concentrations in the original fixing solutions were 0.3, 1.0 and 2 g/100 cm^3. Cells were washed free of excess acrolein before measurement [21].

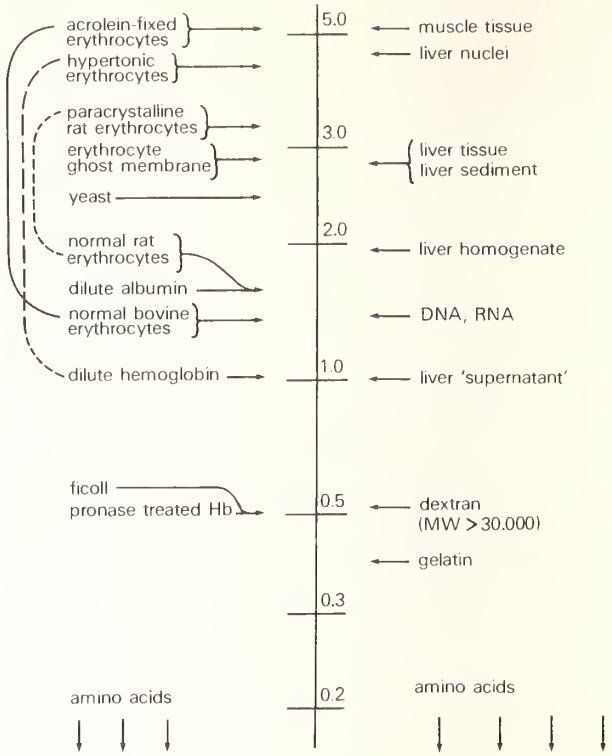

Fig. 8. Comparison of specific absorptions of biological materials using dilute hemoglobin as a reference. All data are for 10 MHz at 25 °C [18].

4. Relaxation Absorption

When stress-strain relationships for a medium depend upon shifts in chemical or structural equilibria, it is possible that a sound wave propagated in the medium will experience relaxation absorption. Specifically, the absorption per wavelength is [22,23].

$$\alpha\lambda = \pi \frac{c^2}{c_s^2}\left(1 - \frac{c_s^2}{c_\infty^2}\right)\frac{\omega\tau}{1 + (\omega\tau)^2} \qquad (1)$$

where τ is the relaxation time of the internal system and c, c_s, c_∞ are the phase velocity, and the low and high frequency limits of the velocity respectively. As implied by the equation, the magnitudes of the absorption and the dispersion in the velocity are related. The relation has been tested quantitatively for hemoglobin [11]. The results are consistent with the hypothesis that a relaxation mechanism is responsible for the absorption [24]. The first velocity dispersion measurements reported for tissues support the hypothesis that relaxation absorption is involved in these materials as well as in macromolecular solutions.[2]

[2]To a very rough approximation we can write [11] $\alpha\lambda \approx (f/c)(\Delta c/\Delta f)$. Kremkau [12] reports for brain values of $\alpha\lambda \approx 0.015$, in agreement with figure 1, and velocity dispersion of around 1 m/s/MHz near 1 MHz.

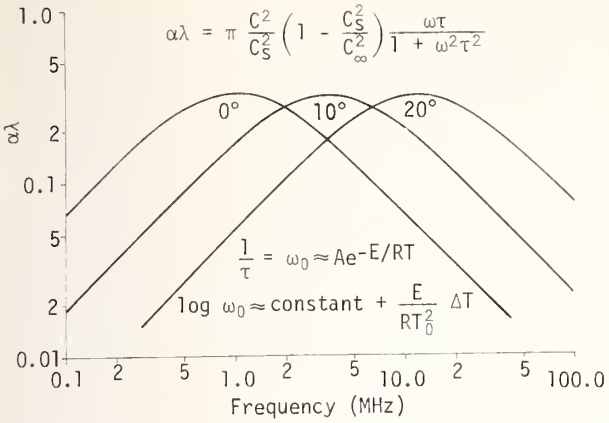

Fig. 9. Relaxation absorption. Log $(\alpha\lambda)$ vs. log frequency is plotted for three temperatues under assumptions discussed in the text. In this example, the activation energy is 20 kcal/mol. The value for $(\alpha\lambda)_{max}$ for the illustration is arbitrary. With this model, the $(\alpha\lambda)$ curves simply shift to the right, with log ω_0 proportional to the increment in temperature.

The frequency dependence of $(\alpha\lambda)$ given by eq. (1) is shown in figure 9. For certain simple reactions which may be perturbed by the sound wave, we may write [25]

$$\frac{1}{\tau} = \omega_0 \approx A\, e^{-E/RT} \qquad (2)$$

where E is the activation energy of the dominant rate process in the internal system, T the absolute temperature, A and R are constants. If a reference temperature T_0 is chosen so that $T = T_0 + \Delta T$, we can write

$$\log \omega_0 \approx \text{constant} + \frac{E}{RT_0^2}\Delta T \ . \qquad (3)$$

The general behavior predicted by figure 9 is seen in a variety of simple systems i.e. the curves of log $(\alpha\lambda)$ vs. log f shift to the right in increments proportional to the change in temperature. This is illustrated with $MnSO_4$ solutions in figure 10 [26]. The temperature coefficient of the absorption is negative if observations are carried out somewhat below the relaxation frequencies, while it is positive at high frequencies. Figure 11 shows the temperature dependence of $(\alpha\lambda)$ for relaxation absorption with activation energies of 20 and 50 cal/mol. As an example, data for lecithin vesicles at 1 MHz are shown [27].

Few biological materials can be characterized by a single relaxation process. Rather, in most cases there appear to be broad distributions of relaxation frequencies, in the case of hemoglobin, for example, extending from below 0.1 MHz to beyond 100 MHz (fig. 1). From our first order model, we would anticipate that increasing temperature would simply shift the curve of log $(\alpha\lambda)$ vs. log f to higher frequencies. Where the slope of this curve is slightly positive this leads to small negative temperature coefficients

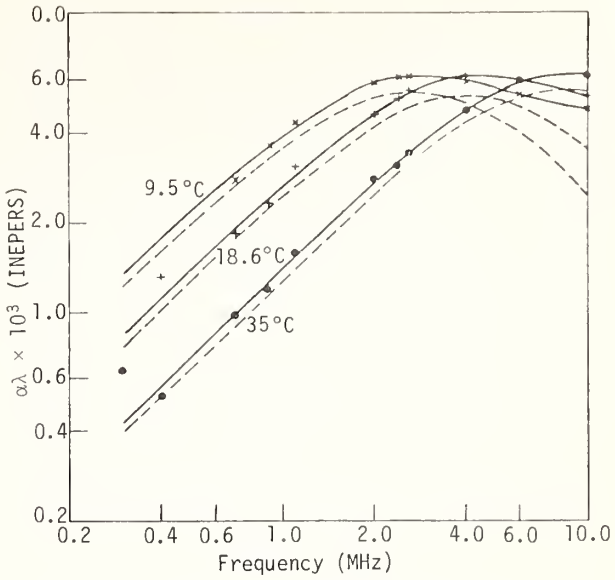

Fig. 10. Absorption of sound in 0.5 molar $MnSO_4$ solutions in water. Dashed curves represent the contribution of the low frequency relaxation to the absorption [26].

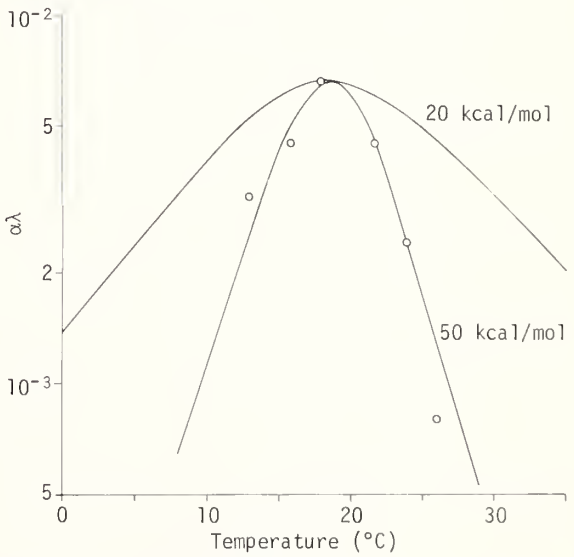

Fig. 11. Relaxation absorption. Log $(\alpha\lambda)$ vs. temperature is plotted for activation energies of 20 and 50 kcal/mol. As an example, data (o) for lecithin vessicles [27] are shown.

for the absorption. Brain [12], blood [11], and heart muscle [10] (fig. 12) appear to have this characteristic. The absorption per wavelength in bone, as reported by Kishimoto [13] decreases with frequency (fig. 13). As anticipated, this leads to a positive temperature coefficient for the absorption. In all of these materials, the activation energies are of the order of a few thousand kilocalories per mole.

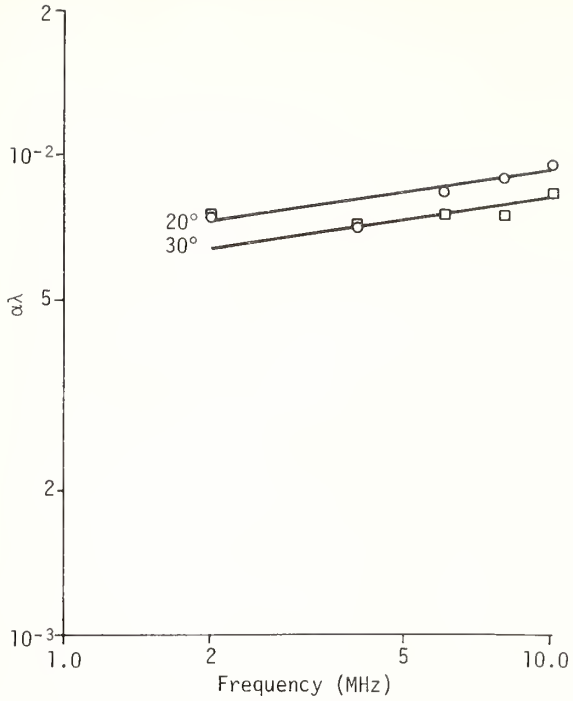

Fig. 12. Absorption of sound by myocardium [10]. The data illustrate the pairing of a positive slope in log (αλ) vs. log frequency with a negative temperature coefficient for the absorption.

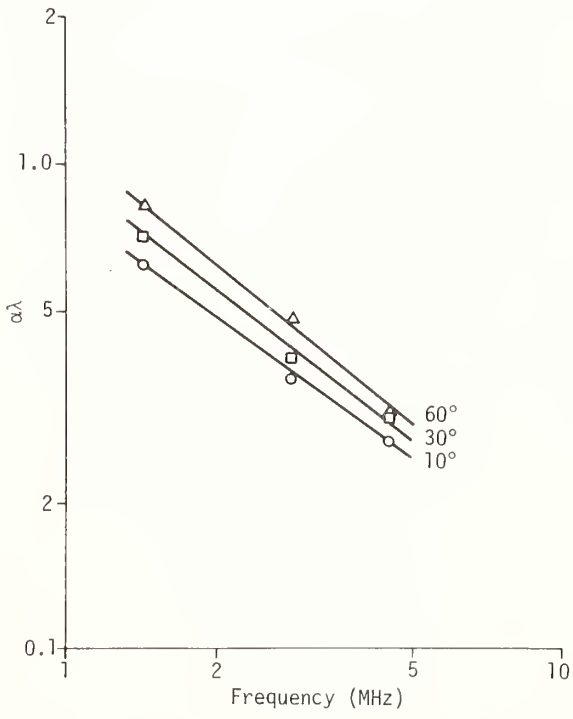

Fig. 13. Absorption of sound by bone [13]. In this case the slope in log (αλ) vs. log frequency is negative and the temperature coefficient of the absorption is positive.

The in vivo data for mouse spinal cord [14] are unique among the limited sample of tissues for which temperature dependence of absorption has been studied (fig. 14). In contrast with other tissues which appear to have many relaxation frequencies, mouse spinal cord at 2 °C shows a frequency dependence of (αλ) which is too strong to be explained even by a single relaxation frequency. In addition, the shape of the log (αλ) vs. log f curve changes with temperature. Because of these unusual properties, mouse spinal cord appears to be a particular candidate for further study. Since temperature studies may provide general information about the properties of internal relaxing systems and in a sense extend the range of frequencies observed, it would be desirable to have this information for a broad range of tissues.

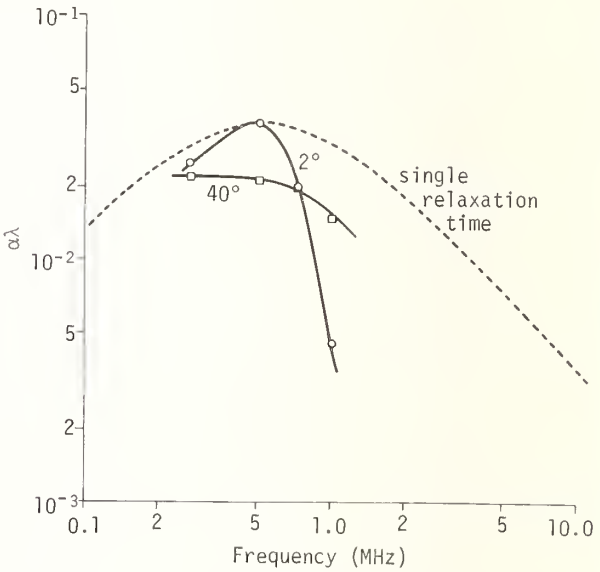

Fig. 14. Absorption of sound by mouse spinal cord [14]. It appears the observations at 2 °C cannot be explained by relaxation mechanisms.

Identification of the specific chemical or structural reactions which are responsible for relaxation absorption in tissues remains the pristine challenge of this field of study. Although some effort has been given to this problem, we must admit almost complete ignorance of the nature of tissue relaxation mechanisms at a meaningful, basic level.

5. Microscopically Inhomogeneous Materials

Although the absorption of sound in blood occurs primarily at the macromolecular level, a significant, measurable, contribution at frequencies below 10 MHz arises from the presence of intact red cells in suspension (fig. 2). Scattering, viscous relative motion, and thermal absorption have been considered as possible mechanisms for this excess loss [17,28-34]. Classical scattering is ruled out on qualitative and quantitative grounds. Relative motion absorption occurs when, because of density differences between suspended particle and suspending medium,

there is relative motion between the two phases with a consequent viscous loss. A comparison of observed, excess, non-protein absorption for suspensions of red cells in physiological saline with that predicted by theory for relative motion absorption is shown in figure 15 [17].

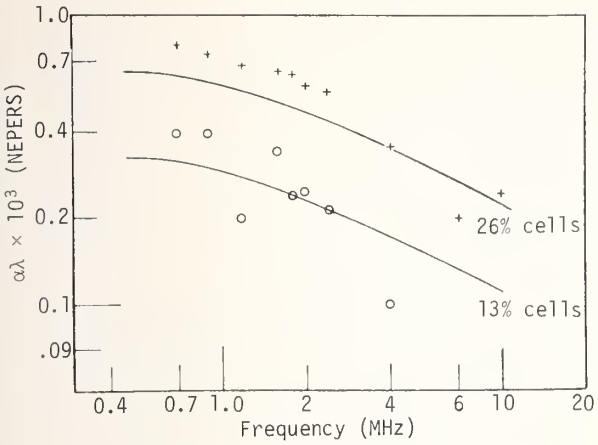

Fig. 15. Comparison of non-hemoglobin absorption in suspensions of red cells in saline with that predicted by relative motion absorption (solid curves). Points are taken from the data in figure 2 and reference [17].

Thermal absorption arises when thermal expansion coefficients and specific heats of particles and the suspending medium differ significantly thus leading to irreversible heat flow between the two phases. If extreme assumptions are made for the thermal properties of blood cells, the predicted thermal asborption is almost as large as that predicted for viscous relative motion [33]. Definitive experiments to compare contributions from the two mechanisms have not been attempted. Present evidence, however, points to relative motion as the dominant process. The suggestion that relative motion may be important in the solid tissues [31,34] remains to be tested.

Acknowledgments

The author wishes to acknowledge the contribution of Dr. Robert Weed for the use of the electron micrograph of a paracrystalline red cell.

This review and much of the research reported has been supported in part by U.S.P.H.S. Grant GM09933.

References

[1] Pohlman, R., Ueber die Absorption des Ultraschalls im menschlichen Gewebe und ihre Abhaengigkeit von der Frequenz, Physik. Z. 40, 159-161 (1939).

[2] Johnston, R. L., Goss, S. A., Maynard, V., Brady, J. K., Frizzell, L. A., O'Brien, W. D., Jr., and Dunn, F., Elements of Tissue Characterization. Part I. Ultrasonic Propagation Properties (this publication, p. 19).

[3] Edmonds, P. D., Bauld, T. J., III, Dyro, J. F., and Hussey, M., Ultrasonic absorption of hemoglobin solutions, Biochim. et Biophys. Acta 200, 174-177 (1969).

[4] Lemons, R. A. and Quate, C. F., Acoustic microscopy: biomedical applications, Science 188, 905-911 (1975).

[5] Marcus, P. W. and Carstensen, E. L., Problems with absorption measurements of inhomogeneous solids, J. Acoust. Soc. Am. 58, 1134-1335 (1975).

[6] Busse, L. J., Miller, J. G., Yuhas, D. E., Mimbs, J. W., Weiss, A. N., and Sobel, B. E., Phase Cancellation Effects: A Source of Attenuation Artifact Eliminated by a CdS Acoustoelectric Receiver in Ultrasound in Medicine, D. White, ed, Vol. 3, pp. 1519-1535 (Plenum Press, New York, 1977).

[7] Hueter, T. F., Visco-Elastic Losses in Tissues in the Ultrasonic Range, Wright Air Development Center. Wright-Patterson AFB, Ohio, Tech. Rept. No. 57-706, ASTIA Doc. No. AD142171 (August, 1968).

[8] Carstensen, E. L., The Mechanism of the Absorption of Ultrasound in Biological Materials, IRE Trans. on Med. Electronics. ME7, 158-162 (1960).

[9] Frizzell, L. A. and Carstensen, E. L., Ultrasonic Heating of Tissues, University of Rochester, Department of Electrical Engineering Technical Report GM09933-20 (November, 1975).

[10] O'Donnell, M., Mimbs, J. W., Sobel, B. E., and Miller, J. G., Ultrasonic attenuation of myocardial tissue: dependence on time after excision and on temperature, J. Acoust. Soc. Am. (in press).

[11] Carstensen, E. L. and Schwan, H. P., Acoustic properties of hemoglobin solutions, J. Acoust. Soc. Am. 31, 305-311 (1959).

[12] Kremkau, F. W., McGraw, C. P., and Barnes, R. W., Acoustic Properties of Normal and Abnormal Human Brain (this publication, p. 81).

[13] Kishimoto, T., Ultrasonic absorption in bones, Acustica 8, 179-180 (1959).

[14] Dunn, F. and Brady, J. K., Ultrasonic absorption in biological media, Biofizika 18, 1063-1066 (1973); Biophysics 18, 1128-1132 (1974).

[15] Frizzell, L. A. and Carstensen, E. L., Shear properties of mammalian tissues at low megahertz frequencies, J. Acoust. Soc. Am. 60, 1409-1411 (1976).

[16] Pauly, H. and Schwan, H. P., Mechanism of absorption of ultrasound in liver tissue, J. Acoust. Soc. Am. 50, 692-699 (1971).

[17] Carstensen, E. L. and Schwan, H. P., Absorption of sound arising from the presence of intact cells in blood, J. Acoust. Soc. Am. 31, 185-189 (1959).

[18] Kremkau, F. W. and Carstensen, E. L., Macromolecular Interaction in Sound Absorption, Proc. of Workshop on Interaction of Ultrasound and Biological Tissues, Battelle Seattle Research Center, Food and Drug Administration, U.S. Dept. of Health Education and Welfare, Rockville, Maryland (1972), pp. 37-42.

[19] O'Brien, W. D. and Dunn, F., Ultrasonic examination of the hemoglobin dissociation process in aqueous solutions of guanidine hydrochloride, J. Acoust. Soc. Am. 50, 1213-1215 (1971).

[20] Ponder, E., The paracrystalline state of the rat red cell, J. Gen. Physiol. 29, 89-102 (1945).

[21] Kremkau, F. W. and Carstensen, E. L., Macromolecular interaction in the absorption of ultrasound in fixed erythrocytes, J. Acoust. Soc. Am. 53, 1448-1451 (1973).

[22] Kremkau, F. W. and Carstensen, E. L., Macromolecular Interaction in the Absorption of Ultrasound in Biological Material, University of Rochester, Department of Electrical Engineering Tech. Report, No. GM09933-18 (April, 1972).

[23] Markham, J. J., Beyer, R. T., and Lindsay, R. B., Absorption of sound in fluids, Rev. of Mod. Phys. 23, 353-411 (1951).

[24] Eigen, M. and deMaeyer, L., Relaxation Methods, in Technique of Organic Chemistry, A. Weissberger, ed., Vol. 8, Part II, pp. 895-1054 (Wiley, New York, 1963).

[25] Stuehr, J. and Yeager, E., The Propagation of Ultrasonic Waves in Electrolytic Solutions, in Physical Acoustics, W. P. Mason, ed., Vol. 2, Part A, pp. 351-462 (Academic Press, New York, 1965).

[26] Carstensen, E. L., Relaxation processes in aqueous solution of $MnSO_4$ and $CoSO_4$, J. Acoust. Soc. Am. 26, 862-864 (1954).

[27] Eggers, F. and Funck, T., Ultrasonic relaxation spectroscopy in liquids, Naturwissenschaften 63, 280-285 (1976).

[28] Epstein, P. S., On the Absorption of Sound Waves in Suspensions and Emulsions, Theodore von Karman Anniversary Volume, California Institute of Technology, Pasadena, California, 1941.

[29] Epstein, P. S. and Carhart, R. R., The absorption of sound in suspensions and emulsions. I. Water fog in air, J. Acoust. Soc. Am. 25, 553-565 (1953)

[30] Urick, R. J., The absorption of sound in suspensions of irregular particles, J. Acoust. Soc. Am. 20, 283-289 (1948).

[31] Fry, W. J., Mechanism of acoustic absorption in tissue, J. Acoust. Soc. Am. 24, 412-415 (1952).

[32] Allegra, J. B. and Hawley, S. A., Attenuation of sound in suspensions and emulsions: theory and experiments, J. Acoust. Soc. Am. 51, 1545-1564 (1972).

[33] Ahuja, A. J., Acoustical properties of blood: a look at the basic assumptions, Med. Phys. 1, 311 (1974).

[34] O'Donnell, M. and Miller, J. G., Mechanisms of Ultrasonic Attenuation in Soft Tissue (this publication, p. 37).

[35] Kessler, L. W., VHF ultrasonic attenuation in mammalian tissue, J. Acoust. Soc. Am. 53, 1759-1760 (1973).

[36] Hawley, S. A. and Dunn, F., Ultrasonic Absorption in Aqueous Solutions of Dextran, J. Chem. Phys. 50, 3523-3526 (1969).

Reprinted from *Ultrasonic Tissue Characterization II*, M. Linzer, ed., National Bureau of Standards, Spec. Publ. 525 (U.S. Government Printing Office, Washington, D.C., 1979).

MECHANISMS OF ULTRASONIC ATTENUATION IN SOFT TISSUE

M. O'Donnell and J. G. Miller

Laboratory for Ultrasonics
Department of Physics
Washington University
St. Louis, Missouri 63130, U.S.A.

Ultrasonic loss mechanisms which arise from the microscopically inhomogeneous nature of soft tissue are investigated over the frequency range ~ 1 to ~ 10 MHz. Contributions to the ultrasonic attenuation due to viscous relative motion losses and thermal losses are shown to exhibit an approximately linear dependence on frequency. Numerical estimates of the attenuation arising from these mechanisms are compared with the results of experiments for a representative substance in each of three attenuation categories: low (blood), medium (heart), and high (skin). Inhomogeneity losses can account for ~ 60 percent of the attenuation observed in heart and skin, and thus may contribute a non-negligible fraction to the attenuation observed in most soft tissue.

Key words: Inhomogeneities; inhomogenity thermal losses; mechanisms; viscous relative motion.

In efforts to account for the ultrasonic attenuation exhibited by soft tissue, two types of mechanisms have been considered: (1) structural or chemical relaxation of the macromolecular constituents [1-3][1], and (2) processes arising from the inhomogeneous nature of tissue, including scattering, viscous relative motion, and thermal losses [1,3-8]. In this paper we estimate the fraction of the total attenuation observed in the 1 to 10 MHz frequency range which is attributable to processes arising solely from the microscopically inhomogeneous nature of soft tissue, as opposed to that fraction presumed to arise from macromolecular relaxation processes.

We consider a model in which a longitudinal ultrasonic wave propagates through tissue which is viewed as a suspension of scatterers in a liquid medium (cytoplasm). For the sake of simplicity all scatterers are considered to be spherical in shape. At an interface between the medium and a scatterer, longitudinal, viscous, and thermal waves may be excited in the suspending medium due to the discontinuity of acoustic and thermal properties at the surface of the scatterer. Energy that is coupled into these waves is lost from the incident ultrasonic beam and thus contributes to the total attenuation that is observed.

For scatterers small compared to the wavelength of the incident wave the reradiated longitudinal wave corresponds to Rayleigh scattering. The effect contributes a term to the attenuation coefficient that varies as the fourth power of frequency and the third power of the scatterer radius for a fixed volume concentration of scatterers. The magnitude of Rayleigh scattering depends upon the square of the difference in adiabatic compressibilities of the scatterer and the suspending medium and upon the square of the difference in densities. The numerical value of the contribution due to Rayleigh scattering is several orders of magnitude lower than the observed attenuation coefficient of soft tissue in the frequency range 1 to 10 MHz [1,2].

Details of the scattering process for scatterers of dimensions which are not small compared to the ultrasonic wavelength are less well understood. (Specular reflections from objects much larger in size than the ultrasonic wavelength are explicitly excluded here.) The general features of the scattering problem indicate that the magnitude of scattering events depends primarily on the square of the differences in densities and compressibilities of the scatterer and the suspending medium. In soft tissue, scatterers of dimensions comparable to ultrasonic wavelengths in the 1 to 10 MHz range (i.e., scatterers of sizes ranging from 0.05 mm to 1 mm) exhibit densities and compressibilities very close to those of the suspending medium. Thus losses arising from these scattering events are expected to represent small contributions to the attenuation coefficient. Such scattering events, however, may be of central importance in scattering and reflection (i.e., 180° backscattering) experiments.

Viscous drag losses arise from the generation of a highly damped viscous wave in the suspending medium. The scatterers attempt to mirror the motion of the suspending medium to an extent determined by a function which depends upon the relative densities of the scat-

[1]Figures in brackets indicate literature references at the end of this paper.

terers and the medium, the ultrasonic frequency, and the viscosity of the medium [4,7]. For fixed frequency, viscosity, and volume concentration of scatterers, the contribution of viscous drag losses to the attenuation coefficient is predicted to rise, reach a maximum, and subsequently fall as a function of scatterer size. A similar rise, plateau, and fall is predicted if viscous relative motion losses are plotted as a function of frequency for fixed scatterer size. Contributions to the attenuation of ultrasound in tissue by viscous relative motion losses were considered by Fry [6], Carstensen and Schwan [1], and Kremkau, Carstensen, and Aldridge [3].

An additional contribution to the ultrasonic attenuation arises from the generation of a highly damped thermal wave at the surface of a scatterer. (Strictly speaking, the viscous drag and thermal effects are coupled, but the strength of this coupling is sufficiently small that it can be ignored [4].) The magnitude of the losses associated with the generation of the thermal wave depends upon frequency and upon the relative heat capacities, coefficients of thermal expansion, and thermal conductivities of the scatterers and suspending medium. At low frequencies the system is in an isothermal limit in which energy is reversibly exchanged between the carrier medium and a scatterer, which closely follow each other in temperature ("isothermal"), so that relatively little loss of energy occurs. At high frequencies the system is in an adiabatic limit in which temperature changes in the suspending medium occur so rapidly that they cannot be communicated to a scatterer. Thus little heat transfer occurs ("adiabatic") and relatively little energy is dissipated. Maximum energy is dissipated in the intermediate range of frequencies where the thermal response of the scatterers to the incident compressional ultrasonic wave lags sufficiently behind that of the suspending medium that substantial energy is dissipated. Thermal losses in inhomogeneous media have been considered by Epstein and Carhart [4], Allegra and Hawley [7], Kremkau, Carstensen, and Aldridge [3], and Ahuja [8].

In order to estimate the contribution to the observed attenuation arising from viscous and thermal effects, it is necessary to identify the relevant scatterers in biological specimens. In principle, all inhomogeneities contribute to the observed attenuation at any frequency. The physical arguments presented above, however, suggest that for a fixed range of frequencies only scatterers exhibiting specific physical properties that define the relatively narrow ranges over which either viscous or thermal losses are near maximum need be considered. Numerical computations discussed below indicate that for the range of scatterer dimensions which results in significant viscous relative motion losses or thermal losses, contributions to the attenuation coefficient exhibit an approximately linear dependence on frequency, i.e., log (attenuation) versus log (frequency) exhibits a slope of 0.8 to 1.2 over the frequency range 1 to 10 MHz. Therefore, the slope of the attenuation versus frequency curve over the range of 1 to 10 MHz (hereafter referred to as the slope of the attenuation) can serve as a useful index of ultrasonic properties. This conclusion, arrived at from theoretical considerations, is consistent with the results of experiments, which indicate an approximately linear dependence on frequency for the ultrasonic attenuation coefficient of soft tissue. The slope of the attenuation represents a desirable index since in transmission experiments it is less susceptible to errors associated with impedance discontinuities and may be less susceptible to errors resulting from phase cancellation effects than is the apparent attenuation coefficient.

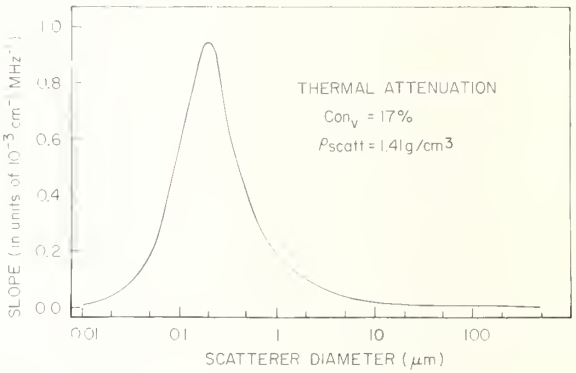

Fig. 1. Slope of the attenuation versus frequency curve over the range 1 to 10 MHz arising from thermal losses plotted as a function of scatterer diameter.

In figure 1 the contribution to the slope of the attenuation arising from thermal losses is plotted as a function of scatterer size. The physical properties of the scatterers and the suspending medium used in calculating the results shown in figure 1 appear in table 1 which is discussed below. As illustrated in figure 1, contributions from thermal losses are largest when the thermal wavelength λ_t of the suspending medium approximately equals 2 π times the radius of the scatterer. (λ_t is on the order of 0.4 to 1.3 μm in the frequency range 1 to 10 MHz.)

The slope of the attenuation which results from the coupling of energy into a viscous wave is plotted as a function of scatterer size in figure 2. As illustrated, viscous relative motion losses are largest when the viscous wavelength λ_v of the suspending medium approximately equals 2 π times the radius of the scatterers. (λ_v is the order of 1.8 to 5.5 μm in the 1 to 10 MHz frequency range.)

Our calculations indicate that viscous relative motion losses dominate thermal losses in the 1 to 10 MHz frequency range for a wide range of scatterer properties consistent with the microscopic anatomy of soft tissue. We thus focus on viscous relative motion losses in an attempt to identify specific physical properties that must be exhibited by the relevant scatterers. The numerical magnitude of the viscous relative motion term is approximately proportional to $(\rho'/\rho - 1)^2$, where ρ' is the density of the scatterer and ρ is the density of the suspending medium. Therefore, significant contributions to the observed attenuation result only from those scatterers which (1) exhibit sizes that maximize viscous relative mo-

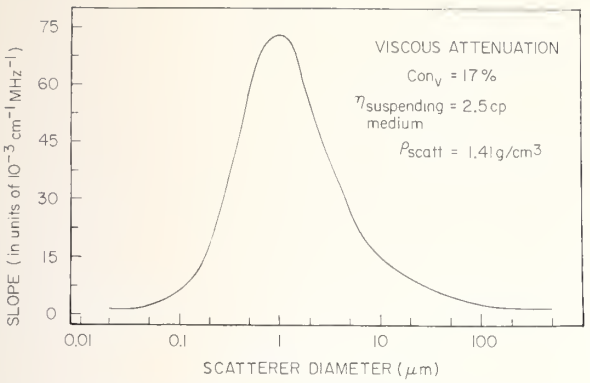

Fig. 2. Slope of the attenuation (1 to 10 MHz) arising from viscous relative motion losses plotted as a function of scatterer diameter.

tion losses, (2) have densities significantly different from that of the suspending medium, and (3) are present in sufficient concentrations. Aggregates of structural protein such as fibrils of collagen or muscle myofibrils appear to be the principal constituents of soft tissue which possess these properties. (Dunn and his colleagues have identified collagen as a significant determinant of the ultrasonic properties of soft tissue, in part because of its large compressional modulus and ubiquity [9,10].)

Limiting our attenuation to scatterers exhibiting the requisite physical properties, we estimate the contribution to the observed attenuation arising from microscopic inhomogeneities. Specific numerical values for the properties of the scatterers and the suspending medium which were used in our calculations are presented in table 1. An attempt has been made to estimate the contribution to the experimentally observed attenuation arising only from viscous and thermal effects for a representative substance in each of three attenuation categories: low (blood), medium (heart), and high (skin). Results of these calculations are summarized in table 2. Losses associated with viscous relative motion are seen to dominate thermal losses in the 1 to 10 MHz range, a feature which appears to be preserved over a wide range of scatterer properties.

The quantitative results presented in table 2 indicate that losses arising solely from microscopic inhomogeneities appear to account for a significant fraction ($\sim$ 60 percent) of the total observed attenuation of heart and skin. These results suggest that inhomogeneity losses may contribute a non-negligible fraction to the attenuation of most soft tissue. Although the exact magnitude of these losses is certain to be altered by the use of more realistic assumptions (e.g., non-spherical scatterers and improved estimates of the values of physical properties specified in table 1), the general conclusions of this study would not be altered if the illustrative numerical results presented in table 2 were in error by 30 percent.

Table 2. Slope of attentuation coefficient-vs-frequency ($cm^{-1}MHz^{-1}$)[a].

Tissue	Viscous	Thermal	Theoretical value[b]	Experimental value	Percent accounted for[c]
Blood (40% Hct)	0.003	0.000	0.003	0.031[d]	10
Heart	0.042	0.001	0.043	0.072[e]	60
Skin	0.101	0.001	0.102	0.170[f]	60

[a] Numerical results presented to 3 significant digits for illustrative purposes only.
[b] Sum of contributions from columns 2 and 3.
[c] Percent of experimentally observed values (column 5) accounted for by sum of contributions (column 4) arising from losses due to microscopic inhomogeneities.
[d] Carstensen, E. L., Li, K., and Schwan, H. P., J. Acoust. Soc. Am. 25, 286-289 (1953).
[e] O'Donnel, M., Mimbs, J. W., Sobel, B. E., and Miller J. G., Ultrasonic Attenuation in Normal and Ischemic Myocardium (this conference).
[f] Oussik, K. T., Kyriazidov, M., Fritch, O. J., and Sear, R. S., Am. J. Phys. Med. 37, 160 (1958).

Table 1. Acoustic and thermal properties of tissue scatterers (T = 20 °C).

Tissue	Scatterers	Size range[a] (μm)	Density (g/cm^3)	Volume concentration % of total volume	Thermal conductivity 10^{-3} cal/s-cm-°C	Coefficient of thermal expansion 10^{-4} deg^{-1}	Specific heat cal/g-°C
Blood (40% Hct)	Red cells	4.6 - 5.6[b]	1.09[b]	40[b]	1.1[b]	1.2[c]	0.8[b]
Heart	Muscle myofibrils	1.0 - 2.0[d]	1.32[d]	18[d]	0.4[c]	1.2[c]	0.4[c]
Skin	Collagen fibrils	0.7 - 1.5[e]	1.41[f]	25[g]	0.4[c]	1.2[c]	0.4[c]
Suspending[h] medium			1.03[b]		1.5[b]	1.4[i]	1.0[b]

[a] Uniform distribution of scatterers with diameters expressed in micrometers.
[b] Ahuja, A. S., Med. Phys. 1, 311-316 (1974).
[c] Estimated.
[d] Bailey, Kenneth, Proteins, H. Neurath and Kenneth Bailey, eds., Chapt. 4 (Academic Press, New York, 1954).
[e] Gross, Jerome, Scientific American, 120-130 (May 1961).
[f] Pomeroy, C. D. and Milton, R. J., J. Soc. Leather Trades Chem. 35, 360 (1951).
[g] Chupvil, M., Physiology of Connective Tissue (Butterworth, London, 1967).
[h] Viscosity (1 to 10 MHz) estimated to be 2.5 centipoise.
[i] Epstein, P. S. and Carhart, R. C., J. Acoust. Soc. Am. 25, 553 (1953).

Acknowledgment

This work was supported in part by grants HL19537, HL17646, and HL07081 from the National Institutes of Health.

Pranoat Suntharothok-Priesmeyer was responsible for production of the text and illustrations.

References

[1] Carstensen, E. L. and Schwan, H. P., Absorption of sound arising from the presence of intact cells in blood, J. Acoust. Soc. Am. 31, 185 (1959).

[2] Pauly, H. and Schwan, H. P., Mechanism of absorption of ultrasound in liver tissue, J. Acoust. Soc. Am. 50, 692 (1971).

[3] Kremkau, F. W., Carstensen, E. L., and Aldridge, W. G., Macromolecular interactions in the absorption of ultrasound in fixed erythrocytes, J. Acoust. Soc. Am. 53, 1448 (1973).

[4] Epstein, P. S. and Carhart, R. C., The absorption of sound in suspensions and emulsions. I. Water fog in air, J. Acoust. Soc. Am. 25, 553 (1953).

[5] Urick, R. J., The absorption of sound in suspensions of irregular particles, J. Acoust. Soc. Am. 20, 283 (1948).

[6] Fry, W. J., Mechanism of acoustic absorption in tissue, J. Acoust. Soc. Am. 24 412 (1952).

[7] Allegra, J. R. and Hawley, S. A., Attenuation of sound in suspensions and emulsions: theory and experiments, J. Acoust. Soc. Am. 51, 1545 (1972).

[8] Ahuja, A. J., Acoustical properties of blood: a look at the basic assumptions, Med. Phys. 1, 311 (1974).

[9] Fields, S. and Dunn, F., Correlation of echographic visualization of tissue with biological composition and physiological state, J. Acoust. Soc. Am. 54, 809 (1973).

[10] O'Brien, W. D. Jr., The Role of Collagen in Determining Ultrasonic Propagation Properties in Tissue, in Acoustical Holography, L. W. Kessler, ed., Vol. 7 (Plenum Press, New York, 1976).

CHAPTER 3

ATTENUATION AND VELOCITY II:

METHODOLOGY AND MEASUREMENTS

Reprinted from *Ultrasonic Tissue Characterization II*, M. Linzer, ed., National Bureau of Standards, Spec. Publ. 525 (U.S. Government Printing Office, Washington, D.C., 1979).

ELEMENTS OF TISSUE CHARACTERIZATION

Part II. Ultrasonic Propagation Parameter Measurements

S. A. Goss, R. L. Johnston, V. Maynard, L. Nider,
L. A. Frizzell, W. D. O'Brien, Jr., and F. Dunn

Bioacoustics Research Laboratory
University of Illinois
Urbana, Illinois 61801, U.S.A.

Methods employed at the Bioacoustics Research Laboratory of the University of Illinois for the determination of ultrasonic propagation properties of biological media are described, with attention devoted to attenuation, absorption and velocity measurements of both longitudinal and shear ultrasonic waves. These include systems specifically for the ultrasonic characterization of soft tissues and for solutions of biologically significant macromolecules. Each method is presented in terms of theory, limitations, applicability, and possible sources of error. Important new techniques from other laboratories are also discussed.

Key words: Ultrasonic absorption; ultrasonic attenuation; ultrasonic instrumentation; ultrasonic measurements; ultrasonic spectroscopy; ultrasonic tissue characterization; ultrasonic tissue parameters; ultrasonic tissue signature; ultrasonic velocity.

1. Introduction

A number of measuring techniques have been developed, or are otherwise employed, at the Bioacoustics Research Laboratory of the University of Illinois in the research efforts associated with the propagation characteristics of ultrasound in biological tissue, and toward a basic understanding of the mechanism(s) responsible for the acoustic properties exhibited by those tissues. These include specialized systems for biological liquids and for soft tissues which are capable of measuring attenuation, absorption, and velocity of longitudinal ultrasonic waves as functions of frequency, temperature and, where appropriate, pH and ambient pressure. In addition, a system is presently being developed to measure the shear acoustical properties of biological materials as a function of frequency and temperature. These techniques, thirteen in all, are described in this paper in terms of parameters measured, theory, application, precision/accuracy, frequency, and temperature range, so that each technique may be assessed separately.

2. Attenuation and Velocity Measurements in Soft Tissue

Attenuation of longitudinal waves in soft tissue specimens are determined using the radiation force, pulse transmission, and standing wave techniques. Velocity measurements in soft tissues can be made by observing the time of flight of an acoustic pulse through a known path length of a tissue sample, and by acoustic interferometry.

A. Attenuation: Radiation Force Method

The phenomenon of radiation force provides a primary method for the measurement of the second order quantities of intensity and power [1-4][1]. Radiation force is a direct result of energy transport by the sound wave, and is equal to the time rate of change of momentum of the wave. Thus a continuous wave incident on a reflecting or absorbing object will produce a time independent force on that object equal to, and in the direction of, the time rate of change of momentum. Consequently, a sensitive balance can be employed to measure the radiation force exerted by an ultrasonic beam incident on a suspended target. It then follows that force, measured as a change in tension of the suspending wire, on a perfectly absorbing target intercepting a vertically directed sound beam is

$$F = \frac{P}{c} \qquad (1)$$

where F is the measured change in tension of the suspending wire, P is the time average power intercepted by the target, and c is the velocity of propagation. Thus, in water, 1 milliwatt of incident power will exert a force equivalent to a weight of 67 μg, which is measured as an apparent target weight change. Similarly, a perfectly reflecting target intercepting a vertically directed sound beam will produce a measurable change in suspension tension, given as

[1]Figures in brackets indicate literature references at the end of this paper.

$$F = \frac{2P}{c} \cos^2\theta \qquad (2)$$

where θ is the angle between the beam axis and the normal to the target surface. Consequently in water, when the target is inclined 45° to the vertical, the sensitivity of the balance is again 67 μg/mW of intercepted power. Thus, a phase insensitive, frequency independent technique for power and intensity attenuation measurements becomes available by interposing a tissue sample between the sound source and the sound intercepting target, by determining that power lost or redirected with the tissue sample in place compared with measured power with the tissue absent [2,5,6]. Care must be taken to insure that the system's sensitivity is actually that that predicted for such idealized cases. The attenuation present in the liquid media (water or physiological saline) will inevitably cause acoustic streaming which will lead to systematic errors in the power estimation. The streaming effect can be minimized by positioning an acoustically transparent barrier of, for example, stretched polyethylene, directly in front of the target.

A second possible source of error is due to the inherent insensitivity of the measurement system to horizontal forces. For maximum accuracy, the main lobe of the sound beam should be directed precisely vertically. Because the beam may contain components of momentum in the plane perpendicular to the main lobe, the radiation force balance method does not respond to all the energy emitted by the source. As the temperature of the target increases due to the fact that energy is being deposited in it, thermal expansion of the target can introduce an error by virtue of increasing its buoyancy and resulting in an apparent target weight change. The ultimate accuracy of the radiation force balance method is limited by noise associated with mechanical vibrations and atmospheric perturbations, which can be reduced by proper design considerations. However, in the presence of pressure gradients, the target is acted on by forces proportional to the target volume, making a small target advantageous.

B. Attenuation: Pulse Transmission Method

The pulse transmission technique is applicable to measurements of sound pressure attenuation in various types of biological specimens [7,8]. The instrumentation consists of a transmitting ultrasonic transducer immersed in a bath (usually physiological saline) which serves as the acoustic coupling medium and aligned axially with either a reflecting surface or a receiving transducer. The associated electronic instrumentation provides an RF pulse to the transmitting crystal and also triggers the sweep of an oscilloscope a variable, but selected, length of time after the initiation of the transmitting pulse. An oscilloscope serves to display the amplified received signal. Measurement of sound attenuation can be performed as follows. First, with no sample in the ultrasonic path, the gain of the receiving amplifier is adjusted to give a signal display of a predetermined amplitude. Then, with the specimen in place, the gain of the system is adjusted, either by increasing the receiving amplifier gain or by removing electrical attenuation in the signal path, to compensate for the loss of acoustic energy in the sample to bring the display trace to the same preselected amplitude. The attenuation measurement is repeated for other samples of the same material, but of varying thicknesses. The measured attenuation values are then plotted versus sample thickness, and the slope of the resulting straight line yields the attenuation per unit length of the specimen.

C. Velocity: Pulse Transit Time Method

Velocity measurements in tissue can be made simply by measuring the time of flight of an acoustic pulse over a known path length of the specimen [9,10]. Differential techniques should be used to minimize uncertainties in path length and time delay measurements, such as the uncertainty of the actual location of the active face of the transducer. If commercial transducers are employed, additional allowances must be made for the quarter-wave impedance matching layer on their surface. Errors may be encountered in time of flight measurements of the acoustic signal in inhomogeneous media, such as tissues. Since a short duration acoustic pulse contains a broad spectrum of components, the frequency dependent effects of velocity dispersion, attenuation, and multiple phase shifts at tissue interfaces, can distort and delay the signal [11]. Techniques which rely on the detection of the leading edge of the received acoustic pulse for timing are prone to the greatest inaccuracies under such distortions.

D. Velocity: Acoustic Interferometric Method

Nearly an order of magnitude improvement in accuracy can be realized by the use of acoustic interferometric techniques employing CW excitation [12,13]. By sandwiching the tissue sample between transmitting and receiving transducers, or between a transducer and a reflecting target, a standing wave is created in the tissue sample. It has been shown that tissue may be distorted in this manner up to 25 percent without affecting the measured velocity [12]. By monitoring the maxima and minima of the received acoustic signal as the path length is changed, the standing wave pattern and the wavelength of sound in the tissue can be measured. This information combined with the frequency employed for the measurement yields the velocity of sound in the sample. Alternatively, the path length may be held fixed and the frequency of excitation changed. The change in frequency necessary to move from one mode in the standing-wave pattern to the next is directly proportional to velocity. The accuracy of such interferometric techniques, under tight temperature control, can reach about 0.1 percent.

E. Attenuation and Velocity: Standing Wave Method

While the measuring techniques described above may be applied to the measurement of the ultrasonic absorption and velocity of most biological tissues, some specimens require specialized techniques.

Lung, by virtue of its extraordinarily high attenuation, presents some problems in determination of its ultrasonic propagation properties. The following method has been developed and yields results in agreement with other similar ones [8].

Briefly, the lung is suspended in the sound field between the sound source and an absorption chamber, to eliminate standing waves beyond the lung. The transient thermoelectric probe [14] provides a convenient acoustic detector to investigate (A) the acoustic field between the specimen and the source, to determine the axial standing wave pattern, and (B) the acoustic field between the specimen and the absorption chamber, to determine the wave amplitude transmitted beyond the lung specimen 15 (see fig. 1). Probing the field in A yields the fraction of incident energy reflected at the lung-saline interface. Assuming that infinitesimal wave acoustics prevails and that the attenuation in the lung is sufficiently great that multiple reflections within the specimen need not be considered, the speed of sound in the lung can be obtained from

$$(\rho v)_{lung} = (\rho v)_{saline}\left(\frac{1}{SWR}\right) \qquad (3)$$

where the ρ's are the known densities and SWR is the observed standing wave ratio (between the source and specimen) and is greater than unity. The attenuation coefficient per unit path length is determined from a knowledge of the energy reflected at the two lung-saline interfaces, the thickness of the sample, and the acoustic intensity detected by the probe in B in accordance with the relation

$$I_1 = I_0 e^{-2\alpha l} \qquad (4)$$

where I_0 and I_1 are, respectively, the acoustic intensities at the lung-saline interface nearest to and farthest from the source, l is the thickness of the sample, and α is the attenuation coefficient.

3. Absorption Measurements in Soft Tissue

The transient thermoelectric method is well suited for determining acoustic absorption in small volumes of highly absorbing liquid or tissue *in vivo* as well as *in vitro*, and may be the only method, applicable to tissues, that measures directly absorption rather than attenuation. As such it is invaluable in determining the portion of attenuation due to absorption *vis-a-vis* that portion due to scattering effects [16,17]. The method requires that a thermocouple junction of small diameter relative to the wavelength be implanted in the sample. The thermocouple and surrounding sample are then exposed to a plane traveling wave ultrasonic field having a temporally rectangular envelope of known intensity. The typical thermoelectric emf response to a 1 second ultrasonic pulse has an initial fast rise which results from conversion of acoustic energy into heat by the viscous forces acting between the thermocouple wire and the sample. This portion of the response approaches equilibrium very quickly with a magnitude that depends mainly upon the thermocouple wire radius, the viscous properties of the sample medium, the sound intensity, and the frequency. The fast rise is followed by a relatively linear rise (in the absence of thermal conduction processes) that is a result of absorption of the ultrasound in the surrounding medium. From a determination of the slope of the *linear* portion of the thermoelectric emf response as a function of time, the absorption coefficient can be calculated using the following relation,

$$\alpha = \frac{\rho C_p K}{2I}\left(\frac{dT}{dt}\right)_0 \qquad (5)$$

where α is the absorption coefficient (cm^{-1}), ρ is the density (g/cm^3), C_p is the specific heat at constant pressure (cal/°C g), K is the mechanical equivalent of heat (4.18 J/cal), I is the acoustic intensity (W/cm^2), and $(dT/dt)_0$ is the initial time rate of change of temperature due to absorption in the medium (°C/s). Effects limiting the

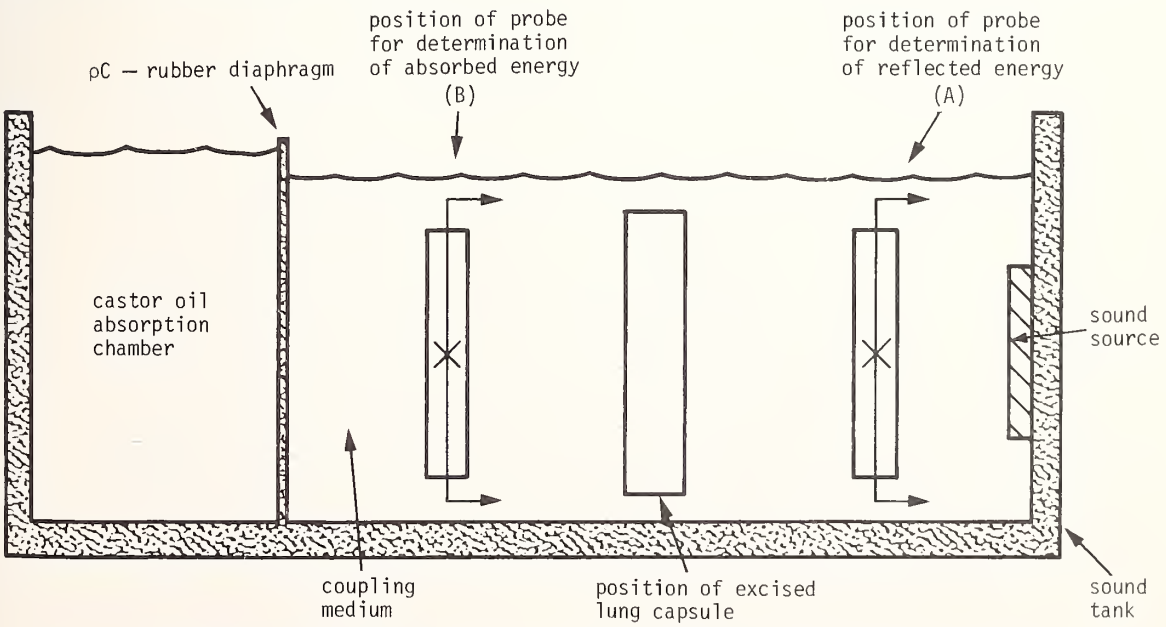

Fig. 1. Schematic diagram of the experimental arrangement for attenuation and velocity measurements in lung using the standing wave method [15].

accuracy of the method include any changes of the thermal properties of the tissue and/or the absorption itself with temperature. Provided the temperature rise during measurement is on the order of one degree or less these effects will be minimal. Dunn [18] has indicated that the total uncertainty in the determination of $(dT/dt)_0$ is of the order of 5 to 10 percent. In application of the transient thermoelectric method the initial value of α is determined by using the ultrasonic intensity that would be present at the site of the junction were the sample absent. The measured depth of the thermocouple and the initial value of α are then used to calculate intensity at the site of the junction by correcting for absorption using an iterative method [18] until the value of α converges (note that if the value of α and/or the depth of the thermocouple are too large, the value of α will not converge).

This technique has been used at frequencies as low as 0.26 MHz [19] and as high as 7 MHz [20] in tissues, but modifications have been used to 2 GHz in fluid media [21]. The lower frequency limit is determined by the value of the absorption, since too low an α yields too low a temperature rise to be detected accurately without having to increase the exposing intensity to unacceptable levels. Also, at low frequencies and absorptions the initial viscous heating portion of the transient thermal emf may become a major portion of the signal, making the subtraction process a relatively erroneous one. At higher frequencies the limitations on accuracy of the method, as described for tissues, are imposed by (1) availability of broad plane wave ultrasonic fields, (2) the size of the thermocouple relative to the wavelength so that the field is affected by scattering from the wire and thermal conduction along it, and ultimately by (3) nonconvergence in the iterative method of depth correction due to high absorption. The latter two limiting effects have not yet been troublesome in the region of application. The method has been found to be very useful and easily applied to most tissues over the frequency range from 0.5 to 4.0 MHz.

4. Absorption and Velocity Measurement in Biological Liquids

The primary mechanism(s) for the absorption of sound in biological material seems to occur at the macromolecular level. Carstensen, Li, and Schwan [22] discovered that the acoustical properties of blood are determined largely by the protein content, and that the absorption coefficient is directly proportional to the protein concentration, whether in solution or within the cell. Pauly and Schwan [23] have demonstrated that nearly two-thirds of the ultrasonic absorption of beef liver lies at the macromolecular level, with the remaining one-third due to structural features of the tissue. Since the primary mechanism for the absorption of sound in tissue seems to occur at the macromolecular level, it has been instructive to investigate the acoustic properties of simpler systems of macromolecules, such as solutions of biopolymers, with the hope that such studies may provide details applicable to the more complex systems.

Three measurement systems have been used at the Bioacoustics Research Laboratory to study acoustic absorption and velocity of solutions and suspensions of biomacromolecules as functions of molecular characteristics, pH, temperature, concentration, and frequency to aid in the elucidation of the mechanisms of interaction between ultrasound and biological tissues.

A. Absorption: High Frequency Method (5 MHz to 200 MHz)

The high frequency system applies pulsed ultrasound to solutions for the purpose of measuring absorption and velocity [24-26]. Two advantages of pulsed ultrasound are that heating effects and standing waves are virtually eliminated. Heating is proportional to the mean power. Using a 10 μs pulse at a repetition frequency of 300 pps results in a signal which is present for only 0.3 percent of the time. Thus the average intensity is much less than the peak intensity, and produces a negligible temperature rise. Since the signal is on for such a small fraction of the time, standing waves are not produced. The basic technique was first described by Pellam and Galt in 1946 [27]. Two transducers, arranged coaxially face each other at opposite ends of a cylindrical tank. The receiving transducer has its position fixed while the sending transducer moves toward or away from it at a constant speed. Assuming the relation governing the process is

$$p(x) = p(o)\, e^{-\alpha x} \qquad (6)$$

where $p(x)$ is the wave pressure amplitude at the distance x from the transmitting transducer, $p(o)$ is the pressure amplitude at $x = o$ (i.e., at the face of the transmitting transducer), and α is the absorption coefficient, the natural logarithm of the ultrasonic pressure amplitude is proportional to the signal path length. The proportionality constant, i.e., the absorption coefficient, can be found by monitoring the pressure as a function of intertransducer distance. A block diagram of the system is shown in figure 2. A pulsed rf signal is amplified, passed through a variable

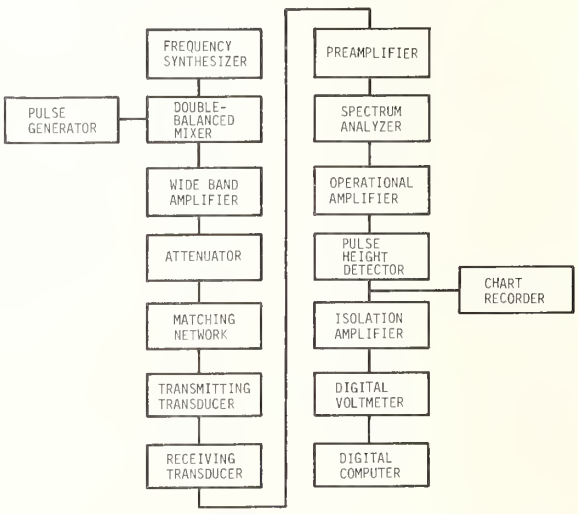

Fig. 2. Block diagram of instrumentation used for high frequency (5 to 200 MHz) ultrasonic absorption measurements in biological liquids.

attenuator, and impedance-matched to the sending transducer. Both transducers are air backed, gold-on-nickel plated X-cut quartz with a fundamental resonant frequency of, for example, 3 MHz, and operated at their odd harmonics. The wave passes through the liquid, where it is attenuated, and impinges upon the receiving transducer. Some of the ultrasound is then reconverted into an electric signal, while the remainder is reflected back through the liquid. A pulse height monitor continually detects the voltage peak of the primary signal (which is linearly proportional to p(x)) as the transducers are moved toward, or away from each other, and converts it to its natural logarithmic value. An on-line computer samples the output of the pulse height detector (a dc voltage proportional to the pulse height) via a digital voltmeter, calculates the attenuation coefficient, and corrects for diffraction effects by the method of Del Grosso [28] yielding the true absorption coefficient. Solute absorption is obtained by subtracting results of a solvent measurement from a solution measurement. Approximately one liter of sample is required for this technique, with measurement error in absorption of about 5 percent over the approximate frequency range 3 to 200 MHz. Greater errors occur in low absorbing liquids at low frequencies and are mainly due to relatively large diffraction effects.

B. Velocity: High Frequency Method

The acoustic velocity can be determined in the high frequency system to within 0.1 percent by measuring the period of the wave in the liquid. This is accomplished by superimposing a reference signal on the received signal, which results in an interference pattern. If the acoustic path length is changed at a constant rate, V_p, the period of this pattern is $T = (\lambda/V_p)$ where λ is the acoustic wavelength. Since $\lambda \doteq c/f$, where f is the excitation frequency, the acoustic velocity is given as $c = TfV_p$. The period T is measured using a time interval counter to determine the time required for the interference signal to go through a greater number (100) of maxima.

C. Absorption: Low Frequency Method (0.3 MHz to 20 MHz)

In the frequency range of 0.3 to 20 MHz, a pulse technique developed by Schwan and Carstensen [29] is employed in order to avoid having to make unreasonable corrections for effects of diffraction phenomena. A sending and a receiving transducer face each other; the former is in the reference liquid and the latter in the test liquid (see fig. 3). An acoustic window separates the two liquids. The distance between the transducers remains constant while the entire transducer ensemble is moved horizontally at a constant speed from a position such that the acoustic path is primarily in the test liquid to a position such that it is primarily in the reference liquid. The reference liquid is chosen to be dispersionless and acoustically well characterized with a sound velocity as near to that of the unknown as possible. Water is an appropriate choice for dilute aqueous solutions. Since the path length is constant, diffraction effects, due to the inequality of the velocities in the two liquids, are corrected by a computer using the method of Del Grosso [28]. Liquid volumes of 1 to 4 liters are used in each chamber, depending upon frequency. As with the high frequency system, measurement error ranges from 2 to 10 percent. The pressure amplitude in the receiving transducer is given by

$$p_r = p_s e^{-\alpha w(d-x)} e^{-\alpha_x x} \qquad (7)$$

where p_s is the pressure amplitude at the sending transducer, and the other symbols are described by figure 3. This equation can be rewritten as

$$\ln p_r = \ln p_s - \alpha_w d + (\alpha_w - \alpha_x)x \qquad (8)$$

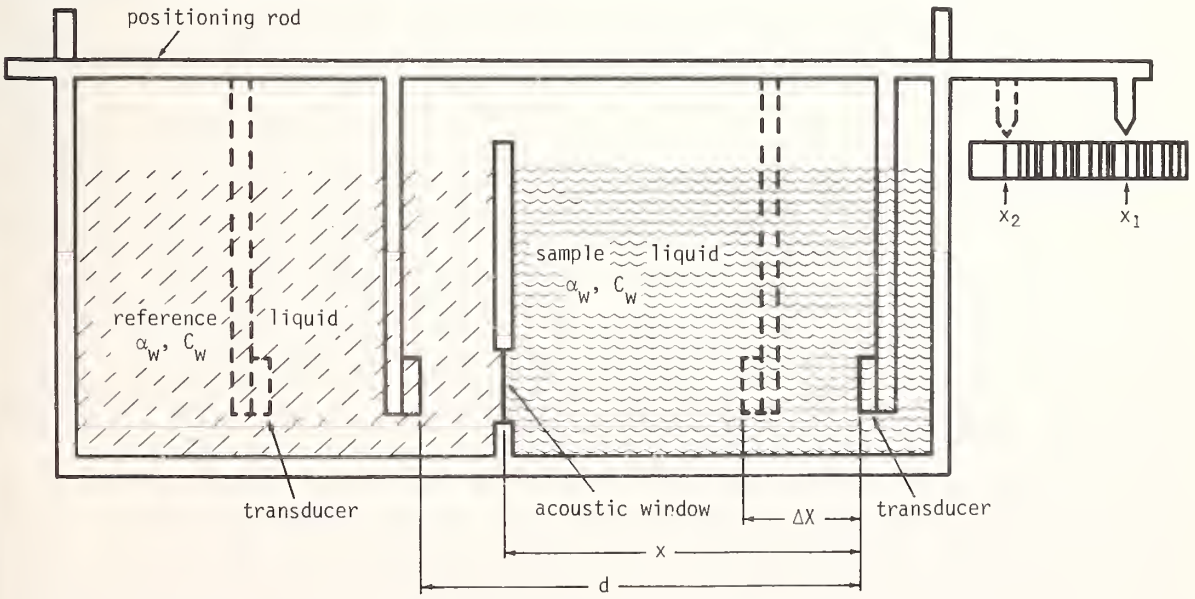

Figure 3. Schematic diagram of apparatus used for ultrasonic absorption and velocity measurements at low frequencies (0.3 MHz to 20 MHz) in biological liquids [24].

and α_x can be obtained graphically from the slope since α_w is known.

As the acoustic window (polyethylene) reflects a negligible, but constant amount of the acoustic energy, it will affect the results only by changing the intercept, i.e., the slope is not affected. Signal processing to obtain the desired absorption coefficient closely resembles that used in the high frequency system, described above [14,24].

D. Velocity: Low Frequency Method

Velocity of the acoustic wave can be determined with the low frequency system to 0.01 percent [30] by superimposing the received and reference signals in the same fashion as was done for the high frequency system. If the velocities in the test and reference liquids are different, moving the transducer assembly will change the acoustic path length. By observing the interference pattern on the oscilloscope, one can position the transducers such that a maximum occurs. If this is position 1 in figure 3, the number n, of acoustic wave lengths between the transducers is given by

$$n = \frac{d - x}{\lambda_w} + \frac{x}{\lambda_x} \qquad (9)$$

If the transducers are moved a distance, Δx, such that the interference pattern undergoes an integral number, m, of 2π phase shifts, the above expression becomes

$$n \pm m = \frac{d - x + \Delta x}{\lambda_w} + \frac{x - \Delta x}{\lambda_x} \qquad (10)$$

where the positive sign applies when the velocity in the test liquid is larger than that of the reference liquid, as is usually the case. Eliminating n between these equations, expressing wavelengths in terms of velocity and frequency, and a rearranging of terms yields

$$c_x = \frac{c_w}{1 \pm \frac{c_w m}{f \Delta x}} \qquad (11)$$

Note that some other procedure must be performed to determine the correct sign.

E. Absorption and Velocity Measurements in Small Liquid Volumes: Resonant Cavity Method

The various methods for determining the acoustic propagation properties of liquids discussed thus far were devised with little consideration for the volume of material necessary for measurement. The minimum volume required in the high frequency system is 500 ml, with greater volumes generally required at lower frequencies to avoid effects due to diffraction phenomena. The necessity for having such large volumes available becomes a serious problem when biological macromolecules are to be treated in solutions (usually in concentrations of 10 percent by weight), since only a few can be examined within the bounds of reasonable economics. It is possible to reduce the specimen volume to less than 50 ml using a resonance technique originally developed by Eggers [31], which employs two X-cut quartz disks, with a fundamental frequency of the order of 2 MHz, separated by a lucite ring, and forming a cylindrical cavity in which the specimen solution is placed. One transducer serves as a transmitter, and the other a receiver. When the transmitting transducer is excited with a sinusoidal voltage, standing waves in the specimen solution result at particular frequencies f_n that obey the resonance equation

$$\rho_q c_q \tan \frac{\pi f_n}{f_q} = \rho_s c_s \begin{bmatrix} -\tan \\ \cot an \end{bmatrix} \frac{\pi}{2} \frac{f_n}{f_s} \qquad (12)$$

where ρ_q and c_q are the density and speed of sound in the quartz transducers, and ρ_s and c_s are the corresponding quantities in the solution. The fundamental frequency of the transducer is f_q, and of the liquid-filled cavity, f_s. At the resonant frequencies f_n, the receiving transducer registers pronounced voltage peaks, whose frequency separation depends on the sound velocity of the specimen solution, and the half-power (3 dB) bandwidth Δf of which is related to the attenuation per wavelength, $\alpha\lambda$. Eggers [31,32] has shown that the velocity of sound v_f in an unknown medium may be related to the velocity of sound in some reference medium v_r by the expression

$$\frac{v_f}{v_r} = \frac{D_f}{D_r} \left| \frac{1 + 2(D_f Z_f - D_r Z_r)}{f_q Z_q} \right| \qquad (13)$$

where Z_f and Z_r are respectively, the acoustic impedance of the unknown and reference medium, and D_f and D_r are the respective separations in frequency units between adjacent resonances for the liquid and reference media, and f_q and Z_q respectively, are the frequency of the quartz and its acoustic impedance. Equation 13 may be approximated by a simpler expression (with a difference of only a few parts per thousand) as

$$\frac{\delta c_f}{c_f} = \frac{\delta f_n}{f_n} \qquad (14)$$

where δc_f is the velocity difference between the unknown and reference media, δf_n is the difference between corresponding resonances, and c_f is the velocity of the reference medium at a frequency f_n. In general, velocity measurements are more difficult to perform than absorption measurements due to temperature drift and other instabilities of the unit. The attenuation of the specimen solution may be calculated from the examination of the quality factor Q of the liquid filled cavity, defined as the frequency f_n divided by the 3 dB bandwidth, Δf_n, of the resonance. This quality factor is a function of the mechanical clamping and the attenuation per wavelength $\alpha\lambda$ of the ultrasonic energy and is expressed as,

$$Q = \frac{f_n}{\Delta f_n} = \frac{\pi}{\alpha\lambda} \qquad (15)$$

The measured Q, however, includes losses associated with attenuation in the solvent, as well as those arising from diffraction, wall effects, imperfect reflections at the quartz surface, etc.,

in addition to the desired excess attenuation due to the solute. Assuming all of these energy losses are additive [32], the measured quality factor Q is given by

$$\frac{1}{Q_{meas}} = \frac{1}{Q_{solute}} + \frac{1}{Q_{extra}} \qquad (16)$$

where Q_{solute} is the quality factor due to sound absorption in the solute, and Q_{extra} includes solvent and other cell losses previously discussed. The excess solute absorption can be obtained by means of a reference measurement in the same cell at the same frequencies with the reference liquid, having equal or very similar sound velocity to insure the same sound field pattern for both measurements. The excess absorption per wavelength in the specimen solution is then obtained from

$$(\alpha\lambda)_{excess} = \pi \left(\frac{\Delta f_s - \Delta f_r}{f_n} \right) \qquad (17)$$

where Δf_s and Δf_r are the corresponding 3 dB bandwidths of the n^{th} resonant peak in the sample and reference liquid, respectively. The application of an overpressure (usually about 10 psi) causes a slight concavity of the transducers, which reduces diffraction and boundary effects, and thereby reduces the minimum frequency of measurement [33]. This technique has been used in our laboratory over the frequency range from 0.5 to 10 MHz.

5. Absorption and Velocity Measurements of Shear Waves in Biological Specimens

A system based on a pulse superposition technique allows measurement of the shear acoustical properties of biological materials of interest [34]. The technique involves phase-amplitude balance to measure the magnitude and phase angle of the reflection coefficient of a shear wave impinging on a quartz-sample interface, and using the known impedance of the quartz, the complex shear specific impedance of the sample being investigated is obtained [35]. From the shear impedance and density, it is possible to calculate the dynamic shear stiffness μ_1, dynamic shear viscosity μ_2, shear velocity c_S, and shear absorption coefficient α_S as shown in the following relationships:

$$\mu_1 = \frac{R_S^2 - X_S^2}{\rho} \qquad (18)$$

$$\mu_2 = \frac{2R_S X_S}{\omega\rho} \qquad (19)$$

$$c_S = \frac{R_S^2 + X_S^2}{\rho R_S} \qquad (20)$$

$$\alpha_S = \frac{\rho\omega X_S}{R_S^2 + X_S^2} \qquad (21)$$

where ρ is the density, ω is the angular frequency, R_S is the real part of the specific shear acoustic impedance and X_S is the imaginary part of the specific shear acoustic impedance. This method has been used to measure the shear acoustic properties of tissues and other biological specimens [36-38]. An improved system utilizing a gated carrier as opposed to a pulsed oscillator approach and an improved ultrasonic unit of beveled AT quartz is being developed that will be useful over the frequency range from 2 to greater than 20 MHz and for temperatures from 10 to 40 °C. These and additional improvements should provide accuracies for the real and imaginary parts of the specific acoustic impedance within ± 100 mech-ohm/cm^2 at 10 MHz, allowing more accurate measurement of impedance close to that for water.

6. Concluding Remarks

The measuring techniques for ultrasonic absorption, attenuation and velocity in biological specimens discussed above have been only those utilized at the Bioacoustics Research Laboratory. There are, however, techniques employed elsewhere which may provide the same information in a more efficient manner. For example, the above discussed methods provide information at discrete frequencies and loci, or, for spatial averages. Spectrum analysis methods [39-41] have been promoted to permit measurements over a somewhat broadened frequency range. The measurement of the spatial distribution of ultrasonic properties such as attenuation or velocity within a specimen may be possible using the algebraic reconstruction from two-dimensional acoustic projections [42,43], although only velocity reconstruction has been considered practical so far.

Recent studies have also considered improvements regarding possible error in established methods of ultrasonic parameter measurements. Artifacts in acoustic attenuation due to phase cancellation effects have been described by Marcus and Carstensen [6], who compared a piezoelectric receiver (phase-sensitive) with a radiation-force receiver (phase-insensitive), and also by Busse et al. [44], comparing the piezoelectric receiver with an acousto-electric receiver. Both studies found that measurements using piezoelectric (phase-preserving) receivers yielded higher apparent attenuation values than those obtained using phase-insensitive receivers. Phase cancellation artifacts are thought to be the source of this error.

Acknowledgment

The authors acknowledge gratefully the partial support for portions of the activities described herein by grants from the National Institutes of Health.

References

[1] Rooney, J. A., Determination of acoustic power outputs in the microwatt-milliwatt range, Ultrasound Med. Biol. 1, 13-16 (1973).

[2] O'Brien, W. D., Jr., Ultrasonic Dosimetry, in Ultrasound: Its Application in Medicine and Biology, F. J. Fry, ed., Chap. 5 (Elsevier, Amsterdam, in press).

[3] Kossoff, G., Balance technique for the measurement of very low ultrasonic power outputs, J. Acoust. Soc. Am. 38, 880-881 (1965).

[4] Hill, C. R., Calibration of ultrasonic beams for biomedical applications, Phys. Med. Biol. 15, 241-248 (1970).

[5] Pohlman, R., Über die Absorption des Ultraschalls im menschlichen Gewebe und ihre Abhängigkeit von der Frequenz, Physik Z. 40, 159-161 (1939).

[6] Marcus, P. W. and Carstensen, E. L., Problems with absorption measurements of inhomogeneous solids, J. Acoust. Soc. Am. 58, 1334-1335 (1975).

[7] Dussik, K. T., Fritch, D. J., Kyriazidou, M., and Sear, R. S., Measurements of articular tissue with ultrasound, J. Phys. Med. 37, 160-165 (1958).

[8] Bauld, T. J. and Schwan, H. P., Attenuation and reflection of ultrasound in canine lung tissue, J. Acoust. Soc. Am. 56, 1630-1637 (1974).

[9] Wladimiroff, J. W., Craft, I. L., and Talbert, D. G., In vitro measurement of sound velocity in human fetal brain, Ultrasound Med. Biol. 1, 377-382 (1975).

[10] Buschmann, W., Voss, M., and Kemmerling, S., Acoustic properties of normal human orbit tissues, Ophtal. Res. 1, 354-364 (1970).

[11] Lange, J. N., Group velocity dispersion due to pulse reflection from a frequency dependent boundary impedance, J. Acoust. Soc. Am. 40, 998-1001 (1966).

[12] Goldman, D. E. and Richards, J. R., Measurement of high frequency sound velocity in mammalian soft tissues, J. Acoust. Soc. Am. 26, 981-983 (1954).

[13] Hueter, T. F., Viscoelastic Losses in Tissues in the Ultrasonic Range, Wright Air Development Center Technical Report 57-706 (1958).

[14] Fry, W. J. and Dunn, F., Ultrasound: Analysis and Experimental Methods in Biological Research, in Physical Techniques in Biological Research, W. L. Nastuk, ed., Vol. IV, Chap. 6, pp. 261-394 (Academic Press, New York, 1962).

[15] Dunn, F. and Fry, W. J., Ultrasonic absorption and reflection by lung tissue, Phys. Med. Biol. 5, 401-410 (1961).

[16] Fry, W. J. and Fry, R. B., Determination of absolute sound levels and acoustic absorption coefficients by thermocouple probes--theory, J. Acoust. Soc. Am. 26, 294-310 (1954).

[17] Fry, W. J. and Fry, R. B., Determination of absolute sound levels and acoustic absorption coefficients by thermocouple probes--experiment, J. Acoust. Soc. Am. 26, 311-317 (1954).

[18] Dunn, F., Temperature and amplitude dependence of acoustic absorption in tissue, J. Acoust. Soc. Am. 34, 1545-1547 (1962).

[19] Dunn, F. and Brady, J. K., Temperature and Frequency Dependence of Ultrasonic Absorption in Tissue, in Proceedings 8th International Congress on Acoustics, Vol. 1, p. 366c (Goldcrest Press, Trowbridge, Wilts., 1974).

[20] Brady, J. K., Goss, S. A., Johnston, R. L., O'Brien, W. D., Jr., and Dunn, F., Ultrasonic propagation properties of mammalian testes, J. Acoust. Soc. Am. 60, 1407-1409 (1976).

[21] Dunn, F. and Breyer, J. E., Generation and detection of ultra-high-frequency sound in liquids, J. Acoust. Soc. Am. 34, 775-778 (1962).

[22] Carstensen, E. L., Li, K., and Schwan, H. P., Determination of the acoustic properties of blood and its components, J. Acoust. Soc. Am. 25, 286-289 (1953).

[23] Pauly, H. and Schwan, H. P., Mechanism of absorption of ultrasound in liver tissue, J. Acoust. Soc. Am. 50, 692-699 (1971).

[24] O'Brien, W. D., Jr., The Absorption of Ultrasound in Aqueous Solutions of Biological Polymers, Ph.D. Thesis, University of Illinois, Urbana, Illinois (1970).

[25] Goss, S. A., The Concentration Dependence of the Ultrasonic Absorption in Aqueous Solutions of Bovine Serum Albumin, M.S. Thesis, University of Illinois, Urbana, Illinois (1974).

[26] Kessler, L. W., Hawley, S. A., and Dunn, F., Semi-automatic determination of ultrasonic velocity and absorption in liquids, Acustica 24, 105-107 (1971).

[27] Pellam, J. R. and Galt, J. K., Ultrasonic propagation in liquids: I. Application of pulse technique to velocity and absorption measurements at 15 megacycles, J. Chem. Phys. 14, 608-614 (1946).

[28] Del Grosso, V.A., Systematic Errors in Ultrasonic Propagation Parameter Measurements Part I--Effect of Free-Field Diffraction, U.S. Naval Research Laboratory Report 6026 (1964).

[29] Schwan, H. D. and Carstensen, E. L., Ultrasonics aids diathermy experiments, Electronics 25, 216-220 (1952).

[30] Carstensen, E. L., Measurement of dispersion of velocity of sound in liquids, J. Acoust. Soc. Am. 26, 858-861 (1954).

[31] Eggers, F., Eine Resonatormethode zur Be-

stimmung von Schall--Geschwindigkeit und Dämpfung an geringen Flüssigkeitsmengen, Acustica 19, 323-329 (1968).

[32] Eggers, F. and Funck, Th., Ultrasonic measurements with milliliter liquid samples in the 0.5-100 MHz range, Rev. Sci. Instrum. 44, 969-977 (1973).

[33] Eggers, F., Funck, Th., and Richman, K. H., High Q ultrasonic liquid resonators with concave transducers, Rev. Sci. Instrum. 47, 361-367 (1976).

[34] Frizzell, L. A., Carstensen, E. L., and Dyro, J. F., Shear properties of mammalian tissues at low megahertz frequencies, J. Acoust. Soc. Am. 60, 1409-1411 (1976).

[35] Moore, R. S. and McSkimin, H. J., Dynamic Shear Properties of Solvents and Polystyrene Solutions from 20 to 300 MHz, in Physical Acoustics, W. P. Mason and R. N. Thurston, eds., Vol. VI, Chap. 4, pp. 167-242 (Academic Press, Inc., New York, 1970).

[36] Dyro, J. F., Ultrasonic Study of Material Related to Atherosclerotic Plaque--Dynamic Viscoelastic Properties of Cholestoric Esters, Ph.D. Thesis, University of Pennsylvania, Philadelphia, Pennsylvania (1972).

[37] Dyro, J. F. and Edmonds, P. D., Ultrasonic absorption and dispersion in cholesteryl esters, Mol. Cryst. Liq. Cryst. 25, 175-193 (1974).

[38] Frizzell, L. A., Ultrasonic Heating of Tissues, Ph.D. Thesis, University of Rochester, New York (1975).

[39] Chivers, R. C. and Hill, C. R., Ultrasonic attenuation in human tissue, Ultrasound Med. Biol. 2, 25-29 (1975).

[40] Lizzi, F., Katz, L., St. Louis, L., and Coleman, D. J., Applications of Spectral Analysis in Medical Ultrasonography, Ultrasonics 14, 77-80 (1976).

[41] Le Croissette, D. H. and Heyser, R. C., Attenuation and Velocity Measurements in Tissue Using Time Delay Spectrometry, in Ultrasonic Tissue Characterization, M. Linzer, ed., National Bureau of Standards Spec. Publ. 453, pp. 81-95 (U.S. Government Printing Office, Washington, D.C., 1976).

[42] Greenleaf, J. F., Johnson, S. A., Lee, S. L., Herman, G. T., and Wood, E. H., Algebraic Reconstruction of Spatial Distributions of Acoustic Absorption Within Tissue From Their Two-Dimensional Acoustic Projections, in Acoustical Holography, P. S. Green, ed., Vol. 5, pp. 591-603 (Plenum Press, New York, 1974).

[43] Greenleaf, J. F., Johnson, S. A., Samayoa, W. F., and Duck, F. A., Algebraic Reconstruction of Spatial Distributions of Acoustic Velocities in Tissue From Their Time of Flight Profiles, in Acoustical Holography, N. Booth, ed., Vol. 6, pp. 71-90 (Plenum Press, New York, 1975).

[44] Busse, L. J., Miller, J. G., Yuhas, D. E., Mimbs, J. W., Weiss, A. N., and Sobel, B. E., Phase Cancellation Effects: A Source of Attenuation Artifact Eliminated by a CdS Acoustoelectric Receiver, in Ultrasound in Medicine, D. White, Ed., Vol. 3, pp. 1519-1535 (Plenum Press, New York, 1977).

Reprinted from *Ultrasonic Tissue Characterization II*, M. Linzer, ed., National Bureau of Standards, Spec. Publ. 525 (U.S. Government Printing Office, Washington, D.C., 1979).

A DEVICE FOR MEASURING ULTRASONIC PROPAGATION VELOCITY IN TISSUE

Bruce D. Sollish

Harry De Jur Diagnostic Instrumentation Laboratory
Department of Electronics
Weizmann Institute of Science
Rehovot, Israel

This paper discusses a device capable of measuring propagation velocity in tissue, both excised and in vivo. The device produces a 4-digit decimal readout of propagation velocity in the specimen relative to that in water. As presently constituted the device is capable of 1 velocity measurement per second, with one additional second required for printout of the result.

The theory of the device is described, and experimental results are presented for solids and soft tissues.

Key words: Propagation velocity; reflection technique; solids; tissue; ultrasound.

1. Introduction

Ultrasonic propagation velocity has been measured in a variety of soft tissues. In a review article, Wells [1][1] has compiled some of the more significant velocity data published in the literature. It would appear that accurate measurement of velocity could help in characterizing soft tissues. Kossoff et al. [2], for example, have measured ultrasonic velocity in the human female breast and have concluded that the results as to characteristics of tissue type correlate reasonably well with the findings of mammography.

One problem in velocity measurement is the need for determining thickness of the tissue along the path of propagation. Thickness can be measured directly or by the method of equivalent water path given by Kossoff [2,3] for transmission and reflection velocity measurement techniques. For each new propagation path through the tissue, another thickness measurement must be made. The process of measuring velocity in a variety of paths through the tissue could therefore be quite time consuming.

In order to eliminate the need to determine tissue thickness along the propagation path, a new pulse-echo method for measuring ultrasound velocity has been developed. This technique utilizes a reflecting surface at a fixed distance from the transducer. The overall propagation path consists of a suitable medium, such as water, and the tissue sample.

Since only the overall distance between the transducer and reflector need be constant, the thickness of the tissue need not be measured. The technique can therefore be readily applied in velocity measurements in different samples or through different paths in the same sample, without repeated thickness calculations. Indeed, the velocity data can be used to compute thickness in the specimen along the propagation path, which can be compared with the thickness as measured directly, for checking the accuracy of the measurement.

A prototype of a device incorporating this reflection technique has been built, for measurements of propagation velocity in solids and in tissue. The following sections describe in more detail the reflection technique, the prototype device implementing the technique, and results of velocity measurements in solids and in tissue.

2. Description of the Technique

The method used for measuring propagation velocity is illustrated in figure 1. A flat reference reflecting surface is positioned at a convenient fixed distance from the ultrasonic transducer. Both are immersed in a suitable propagating medium such as distilled water. An A-mode pulse-echo device displays an echo due to the reflecting surface. This echo is a reference echo for the remainder of the velocity measurement.

The tissue specimen is next interposed between the transducer and the reflector as shown in the figure. The A-scope is adjusted to display the echoes corresponding to the following interfaces: the anterior boundary of the specimen, the posterior boundary of the specimen, and the reflector surface as returned through the specimen. The reflector echo is shifted in time from its reference position if the velocity in the specimen is different from that in the medium.

As shown in the figure, there are in general two configurations for velocity measurement. In the first configuration, the specimen is positioned somewhere in between the transducer and the reflector. In this case four echoes of in-

[1]Figures in brackets indicate literature references at the end of this paper.

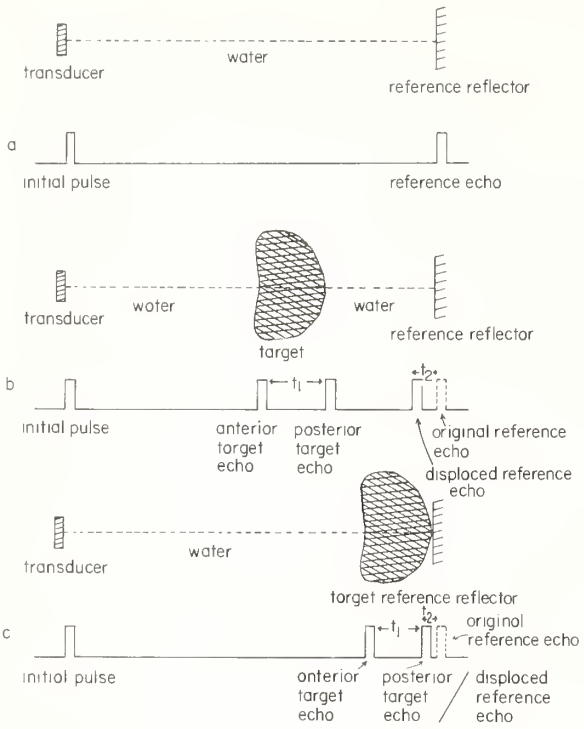

Fig. 1. Reference reflector technique for velocity measurements.
a) initial calibration
b) target interposed between transducer and reference reflector
c) target in contact with reference reflector.

terest are produced. In the second configuration, the specimen is positioned so that its posterior boundary is coincident with the reflector. In this case, there are only three echoes to consider. The second configuration is readily adapted for use in velocity measurements made via a water bag, in which case the specimen and the reflector lie outside the water bag.

For either configuration, velocity in the sample is calculated as follows. Denote the distance between the transducer and reflector by L, the thickness of the specimen by ℓ, the velocity in the medium by V_0, and the velocity in the specimen by V. Let the time between the anterior and posterior echoes from the specimen be T_1, and let the time displacement of the reflector echo due to interposition of the specimen be T_2. Then the following equations apply for T_1 and T_2:

$$T_1 = 2\ell/V \tag{1}$$

$$T_2 = \frac{2L}{V_0} - \left[\frac{2(L-\ell)}{V_0} + \frac{2\ell}{V}\right]$$

$$= 2\ell\left(\frac{1}{V_0} - \frac{1}{V}\right) \tag{2}$$

From these equations, the ratio of propagation velocity in the specimen to that in the medium is

$$V/V_0 = 1 + T_2/T_1 \tag{3}$$

We note that T_2 is positive if the reflector echo is displaced toward the transducer when the specimen is in position, and negative if the reflector is displaced away from the transducer.

The thickness of the specimen along the path of propagation can be calculated from the above equations, as

$$\ell/\ell_0 = V/V_0 \tag{4}$$

where

$$\ell_0 = \frac{V_0 T_1}{2} \tag{5}$$

We note that ℓ_0 is the thickness of the specimen measured by the A-scope calibrated for velocity in the medium.

The significance of eqs. (1) through (5) is that the ratio of T_2 to T_1 is independent of the thickness ℓ of the specimen. Accurate measurement of times T_1 and T_2 will give an accurate measurement of velocity in the specimen relative to velocity in the medium. Even if the specimen is repositioned or if a different specimen is examined, T_1 and T_2 will both change accordingly, as long as the transducer to reflector distance remains unchanged. Thus, the technique enables rapid velocity measurements in a variety of tissues, as long as the reference echo is returned through the specimen.

3. Description of the Device

A block diagram of a device utilizing the reference reflector technique for measuring ultrasound velocity is shown in figure 2. An A-scope and an oscilloscope are required. In addition, a printer may be added for hard copy output of velocity data.

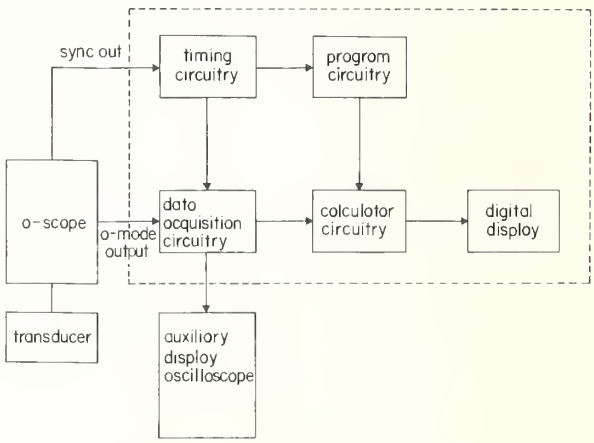

Fig. 2. Block diagram of velocity measurement device and associated equipment.

Operation of the system is as follows. Before the specimen is immersed in water, the A-scope is adjusted to display the echo due to the reference reflector. The A-mode ("video") signal is fed to the data acquisition circuit, passing through a

time-gated threshold detector and a pulse shaper. The processed echo from the reflector is displayed on the oscilloscope, together with a pulse whose position on the display is variable. The user presets the time delay of the variable pulse, so that the pulse overlaps the reference echo, as seen on the oscilloscope and confirmed by a front-panel LED indicator. This procedure, which stores in the data acquisition circuitry the propagation time from the transducer to the reflector, is performed only once before the specimen is inserted. At any time, calibration may be checked by removing the specimen, and noting if the overlap condition is resumed.

Following storage of the reference echo, the specimen is interposed between the transducer and the reflector. The data acquisition circuit, by adjustment of the time-gated threshold detector, eliminates internal echoes from within the sample. The present velocity device implements the configuration of figure 1c. Therefore only two echoes remain after processing: the anterior echo of the specimen and the echo at the interface between the specimen and reflector.

The data acquisition circuit now contains three pulses: the two echoes processed from the tissue specimen and the preset pulse supplied by the user as described earlier. Two gates are derived from these pulses. The first gate is opened by the anterior pulse and closed by the specimen-reflector boundary echo. The second gate is opened by the specimen-reflector boundary echo and closed by the preset pulse or opened by the preset pulse and closed by the specimen-boundary echo, depending on which signal arrives first. In the latter case, a flag is sent out to the calculator circuit to perform a subtraction instead of an addition, as discussed later.

Each gate enables one of two 4-digit BCD counters clocked at a rate of 15 MHz. By the end of the second gate, two data words have been loaded into the counters. These two 4-digit words, corresponding to T_1 and T_2 in eq. (3), provide all the information required for calculating velocity in the specimen (relative to water). The maximum count of 9999 corresponds to a round-trip travel time through 500 mm of water.

A 10-step hard-wired program sequentially controls the operation of a 4-function calculator chip. These steps include clearing the calculater, entering the values T_1 and T_2, performing the arithmetic operations of eq. (3), and displaying the result to 4 significant digits via a front-panel LED display. In the event of a flag generated by the data acquisition circuitry, the program treats T_2/T_1 as a negative number. If desired, the results of each measurement are printed by an IBM output writer, 10 measurements to a line.

The timing circuitry maintains synchronization among all elements of the velocity measuring system. When the user presses the start button after checking on the oscilloscope that the correct echoes are present, the timing circuit insures that only a single set of data words enters the calculator until calculation and printout of the results are complete. Using a free-running start signal, a new velocity value is calculated and printed every two seconds.

4. Experimental Results

A. Measurements of Velocity in Solids

Before conducting measurements of ultrasound velocity in tissues, it was necessary to check the accuracy of the reference reflector velocity technique and its implementation in the device described in the previous section. For this purpose three objects were chosen: a 4-mm thick slab of polyvinylchloride (PVC), a 6-mm thick slab of perspex, and a 10-mm thick combination of the two materials. The ultrasonic frequency was 5 MHz. Fifty velocity measurements were made for each object.

Results of measurements of velocity in the three test objects are given in table 1. Absolute values of velocity are found by multiplying the respective relative values by the ultrasound velocity in water, 1498 m/s. The standard deviations vary from about 0.3 to 0.5 percent of the measured values.

Table 1. Velocity measurements of selected solids.

Polyvinylchloride (PVC)

Relative velocity data ($\times 10^{-3}$)

1486	1486	1479	1472	1486	1479	1479	1486	1486	1486
1486	1486	1500	1500	1486	1486	1479	1479	1486	1479
1486	1486	1500	1486	1486	1500	1486	1486	1486	1500
1486	1500	1486	1486	1486	1486	1472	1479	1500	1479
1500	1486	1486	1486	1486	1472	1472	1486	1486	1486

Average relative velocity: 1.4860
Average absolute velocity: 2226.0 m/s
Standard deviation: 11.2 m/s

Perspex

Relative velocity data ($\times 10^{-3}$)

1822	1811	1811	1811	1811	1811	1811	1822	1822	1811
1811	1820	1811	1811	1822	1811	1811	1820	1811	1811
1811	1820	1820	1800	1811	1822	1811	1811	1808	1800
1822	1811	1811	1800	1820	1811	1811	1811	1822	1820
1811	1811	1820	1820	1811	1811	1831	1811	1820	1811

Average relative velocity: 1.8138
Average absolute velocity: 2717.1 m/s
Standard deviation: 9.4 m/s

PVC-perspex combination

Relative velocity data ($\times 10^{-3}$)

1670	1664	1664	1668	1674	1668	1674	1668	1668	1664
1664	1658	1664	1668	1664	1664	1670	1670	1674	1664
1658	1664	1664	1664	1664	1664	1664	1674	1658	1664
1658	1664	1674	1674	1670	1674	1668	1664	1664	1664
1668	1668	1668	1664	1674	1658	1674	1658	1668	1668

Average relative velocity: 1.6664
Average absolute velocity: 2496.3 m/s
Standard deviation: 7.2 m/s

To check the accuracy of the results obtained for each object, the thickness given by eqs. (4) and (5) was compared to the thickness measured by a caliper. Propagation times were respectively 3.60 μs, 4.42 μs, and 8.02 μs in the PVC, perspex, and PVC-perspex combination. The corresponding thicknesses calculated from the data and eqs. (4) and (5) are 4.003 mm, 6.005 mm, and 10.01 mm, respectively, which are within 0.1 percent of the measured values.

B. Measurements of Velocity in Soft Tissues

In order to demonstrate measurement of velocity in soft tissue, a sample of fat in vitro and two human forearms in vivo were examined. As previously, the insonifying frequency was 5 MHz and 50 individual velocity measurements were taken for each target. Results of the measurements are given in table 2.

Table 2. Velocity measurements of soluble soft tissues.

Fat (bovine)

Relative velocity data ($\times 10^{-3}$)

0987	0987	0987	0987	0987	0987	0987	0987	0991	0991
0991	0991	0991	0987	0987	0991	0987	0987	0987	0991
0987	0987	0987	0991	0987	0991	0991	0991	0987	0987
0991	0987	0991	0987	0991	0991	0987	0991	0983	0991
0991	0987	0987	0987	0991	0987	0987	0987	0987	0987

Average relative velocity: 0.9884
Average absolute velocity: 1480.7 m/s
Standard deviation: 3.1 m/s

Forearm (subject A)

Relative velocity data ($\times 10^{-3}$)

1057	1058	1058	1058	1057	1057	1058	1057	1057	1056
1056	1057	1057	1057	1057	1057	1058	1057	1058	1058
1057	1057	1057	1057	1056	1057	1057	1057	1057	1057
1056	1057	1056	1056	1057	1057	1057	1057	1057	1057
1057	1058	1057	1059	1057	1057	1057	1057	1056	1056

Average relative velocity: 1.0570
Average absolute velocity: 1583.4 m/s
Standard deviation: 1.0 m/s

Forearm (subject B)

Relative velocity data ($\times 10^{-3}$)

1056	1056	1055	1055	1056	1056	1055	1056	1055	1055
1056	1055	1055	1056	1056	1055	1056	1056	1056	1055
1055	1056	1055	1055	1056	1055	1054	1053	1054	1053
1053	1053	1053	1054	1054	1055	1054	1054	1054	1053
1054	1054	1054	1053	1054	1053	1053	1054	1053	1053

Average relative velocity: 1.0546
Average absolute velocity: 1579.8 m/s
Standard deviation: 1.7 m/s

The specimen of bovine fat was refrigerated for several days and then warmed to room temperature before insonification. The velocity of 1481 m/s is approximately 1 percent higher than the velocity for cow fat given by Goldman and Hueter [4], but well within the limits for mammalian fat in general. The standard deviation in the present measurement is about 0.2 percent.

The next measurements were made in the forearms of two male subjects, the same age (27). Care was taken to investigate the same portion of forearm of each subject. The average velocities in the two subjects, 1583 m/s and 1580 m/s, respectively, lie within the range given by Goldman and Hueter for human limbs. The standard deviations are of the order of 0.1 percent of the measured velocities. More data would be required to determine if the difference in velocity between the two subjects is statistically significant.

5. Conclusion

A device for measuring ultrasonic propagation velocity in tissue using a reference reflector has been described. On the basis of experimental results in solids and soft tissue, it appears that velocity measurements accurate to within 0.2 percent can be achieved with the device.

An improved model is now under construction. It will incorporate microprocessor-based circuitry for increasing the number of measurements at a single location to 500 per second. This will increase the precision of the measured velocity as well as eliminate problems of motion during measurement. The new device should enable scanning a structure such as the breast with the object of studying local variations in propagation velocity.

Acknowledgments

The author wishes to express his gratitude to the Harry de Jur Foundation and the Rose Teitelbaum Cancer Research Foundation for their partial support of this research. The author would also like to thank Professor E.H. Frei, and Y. Dreier, I. Gonen, E. Grinwald, A. Kuprak, J. Leibovitz, and M. Moshitzky of the Weizmann Institute for their roles in the project.

References

[1] Wells, P. N. T., Absorption and dispersion of ultrasound in biological tissue, Ultrasound in Med. and Biol. 1, 369-376 (1975).

[2] Kossoff, G., Fry, E. K., and Jellins, J., Average velocity of ultrasound in the human female breast, J. Acoust. Soc. Am. 53, 1730-1736 (1973).

[3] Kossoff, G., Reflection Techniques for Measurement of attenuation and velocity, in Ultrasonic Tissue Characterization, M. Linzer, ed., National Bureau of Standards Spec. Publ. 453, pp. 135-139 (U.S. Government Printing Office, Washington, D.C., 1976).

[4] Goldman, D. E., and Hueter, T. F., Tabular data on the velocity and absorption of high frequency sound in mammalian tissues, J. Acoust. Soc. Am. 28, 35-78 (1956).

Reprinted from *Ultrasonic Tissue Characterization II*, M. Linzer, ed., National Bureau of Standards, Spec. Publ. 525 (U.S. Government Printing Office, Washington, D.C., 1979).

MEASUREMENT OF THE TEMPERATURE DEPENDENCE OF THE VELOCITY OF ULTRASOUND IN SOFT TISSUES

T. Bowen, W. G. Connor, R. L. Nasoni, A. E. Pifer, and R. R. Sholes

Departments of Physics and Radiology
University of Arizona
Tucson, Arizona 85724, U.S.A.

The velocity of 5 MHz ultrasound is being measured in tissue samples in order to evaluate the feasibility of non-invasive monitoring of temperature distributions produced during hyperthermia treatments. By employing a pulsed-ultrasound technique in which the time of the first zero-crossing of the received signal is recorded, the velocity measurements are insensitive to reflections and to changes of attenuation. Results in the 35 to 45 °C range for fresh canine tissues, such as kidney, liver, and muscle, indicate that the rate of velocity change with temperature is correlated with the magnitude of the ultrasonic velocity, but the relationship appears to be altogether different for tissue fat. The results give encouragement to carry out the more extensive measurements, particularly in vivo, which would be needed to determine feasibility of an ultrasonic temperature monitoring system.

Key words: Non-invasive temperature monitoring; soft tissue; temperature dependence; ultrasound velocity; zero crossing detection.

1. Introduction

There has been increasing interest recently in hyperthermia as a promising modality for control of some types of malignancies [1-3][1]. In such treatments the tissue temperature must be raised from the usual body temperature of 37 °C to approximately 43 °C for a period of one-half to one hour. If the temperature is accidentally a few degrees higher, all cells will be killed; if a few degrees lower, the effect of the treatment will be negligible. A non-invasive temperature monitoring system is needed for this application. In addition, such a system might find other diagnostic applications where thermal anomalies are caused by changes in the circulatory system or in metabolic processes.

An ultrasonic temperature monitoring system might be devised for soft tissue if some ultrasonic characteristic varies in a known way with temperature. The most promising parameters appear to be ultrasonic velocity and attenuation. Earlier work on transmission-type tomographic image reconstruction systems [4] indicated that velocity data gives much more reproducible results. However, the task of utilizing velocity changes to measure temperature is not an easy one. At 37 °C the velocity of sound in water changes 1.8 m/s per °C or about 0.12 percent per °C. It is clear when one examines results for the velocity of ultrasound in any particular tissue type that the variation from one sample to another is much larger than the variation over a 10 °C temperature range; consequently, one cannot hope to measure temperature ultrasonically. However, it still might be possible to measure temperature changes ultrasonically, making use of the fact that the initial reference temperature, 37 °C, is known to be quite uniform and corrections for regional differences are also known.

Suppose it is desired to monitor a temperature change from body temperature (37 °C) to a treatment temperature in the neighborhood of 43 °C within ± 10 percent for each tissue type in the region of interest. It is the purpose of this work to discuss the first experimental step toward answering whether or not this property of soft tissue can be predicted with such accuracy.

2. Experimental Arrangement

The experimental arrangement for the in vitro measurement of ultrasonic velocity in 1 to 10 cm thick tissue samples as a function of temperature is shown schematically in figure 1. The pulse generator provides a pulse which shock excites the 12.7 mm diameter 5 MHz ultrasound transmitter immersed in the water temperature bath. This pulse also starts the digital timer. The oscilloscope serves only to visually monitor the system; its trace is initiated by a trigger pulse from the pulse generator whose timing can be delayed or advanced relative to the main pulse so as to observe any part of

[1]Figures in brackets indicate literature references at the end of this paper.

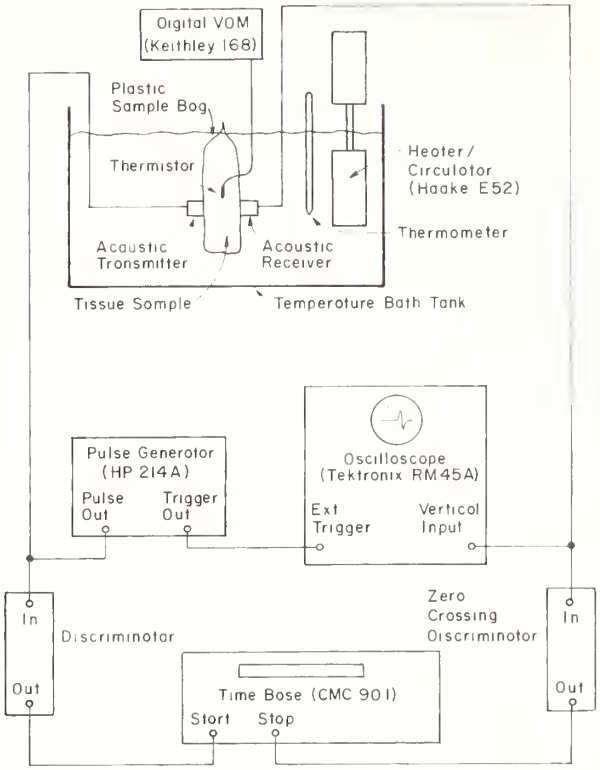

Fig. 1. Block diagram of the experimental arrangement for in vitro measurements of ultrasound velocity as a function of temperature.

the signal at the receiver. The output of the 12.7 mm diameter ultrasound receiver, which is also immersed in the temperature bath, is connected both to the vertical oscilloscope input for observation of its amplitude and to a zero-crossing discriminator whose output stops the digital timer. The digital timer measures to the nearest 0.01 μs the transit time plus a fixed time related to the delays in the system not connected with the sound propagation. The fixed delays are found by an extrapolation to zero separation of a series of measurements of transit time in water as a function of separation within the errors of measurement. This agrees with the results of others who have found that, although the pressure distribution in the near field is very complicated, the average pressure sensed by a detector whose dimensions are large compared to a wavelength behaves like a plane wave [5]. Adjustment of the width of the shock excitation pulse from the pulse generator can provide a signal at the receiver in which only one or two cycles have large amplitude.

The zero-crossing discriminator is an essential component to define a time reference in a received signal burst. Its operation is illustrated in figure 2. By initiating discriminator action at the occurrence of the first zero crossing, the timing becomes independent of received signal amplitude. This is important when studying the temperature dependence of sound velocity as the attenuation (hence, the received

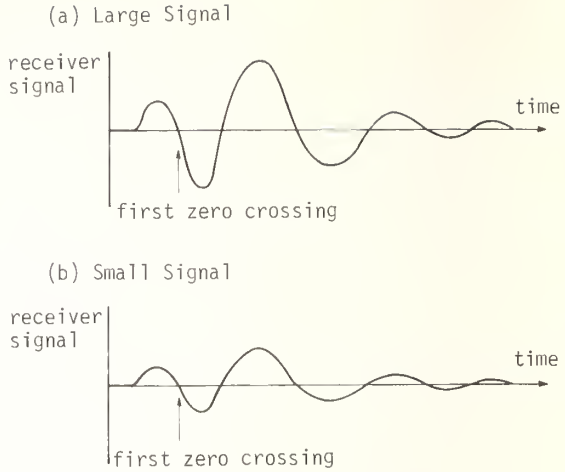

Fig. 2. The first zero-crossing is shown for a large signal (a) and a small signal (b) to illustrate that its position in time remains unaffeced by changes of amplitude.

signal amplitude) also varies with temperature. A pulsed ultrasound system with the timing referenced to the first zero crossing not only is very stable in operation [6], but also is comparatively immune to the effects caused by multiple reflections, as these only disturb a later part of the received signal.

The frequency dependence of ultrasonic velocity and attenuation in tissue affects the shape of the received signal, which could introduce timing shifts. The change of velocity with frequency, or dispersion, causes the pressure pulse to propagate with a group velocity differing slightly from the phase velocity of a continuous wave. Tissue dispersion is typically 0.1 to 1.0 m/s per MHz [7], which at 5 MHz shifts the group velocity 0.5 to 5 m/s above the phase velocity. For sample thicknesses on the order of 2 cm the first zero crossing is still propagating with a velocity nearly equal to the group velocity, and only the leading edge of the first one-half cycle is distorted because the pulse is moving faster than its constituent frequency components [8]. A small velocity shift of this magnitude would have little effect upon the observed rate of change with temperature.

The increasing attenuation at higher frequencies in tissue changes the signal waveform with changing depth. However, the shape of the received waveform was not observed to change significantly over the 35 to 45 °C range of temperatures at fixed depth.

For path lengths on the order of 2 cm the transit time jitter is less than 0.001 μs. The 0.01 μs least count of the digital timer presently limits the timing precision, but this can be greatly improved with the same time digitization by adding an event counter and digital logic so that the transit time is automatically accumulated for, say, 1000 transmitted pulses. However, this improvement will come about only if the time reference oscillator is not synchronized with the start of the transit time measurement.

For samples more than a few centimeters thick, which may often be encountered for in vivo measurements, the optimum ultrasound frequency may be somewhat less than the 5 MHz initially employed. If V(t) is the received transducer voltage as a function of time near the first zero crossing and if the voltage error in detecting the true zero point is given, it is desired to maximize dV/dt at the zero crossing. This would be proportional in the near field to f exp (-βaf), where a is the spacing between transducers and βf is the ultrasonic amplitude attenuation coefficient for the tissue being examined. This function is maximum when βaf = 1, or $f = (\beta a)^{-1}$. For example, $\beta \approx 0.01$ μs-mm^{-1} is typical for many soft tissues, so if a = 100 mm, f = 1 MHz. This result can be easily generalized for cases where the voltage error or noise is frequency dependent.

In a typical data-taking run, the temperature of the bath is increased at a rate of 0.4 °C/min. The rate must be reasonably high so that changes do not take place in the tissue which are a function only of time. However, the higher the rate of change of temperature, the greater the lag of temperature at the center of the sample. In order to correct the data for this temperature lag, a thermistor is inserted at the center of the sample to monitor the temperature difference with respect to the bath. It can be shown from the solution of the one-dimensional heat-diffusion equation when the temperature at the surfaces is a linear function of time that the average temperature along the ultrasound path at time t, Θ(t), is approximately given by:

$$\Theta(t) \cong \frac{1}{3}\,\Theta_{bath}(t) + \frac{2}{3}\,\Theta_{thermistor}(t)\ ,$$

where $\Theta_{bath}(t)$ and $\Theta_{thermistor}(t)$ are the temperatures at time t of the bath (and sample surfaces) and center thermistor, respectively.

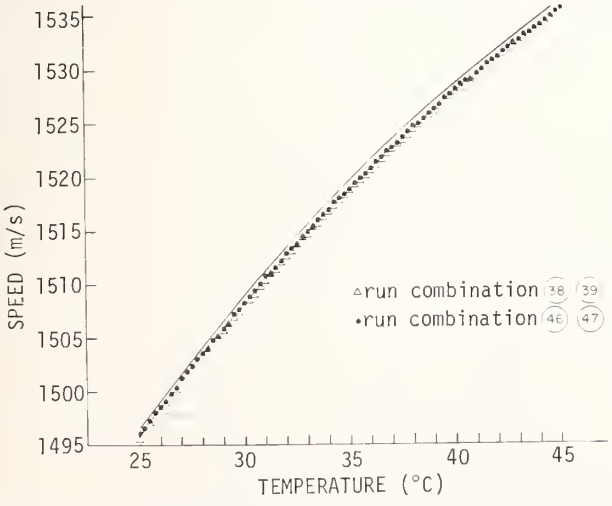

Fig. 3. The speed of ultrasound as a function of temperature for water. The points represent data obtained in this work. The solid curve represents the results of J. R. Lovett, J. Acoust. Soc. Amer. 45, 1051 (1969).

For samples more than a few centimeters thick and for in vivo measurement, other methods of heating the sample may be necessary to avoid large temperature inhomogeneities. This may often necessitate synchronized alternate pulsing of the heat source and the ultrasound transmission to avoid spurious electrical pickup.

Data obtained with the system outlined above for water is illustrated in figure 3. Note the excellent agreement when the rate of variation with temperature is compared with results obtained by others [9].

3. Results

Freshly excised samples of canine skeletal muscle, liver, kidney, spleen, brain, and fat were measured within one hour after sacrifice of the animal. Each run began at approximately 35 °C. When approximately 45 °C was reached the temperature was held constant for at least 30 minutes to verify that the observed changes were attributable to the changes of temperature and not to tissue degeneration. Some data were taken where the temperature was held constant at other values between 35 and 45 °C; no runs gave evidence of ultrasound velocity changes due to tissue degeneration for samples within the first hour after sacrifice. At later times (> 60 minutes after sacrifice), velocity changes (occasionally dramatic decreases) at constant temperature were observed with muscle samples. Each data run was least-square fitted to a polynomial in temperature containing linear and quadratic terms.

Table 1. Ultrasound velocity at 37 °C and rate of change of ultrasound velocity with temperature, dv/dΘ, at 37, 40, 43 °C for fresh canine tissue samples, water, and corn oil.

Tissue type	Sound velocity at 37 °C (m/s)	(dv/dΘ)[(m/s)/°C] 37 °C	40 °C	43 °C
Skeletal muscle	1589.1	1.23	1.03	0.82
Skeletal muscle	1603.3	1.13	0.92	0.71
Skeletal muscle	1588.8	1.16	0.95	0.78
Skeletal muscle	1591.6	1.08	0.87	0.65
Liver	1591.7	0.93	0.78	0.62
Liver	1594.8	1.13	0.96	0.80
Liver	1604.0	0.99	0.72	0.46
Kidney	1570.2	1.35	1.16	0.98
Kidney	1566.5	1.29	1.11	0.93
Kidney	1571.1	1.29	1.11	0.94
Brain (white matter)	1563.2	0.67	0.62	0.26
Spleen	1601.3	1.31	1.07	0.84
Water	1522.5	1.84	1.66	1.48
Stomach fat (fresh)	1411.9	-2.89	-2.85	-2.86
Stomach fat (refrig. 5 h)	1412.9	-3.43	-2.86	-2.91
Corn oil	1420.0	-2.75	-2.58	---

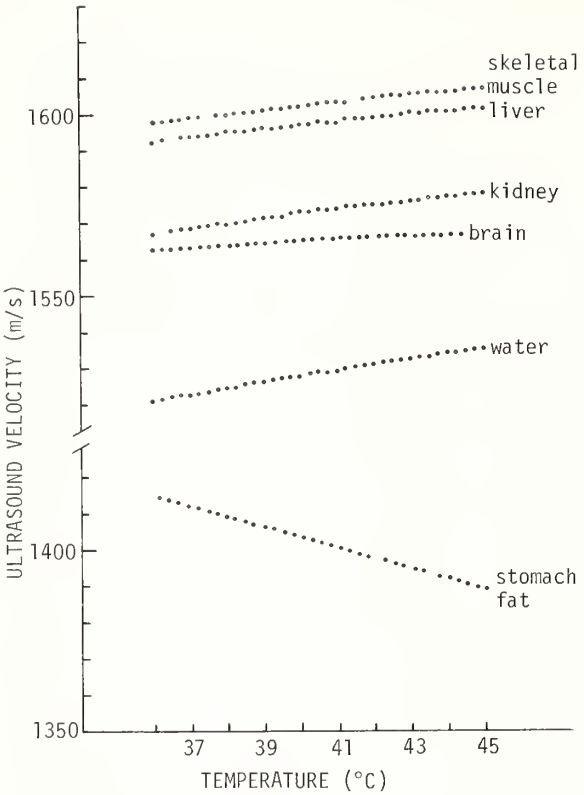

Fig. 4. Typical data showing the dependence of ultrasound velocity on temperature for fresh canine skeletal muscle, liver, kidney, brain (white matter), and stomach fat, as well as for water.

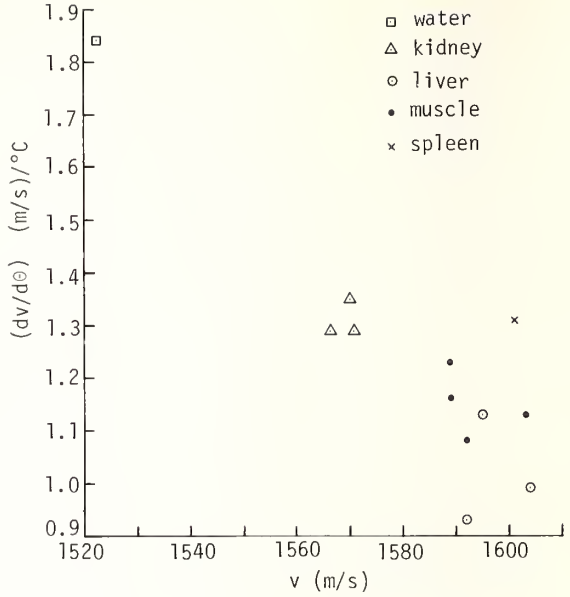

Fig. 5. The rate of change of ultrasound velocity with temperature, dv/dΘ, at 37 °C is plotted as a function of the corresponding ultrasound velocity, v, at 37 °C for each fresh canine tissue sample and for water.

The results are listed in table 1 along with the results for water and corn oil for comparison. Typical curves of ultrasound velocity versus temperature are shown in figure 4. In every case, the variation of ultrasound velocity with temperature, dv/dΘ, is less than the corresponding value for water, actually reversing sign for fat. For tissues other than fat at a specified temperature, a negative correlation between the magnitude of the ultrasound velocity, v, and dv/dΘ is apparent. This is shown in figure 5, where dv/dΘ at 37 °C is plotted against v at 37 °C for each sample (except brain and fat) and for water. Except for one data point for liver and the single point for spleen in figure 5, there appears to be a close connection between dv/dΘ and v for water and soft tissues having high water content.

4. Conclusions

The results of this study are encouraging in two respects: (1) Changes of ultrasound velocity in soft tissues with temperature can be simply, yet accurately, measured with readily available digital electronic circuitry. (2) The rate of change of ultrasound velocity in soft tissues with high water content in this study fell within ± 10 percent of a prediction based only upon the magnitude of the velocity itself for 9 out of 12 samples. However, it is already apparent that the relative fat content of various tissues may be an important parameter. Before any conclusions can be reached concerning the feasibility of non-invasive ultrasonic temperature monitoring, further measurements, especially in vivo, must more precisely ascertain the predictability of ultrasonic velocity temperature dependence in soft tissues.

References

[1] Gerner, E. W., Connor, W. G., Boone, M. L. M., Doss, J. D., Mayer, E. G., and Miller, R. C., Radiology 116, 433 (1975).

[2] Miller, R. C., Connor, W. G., Heusinkveld, R. S., and Boone, M. L. M., Prospects for Hyperthermia in Human Cancer Therapy, Part I: Hyperthermic Effects in Man and Spontaneous Animal Tumors (to be published).

[3] Pettigrew, R. T., Galt, J. M., Ludgate, C. M., Horn, D. B., and Smith, A. N., Br. J. Surg. 61, 727 (1974).

[4] Greenleaf, J. F. and Johnson, S. A., Algebraic Reconstruction of Spatial Distributions of Acoustic Velocity and Attenuation in Tissue from Time-of-Flight and Amplitude Profiles, in Ultrasonic Tissue Characterization, M. Linzer, ed., National Bureau of Standards Spec. Publ. 453, pp. 109-119 (U.S. Government Printing Office, Washington, D.C., 1976).

[5] Rschevkin, S. N., The Theory of Sound, pp. 440-444 (Macmillan, New York, 1963).

[6] Lees, S., Gerhard, F. B. Jr., and Oppenheim, F. G., Ultrasonics 11, 269 (1973).

[7] Carstensen, E. L. and Schwan, H. P., J. Acoust. Soc. Amer. 31, 305 (1959); Carstensten, E. L., Absorption of Sound in Tissue (this publication, p. 29).

[8] Icsevgi, A. and Lamb, W. E. Jr., Phys. Rev. 185, 517 (1969). Section IV of this paper gives an elegant and clear explanation of the behavior of the pulse velocity when the group velocity exceeds the phase velocity.

[9] Lovett, J. R., J. Acoust. Soc. Amer. 45, 1051 (1969).

Reprinted from *Ultrasonic Tissue Characterization II*, M. Linzer, ed., National Bureau of Standards, Spec. Publ. 525 (U.S. Government Printing Office, Washington, D.C., 1979).

ULTRASONIC ATTENUATION IN NORMAL AND ISCHEMIC MYOCARDIUM

M. O'Donnell, J. W. Mimbs, B. E. Sobel, and J. G. Miller

Washington University
St. Louis, Missouri 63130, U.S.A.

The ultrasonic attenuation coefficient of dog myocardium was measured in vitro over the frequency range 2 to 10 MHz. Changes in the attenuation of normal myocardium were measured as a function of time after excision at fixed temperatures. Results of measurements made on tissue maintained at 35 °C revealed progressive changes in the attenuation as a function of time, presumably indicative of tissue degradation. Results of measurements at 19.5 °C, however, showed no significant changes in attenuation up to 4 hours following excision. The temperature dependence of the attenuation was measured over the range ∿ 20 °C to ∿ 37 °C, yielding the result that the attenuation coefficient at 37 °C is about 20 percent lower than that at 20 °C. The attenuation coefficient was measured in vitro at ∿ 20 °C in hearts from dogs previously subjected to coronary occlusion and sacrificed at intervals ranging from 15 minutes to 3 days following occlusion. Results of these measurements indicate a modest decrease in the attenuation of ischemic tissue measured at 15 minutes, 1 hour, 6 hours and 24 hours, and an increase in attenuation of ischemic regions studied 3 days following occlusion.

Key words: Ischemic injury; myocardial infarction; ultrasonic attenuation.

1. Introduction

Previous reports from our laboratory presented the ultrasonic attenuation in normal myocardium and in myocardium subjected to ischemic injury from dogs sacrificed 4 to 11 weeks after coronary artery occlusion. In this report, we present the results of a new series of attenuation measurements on dog left ventricle. Results from this series of measurements are analyzed to: (1) contrast attenuation in normal and ischemic zones of tissue from animals sacrificed 15 minutes, 1 hour, 6 hours, 24 hours, and 3 days following coronary occlusion, (2) examine changes in the ultrasonic attenuation of tissue in vitro at fixed temperatures as a function of time after excision, and (3) examine the temperature dependence of the ultrasonic attenuation of tissue in vitro.

2. Methods

A. Ultrasonic analysis

The instrumentation employed for ultrasonic analysis is depicted in figure 1. The transmitting transducer and driver yielded an ultrasonic pulse with frequency components of sufficient amplitude to permit operation over a range of 2 to 10 MHz. Details of transducer design are discussed subsequently. Under control of a timing unit, broadband ultrasonic pulses were gated into a slowly sweeping analogue spectrum analyzer. Output pulses from the spectrum analyzer, comprising the logarithm of the Fourier transform of the received ultrasonic pulses, were converted by a sample-and-hold unit into a slowly varying (dc) signal. As the spectrum analyzer was slowly swept through frequency, the output of the sample-and-hold and a voltage corresponding to the frequency being analyzed by the spectrum analyzer were transmitted to two analogue-to-digital converters (ADC's). The digital outputs from the ADC's were recorded on magnetic tape for subsequent analysis.

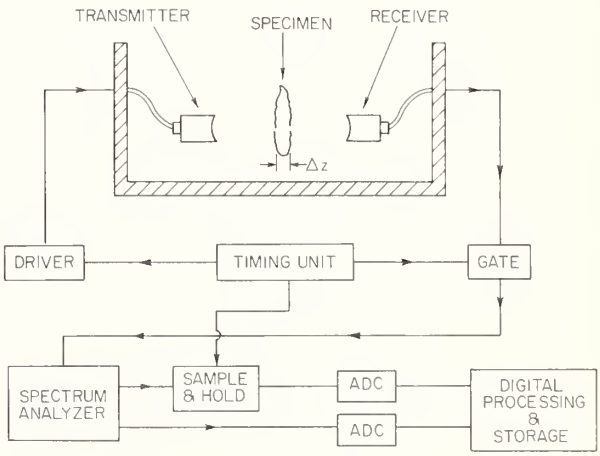

Fig. 1. Block diagram of the ultrasonic instrumentation used in this study.

The procedure used for the quantitative measurement of the attenuation following transmission of ultrasound through tissue has been described in detail in previous reports [1,2][1] and is similar to a substitution technique developed by Schwan

[1]Figures in brackets indicate literature references at the end of this paper.

and Carstensen [3]. If reflections at saline-tissue interfaces can be neglected (and in the absence of artifacts arising from phase cancellation effects), the ultrasonic attenuation coefficient α_t of tissue of thickness Δz is given by

$$\alpha_t = \frac{[V_A(\nu) - V_B(\nu)]}{\Delta z \log_{10} e} \qquad (1)$$

where the term $[V_A(\nu) - V_B(\nu)]$ represents the signal loss, which is obtained by subtracting the logarithmic output of the spectrum analyzer in the presence of tissue $[V_B(\nu)]$ from that recorded in the absence of tissue $[V_A(\nu)]$. The signal loss (expressed in decibels) is calibrated by comparison with an electronic attenuation standard.

Figure 2 illustrates the use of the method to determine the attenuation coefficient of a test object, a flat polyethylene plate of Δz = 0.5 cm. The left panel of figure 2 exhibits a plot of $V_A(\nu)$ with no specimen present (upper curve) and a plot of $V_B(\nu)$ with the polyethylene specimen present (lower curve). The result of subtraction of the two curves in the left panel of figure 2 is displayed as the attenuation-frequency plot in the right panel, with data points calculated according to eq. (1). For cases in which reflections from saline-specimen interfaces cannot be neglected, the slope of the attenuation coefficient versus frequency curve displayed in figure 2 remains a valid ultrasonic index, although the attenuation coefficient α_t may not. (The ultrasonic pulse length used in these studies was less than 0.05 cm in a polyethylene plate of Δz = 0.5 cm. Thus standing wave effects could not occur.)

A possible source of artifact in the apparent attenuation coefficient α_t as determined from eq. (1) arises from phase cancellation effects [1,2]. Phase cancellation effects may occur if inhomogeneities in the tissue distort the ultrasonic field presented to a spatially extended piezoelectric receiving transducer. These wavefront distortions may result from transmission of ultrasound through tissue with variations in surface characteristics, internal structural characteristics, or both. When the wavefronts incident upon a piezoelectric receiver are distorted, the generated electrical signal is degraded because of the phase sensitive nature of the receiver. Phase cancellation effects can induce artifacts into attenuation data which might be interpreted incorrectly as reflecting only the absorption and scattering properties of a specimen [1,2,4].

An intensity sensitive ultrasonic receiving transducer which is inherently insensitive to phase cancellation effects is under continuing development in our laboratory [1,2]. This transducer makes use of the acoustoelectric effect in single crystal cadmium sulfide to convert the intensity of an incident ultrasonic wave into an electronic current in the semiconducting crystal. An illustration of phase cancellation effects is presented in figure 3, which contrasts the performance of a piezoelectric and an acoustoelectric transducer of equal diameters (1.3 cm). The upper panel of figure 3 illustrates the apparent attenuation coefficient as a function of frequency for four adjacent sites of dog left ventricle measured with the piezoelectric receiver. Marked variability is observed in data obtained from four morphologically similar regions. The lower panel depicts the results of measurements on the identical four sites; however, the intensity sensitive acoustoelectric receiver was used. The data of the lower panel exhibit more uniform consistency, presumably reflecting the reduction or elimination of artifacts due to phase cancellation.

The present configuration of the acoustoelectric receiver is cumbersome and would not permit the rapid collection of data that was required in experiments on ischemic tissue (see below). All data reported here were obtained using identical focused piezoelectric transducers (1.3 cm diameter, 5 cm focal distance) for transmitter and receiver. By positioning the specimen of interest so that it lay entirely within the depth of field of the focused transducers, phase cancellation artifacts were minimized. A comparison of the performance of the focused transducers and the acoustoelectric receiver is shown in figure 4. In this figure the apparent attenuation coefficient versus frequency plots obtained from analysis of the identical four adjacent sites of left ventricle are presented. The upper panel presents data obtained with the

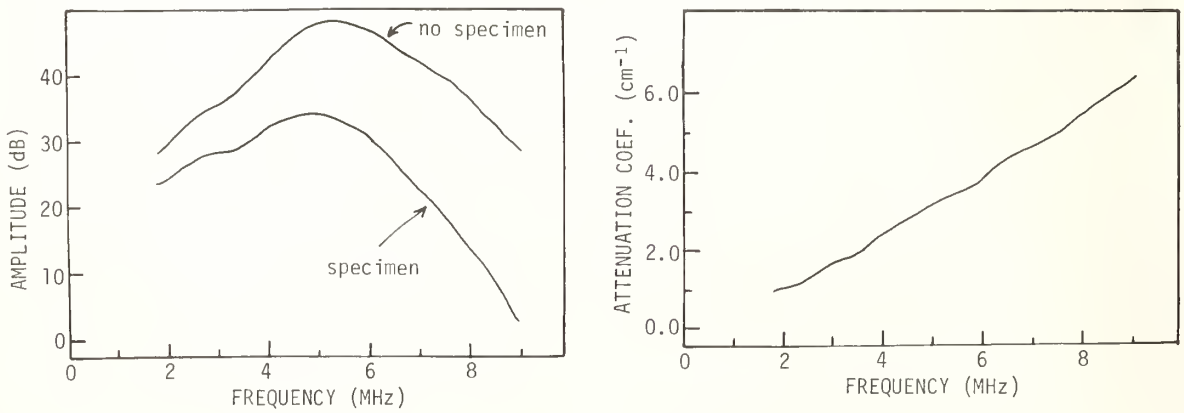

Fig. 2. The left panel is a plot of $V_A(\nu)$ obtained without a specimen and $V_B(\nu)$ obtained with a specimen (a polyethylene plate of Δz = 0.5 cm in this case). The right panel depicts the attenuation versus frequency plot determined using eq. (1) and the data shown in the left panel.

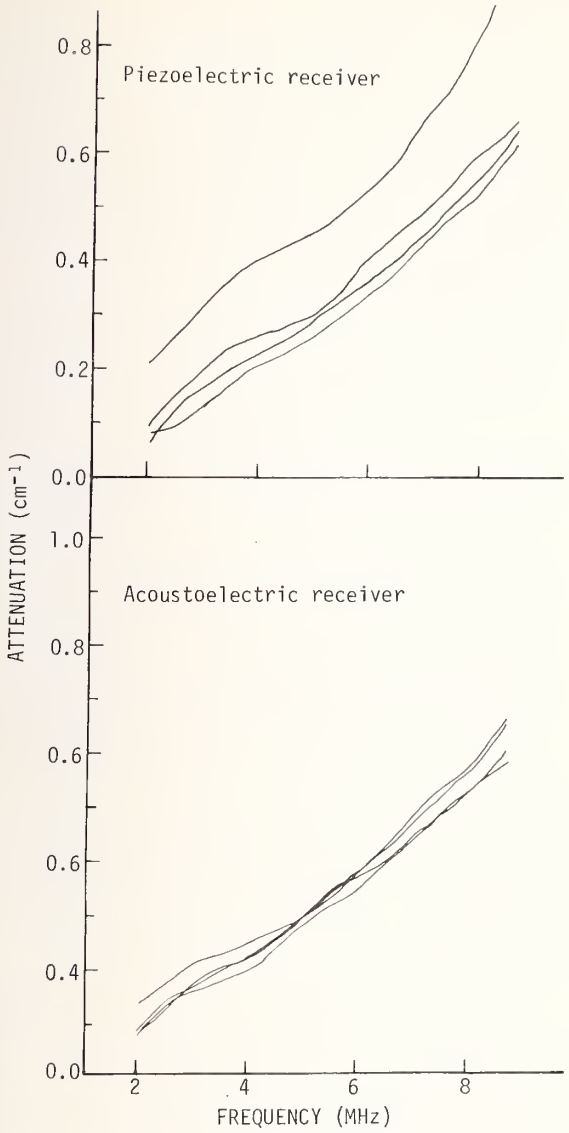

Fig. 3. Planar piezoelectric transmitter. The upper panel depicts the apparent attenuation coefficient as a function of frequency for four contiguous sites of dog left ventricle measured with a 1.3 cm diameter planar piezoelectric receiver. The lower panel depicts the results of measurements on the identical four sites using a 1.3 cm diameter intensity sensitive acoustoelectric receiver.

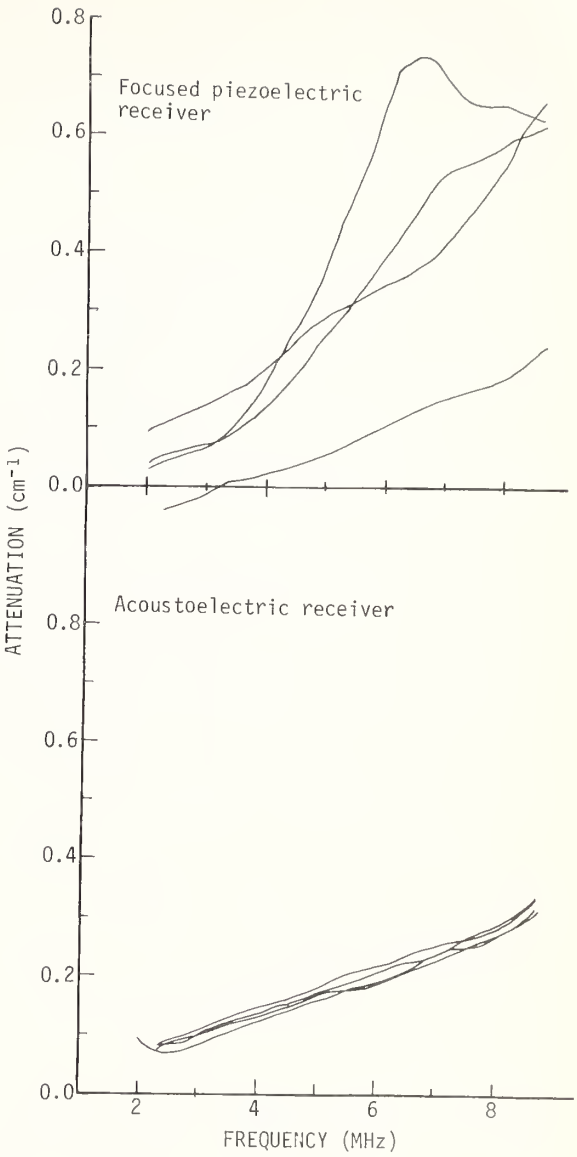

Fig. 4. Focused piezoelectric transmitter. The upper panel illustrates the apparent attenuation coefficient as a function of frequency for four contiguous sites of dog left ventricle measured using a 1.3 cm diameter focused (5 cm focal distance) piezoelectric receiver. The lower panel depicts the results of measurements on the identical four sites, using a 1.3 cm diameter acoustoelectric receiver.

focused piezoelectric receiver and the lower panel presents data obtained with the acoustoelectric receiver. A focused piezoelectric transmitter was used to obtain the results shown in both panels of figure 4. The focused piezoelectric transducer arrangement (fig. 4) is seen to offer significant improvement over the planar piezoelectric transducer arrangement of figure 3. Data reproducibility and consistency remain, however, more satisfactory with the use of the acoustoelectric receiver.

In an attempt to quantitate the extent to which phase-cancellation effects resulted in degradation of attenuation-frequency data, a statistical index was developed. Because phase cancellation effects in attenuation-frequency data may manifest themselves as erratic (non-monotonic) frequency dependences (in contrast with the expected monotonic variation of attenuation with frequency), one method of segregating the data is on the basis of a statistical test of the goodness of a fit to a monotonic curve. Using a

three parameter fit to the measured signal loss data [$(V_A - V_B)$ of eq. (1)], a root mean square deviation (RMSD) was calculated. The RMSD was defined by

$$\text{RMSD} = (\nu_2 - \nu_1)^{-1} \left\{ \int_{\nu_1}^{\nu_2} [y_m(\nu) - y_c(\nu)]^2 \right\}^{\frac{1}{2}} d\nu \quad (2)$$

where ν is the ultrasonic frequency, $(\nu_2 - \nu_1)$ defining the frequency interval of the measurements. $y_m(\nu)$ is the measured signal loss at frequency ν, and $y_c(\nu)$ is the calculated signal loss, determined by a least squares three parameter fit to the data. The units of RMSD are the same as those of $y(\nu)$, in this case decibels (dB). The value of RMSD was used to quantitate the degree of non-monotonicity and thus to estimate in a relative fashion the contribution of phase cancellation effects. Large values of RMSD would be expected whenever substantial phase cancellation contributions influenced the apparent attenuation.

The application of this approach is demonstrated in figure 5, which illustrates our progress in systematically reducing artifacts due to phase cancellation. The calculated RMSD for each attenuation-frequency curve obtained with several transducer combinations is shown. Data obtained in 20 measurements with a 1.3 cm diameter planar piezoelectric receiver are shown in panel A and in 44 measurements using a 0.2 cm diameter planar piezoelectric receiver in panel B. In both cases the transmitter was a 1.3 cm diameter planar piezoelectric transducer. The reduced RMSD's of

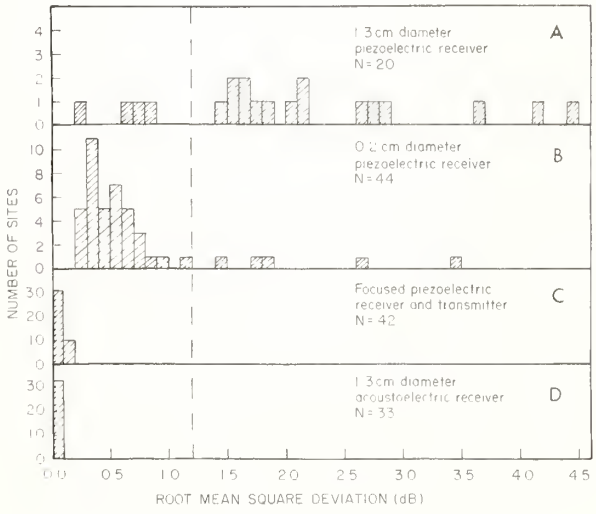

Fig. 5. Histogram showing the range of calculated root mean square deviations (RMSD's) of attenuation-frequency curves determined with four different transducer configurations.

panel B as compared with panel A presumably reflect a decrease in the phase cancellation artifacts achieved by reducing the area over which the ultrasonic field was integrated. Panel C exhibits the results of measurements on 42 sites made with a focused transducer pair and demonstrates substantial improvement over the arrangements of panels A and B. (It should be noted, however, that substantial artifacts due to phase cancellation occur in the presence of intervening tissue located outside of the focal zone. Thus, for future applications in vivo, the use of a focused transducer does not appear to be a satisfactory method for minimizing artifacts due to phase cancellation.) The results of the measurements on 33 sites using the acoustoelectric receiver are presented in panel D of figure 5. The very small RMSD's obtained with the intensity sensitive acoustoelectric receiver reflect the inherent freedom from phase cancellation artifacts, making a transducer of this design potentially suitable for future in vivo applications.

B. Tissue preparation and independent indices of pathology

All measurements were carried out in vitro on myocardial tissue obtained from adult, mongrel, 15 to 30 kg dogs. In studies of ischemic injury, each dog was intubated after anesthesia with sodium pentobarbital (25 mg/kg, intravenously), placed on a Harvard respirator, ventilated with room air, and subjected to a left thoracotomy via the fifth interspace. The pericardium was incised, and the left anterior descending coronary artery dissected free immediately distal to the first ventricular branch and ligated. The pericardium was left open. For dogs studied at 6 hours, 24 hours, and 3 days following occlusion, the chest was closed conventionally, with intrapleural suction maintained for at least one hour via a chest tube.

At the time of sacrifice, each animal was again anesthetized with sodium pentobarbital (50 mg/kg, intravenously). The heart was rapidly excised and placed in a 0.9 percent NaCl solution. To prepare the tissue for ultrasonic analysis an incision was made at the root of the aorta, continued inferiorly along the left ventricular surface of the interventricular septum to the apex, and extended posteriorly and superiorly, terminating at the base of the heart. This permitted prompt excision of a segment of the left ventricular anterior and apical wall. This segment comprised the area of infarction and surrounding area of normal myocardium in all animals subjected to coronary ligation. (We note that this segment was measured unaltered, i.e., no additional preparation such as further slicing to achieve flat or parallel surfaces was undertaken.) Except as noted, ultrasonic analysis was initiated within 5 minutes following the death of the animal, and completed within 45 minutes.

Tissue from animals sacrificed at 24 hours and 72 hours following coronary occlusion was analyzed biochemically for creatine kinase (CK) content, an established index of tissue pathology. One centimeter diameter biopsies corresponding to regions of ultrasonic analysis were obtained immediately following ultrasonic measurement. To facilitate comparison of data from different animals, regional CK activity was expressed as the percentage of depletion compared to activity in normal myocardium from the same animal. Sites with CK depletion of greater than 40 percent were classified as ischemic and those with CK depletion less than 20 percent were classified as normal.

For dogs sacrificed from 15 minutes to 6 hours following occlusion, colloidal carbon black was

injected into the left atrium fifteen seconds prior to killing the animal for the purpose of differentiating regions of ischemic and normal myocardium. Regions of ischemia did not change color after injection, while non-ischemic regions rapidly were stained black. Visual inspection of the tissue after excision was used to differentiate normal from ischemic tissue. Analysis of 60 sites from 4 control dogs indicated that the presence of dye did not alter the ultrasonic measurements of normal myocardium.

3. Results

Prior to addressing questions related to ischemic injury, it is necessary to determine experimentally the range of variability introduced into the results of ultrasonic attenuation measurements in vitro by variables such as: (1) the time interval that elapses between the sacrifice of the dog and the ultrasonic measurement, (2) the temperature of the tissue during ultrasonic measurement, and (3) the specific region of the left ventricle that is analyzed.

A. Time interval between sacrifice and measurement

In an effort to estimate the extent to which tissue degradation compromises the results of in vitro measurements, the ultrasonic attenuation coefficient of dog myocardium was measured at constant temperature as a function of time following excision. All experiments were performed in a 0.9 percent NaCl bath with temperature regulated to ± 0.2 °C by means of a controller and recirculator.

In table 1 data are displayed as a function of time following excision for experiments performed at two temperatures: (1) 19.5 °C (analysis of 27 regions from 3 hearts) and (2) 35 °C (analysis of 27 regions of 3 additional hearts). The ultrasonic attenuation coefficient as a fraction of frequency was approximately independent of time up to 4 hours following excision for tissue maintained at 19.5 °C. When the temperature was maintained at 35 °C, however, a definite change with time was observed. For measurements at 35 °C, the value of the slope of a least squares line fit to the attenuation versus frequency data changed from (0.061 ± 0.003) $cm^{-1}MHz^{-1}$ (mean ± standard error (S.E.)) at 15 minutes following sacrifice to (0.071 ± 0.003) $cm^{-1}MHz^{-1}$ at 4 hours following sacrifice. It thus appears that no statistically significant changes in attenuation occur for periods up to several hours following excision for tissue maintained at approximately 20 °C, although small (∿ 15 percent) but significant changes occur over that time interval for tissue maintained at 35 °C. These results motivated the choice of 20 °C as the temperature at which the extensive series of measurements on ischemic and normal myocardial tissue in vitro reported below were carried out.

Table 1. Ultrasonic attenuation of normal myocardium as a function of time after excision.

Time after excision	Number of sites	Number of dogs	Temp. °C	Attenuation coefficient (cm^{-1}) (mean ± SE) 2 MHz	4 MHz	6 MHz	8 MHz	10 MHz	Slope of α vs frequency (cm^{-1} MHz^{-1})
15 min	27	3	19.5	0.10 ± 0.02	0.19 ± 0.02	0.34 ± 0.02	0.38 ± 0.03	0.65 ± 0.03	0.072 ± 0.002
2 h	27	3	19.5	0.10 ± 0.02	0.20 ± 0.02	0.36 ± 0.02	0.50 ± 0.03	0.70 ± 0.03	0.075 ± 0.002
4 h	27	3	19.5	0.10 ± 0.02	0.20 ± 0.02	0.35 ± 0.02	0.49 ± 0.03	0.69 ± 0.03	0.075 ± 0.002
15 min	27	3	35	0.09 ± 0.02	0.17 ± 0.03	0.30 ± 0.03	0.43 ± 0.03	0.56 ± 0.04	0.061 ± 0.003
2 h	27	3	35	0.09 ± 0.02	0.19 ± 0.03	0.34 ± 0.03	0.47 ± 0.03	0.61 ± 0.04	0.068 ± 0.003
4 h	27	3	35	0.11 ± 0.02	0.22 ± 0.03	0.37 ± 0.03	0.52 ± 0.03	0.64 ± 0.04	0.071 ± 0.003

B. Temperature dependence of the attenuation

To relate the results obtained at 20 °C to what might be expected if the measurements were carried out at 37 °C, an additional series of experiments was designed to elucidate the temperature dependence of the attenuation in a manner relatively independent of effects arising from tissue degradation. Results from the previous series of experiments (table 1) suggested the possibility that tissue might be temporarily stored at approximately 20 °C without undergoing significant degradation between measurements made at elevated temperatures. Using this approach, four freshly excised hearts were used for a measurement of the attenuation at 20.5 °C, 25 °C, 30 °C, and 37 °C. Each segment of left ventricle was placed in a 20.5 °C bath and analyzed ultrasonically immediately after excision. After analysis at this temperature, the tissue sample and holder were removed from the measurement bath and placed in a storage bath which was maintained at 19.5 °C. The measurement bath was heated to 25 °C and regulated to maintain this temperature to ± 0.2 °C. Upon stabilization of the temperature at 25 °C, the sample and holder were reinserted into the original bath and allowed to equilibrate, whereupon the ultrasonic attenuation was measured. The same procedure was repeated for measurements at 30 °C and 37 °C, with the entire process lasting about 80 minutes. To check the validity of this method for identifying the true temperature dependence, the attenuation obtained at 37 °C using the above procedure was compared to the attenuation measured at 37 °C for 3 additional freshly excised hearts at 27 sites. The slope of the attenuation for these measurements made at 37 °C within minutes of ex-

Table 2. Ultrasonic attenuation of normal myocardium as a function of temperature.

Number of sites	Number of dogs	Temp. °C	Attenuation coefficient (cm^{-1}) (mean ± SE) 2 MHz	4 MHz	6 MHz	8 MHz	10 MHz	Slope of α vs frequency (cm^{-1} MHz^{-1})
36	4	20.5	0.10 ± 0.02	0.19 ± 0.02	0.34 ± 0.03	0.48 ± 0.03	0.64 ± 0.03	0.071 ± 0.002
36	4	25	0.10 ± 0.02	0.19 ± 0.02	0.33 ± 0.03	0.45 ± 0.03	0.61 ± 0.03	0.068 ± 0.002
36	4	30	0.10 ± 0.02	0.17 ± 0.02	0.31 ± 0.03	0.43 ± 0.03	0.58 ± 0.03	0.064 ± 0.002
36	4	37	0.11 ± 0.02	0.19 ± 0.02	0.31 ± 0.03	0.41 ± 0.03	0.56 ± 0.03	0.058 ± 0.002

cision was (0.060 ± 0.002) cm^{-1} MHz^{-1} in good agreement with the value 0.058 ± 0.002 cm^{-1} MHz^{-1} measured at 37 °C for the 36 sites of tissue stored at 19.5 °C between measurements. This result suggests that the procedure is methodologically sound.

Results of this series of experiments on 36 regions from 4 hearts designed to determine the temperature dependence of the attenuation coefficient are presented in table 2. The slope of a least squares line fit to the attenuation-frequency data decreases approximately linearly with increasing temperature over the range 20.5 °C to 37 °C, with the value at 37 °C being about 20 percent less than that at 20.5 °C.

C. Regional variations in attenuation

In order to identify possible variations in the attenuation coefficient as a function of the region of the left ventricle that was analyzed, 102 sites from 4 dogs not subjected to coronary ligation were studied and the results segregated into 4 groups based on the region investigated. Data from these experiments are presented in table 3. Values of the attenuation coefficient for regions in the mid-posterior and apical aspects of the left ventricle were essentially identical. Somewhat higher values were exhibited by regions in the papillary muscles and generally lower values were exhibited by regions near the base of the heart. These results are summarized in figure 6, utilizing the slope of a least squares line fit to the attenuation coefficient versus frequency plots for comparative purposes.

Based on the results of this study of regional variability of the ultrasonic attenuation coefficient of normal myocardium, subsequent studies were conducted primarily on sites from mid-posterior and apex, avoiding sites from the papillary muscles and the base. With this approach, the value of the slope of the attenuation for normal left ventricle, as determined from measurements at 245 discrete sites from 36 dogs, was (0.072 ± 0.001) cm^{-1} MHz^{-1} (mean ± S.E.).

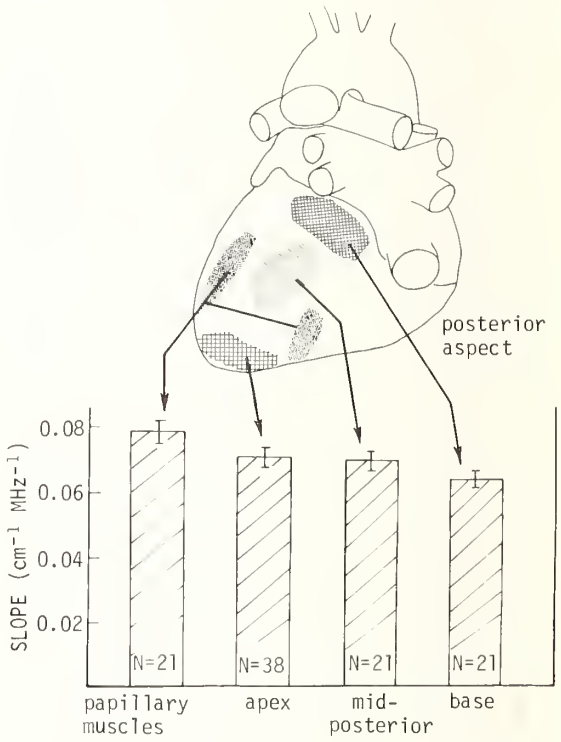

Fig. 6. Regional variation of the slope of the attenuation (2 to 10 MHz) in normal myocardium.

Table 3. Regional variation of ultrasonic attenuation in normal myocardium.

Description	Number of sites	Number of dogs	Temp. °C	Attenuation coefficient (cm^{-1}) (mean ± SE) 2 MHz	4 MHz	6 MHz	8 MHz	10 MHz	Slope of α vs frequency (cm^{-1} MHz^{-1})
Base	21	4	20	0.11 ± 0.02	0.20 ± 0.02	0.34 ± 0.02	0.46 ± 0.03	0.62 ± 0.03	0.064 ± 0.002
Mid-posterior	21	4	20	0.10 ± 0.02	0.19 ± 0.02	0.34 ± 0.02	0.48 ± 0.03	0.64 ± 0.03	0.070 ± 0.002
Apex	39	4	20	0.10 ± 0.02	0.19 ± 0.02	0.35 ± 0.02	0.49 ± 0.03	0.65 ± 0.03	0.071 ± 0.002
Papillary muscles	21	4	20	0.13 ± 0.02	0.26 ± 0.02	0.41 ± 0.02	0.55 ± 0.03	0.76 ± 0.03	0.079 ± 0.002

D. Effects of ischemic injury

To investigate changes in physical properties of tissue resulting from ischemic injury, ultrasonic measurements were carried out on freshly excised hearts previously subjected to coronary occlusion for intervals of 15 minutes, 1 hour, 6 hours, 24 hours, and 3 days. Results of these measurements are summarized in table 4. The attenuation measured at 15 minutes, 1 hour, 6 hours, and 24 hours following coronary occlusion is lower than that exhibited by normal myocardium, while that at 3 days following occlusion is higher than that of normal.

The attenuation values reported in table 4 represent averages of the values obtained for all sites analyzed. Results illustrated in figures 4 and 5 suggest that artifacts arising from phase cancellation effects may occur in data obtained using the focused transmitter-focused receiver configuration. To eliminate measurements exhibiting probable phase cancellation effects from further consideration, an index based on RMDS (eq. 2) was used to segregate the data. Attenuation coefficient *versus* frequency curves exhibing RMSD's greater than 0.25 dB were deleted from further consideration. The value 0.25 dB was selected for segregating the data because it represents an RMSD two times the maximum RMSD exhibited by data obtained using the phase cancellation insensitive acoustoelectric receiver. The results of segregating the data in this way are illustrated in table 5. The average values of the slope of the attenuation *versus* frequency curves are presented for two groups: (1) data including sites exhibiting phase cancellation effects, and (2) data excluding sites exhibiting phase cancellation effects. A comparison of the number of sites contributing to the average slope in each group indicates that a modest but significant number of attenuation *versus* frequency curves were compromised by phase cancellation effects.

The results of experiments on normal and ischemic myocardium are summarized in figure 7. The average slope of the attenuation (last column of table 5) is shown at 15 minutes, 1 hour, 6 hours, 24 hours, and 3 days following coronary occlusion. The slope of the attenuation of ischemic myocardium is significantly lower than that of normal myocardium for times ranging from 15 minutes through 24 hours following coronary occlusion and is significantly larger at 3 days following occlusion.

Table 4. Ultrasonic attenuation of normal and ischemic myocardium.

Description	Number of sites	Number of dogs	Temp. °C	Attenuation coefficient (cm^{-1}) (mean ± SE) 2 MHz	4 MHz	6 MHz	8 MHz	10 MHz	Slope of α *vs* frequency (cm^{-1} MHz^{-1})
Normal	245	36	20	0.10 ± 0.02	0.19 ± 0.02	0.33 ± 0.02	0.48 ± 0.03	0.65 ± 0.03	0.072 ± 0.001
Time after occlusion									
15 min	56	5	20	0.10 ± 0.02	0.17 ± 0.02	0.32 ± 0.02	0.43 ± 0.03	0.57 ± 0.03	0.063 ± 0.003
1 h	64	8	20	0.09 ± 0.02	0.17 ± 0.02	0.32 ± 0.02	0.43 ± 0.03	0.57 ± 0.03	0.063 ± 0.003
6 h	59	5	20	0.08 ± 0.02	0.15 ± 0.02	0.30 ± 0.02	0.44 ± 0.03	0.57 ± 0.03	0.066 ± 0.002
24 h	29	11	20	0.08 ± 0.02	0.16 ± 0.02	0.29 ± 0.02	0.43 ± 0.03	0.59 ± 0.03	0.067 ± 0.002
3 d	31	7	20	0.11 ± 0.02	0.20 ± 0.02	0.38 ± 0.02	0.52 ± 0.03	0.69 ± 0.03	0.079 ± 0.002

Table 5. Slope of the ultrasonic attenuation of normal and ischemic myocardium.

Description				Including sites exhibiting phase cancellation effects		Excluding sites exhibiting phase cancellation effects	
Time after coronary occlusion	Number of dogs	Temperature °C	Character of sites	Number of sites	Slope (cm^{-1} MHz^{-1})	Number of sites	Slope (cm^{-1} MHz^{-1})
15 min	5	20	normal	58	0.073 ± 0.003	45	0.072 ± 0.003
15 min	5	20	ischemic	56	0.063 ± 0.003	49	0.062 ± 0.002
1 h	8	20	normal	69	0.072 ± 0.003	52	0.071 ± 0.003
1 h	8	20	ischemic	64	0.063 ± 0.003	57	0.062 ± 0.003
6 h	5	20	normal	59	0.072 ± 0.002	51	0.072 ± 0.002
6 h	5	20	ischemic	59	0.066 ± 0.002	49	0.064 ± 0.002
24 h	11	20	normal	29	0.073 ± 0.002	24	0.068 ± 0.002
24 h	11	20	ischemic	29	0.067 ± 0.002	27	0.060 ± 0.002
3 d	7	20	normal	30	0.072 ± 0.002	25	0.072 ± 0.001
3 d	7	20	ischemic	31	0.079 ± 0.002	28	0.082 ± 0.002

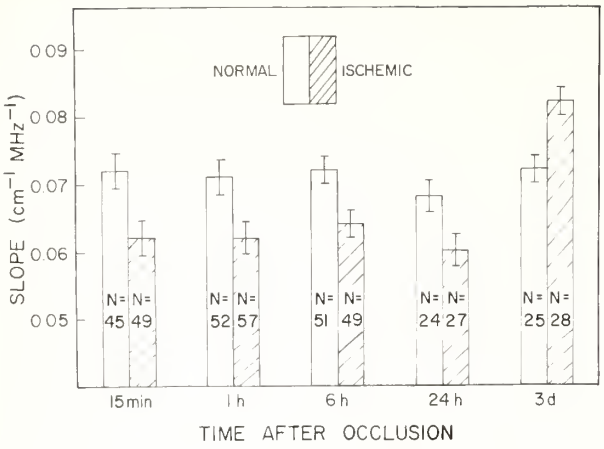

Fig. 7. Slope of the ultrasonic attenuation (2 to 10 MHz) for normal and ischemic myocardial tissue determined at specified intervals following coronary occlusion.

4. Discussion

Emphasis in the present studies was placed on systematic measurements making use of carefully defined control experiments. Either creatine kinase depletion or reduced uptake of colloidal carbon was used as an independent index for documenting myocardial ischemia. Care was taken to eliminate artifacts due to ultrasonic phase cancellation effects, a potentially significant source of variability in attenuation coefficient measurements. Methods suitable for conducting meaningful experiments on excised tissue were developed and validated. Results of the study addressing the problem of tissue degradation following excision led to the choice of $\sim$ 20 °C rather than 37 °C for the present series of investigations. The possibility of significant changes in the ultrasonic properties of tissue measured in vitro as a function of time following excision was considered by Hueter [5], and more recently by Frizell and Carstensen [6], and by Bamber et al. [7]. Previous studies examined changes for time intervals substantially larger (tens of hours) than the present experiments, which had the more limited goal of defining the range of validity of attenuation measurements on freshly excised tissue.

The temperature dependence of the attenuation of normal myocardium was measured over the range $\sim$ 20 °C to $\sim$ 37 °C using a technique designed to minimize artifacts arising from tissue degradation. Results of these measurements suggest that the data obtained at 37 °C might be expected to differ by only about 20 percent from that obtained at 20 °C. However, these limited measurements on normal myocardium do not adequately address the possibility of differences in the temperature dependence of the attenuation exhibited by ischemic as opposed to normal tissue.

Results of this study indicate a small decrease in the attenuation in the early stages of a myocardial infarct (up to 24 hours following coronary occlusion). Although mechanisms responsible for the attenuation of soft tissue are inadequately understood [8], a decrease in attenuation might be expected to accompany edema, which is a recognized correlate of recent ischemic injury. If the small decrease in attenuation of ischemic tissue is corroborated by measurements in vivo, the use of an index based on the ultrasonic attenuation to characterize the state of myocardium might be approached. Efforts to use an index based on attenuation to characterize the state of myocardial tissue might utilize each heart as its own control thus abrogating data variability due to regional myocardial variations as documented in table 3.

An increase in attenuation over that of normal myocardium is observed in tissue subjected to ischemic injury and measured three days following coronary occlusion. Previous reports from this laboratory documented substantial increases in attenuation in tissue studied 4 to 11 weeks after coronary occlusion [2,9]. This increase in attenuation, evident at three days following occlusion and reaching substantial magnitude weeks after occlusion, appears to be related to the onset of scar formation, reflecting the increase in the collagen content of necrotic tissue.

Acknowledgments

Lawrence J. Busse carried out the investigations of phase cancellation effects described in the text and presented in figures 3, 4, and 5. Pranoat Suntharothok-Priesmeyer was responsible for production of the text and illustrations.

This work was supported in part by grants HL19537, HL17646, and HL07081 from the National Institutes of Health.

References

[1] Busse, L. J., Miller, J. G., Yuhas, D. E., Mimbs, J. W., Weiss, A. N., and Sobel, B. E., Phase Cancellation Effects: A Source of Attenuation Artifacts Eliminated by a CdS Acoustoelectric Receiver, in Ultrasound in Medicine, D. White, ed., vol. 3, pp. 1519-1535 (Plenum Press, New York, 1977).

[2] Miller, J. G., Yuhas, D. E., Mimbs, J. W., Dierker, S. B., Busse, L. J., Laterra, J. J., Weiss, A. N., and Sobel, B. E., Ultrasonic Tissue Characterization: Correlation Between Biochemical and Ultrasonic Indices of Myocardial Injury, in Proceedings 1976 IEEE Ultrasonics Symposium 79, 33-43 (Cat. No. CH 1120-43U, IEEE, New York, 1976).

[3] Schwan, H. P. and Carstensen, E. L., Ultrasonics aids in diathermy experiments, Electronics, 216-220 (July 1952).

[4] Marcus, P. N. and Carstensen, E. L., Problem with absorption methods of inhomogeneous solids, J. Acoust. Soc. Am. 58, 1334-1335 (1975).

[5] Hueter, T.A., WADC Tech. Rept. 57-706 (1958).

[6] Frizell, L. A., Ultrasonic Heating of Tissue, Ph.D. Thesis, University of Rochester (1976) (unpublished).

[7] Bamber, J. C., Fry, M. J., Hill, C. R., and Dunn, F., Ultrasonic attenuation and backscattering by mammalian organs as a function of time after excision, Ultrasound in Medicine and Biology 3, 15-20 (1977).

[8] See the references listed in O'Donnell, M. and Miller, J. G., Mechanisms of Ultrasonic Attenuation in Soft Tissue (this publication, p. 37).

[9] Yuhas, D. E., Mimbs, J. W., Miller, J. G., Weiss, A. N., and Sobel, B. E., Changes in Ultrasonic Attenuation Indicative of Regional Myocardial Infarction, in Ultrasound in Medicine, D. W. White, ed., vol. 3, 1883-1894 (Plenum Press, New York, 1977).

Reprinted from *Ultrasonic Tissue Characterization II*, M. Linzer, ed., National Bureau of Standards, Spec. Publ. 525 (U.S. Government Printing Office, Washington, D.C., 1979).

ACOUSTIC MICROSCOPIC ANALYSIS OF MYOCARDIUM

Donald E. Yuhas and Lawrence W. Kessler

Sonoscan Inc.
720 Foster Avenue
Bensenville, Illinois 60106, U.S.A.

Acoustic microscopy can be employed to measure variations in the ultrasonic attenuation and velocity over spatial dimension of tens of micrometers. Knowledge of the interactions at this fine-structure level provides a more complete understanding of the response of tissues at diagnostic frequencies. In this article we investigate the ultrasonic characteristics of formalin-fixed infarcted and normal myocardium at the microscopic level. The elastic microstructure of normal tissues is found to be uniform over spatial dimensions of hundreds of micrometers. The attenuation coefficient α, at 100 MHz, ranges from 37 to 68 cm^{-1} while the velocity varies less than ± 20 m/s. Acoustic anisotropy, attributed to muscle fiber orientation, is found to be a primary source of attenuation variability. The elastic microstructure in the zones of infarction is very distinct from that in normal zones. With infarction, variations in the attenuation ranging from 38 to 100 cm^{-1} occur over dimensions of hundreds of micrometers. Accompanying this variability in attenuation is a wide distribution of velocity. The most highly attenuating regions in the infarcted tissue show localized increases in the velocity of more than 75 m/s. Such large variations in sonic velocity are sufficient in magnitude to be an important source of phase cancellation in low frequency attenuation measurements. Additionally, the 100 MHz data indicate that the frequency dependence of the attenuation coefficient observed in the 1 to 10 MHz range for infarcted and normal myocardium may not hold in the 10 to 100 MHz frequency interval.

Key words: Acoustic microscopy; anisotropy; attenuation; elastic microstructure; infarct; interferogram; phase cancellation; myocardium; velocity.

1. Introduction

The complete ultrasonic characterization of tissue can be divided into two distinct levels of interaction: 1) structures greater than the wavelength of diagnostic ultrasound and 2) structures that are finer. The larger structures give rise to specular reflections which are used to define the outlines of tissues and organs seen in conventional B-scan echograms. The finer structures give rise to characteristic scattering properties of tissue and are also responsible for intrinsic attenuation and velocity. It is this sensitivity to fine structure, that makes the diagnostic frequency ultrasonic parameters so important in determining tissue pathologies.

As an aid to understanding the low frequency scattering, attenuation, and velocity data, direct visualization of the finer structures is desirable. Conventional microscopy (optical and electron) can be used to delineate various structural components, but these methods do not provide the required information regarding the ultrasonic properties of the tissue.

On the other hand, the elastic microstructural information obtained through acoustic microscopy is directly applicable to the lower frequency (1 to 10 MHz) characteristics. Acoustic microscopy provides a means for visualizing directly the elastic architecture as well as for measuring variations in the ultrasonic attenuation and velocity properties over areas tens of micrometers in diameter. By using this technique, valuable insight can be gained into mechanisms responsible for the attenuation of sound as well as factors which influence tissue characterization measurements at lower frequencies.

This preliminary study consists of a series of acoustic microscope observations of myocardial tissue. Previous reports have shown that quantitative changes in ultrasonic attenuation over the frequency range 2 to 10 MHz are associated with regional myocardial infarction [1-4][1]. The ultrasonic attenuation in normal tissue was found to exhibit a linear frequency dependence, while infarcted tissue exhibits a significant quadratic dependence. As a clue to elucidating the nature of the change in attenuation at lower frequencies, acoustic microscopy was used to investigate the elastic microstructure of normal and infarcted myocardium.

2. Methods

Acoustic micrographs were obtained with a commercially available 100 MHz scanning laser acoustic

[1]Figures in brackets indicate literature references at the end of this paper.

microscope, SONOMICROSCOPE 100. A brief description of the technique is presented here for completeness. For a more detailed description, the reader may refer to the listed references [5-9].

Figure 1 illustrates the instrumentation used to produce 100 MHz acoustic micrographs. A sample is placed on a glass stage between an insonifying transducer and receiver. The transmitting transducer is a piezoelectric element which is bonded to a glass substrate, and the receiver is a scanning focused laser beam. The acoustic energy is coupled to the specimen through the glass substrate without need for an acoustically lossy water bath. The specimen is moistened with liquid to ensure good acoustic coupling. The sound is transmitted through the sample at an angle of 10° with respect to the normal. In order to provide a specularly reflecting surface for the scanning laser beam receiver, the specimen is covered with a partially silvered coverslip. The coverslip allows a small amount of light to penetrate to the sample and render an optical view simultaneously with the acoustic.

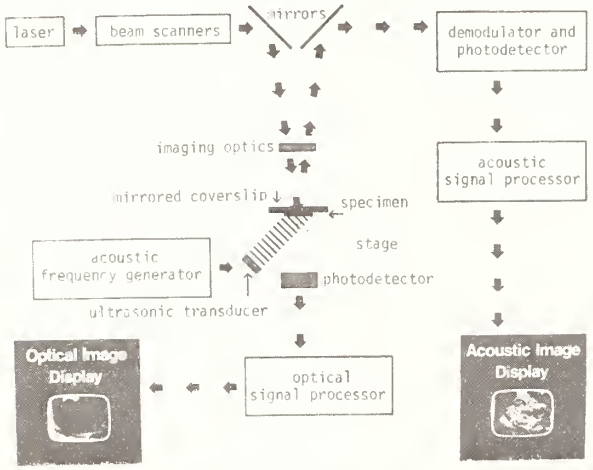

Fig. 1. Schematic diagram of the acoustic microscope used in this study. The instrument employs a scanning laser beam technique for detecting the amplitude and phase of acoustic energy transmitted through the sample. Acoustic and optical images are produced simultaneously and are presented on separate monitors.

The acoustic energy transmitted through the specimen imparts a slight oscillatory mechanical perturbation to the coverslip surface. The amplitude of these perturbations, which vary at the acoustic frequency, is inversely proportional to the localized ultrasonic attenuation properties in the underlying sample. By sensing the perturbations and displaying the signal on a TV monitor, an acoustic image is formed. Images are obtained in real time and displayed at a magnification of about 70 X. The bright regions seen on the acoustic micrographs correspond to areas of high transmission through the sample, whereas the darker areas correspond to regions of higher ultrasonic attenuation.

Quantitative attenuation measurements of the tissue observed in the microscope can be made anywhere within the field of view by an optical technique described previously [10]. With the sample in place, an acoustic image is obtained. Areas of interest are noted and readings of the image brightness are obtained with a light meter. Once the image brightness is recorded the sample is removed and replaced by an equivalent thickness of coupling medium. For this work formalin (10 percent formaldehyde) was used. Electrical attenuation is then inserted into the electro-acoustic signal path to restore the image brightness to its previous level. Although the acoustic field is quite uniform, care was taken to ensure that the same region of sound field was measured for the cases with and without the sample in place. Using this technique, attenuation can be measured over an area as small as 5×10^{-5} cm^2. The sensitivity of the photo cell used in these studies permitted discrimination of sound levels to within ± 1 dB, which introduced a 3 to 8 percent uncertainty in the measured attenuation coefficient. Because the acoustic image of the specimen is observed during the course of the measurement procedure, it is possible to select regions of low contrast structural details, thereby assuring the attenuation values obtained were free from artifacts arising from vessels or fluid filled cavities.

In addition to recording the transmissivity of specimens, the scanning laser acoustic microscope is equipped with an acoustic interferogram mode of operation. Acoustic interferograms display the localized distribution of transit times through the sample. For specimens of uniform thickness these transit time variations are directly related to localized variations in sonic velocity. Interferograms can be conceptualized with reference to figure 2. In this schematic, an ultrasonic plane wave is incident on the sample at an angle with respect to the normal. The intersection of the wavefronts with the plane below the specimen results in a series of fringes (indicated by the dots) which run in and out of the plane of the page. Using phase sensitive detection, the positions of these equiphase lines are displayed on

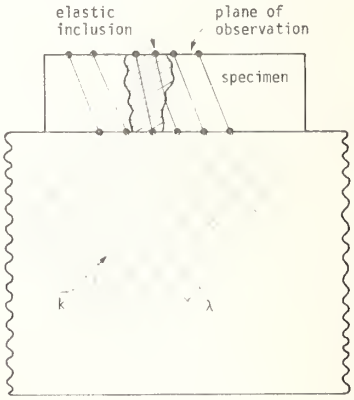

Fig. 2. Model for conceptualizing acoustic interferograms. As a plane wave propagates through a sample, regions of velocity variations cause refraction. The resulting wavefronts are displaced as they arrive at the sample surface as shown by the dots. The lateral position of the wavefronts (fringes) are a function of the change in velocity and can be calculated from the formulas given in the text.

the image monitor. Figure 3 is a micrograph of an interferogram recorded with no specimen on the stage. In this case the interferogram lines (fringes) are straight and parallel. Going from left to right, each successive interference fringe represents an increase in transit time through the glass stage of exactly one period of oscillation (10 nanoseconds at 100 MHz).

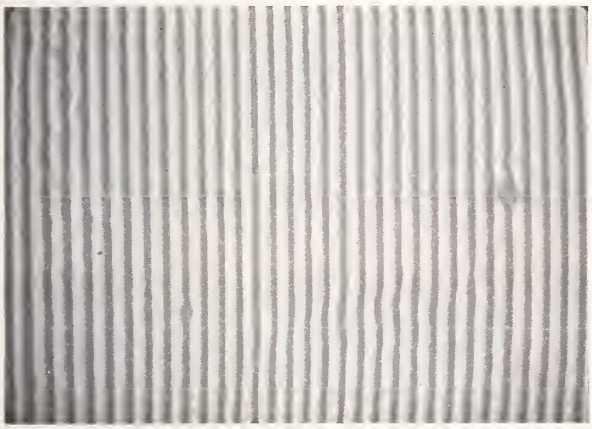

Fig. 3. Interferogram obtained eith no sample on the microscope stage showing equally spaced, parallel, interference fringes. This is the same type of interferogram that would be obtained on a sample that exhibited no regional changes in sonic velocity.

Figure 2 also illustrates the effect of elastic inhomogeneity on the position of the interferogram fringes. As the wave enters the sample it refracts according to Snell's law. In the areas of the sample with uniform propagation velocity (white areas) the separation of successive fringes after propagating through the specimen is the same as that measured with no sample. When structures with variations in propagation velocity are present, illustrated by the hatched area, the separation of successive fringes in the vicinity of the elastic inclusion changes. The magnitude of the fringe shift, N, is directly related to the propagation velocities of the two components by the following relations [11]:

$$N = \frac{\Delta t \sin \theta_1}{\lambda_1} (\cot \theta_1 - \cot \theta_2) \qquad (1)$$

where N is the dimensionless magnitude of the lateral fringe shift normalized by the unperturbed fringe spacing: λ_1 is the wavelength of sound in region 1 of the specimen; Δt is the specimen thickness; and θ_1 and θ_2 are the propagation angles in regions 1 and 2 respectively.

The relationship between the propagation angles and the sonic velocity is given by Snell's law:

$$\frac{\sin \theta_1}{c_1} = \frac{\sin \theta_2}{c_2} \qquad (2)$$

where c_1 and c_2 are the respective propagation velocities.

Using eqs. (1) and (2) and knowing the magnitude of the sonic velocity of one component in the field of view, the sonic velocities of all other areas can be determined. The primary factor determining the sensitivity of the technique for measuring variations in velocity is the sample thickness. For the sample thicknesses used in this study, a displacement of a fringe by 1/10 of the unperturbed fringe spacing (i.e., N = 0.1) corresponds to a velocity change of 5 m/s.

3. Myocardial Samples

The specimens used in this study[2] were taken from regions of formalin-fixed canine myocardium. Sections .05 ± .005 cm in thickness were made in several different myocardial regions extending from the apex to the base of the heart. The plane of dissection was oriented approximately at an angle of 45° with respect to the long axis of the heart and each section extended from epicardial to endocardial surface. Samples were taken from regions of infarcted and non-infarcted tissues with the regions of infarction lying nearer to the apex of the heart. Analysis was carried out on section taken from a single heart which had been formalin fixed for more than a year and was originally excised 4 weeks after coronary occlusion.

4. Results

Figure 4 presents an acoustic micrograph (a) and interferogram (b) obtained on a myocardial section taken from a non-infarcted region. Brightness variations in this micrograph (fig. 4a) generally range from light to dark grey. A band of lighter material approximately 1 mm wide can be seen running almost vertically through the central portion of the micrograph. On either side of this acoustically transmissive region are darker areas oriented both perpendicular and parallel to the band. Except for the dark structure (indicated by the arrow), which is attributed to a vessel, the change in brightness between the various regions is relatively subdued and gradual. The interferogram of this region (fig. 4b) shows a uniform sonic velocity distribution. Only the area indicated by the arrow exhibits an abrupt disruption of the interferogram lines showing a slight increase of sonic velocity of 20 m/s. Throughout most of the sample the lateral shifts in the interferogram lines going from the top to the bottom of the micrograph over the entire field are less than .4 fringes indicating velocity changes of less than ± 10 m/s in the vertical direction.

Figure 5 illustrates an interesting effect, that of acoustic anisotropy in myocardial tissue. These micrographs were obtained on the same sample shown in figure 4; however, the sample has been rotated 90° in the plane of the stage. Recall that the angle of insonification is approximately 10° from the specimen normal. Thus, while the major component of the propagation vector K is perpendicular to the sample, a small off-axis component leads to some dramatic changes in image contrast on rotation. The amplitude micrograph shown in figure 5a reveals two distinct regions. The upper half of the micrograph shows acoustic morphology similar to that observed in the previous micrographs. The lower half of the micro-

[2]Samples provided courtesy of Washington University, Division of Cardiology, St. Louis, Missouri.

(a)

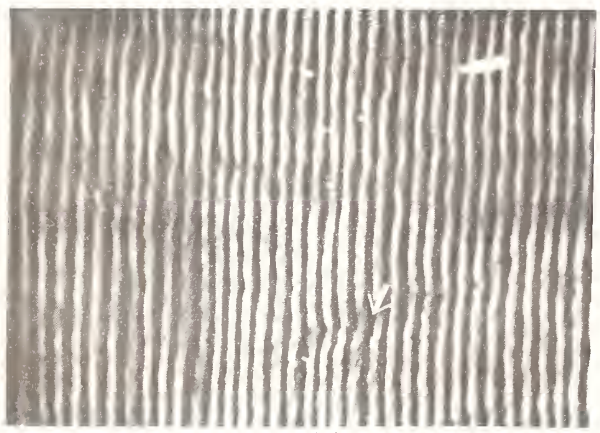

(b)

Fig. 4. Acoustic amplitude micrographs (a) and interferogram (b) of normal myocardium. The field of view in each micrograph is 2.3 by 3.0 mm and the sample thickness is 500 micrometers. In the amplitude micrograph the light areas are regions of low attenuation. The interferograms are arranged so that a lateral shift to the right corresponds to a region of increased velocity and a shift to the left, lower velocity. A shift of one fringe corresponds to a velocity change of 50 m/s. Typical variations in this sample are ± 10 m/s.

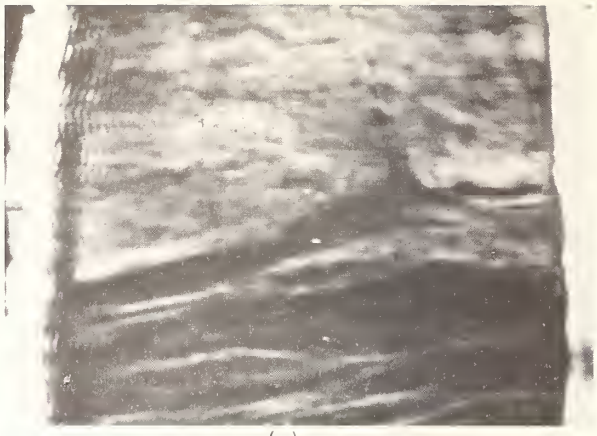

(a)

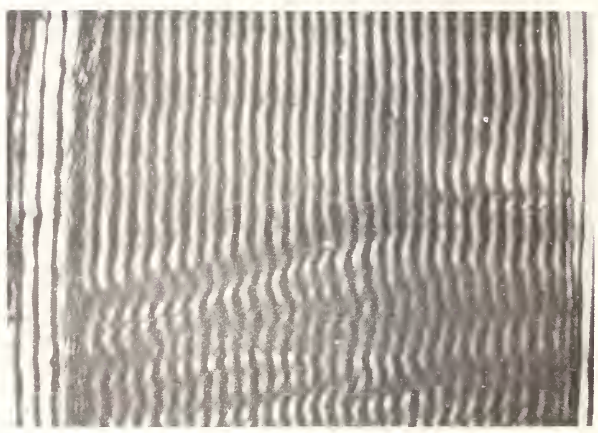

(b)

Fig. 5. Acoustic amplitude micrograph (a) and interferogram (b) of the same region depicted in figure 4 after sample rotation (counter-clockwise) by 90°. The dramatic changes in these images compared to figure 4 are due to the tissue being anisotropic acoustically.
The top portion of the interferogram shows velocity variations of ± 5 m/s, while variations of 40 m/s are seen in the lower portion of the micrograph.

graph is significantly different, showing bands of acoustically light and dark material running horizontally across the field of view. The change of acoustic contrast is abrupt across these boundaries and their morphology suggests that they arise from muscle fiber orientation. In this micrograph the off-axis component of the propagation vector k is parallel to the acoustic striations seen in the micrograph, i.e. with the grain, whereas in the previous figure it is perpendicular or across the grain.

It should be emphasized here that the portion of the sample comprising the lower half of this field of view (fig. 5a) is the same area as that imaged in the left half of figure 4a. Some of the most highly attenuating areas seen in figure 5a become the least attenuating areas as the sample is rotated in the sound field. The acoustic interferogram of the same region is shown in figure 5b. Again, the spatial distribution character of sonic velocity in the upper portion of the micrograph is similar to that seen in figure 4b. The sonic velocity in this region is 1580 m/s with typical variations less than ± 5 m/s. In the darker regions the interferogram lines become quite jagged, indicative of sharply localized changes in sonic velocity. Typical shifts here are on the order of 0.8 normalized fringes, corresponding to an increase in velocity of 40 m/s.

Figures 6a and 6b show a comparison between interferograms obtained on normal and infarcted tissue. The interferogram obtained on the normal

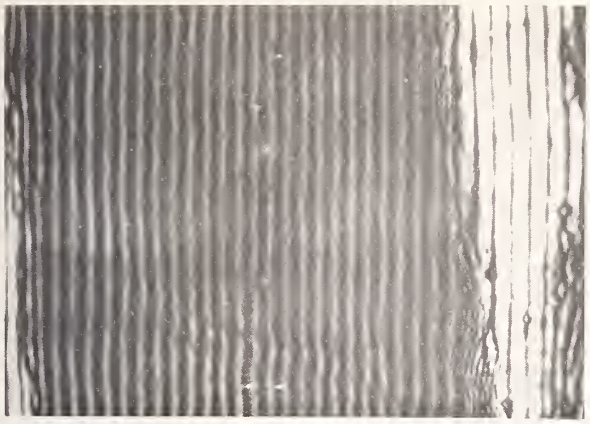

(a)

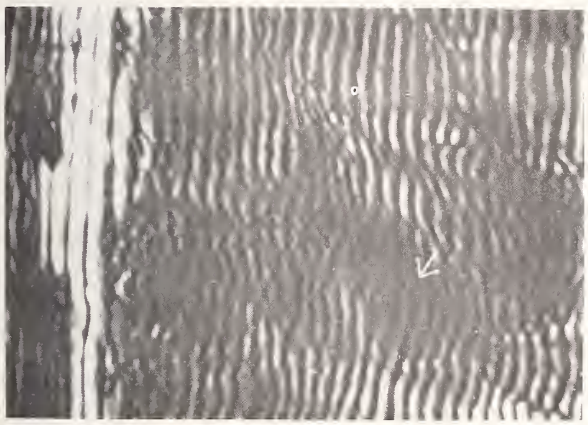

(b)

Fig. 6. Interferograms comparing normal and infarcted tissue. (a) Interferogram of normal tissue shows uniform attenuation and velocity. Velocity variations are typically ± 5 m/s. (b) Interferogram of infarcted tissue. Both attenuation and sonic velocity are highly variable. Typically, the highly attenuating areas show increased sonic velocity, for example, the region indicated by the arrow has a velocity of 75 m/s higher than the surrounding tissue.

specimen (fig. 6a) shows similar characteristics as discussed previously, i.e. uniform attenuation and velocity over the field of view. In contrast, the most distinctive feature of the infarcted tissue (fig. 6b) is its overall microelastic inhomogeneity. There are small regions of this micrograph which show uniform velocity profiles and attenuation characteristics (similar to normal tissue), however, there also exists a number of highly attenuating (darker) areas. These dark areas show increases in sonic velocity of more than 75 m/s compared to that seen in the neighboring tissue. The complex interference fringe pattern indicates that, in the infarcted zones, there is considerable variation in the sonic velocity on a microscopic scale.

On several sections, ultrasonic attenuation measurements were made at 100 MHz. The results

Table 1. Summary of 100 MHz attenuation measurements.

Section	Attenuation range (cm^{-1})	Number of measurements
A non-infarct	48	1
B non-farct[a]	43[b]	2
B non-infarct[c]	41 - 68	2
C non-infarct	37 - 61	2
D infarct	38 - 100	5
E infarct	27 - 70	5

[a] Off-axis component of sound is perpendicular to grain.
[b] Off-axis component of sound is parallel to grain.
[c] Typical value.

are presented in table 1. Sections A through C were obtained from normal regions while sections D and E were obtained from zones of infarction. Each attenuation measurement was made on a small region of tissue ($1 \times 10^{-4} cm^2$) and, in general, several different areas on each section were measured. The range of attenuation measured in a section is given in column 2 of the table. The variations tabulated here represent structural variations in the tissue as opposed to uncertainties in the measurement technique (which are on the order of ± 10 percent). The number of measurements made on each section was governed primarily by the image contrast as seen on the TV monitor. Areas that looked distinct on the monitors were subsequently measured. Thus, sections with uniform attenuation properties were subjected to fewer measurements than sections displaying a variety of brightness levels.

The attenuation values obtained in the 3 sections of normal tissue range from 37 to 68 cm^{-1}. For section B, two entries are presented in the table corresponding to the two different orientations of the section in the sound field. The first entry, $B_{\perp}$, represents measurements made on section B in the orientation depicted in figure 4a, while the second entry, $B_{\parallel}$, presents measurements made in the orientation depicted in figure 5a. The attenuation measured in the B orientation show relatively minor variations from the typical value of 43 cm^{-1}. In contrast, measurements on the same section in the $B_{\parallel}$ orientation yield values ranging from 41 to 68 cm^{-1}. Perhaps the most striking feasure of the acoustic anisotropy is the observation that the same area that yields an attenuation coefficient of 45 cm^{-1} in orientation $B_{\perp}$ gives a value of 68 cm^{-1} in the $B_{\parallel}$ orientation. Thus, variations in attenuation which are attributed solely to anisotropic propagation are of the same magnitude as variations observed in different sections.

The attenuation measured in the zones of infarction serve to quantify the visual impression given by the acoustic micrographs. Infarcted zones show inhomogeneous attenuation properties with variations ranging between 27 and 100 cm^{-1} for the two sections analyzed. The highly attenuating zones with attenuation coefficients in excess of 70 cm^{-1}, are morphologically distinct from any features present in the non-infarcted regions.

5. Discussion

This study presents some acoustic microstructure characteristics of myocardial tissue at a frequency of 100 MHz. The features revealed in the acoustic micrographs as well as the quantitative attenuation and velocity data can lead to important conclusions with regard to the complete ultrasonic characterization of tissues.

First of all, 100 MHz acoustic micrographs can be used to distinguish between and recognize infarcted and normal tissue. The most distinctive feature of the infarcted zone is the high degree of localized variations in attenuation and velocity. Such acoustic contrast could result from fibrous scar tissue distributed in a matrix of normal myocardium. The highly attenuating, high sonic velocity regions can be attributed to areas of substantial scar. This identification is consistent with lower frequency measurements on tissues rich in collagen [12].

Secondly, significant acoustic anisotropy, arising from muscle fiber orientation, has been observed at 100 MHz. One of the sections analyzed (sample B) showed a large orientational dependence, and this may have been due to the particular geometry of the fibers. With a small component of the propagation vector K along the fiber an increase in attenuation was observed. This is in the same direction as the attenuation anisotropy previously observed in striated muscle at lower frequencies [13]. The magnitude of change in attenuation is rather substantial, 45 to 68 cm^{-1}, indicating that structural aspects and tissue architecture play an important role in determining overall attenuation. The orientation effect favors scattering type loss mechanism.

Thirdly, the large velocity variations measured in the infarcted tissue may have important consequences for low frequency attenuation measurements. Phase cancellation losses have been implicated as a primary source of artifact in attenuation measurement made using piezoelectric receivers [14,15]. Although small diameter ($\sim$ .2 cm) receiving transducers or confocal pairs of transducers can be used to minimize phase cancellation loss, they do not completely eliminate it. Phase cancellation occurs when inhomogeneities in the tissue distort the ultrasonic phase fronts presented to a spatially extended piezoelectric receiving transducer. The interferogram, figure 6b, displays the high degree of wavefront distortion which actually occurs in infarcted myocardium. Quantitatively, the distortion is greater than 1.5 fringes or 540° in phase over a distance which is smaller than the diameter of the small receiving transducer (.2 cm) measurement reported at lower frequency [2-4].

Lastly, it is interesting to compare the attenuation measurements made at 100 MHz with those obtained at lower frequencies. Figure 7 is a plot of the attenuation coefficient divided by frequency (α/f) vs f. The data in the frequency range 2 to 10 MHz were reported previously and are average attenuation values obtained on fresh myocardium excised 4 to 5 weeks after vascular occlusion [4]. On the other hand, the 100 MHz data, taken from table 1, represent the range of attenuation values in the infarcted and non-infarcted zones.

Analysis of figure 7 indicates that for normal tissue, in the frequency interval 2 to 10 MHz, α/f has a relatively constant value of .07 cm^{-1} MHz^{-1}.

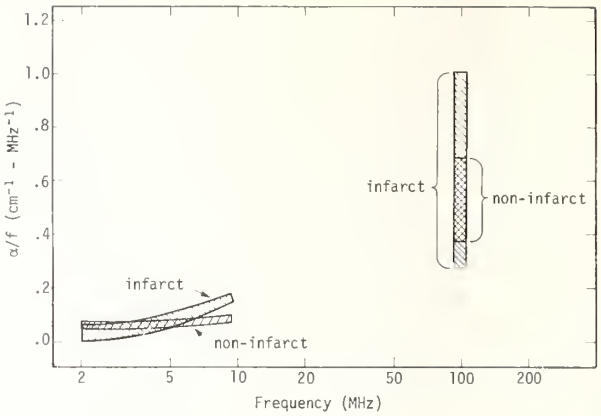

Fig. 7. Comparison of 100 MHz attenuation data with that obtained at lower frequencies for infarcted and non-infarcted myocardium. Low frequency data are taken from the work of Miller et al. [4] while the 100 MHz data are from table 1.

The 100 MHz values reported here are substantially higher (.37 to .68 cm^{-1} MHz^{-1}). For the infarcted tissue, the 2 to 10 MHz α/f values increase with frequency. Linear extrapolation of these data would predict a value of 1.9 cm^{-1} MHz^{-1} at 100 MHz. However, the most highly attenuating regions observed in the infarcted zones at 100 MHz have α/f values of 1.0 cm^{-1} MHz^{-1}, a value significantly lower than that predicted. Thus, the α/f versus f dependence for normal and infarcted tissue predicted in the range 1 to 10 MHz may no longer hold in the interval 10 to 100 MHz.

The following limitations to this conclusion should be pointed out. First of all, the referred to low frequency data were obtained on freshly excised tissue, while this 100 MHz investigation used formalin fixed tissues. Although data obtained on other tissues, e.g., kidney, indicate that the effect of formalin on the overall attenuation values at 100 MHz may not be significant [10], this has not yet been verified for the myocardium. The second point concerns orientation effects. The lower frequency measurements were made by transmitting sound through the myocardial wall roughly perpendicular to the epicardial surface, while the 100 MHz measurements were done in a plane perpendicular to this. Results presented in this study indicate the presence of an orientational effect on the acoustic properties.

Although more comprehensive work needs to be done to quantify the extent to which orientation and fixing influence the acoustic properties, the results of this study show that high frequency acoustic microscopy can play an important role in the understanding and characterization of tissues at diagnostic frequencies.

Acknowledgment

The stimulating discussions with W. D. O'Brien, University of Illinois are gratefully acknowledged.

References

[1] Lele, P. P. and Namery, J., A computer-based ultrasonic system for detection and mapping

of myocardial infarcts, in Proc. San Diego Biomed. Symp. 13, 121 (1972).

[2] Yuhas, D. E., Mimbs, J. W., Miller, J. G., Weiss, A. N., and Sobel, B. E., Changes in Ultrasonic Attenuation Indicative of Regional Myocardial Infarction, in Ultrasound in Medicine, D. White, ed., Vol. 3 (Plenum Press, New York, 1977).

[3] Mimbs, J. W., Yuhas, D. E., Miller, J. G., Weiss, A. N., and Sobel, B. E., Detection of myocardial infarction in vitro based on altered attenuation of ultrasound, Circulation Research (in press).

[4] Miller, J. G., Yuhas, D. E., Mimbs, J. W., Dierken, S. B., Busse, L. J., Weiss, A. N., and Sobel, B. E., Ultrasonic Tissue Characterization: Correlation between Biochemical and Ultrasonic Indices of Myocardial Injury, in Proc. of IEEE Ultrasonic Symposium, J. deKlerk and B. McAvoy, eds., Cat. No. 76 Ch. 1120-4SU, p. 33 (Annapolis, 1976).

[5] Korpel, A., Kessler, L. W., and Palermo, P. R., An acoustic microscope operating at 100 MHz, Nature 232, 110 (1971).

[6] Kessler, L. W., Korpel, A., and Palermo, P. R., Simultaneous acoustic and optical microscopy of biological specimens, Nature 239, 111 (1972).

[7] Kessler, L. W., Palermo, P. R., and Korpel, A., Practical High Resolution Acoustic Microscopy, in Acoustical Holography, G. Wade, ed., Vol. 4, p. 51 (Plenum Press, New York, 1972).

[8] Kessler, L. W., Palermo, P. R., and Korpel, A., Recent Developments with the Scanning Laser Acoustic Microscope, in Acoustical Holography, P. S. Green, ed., Vol. 5, p. 15 (Plenum Press, New York, 1974).

[9] Kessler, L. W., The Sonosmicroscope, in Proc. of IEEE Ultrasonic Symposium, J. deKlerk, ed., p. 735, Cat. No. 74-CHO-896-1 SU (IEEE, New York, 1974).

[10] Kessler, L. W., VHF ultrasonic attenuation in mammalian tissue, J. Acoust. Soc. Am. 53 1759 (1973).

[11] Kessler, L. W., Tissue Characterization by Means of Acoustic Microscopy, in Ultrasonic Tissue Characterization, M. Linzer, ed., Spec. Publ. 453, p. 261 (U.S. Government Printing Office, Washington, D.C., 1976).

[12] O'Brien, W. D., Jr., The Role of Collagen in Determining Ultrasonic Propagation Properties in Tissue, in Acoustical Holography, L. W. Kessler, ed., Vol. 7 (Plenum Press, New York, 1977).

[13] Dussik, K. T. and Fritch, D. J., Determination of Sound Attenuation and Sound Velocity in the Structures Constituting the Joints and of the Ultrasonic Field Distribution within the Joints on Living Tissues and Anatomical Preparations, both in Normal and Pathological Condition, Progress Report, Project A454, Public Health Service, April (1955), September (1956).

[14] Marcus, P. N. and Carstensen, E. L., Problems with absorption methods of inhomogeneous solids, J. Acoust. Soc. Am. 58, 1334 (1975).

[15] Busse, L. J., Miller, J. G., Yuhas, D. E., Mimbs, J. W., Weiss, A. N., and Sobel, B. E., Phase Cancellation Effects: A Source of Attenuation Artifact Eliminated by a CdS Acoustoelectric Receiver, in Ultrasound in Medicine, D. White, ed., Vol. 3, pp. 1519-1535 (Plenum Press, New York, 1977).

Reprinted from *Ultrasonic Tissue Characterization II*, M. Linzer, ed., National Bureau of Standards, Spec. Publ. 525 (U.S. Government Printing Office, Washington, D.C., 1979).

ACOUSTIC PROPERTIES OF NORMAL AND ABNORMAL HUMAN BRAIN

F. W. Kremkau, C. P. McGraw, and R. W. Barnes

Bowman Gray School of Medicine
Winston-Salem, North Carolina 27103, U.S.A.

Attenuation and propagation speed at 1, 3, and 5 MHz and specific acoustic impedance at 2 MHz were measured in vitro in 10 tissue samples from 8 abnormal human brains. The results were compared to values resulting from a study of 5 normal human brains reported elsewhere. Conclusions from literature review are that attenuation is lower in gliobastoma than in normal brain and attenuation, propagation speed and impedance are higher in meningioma than in normal brain. Conclusions from the data of the present study are that subarachnoid hemorrhage appears acoustically normal; infarcts have normal attenuation but increased speed; clots, intracerebral hemorrhage, and metastases have increased attenuation and speed; hydrocephalic brain has very low attenuation and low speed. In general, it appears that abnormal conditions produce increases in all three acoustic properties studied.

Key words: Attenuation; brain tumor; clot; hemorrhage; hydrocephalus; impedance; infarct; speed; ultrasonic.

1. Introduction

As part of a study of acoustic properties of normal and abnormal tissues, attenuation and propagation speed at 1, 3, and 5 MHz and specific acoustic impedance (hereafter called impedance) at 2 MHz were measured in vitro in 10 tissue samples from 8 abnormal human brains.

Results from our study of 23 tissue samples from 5 normal human brains are reported elsewhere [1][1]. The important observations were:

(a) attenuation measured with piezoelectric transducers resulted in higher values (0 to 50 percent) than those obtained using radiation force method;
(b) attenuation (using transducer method) was 0.9 dB/cm at 1 MHz and was a function of $f^{1.1}$ over the range 1 to 5 MHz;
(c) propagation speeds at 1 MHz were 1546 and 1539 m/s for fresh and fixed tissues, respectively;
(d) speed dispersion was 2 ms^{-1} MHz^{-1} and 1.6 ms^{-1} MHz^{-1} for fresh and fixed tissues, respectively;
(e) white matter had attenuation 1.4 times that for gray;
(f) attenuation of adult brain was 2.7 times that for infant;
(g) one day aging reduced attenuation up to 20 percent;
(h) attenuation depended upon temperature to the power -0.1 and -0.5 at 1 and 5 MHz, respectively;
(i) propagation speed as a function of temperature exhibited a minimum at approximately 15 °C.

The differences between white and gray matter and between infant and adult attenuation can be explained on the basis of tissue water content. The minimum in propagation speed with respect to temperature may indicate a sensitivity to the crystal-liquid crystal phase transition for membrane phospholipid bilayers.

There are several reports in the literature regarding the acoustic properties of normal and abnormal human brain tissue. A review of the data for normal brain may be found in our earlier report [1]. In addition, reported values for impedance are 1.59 x 10^6 MKS rayl (kg/m^2s) for "brain" [2], 1.60 for cerebellum [2], 1.51 for cerebrum [3], and 1.52 for white matter [4].

An early paper by Wild and Reid [5] showed differences in received echo patterns for normal brain and several malignant and benign tumors. More recently Fishman, Heyser, and Le Croissette [6] reported high attenuation in tumor regions of human brain sections using qualitative transmission images. A summary of the data for abnormal brain is given in table 1. Only tumors are cited as no other abnormality was found in the literature. Table 2 shows an attempt to simplify this summary and draw some conclusions from it. It lists reports of greater (+), equal (=), or lesser (-) values for attenuation, speed, or impedance as compared to the same authors' values for normal brain tissue. Citing only those situations where at least two reports are in agreement, the following are concluded:

(a) attenuation is lower in glioblastoma than in normal brain;
(b) attenuation is higher in meningioma than in normal brain;
(c) propagation speed and impedance are higher in meningioma than in normal brain.

[1]Figures in brackets indicate literature references at the end of this paper.

Table 1. Attenuation, propagation speed, and impedance for several brain tumors--literature summary.

Tissue	Frequency (MHz)	Attenuation (dB/cm)	Speed (m/s)	Impedance (10^6 MKS rayl)	Reference
acoustic neurinoma	4	-	1522-1547	1.57-1.62	2
	5	6-8	-	-	7
arachnoidal sarcoma	4	-	1530	1.58	2
astrocytoma	5	7	-	-	7
	-	-	1660	1.71	8
	-	-	1545	-	9
	-	-	1517[a]	1.64[a]	9
craniopharyngioma	5	9-12	-	-	7
ependymoma	4	-	1537-1545	1.60-1.62	2
	5	9	-	-	7
	2	-	1501	1.54	9
glioblastoma	5	6-9	-	-	7
	5	3.3[a]	-	-	10
	3	20[a]	-	-	11
	1	0.5	-	-	12
	1	0.5	-	-	13
glioma	4	-	1525-1547	1.57-1.61	2
	2	-	1529	1.56	9
	2	-	1500	1.54	9
medulloblastoma	5	8-11	-	-	7
meningioma	4	-	1540-1550	1.61-1.64	2
	5	10-13	-	-	7
	-	-	1640	1.72	3
	2	-	1546-1569	-	9
	2	-	1524[a]	1.57[a]	9
	5	6.3[a]	-	-	10
	1	0.9-1.2	-	-	12
	1	0.6-1.2	-	-	13
	5	35	-	-	14
metastatic adenocarcinoma	-	-	1590	1.68	3
	1	0.3	-	-	12
metastatic carcinoma	4	-	1535	1.60	2
	5	8-10	-	-	7
	5	4.3[a]	-	-	10
	5	-	-	1.52	4
oligodendroglioma	5	7	-	-	7
pinealoma	5	9	-	-	7
pituitary adenoma	5	7	-	-	7
retinoblastoma	-	-	1600	1.67	3
spongioblastoma	4	-	1532	1.59	2

[a]Formalin fixed samples.

Table 2. Attenuation, propagation speed, and impedance are higher than (+), equal to (=), or lower than (-) that for normal tissue as measured by the same authors. There is a consensus that glioblastoma has lower attenuation and that meningioma has higher attenuation, speed, and impedance.

Tumor	Attenuation	Speed	Impedance	Reference
acoustic neurinoma		+	+	2
	-			7
arachnoidal sarcoma		-	-	2
astrocytoma	-			7
		+	+	8
craniopharyngioma	+			7
ependymoma		+	+	2
	+			7
glioblastoma	-			7
	-			10
	+			11
	-			12
	-			13
glioma		=	=	2
medulloblastoma	+			7
meningioma		+	+	2
	+			7
		+	+	3
	+			10
	+			12
	+			13
	+			14
metastatic adenocarcinoma		+	+	3
	-			12
metastatic carcinoma		+	+	2
	=			7
	+			10
			=	4
oligodendroglioma	-			7
pinealoma	=			7
pituitary adenoma	-			7
retinoblastoma		+	+	3
spongioblastoma		=	=	2

2. Materials and Methods

Normal and abnormal human brain tissue samples were obtained at autopsy. Measurements were made at 37 °C after at least 24 hours of fixation in 10 percent formalin. Except during measurement, tissues were stored at 4 °C. Tissue samples were cut to fill the sample holder - a Teflon® ring with inner diameter 33 mm, outer diameter 45 mm, and (sample) length 15 mm. Saran® membranes were stretched over both sides of the chamber to provide flat tissue surfaces and acoustic windows. The sample holder fit into a guide in a temperature controlled water bath which provided consistent placement (within 1 mm in each coordinate) relative to source and receiver transducers. The transducers were one inch diameter Valpey-Fisher polished 1 MHz X-cut quartz. The source transducer was driven by an Arenberg PG-650C pulsed oscillator. Bursts were typically 20 cycles long and reasonably characterized by a single (fundamental) frequency. The receiver transducer was connected to the input of a 7A18 amplifier in a Tektronix 7904 oscilloscope with a 7B92 dual time base. Amplitude of received burst, with and without tissue sample between transducers, was measured and attenuation coefficient, calculated from the following relation:

$$m = \frac{1}{d}\left[20 \log_{10} \frac{A_o}{A_1} - m_c\right] + m_w$$

where m and m_w are attenuation coefficients in dB/cm of tissue sample and water, respectively, m_c is window loss in dB, d is sample thickness in cm, A_o is received amplitude with sample not present (water path), and A_1 is received amplitude with sample present. Amplitudes were measured with precision ± 2 percent or better and accuracy (based on Tektronix specification) within 2 percent. Measurements were taken at 1, 3, and 5 MHz. Corrections for m_c and m_w are normally less than 1 percent except m_c at 3 and 5 MHz (typically 2 and 7 percent, respectively). The value for m_c is obtained by measuring the received amplitude change when a water filled chamber is inserted between the transducers. Additional reflection loss resulting from impedance discontinuity between water and tissue is not significant.

Propagation speed was calculated using the arrival time change occurring when the sample was inserted between source and receiver transducers. $c = d/(t_2 - t_s)$ where c is propagation speed in the tissue sample in m/s, d is sample thickness in meters, t_1 is propagation time in seconds in d path length of water, and t_s is arrival time change in seconds when sample is introduced into sound path. Arrival time changes are typically 200 to 400 ns read to a precision of ± 10 ns and accuracy (based on Tektronix specification) within 5 percent. Measurements were taken at 1, 3, and 5 MHz.

Acoustic impedance was measured using the method of Gregg and Palagallo [4]. A Parametrics Pulser/Receiver 5050PR was used with a Hoffrel 310A 2.0 MHz, 13 mm diameter diagnostic transducer. Display was produced on the Tektronix 7904 oscilloscope.

3. Results

The results of seven abnormal conditions are given in table 3. With respect to attenuation and propagation speed, the following observations are made:

(a) subarachnoid hemorrhages appear normal acoustically;
(b) infarcts have normal attenuation but increased speed;
(c) clots, intracerebral hemorrhage, and metastases have increased attenuation and speed;
(d) hydrocephalic brain has very low attenuation and low propagation speed.

Impedance values do not correlate well with tissue type or with propagation speed values.

Table 3. Acoustic properties for seven abnormal conditions in human brain.

Tissue	Attenuation (dB/cm)			Speed (m/s)	Impedance (10^6 MKS rayl)
	1 MHz	3 MHz	5 MHz	1 MHz	2 MHz
normal[a]	0.9	2.8	5.2	1539	1.43
metastatic lung carcinoma	1.5	5.6	11.0	1568	1.56
ventricular clot[b]	2.3	9.6	12.2	1575	1.55
subarachnoid hemorrhage[c]	0.9	3.2	5.6	1535	1.73
intracerebral hemorrhage	1.9	8.2	12.8	1553	1.78
hemorrhagic infarct with necrosis	0.9	3.0	5.7	1552	1.72
Island of Riel infarct	0.9	3.2	6.6	1556	1.46
hydrocephalus	0.2	0.8	1.3	1516	2.13

[a] See reference [1]. Impedance value was obtained by measurement on one normal brain of the five studied with respect to attenuation and propagation speed.
[b] Mean of three samples.
[c] Mean of two samples.

4. Discussion

In general, it appears that abnormal conditions produce increases in all three acoustic properties studied. The measured metastatic carcinoma values agree reasonably well with those of others [4,7] (see table 1). The low attenuation for hydrocephalus is similar to that reported for infant brain where high water content was suggested as an explanation [1]. The low propagation speed for hydrocephalus was not observed in the normal infant. Our results show normal attenuation for infarcts (1 to 5 MHz). Miller et al. [15] observed an increase in attenuation for dog heart after infarct but this was evidenced only at frequencies above 5 MHz. Lele and Namery [16] reported increased attenuation above 2 MHz for infarcted dog heart compared to normal. They also observed reduced impedance for infarct which was not observed in our study of brain.

Few of these abnormal tissues have been studied by more than one group. Much more data will be required before confident generalizations can be agreed upon.

Acknowledgments

The authors are grateful for technical assistance from Ms. S. Gaskey.

This work was supported in part by NINCDS Contract NO1-NS-4-2304.

References

[1] Kremkau, F. W., McGraw, C. P., and Barnes, R. W., Ultrasonic attenuation and preparation speed in normal human brain, submitted for publication, J. Acoust. Soc. Am.

[2] Schiefer, W., Kazner, E., and Kunze, S., Clinical Echo-Encephalography, pp. 67-68 (Springer-Verlag, New York, 1968).

[3] Ishikawa, S., Yukishita, K., and Ito, K., Ultrasonic attenuation in brain (7th report), Jap. Med. Ultrasonics 3, 33 (1965), quoted in reference 7.

[4] Gregg, E. C. and Palagallo, G. L., Acoustic impedance of tissue, Investigative Radiol. 4, 357-363 (1969).

[5] Wild, J. J. and Reid, J. M., The effects of biological tissues on 15-mc pulsed ultrasound, J. Acoust. Soc. Am. 25, 270-280 (1953).

[6] Fishman, L. S., Heyser, R. C., and Le Croissette, D. H., Ultrasonic transmission measurements in human brain sections, Radiology 112, 211-213 (1974).

[7] Ishikawa, S., Yukishita, K., Sato, K., Ito, K., and Wagai, T., Ultrasonic attenuation in brain tissue (the 7th report), Jap. Med. Ultrasonics 3, 48 (1965).

[8] Uematsu, S. and Walker, A. E., A Manual of Echoencephalography, p. 40 (Williams and Wilkins, Baltimore, 1971).

[9] Van Venrooij, G. E. P. M., Measurement of ultrasound velocity in tissue, Ultrasonics 9, 240-242 (1971).

[10] Tanaka, K., Yukishita, K., Ito, K., Ehara, K., and Watanabe, H., Ultrasonic diagnosis of brain tumors, Proc. Intl. Symp. on Echo-Encephalography, (1967), pp. 38-44, quoted in Erikson, K. R., Fry, J. J., and Jones, J. P., Ultrasound in medicine - a review, IEEE Trans. Sonics Ultrasonics SU-21, 144-170 (1974).

[11] Le Croissette, D. H. and Heyser, R. D., Attenuation and Velocity Measurements in Tissue Using Time Delay Spectrometry, in Ultrasonic Tissue Characterization, M. Linzer, ed., National Bureau of Standards Spec. Publ. 453, pp. 81-95 (U.S. Government Printing Office, Washington, D.C., 1976).

[12] Oka, M. and Yosioko, K., Ultrasonic absorption of human brain tissue, Paper #1302 presented at World Congress of Ultrasound in Medicine, San Francisco (1976).

[13] Nakaima, N., Study of the ultrasonic attenuation of brains bearing tumors, J. Wakayama Med. Soc. 27, 69-106 (1976).

[14] Kikuchi, Y., Tanaka, K., and Wagai, T., Early cancer diagnosis through ultrasonics, J. Acoust. Soc. Am. 29, 824-833 (1957).

[15] Miller, J. G., Yuhas, D. E., Mimbs, J. W., Dierker, S. B., Busse, L. J., Laterra, J. J., Weiss, A. N., and Sobel, B. E., Ultrasonic tissue characterization: correlation between biochemical and ultrasonic indices of myocardial injury, IEEE Ultrasonics Symposium Proceedings (1976) IEEE Catalogue No. 76 CH 1120-5SU, pp. 33-43.

[16] Lele, P. P. and Namery, J., A Computer-Based Ultrasonic System for the Detection and Mapping of Myocardial Infarcts, in Proceedings San Diego Biomedical Symposium, pp. 121-132, San Diego Biomedical Symposium, San Diego, California, 1974.

Reprinted from *Ultrasonic Tissue Characterization II*, M. Linzer, ed., National Bureau of Standards, Spec. Publ. 525 (U.S. Government Printing Office, Washington, D.C., 1979).

FREQUENCY DEPENDENT ATTENUATION OF MALIGNANT BREAST TUMORS STUDIED BY THE FAST FOURIER TRANSFORM TECHNIQUE

E. Kelly Fry, N. T. Sanghvi, and F. J. Fry

Indiana University School of Medicine and
Indianapolis Center for Advanced Research
Indianapolis, Indiana 46202, U.S.A.

and

H. S. Gallager

The University of Texas System/Cancer Center
Houston, Texas 77025, U.S.A.

The work discussed in this paper comprises one aspect of an experimental design concerned with the use of multi-discipline examination methods to provide detailed information on the interaction of normal and malignant breast tissues with a high frequency sound field. The complete experimental design included x-ray and needle biopsy examination of the breast of a patient prior to mastectomy, followed by: x-ray examination of the excised breast (the malignant tumor remained intact in the excised breast); ultrasound visualization and FFT studies of the formalin-fixed, excised breast specimen; x-ray examination of 0.5 cm thick, whole breast sections of the tissue; and, finally, sectioning and histological staining of the primary malignant tumor region and other tissue areas of interest. Emphasis is given in this preliminary report to a study of attenuation of the sound beam as a function of frequency for specific tissue paths (i.e., from skin to back surface of the excised breast), which included (1) the malignant tumor, (2) the nipple and (3) the areola.

For the tissue path which included the malignant tumor, the FFT studies indicate that the attenuation for the full range of frequencies studied (1.1 to 4.4 MHz) was greater than that of any other area of the breast. A significant result of the investigations reported in this paper is the determination that this analytical technique is feasible and can yield data on malignant and normal regions of breast tissue which correlate with the ultrasound visualization imaging information and with the tissue structure information as revealed by histological examination.

Key words: Attenuation of areola; attenuation of breast tissue; attenuation of malignant tumors; breast cancer detection; breast carcinoma; breast examination techniques; FFT techniques for breast; histology of breast tumors; signal processing for tissue; x-ray examination of breast.

1. Introduction

At the present time, ultrasound visualization techniques, if used in conjunction with other clinical examination methods, can improve the level of success in the differential diagnosis of breast pathologies [1][1]. However, the theoretical capability of ultrasound for providing a successful method of early detection of breast cancer is not presently realized, in part because of the lack of sufficient clinical studies with this method and, in addition, because of the need for more basic experimental studies on the interaction of ultrasound and breast tissue. There is, in fact, a serious need for relatively sophisticated investigations concerned with (1) the complex structure of normal breast in terms of its interaction with sound fields and (2) the variability in structural features of malignant tumors (including those in the same pathology classification) insofar as this variability is significant to medical diagnostic data obtained by ultrasound examination of such tumors.

The experimental work discussed in this paper comprises one aspect of an overall approach of using multi-discipline examination methods, namely, x-rays, ultrasound visualization, signal processing of ultrasound transmission data (i.e., Fast Fourier Transform (FFT) techniques) and histological techniques to provide detailed information on the structural features of breast tissue and their interaction with a high frequency sound field. In the initial experimental stages,

[1]Figures in brackets indicate literature references at the end of this paper.

procedures such as the FFT are best performed on an excised breast. A special preparation, namely, an excised, formalin-fixed breast with a known intact malignant tumor, was used in the investigations discussed in this paper. Detailed examination of such breasts, by both standard and experimental breast cancer detection methods, and the correlation of the results with tissue structure information provided by histological investigations, can yield data that is pertinent to early breast cancer detection [2-8]. The rationale, validity and value of studying such fixed, whole specimens by ultrasound visualization techniques have been discussed in detail by Kelly Fry and Gallager in a previous publication [8]. Additionally, Calderon et al. have published results of an investigation on the ultrasound attenuation values of formalin-fixed breast tumors [9].

In capsule form, the overall experimental design called for collection of data first by x-ray examination of the breast of the patient prior to surgery, followed by: x-ray examination of the excised breast; detailed ultrasound visualization and FFT studies of the formalin-fixed excised breast specimen; whole breast sectioning of the tissue in blocks of approximately 0.5 cm in thickness; x-ray examination of each of these cross sections and, finally, sectioning and histological staining of the primary malignant tumor region and other tissue areas of interest.

The FFT studies were considered in the nature of a feasibility study and it is in that regard they are reported in this paper. Emphasis is given in this preliminary report to a study of attenuation of the sound beam both in the region of the malignant tumor and in other areas of the breast tissue (such as nipple and areola) as a function of frequency. As used in this paper, the term "attenuation" designates all losses in sound pressure amplitude or intensity as the acoustic beam traverses the tissue, including those due to specular reflection, scattering, refraction, absorption and diffraction.

Both the location (as revealed by x-ray examination of the whole, excised breast) and the malignant character of the primary mass (as revealed by needle biopsy) were known at the time of the ultrasound visualization and FFT studies. At the time of this writing, the histological classification of the primary malignant tumor has been determined and detailed histological studies are underway. The precise correlations between information revealed by histology, ultrasound visualization and FFT techniques will be the subject of a later paper.

2. Experimental Methods

The tissue specimen used in the subject study was an excised, formalin-fixed, left breast of a female subject who was 49 years of age at the time of the mastectomy. Since the diagnosis of breast carcinoma had been made by x-ray and needle biopsy prior to surgery, the mastectomy was carried out without a surgical biopsy so that the excised breast contained the previously detected malignant mass in an essentially undisturbed state. After excision, the breast was made to assume its approximate normal contour by pinning it to a layer of paraffin, was x-rayed and then formalin-fixed. The fixation process consisted of covering the pinned breast with 10 percent formalin solution, completely draining this solution and adding a fresh formalin solution every other day for a total period of two weeks. After the completion of this process, the breast was maintained in formalin solution except for periods of ultrasonic examination.

The instrumentation used for pulse-echo examination of the excised breast was a linear scan, B-mode visualization system which included a variety of types of transducers. Only two of these transducers were used as transmitters in the FFT studies, namely, 1.1 MHz and 4.4 MHz center frequency units. Most of the FFT studies were carried out with the 4.4 MHz unit and the results obtained with this transducer will be discussed in this paper. This transducer has a diameter of 1.9 cm, a 7.5 cm focal length, a midband frequency response of 4.4 MHz, a band width of 3 MHz just above noise, and 1 MHz at the 3 dB point.

During the visualization scanning procedures, the breast and examining transducers were completely immersed in mammalian Ringer's solution at room temperature (23 °C) so that there was direct fluid coupling of the ultrasound to the tissue. Both transverse (medial-to-lateral) and longitudinal (superior-to-inferior) scans were taken at distance intervals of 1 to 2 mm. In order to relate data recorded on the echograms to specific areas of the tissue, an anatomical landmark on the tissue (such as the center of the nipple or the center of a prominent skin discoloration over the area of abnormality) was selected and a highly reflective and attenuating acoustic target placed on this landmark. With the focus of the transducer set on the target center, the echogram of the breast tissue showed a distinct, easily identified front surface reflection and an attenuation shadow of the target. Since the linear coordinates (X and Y) were recorded for each echogram, subsequent scans of the tissue with the target removed could be directly related to the chosen anatomical landmark. These surface landmarks were subsequently used in the FFT experiments for identification of desired sound transmission tissue paths.

For the ultrasound attenuation studies in the transmission mode, the previously described axisymmetric focused transducer was used as a transmitter, and a 4 mm diameter, 10 MHz frequency, PZT ceramic sandwich-type piezoelectric probe was used as a receiver. A Panametrics Model 5050R unit pulse-excited the transmitter, and a series unit step attenuator was used to attenuate the ultrasonic received signals prior to their entrance into an amplifier receiver. The breast preparation was mounted on a three-motion coordinate system in a temperature controlled mammalian Ringer's bath (average temperature 23 °C) and positioned between the sending and receiving transducers, with the anterior aspect of the tissue facing the sending transducer (fig. 1). With this arrangement, any area of the tissue could be easily examined and the tissue could be moved in 1 mm steps in the three-axis coordinate system.

In order to record the system's reference waveform, transmitter and receiver transducers were placed facing each other and adjusted in position to receive the optimum plane wave acoustic signals. A linearity test of the system was performed by setting the attenuator unit at different values and comparing the corresponding outputs of the FFT

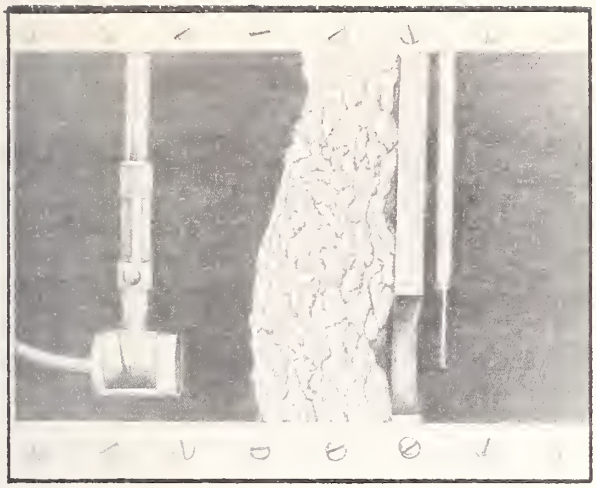

Fig. 1. Experimental arrangement of examining transducer (left), excised breast (side view) and receiving transducer.

spectrum. The system was found to be accurate to ± 1 dB in the useable frequency band, for any particular transmitting transducer. The received ultrasonic waveforms were digitized at a sampling rate of 10 or 20 nanoseconds using an eight bit Biomation Model 8100 digitizer and then transferred to a PDP-11/45 computer. Generally, four waveforms were digitized for each tissue region of interest (i.e., nipple, areola, etc.), stored on a computer disc, and later processed using a 1024 point FFT. In order to obtain attenuation and phase-angle versus frequency plots, they were deconvolved with the original system's reference waveform. The waveforms were transformed into the frequency domain and the absolute amplitude for each waveform was compared with the amplitude of the reference waveform for the relative attenuation measurement. To obtain the phase angle for each waveform, the phase was compared with the reference waveform and subsequently linearized for each frequency. For optimum frequency resolution, appropriate sampling intervals were selected on the Biomation digitizer. The output was presented in a graphical form in three different formats; namely, normalized pressure amplitude, attenuation and phase-angle spectra. The phase-angle data is presented in a separate paper [10].

The tissue was sampled at various selected regions by moving the specimen across the ultrasound beam on the three-axis system. The regions of interest chosen for this study were specific tissue paths (i.e., from skin to back surface of the specimen) which included 1) the malignant tumor, 2) the nipple and 3) the areola. In that regard, eighteen separate transmission mode studies were made in the tumor path, nine in the areola path and eight in the nipple path. In addition, the upper inner aspect of the breast was chosen as representative of normal, middle-aged, mammary adipose tissue and test ultrasound transmissions were made in that region.

Following completion of the FFT studies, the tissue was longitudinally sliced to produce whole breast sections from 5 to 8 mm in thickness. Each of these cross sections was x-rayed and the radiographs studied to determine which specific regions of the breast would be further examined by means of histological techniques. Tissue cubes 2 x 2.5 cm in overall dimensions were excised from the selected regions of interest and prepared for histological study. The primary malignant mass was included in one of these cubes of tissue.

3. Results

The ongoing histological studies indicate that the primary malignant mass was an invasive carcinoma of duct cell origin with an intermediate degree of differentiation. The mass was multinodular, fairly well circumscribed but not encapsulated, with a dense fibrotic center and a peripheral shell (3 to 4 mm thickness) of neoplastic cells. The fibrotic tissue, representing the major tumor mass, was highly collagenous but the cellular shell had a minimum deposit of collagen.

Included in the illustrations shown in this paper are duplications of the recorded system reference waveform (normalized pressure amplitude versus frequency) for sound wave transmission through Ringer's solution, compared to the waveforms recorded for sound transmission through breast tissue immersed in Ringer's solution. Such pressure amplitude graphical displays are presented in order to demonstrate the characteristics of the reference waveform and the dynamic range limitations of the system.

Before discussing the results obtained for the tissue path that included the malignant tumor, it is of interest to consider the attenuation values obtained for the areola and nipple tissue path regions of the breast which, on the basis of the x-ray examination, can be assumed normal. In calculating precise attenuation values, on the basis of the recorded, normalized pressure amplitude values, the tissue path length was taken as the distance between the anterior surface of the skin overlying the nipple or areola and the posterior surface of the breast specimen (as determined by the previously obtained ultrasound visualization images of the breast specimen). Therefore, it is emphasized here that the attenuation values shown in figures 3 and 4 are not specifically for areola or nipple, but are for the tissue path that includes these structures.

Figure 2 presents reoorded pressure amplitude waveforms for four sound transits through the nipple at entrance points separated by 2 mm of surface tissue. These waveforms show the maximum variability in pressure amplitude (differences in pressure amplitude for waveforms A, B, C, D) found for the nipple region. The attenuation frequency spectrum plot for the nipple path shown in figure 3 is based on the pressure amplitude waveforms shown in figure 2 and the tissue path length (surface of nipple to back surface of the specimen) traversed by the sound wave.

Figure 4 is the attenuation frequency spectrum for the areola region of the breast. As in the case of the nipple, this data is also based on differences in pressure amplitude response curves (three sound transits through the areola region at entrance points separated laterally by 1 mm of surface tissue) and the tissue path length (areola skin to back surface of the specimen). All other sound transmissions in the areola path gave results within the range of values shown in figure 4. The tissue region of greatest attenuation, as shown in figure 4, was located closer to the nipple in comparison to the other two sound transit regions.

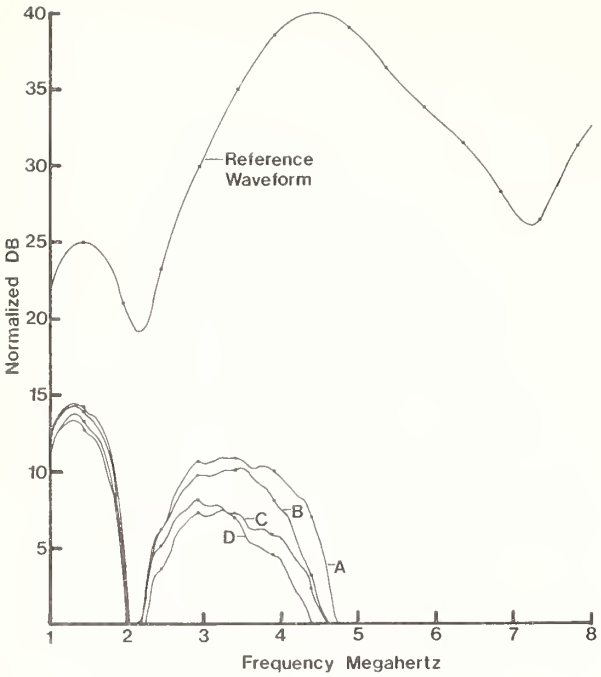

Fig. 2. Computer recorded display of: (a) reference waveform for ultrasound transmission through Ringer's solution only; (b) waveforms A, B, C, D for ultrasound transmission through four separate regions of the "nipple tissue path" of an excised, formalin-fixed breast immersed in Ringer's solution.

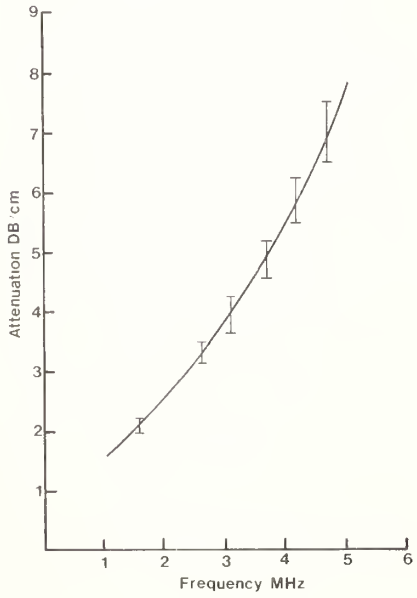

Fig. 3. Attenuation frequency spectrum for "nipple tissue path" based on waveforms shown in figure 2.

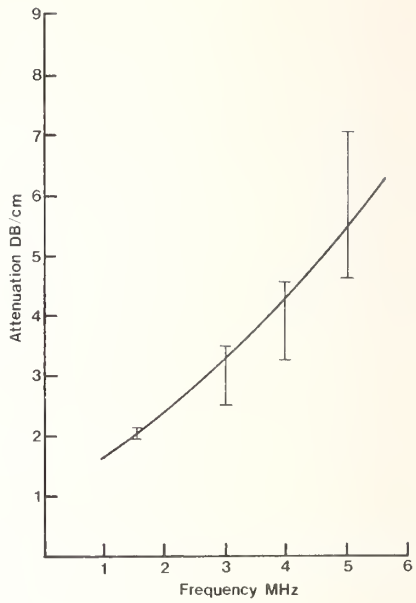

Fig. 4. Attenuation frequency spectrum for "areola tissue path" based on three sound transmissions through separate regions of the areola.

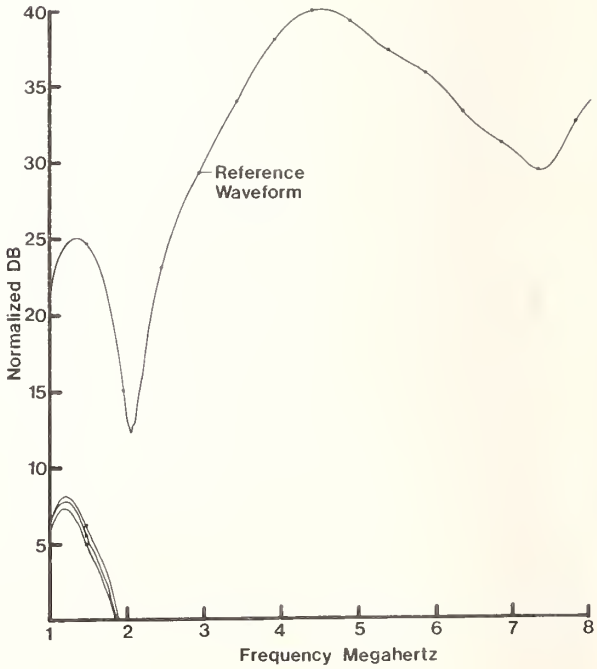

Fig. 5. Computer recorded display of: (a) reference waveform for transmission through Ringer's solution only; (b) three waveforms for ultrasound transmission in separate regions of the "tumor tissue path" of an excised, formalin-fixed breast immersed in Ringer's solution.

The waveform recordings shown in figure 5 resulted from three sound transits in the tumor tissue path, with each of the test points separated by 1 mm of tumor tissue in terms of skin surface distance. In contrast to results obtained in all other tested regions of the breast, the recorded waveform data show a total lack of recorded pressure amplitude response in the higher frequency regions. This result indicates that there is at least 40 dB of amplitude loss, for the tissue path from skin to back surface, in the frequency regions above approximately 2 MHz. At the lower end of the frequency spectrum, pressure amplitude response was recorded but, as shown later in this paper, the level of these pressure amplitudes indicates a greater attenuation for the tumor tissue path than for that of the nipple tissue path.

For the main body of the primary malignant tumor, the overlying tissue is approximately 1.5 cm in depth (from skin to anterior border of overt mass); the tumor has a diameter of 1.5 cm in depth and the tissue below the tumor is approximately 2 cm in depth. X-ray examination of the excised breast indicated the tissues surrounding the tumor were primarily fatty in nature. Consequently, if the attenuation for the 3.5 cm of tissue surrounding the tumor is considered to be that of normal breast adipose tissue and, further, if the attenuation value for such tissue is assumed comparable to that found in the present studies for tissue paths (skin to back of tissue) through other fatty regions of the breast, namely, 2.5 dB/cm at 2.0 MHz, then the tissues surrounding the tumor account for 8.8 dB of the attenuation. It should be noted that the 2.5 dB/cm value for breast adipose tissue is in general agreement with that found by Calderon et al. [9], namely 2.3 dB/cm at 2.25 MHz for formalin-fixed, excised, normal breast tissue. Deducting the 8.8 dB from the 40 dB maximum dynamic range response of the system and taking into account the 1.5 cm tumor path, it is found that the attenuation for the malignant tumor itself is 21 dB/cm at a frequency of 2 MHz. Since this value is in general agreement with that of Calderon et al. who found an attenuation of 20 dB/cm at 2.25 MHz for formalin-fixed, excised, malignant breast tumors, it is expected that the 40 dB dynamic range limitation, which represents a factor of 100 in pressure amplitude and 10,000 in intensity, is close to an adequate dynamic range response.

Carrying out the same type of calculation, using the pressure amplitude data shown in figure 5 for the lower frequencies, gives an attenuation value for the malignant mass of 8 dB/cm at a frequency of 1.5 MHz. This is calculated on the basis of 3.5 cm of normal fatty breast tissue, with an attenuation value of 2.0 dB/cm at 1.5 MHz (as found for other normal fatty regions of this breast specimen) and a 1.5 cm depth of tumor mass.

Of the total of 18 separate runs through the tumor tissue path, with the exception of two sound transits in a particular region of this path, all recorded results indicated that for frequencies above 2 MHz there apparently was total attenuation of the sound wave (i.e., within the 40 dB recording level capability of the system). The exceptional cases showed 1) a pressure amplitude waveform that was highly, but not completely, attenuated by the tumor path and thus was within the 40 dB maximum dynamic range of the system and 2) for a sound transit in an area just 2 mm laterally distant from that of number one above, a pressure amplitude waveform which had precisely the same frequency spectrum, pressure amplitude response as that found for normal fatty regions of the breast. On the basis of this result, it was assumed, prior to the histological examination, that the tumor included a border region of less density (conjectured to be a mixture of normal and neoplastic tissue) than the central mass and an adjacent region of distinct adipose tissue. Based on pressure amplitude data and the known tissue path, an attenuation value of 13 dB/cm at a frequency of 2 MHz was calculated for this border area of neoplastic tissue.

The histological studies, to date, clearly show adipose tissue immediately adjacent to and surrounding the malignant mass, thus accounting for the characteristics of the waveform which duplicated those of the fatty regions of the breast. The 3 to 4 mm thick neoplastic shell located adjacent to the adipose tissue and surrounding the fibrotic center of the tumor presumably accounted for the 13 dB/cm attenuation value.

4. Discussion

At the present time, in clinical studies concerned with the use of pulse-echo methods for breast examination, differential diagnosis is primarily based on the characteristics of the wall of the tumor, the presence and nature of the echoes from the internal structure of the tumor and the existence or absence of a shadowing phenomenon resulting from the attenuation of acoustic energy by a malignant mass. In evaluating each of these parameters, considerable emphasis and reliance is placed on the so-called "attenuation shadow" which, when present, is generally considered to be indicative of the presence of a malignant mass. However, precise knowledge regarding attenuation characteristics of normal, benign and malignant breast tissue is extremely limited. This is a serious deficit since its consequence may be misdiagnosis of the benign or malignant nature of a breast tumor.

Considerable care should be used in interpreting attenuation shadows produced by pulse-echo examination of breast, with specific regard to the question of whether normal or benign tissues can produce significant shadowing effects. In that regard, Kobayashi has found that fat necrosis results in an attenuation shadowing comparable to that produced by a malignant mass, as judged by pulse-echo visualization [11]. Calderon et al.'s studies at a frequency of 2.25 MHz of formalin-fixed excised breast tissue gave values of 20 dB/cm for malignant masses, 9 dB/cm for benign masses and approximately 2.3 dB/cm for normal breast tissue surrounding the tumors [9]. Although there is a significant difference between attenuation values for benign and malignant tumors as found by these investigators, it must be realized that in the clinical pulse-echo methods, differential diagnosis is made on the basis of a comparison between the image pattern of the overt mass and that of the surrounding normal tissue. Therefore, the Calderon et al. data indicate that for pulse-echo techniques in which the sound beam makes two passes through the breast, common sized benign tumors (2 cm and above) with an attenuation of 9 dB/cm could result in shadowing in relation to surround-

ing normal tissue with an attenuation value of 2.3 dB/cm. Additionally, the first author of this paper recently found, in the case of several clinical patients, each with an overt, benign mass within the breast (identified by x-ray examination and confirmed by surgical biopsy), that the echograms obtained using standard pulse-echo methods at frequencies of 4.4 MHz to 5.0 MHz displayed distinct shadows in the region of the mass. The significance of this result, insofar as the present paper is concerned, is the recognition of the need for quantitative attenuation data on multiple types of benign and malignant breast tumors, as opposed to simple visual inspection of shadow phenomena of such masses and consideration of whether signal processing techniques may provide some of the needed data [12].

The FFT studies discussed in this paper, for the tissue path which included the malignant tumor, showed that the attenuation for the full range of frequencies studied (1.1 to 4.4 MHz) was greater for this tissue path than for that of any other area of the breast. Further, these findings were consistent with those found in the visualization echograms, that is to say, even at a frequency of 1.1 MHz, this specific tumor could be recognized by "pale shadowing," while at the higher frequencies the attenuation shadow was more opaque and formed a distinctive border in relation to adjacent tissue.

From the viewpoint of possible in vivo breast examinations by FFT methods, it is of interest that in the present study the dual structural components of the tumor (as shown by the two attenuation values) and the adipose tissue surrounding the tumor were recognized prior to any histological investigations. Further, the finding that the total malignant mass was attenuating but the greater attenuation was in the region of fibrosis agrees with earlier studies [8] relating attenuation (as judged by nonquantitative pulse-echo methods) of breast tumors with specific tumor tissues (as revealed by detailed histological studies). The highly collagenous nature of the primary malignant mass combined with its high attenuation values and the minimum collagen content of the surrounding cellular shell is of interest in regard to the relative importance of elastic properties versus physical structural make-up for sound reflection and transmission through overt tissue masses [13]. The ongoing histological studies and the preliminary phase-angle data may provide some information on this aspect [10].

There are many factors, both tissue and instrumentation related, associated with the attenuation in the nipple path region as determined by the FFT ultrasound transmission studies discussed in this paper. Included in the tissue aspects are the nonuniform structure of the skin surface and the variable tissue components within the nipple and in the regions deep to the nipple. Although the above factors may be significant, information which is relevant to present pulse-echo clinical techniques can be derived from the preliminary FFT data without complete analysis of such parameters. In that regard, for example, the results shown in figure 3 are important in relation to detection of an overt breast mass located in the region directly posterior to the nipple. If pulse-echo techniques are applied to scan directly over the nipple region, there may be a lack of success in detecting such masses (particularly at frequencies of the order of 5 MHz) because of their location in the attenuating path of the nipple. For the purposes of tumor detection, therefore, the tissues deep to the nipple should be viewed by scanning from the side regions of the breast and by using lower frequencies. These two approaches to visualizing structures deep to the nipple were successfully applied by the present authors in the case of the excised breast discussed in this paper, and breasts studied in vivo.

To accomplish the overall aim of the studies carried out in this preliminary investigation, that is, to correlate x-ray, visualization, FFT analysis and histological findings, requires extensive and time-consuming investigations. However, if some of the significant parameters that are relevant to differential diagnosis of breast tumors by ultrasonic techniques are to be determined by methods other than the necessarily slow process of interpreting ultrasound clinical data, such detailed investigations are necessary. A significant result of the investigation reported in this paper is the determination that this computer based, signal processing technique is feasible and can yield data on malignant and normal regions of breast tissue. It also appears evident from these experiments that similar investigations could be carried out on freshly excised whole breast tissue. If such investigations are successful, then this technique could be considered for application to breast patient examination. Success in that regard could lead directly to development of an ultrasound breast examination technique which might eventually limit the need for surgical biopsy to a small number of exceptional cases.

Acknowledgments

Grateful acknowledgment is made to the assistance of George W. Gardner, ultrasound technologist, in all aspects of the above studies.

This research was supported by the Grace M. and Ralph W. Showalter Residuary Trust, and by the Indianapolis Center for Advanced Research, Inc.

References

[1] Kobayashi, T., Review: Ultrasonic Diagnosis of Breast Cancer, in Ultrasound in Medicine and Biology, Vol. 1 (1975), pp. 383-391.

[2] Gallager, H. S. and Martin, J. E., The Pathology of Early Breast Cancer, in Breast Cancer: Early and Late, The University of Texas, M. D. Anderson Hospital, pp. 37-50 (Year Book Medical Publishers, Inc., Chicago, 1968).

[3] Gallager, H. S. and Martin, J. M., The study of mammary carcinoma by mammography and whole organ sectioning, Cancer 23 (4), 855-873 (1969).

[4] Fry, E. Kelly, Franklin, T. D., Jr., and Gallager, H. S., Ultrasound Visualization of Excised Breast Tissue: An Experimental Approach to the Problem of Precise Identification of Structure from Echogram Data, Acoustical Society of America meeting, Washington, D.C., April (1971).

[5] Fry, E. Kelly, Gallager, H. S., and Franklin,

T. D., Jr., In Vivo and In Vitro Studies of Application of Ultrasonic Visualization Techniques for Detection of Breast Cancer, in Proc., IEEE Ultrasonics Symposium, Miami, Florida, December (1971).

[6] Martin, J. E. and Gallager, H. S., Reflections on Benign Disease: A Radiographic-Histologic Correlation, in Early Breast Cancer Detection and Treatment, H. S. Gallager, ed., pp. 177-181 (John Wiley and Sons, New York, 1976).

[7] Fry, E. Kelly, The Use of Ultrasound Methods to Detect Changes in Breast Tissue Which Precede the Formation of a Malignant Tumor, in Acoustical Holography, L. W. Kessler, ed., pp. 1-20, Vol. 7 (Plenum Publishing Corp., New York, 1977).

[8] Fry, E. Kelly and Gallager, H. S., A Research Approach to Visualization of Breast Tumors by Ultrasound Methods, in Ultrasound: Its Application in Medicine and Biology, F. J. Fry, ed. (Elsevier Scientific Publishing Co., Amsterdam, 1978).

[9] Calderon, C., Vilkomerson, D., Mezrich, R., Etzold, K. F., Kingsley, B., and Haskin, M., Differences in the attenuation of ultrasound by normal, benign and malignant breast tissue, J. Clin. Ultrasound 4 (4), 249-254 (1976).

[10] Fry, E. Kelly, Sanghvi, N. T., Fry, F. J., Gardner, G. W., and Gallager, H. S., Determination of Alterations of Phase Angle of Ultrasound Transmitted Through a Malignant Breast Tumor: A Preliminary Investigation, in Ultrasound in Medicine, D. White, ed., Vol. 4 (Plenum Publishing Corp., New York, 1978).

[11] Kobayashi, T., Takatani, O., Hattori, N., and Kimura, K., Study of sensitivity-graded ultrasonotomography of breast tumor (preliminary report), Med. Ultrasonics 10 (1), 38-40 (1972).

[12] Lizzi, F., Katz, L., St. Louis, L., and Jackson-Coleman, D., Applications of spectral analysis in medical ultrasonography, Ultrasonics 14 (2), 77-80, March (1976).

[13] Fields, S. and Dunn, F., Correlation of echographic visualizability of tissue with biological composition and physiological state, J. Acoust. Soc. Amer. 54 (3), 809-812 (1973).

Reprinted from *Ultrasonic Tissue Characterization II*, M. Linzer, ed., National Bureau of Standards, Spec. Publ. 525 (U.S. Government Printing Office, Washington, D.C., 1979).

CORRELATION OF ULTRASONIC ATTENUATION WITH CONNECTIVE TISSUE CONTENT IN BREAST CANCERS

Toshiji Kobayashi

Division of Clinical Electrophysiology
Department of Internal Medicine
National Cancer Center Hospital
5-1-1, Tsukiji, Chuo-ku, Tokyo-104, Japan

In recent years, ultrasonic techniques have been applied to the diagnosis of breast cancer. Various characteristics suggestive of tumor pathology have been determined. In this paper, some of these signs, such as the acoustic middle shadow and the complete disappearance of the distal limit of the tumor mass echo, are correlated with the connective tissue content of various breast cancers. Because of the high acoustic impedance of connective tissue relative to the other tissues, tumors rich in connective tissue are believed more strongly to attenuate the ultrasonic waves and thus to cause shadows in the tissues beyond them.

Key words: Attenuation; breast cancer; cancer; connective tissue; differential diagnosis; medullary carcinoma; papillary carcinoma; scirrhous carcinoma; shadowing; ultrasound.

1. Introduction

Because of its noninvasive nature, diagnostic ultrasound is a good clinical tool for the fine visualization of soft tissue pathologies. This technique has been applied in the past several years to the differential diagnosis of breast tumors with high diagnostic accuracies. Echographic criteria for differentiating malignant and benign lesions have been reported by several investigators [1-8][1].

Echographic patterns of shadowing beyond tumors (retromammary shadowing) provide reliable and accurate diagnostic information for the diagnosis of breast cancer. In this paper, various malignant signs, such as the acoustic middle shadow sign and the complete disappearance of the distal limit of the tumor mass echo, are shown to be correlated with the connective tissue content within the breast cancer. Because of the high acoustic impedance of connective tissue relative to the other tissue, tumors rich in connective tissue are believed more strongly to attenuate the ultrasonic waves and thus to cause shadows in the tissues beyond them.

2. Method and Results

During the past five years, 1617 cases of palpable breast tumors were examined echographically and all cases with breast cancer were verified by mastectomy. This material forms the basis of this retrospective study. The method of examination is shown in figure 1. The criteria for the differential diagnosis of breast tumors can be divided into three major categories comprising (1) the boundary echoes and shape, (2) internal echoes, and (3) shadowing, as illustrated in figure 2.

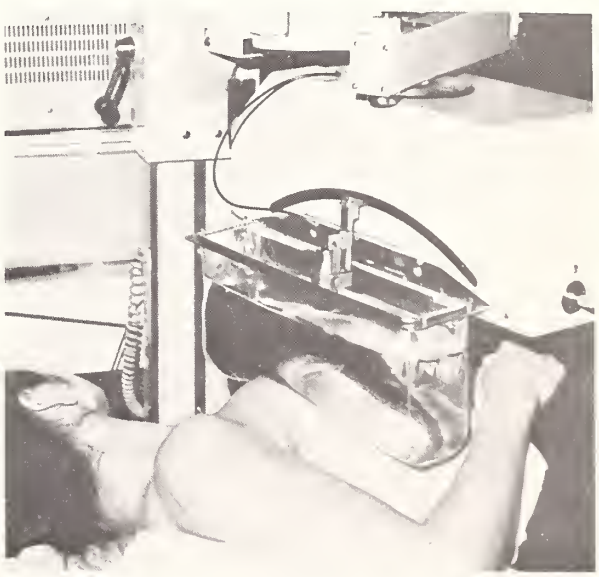

Fig. 1. Method of scanning the breast. The 5 MHz probe is moved automatically along the arc of a circle, and ultrasonic coupling to the patient is through the water in the flexible plastic bag.

[1]Figures in brackets indicate literature references at the end of this paper.

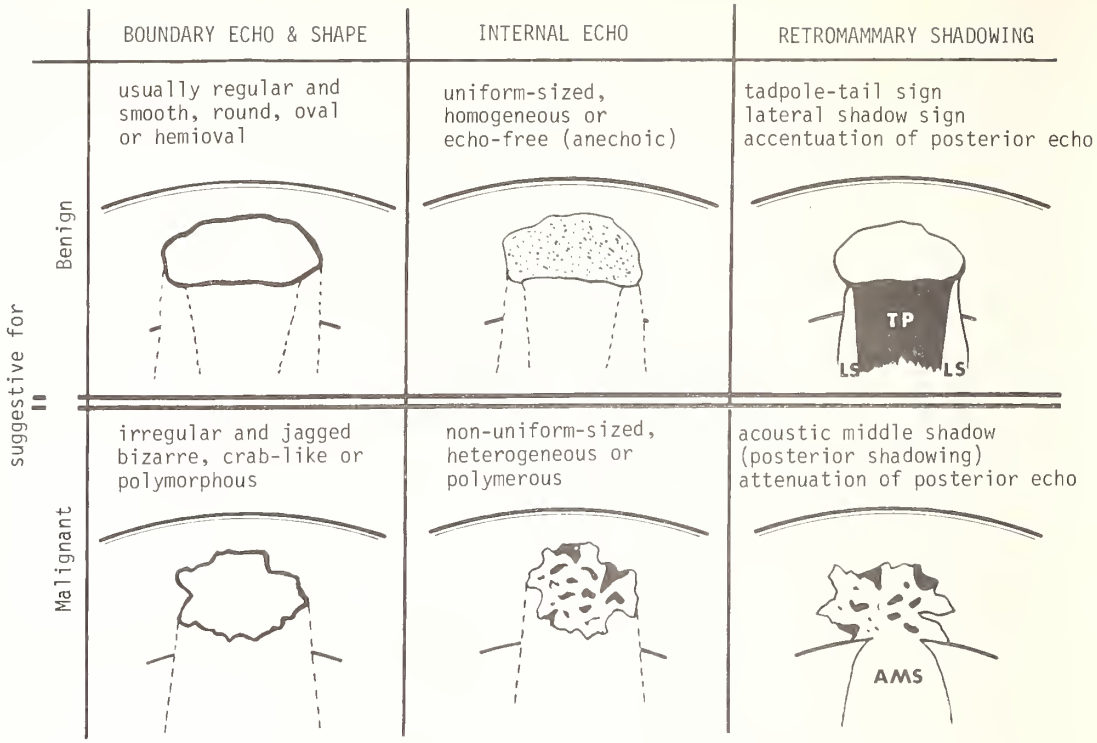

Fig. 2. Diagram illustrating echogram appearances for differential diagnosis of benign and malignant tumors.

The first two categories, that is, the boundary echoes and shape, and internal echoes, result from echo patterns mainly confined to the tumor mass itself or its vicinity. The third category, shadowing, is a result of various attenuation mechanisms such as multiple reflections, changes in beam velocity, and scattering due to the impedance discontinuities within the tumor.

The boundary echoes provide important diagnostic information, producing outlines which are usually irregular in the case of breast cancers, and regular in the case of benign lesions, such as cysts and fibroadenomas. A cancerous tumor is uneven with a jagged edge, sometimes triangular, rectangular or irregular in shape, whereas a benign tumor is usually round, oval or hemioval. Moreover, the internal echo pattern in a malignant tumor is usually irregular both in size and distribution, in contrast with the either homogeneous or anechoic internal echo pattern of a benign lesion.

Other differential diagnostic criteria result from echo patterns due to multiple reflections from the tumor mass, modifying the shadowing. It is this phenomenon which is the principal subject of this paper. The tadpole-tail sign arises from the low energy loss in the beam as it passes normally through the distal wall of a cyst leaving sufficient energy to cause multiple reflections or "ringing" between the distal cyst wall and the chest wall. The difference in the velocities in tissue and cyst may play an important role in causing this pattern. This sign is usually not seen in the majority of malignant lesions except in some cases of medullary carcinoma. The lateral shadow sign is believed to be formed by the almost total reflection of the ultrasonic beam at the lateral wall of cystic lesions as, for example, with benign tumors [6]; an explanation of the formation of this sign has recently been published [9].

A characteristic of malignant lesions designated as "acoustic middle shadow sign" is sometimes observed. This phenomenon is believed to be caused by the high attenuation of the ultrasonic energy by malignant tumor tissue, due to large acoustic impedance discontinuities within such tissue.

The reliability of these various signs for the differential diagnosis of various histological types of breast cancer is seen in table 1. Diagnostic accuracy is greatest in scirrhous carcinoma and lowest in medullary carcinoma.

Echographic characteristics suggestive of malignant lesions, such as the acoustic middle shadow sign and the complete disappearance of the distal limit of the tumor mass echo, have been correlated with the connective tissue content of tumor masses for various histological types of breast cancer. The grading of the connective tissue content was divided into three categories based on the observation of many microscopic field specimens. These categories were expressed as follows: 1) the connective tissue over 75 percent (rich), 2) 25 to 75 percent (moderate) and 3) less than 25 percent (poor). The specimens were stained by hemtoxylin and eosin and are shown magnified by approximately 100.

The results of the analysis are shown in tables 1, 2, 3 and 4. The acoustic middle shadow sign as well as the complete disappearance of the distal limit of the tumor mass echo, were most frequently seen in the cases with abundant connective tissue, whereas the tadpole-tail sign and the lateral shadow sign were often seen in cases with little connective tissue content, mainly in medullary carcinoma. These analyses were carried out on 12 cases of various breast cancers (4 scirrhous carcinomas, 5 papillary carcinomas and 3 medullary carcinomas).

Table 1. Reliability of various criteria for the differential diagnosis of breast cancer (53 cases).

Appearance typical of tumor histological type		Type of carcinoma	Medullary		Papillary		Scirrhous	
		Diagnostic accuracy rate	20/24	(83%)	13/15	(87%)	14/14	(100%)
	Malignant	Complete disappearance of distal limit of tumor echo	17/24	(70%)	12/15	(80%)	11/14	(78%)
		Irregular boundary echo	23/24	(95%)	14/15	(93%)	11/14	(78%)
		Acoustic middle shadow sign	18/24	(75%)	11/15	(73%)	14/14	(100%)
	Benign	Bilateral disappearance of distal limit of tumor echo	4/24	(17%)	1/15	(0.6%)	0/14	(0%)
		Tadpole-tail sign	4/24	(17%)	2/15	(1.3%)	0/14	(0%)
		Lateral shadow sign	4/24	(1.3%)	2/15	(1.3%)	0/14	(0%)

Table 2. Connective tissue content of 12 cases of carcinoma. Rich = over 75 percent; moderate = 25 to 75 percent; poor = less than 25 percent. High consistency is indicated by (+++), intermediate consistency by (++), and low consistency by (+).

	Connective tissue content			Nonconnective tissue content		
	rich	moderate	poor	rich	moderate	poor
1) Scirrhous carcinoma (T1)	(+++)					(+)
2) Scirrhous carcinoma (T1)	(+++)					(+)
3) Scirrhous carcinoma (T2)	(+++)					(+)
4) Scirrhous carcinoma (T2)		(++)			(++)	
5) Papillary carcinoma (T1)		(++)			(++)	
6) Papillary carcinoma (T1)		(++)			(++)	
7) Papillary carcinoma (T2)		(++)			(++)	
8) Papillary carcinoma (T2)	(+++)					(+)
9) Papillary carcinoma (T2)	(+++)					(+)
10) Medullary carcinoma (T1)	(+)		(+++)			
11) Medullary carcinoma (T2)	(+)		(+++)			
12) Medullary carcinoma (T2)	(+)		(+++)			

Table 3. Correlation between appearance of various echo signs and connective tissue contents in 12 cases of carcinoma, classified according to echo signs. Signs indicated by circled letters in the table have the higher reliabilities. A = acoustic middle shadow sign; C = complete disappearance of distal limit of tumor mass echo; N= no change of shadow or intermediate pattern; T = tadpole-tail sign; L = lateral shadow sign.

	Connective tissue content														
	rich					moderate					poor				
1) Scirrhous carcinoma (T1)	(A)	(C)	N	T	L	A	C	N	T	L	A	C	N	T	L
2) Scirrhous carcinoma (T1)	(A)	(C)	N	T	L	A	C	N	T	L	A	C	N	T	L
3) Scirrhous carcinoma (T2)	(A)	C	N	T	L	A	(C)	N	T	L	A	C	N	T	L
4) Scirrhous carcinoma (T2)	A	C	N	T	L	A	C	N	(T)	(L)	A	C	N	T	L
5) Papillary carcinoma (T1)	A	C	N	T	L	A	C	N	(T)	(L)	A	C	N	T	L
6) Papillary carcinoma (T1)	A	C	N	T	L	A	C	N	(T)	(L)	A	C	N	T	L
7) Papillary carcinoma (T2)	A	C	N	T	L	A	C	(N)	T	L	A	C	N	T	L
8) Papillary carcinoma (T2)	(A)	(C)	N	T	L	A	C	N	T	L	A	C	N	T	L
9) Papillary carcinoma (T2)	(A)	(C)	N	T	L	A	C	N	T	L	A	C	N	T	L
10) Medullary carcinoma (T1)	A	C	N	T	L	A	C	N	T	L	A	C	N	(T)	(L)
11) Medullary carcinoma (T2)	A	C	N	T	L	A	C	N	T	L	A	C	N	(T)	(L)
12) Medullary carcinoma (T2)	A	C	N	T	L	A	C	(N)	T	L	A	C	N	T	L

Table 4. Correlation between appearance of various echo signs and connective tissue contents in 12 cases of carcinoma, classified according to carcinoma type. (S) = scirrhous carcinoma; (P) = papillary carcinoma; (M) = medullary carcinoma.

	Connective tissue content			Nonconnective tissue content		
	rich	moderate	poor	rich	moderate	poor
Acoustic middle shadow sign	(S) (S) (S) (P) (P)					(S) (S) (S) (P) (P)
Complete disappearance of distal limit of tumor mass echo	(S) (S) (P) (P)	(S)			(S)	(S) (S) (P) (P)
Tadpole-tail sign		(P) (P)	(M) (M)	(M) (M)	(P) (P)	
Lateral shadow sign		(P) (P)	(M) (M)	(M) (M)	(P) (P)	
No shadow or intermediate pattern		(P) (M)			(P) (M)	

3. Demonstration of Typical Echograms and Tissue Characteristics

Tables 3 and 4 show the correlations between the amount of connective tissue and the various echo patterns described in the following paragraphs.

A. Scirrhous Carcinoma (T1 and T2)

A series of echograms recorded by the sensitivity-graded method [6] show typical patterns of shadowing (acoustic middle shadow sign) suggestive of T2 malignancy (fig. 3).

The distal limit of the tumor mass echo gradually fades as the attenuation increases, as may be seen on the echograms taken at -15 to -20 dB attenuation, and finally completely disappears. The microscopic picture shows the tissue type content to be predominantly connective in cellular structure. The echogram in figure 4 is a typical pattern of early scirrhous carcinoma (T1), showing the acoustic middle shadow underneath the tumor mass echo. Histologically, the connective tissue component is predominant.

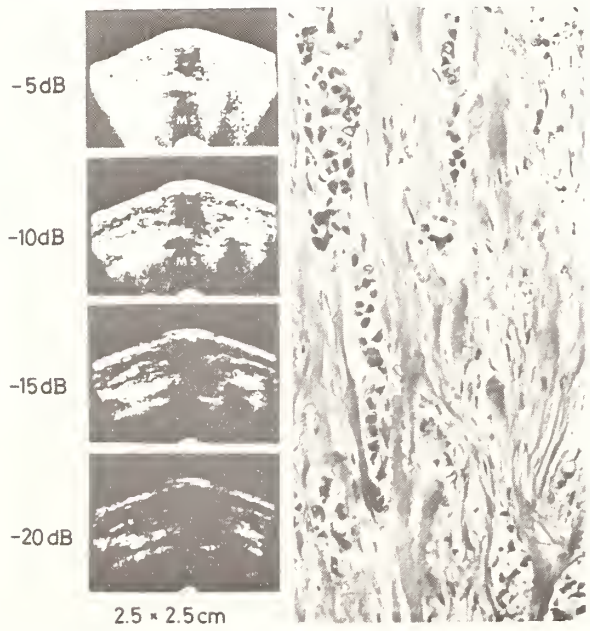

Fig. 3. Echograms of breast with T2 scirrhous carcinoma (acoustic middle shadow sign) recorded at a range of sensitivities, together with corresponding histological section magnified approximately 100 times.

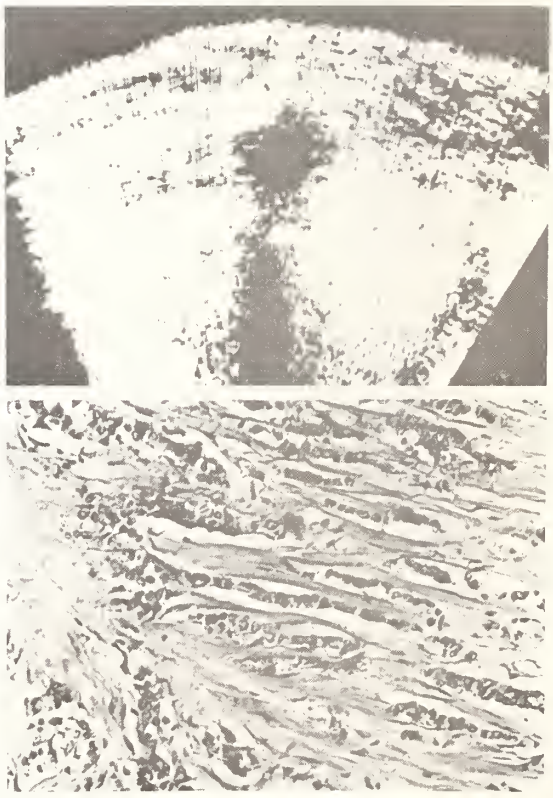

Fig. 4. Echogram of breast with T1 scirrhous carcinoma (acoustic middle shadow sign), together with corresponding histological section magnified approximately 100 times.

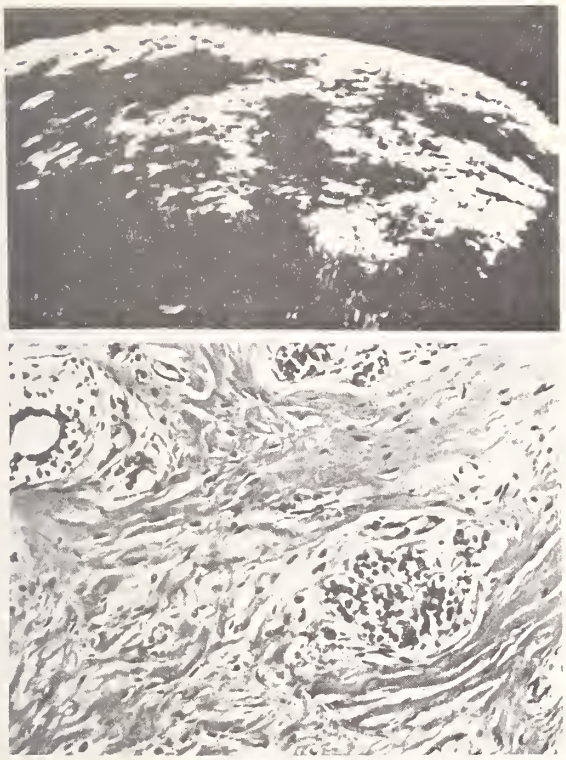

Fig. 5. Echogram of breast suggesting T1 scirrhous carcinoma (acoustic middle shadow sign), together with confirmatory corresponding histological section magnified approximately 100 times.

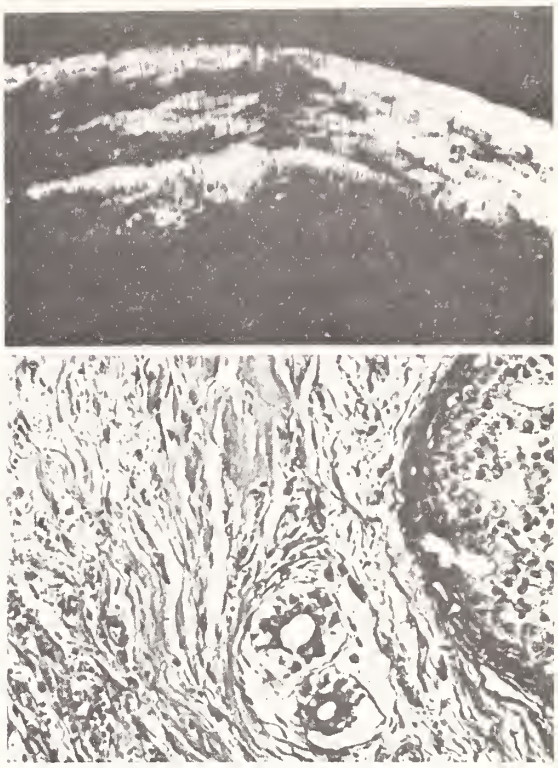

Fig. 6. Echogram of breast with papillary carcinoma (note absence of acoustic middle shadow and tadpole-tail signs), together with corresponding histological section magnified approximately 100 times.

The echogram in figure 5 shows another typical acoustic middle shadow pattern suggestive of T1 malignancy. The microscopic picture also shows rich connective tissue.

These results suggest that rich connective tissue content may play an important role in producing the acoustic middle shadow sign and in the complete disappearance of the distal limit of the tumor mass echo in clinical echograms of scirrhous carcinoma.

B. Papillary Carcinoma (T1)

The echogram of early papillary carcinoma shows a typical attenuation of the shadowing, so that the acoustic middle shadow sign is not clear. Moreover, the typical benign signs such as tadpole-tail sign and the lateral shadow sign do not appear either (fig. 6.).

The histological picture shows connective tissue and nonconnective tissue approximately evenly distributed. Therefore, this pattern of papillary carcinoma may lie in between those of scirrhous carcinoma and medullary carcinoma (see C below) with respect to the connective tissue content. This kind of evenly-distributed connective and nonconnective tissue produces an equivocal echographic pattern which makes it difficult correctly to diagnose early papillary carcinomas.

C. Medullary Carcinoma (T2)

This echogram shows a rather homogeneous internal echo, mimicking a benign cyst, and an atypical tadpole-tail shorter than that of tadpole-tail usually seen in the case of benign tumors (fig. 7). Consequently correct diagnosis is rather difficult. The histological picture shows rich non-connective tissue content, and especially abundant and uniformly distributed tumor cells. This kind of homogeneous and even distribution of tumor cells should produce little sonic reflection from within the tumor mass, thus mimicking the pattern of benign cysts.

4. Discussion

In the past several years, researchers have hypothesized that the ultrasonic characteristics of malignant breast tumors could be attributed to the increased attenuation of ultrasonic energy by the cancerous tissue with greater internal acoustic impedance discontinuities, and hence increased scattering losses, as compared with those with normal breast tissue and benign breast tissues.

In direct measurements of the attenuation of ultrasound within 18 samples of various normal, benign and malignant breast tissues, significant differences have been found [10]. At 2.25 MHz, malignant tissue had the highest attenuation (1.2 dB per wavelength), whilst benign tissues had a median value of 0.6 dB per wavelength. These results support the hypothesis.

From a histological standpoint, the percentage of connective tissue (consisting of fibroblasts

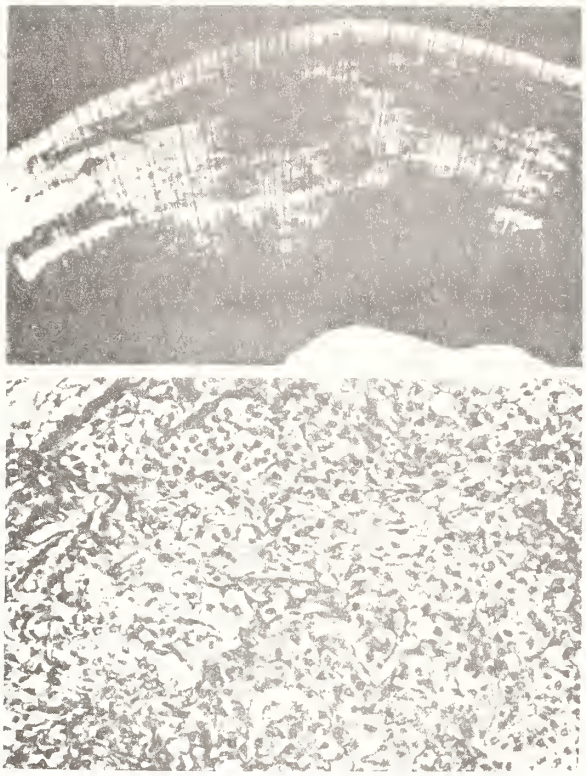

Fig. 7. Echogram of breast with T2 medullary carcinoma (the tadpole-tail sign is shorter than that generally seen with benign tumors), together with corresponding histological section magnified approximately 100 times.

and fibrous tissue) has been suggested to be one of the principal factors responsible for ultrasonic attenuation in neoplastic tissue [11].

In an analysis [12] of 53 cases of breast cancer for the incidence of the appearance of various echographic characteristics such as the acoustic middle shadow sign, the complete disappearance of the distal limit of the tumor mass echo was suggestive of malignancy, and the tadpole-tail sign and the lateral shadow sign was suggestive of a benign condition. Diagnostic accuracy rates were 100 percent, 87 percent and 83 percent in scirrhous carcinoma, papillary carcinoma and medullary carcinoma respectively, as may be seen in table 1. It is interesting to note that the tadpole-tail sign and the lateral shadow sign appeared most rarely, and the disappearance of the distal limit of the tumor echo was most frequent, in medullary carcinomas. Generally these signs suggest benign lesions, and this may account for the fact that the lowest diagnostic accuracy is obtained with medullary carcinomas.

The connective tissue content seems to be generally rich in scirrhous carcinoma and poor in medullary carcinoma. The tumor cellular component usually predominates within the nonconnective tissue of medullary carcinoma and this tissue structure may be responsible for the bioacoustical homogeneity observed within the tumor mass. This homogeneity in medullary carcinoma may produce less attenuation of ultrasonic energy, resulting in shadowing suggestive of benign tumors, such as the tadpole-tail sign and the lateral shadow sign. In the present investigation, these echographic characteristics appear regardless of the tumor size and the location of the tumor mass within the breast.

Medullary carcinoma has lower attenuation than other types of carcinoma [10]; its measured value at 2.25 MHz falls in a range comparable to that of benign tumor tissue, whereas the attenuation is highest in scirrhous carcinomas followed by papillary carcinomas. It is interesting to note that the discrimination on the basis of attenuation was very clear between normal breast tissue, benign tumors, and malignant tumors, except for the case of medullary carcinoma. This finding is in agreement with the hypothesized echographic origin of the medullary carcinomas even at the frequency of 5 MHz used in the present analysis.

As to the other factors contributing to the echographic characteristics of tumors, especially irregular and nonsmooth boundary echoes of various carcinomas, the incident rate of its irregularity is 95 percent for medullary carcinoma, 93 percent for papillary carcinoma and 78 percent for scirrhous carcinoma. This kind of irregularity may be closely related with infiltrative pattern of cancerous cells, and the reflection coefficient at the tumor interface as well as other factors.

It should be emphasized that the correlation of clinical echographic signs with the histological characteristics of the tumors does not imply that in any given case, a particular sign is indicative of any histological type. Because of inadequacies of the clinical equipment used in this study, these correlations should only be considered qualitative. The principal conclusion is that the amount of connective tissue within the tumor mass may play an important role in the formation of the acoustic middle shadow sign and the complete disappearance of the distal limit of the tumor mass echo, and that it is probably due to the increased ultrasonic attenuation caused by the high acoustic impedance of the connective tissue.

References

[1] Baum, G., Ultrasonic Examination of the Breast, in Fundamentals of Medical Ultrasonography, G. Baum, ed., pp. 380-402 (Putnam's Sons, New York, 1975).

[2] Cole-Beuglet, C. and Beique, R. A., Continuous ultrasound B-scanning of palpable breast masses, Radiology 117, 123-128 (1975).

[3] Fujii, T., Izuo, M., Kishi, S., Yokomori, T., and Fujimori, M., The results and the evaluation of ultrasonic diagnosis of breast disease, J. Jap. Soc. Cancer Therap. 8, 253-

[4] Hirose, M. and Furuki, R., Ultrasonic diagnosis of breast disease, Proc. 17th Meeting Jap. Soc. Ultrasonics Med. 17, 37-38 (1971).

[5] Jellins, J., Kossoff, G., Reeve, T. S., and Barraclough, B. H., Ultrasonic grey scale visualization of breast disease, Ultrasound Med. & Biol. 1, 393-404 (1975).

[6] Kobayashi, T., Takatani, O., Hattori, N., and Kimura, K., Differential diagnosis of breast tumors: The sensitivity graded method of ultrasonotomography and clinical evaluation of its diagnostic accuracy, Cancer 33, 940-951 (1974).

[7] Pluygers, E., Diagnostic ultrasonore, par echographie A et B, des affections Mammaires, J. Belge. Radiol. 58, 15-29 (1975).

[8] Wagai, T., Tsutsumi, M., and Takeuchi, H., Diagnostic Ultrasound in Breast Diseases, in Present and Future of Diagnostic Ultrasound, I. Donald and S. Levi, eds., pp. 148-161

[9] Okujima, M., Refraction of ultrasonic beam incident near circumference of spherical medium, Proc. Jap. Soc. Ultrasonics Med. 29, 231-232 (1976).

[10] Calderon, C., Vilkomerson, D., Mezrich, R., Etzold, K. E., Kingsley, B., and Haskin, M., Differences in the attenuation of ultrasound by normal, benign and malignant breast tissue, J. Clin. Ultrasound 4, 249-254 (1976).

[11] Field, S. and Dunn, F., Correlation of echographic visualization of tissue with biological composition and physiological state, J. Acoust. Soc. Am. 54, 809-812 (1973).

[12] Kobayashi, T., Takatani, O., Hattori, N., and Kimura, K., Clinical investigation for the differential diagnosis of breast tumor by means of the sensitivity graded method of ultrasonotomography (fourth report) - Analytical re-appraisal of diagnostic criteria in echographic and mammographic findings, Proc. 24th Meeting Jap. Soc. Ultrasonics Med. 24, 147-148 (1973).

Reprinted from *Ultrasonic Tissue Characterization II*, M. Linzer, ed., National Bureau of Standards, Spec. Publ. 525 (U.S. Government Printing Office, Washington, D.C., 1979).

THE ATTENUATION OF SELECTED SOFT TISSUE AS A FUNCTION OF FREQUENCY

D. H. Le Croissette, R. C. Heyser, P. M. Gammell, and J. A. Roseboro

Jet Propulsion Laboratory
California Institute of Technology
Pasadena, California 91103, U.S.A.

and

R. L. Wilson[1]

School of Medicine
University of Southern California
Los Angeles, California 95033, U.S.A.

Measurements of attenuation versus frequency have been made on pancreas, kidney, fat and liver specimens of hog tissue. Hogs were of the "Berkshire" variety and the tissue obtained from a slaughterhouse. The measurements were taken under controlled conditions of temperature and formalin fixing to determine the effects of aging and fixing on the tissue. A swept-frequency transmission system was used operating over the range of about 1.5 to 9.5 MHz. The curves show the changes occurring in fresh tissue as a result of several days of aging at refrigerator temperatures (5 °C) and the effects of fixing the tissue in formalin immediately post-mortem or after several days of 5 °C storage. All measurements were made at 37 °C.

Key words: Attenuation; tissue properties; transmission; ultrasound.

1. Introduction

The recent interest in characterizing soft tissue by ultrasound is based upon measurements made as early as 1952 [2][2] and later observations by scientific investigators attempting to lay the groundwork for a new technique of ultrasonic diagnosis. The work reported here is the start of a systematic attempt to measure the attenuation of soft tissue as a function of frequency. This topic was chosen because of the belief, substantiated by initial measurements [2], that there is a variation in the attenuation of ultrasound through tissue as a function of frequency that can be correlated with the pathological state of the tissue. The measurements reported here were made on excised tissue obtained from hogs. This paper reports data obtained from fresh, aged and fixed specimens.

In a typical pulse-echo ultrasound imaging system, the frequency variation of attenuation cannot usually be identified. Furthermore, the increase in attenuation of normal tissue as a function of frequency tends to mask the high frequency behavior of tissue when a measurement is made over a long path length, i.e., far from the transducer. These two factors have made the identification of pathological tissue by its frequency-dependent characteristic unlikely and so this phenomenon plays little part in the subjective pattern recognition techniques used in contemporary diagnostic ultrasonography. It is believed, however, that if an identification mechanism based on frequency-dependent phenomenon can be found, suitable instrumentation will be devised for tissue identification.

Measurements on tissues of known pathologies can greatly increase the knowledge of tissue characterization needed to develop such instrumentation. Specimens obtained from cadavers are especially useful since the individual organ can be studied. Most autopsy material, however, is not available until after a one or two-day delay. Furthermore, the general availability of pathological tissue is greatly enhanced if a study is not constrained to specimens a few hours old. This study is therefore to determine the acoustic attenuation characteristics of several organs as a function of time after death and after fixing in formalin solution.

2. Methodology

There are two major methods for examining the ultrasonic propagation behavior of tissue as a function of frequency. The most popular method [3-5] uses the frequency spectrum that is emitted by a heavily damped transducer operated in a pulse mode. This method is capable of giving useable data at frequencies several times the natural resonant frequency of the crystal with adequate signal-to-noise ratios. By contrast,

[1]Current address: Harbor General Hospital, Torrance, California 90509.

[2]Figures in brackets indicate literature references at the end of this paper.

the technique used in this work does not pulse the transducer but sweeps the operating frequency over a wide band. This technique [6], known as Time Delay Spectrometry (TDS), reduces the effects of multipath propagation and reverberation by using a swept frequency transmitter and receiver so that the frequency acts as a "time tag" to the signal. The sweep of the receiver is delayed from that of the transmitter so it will only respond to the signals with the proper time delay. This discriminates against signals with different arrival times, especially those due to reverberation and multipath propagation.

The data were taken with a standard swept-type spectrum analyzer-tracking generator which has been modified by offsetting the tracking generator by a constant frequency. A Panoramic SPA-3 spectrum analyzer and Panoramic G6 tracking generator were used. This tracking generator can be adjusted to compensate for the time of transit of the ultrasound through the sample. A sweep rate of 100 $MHz \cdot s^{-1}$ and 3 dB intermediate frequency bandwidth of 600 Hz were used. If the sweep frequency versus time of the spectrum analyzer is linear, this constant frequency offset will exactly compensate for a constant time delay of the ultrasound through the specimen. The time delay will be constant across the frequency sweep if both the specimen and the medium in which it is immersed are nondispersive. Dispersion of the medium and the sample will not affect the measurements by more than 1 dB, provided the average velocity of the sample and medium does not change by more than 1 percent. Linearity requirements on the sweep of the spectrum analyzer are extreme, however.

The measurements were made over the frequency range 1.5 to 9.4 MHz. Two Aerotech Alpha transducers were used. The 10 MHz, 0.63 cm diameter (0.25 inches) transducers were selected so that the resonant frequency was just above the range of interest. This frequency was chosen so that the transducer sensitivity increased with frequency over the band. This compensates for the increase in tissue attenuation with frequency to give a more nearly constant signal-to-noise ratio over the selected frequency spectrum. The specimen was located midway between the transducers, which were 12 cm apart.

3. Specimen Handling

Specimens of tissue from hogs were studied no more than four hours after slaughter. The tissue type and the time sequence of the measurements are shown in figure 1. All specimens were heat sealed in a plastic bag containing either 0.9 percent saline or formaldehyde diluted 10:1 with water (i.e., approximately 4 percent). The liver specimens were sliced to approximately 15 mm thickness; the kidney and pancreas specimens were studied intact. The backfat specimen was left in the form of a slab as it was stripped from the carcass. The thickness of all of the specimens was calipered at the locations studied. Fat is normally removed one day after slaughter which accounts for the one-day delay shown in figure 1(b).

Figures 2 through 9 show the measured attenuation versus frequency for the hog tissue at 37 °C. Four or five locations on each specimen were studied. Obvious ducts, vessels, and tapered edges were avoided. In the case of the kidney, measurements were not made in the central portion, which contains the large vessels and the renal pelvis. All of the kidney measurements were made in the region of the pyramids, and so include both cortical and medullary matter. The locations studied on any given specimen can be identified by the shape of the symbol used on figures 2 through 5. That is, the circle, square, or triangle represents the same visible location on the specimen when studied on the day of slaughter, five days later, and after fixing. Care was taken to avoid multipath effects by visual inspection of the area of the specimen and by observing the spectrum analyzer for obvious signs of multipath interference. Since no fine structure was observed in the attenuation versus frequency curves, the data are reported at 0.5 MHz intervals.

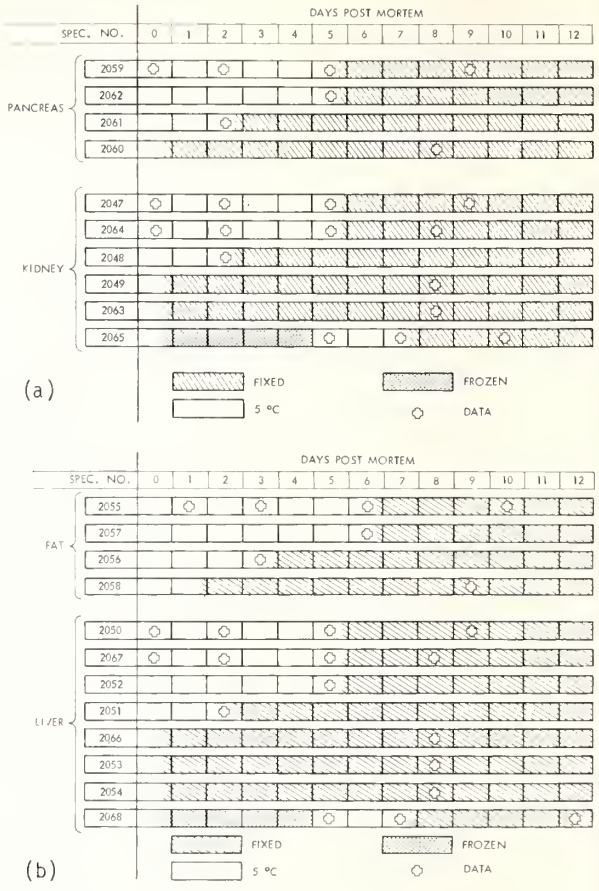

Fig. 1. Specimen history: (a) pancreas and kidney, (b) fat and liver.

Each specimen was measured at four or five points. This is a compromise between sampling enough locations to insure that the measurements are representative and reducing experiment time to a minimum. Since tissue is known to deteriorate rapidly at 37 °C, it is important that the experiment time be kept as short as possible. Stray air bubbles that initially clung to the specimen were gently brushed away. No gas evolution was subsequently observed visually.

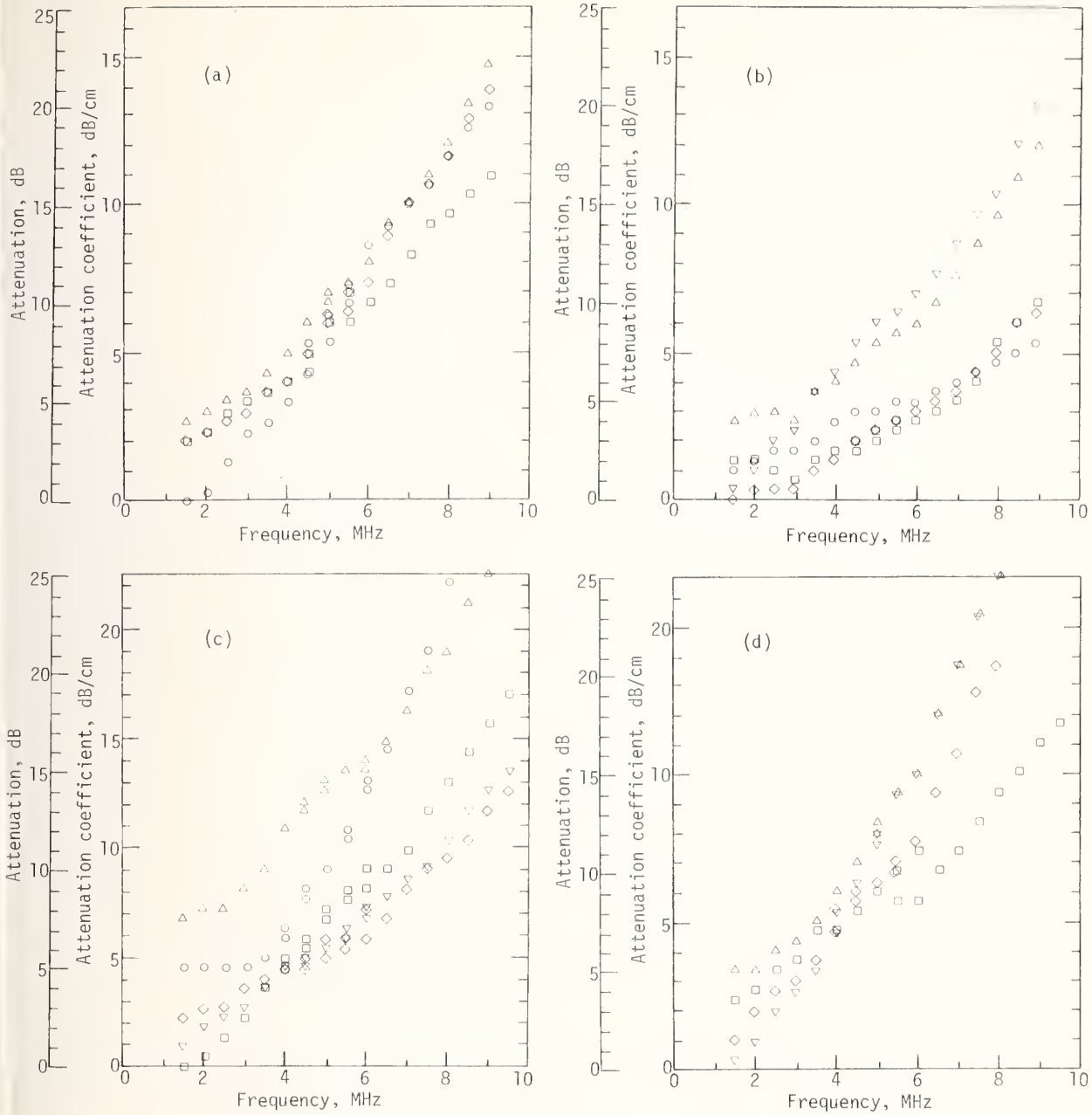

Fig. 2. Attenuation versus frequency for hog pancreas: (a) 6 hours post-mortem (fresh), (b) 5 days post-mortem (fresh), (c) 5 hours post-mortem (fixed), (d) 5 days post-mortem (fixed).

These measured values of tissue attenuation exhibit considerable variability. At this stage in the experiments it was considered that little was to be gained by applying statistical analysis on the four or five readings taken although it is recognized that a mean and variance will be meaningful on readings from a higher number of points. Accordingly, the averaged or summarized data are presented in the form of band diagrams in figures 6 through 9. These bands were selected to follow the data with no more than 10 percent of the points falling outside of the band.

4. Data Acquisition

The response of the system was recorded with attenuations of 0, 5, 10, 15, 20, 25, and 30 dB switched into the system. The response with the specimen between the transducers was then recorded on the same polaroid film. Since the sweep of the spectrum analyzer only covers a 5.5 MHz range in the present equipment, it was necessary to take the data in two parts. As a check, readings taken from both spectra are reported in the range of overlap, which is 4.5 to 5.5 MHz. If only one reading is reported at a given loca-

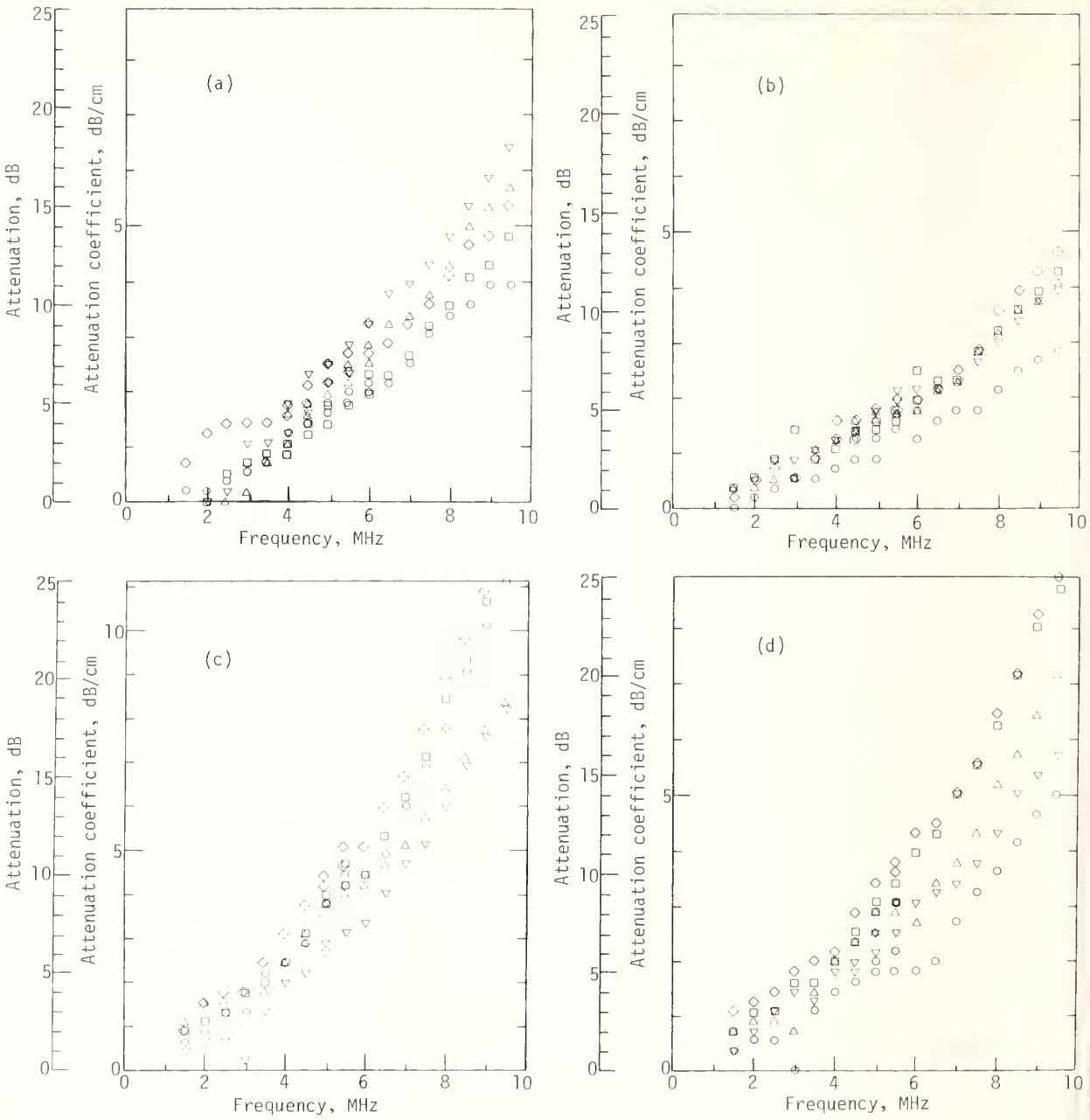

Fig. 3. Attenuation versus frequency for hog kidney: (a) 3 hours post-mortem (fresh), (b) 5 days post-mortem (fresh), (c) 4 hours post-mortem (fixed), (d) 5 days post-mortem (fixed).

tion on the specimen then the readings from the upper and from the lower spectra agree within 0.5 dB. Since the calibration spectra are obtained for 5 dB increments, interpolation to the nearest 1 dB is reliable. For smoothness in plotting the data, the graphs are plotted to the nearest 0.5 dB, although no significance should be attached to changes of less than 1 dB. The accuracy of the data is believed to be generally ± 1 dB, with rare deviations of ± 2 dB. Measurements using standard, non-biological samples show a system repeatability error of ± 0.5 dB.

5. Measurements

Figure 2 shows the plot of attenuation versus frequency for hog pancreas under four conditions; (a) six hours post-mortem (fresh), (b) five days post-mortem (fresh), (c) fixed five hours post-mortem, and (d) fixed five days post-mortem. Storage of the fresh tissue at 5 °C results in a decreased attenuation particularly at the higher frequencies. These data do not seem conclusive, however, since figure 2(b) shows a bimodal distribution of readings. The organ lacks rigidity and so accurate placement and replacement of the

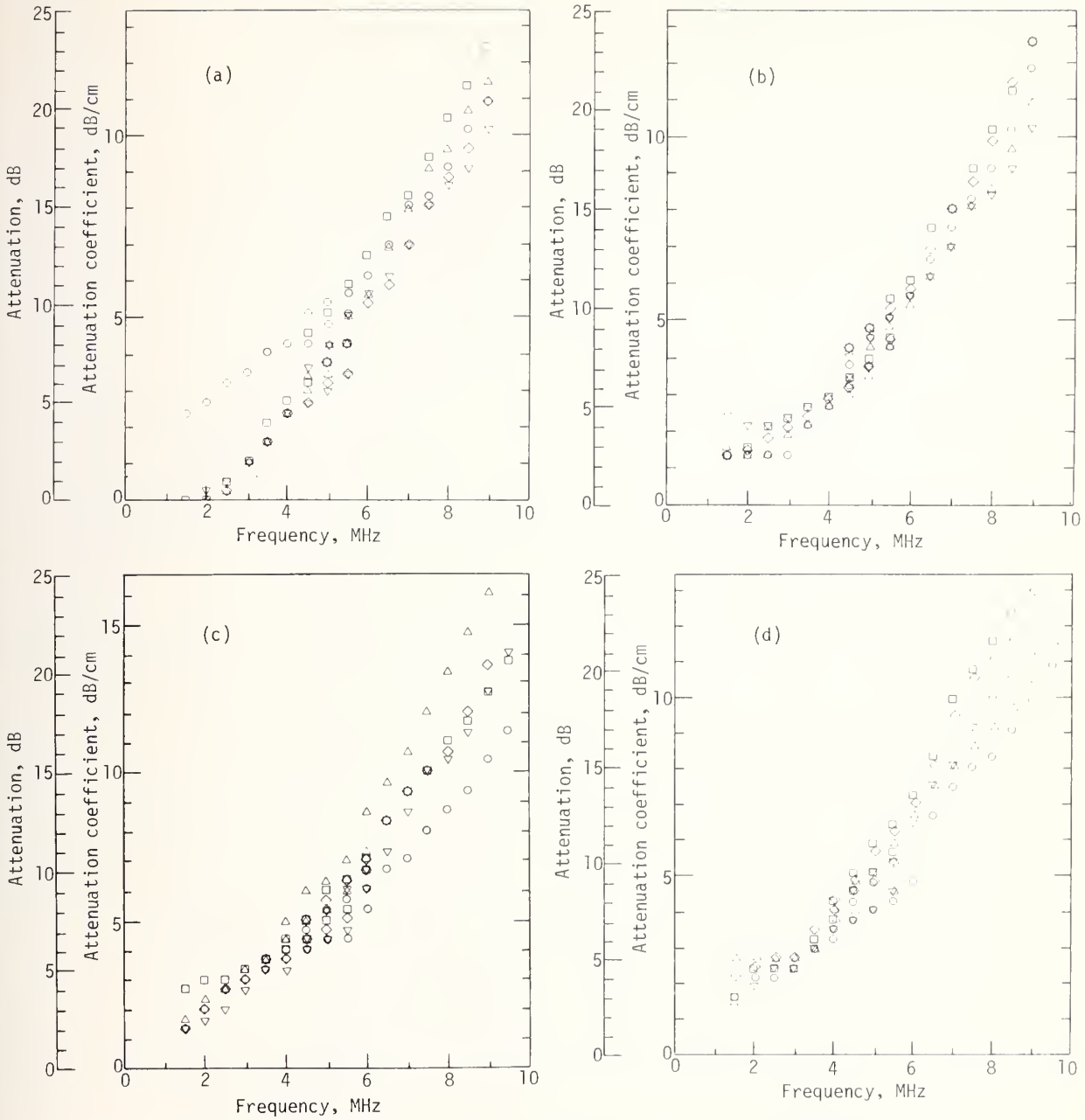

Fig. 4. Attenuation versus frequency for hog backfat: (a) 1 day post-mortem (fresh), (b) 6 days post-mortem (fresh), (c) 1 day post-mortem (fixed, (d) 6 days post-mortem (fixed).

transducers on these specimens is very difficult. In addition, the pancreas contains lobules of glandular tissue on the order of 1 cm, interspersed with fat. It is therefore considered that the wide spread in data can be accounted for by the lack of rigidity and the inhomogeneity of the specimen. Figure 6 shows the bands of attenuation versus frequency for the fresh specimens under two conditions; six hours and five days post-mortem.

The measurements on fresh and fixed kidneys are shown in figure 3 and the corresponding bands of attenuation are given in figure 7. For the fresh specimens, storage of the tissue at 5 °C for five days has resulted in a decrease in attenuation, especially at the higher frequencies. Measurements taken 48 hours post-mortem (not reported here) lie between the two values. This decrease is just sufficient to separate the band curves. The attenuation of fixed tissue is above that of the tissue just post-mortem.

Figures 4 and 8 made on hog fat show that there is little effect of aging on the attenuation characteristics. Little significance can be placed on the differences at low frequencies shown in figure 8 since the attenuation is only of the order of

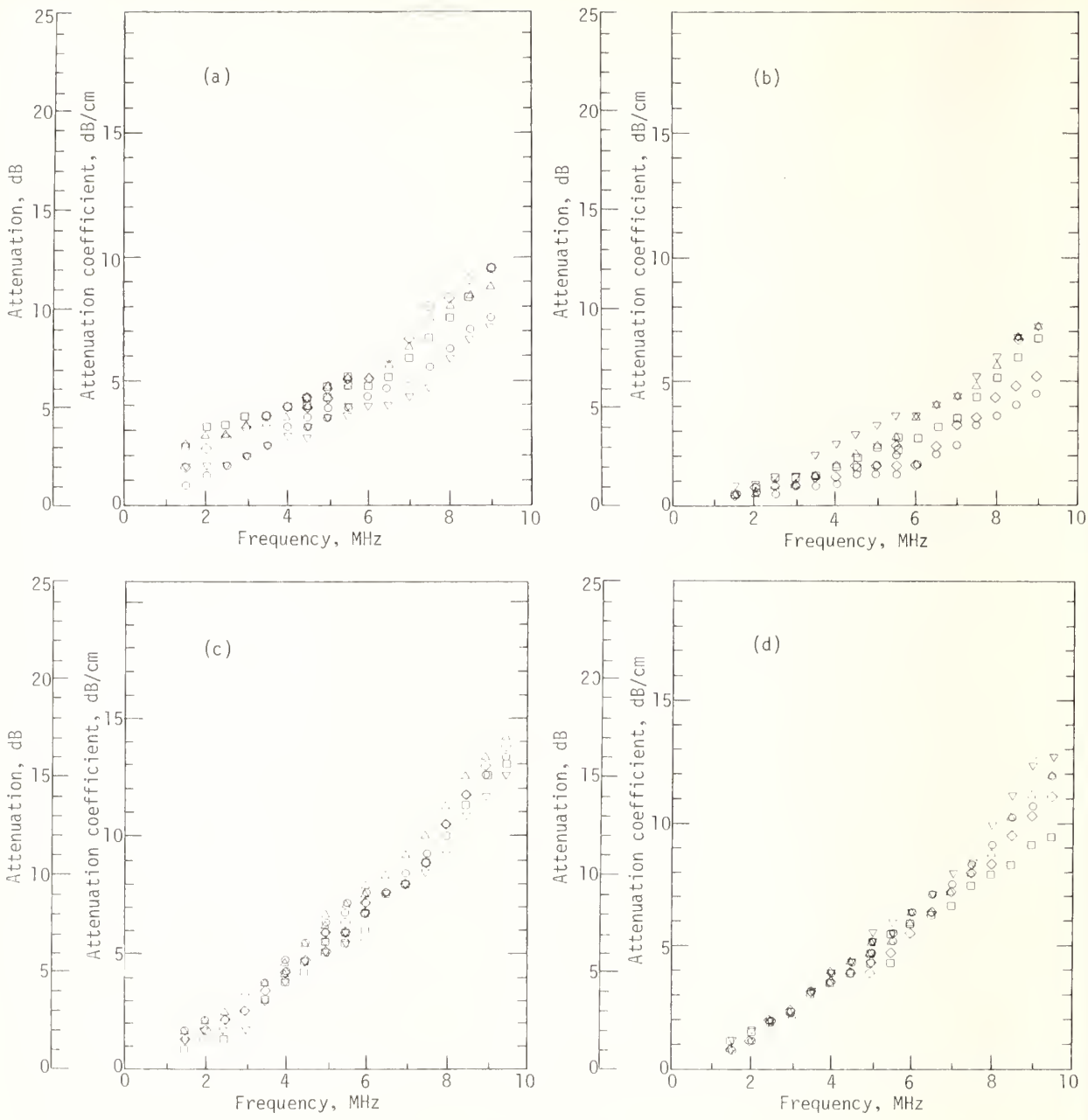

Fig. 5. Attenuation versus frequency for hog liver: (a) 5 hours post-mortem (fresh), (b) 5 days post-mortem (fresh), (c) 5 hours post-mortem (fixed), (d) 5 days post-mortem (fixed).

the uncertainties in the measurements. Fixing the specimens gives a slightly higher attenuation. There is considerable difference between this fat and typical fat found in human studies so that these data should be applied with caution. Hog fat is white and of a uniform texture whereas human fat is yellow and has a lobular structure with connective tissue interspersed.

Figures 5 and 9 show the data for hog liver. Here the storage of a fresh specimen results in a lower attenuation over a five-day period. The fixed specimens show increased attenuation. The data bands are fairly narrow probably because of the homogeneity of the tissue at the resolution level studied.

These tissue specimens were stored at 5 °C and heated to the measurement temperature of 37 °C over about a one-hour period. Following this procedure, each specimen was returned to the refrigerator for storage until the next measurement was made or until the specimen was fixed. For comparison, some specimens were held undisturbed at 5 °C until a single measurement was taken. No significant difference in attenuation could be seen between the two groups.

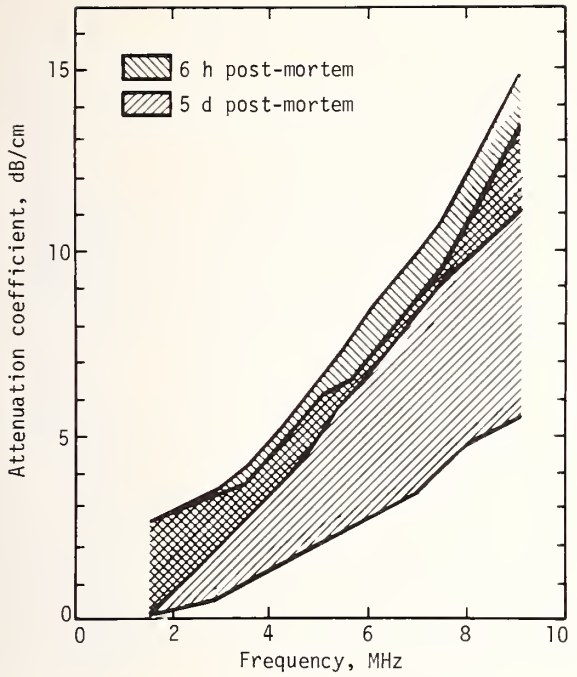

Fig. 6. Attenuation versus frequency data bands for hog pancreas: 6 hours and 5 days post-mortem (fresh).

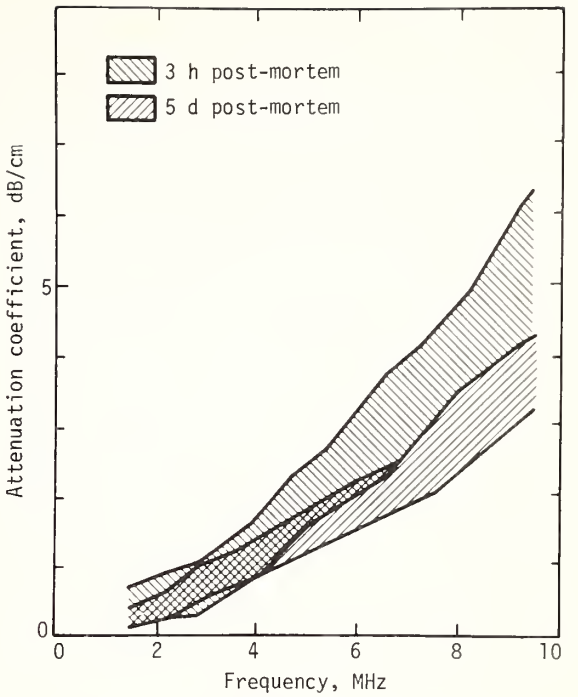

Fig. 7. Attenuation versus frequency data bands for hog kidney: 3 hours and 5 days post-mortem (fresh).

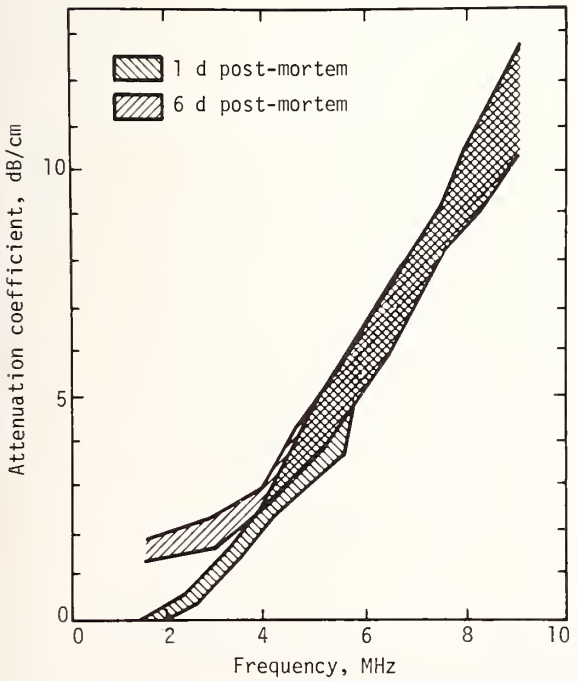

Fig. 8. Attenuation versus frequency data bands for hog backfat: 1 day and 6 days post-mortem (fresh).

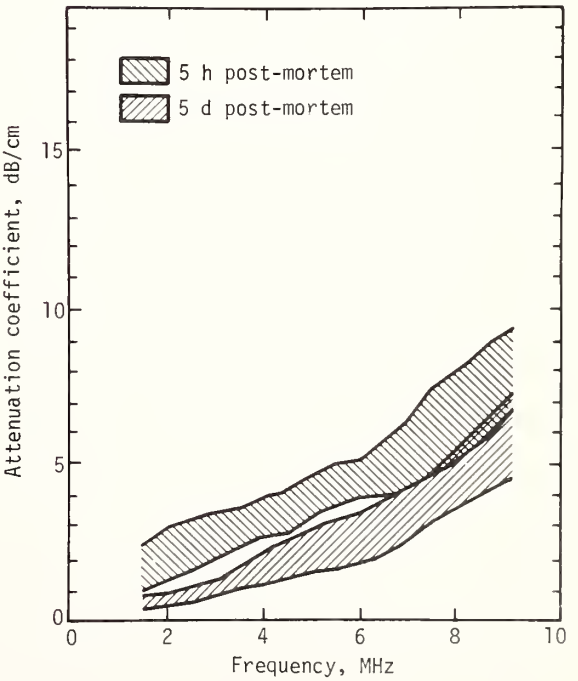

Fig. 9. Attenuation versus frequency data bands for hog liver: 5 hours and 5 days post-mortem (fresh).

6. Discussion

The accuracy of these measurements relies upon the internal sweep linearity of the spectrum analyzer to provide a constant time delay across the frequency band matching the constant transit time of the sound energy through the specimen. Slight non-linearities in the sweep were observed to give an error as high as 1 dB in the measured attenuation. Some indication of this error may be seen in the region between 4.5 and 5.5 MHz. In practice, two sets of data were taken; the lower half extended from 1.5 to 5.5 MHz and the upper part from 4.5 to 9.5 MHz. Small errors in the overlapping region are indicated by two values being plotted with the same symbol. In many cases identical values were obtained or the error was small. Since these measurements were taken, a new system has been built in which the sweeps of the transmitter and receiver are obtained from digitally programmed phase-coherent synthesizers. This will insure that the system is aligned over the entire frequency range of 1 to 10 MHz and will materially improve the quality of the data.

Acknowledgment

This paper presents the results of one phase of research conducted at the Jet Propulsion Laboratory, California Institute of Technology for the National Science Foundation, by agreement with the National Aeronautics and Space Administration.

References

[1] Wild, J. J. and Reid, J. M., Further pilot echographic studies on the histologic structure of tumor of the living and intact human breast, Am. J. Pathol. 28, 831-861 (1952).

[2] Le Croissette, D. H. and Heyser, R. C., Attenuation and Velocity Measurements in Tissue Using Time Delay Spectrometry, in Ultrasonic Tissue Characterization, M.Linzer, ed., National Bureau of Standards Spec. Publ. 453, pp. 167-196 (U.S. Government Printing Office, Washington, D.C., 1976).

[3] Lele, P. P., Mansfield, A. B., Murphy, A. I., Namery, J., and Senapati, N., Tissue Characterization by Ultrasonic Frequency-Dependent Attentuation and Scattering, in Ultrasonic Tissue Characterization, M. Linzer, ed., National Bureau of Standards Spec. Publ. 453, pp. 167-196 (U. S. Government Printing Office, Washington, D.C., 1976).

[4] Lizzi, F. L. and Laviola, M. A., Tissue signature characterization using frequency domain analysis, Ultrasonics Symposium Proceedings (IEEE), pp. 714-719, 1976.

[5] Miller, J. G., Yuhas, D. E., Mimbs, J. W., Dierker, S. B., Buse, L. J., Laterra, J. J., Weiss, A. N., and Sobel, B. E., Ultrasonic tissue characterization: correlation between biochemical and ultrasonic indices of myocardial injury, Ultrasonics Symposium Proceedings (IEEE), pp. 33-43, 1976.

[6] Heyser, R. C. and Le Croissette, D. H., A new ultrasonic imaging system using Time Delay Spectrometry, Ultrasound in Med. and Biol. 1, 119-131 (1974).

CHAPTER 4

SCATTERING AND ATTENUATION

Reprinted from *Ultrasonic Tissue Characterization II*, M. Linzer, ed., National Bureau of Standards, Spec. Publ. 525 (U.S. Government Printing Office, Washington, D.C., 1979).

CLINICAL SPECTRUM ANALYSIS TECHNIQUES FOR TISSUE CHARACTERIZATION

Frederic L. Lizzi and Marek E. Elbaum

Riverside Research Institute
80 West End Avenue
New York, New York 10023, U.S.A.

A spectrum analysis system is being used in a clinical measurement program to examine the reflectance characteristics of intraocular structures. The on-line system computes power spectra descriptive of echoes returned from well-defined tissue segments chosen by the examiner. Clinical data are digitized for subsequent post-processing and cataloguing. This paper presents an overview of the theoretical analysis used to formulate system design and to guide data interpretation. The analysis accounts for stochastic tissue architectures and treats the specific illumination conditions employed in the system. The paper also discusses system parameters as related to observable tissue characteristics and presents typical test data and clinical spectra for several pathologic conditions.

Keywords: Clinical ultrasound; ocular tumor; power spectra; Rayleigh scattering; ultrasonic spectrum analysis.

1. Introduction

Within the past few years, a variety of advanced techniques have been employed to measure the ultrasonic properties of soft-tissue structures [1-3][1]. This paper describes a clinical spectrum analysis technique [4] which has been used to measure the frequency-domain characteristics of ultrasonic backscatter from tissues of the eye and orbit. The technique employs a clinical, on-line system together with computer post-processing and data cataloguing. Following laboratory verification, an extensive series of clinical measurements has been carried out. The in vivo spectral data base is now being evaluated in terms of potential diagnostic significance and is also being employed in analytic modelling of tissue reflectance.

The spectrum analysis techniques have been designed to accommodate the stochastic nature of clinically relevant tissue structures, such as ocular tumors and vitreous hemorrhages. These structures exhibit randomness in terms of the size, orientation, and/or spatial position of their constituent internal scattering centers. Single reflectance measurements made on such stochastic entities exhibit a significant degree of statistical fluctuation which can preclude the reliable identification of pertinent tissue characteristics. Accordingly, the spectrum analysis techniques described below incorporate on-line ensemble averaging: the resulting power spectra determinations constitute statistically stable descriptors of tissue properties. In addition, compensatory procedures are employed to account for extraneous spectral weighting introduced by the transfer functions of transducers and electronic subsystems.

The spectral techniques can ultimately be employed clinically to examine organs other than the eye. However, their in vivo application is now practicable in ocular examinations since the media of the eye do not present additional constraints found in other organs. If transmission through the ocular lens is avoided [5], acoustic attenuation and refraction do not present significant obstacles in viewing intra-ocular structures at center frequencies higher than 10 MHz. The large bandwidths that can be realized at these high frequencies permit spectral sensitivity to morphological features whose scale sizes are significantly less than 0.5 mm. In addition, the narrow beamwidths (e.g., 0.3 mm) available at these center frequencies provide precise spatial definition of tissue segments to be analyzed and permit meaningful ensemble averaging, even within small tissue volumes.

To date well over 200 clinically derived spectra of normal and abnormal structures have been acquired, processed, and catalogued in disease-indexed digital files. Previous publications have discussed the operation of the spectrum analysis system and presented clinical findings [6,7]. This paper first outlines the analytic framework which has guided system design, clinical operation, and data interpretation. It then describes system operation emphasizing the relations between system performance parameters and observable tissue characteristics. Lastly, it presents representative test results for comparison with clinical data obtained for several ocular pathologies.

2. Outline of Analytic Framework

The clinical deployment of the spectrum analysis techniques employed in the present system has been

[1]Figures in brackets indicate literature references at the end of this paper.

guided by an analysis which accounts for both the stochastic nature of tissue architectures and the geometry and temporal spectrum of the ultrasonic illumination beam. This analysis is presented in outline form to facilitate discussions in following sections. (A more comprehensive treatment will be presented elsewhere [8].)

The analysis is discussed, first, in terms of its general formulation which accounts for the use of focused illumination conditions. Second, tissue architectures which are statistically stationary are discussed. Lastly, attention is given to tissues which can be modelled as randomly distributed Rayleigh scatterers.

A. Basic Formulation

The geometry involved in the analysis is shown in figure 1. A focused transducer emits a short, broadband ultrasonic pressure pulse. Radio frequency echo signals received from scatterers within a range-gated segment (O-L) are subjected to spectrum analysis. The range gate is positioned within the focal volume of the transducer and its time duration is chosen to be much larger than the duration of echoes from a single scatterer. The transmission characteristics of all intervening structures are assumed to be statistically homogeneous and to result in negligible attenuation.

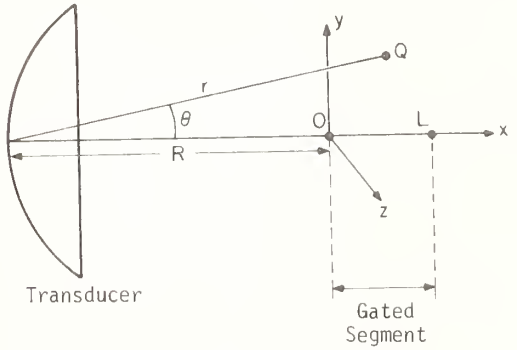

Fig. 1. Geometry for spectrum analysis measurements.

The received signals are analyzed in the frequency domain. The classic results obtained by O'Neil [9] are applicable for the weakly focused transducers used in this program. These results show that, at a point Q in the focal zone, the incident wave is essentially planar and its pressure amplitude is given by

$$p'(\omega) = jkA\, P(\omega)\frac{e^{-jkr}}{2\pi r}F(r,\theta) \qquad (1)$$

where $k = \omega/c$ is the wave number; ω and c are radian temporal frequency and propagation velocity, respectively; $P(\omega)$ is the pressure amplitude at the transducer surface with area A. The function $F(r,\theta)$ describes the beam pattern at a constant range from the transducer and is equal to $2J_1(k\,a \sin\theta)/(k\,a \sin\theta)$ where $J_1(\beta)$ represents a Bessel function of the first kind and first order with argument β.

It is useful to simplify this expression at the outset. By virtue of the narrow angular beamwidths (e.g., 0.3 degree) and small fractional range segments, L/R, that are of interest, the beam pattern over the gated segment can be expressed as a function of cross-sectional arguments only: i.e., $F(r\theta) = F(y,z)$. Also, the range, r, can be replaced by R + x. Thus, eq. (1) can be rewritten as

$$p'(\omega) = (j\omega A/c)P(\omega)\frac{e^{-j\omega R/c}}{2\pi R}e^{-j\omega x/c}F(y,z)\ . \qquad (2)$$

The backscatter from the gated tissue volume is characterized in terms of a scattering function, $S(\omega; x,y,z)$. This function relates the amplitude of the incident pressure at a point (x,y,z) within the volume of interest to the strength of the backscattered spherical wave originating at that point. The backscattered wave is sensed by the transducer which responds to the spatial average of the pressure distribution generated over its surface. The spatially averaged pressure received from each scattering element is proportional to $F^2(y,z)$ and can be readily calculated by using the coordinate system employed by O'Neil [9]. The total received pressure is then obtained by integration over the gated volume, V_m

$$p_m(\omega) = B(\omega)\int_{V_m} S(\omega; x,y,z)F_m^2(y,z)e^{-j2\omega x/c}dxdydz \qquad (3a)$$

where $B(\omega)$ is

$$B(\omega) = (j\omega A/c)P(\omega)\frac{e^{-j2\omega R/c}}{(2\pi R)^2} \qquad (3b)$$

and the sub-index m indicates the m^{th} measurement.

As a first approximation for many tissues of interest, $S(\omega; x,y,z)$ characterizes weak scattering of identical, randomly distributed, isotropic scattering elements. Under these conditions it is convenient to factor the scattering function as follows

$$S(\omega; x,y,z) = H(\omega)N(x,y,z)\ . \qquad (4)$$

Here $H(\omega)$ defines the reflectance characteristic of a single scattering element while $N(x,y,z)$ describes their effective spatial concentration. With eqs. (3) and (4), the total received pressure in the m^{th} measurement can be written as a Fourier transformation, with respect to axial range, of the product of the gating function $G(x)$ and a function characterizing the weighted concentration of tissue elements; i.e.

$$p_m(\omega) = B(\omega)H(\omega)\int_0^\infty\left[G(x)\int_{-\infty}^{\infty}\int_{-\infty}^{\infty}N(x,y,z)F_m^2(y,z)dydz\right]e^{-j2\omega x/c}dx\ . \qquad (5)$$

The function $G(x)$ describes the length of the range gate and the range-weighting function (e.g., Ham-

ming) applied in the measurement. Denoting the Fourier integral by $Q_m(\omega)$, eq. (5) can be rewritten as

$$p_m(\omega) = B(\omega)H(\omega)Q_m(\omega) \tag{6}$$

It is important to notice the stochastic nature of $Q_m(\omega)$ resulting from the stochastic nature of the tissue concentration function, N(x,y,z). Qualitatively, for equal, but non-overlapping tissue volumes, $p_m(\omega)$ can vary randomly from measurement to measurement, as different tissue realizations are illuminated with the ultrasonic beam. This stochastic process can be meaningfully characterized in terms of the power spectrum, $\hat{p}$, computed by forming an ensemble average of the modulus-square of $p_m(\omega)$; i.e.,

$$\hat{P} = \frac{1}{M}\sum_{m=1}^{M} |p_m(\omega)|^2 \tag{7a}$$

$$= |B(\omega)|^2 \; |H(\omega)|^2 \; M^{-1}\sum_{m=1}^{M} |Q_m(\omega)|^2 \tag{7b}$$

In the present technique, the ensemble average is computed from a series of observations of $|p_m(\omega)|^2$ taken along adjacent, non-overlapping beam headings within the examined tissue. The resulting function $\hat{p}$ then constitutes an estimate of the "true" power spectrum, $\langle p \rangle$. (The symbol $\langle \cdot \rangle$ refers to ensemble averaging over all realizations of the structure of interest.)

The statistical fluctuations associated with estimates of $\langle \hat{p} \rangle$ are of significant practical importance. For tissues characterized by a Gaussian-distributed concentration function and a correlation volume much smaller than the sampling volume, V_m, $p_m(\omega)$ has a Gaussian distribution and $|p_m(\omega)|^2$ obeys Chi-square statistics. (Tissues which possess many independent scattering centers within V_m obey these statistics as well by virtue of the law of large numbers.)

It follows from the properties of the Chi-square distribution that independent measurements of $|p_m(\omega)|^2$ exhibit significant variability; in fact, at any value of ω, the standard deviation, σ, of such measurements is equal to their mean value, $\langle p \rangle$. The relative fluctuations which persist after averaging M independent realizations of $|p_m(\omega)|^2$ can be assessed from the ratio

$$\frac{\langle \hat{P} \rangle \pm \sigma}{\langle \hat{P} \rangle} = 1 \pm M^{-\frac{1}{2}} \tag{8}$$

In spectral measurements, this degree of fluctuation is evidenced at each value of ω producing a statistical "ripple" of the above magnitude about the mean spectral shape. This result has been employed to select a value of M that is suitable for clinical measurements as discussed below.

B. Statistically Stationary Architectures

If the concentration function, N(x,y,z), is a weakly stationary process, then its autocorrelation function can be expressed as

$$\langle N(x,y,z)N(x_1,y_1,z_1)\rangle = R_N(\Delta x,\Delta y,\Delta z) \tag{9}$$

where $\Delta x = x-x_1$, $\Delta y = y-y_1$, $\Delta z = z-z_1$. For this case, substitution into eqs. (5) through (7) can be carried out with considerable simplification. The expected value of $\hat{p}$, taken in the sense of an average over the ensemble of tissue realizations becomes

$$\langle \hat{P} \rangle = \langle |p_m(\omega)|^2 \rangle \tag{10}$$

$$= |B(\omega)|^2 \; |H(\omega)|^2 \int_{-\infty}^{\infty}\int_{-\infty}^{\infty}\int_{-\infty}^{\infty} R_G(\Delta x)\; R_F(\Delta y,\Delta z)$$

$$R_N(\Delta x,\Delta y,\Delta z) \times e^{-j2\omega\Delta x/c}\; d(\Delta x)d(\Delta y)d(\Delta z)$$

where R_G and R_F are the autocorrelation functions of the gate function, G, and directivity function, F^2, respectively.

For a limiting case that is of practical interest here, the correlation volume defined by the system-related functions R_G and R_F is much larger than that of the tissue function R_N. Equation (10) can then be approximated as

$$\langle \hat{P} \rangle \cong |B(\omega)|^2 \; |H(\omega)|^2 \; R_G(0)\; R_F(0,0)\; T(\omega) \tag{11}$$

where $T(\omega)$ depends only on the tissue structure and is given by

$$T(\omega) = \int_{-\infty}^{\infty}\left[\int_{-\infty}^{\infty}\int_{-\infty}^{\infty} R_N(\Delta x,\Delta y,\Delta z)\; d(\Delta y)d(\Delta z)\right] \tag{12}$$

$$e^{-j2\omega\Delta x/c}\; d(\Delta x)\;.$$

C. Spatial Distribution of Rayleigh Scatterers

The above discussions are applicable directly to tissues which can be modelled as a set of randomly distributed, discrete Rayleigh scatterers: i.e., scatterers whose sizes are much smaller than the illumination wavelengths. We next treat the case where the number of Rayleigh scatterers within a unit volume is a Poisson process; i.e.,

$$N(x,y,z) = \sum_{i=1}^{K} \delta(x-x_i)\; \delta(y-y_i)\; \delta(z-z_i) \tag{13}$$

where δ is the Dirac delta function and (x_i,y_i,z_i) are the random coordinates of the ith scatterer which are uniformly distributed over the inspected tissue volume. K is the number of scatterers per unit volume and obeys Poisson statistics with parameter $\langle K \rangle$. It follows [10] that R_N, the autocorrelation function of N, is

$$R_N = \langle K \rangle\; \delta(\Delta x)\; \delta(\Delta y)\; \delta(\Delta z) + \langle K \rangle^2 \tag{14}$$

Using eq. (14) for R_N in eq. (10), one obtains

$$\langle \hat{P} \rangle = |B(\omega)|^2 \, |H(\omega)|^2 \left\{ \langle K \rangle R_G(0) R_F(0,0) + \right. \tag{15}$$

$$\left. \langle K^2 \rangle \, |\tilde{G}(\omega)|^2 \int_{-\infty}^{\infty} \int_{-\infty}^{\infty} R_F(\Delta y, \Delta z) \, d(\Delta y) d(\Delta z) \right\}$$

where $\tilde{G}(\omega)$ is the Fourier transform of $R_G(\Delta x)$.

The first term in eq. (15), proportional to the expected number of scatterers, is identified with non-coherent scattering. The second term, proportional to the square of the expected number of scatterers, is identified with coherent scattering. The relative contributions of both components to the total measurement varies with frequency. The non-coherent spectral component is distributed over the frequency domain, whereas the coherent component primarily contributes at zero frequency providing that the power spectrum $|\tilde{G}(\omega)|^2$ can be adequately approximated as a Dirac delta function at the frequency origin.

In practice, non-coherent spectra predominate in clinical observations. This occurs because spectral observations are carried out at high frequencies and a time-weighting function is used to suppress the sidelobes of $|\tilde{G}(\omega)|^2$. These sidelobes fall-off at a rate which is more rapid than the ω^{-2} characteristic associated with a rectangular gating function.

Equation (15) can be used to address the topic of spectral normalization. The non-coherent term is proportional to $|H(\omega)|^2$ which for Rayleigh scatterers has an ω^4 dependence. However, other system-related terms are also frequency-dependent. To account for these factors, spectral data are normalized using calibration spectra obtained from a flat, water-glass interface viewed at normal incidence and located at R + L/2. It can be shown that this normalization removes the system-related frequency dependence in the non-coherent component of eq. (15) and that the normalized spectrum is indeed proportional to ω^4. Experimental results verifying this conclusion are presented in a subsequent section.

These results and those of preceding sections are applicable to a variety of tissue structures. However, all tissues of interest do not fall within simple categories and further analysis is warranted to treat more complex tissue structures and to investigate the most appropriate approaches to data normalization. Such analyses are being conducted as the clinical data base is expanded and histologic preparations become available.

3. Spectrum Analysis System

The spectrum analysis techniques described above have been implemented with an on-line clinical system. The system is integrated with a high-resolution A- and B-scan instrument which is employed routinely in ophthalmic examinations (fig. 2). The operation of the system is described elsewhere [6] and is only briefly summarized here. The tissue segment to be analyzed is selected by observing A- and B-scan displays in which the position of the moveable, system range gate is superimposed. These displays are also monitored to insure that the beam does not traverse the absorptive ocular lens and that the tissue segment to be analyzed lies within the transducer's focal zone.

After the range gate has been placed over the desired tissue segment, processing is initiated. First, the gated rf echo complex is multiplied by a time-weighting function to suppress spectral side lobes which would prevent accurate measurements of steeply rising or falling spectra. Then, the gated signals are applied to a scanning electronic spectrum analyzer which computes the desired spectrum comprised of 50 spectral elements occupying adjacent 300-KHz frequency bands.

An ensemble of these spectra are computed along 13 adjacent, non-overlapping beam headings and entered into an on-line averager. The spectral ensemble is obtained by executing a slow sector scan during which an optical encoder initiates a spectrum analysis computation each time the trans-

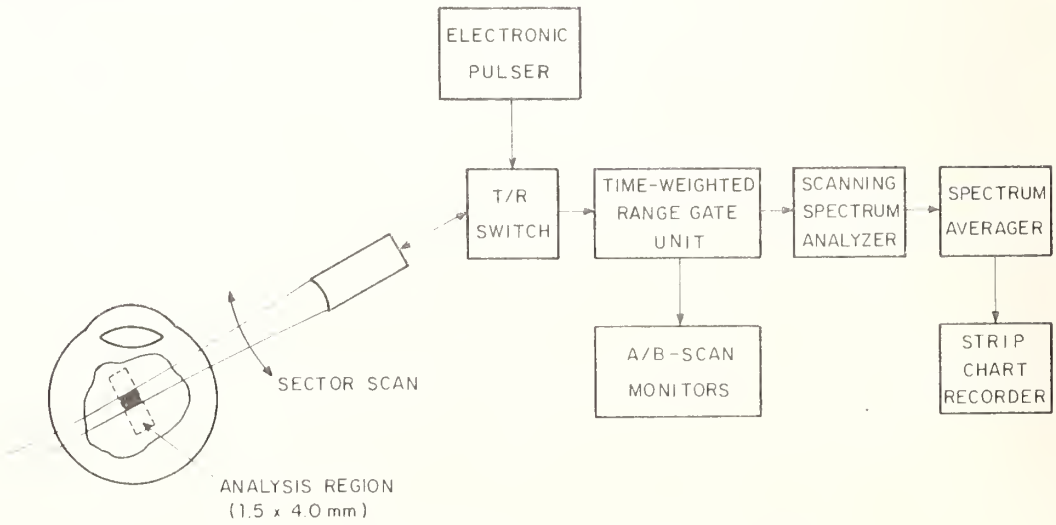

Fig. 2. Configuration of spectrum analysis system.

ducer heading is incremented by one angular beamwidth (0.3 degrees at 10 MHz). (In practice, 100 partly redundant spectra are averaged to improve electronic signal-to-noise ratios.) Averaged spectra are presented on a strip chart recorder which also displays frequency and amplitude calibration signals for use in subsequent processing.

After each examination session, calibration spectra are recorded from an optically flat glass plate situated at each of the ranges used in tissue measurements. The calibration spectra and tissue spectra are subsequently digitized and entered into a computer for spectral normalization, smoothing, regression analysis, and data cataloguing.

Table 1 lists the salient system parameters which influence the detail with which tissue characteristics such as $|H(\omega)|^2$ and $T(\omega)$ can be examined. As discussed below, the frequency coverage, spectral resolution, and number of non-overlapping beam positions are of central importance in tissue studies.

Table 1. Nominal system parameters.

Frequency coverage	5 to 13 MHz
Spectral resolution	
Gating function	0.6 MHz
Spectrum analyzer	0.3 MHz
Gated range segment	1.5 mm
Lateral scan dimension	4 mm
Beam width (10 MHz)	0.3 mm
Number of distinct beam positions	13
Dynamic range	30 to 35 dB

The frequency coverage achievable in spectral measurements has been found to approximate the 20-dB system bandwidth as defined by glass plate spectra. This coverage is nominally 5 to 13 MHz for a broadband transducer with a 10 MHz resonant frequency. Beyond this range, limited signal-to-noise ratios are encountered and spectral normalization can become inaccurate. The available frequency coverage determines the spectral characteristics of tissue elements with specific scale sizes. Within the above frequency range, Rayleigh scattering is encountered for spherical elements whose diameters are less than 35 μm. As discussed below, membranes, or periodic features, with axial dimensions larger than 100 μm will produce periodic spectra with at least one spectral cycle displayed over the achievable 8 MHz coverage. In addition, tissue septa whose thicknesses are less than 30 μm will exhibit monotonically rising spectra.

Spectral resolution is determined by the 2-μs gate duration and the weighting function. These variables have been chosen to achieve a 0.6 MHz resolution while the spectrum analyzer employs a 0.3 MHz filter bandwidth. The short gate duration corresponds to a 1.5 mm tissue depth permitting analysis within small ocular tumors and avoiding significant signal weighting due to attenuation within the gated echo complex.

The number of independent spectra which are ensemble averaged is an important factor in assessing the residual statistical fluctuation with estimations of mean spectral shape and amplitude. Usually, 13 spectra from non-overlapping beam positions are used to form the ensemble average. For the conditions described with reference to eq. (8), a statistical spectral "ripple" of approximately ± 1 dB is expected. While spectral fluctuations are often confined within this range, there are situations where significantly larger excursions occur suggesting that the analyzed tissues exhibit relatively large correlation volumes.

(Further analyses of these parameters in terms of the accuracies of spectral slope and attenuation estimations have been presented in a previous publication [7].)

4. Representative Results

Before clinical deployment, the performance of the spectrum analysis system and the applicability of the theoretical approach was verified on a number of test targets. One type of test target was a thin plastic membrane immersed in distilled water and viewed at normal incidence. For this target, $N(x,y,z)$ is proportional to $\delta(x-x_0) - \delta(x-x_0-D)$ where D represents thickness and x_0 locates the proximal membrane surface. From eq. (5) and (7), the calculated power spectrum, is proportional to $\sin(2\pi fD/c)$ so that spectral minima will occur at frequencies separated by an interval equal to $c/2D$. The observed spectrum, shown in figure 3, exhibits a scalloped shape in agreement with this result. The measured frequency interval between successive spectral minima is 3.6 MHz which corresponds to a calculated thickness of 360 μm. This value is within 5 percent of the measured membrane thickness.

Spectral data were also obtained for dilute solutions of plastic microspheres with 25 μm diameters. These dilute solutions insure that single scattering from points is approximated over the spectral measurement band. Moreover, it is reasonable to assume that their spatial distribution forms a Poisson process since the random position of each scatterer should be independent and uniformly distributed within the analyzed volume. Accordingly, measured spectra should be described by eq. (15).

Figure 4 shows normalized spectra measured for two microsphere concentrations. The spectral curves agree very closely with the ω^4 dependence expected from the normalized, non-coherent spectral component in eq. (15). In addition, a fourfold change in microsphere concentration was found to produce a proportional 6-dB change in spectral amplitude. This amplitude change is consistent with non-coherent scattering, in which received spectral power is proportional to the mean number of scattering particles.

Clinical measurements have been carried out on a wide variety of normal and diseased structures in the eye and orbit. In vivo data on more than 200 cases have been acquired and digitally catalogued as part of an on-going research effort. The following paragraphs review some of the observed spectral features which relate directly to cases treated in the preceding discussions of analytic and experimental results.

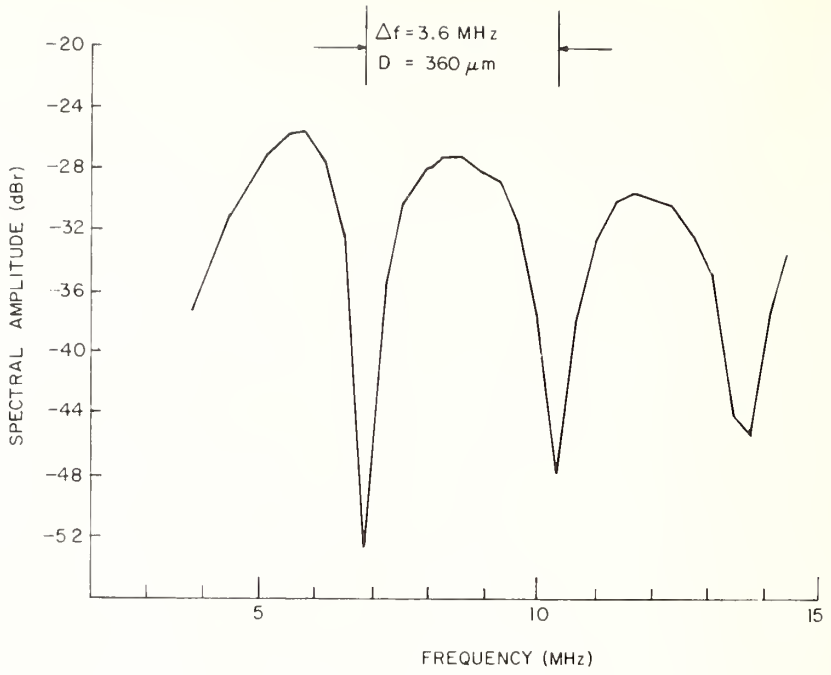

Fig. 3. Spectrum of echoes from plastic membrane.

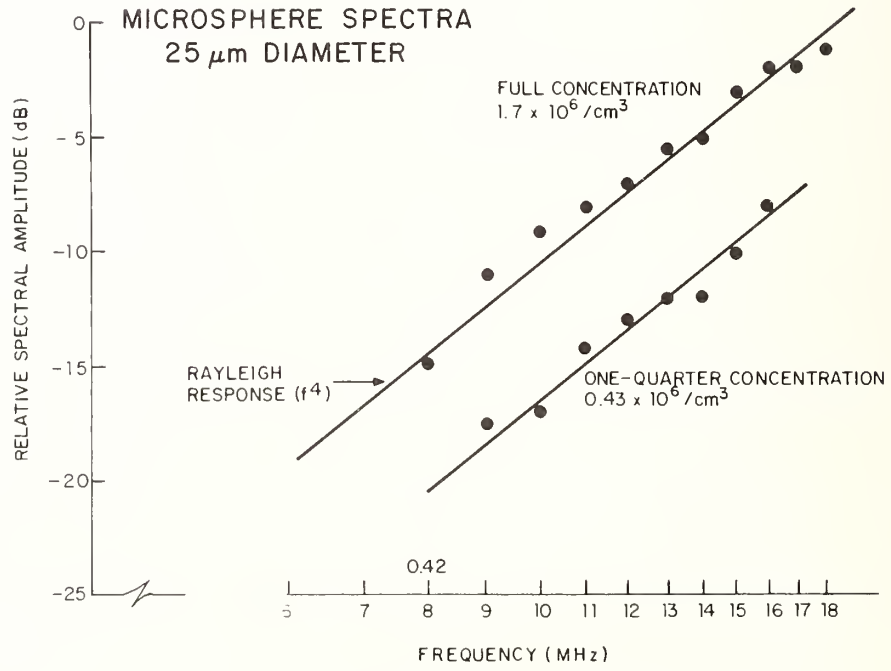

Fig. 4. Spectra obtained for two concentrations of dilute microsphere suspensions.

Detached retinas, observed prior to the development of gross degenerative processes, constitute thin membranes bounded, anteriorly, by vitreous humor and, posteriorly, by fluid exudate. Spectra obtained from these structures display a marked scalloped appearance similar to that seen for the plastic membrane (fig. 3). This fact is demonstrated in figure 5 which shows clinical spectra in decibels relative to a glass plate (dBr) obtained from three different cases of retinal detachments. Retinal thickness can be computed from the frequency repetition interval of these spectra. Using a nominal propagation velocity of 1.5 mm/μs for the retina, the computed values in the illus-

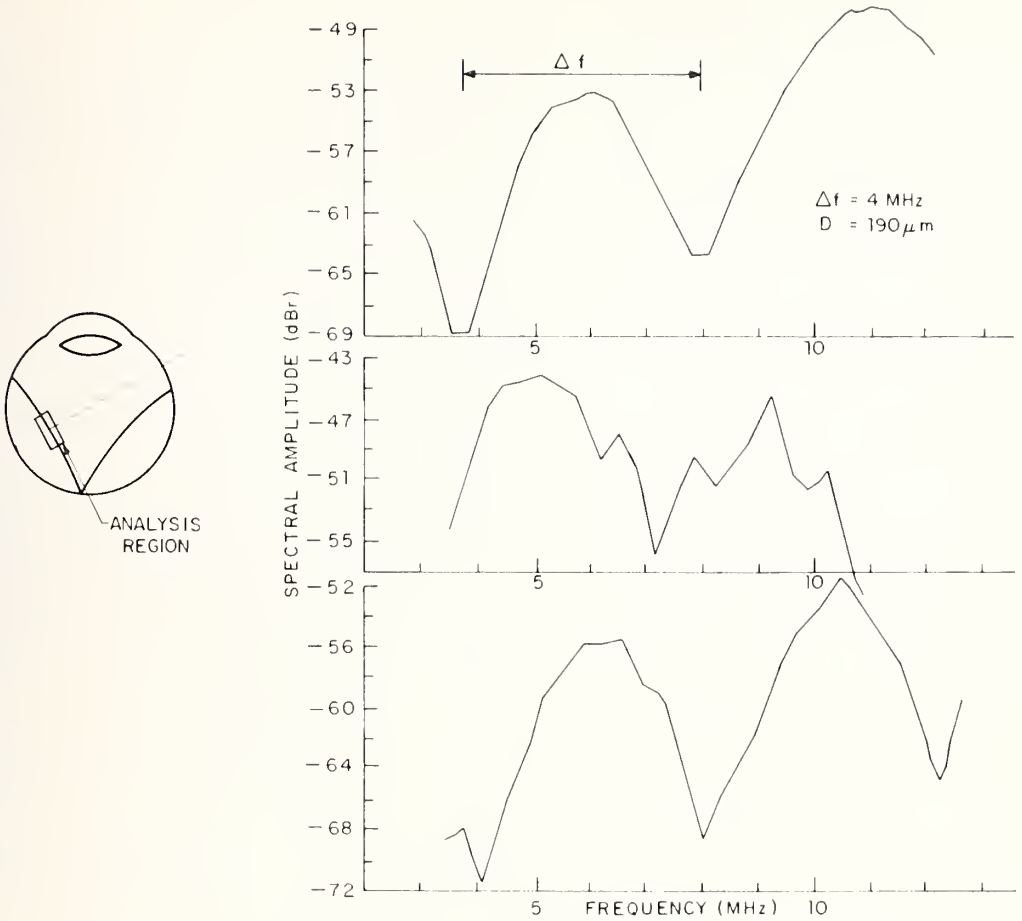

Fig. 5. Clinical spectra obtained for detached retina (3 cases). dBr units indicate dB levels with respect to glass plate spectra.

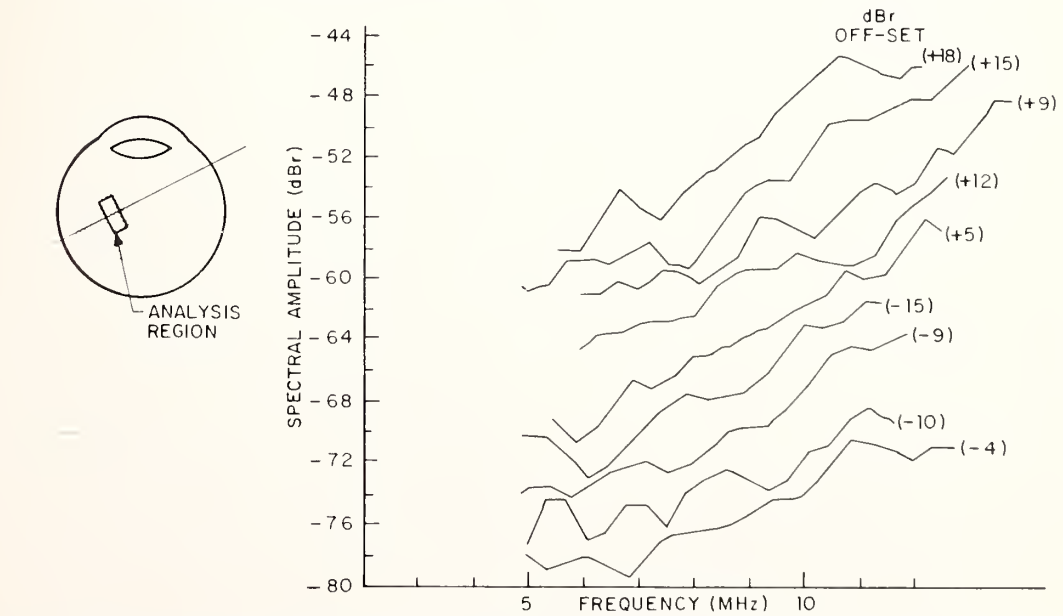

Fig. 6. Clinical spectra obtained for vitreous hemorrahages (9 cases). Spectral amplitudes have been off-set by indicated values.

trated cases are on the order of 190 μm and are consistent with expected retinal dimensions.

Vitreous hemorrhages have been studied extensively with the spectrum analysis system. In their unorganized state, these hemorrhages contain randomly placed aggregations of hemorrhagic debris dispersed in sections of the vitreous humor. Unorganized hemorrhages consistently produce spectra whose amplitudes increase markedly with increasing frequency as shown in figure 6. The rate of increase can sometimes be as rapid as the f^4 characteristic associated with Rayleigh scattering: this fact indicates scattering from a uniform distribution of elements that are smaller than 35 μm. Spectral amplitudes are typically -70 dBr near 5 MHz: these very low levels can often be exceeded by returns from isolated specular reflectors or, in the extreme, by the system noise level. At higher frequencies, the spectral amplitudes produced by hemorrhagic debris are significantly larger and exceed these background levels.

Occasionally, other spectral shapes have been observed within an examined vitreous hemorrhage. They indicate a possible high-density packing or organization of the hemorrhagic debris. The presence of membranes has also been found to affect the observed spectral shape. For example, figure 7 shows the scalloped spectra received from a range-gated volume which contained both hemorrhagic debris and a thickened intravitreal membrane.

5. Conclusion

The analysis outlined in the preceding sections has proven extremely useful in designing the spectrum analysis system and in selecting system parameters, such as gate dimensions, for clinical application. It has also formed a constructive framework for interpreting in vivo data, especially for detached retinas, vitreous hemorrhages, and intra-vitreal dispersions of cholesterol aggregations.

The analysis is being extended to accommodate more complex tissue architectures. This effort is proceeding using clinically measured spectra and subsequent histologic preparations when available. Of particular interest are intra-ocular tumors such as malignant melanomas and metastatic carcinomas.

Other topics under investigation include the use of spectral data to estimate tissue attenuation characteristics. Presently, attenuation estimates are formed from ratios of power spectra measured at sequential range sites separated by ΔR. If the examined tissue architecture satisfies certain conditions (e.g., statistical homogeneity), then such ratios describe the attenuation experienced within ΔR. Spectral data indicate that this approach is appropriate for some tissues (e.g., orbital fat) but is not applicable to other tissues (e.g., heterogeneous tumors). In these latter cases, spectral ratios might serve as a useful index of statistical homogeneity.

As the clinical data base is expanded, these investigations can proceed toward the ultimate goal of applying spectrum analysis techniques to supplement conventional A- and B-scan ultrasonography.

Acknowledgments

The authors wish to acknowledge the collaboration of D. Jackson Coleman and Louise Franzen in the clinical aspects of this work. They also wish to thank Angel Rosado for his assistance in data processing.

Portions of this work were supported by Public Health Service Grants EY-01212-04 and EY-01218-04 from the National Eye Institute.

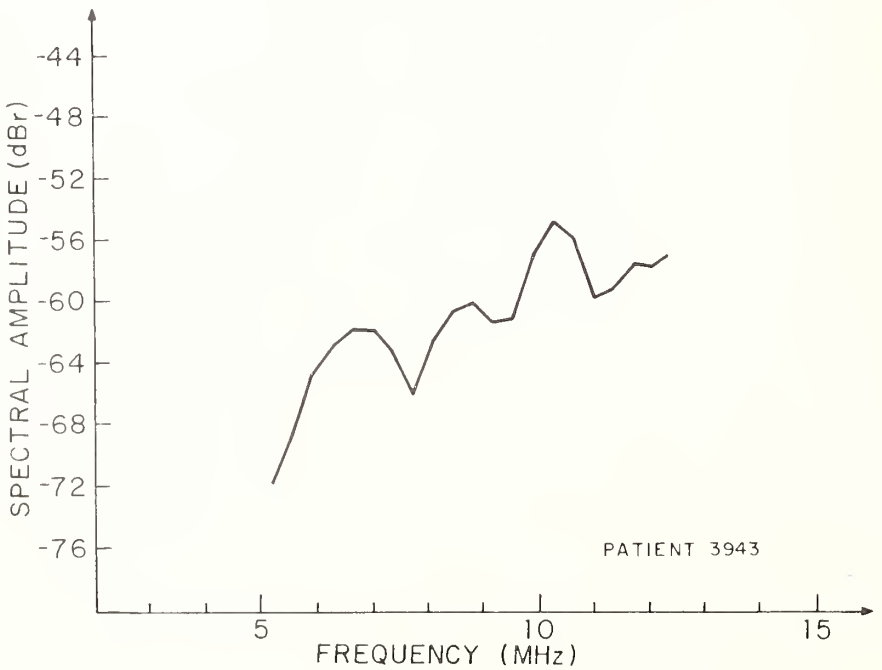

Fig. 7. Clinical spectrum obtained for a vitreous hemorrhage and associated intravitreal membrane.

References

[1] Waag, R., Lerner, R., and Gramiak, R., Swept-Frequency Ultrasonic Determination of Tissue Macrostructure, in Ultrasonic Tissue Characterization, M. Linzer, ed. National Bureau of Standards Spec. Publ. 453, pp. 213-230 (U.S. Government Printing Office, Washington, D.C., 1976).

[2] Lele, P. and Namery, J., A Computer-Based Ultrasonic System for the Detection and Mapping of Myocardial Infarcts, in Proceedings of the San Diego Biomedical Symp. 13, 121-132 (1974).

[3] Sigelmann, R. and Reid, J., Analysis and measurement of ultrasound backscattering from an ensemble of scatterers excited by sine-wave bursts, J. Acoust. Soc. Am. 5, 1351-1355 (1973).

[4] Lizzi, F. L., St. Louis, L., and Coleman, D. J., Applications of spectral analysis in medical ultrasonography, Ultrasonics 14 (2), 77-80 (1976).

[5] Lizzi, F., Burt, W., and Coleman, D. J., Effects of ocular structures on the propagation of ultrasound in the eye, Arch. Ophthalmol. 84, 635-640 (1970).

[6] Lizzi, F., Laviola, M., and Coleman, D. J., Ultrasonic Tissue Characterization Using Spectrum Analysis, in Proceedings of SPIE/SPSE Conference on Application of Optical Instrumentation in Medicine V, Society of Photo-Optical Instrumentation Engineers, Palos Verdes Estates, California, pp. 322-328 (1976).

[7] Lizzi, F., Laviola, M., and Coleman, D. J., Tissue Signature Characterization Utilizing Frequency Domain Analysis, in Proceedings of IEEE Ultrasonics Symposium 1976, Institute of Electrical and Electronics Engineers, Inc., New York, pp. 714-719 (1976).

[8] Lizzi, F. and Elbaum, M., Ultrasonic Spectrum Analysis Techniques in Medical Ultrasound, Riverside Research Institute Technical Report, Riverside Research Institute, New York, N.Y. (in preparation).

[9] O'Neil, H., The theory of focussing radiators, J. Acoust. Soc. Am. 21, 516-526 (1949).

[10] Pratt, W. Laser Communications Systems, pp. 255-262 (John Wiley and Sons, New York, 1969).

Reprinted from *Ultrasonic Tissue Characterization II*, M. Linzer, ed., National Bureau of Standards, Spec. Publ. 525 (U.S. Government Printing Office, Washington, D.C., 1979).

TISSUE CHARACTERIZATION IN VIVO BY DIFFERENTIAL ATTENUATION MEASUREMENTS

Salavatore Lévi and José Keuwez

Ultrasound Lab and F.R.E.S.E.R.H., Hôpital Brugmann
Université Libre de Bruxelles, Brussels, Belgium

A practical ultrasound method has been applied for the differentiation in vivo of pelvic tumors. This method has the advantage of being applicable during usual ultrasonic examination and does not require information about the tissues involved, nor the surrounding tissues.

The method is based upon the fact that the ultrasonic attenuation increases with frequency; the comparison of the echoes from the posterior and anterior boundaries of the tumor leads to a coefficient of differential attenuation. This coefficient has been determined in examinations of 95 gynecological patients; the organs and tumors explored were normal uteri, leiomyomas and ovarian cysts. The values of the coefficient of differential attenuation obtained for these three categories of tissue are sufficiently separated, which enables us to make a differentiation.

Key words: Characterization; differential attenuation; tumor; ultrasound.

1. Introduction

Ultrasound has been shown to be effective in the diagnosis of tumors and is generally capable of differentiating between solid and liquid components. The current acoustic methods, which have been applied for a number of years, give dependable results in 93 percent of the leiomyoma cases and in 84 percent of the cases involving ovarian cysts [1][1].

Ultrasonic imaging has reached a high level of accuracy, especially with the application of "grey-scale" techniques. However, other aspects of diagnostic ultrasound have not yet reached their full potential. More precise information on the viscoelastic properties of tissues, especially those of tumors, should be the next step in research on diagnostic methods.

Quantitative studies should produce more meaningful numerical data regarding the various types of tumors investigated. Such data will be representative of the acoustical properties of the tissues and complete the subjective data produced by imaging.

One of the most important of these properties is the attenuation of sound. The loss in acoustic intensity in travelling through the biological tissues is caused mainly by absorption and scattering. These causes may be grouped under the term "attenuation". It is difficult to assess the individual contribution of these mechanisms (absorption, scattering, ...) and it is therefore quite preferable to confine oneself to examining attenuation as a whole.

The importance of the various mechanisms is dependent on the wave frequency; therefore the attenuation is a function of frequency. The attenuation is a characteristic of a tissue, but generally it is quite impossible to measure it in vivo without invasive techniques. We chose the determination of the variation of the attenuation with frequency as a basis for the differentiation of tissues [2-4]. A similar concept has been proposed by Kossoff [5,6], but no results have been published. For a good understanding, we envisioned a model similar to that published by Hill [7].

2. Model and Analysis

The following analysis is approximate and does not take into account various mechanisms which could be important. The objective of this analysis is to give an idea of the relation between the ultrasonic properties of tissues under investigation and the coefficient of differential attenuation which will be defined below.

Generally any mass[2] consists of several layers of tissue which have their own properties; for example, the uterine fibroma in which a layer of normal muscle surrounds pathological tissues. The model (fig. 1) has been constructed in order to represent the different layers of the region under investigation and of the mass. Each layer is characterized by an acoustic absorption coefficient, and each interface by a back-scattering cross-section (σ). (σ is used here to take account of all the mechanisms which contribute to the loss of energy at this interface.)

These layers are separated into two sets; p layers between the transducer and the mass, the mass being constituted of r - p = n layers. In each layer, one of the important mechanisms in

[1]Figures in brackets indicate literature references at the end of this paper.

[2]In this paper, the term "mass" will include the normal uterus, leiomyoma, and cyst.

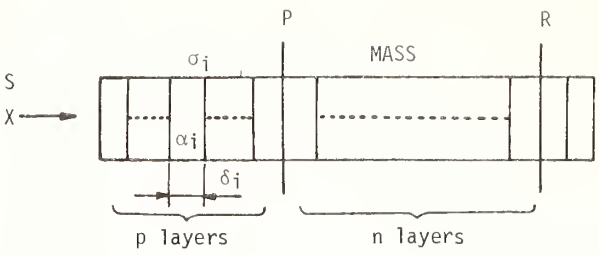

Fig. 1. Model of the different layers of the region under investigation.

which acoustic energy is degraded as heat by internal friction of viscosity is the absorption. This loss of acoustic energy follows the relation given by the equation:

$$A = A_0 \exp(-\alpha x) \tag{1}$$

where α is the amplitude absorption coefficient, A_0 and A are, respectively, the wave amplitude at some reference point and the amplitude at a further distance, x, from that reference point.

Let us consider a sound wave propagating from the source S to the point R (fig. 1). The amplitude of that wave at R is given by

$$A(R,\nu) = A_0(\nu)\ \bar{\sigma}(R,\nu)\ \exp(-\alpha_1(\nu)\delta_1) \tag{2}$$

$$\ldots\ \exp(-\alpha_r(\nu)\delta_r)$$

where ν is the wave frequency, α_i and δ_i are, respectively, the amplitude absorption coefficient and the thickness of the layer i; $\bar{\sigma}(\nu)$ is a factor which describes the decrease of amplitude at the several interfaces. The amplitude, SA, of the reflected wave coming from R on to the transducer is related as follows:

$$SA(R,\nu) = A_0(\nu)\ \sigma(R,\nu)\ \exp(-2 \sum_{i=1}^{r} \alpha_i\delta_i) \tag{3}$$

If (ν_1,ν_2) are two different frequencies, let us consider the ratio of the amplitudes $SA(R,\nu_1)$ and $SA(R,\nu_2)$; according to eq. (3), this ratio is given by the following equation:

$$\ln \frac{SA(P,\nu_1)}{SA(R,\nu_2)} = \ln \frac{A_0(\nu_1)}{A_0(\nu_2)} + \ln \frac{\sigma(R,\nu_1)}{\sigma(R,\nu_2)} \tag{4}$$

$$- 2 \sum_{i=1}^{r} (\alpha_i(\nu_1)-\alpha_1(\nu_2))$$

Similarly, (see fig. 1)

$$\ln \frac{SA(P,\nu_1)}{SA(P,\nu_2)} = \ln \frac{A_0(\nu_1)}{A_0(\nu_2)} + \ln \frac{\sigma(P,\nu_1)}{\sigma(P,\nu_2)} \tag{5}$$

$$- 2 \sum_{i=1}^{p} (\alpha_i(\nu_1)-\alpha_i(\nu_2))$$

Now we introduce J as the difference of eqs. (4) and (5).

$$J = \ln \frac{SA(R,\nu_1)}{SA(R,\nu_2)} - \ln \frac{SA(P,\nu_1)}{SA(P,\nu_2)} \tag{6}$$

$$J = \ln \frac{\sigma(R,\nu_1)}{\sigma(P,\nu_1)} - \ln \frac{\sigma(R,\nu_2)}{\sigma(P,\nu_2)} \tag{7}$$

$$- 2 \sum_{i=p+1}^{r} (\alpha_i(\nu_1)-\alpha_i(\nu_2))\delta_i$$

Equation (6) can be written in the following form:

$$\frac{J}{2d} = (\eta(\nu_1) - \eta(\nu_2)) - (\bar{\alpha}(\nu_1) - \bar{\alpha}(\nu_2))$$

$$= \Delta\eta - \Delta\bar{\alpha}$$

where

$$\sum_{i=p+1}^{r} \alpha_i\delta_i = \bar{\alpha}d \quad (d = \text{thickness of the mass}) \tag{10}$$

$$\ln \frac{\sigma(R,\nu)}{\sigma(P,\nu)} = 2d\eta(\nu) \tag{11}$$

Examining eq. (8), we see that J/2d depends only on the ultrasonic properties of the layers comprised between P and R; J/2d is a characteristic of the mass and tells us about the variation of attenuation with frequency.

Let us remark that, for the calculation of the value of J, we only need the knowledge of four amplitudes, and no information is required about the tissues involved nor the surrounding tissues.

3. Materials and Methods

We have defined eq. (6)

$$J = \ln \frac{SA(R,\nu_1)}{SA(R,\nu_2)} - \ln \frac{SA(P,\nu_1)}{SA(P,\nu_2)} \tag{12}$$

which is the basic equation for characterization based upon differential attenuation. For the calculation of J it is necessary to measure the amplitudes of the waves reflected by the anterior and posterior boundaries of the mass. This measurement must be performed at two frequencies (ν_1 and ν_2). Theoretically, it is possible to undertake these measurements with a single pulse [6], however, we have chosen to adapt eq. (10) by considering that these amplitudes are for waves generated by two relatively narrow band (0.5 MHz) transducers.

These amplitudes have been measured with the ultrasonic equipment "Kretz-Combison I" [2-4]. For each amplitude measurement, all the settings were identical except that of the master gain. This last one was adequately adjusted to obtain an amplitude of given level on the A-Scope for the echo of interest (I). The corresponding reading

$L(I,\nu)$ (in dB) was used in the following equation based on eq. (12)

$$\gamma = \frac{1}{2d} L(R,\nu_1) - L(R,\nu_2) - (L(P,\nu_1) - L(P,\nu_2)) \quad (13)$$

where d = dimension of the mass. We call γ the coefficient of differential attenuation. This attenuation coefficient has been determined in examining 95 gynecological patients. The masses under investigation were the normal uterus, leiomyoma and cyst. The nominal frequencies were 2 MHz and 4 MHz.

4. Results

At present, twelve cases have been labeled as normal uterus, and 34 other cases have been classified as leiomyoma or cyst after surgery. We plotted the values of the differential attenuation coefficient, γ, versus the dimension, d, of the mass (fig. 2). The plot shows that γ is not influenced by d and that the γ belonging to the three categories of tissues (normal uterus, leiomyoma and cyst) are quite characteristic. Some cysts have shown an abnormally high differential attenuation for masses with liquid content; we also obtained negative values for some cysts, however, this peculiarity has been reported and explained [8]. The values of γ for the normal uterus are higher than those obtained for the leiomyoma, which is in agreement with the ultrasonic properties of these tissues and with previous results [4]. The results of the statistical analysis are shown in table 1.

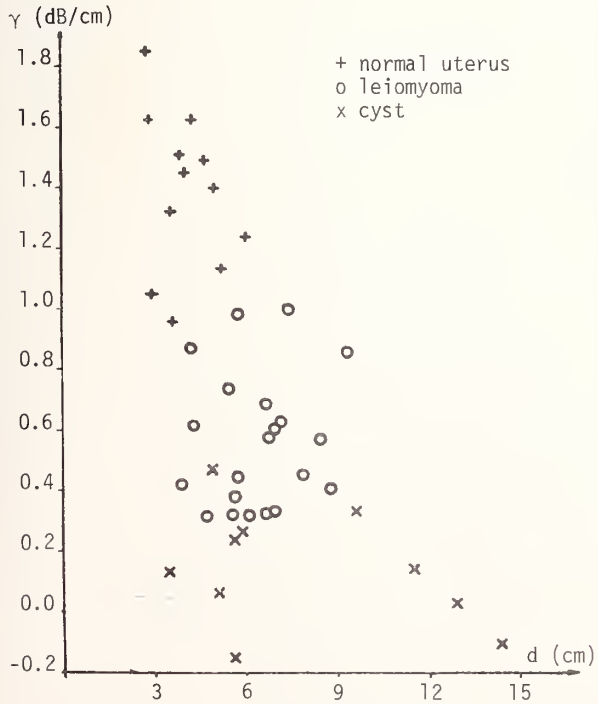

Fig. 2. Plot of the values of the differential attenuation coefficient, γ, versus the dimension, d, of the mass.

Table 1. Statistical analysis.

Organ	No.	Mean	γ(db/cm) S.D.
Normal uterus	12	1.39	0.27
Leiomyoma	22	0.57	0.22
Cyst	10	0.13	0.20

The absolute values are not interesting by themselves because γ is also depending on the instrumentation.

5. Comments and Discussion

If in vitro it is possible to imagine transmission methods, it is more difficult in vivo where generally only reflections methods are applicable. Unfortunately, it is not enough to know the amplitude of the reflected signals to tell something about the tissues involved. It is also necessary to know the properties and the orientation of the interfaces which have partially reflected the sound waves.

When working in vitro, the samples can generally be chosen, cut and positioned as desired. In vivo, many constraints have to be taken into account. Theoretically our method avoids some of them; for instance no information concerning the surrounding tissues is required. However, difficulties due to the orientation of the interfaces remain. Sometimes it was difficult to obtain a posterior echo because of the orientation of the tumor with respect to the abdominal wall. The orientation is also affected by the cardio-respiratory movements. Besides the difficulties of measurement, one should be aware that the refraction properties are frequency dependent. This could cause important differences in amplitude when using two frequencies ν_1 and ν_2 at oblique incidence. The dispersion of our results can in part be explained by this last discussion as well as by considering effects due to the beam geometry.

We characterized our transducers [4]; however this characterization was made in a nonattenuating medium (water). In our experiments the sound was propagating into an inhomogeneous and attenuating medium (for instance the abdominal wall) which could strongly influence the beam geometry. Therefore it is illusory to pursue this discussion based on our transducer characterization. However one must be aware that the beam geometry can dominate the results. That is probably the reason we did not obtain coherent results when working with other transducers. This method, as it is applied, considerably extends the duration of the examination, which is generally performed with a full bladder. Under these circumstances it is difficult for the patient to lie still. Technical improvements are necessary.

6. Conclusion

The characterization of tissues based upon the variation of attenuation with frequency seems to be suitable and helpful in cases where scans alone do not permit an accurate diagnosis. However, we would like to emphasize that it was not always possible to determine the coefficient of differential attenuation, for several reasons developed

in the previous paragraph. The results reported in this paper are those obtained for frequencies of 4 and 2 MHz; however, we also determined this coefficient for frequencies of 2 and 1 MHz. The results obtained in this last case were incoherent and the overlap between the three categories of tumors investigated was important.

The various inconveniences described above should be resolved by a better choice of transducers and the way of determining the various amplitudes required for the computation of the coefficient of differential attenuation.

Acknowledgments

We wish to thank Professor R. C. Eggleton (Indianapolis Center for Advanced Research, Indianapolis, Indiana) for helpful suggestions in preparing this paper, and Mrs. J. Drake for her secretarial assistance.

References

[1] Levi, S. and Delval, R., Value of ultrasonic diagnosis of gynecological tumors in 370 surgical cases, Acta Obstet Gynecol Scand 55 261-266 (1976).

[2] Levi, S., Essai d'analyse quantitative des échogrammes de tumeurs pelviennes; Journées d'Etudes sur les Ultrasons Appliqués à la Médicine, Nancy (1974), Résumé des Communications, p. 40.

[3] Levi, S., An Attempt to Differentiate Pelvic Tumors in Vivo by Attenuation Measurements, in Abstracts of the 2nd World Congress on Ultrasonics in Medicine, p. 81 (Junge und Sohn, Muchen, 1975).

[4] Levi, S. and Keuwez, J., An Attempt to Find a Differential Attenuation Coefficient for Ultrasonic Diagnosis of Pelvic Tumors in Vivo, in Ultrasound in Medicine, Vol. 3B, p. 1989 (Plenum Press, New York, 1977).

[5] Kossoff, G., Display techniques in ultrasound pulse echo investigations; a review, J. Clin. Ultrasound 2, 61 (1974).

[6] Kossoff, G., Reflection Techniques for Measurements of Attenuation and Velocity, in Ultrasonic Tissue Characterization, M. Linzer, ed., National Bureau of Standards Spec. Publ. 453, pp. 135-139 (U.S. Government Printing Office, Washington, D.C., 1976).

[7] Hill, C. R., Echoes from Human Tissues, in Ultrasonics International '75 Conference Proceedings, 24-26 March 1975, Imperial College, London, pp. 20-22 (Guildford IPC Science and Technology Press Ltd., London, 1975).

[8] LeCroissette, D. H. and Heyser, R. C., Attenuation and Velocity Measurements in Tissue Using Time Delay Spectrometry, in Ultrasonic Tissue Characterization, M. Linzer, ed., National Bureau of Standards Spec. Publ. 453, pp. 81-95 (U.S. Government Printing Office, Washington, D.C., 1976).

Reprinted from *Ultrasonic Tissue Characterization II*, M. Linzer, ed., National Bureau of Standards, Spec. Publ. 525 (U.S. Government Printing Office, Washington, D.C., 1979).

STATISTICAL ESTIMATION OF THE ACOUSTIC ATTENUATION COEFFICIENT SLOPE FOR LIVER TISSUE FROM REFLECTED ULTRASONIC SIGNALS

Roman Kuc,[1,2] Mischa Schwartz,[1] Nathaniel Finby,[2] and Frank Dain[2]

[1]Department of Electrical Engineering and Computer Science
Columbia University
New York, New York 10027, U.S.A.

[2]Department of Radiology
St. Luke's Hospital Center
New York, New York 10027, U.S.A.

The acoustic attenuation coefficient measured in dB/cm is known to increase linearly with frequency for liver tissue. The slope of this linear function, denoted by β, has been shown by other investigators to be an indicator of tissue state. β is usually measured from the change in the log spectrum experienced by an acoustic pulse when it is transmitted through the tissue. This paper presents research in estimating β from the reflected signals which are currently used in the clinical environment to generate diagnostic images. The reflected signals from internal tissue structures (in liver - the vascular and biliary systems) are distorted by the irregular reflector shapes. By modeling the roughness of the typical acoustic reflector, the distribution of the received spectra can be derived and the 95 percent confidence limits for the measured β can be calculated. The confidence limits are presented in terms of the tissue size and average reflector density. Experimental results using the reflected signals from *in vitro* refrigerated and formalin-fixed liver sections are presented.

Key words: Computer processing; estimation theory; liver attenuation; spectral analysis; statistical modeling; ultrasonic tissue characterization.

1. Introduction

As an acoustic pulse propagates through liver tissue it experiences a frequency dependent attenuation. Pauly and Schwan [1][1] observed that the acoustic attenuation was a linear function of frequency and postulated that this behavior was primarily the result of macromolecular relaxation processes. Lele *et al.* [2] confirmed the linear frequency dependence of the acoustic attenuation and in addition experimentally demonstrated that the slope of the linear dependence increased for necrotized tissue. Lele's experiments were performed by transmitting an acoustic pulse of known shape through a thin liver section and observing the change in the log power spectrum as the pulse propagated through the tissue. In this paper we discuss our work in estimating the slope of the linear frequency dependent attenuation, which we denote by the coefficient β, from the reflected acoustic signals, typical of those currently used in the clinical environment to generate the acoustic images.

The reflections observed from liver tissue are caused primarily by the vascular and biliary systems that permeate the liver volume. Because the typical reflector encountered within the liver is neither plane nor normally incident to the incident pulse, the log spectra of the reflected signals are distorted. In this paper we account for the distortion caused by the irregularly shaped reflector by modeling the reflector as a random linear filter having an impulse response which is a sample function from a zero mean, white Gaussian process. From this assumed model we can derive the distribution of the observed sample spectrum. Using this distribution we can calculate confidence intervals for the resulting estimates of β. Finally, we predict the sensitivity of the estimator on the tissue thickness, L, by assuming that the liver tissue has a reflector density μ reflectors per cm. Experimental results using *in vitro* refrigerated and fixed liver tissue specimens will be compared to the analytically predicted performance.

[1]Figures in brackets indicate literature references at the end of this paper.

2. Acoustic Attenuation of Liver Tissue

We first describe the experimental procedure that we use to measure β from transmitted pulses. This is used to verify the reflection measurements. The power spectrum of the incident pulse, denoted by $S_X(f)$ in figure 1, is found by reflecting the pulse from a plane, normally incident reflector

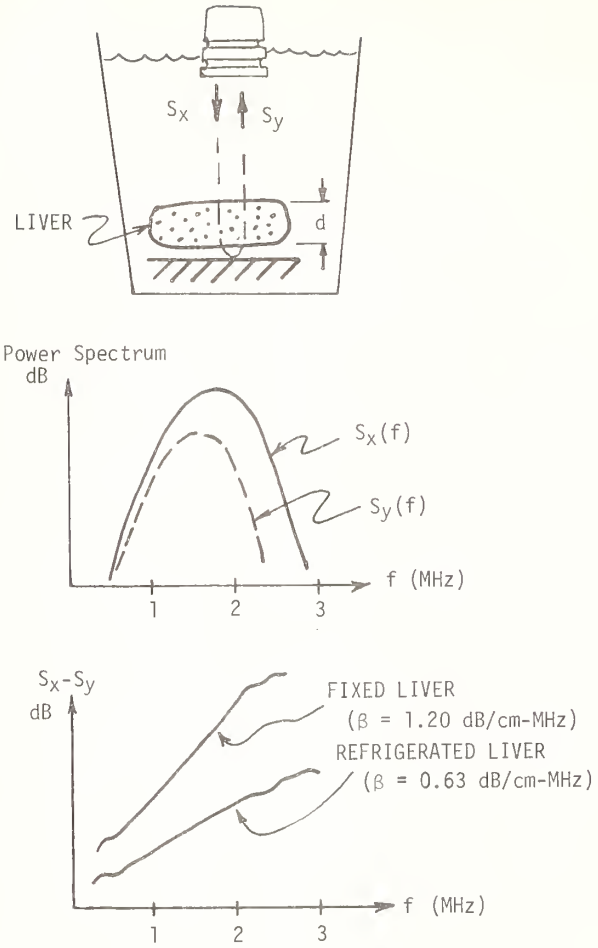

Fig. 1. Transmission experimental configuration results. An acoustic pulse propagates through liver sample having thickness d, is reflected by plane, normally incident reflector and propagates through sample a second time. The liver acts like a low pass filter, attenuating the high frequencies in the power spectrum. The difference between the power spectra is found to be linear with a slope which is an indicator of tissue state. The parameter β is the observed slope divided of twice the tissue thickness.

with no tissue in the acoustic path. The power spectrum of the pulse transmitted through the tissue of thickness d back to the transducer is denoted by $S_Y(f)$. The effect of the tissue acoustic attenuation can be found by taking the log spectral difference (in dB) of the two spectra. For a linearly frequency dependent acoustic attenuation this will be equal to

$$10 \log S_X(f) - \log S_Y(f) = 2 \beta df \qquad (1)$$

The value of β, in units of dB/cm-MHz, for a given tissue can be measured by dividing the observed slope of the log spectral difference by the acoustic path length through the tissue. For reflected signals the acoustic path length is equal to twice the tissue thickness.

The average values of β that we obtained for in vitro refrigerated and fixed liver specimens are shown in figure 1. These values agree with those found by other researchers [1,2]. The transmission technique works well when thin, parallel cut sections of tissue are used. When large heterogeneous tissue specimens, or tissue specimens which have irregular shapes are used, the propagating pulse becomes distorted producing artifacts in the measurements [3,4].

We will extend this technique of measuring β to signals reflected from tissue structures by subtracting the log spectra of signals from two reflectors within the tissue. But because of the distortion to the spectra caused by the irregular reflectors the observed spectral difference will be a distorted linear function. The coefficient β will be estimated by fitting a straight line to the spectral difference and dividing by the round-trip distance between the reflector locations. In order to find a suitable estimation technique and the confidence intervals for the resulting estimate we will derive the distribution of the distortion to the log spectrum in the next section.

3. Reflector Model

We propose to model the irregular reflector as a random linear filter with an impulse response, denoted by r(n) for n = 1, 2, ..., KT_s, which is a sample function from a zero mean, white Gaussian process. The probability density function (p) of r(n) is then given by

$$p(r(n)) = \frac{1}{\sqrt{2\pi}\,\sigma_r} \exp\left[-\frac{r^2(n)}{2\sigma_r^2}\right] \qquad (2)$$

For a white Gaussian process, the values of r(n) and r(m) for sampling times $n \neq m$ are independent. This appears to be a reasonable assumption in this work, considering the irregularity of the reflecting vascular structures [5]. This is verified by the experimental results to be described later.

If $S_X(f)$ is the power spectrum of the acoustic pulse incident to the reflector having the impulse response r(n), then the power spectrum of the reflected signal, $S_R(f)$, can be written as

$$S_R(f) = |R(f)|^2 S_X(f) \qquad (3)$$

where $|R(f)|^2$ is the power transfer function of the reflector [6].

We will estimate β from the log spectral difference. The logarithm (in units of dB) of eq. (3) is equal to

$$10 \log S_R(f) = 10 \log S_X(f) + 10 \log |R(f)|^2 \qquad (4)$$

$$= 10 \log S_X(f) + n(f) \,. \qquad (5)$$

The last equation indicates that the effect of an irregular reflector is an additive distortion to the log spectrum of the incident pulse at the reflector location. Furthermore, since the reflector impulse response is assumed to be zero mean, white Gaussian, it can be shown [6] that the random variables

$$C_i = |R(f_i)|^2 \qquad (6)$$

are mutually independent and have an exponential distribution (the chi-square distribution with two degrees of freedom), at frequencies f_i which are separated by the fundamental frequency, $F = 1/KT_s$.

Since we are seeking the distribution of the distortion in the log spectral domain (in dB) we set

$$n_i = 10 \log C_i = 10 \log |R(f_i)|^2 \tag{7}$$

Using the relation for the pdf of a transformed random variable [7,8] the pdf of the distortion to the log spectrum n_i is found to be equal to

$$p(n_i) = \frac{1}{4.34\ \sigma_r^2 T_s} \exp\left[\frac{n_i}{4.34} - \frac{e^{\frac{n_i}{4.34}}}{\sigma_r^2 T_s}\right] \tag{8}$$

for $-\infty < n_i < \infty$. This distribution is shown in figure 2a.

If we let $h = \ln \sigma_r^2 T_s$, then $\sigma_r^2 T_s = e^h$. Eq. (8) can then be written

$$p(n_i) = \frac{1}{4.34} \exp\left[\frac{n_i}{4.34} - h - e^{\frac{n_i}{4.34} - h}\right] \tag{9}$$

This last result shows that the effect of the variance of the reflector impulse response σ_r^2 on the distribution of the log spectral distortion is only a shift by an amount h.

We shall now describe the technique we have developed to partition the total reflected signal from a liver tissue into segments which are used for calculating the sample spectra of the returns from the irregular reflectors.

4. Processing of Reflected Data

An acoustic pulse having an arbitrary power spectrum $S_X(f)$ propagates into a tissue medium and reflections due to changes in tissue acoustic impedance are detected by the transducer. A typical reflected signal denoted by y(n), is shown in figure 3. The envelope of y(n) is calculated by rectifying the sample values and low pass filtering with a digital nonrecursive filter. The envelope is observed to contain a series of N maxima which have random amplitudes and occurrence times. We assume that the occurrence of a maximum, or peak, in the reflected signal envelope indicates the presence of an irregular reflector. This is the same assumption used in the equipment producing sonograms in the clinical environment. The time series is divided into N nonoverlapping data segments corresponding to the signals returned from the individual reflectors.

The shape of the reflected signal envelope suggests a way of segmenting the reflected data. For our reflected signal analysis the data was segmented about the peaks in the envelope using the locations of the adjacent minima to delimit the segment. Each segment is then assumed to represent the return from an irregular reflector, with the position of the envelope peak in the total reflected signal defined as the reflector location within the tissue. This procedure produces a set

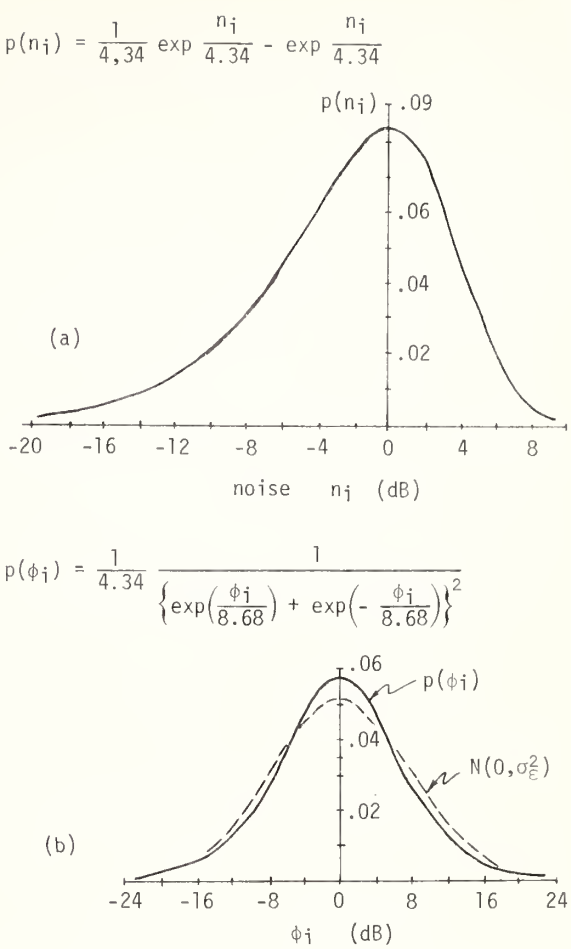

Fig. 2. Reflection experimental configuration and procedure. An acoustic pulse is emitted and the reflection from the liver tissue parenchyma are detected. For the emitted signal shown, a typical reflected signal contains a series of peaks which have random amplitudes and occurrence times. These are most evident in the envelope. The received signal is divided into segments delimited by the envelope mimma. The power spectra are calculated and β is estimated from the spectral differences using least squares.

of nonoverlapping data segments which are assumed to be statistically independent.

The data segment corresponding to the k^{th} reflector will be denoted by $y_k(n)$, $n = 1,2,\ldots,M_kT_s$. The sample power spectrum, denoted by $S_k(f)$, is calculated from $y_k(n)$ by using the squares of the cosine and sine transforms given by

$$S_k(f) = \frac{T_s}{M_k}\left\{\left(\sum_{n=1}^{M_kT_s} y(n)\cos 2\pi fn\right)^2 + \left(\sum_{n=1}^{M_kT_s} y(n)\sin 2\pi fn\right)^2\right\} \tag{10}$$

Because of the symmetry of the power spectrum it suffices to consider the positive frequencies only.

In a manner similar to the transmission experiment we will calculate the differences between the sample spectra to estimate the value for β. For N segments there are N/2 independent spectral differences as shown in figure 3. From each observed spectral difference we will estimate a value for β, denoted by β_k for the k^{th} spectral difference. The estimate for β using the entire reflected signal will be taken as the average of these individual estimates. A technique for pairing the segments to minimize the estimator variance will be discussed later.

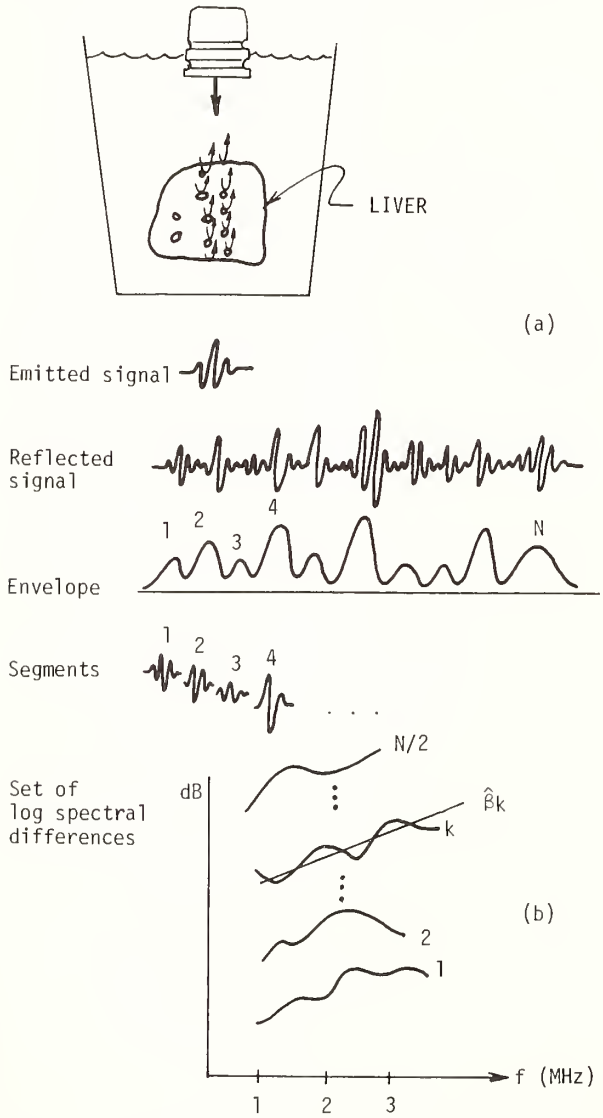

Fig. 3. Probability density functions. With the rough boundaries modeled as linear filters with random zero-mean Gaussian impulse responses, the values of the power spectrum at the harmonic frequencies are independent and distributed as the function shown in (a). The values of the power spectral difference at the harmonic frequencies are also independent and distributed as the function shown in (b).

The power spectrum of the incident pulse has significant energy only in a band of frequencies, from f_L (for lower) to f_U (for upper). It is in this usable range that the log power spectral difference given in eq. (1) will be approximately linear. Outside this range noise effects cause random deviations. The set of frequencies f_i separated by the fundamental frequency spacing are confined to be within this usable range, i.e.,

$$f_i \in [f_L, f_U] \tag{11}$$

In the analysis we shall assume that there are m frequencies within the usable range, with f_1 defined as the smallest.

5. Distribution of the Log Spectral Difference

Now let us consider the log spectral difference between the returns from two irregular reflectors, ℓ and j (ℓ<j), separated by a distance $d_{\ell j}$. If the corresponding power spectra of the reflected signals are denoted by $S_\ell(f)$ and $S_j(f)$, then their log spectral difference in dB at the harmonic frequencies is equal to

$$\begin{aligned} z_i &= 10 \log S_\ell(f_i) - 10 \log S_j(f_i) \\ &= 10 \log S_{X_\ell}(f_i) - 10 \log S_{X_j}(f_i) \\ &\quad + n_\ell(f_i) - n_j(f_i) \end{aligned} \tag{12}$$

for i = 1, 2, ..., m

where $S_{X_k}(f)$, k = ℓ, j, is the power spectrum of the propagating pulse at the k^{th} reflector. For a tissue with a linearly increasing attenuation with frequency, the difference between the propagating pulse log spectra is the same as the transmission experiment results given in eq. (1). In our case, it is equal to

$$10 \log S_{X_\ell}(f_i) - 10 \log S_{X_j}(f_i) = 2\beta d_{\ell j} f_i \tag{13}$$

for i = 1, 2, ..., m.

If the difference of the spectral distortions at the harmonic frequencies is defined as

$$\varepsilon_i = n_\ell(f_i) - n_j(f_i) = n_{i,\ell} - n_{i,j} \tag{14}$$

then eq. (12) can be written as

$$z_i = 2\beta d_{\ell j} f_i + \varepsilon_i \tag{15}$$

for i = 1, 2, ..., m.

In words, this last result states that the log spectral difference between two reflected signals at the harmonic frequencies is a distorted linear function of frequency with a slope equal to the value of β, the coefficient to be estimated, and the round-trip distance between the reflectors.

The distortion enters as an additive noise term. Since ε_i is the difference of random variables which are independent and identically distributed (iid) at the harmonic frequencies, ε_i is also iid and the variances are equal at the harmonic frequencies. Therefore, we can drop the i subscript and denote the variance by σ_ε^2. We can show that σ_ε^2 is independent of the individual reflector variances and is equal to 62 $(dB)^2$ [7]. Therefore, the distortions to the straight line calculated by using the log spectra from any two reflectors will have the same variance as the reflectors are spaced farther apart (larger $d_{\ell j}$) the slope of the log spectral difference will increase. But since the statistical roughness is assumed to be constant for all reflectors, the distortions should remain the same. We shall use this fact later in how we pair segments to calculate the spectral difference.

Since the attenuation coefficient β affects only the slope in eq. (15), the mean value of the distortion ε_i can be eliminated by translating the axes. This can be accomplished by defining new variables $Z_i = z_i - \bar{z}$ and $F_i = f_i - \bar{f}$ where

$$\bar{z} = \frac{1}{m} \sum_{i=1}^{m} z_i \tag{16a}$$

and

$$\bar{f} = \frac{1}{m} \sum_{i=1}^{m} f_i \tag{16b}$$

The statistical model with zero mean distortion and centered frequency axis can be written as

$$Z_i = 2\beta d_{\ell j} F_i + \phi_i \tag{17}$$

for i = 1, 2, ..., m.

The pdf of the additive noise term ϕ_i with zero mean can be shown [7] to be equal to

$$p(\phi_i) = \frac{1}{4.34} \frac{1}{\left(e^{\frac{\phi_i}{8.68}} + e^{\frac{-\phi_i}{8.68}} \right)^2} \tag{18}$$

We plot $p(\phi_i)$ in figure 2b. For comparison we also show the Gaussian pdf having mean 0 and variance $\sigma_\varepsilon^2 = 62$, in dashed lines. Because of their similarity, we will approximate ϕ_i by a Gaussian random variable having mean 0 and variance σ_ε^2, i.e., i.e.,

$$p(\phi_i) = \frac{1}{\sqrt{2\pi}\,\sigma_\varepsilon} e^{-\frac{\phi_i^2}{2\sigma_\varepsilon^2}} \tag{19}$$

The statistical model given by eq. (17) describes the log spectral difference between 2 reflectors separated by distance $d_{\ell j}$. The entire reflected signal contains N segments from which we can calculate N/2 independent log spectral differences. We will show later that depending on how the segments are paired it may be desirable to use N' differences from which to estimate β, where $N' \le N/2$. The statistical model using the entire reflected signal can be written

$$Z_{ik} = 2\beta d_k F_i + \phi_{ik} \tag{20}$$

for i = 1, 2, ..., m
k = 1, 2, ..., $N' \le \frac{N}{2}$

where Z_{ik} is the observed value of the k^{th} log spectral difference (after the mean value is subtracted) at frequency F_i using signals from reflectors spaced d_k apart.

6. Derivation of Maximum Likelihood Estimator for β

The results of the previous section indicated that the additive distortions to the log spectral difference are closely approximated by independent and identically distributed Gaussian random variables with mean zero and variance σ_ε^2.

Under these conditions the maximum likelihood estimate of β, denoted by β_{ML}, is found to be equal to

$$\hat{\beta}_{ML} = \frac{\sum_{k=1}^{N'} d_k^2 \hat{\beta}_k}{\sum_{k=1}^{N'} d_k^2} \tag{21}$$

where

$$\hat{\beta}_k = \frac{1}{2d_k} \frac{\sum_{i=1}^{m} Z_{ik} F_i}{\sum_{i=1}^{m} F_i^2} \tag{22}$$

is the maximum likelihood estimate of β using only the information in the k^{th} spectral difference. It can be shown that this estimator is efficient, i.e., it has the smallest variance of any unbiased estimator [7]. The variance of the resulting estimator can be shown to be equal to

$$\mathrm{Var}\left[\hat{\beta}_{ML}\right] = \frac{\sigma_\varepsilon^2}{4 \sum_{k=1}^{N'} d_k^2 \sum_{i=1}^{m} F_i^2} \tag{23}$$

For notational convenience let us define S as

$$S = \frac{\sigma_\varepsilon^2}{\sum_{i=1}^{m} F_i^2} \tag{24}$$

The estimator variance given in eq. (21) can then be written as

$$\mathrm{Var}\left[\hat{\beta}_{ML}\right] = \frac{S}{4 \sum_{k=1}^{N'} d_k^2} \tag{25}$$

We want to minimize the estimator variance by properly selecting the segments used in calculating the spectral difference. If adjacent peaks are chosen, all the d_k's will be small and the variance will be large. Physically, this occurs because the acoustic attenuation doesn't affect the signal significantly for small tissue distances while the irregular boundary effects are large. If we take segments far apart so that the effect of acoustic attenuation is more apparent, the number of spectral differences N' becomes smaller. We will find the optimum separation by considering a simple tissue model.

For heuristic purposes let us consider a statistically homogeneous tissue L cm long and having a reflector density equal to μ reflectors per cm. The average spacing between reflectors is $1/\mu$ and the average number of peaks in the reflected signal is $N = \mu L$. If the segments to be used in calculating the log spectral difference are chosen such that the distances between them are constant and equal to $d_n = n/\mu$, $N/2 \leq n \leq N-1$, the number of independent differences that can be formed is equal to $N' = N-n$. The minimum variance can be shown to occur for $n = 2N/3$. Then from eq. (25) we find the minimum variance to be

$$\mathrm{Var}\left[\hat{\beta}_{ED}\right]_{min} = \frac{S}{\frac{16}{27}\frac{N^3}{\mu^2}} \tag{26}$$

The ED denotes equal distance separations between reflectors. To relate this to tissue size we substitute $N = \mu L$ to get

$$\mathrm{Var}\left[\hat{\beta}_{ED}\right]_{min} = \frac{S}{\frac{16}{27}\mu L^3} \tag{27}$$

Recalling that $\mu L = N$ we can write eq. (27) as

$$\mathrm{Var}\left[\hat{\beta}_{ED}\right]_{min} = \frac{S}{\frac{16}{27} N \cdot L^2} \tag{28}$$

This shows that in addition to decreasing as $1/N$, the variance also decreases as $1/L^2$. This demonstrates quantitatively the intuitive result that for larger tissues, the acoustic attenuation becomes increasingly discernible relative to the boundary distortion.

7. Confidence Intervals for the Estimator

In the previous section we derived the variance of the ED estimator as a function of tissue size and reflector density. For Gaussian random variables, the 95 percent confidence interval is defined as an interval 1.96 times the square root of the variance about the estimate of the parameter. From eq. (27) the confidence interval width is given by

$$\left(-\frac{c_1}{\mu^{1/2}L^{3/2}}, \frac{c_1}{\mu^{1/2}L^{3/2}}\right) \tag{29}$$

with $c_1 = \sqrt{27/16}\, S$. For a given reflector density μ the confidence intervals will indicate the tissue size required for a desired estimator resolution.

We will now present some experimental results using refrigerated and formalin-fixed liver tissue specimens.

8. Experimental Results

A 2.0 MHz transducer was used to obtain data from in vitro refrigerated and fixed liver specimens. The thickness of the refrigerated liver was 6.7 cm. After 1 month of formalin-fixation the tissue size was 7.5 cm. From transmission tests the average values of β were observed to be equal to 0.63 dB/cm-MHz for refrigerated liver and 1.20 dB/cm-MHz for formalin-fixed liver. These values agree favorably with those observed for refrigerated liver by Pauly and Schwan [1] and for formalin-fixed liver by Lele [2]. The usable bandwidth was determined from the transmission experiments to be 1.2 to 2.4 MHz. The envelope of the reflected signal was calculated by using a 15 point lowpass filter with a Gaussian shape truncated at $\pm 3\sigma$. This particular filter was chosen because its impulse response matched the envelope of the incident pulse. With this filter the average density of peaks, μ, in the reflected signal envelope was observed to be equal to 7. The data were partitioned into non-overlapping segments delimited by the locations of the envelope minima. The same power spectrum was calculated for each segment by using eq. (10). The coefficient β was estimated from the difference of spectra separated by a distance approximately equal to $2L/3$, where L is the total size of the tissue.

In the above analysis we were concerned with the estimator performance as a function of tissue size. In order to verify the predicted performance of the confidence intervals with respect to tissue size, small tissue sizes were simulated by taking the equivalent amount of data from the total signal reflected from the liver, starting at the beginning of the record. The results then indicate the experimental performance of the estimator as the tissue size is increased. The confidence intervals, instead of being taken about the estimated value, for purposes of comparing the results of different runs, are taken about the average values of β observed from the transmission experiments.

With the 15 point filter the average segment size was 18 samples at $T_S = 0.1$ μs, producing a fundamental frequency equal to 0.6 MHz. Two independent values per spectrum, located at 1.5 ($F_1 = -.3$) and 2.1 ($F_2 = +.3$) MHz were used. From eq. (24) the resulting value for S is 345. For $\mu = 7$ the variance given by eq. (27) is equal to

$$\mathrm{Var}\left[\hat{\beta}_{ED}\right] = \frac{83}{L^3} \tag{30}$$

From eq. (29) the resulting 95 percent confidence intervals are given by

$$CI = \left(\hat{\beta} - \frac{18}{L^{3/2}}, \hat{\beta} + \frac{18}{L^{3/2}}\right) \tag{31}$$

The ED estimates as a function of tissue size for 4 independent (nonoverlapping) runs, denoted

by R1 through R4, through refrigerated liver are shown in figure 4. The 95 percent conficence intervals are indicated. From the figure it is noted that the confidence intervals are a reasonable prediction of the estimator performance: wider variations and extreme values are found at the smaller tissue sizes with the variations decreasing as the tissue size increases. The confidence intervals are rather wide indicating that large tissue sizes are required to determine β accurately with this technique.

The estimates for 6 independent runs, F1 to F6, through fixed liver are shown in figure 5. The confidence intervals are centered about the average value of β observed for fixed liver. Again the confidence intervals reasonably predict the observed performance.

The averages of the independent runs for refrigerated and fixed livers are shown in figure 6. The confidence intervals have been reduced to account for the averages of independent values (by 1/2 for refrigerated liver, by $1/\sqrt{6}$ for fixed liver). Here again the confidence intervals are consistent with the observed results. Even for the averaged estimates the reduced confidence intervals are still

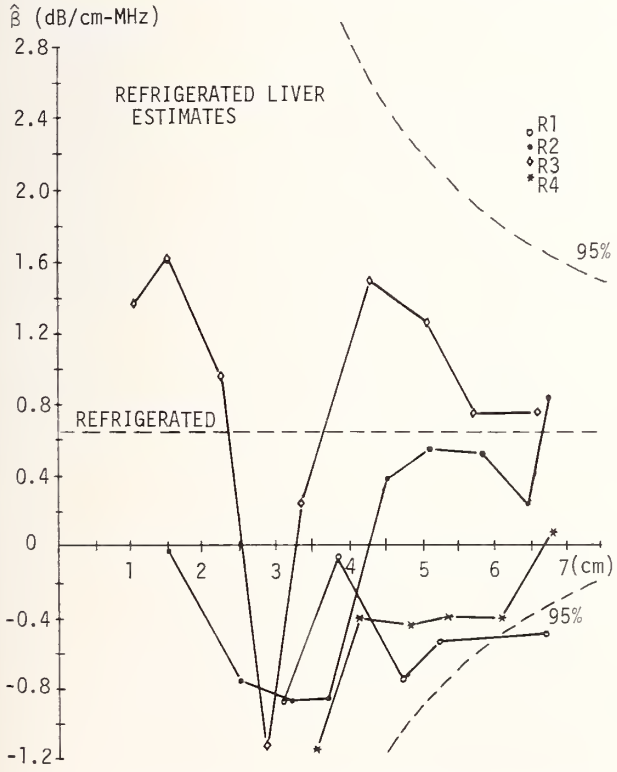

Fig. 4. β estimates for refrigerated liver. The theoretically derived 95 percent confidence intervals are shown in dashed lines as a function of liver size. The curves are centered about the value observed from transmission results. The larger the liver the more data is produced and the better the resulting estimate. Experimental results from four runs R1 to R4 are shown. Smaller liver sizes were simulated by taking equivalent sections of data from the total reflected signal.

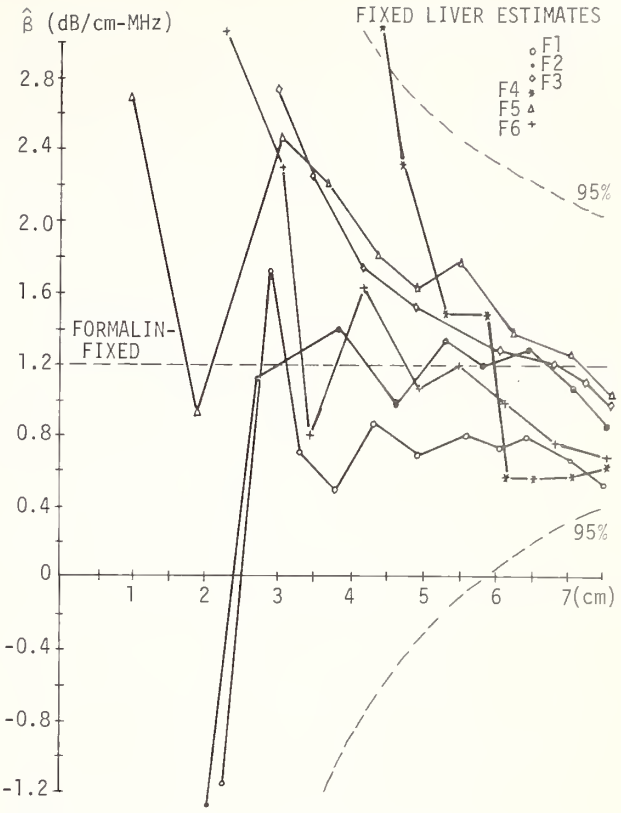

Fig. 5. β estimates for formalin-fixed liver. The confidence intervals are shown in dashed lines as a function of liver size. The curves are centered about the value observed from transmission results. Experimental results are shown for six runs F1 to F6.

overlapped at 8 cm. Even though the experimental results shown here differ noticeably for refrigerated and fixed liver, the fixed liver estimates are close to the upper confidence interval predicted for refrigerated liver.

9. Conclusion

The first order model of the irregular reflector presented in this paper offers a reasonable description of the actual results obtained from refrigerated and fixed liver samples. The resulting confidence intervals, however, are wide and overlap significantly indicating that a large amount of data is required for a reasonable estimator resolution. The spread in the estimates predicted by the confidence intervals are due to the wide variations possible in the reflected signal power spectrum caused by the white Gaussian impulse response model of the irregular reflector. To decrease the confidence intervals, and hopefully the resulting experimental estimates, a more accurate model of the typical reflector is required. In the reflector model assumed here we have ignored possible deterministic reflections and have assumed the reflector effects to be completely random. We plan to study an improved model, combining both deterministic and random effects, for which better estimation techniques can be derived to produce more accurate estimates from smaller tissue samples.

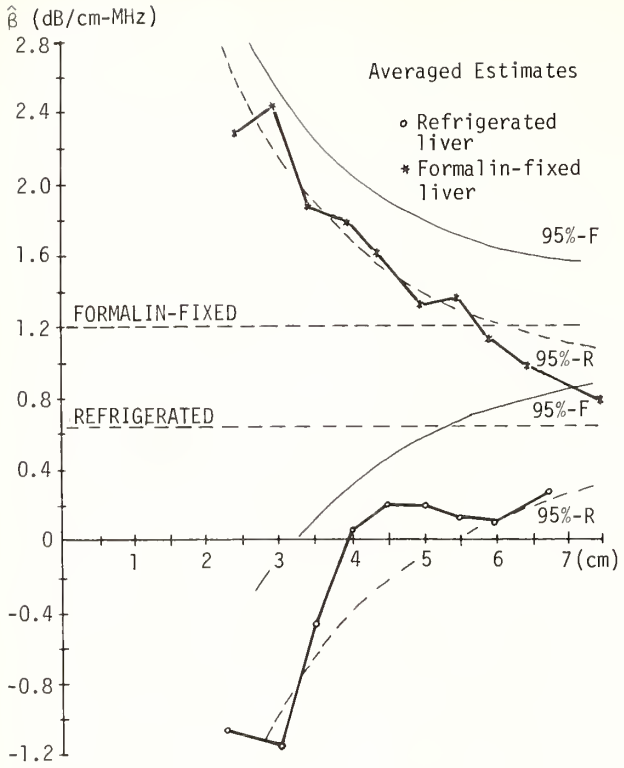

Fig. 6. Comparison averaged β estimates for refrigerated and fixed livers. The respective confidence intervals are indicated about the values observed in transmission experiments. The averages of the 4 refrigerated liver runs and 6 formalin-fixed liver runs indicate a separation in their values.

Acknowledgment

This research was made possible by the loan of the fast analog-to-digital converter and paper tape unit by the Picker Corporation.

References

[1] Pauly, H. and Schwan, H. P., Mechanism of absorption of ultrasound in liver tissue, J. Acoust. Soc. Am. 50, 792-99 (1971).

[2] Lele, P. D., Mansfield, A. B., Murphy, A. I., Namery, J., and Senepati, N., Tissue Characterization by Ultrasonic Frequency-dependent Attenuation and Scattering, in Ultrasonic Tissue Characterization, M. Linzer, ed., pp. 167-96, National Bureau of Standards Spec. Publ. 453 (U.S. Government Printing Office, Washington, D.C., 1976).

[3] Miller, J. G., Yuhas, D. E., Mimbs, J. W., Dierker, S. B., Busse, L. J., Laterra, J. J., Weiss, A. N., and Sobel, B. E., Ultrasonic Tissue Characterization, 1976 IEEE Ultrasonics Symposium Proc., 76 CH 1120-5SU, 33-43 (1976).

[4] Kuc, R., Schwartz, M., and Von Micsky, L., Parametric Estimation of the Acoustic Attenuation Coefficient Slope for Soft Tissue, 1976 IEEE Ultrasonics Symposium Proc., 76 CH 1120-5SU, 44-47 (1976).

[5] Elias, H. and Sherrick, J. S., Morphology of the Liver (Academic Press, New York, 1969).

[6] Jenkins, G. N. and Watts, D. G., Spectral Analysis and Its Applications (Holden-Day, San Francisco, 1968).

[7] Kuc, R., Statistical Estimation of the Acoustic Attenuation Slope for Liver Tissue, Ph.D. Dissertation, Columbia University (1977).

[8] Schwartz, M., Information Transmission, Modulation, and Noise (McGraw-Hill, New York, 1970).

[9] E. Parzen, Modern Probability Theory and Its Applications (Wiley, New York, 1967).

CHAPTER 5

SCATTERING

Reprinted from *Ultrasonic Tissue Characterization II*, M. Linzer, ed., National Bureau of Standards, Spec. Publ. 525 (U.S. Government Printing Office, Washington, D.C., 1979).

AN ULTRASONIC TISSUE SIGNATURE FOR THE LUNG SURFACE

Theodore L. Rhyne[1]

Massachusetts Institute of Technology
and Massachusetts General Hospital
Cambridge, Massachusetts 02139, U.S.A.

The normal lung surface is modeled as a statistically rough surface composed of the air-containing alveolar sacs at the periphery. The ultrasonic reflection (scatter) from the rough surface is analyzed as a random process and a frequency signature, which depends upon alveolar sac radii statistics, is predicted for the reflectance. Pulse-echo ultrasonic instrumentation for the measurement of the absolute reflectance from the lung surface is presented. Lung reflectance data confirming the lung surface frequency signature is presented for humans. Applications of the model are discussed to the detection of pulmonary embolism, atelectasis, pulmonary edema, and chronic lung disease.

Keywords: Detection of lung disease; frequency signature; statistical scattering; tissue signature; ultrasonic scattering; ultrasound.

1. Introduction

Ultrasonic characterization of tissue represents a considerable challenge to the researcher in that he must exploit essentially "second order" phenomena while current clinical techniques have already exploited the "first order" phenomena. The "second order" phenomena (dispersion, reflection, scattering, movement, etc.) are often measurable only after suitable instrumentation has been developed. The researcher is especially challenged to select from an infinity of possible instrumentation approaches and plausible phenomena in order to arrive at a clinically useful diagnostic technique. The work reported here is the development of a tissue characterization for the normal lung surface using an analytical approach. The approach is quite possibly as significant as the results since it offers a path through the complex decisions involving instrumentation design, study of phenomena, and definition of the useful measurement.

The analytical approach used here is summarized in the four interactive steps outlined below. The interplay of each step can be followed as the normal lung model is developed.

1) Calibration of the transmitter-receiver circuitry and transduction process to either an absolute or traceable standard for measurement of tissue acoustic properties that are independent of the instrumentation.

2) Design of the transmitted acoustic signal waveform to accentuate the desired tissue phenomena.

3) Development and validation of analytical models for the tissue target which characterize the measurable acoustic phenomena of tissue in the normal and diseased states.

4) Development of signal processing operations performed by the instrumentation to detect and quantify echo parameters that characterize the normal and diseased states of the tissue.

2. Normal Lung

The lung is a very large organ whose surface lies within a few centimeters of the skin over most of the chest. As shown in figure 1a, a transducer coupled to the skin may direct ultrasonic waves through the soft tissues of the intercostal space that lies between adjacent ribs. If a sufficiently small transducer is utilized, the lung surface can be examined with no interference from nearby ribs.

A normal lung has a gross density that is approximately one third that of water. Thus, the lung is approximately two thirds air and one third soft tissue. At the periphery the schematic of the magnified lung surface in figure 1b indicates the relationship of the air-containing alveolar sacs to the soft tissues that surround the sacs. The alveolar sac is the end-respiratory airway and is divided up into the familiar alveolar chambers.

The marked difference in acoustic impedance between the air and the surrounding soft tissue causes nearly perfect reflection at the air to soft tissue boundary. For our purposes we postulate an "ultrasonic" lung surface which is a roughened planar surface composed of the outer walls of the multitude of peripheral alveolar sacs that lie just inside the pleural membrane.

The physical lung surface (as opposed to the "ultrasonic" surface) is a pleural membrane which forms a unique bearing with a second pleural membrane that is attached to the inside of the chest

[1]Current Address: Bolt, Beranek and Newman, Inc., 50 Moulton Street, Cambridge, MA 02138.

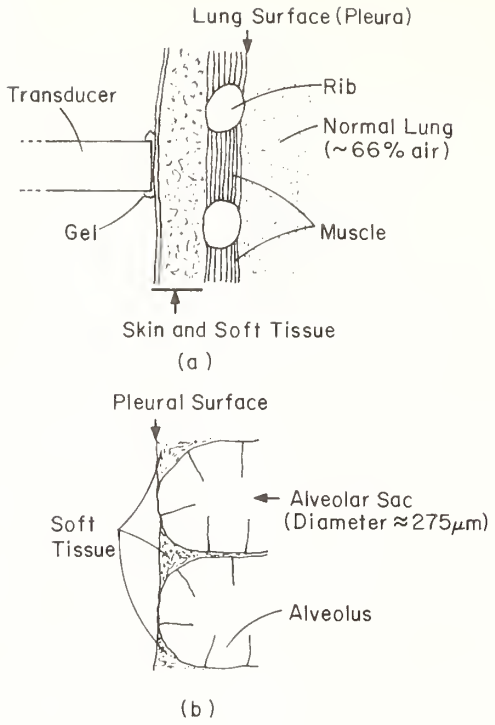

Fig. 1. Schematic representation of the chest and lung surface; (a) cross section of the chest wall; (b) enlarged cross section of the lung surface.

wall. During respiration the lung moves laterally within the chest on this pleura-fluid-pleura bearing. Since the bearing is composed of soft tissue and is only a few tens of a micrometer thick, it does not contribute a significant echo in comparison to the "ultrasonic" lung surface. Furthermore, the lateral motion of the lung permits the lung surface to be scanned during respiration by a transducer held stationary with respect to the chest wall.

The geometry of the lung examination is provided in figure 2. A radiating and receiving transducer located at the skin is represented by a circular disk which is the aperture of the transducer. The radiating and receiving disk observes the lung surface through the soft tissue of the intercostal space, which is a uniformly lossy media. The "ultrasonic" lung surface is a rough surface normal to the disk and of infinite extent. The rough surface may move laterally with no change in range, thus presenting new portions of its surface to the area directly underlying the disk.

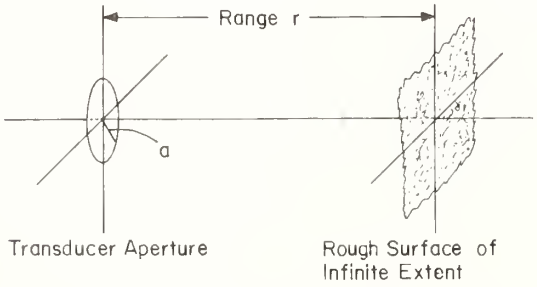

Fig. 2. Geometry for the examination of the lung surface by a transducer with a circular aperture.

3. Calibrated Instrumentation and Signal and Design

Wave propagation between the radiating (and receiving) aperture and lung surface forms a central issue in the calibrated measurement of echoes reflected from the lung surface. If we further simplify the situation represented in figure 2 to a lossless media and a flat perfectly reflective plane, we have a classic radiation (or diffraction) problem. By virtue of the finite size of the radiating and receiving disk plus the wave speed of the media, waves launched by the disk produce filtered echoes as they reflect from the plane and return to the disk. The radiation (or diffraction) filter response is given in Appendix A as developed in the literature [1][2]. If the response is graphed as in figure 3 for a representative situation, we see that the radiation filter is a high pass filter. The nearly flat response of the radiation filter depends on the selection of aperture size, frequency, and range so that the surface lies within the near-field of the transducer. This is the case for the lung surface measurements. Subsequently, the radiation filter will be used both for calibration and adjustment of lung surface data.

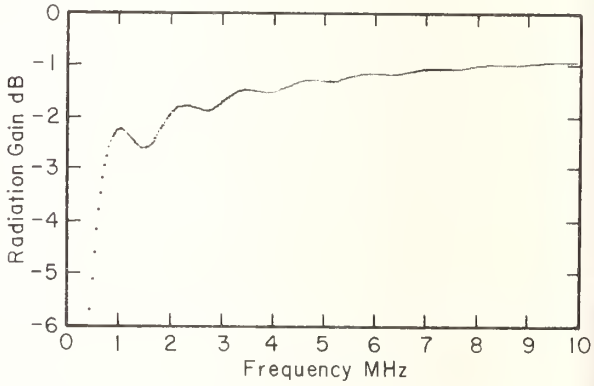

Fig. 3. Frequency response of the radiation filter between a radiating disk of radius 0.0125 inch and a flat perfectly reflecting plane 1.5 cm distant.

The pulse echo instrumentation is diagrammed in the network of figure 4. It consists of a transmitter, a receiver, and a transducer, each linearly coupled to a common transmission system. The transmitting waveform V_t excites the system. The waveform $V_t(t)$ propagates through the transmission line to the transducer. The transducer couples the electrical domain to the acoustic radiation field. Energy launched by the radiating disk of figure 2 is represented as energy consumed in the radiation resistance. Conversely, echoed waves striking the disk are represented by the wave

[2]Figures in brackets indicate literature references at the end of this paper.

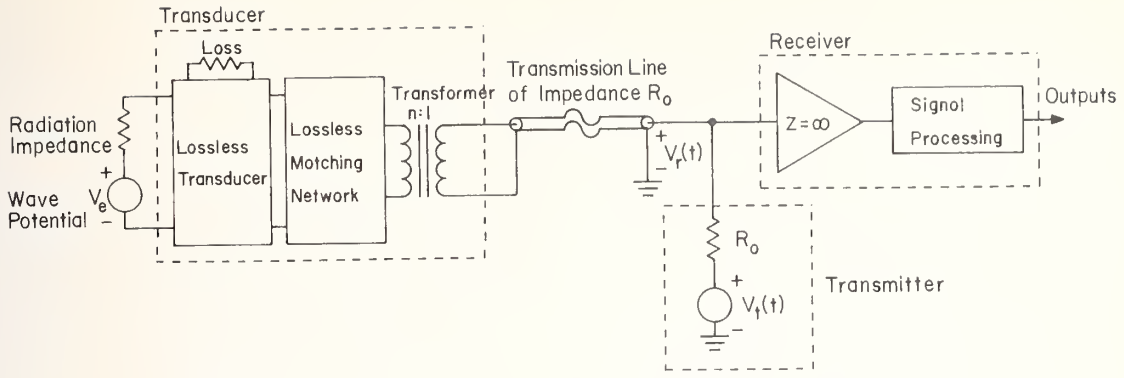

Fig. 4. Schematic of pulse-echo ultrasonic instrumentation.

potential $V_e(t)$. The radiated waveform is $V_t(t)$ as filtered by the transmission line and the transducer. The received waveform $V_r(t)$ is the wave potential $V_e(t)$ as filtered once again by the transducer and transmission line.

If the transmitter (plus receiver) matches the impedance of the transmission line, then the filtration of the transmission line consists of simple time delays of the transmitted and received signals. Also,the impedance presented to the transducer is R_o in series with $V_t(t)$. Thus, matching effectively removes the transmission line from the network of figure 4. The net effect of the instrumentation is the filtration of transmitted and received signals by the transducer.

In order to measure transducer response and the magnitude of echoes from a target, it becomes important to define a measure of absolute signal loss. This is done by energy conservation of the energy in the transmitted wave $V_t(t)$, a portion of which ultimately returns as the received echo $V_r(t)$. Loss is defined here as the ratio of the exchangeable power of the transmitter to the received power in eq. (1). This is more conveniently expressed as the gain (always less than unity) or transfer gain in eq. (2) which can be expressed in decibel or magnitude notation.

$$\text{Loss (dB)} = 10 \log_{10} \frac{(V_t^2)/(4R_o)}{(V_r^2)/(R_o)} = 20 \log_{10} \frac{V_t}{2V_r} \qquad (1)$$

$$\text{gain} = \frac{2V_r}{V_t} \qquad (2)$$

Since the transmitted acoustic waveform is determined by $V_t(t)$, we are free to choose it so as to accentuate some property of the target. Here, the magnitude of the lung surface echo is the important property. Furthermore, the returned lung echo will be corrected by the radiation filter and transducer filter magnitudes. Therefore, we select a transmitted waveform which is a carrier burst of sufficient duration to allow the transducer and the radiation process to reach their steady-state or Fourier responses. The transmitted pulse waveform is completely described by the magnitude, frequency, and duration of the sinusoidal carrier. Conversely, the carrier burst must be sufficiently short in time to allow range discrimination of the lung echo from other echoes. The values for V_t and V_r utilized in loss calculations are the instantaneous values of the envelopes of carrier waves.

The transducer frequency response is experimentally determined as an absolute quantity using the selected signals, the definition of loss, the radiation filter correction (fig. 3), and an experimental geometry as in figure 2 (with a flat perfectly reflective planar test target) [2]. It is interesting to note that absolute dosimetry may be determined as the power dissipated in the radiation resistance of figure 4 [2,3]. The transducer of figure 4 provides a transformer and a lossless matching network in addition to the transducing plate and associated radiation and dissipation loads. Modeling of the transducing disk is extensively discussed elsewhere [2,3] where it is shown that a simple model for transducer gain exists at half-wave resonance. Also, it is shown that optimum loop sensitivity results from adjustment of the transformer for impedance matching of transmitter to transducer impedances. The adoption of a transmission system impedance plus specification of transducer transfer function could form the basis of standardization for pulse echo instrumentation.

4. Scattering Model for the Lung Surface

Returning to the measurement of the reflection from the lung surface depicted in figure 2, we are motivated by the microscopic structure to model the lung as a randomly rough surface. The essential difference between the flat surface of figure 3 and a rough surface is that the rough surface has a finite thickness or scattering depth and is said to be range-spread. Mathematically, this is described in eq. (3) as an integration over all range of some range-spread function $m(\cdot)$ with the impulse response of the radiation coupling $f(\cdot,\cdot,\cdot)$, which is the time domain pair to eq. (A-1).

$$r(t) = \int_0^\infty f(r,a,t)\, m(r)\, dr \qquad (3)$$

For a "thinly rough" surface we may expand the function $f(r,a,t)$ about some fixed range (r_o), make a change of variables for fixed wave speed c, and thus turn the equation into the time convolution in eq. (4).

$$r(t) = \int_{-\infty}^{\infty} f(r_0,a,t-\tau)\,\frac{c}{2}\,\frac{m(c\tau)}{2}\,d\tau \qquad (4)$$

Equation (4) is highly significant in that the received signal r(t) is the result of a linear filtration in cascade with the radiation filter of eq. (A-1). The frequency equivalent of eq. (4) is simply a product of transfer functions in eq. (5), where G(f) is the transfer function associated with m(·).

$$R(f) = F(r,a,f)\,G(f) \qquad (5)$$

The filter G(f) and its transform pair $\frac{1}{2}c\,m(\frac{1}{2}c\tau)$ represent the filtration of a randomly rough surface and, therefore, are themselves random. In a sense the precise G(f) depends upon the particular ensemble of scattering elements that lie in the field pattern of the transducing disk of figure 2. The value of the Fourier function G(f) is the magnitude (and phase) of the reflection due to a long carrier burst. By allowing the transducer, radiation filter, and reflection filter to reach steady-state as discussed above, one may make direct measurement of the magnitude of G(f). The measured value will vary as different ensembles of scattering elements sweep in front of the transducer. The characterization of the lung surface lies in relating the statistical properties of the lung surface to the probability density function (and its mean and variance) for the random variable |G(f)|.

A randomly rough surface representing the normal lung consists of a planar array of the alveolar sac wall segments shown in figure 1(b). Between adjacent alveolar sac chambers cusp-like regions are formed which contain soft tissue which readily support wave propagation. The depth of these cusps constitutes the thickness or scattering depth of the "ultrasonic" lung surface. The lung surface is characterized as having a mean scattering depth (w_0) and standard deviation of scattering depth (σ_w). Figure 1(b) indicates that the scattering depth w_0 is approximately equal to the mean radius of the peripheral alveolar sacs. If the wavelength of the ultrasound is very much greater than w_0 one expects the surface to reflect as though it were flat. Conversely, at some critical wavelength related to the mean scattering depth w_0 one would expect destructive interference. The degree of the destructive interference would of course depend upon the regularity of the scattering surface with greater destructive interference occurring for smaller σ_w.

Using the above model for the lung surface plus several additional assumptions the probability density function plus its mean and standard deviation for |G(f)| are predicted in Appendix B. The density function is a Ricean function whose shape depends upon w_0, σ_w, and the frequency f. The most significant measurable properties of |G(f)| are the mean ($\bar{Z}$) and standard deviation (σ_z) given in figure 5 as functions of frequency. At lower frequencies the curves approach those of a perfect reflector (0dB). Conversely, there is a destructive interference minimum at a frequency where one-half a wavelength equals the mean scattering depth w_0. Figure 5(a) demonstrates the dependence of the dip frequency on w_0. In figure 5(b) we note that the depth of the dip increases for greater regularity in the scattering depth (smaller σ_w).

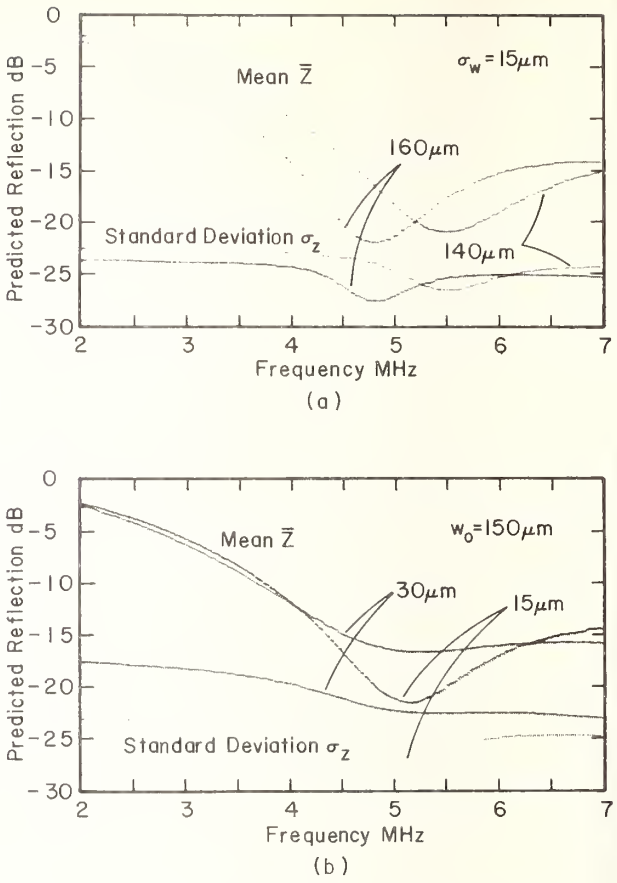

Fig. 5. Families of curves for the mean $\bar{Z}$ and standard deviation σ_z of the predicted echo amplitude, dB versus frequency; (a) curves for two values of scattering depth w_0 and fixed σ_w; (b) curves for two values of σ_w and fixed w_0.

5. Experimental Results

Experimental measurement of the lung surface reflection can be made to confirm the above model. Measured values are corrected for radiation, transducer, transmitted voltage, and bulk tissue effects as in eq. (6). The resulting experimental value (Y) is

$$Y = \frac{2V_r\ 10^{(1/20)2rf0.897\ 10^{-6}}}{|F(r,a,f)|\ V_t\ |T(f)|^2} \qquad (6)$$

is a measure of the absolute reflectivity |G(f)| of the lung surface at the frequency f. In the equation V_r and V_t are envelopes of sinusoids as discussed earlier. The function $|T(f)|^2$ is the measured transducer loop transfer function and F(r,a,f) is the radiation transfer function for range r and frequency f. Correction is made for bulk tissue loss using an attenuation constant of 0.897 dB/cm.

By averaging over many values of Y at a single frequency for successive pulse echo transmissions with the lung surface scanning before the transducer, we arrive at the mean reflectance $\bar{Y}$ for

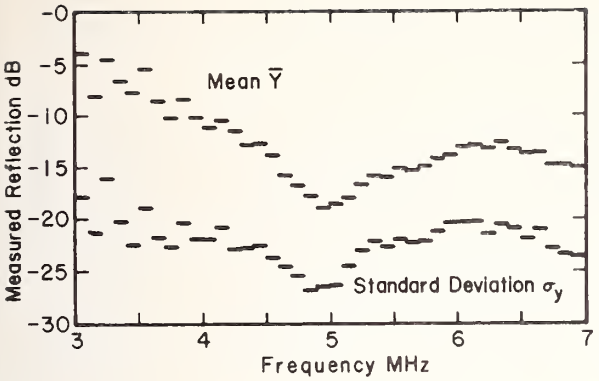

Fig. 6. Experimental data for the mean and standard deviation of lung reflection Y for a normal human volunteer.

that frequency. Similarly, one may compute the standard deviation (σ_Y) for Y over the data for a single frequency. When multiple frequencies are examined and the data reduced for $\bar{Y}$ and σ_Y, the experimental data in figure 6 is arrived at. Note that the destructive dip is present near 5.2 MHz and the curve rises toward 0 dB at lower frequencies. A more extensive discussion shows close correlation between the predicted probability density function of Appendix B and experimental histograms [2,3]. These data confirm the analytical model of tissue thus completing step 3 in the approach to tissue characterization.

6. Applications

The final element in the approach to tissue characterization is to define the signal processing functions of figure 4 to perform some clinically useful application. Two areas of application are suggested for the normal lung tissue signature developed here, they are: a) detection of acute infiltrative disease and b) detection of chronic pulmonary disease.

The normal lung surface strongly reflects the ultrasound due primarily to the presence of air at the periphery. Several diseases, including pneumonia, edema, atelectasis, and pulmonary embolism, which acutely alter the air content at the periphery should be detectable as a departure from the normal model. Preliminary clinical evidence suggests that reductions in lung reflectivity from 10 dB to 30 dB are associated with these acute diseases [2,3]. An optimal method of detecting the reduction in reflection has been suggested [2,3] utilizing the predicted probability density function to determine a sufficient statistic which is the root mean square reflection. An ultrasonic instrument embodying this technique is shown in figure 7. The performance of this detection scheme can be evaluated in terms of probability for false positive and false negative with the testing threshold (T) set to optimize performance.

The chronically abnormal lung can be postulated to produce reflection functions differing from those of figures 5 and 6 due to rearrangement of tissue structures at the periphery of the lung. Diseases such as emphysema and pleural diseases are of clinical interest. Figure 8 demonstrates the reflection data ($\bar{Y}$,σ_Y) for a subject with severe chronic pulmonary disease. The destructive interference dip has been suppressed presumably by the higher variance in the scattering depth (σ_W) of the diseased structures at the periphery. Indeed, if a greater value of σ_W is used in the model of figure 5(b) the dip becomes obliterated. A suggested application to chronic disease is to fit predicted curves to experimental data and take the resulting scattering parameters w_o and σ_W as indices of the lung surface [2,3].

The above applications depend upon detecting departures from the normal model. Further development of this tissue characterization approach suggests developing detailed models (step 3) for the diseased states so that further clinical applications can be defined (step 4).

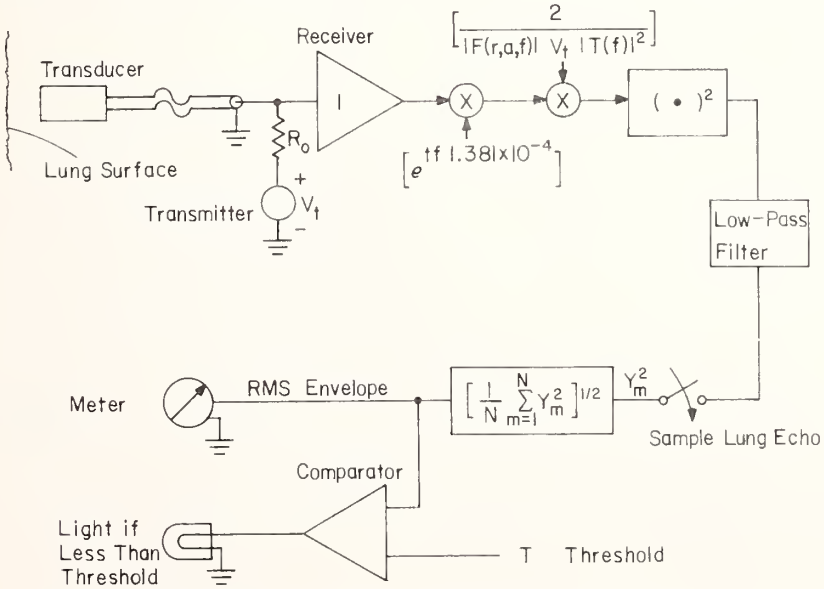

Fig. 7. Ultrasonic instrument for detecting acute lung disease using a sufficient statistic for testing against a threshold.

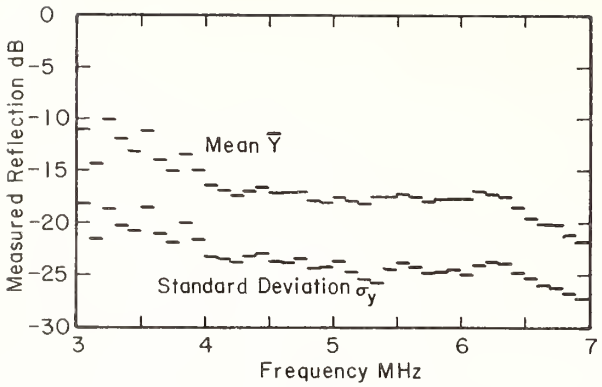

Fig. 8. Experimental data for the mean and standard deviation of lung reflection Y for a subject with severe chronic pulmonary disease.

Appendix A
Radiation Filter Response

The radiation filter response reported in the literature [1] and tabulated [2] is given in eq. (A-1) for the definitions in eqs. (A-2). It is an exact solution to the radiation coupling between two coaxial disks spaced at distance 2r apart.

$$F(r,a,f) = \left[\cos(2\pi f t_3) + j\sin(2\pi f t_3)\right] \qquad \text{(A-1)}$$

$$- \frac{c^2}{a^2} t_3 t_4 \left[\frac{t_4 + t_2}{t_4 + t_1}\right]^{1/2}$$

$$\left[J_0(2\pi f t_3) + jJ_1(2\pi f t_3)\right]$$

$$+ \frac{c^2}{a^2} t_3^2 \left[\frac{t_4 + t_2}{t_4 + t_1}\right]^{1/2}$$

$$\left[1 - \frac{\frac{1}{2}t_4}{t_4 + t_1} + \frac{\frac{1}{2}t_4}{t_4 + t_2}\right]$$

$$\left[J_0(2\pi f t_3) - \frac{J_1(2\pi f t_3)}{2\pi f t_3} + jJ_1(2\pi f t_3)\right]$$

$$+ \text{higher terms}$$

$$t_1 = 2r/c \qquad \text{(A-2a)}$$

$$t_2 = \left[\frac{4a^2 + 4r^2}{c^2}\right]^{1/2} \qquad \text{(A-2b)}$$

$$t_3 = \tfrac{1}{2}(t_2 - t_1) \qquad \text{(A-2c)}$$

$$t_4 = \tfrac{1}{2}(t_2 + t_1) \qquad \text{(A-2d)}$$

In the equations c is the wave speed, f is the frequency, a is the disk radius, and r is the range between disk and plane. The functions J_0, J_1 are Bessel functions of the first kind.

Appendix B
Detailed Scattering Function for the Lung Surface

This appendix is a summary of a more detailed development of the scattering function for the lung given elsewhere [2,3]. The range spread function m(r) is considered to be the incremental reflectance of the rough surface due to surface elements between r and r+dr in range. In order to simplify the development the following assumptions are made:

1) Reflection is a first order scattering process involving no shadowing of reflective elements nor multiple reflection among elements.
2) The dimensions of roughness elements are small compared to the diameter of the transducer.
3) The soft tissue to air interfaces perfectly reflect with no other loss mechanism.
4) The disk is normal to the surface.
5) The scattering depth is thin compared to variations in the radiation transfer function.
6) The incremental reflectance from an individual scattering element is of constant amplitude over the depth of the element.
7) The scattering elements are statistically independent.
8) The lung surface approaches a flat perfectly reflective plane as the frequency approaches zero.

The transfer function for an individual scattering element of depth w_m is given in eq. (B-1). The overall transfer function is a sum over a large number of individual scattering elements in eq. (B-2).

$$L(f,w_m) = \frac{k}{j^2\pi f}\left[1 - e^{\frac{-j2\pi f 2w_m}{c}}\right] \qquad \text{(B-1)}$$

$$F(f) = \frac{1}{N}\sum_{M=1}^{N} L(f,w_m) \qquad \text{(B-2)}$$

Invoking the central limit theorem G(f) becomes a Gaussian random variable with independent real and imaginary parts with means R_0, Q_0 and variance σ^2. When the value of k in eq. (B-1) is adjusted to normalize the magnitude as in assumption 8, the essential values for R_0, Q_0 and σ^2 are arrived at in eqs. (B-3) and (B-4).

$$R_0^2 + Q_0^2 = \frac{c^2}{4w_0^2(2\pi f)^2}\left[1 + e^{\frac{-4\sigma w^2(2\pi f)^2}{c^2}}\right.$$

$$\left. - 2\cos\frac{(2w_0 2\pi f)}{c} e^{\frac{-2\sigma w^2(2\pi f)^2}{c^2}}\right] \qquad \text{(B-3)}$$

$$\sigma^2 = \frac{c^2}{8w_o^2(2\pi f)^2}\left[1 - e^{\frac{-4\sigma w^2(2\pi f)^2}{c^2}}\right] \qquad \text{(B-4)}$$

If we are concerned only with the magnitude Z of G(f) the probability density function becomes Ricean as in eq. (B-5). The mean and a variance of the magnitude are given in eqs. (B-6) and (B-7) respectively. The functions $I_o(\cdot)$ and $I_1(\cdot)$ are modified Bessel functions.

$$p_z(Z) = \frac{Z}{\sigma^2} e^{\frac{-(Z^2 + R_o^2 + Q_o^2)}{2\sigma^2}} I_o\frac{Z(R_o^2 + Q_o^2)}{\sigma^2},$$

$$Z \geq 0 \qquad \text{(B-5)}$$

$$\bar{Z} = e^{\frac{-(R_o^2 + Q_o^2)}{4\sigma^2}} \frac{\sigma^2\pi}{2}^{\frac{1}{2}} \left[\left(1 + \frac{R_o^2 + Q_o^2}{2t^2}\right) I_o \frac{R_o^2 + Q_o^2}{4t^2}\right.$$

$$\left. + \frac{R_o^2 + Q_o^2}{2t^2} I_1\left(\frac{R_o^2 + Q_o^2}{4t^2}\right)\right] \qquad \text{(B-6)}$$

$$\sigma_z^2 = R_o^2 + Q_o^2 + 2\sigma^2 - \bar{Z}^2 \qquad \text{(B-7)}$$

The mean squared lung surface reflectance in eq. (B-8) expresses the energy scattered at a given frequency. This function is essentially the scattering function discussed in radar.

$$\overline{|G(f)|^2} = \overline{z^2} = R_o^2 + Q_o^2 + 2\sigma^2 \qquad \text{(B-8)}$$

Acknowledgments

This paper is essentially a summary of work reported in the three references cited. It was felt that it would be useful to the reader to report the essential results here in summary form and to refer the interested reader to the more extensive discussions and numerous literature citations to be found in the basic papers.

The work summarized here and in the basic papers was supported by the Ambrose Monell Foundation and the G. Unger Vetlesen Foundation.

References

[1] Rhyne, T. L., Radiation coupling of a disk to a plane and back or a disk to a disk: An exact solution, J. Acoust. Soc. Am. 61, 318-324 (1977).

[2] Rhyne, T. L., Acoustic Instrumentation and Characterization of Lung Tissue (Forest Grove, Oregon, 1977).

[3] Rhyne, T. L., Sonar Characterization of Tissue as Applied to the Lung, Sc. D. Thesis, Department of Electrical Engineering and Computer Science, Massachusetts Institute of Technology, Cambridge, Massachusetts (1976).

Reprinted from *Ultrasonic Tissue Characterization II*, M. Linzer, ed., National Bureau of Standards, Spec. Publ. 525 (U.S. Government Printing Office, Washington, D.C., 1979).

ANGLE SCAN AND FREQUENCY-SWEPT ULTRASONIC SCATTERING CHARACTERIZATION OF TISSUE

R. C. Waag, P. P. K. Lee, R. M. Lerner, L. P. Hunter, R. Gramiak, and E. A. Schenk

Departments of Electrical Engineering, Radiology, and Pathology
University of Rochester
Rochester, New York 14627, U.S.A.

Ultrasonic wave interference has been applied to characterize tissue by measuring scattered wave intensity as a function of frequency and angle. A theory of acoustic wave propagation and scattering in an inhomogeneous medium has been employed to show that received ultrasound may be expressed in terms of medium refractive index variations via a Fourier transform. Using a computer-based system, measurements were made on model targets and post-mortem liver specimens. Model studies demonstrate that regular scatterer spacing can be inferred from measured diffraction data by Fourier inversion and that scattering differences can be observed from random media consisting of particles of different average sizes. Scattering from liver indicates there is significantly more energy scattered at small angles than is backscattered. Correlation of ultrasound scattering with structure observed through a microscope has been obtained by computing the diffraction pattern of the two-dimensional optical transmittance images acquired through a microscope-TV chain attached to the computer. Average particle sizes of the model random media determined by Fourier analysis that exhibited diffraction rings of the digitized cross-sections yielded scattering predictions which were in agreement with measured acoustic data.

Key words: Angular scattering; characterization of tissue; optical correlation; scattering; swept-frequency diffraction.

1. Introduction

Although ultrasound has been widely accepted as a valuable diagnostic tool in medical imaging, its use in quantitative characterization of tissue is just beginning to emerge. Among methods which employ amplitude, phase, frequency, and attenuation of ultrasound signals, diffraction-based techniques offer the potential of characterizing acoustic scattering element distribution on a scale corresponding to the wavelength within a finite volume probed by the ultrasound beam [1-6][1]. Success of wave interference methods in x-ray studies of materials as well as in atmospheric probing by radar motivates the development of the methodology for acoustic studies of tissue. However, realization of practical tissue characterization systems based on diffraction require more detailed understanding of the acoustic scattering process, including development of useful models and knowledge of practical measurement limitations.

In this paper, our ultrasonic scattering studies of model targets and preliminary results from liver tissue are described. A model is developed to show the fundamental relationship between scattered acoustic waves and tissue structure. The measurements demonstrate feasibility of the method and identify problems. The results indicate the promise of the concept but point out the need for additional data to characterize tissue.

Our research combining angle scanning and frequency sweeping is intended to provide a foundation for characterization of tissue by its ultrasonic scattering properties.

2. Theoretical Basis

A. Acoustic Scattering Model

The model we use relates the scattered intensity to the acoustic structure of the tissue and indicates that different levels of organization may be studied with ultrasound by appropriate choice of frequency and geometry. The resulting acoustic characterization can then be compared to microscopic determinations of structure to establish tissue pathology. The theory is analogous to that used in x-ray diffraction of amorphous materials and allows the structure of the medium to be inferred from measurements of the scattered acoustic wave.

The tissue is modeled as an inhomogeneous medium in which the acoustic properties exhibit variations from point to point. Since wave propagation is affected by the local environment, wavefronts are distorted and scattered. The derivation has followed the basic approach used in modeling wave propagation and scattering for acoustic studies of the lower atmosphere [7].

[1]Figures in brackets indicate literature references at the end of this paper.

The analysis begins with consideration of a plane wave propagating through a lossless unbounded medium which has small variations in refractive index. Small values of absorption do not change the basic relationships [6].

Assuming a monochromatic incident plane wave, weak single scattering, and a receiver in the far-field, the resulting scattered wave velocity potential $\phi_1(\underset{\sim}{r},k)$ is given by

$$\phi_1(\underset{\sim}{r},k) = \frac{A_o k^2 e^{ikr}}{2\pi r} \int_{V'} e^{i\underset{\sim}{k}\cdot\underset{\sim}{r}'} n_1(\underset{\sim}{r}')dV' \qquad (1)$$

in which

A_o = incident plane wave amplitude
k = incident wave number
$\underset{\sim}{K}$ = scattering wave vector
$n_1(\underset{\sim}{r}')$ = variations of acoustic refractive index
V' = scattering volume
r = distance from the scattering volume center to the reception point

Thus, the velocity potential at a receiving point r is equal to the product of a frequency-dependent factor and the three-dimensional spatial Fourier transform of the acoustic refractive index variations.

The theory also relates the mean square value of velocity potential to the correlation function of the acoustic refractive index variations in a random medium if the variations are stationary in space. The relation is

$$\langle|\phi_1(\underset{\sim}{r},k)|^2\rangle = \frac{A_o^2 k^4 V'}{4\pi^2 r^2} \int_{V'} e^{i\underset{\sim}{K}\cdot\underset{\sim}{\rho}} B_{n_1}(\underset{\sim}{\rho})dV' \qquad (2)$$

where

$$B_{n_1}(\underset{\sim}{\rho}) = \langle n_1(\underset{\sim}{r}')n_1(\underset{\sim}{r}' + \underset{\sim}{\rho})\rangle$$

where $\langle\ \rangle$ denotes ensemble averaging. This shows that the average intensity of the scattered wave is proportional to the three-dimensional spatial Fourier transform of the correlation function of the acoustic refractive index variations.

The expression for the mean square velocity potential allows determination of the correlation function of the acoustic refractive index variations in the medium by inversion of the transform relating the measured average scattered intensity as a function of scattering vector [8]. Alternatively, a specific form for the correlation function can be employed to evaluate the average scattered intensity for comparison with experimental data. The latter approach has been used to evaluate scattering from a cloud of scatterers assuming a correlation function with a Gaussian shape modified to remove the dc spectral component [9]. Neglecting density variations, the resultant expression for the scattered intensity per unit incident intensity is

$$\frac{I_{is}}{I_i} = NV\frac{\sqrt{2\pi}}{9}\frac{k^4a^6}{r^2}|\gamma_K|^2 \times \left(\frac{1}{8}k^2a^2\sin^2\frac{\nu}{2}\right)e^{-2k^2a^2\sin^2\frac{\nu}{2}} \qquad (3)$$

ν = scattering angle
NV = mean number of scatterers in sample volume
a = mean radius of the particles
γ_K = mean value of compressibility variations between scatterers and medium

The result predicts that smaller particles scatter more energy off-axis than large particles for a fixed incident frequency.

B. Optical Correlation

Optical data for comparison to ultrasound angle scattering data can be obtained by computing the diffraction pattern of a sample region with variable transmission representing spatial distribution of scattering inhomogeneities. In the far-field of a plane through the region, the diffracted optical field is given in terms of the two-dimensional Fourier transform of the transmission pattern [10].

$$\psi(\underset{\sim}{r}) = \frac{Ae^{-ikr}}{r} \int_S T(\underset{\sim}{r}')e^{i\underset{\sim}{k}\cdot\underset{\sim}{r}'}\,d\underset{\sim}{r}' \qquad (4)$$

where

A = constant

$\underset{\sim}{k} = \frac{2\pi}{\lambda}\frac{\underset{\sim}{r}}{r}$

$T(\underset{\sim}{r}')$ = transmittance of aperture S

The intensity of $I(\underset{\sim}{r})$ of the pattern is then

$$I(\underset{\sim}{r}) = \psi(\underset{\sim}{r})\psi^*(\underset{\sim}{r})$$

The dimensions over which diffraction occurs are determined by the wavelength or, equivalently, the sampling interval of the optical transmittance and can be readily chosen in analysis to yield a scale comparable to that in ultrasound diffraction. Averaging the two-dimensional diffraction intensity patterns of any collection of typical cross-sections in the region results in a statistical characterization of diffraction by a random medium.

For an isotropic random medium with local order, the predicted average diffracted intensity takes the form of concentric rings [11]. The spacing of the rings gives nearest neighbor distance while the width of the rings is a measure of the spread in scatterer size and the number of visible rings indicates ranges of local order. Optical diffraction also allows quantitative determinations of parameters describing known optical morphology for comparison with similar parameters derived ultrasonically when there is no order since the width or general shape of the power spectra can be used in these cases.

3. Experimental Methods

A. Acoustic Scattering

Initial studies employed frequency sweeping with fixed transducer-target orientation. The scattering experiments were performed in a water-filled tank containing a fixture on which transducer holders were mounted. The holders could be angled to align the ultrasonic beams and could be slid along the fixture as well.

The electronic instrumentation used for this investigation consisted of a transmitter capable of frequency sweeping, a range-gated receiver and a recorder. Bursts of ultrasound were gated from a variable frequency master oscillator to a power amplifier which drives a wideband 9.5 mm diameter transducer with a 5 MHz center frequency. The frequency of the master oscillator was slowly swept over a range of 2 to 8 MHz by a linear ramp function that produced negligible carrier frequency variation over any single pulse.

The scattered ultrasound pressure was detected by a receiving transducer matched to that used for transmission and the amplified RF signal was energy-detected to give a video signal proportional to the incident wave peak intensity which was then recorded.

Arrays of cylinders were studied to provide information about the influence of geometric alignment and beam uniformity. The scatterer positions for array measurements were established by five sets of uniformly spaced grooves two centimeters in length. A rubber sheet was used to shield the holder exposing only one set of wires for acoustic measurements. The center of the array was nominally set at the intersection of the transducer beams for each study with the array elements lying along the bisector of the angle formed by the beams.

The energy detector output was bandpass filtered to produce a signal that was displayed as a function of frequency on the face of an oscilloscope for photographic recording. The analog curves were sampled at 0.115 MHz intervals and quantized into integers in the range 0 to 255 for calculation of Fourier transforms.

Ultrasound scattering as a function of angle was measured in a water tank using an acoustic diffractometer [12] that provided precise control of transducer position relative to the scattering volume. The scattering medium was contained in a cylindrical column 28 mm in diameter by a .0254 mm thick cellulose tubing that minimized reflected energy loss at the perimeter of the sample. Transmitting and receiving transducers containing 4.76 mm radius ceramic disks as active elements were rotated in equal increments but opposite directions about the axis of the cylindrical sample. Transmitter and receiver distances from the axis of rotation were each equal to 13.6 cm. This scanning procedure maintains a constant scattering vector direction while changing the scattering angle, ν, and hence the scattering vector magnitude. The centers of transducer rotation were maintained to within $\pm$ 0.3 mm during the angle scan.

The electronics were the same as in the swept-frequency measurements. The receiver electronics were also the same as used in the previous studies except that a log amplifier was added to accommodate both the small off-axis scattering and the large direct transmission signals. The energy detected output was sampled by the computer and recorded in digital form along with appropriate positional information for statistical analysis and display.

A typical scattering experiment consisted of sixteen angle scans taken at 2.5 mm increments along the axis of the cylindrical sample. In each angle scan, data was collected at 163 equally spaced increments of 2° from a scattering angle of -153° to 165°. The transmitted tone burst was 10 μs long while the receiver gate was 6 μs long and centered in the scattering volume.

Fresh samples of pig liver and human liver samples obtained at autopsy have also been studied ultrasonically by angle scanning and varying frequency. Cylindrical plugs were taken from peripheral regions near the capsule to minimize the inclusion of large vessels. Transmit pulse length and receiver gates were set as in the random medium model studies to minimize inclusion of specular reflectors from the surface.

B. Optical Data

Optical data was acquired under computer control by sampling a TV image obtained through a transmission microscope. Drops of the particle suspensions were spread over a microscope slide and typical areas digitized. Five different images from a smear of each particle suspension were obtained for analysis. The individual images consisted of 8-bit samples representing light intensity transmission over a field of 1.7 mm spanned by 384 x 384 matrix elements.

The cylindrical liver specimens were fixed in formalin and standard sectioning and staining procedures used to evaluate histomorphologic changes in the sections that were studied ultrasonically. Each stained section was digitized into a 256 x 256 matrix covering a field of 4.5 mm. In the optical studies of liver tissue, a Van Gieson connective tissue stain was employed to bring out structures believed to cause ultrasonic scattering and the computed average power spectra were used to characterize the architecture for comparison with ultrasound angle scan data.

The digital representations of the optical images obtained through the microscope-TV system were enhanced to improve the contrast between the particle boundaries and the background. This was accomplished by forming histograms of original image amplitudes and using these histograms to develop mappings that spread the original light intensity transmission values over wider ranges. The far-field diffraction pattern of each optical image was obtained by a two-dimensional Fourier transformation implemented using an integer FFT algorithm. The log magnitude of the resultant spectra was calculated to facilitate display of a wide range of spatial frequency amplitudes. Averages of the log magnitude spectra from the five sample functions of the same particle size distribution were computed. The spherical symmetry of this spectral estimate was used to produce additional smoothing by averaging spatial frequency amplitudes determined along radii spaced 1° apart. The results were used to find average nearest neighbor distances.

4. Results

Data was collected by frequency scanning 10 mil monofilament nylon cylinders in arrays with spacings of 0.72 and 1.52 mm at a range of 11.0 cm and a Fourier transform was applied to infer the spacings (fig. 1). The influence of transmitter range on measurements of diffraction by an array spacing of 1.52 mm was observed for ranges of 4.5 and 11.5 cm (fig. 2). The distances (0.78 and 1.55 mm) indicated by the peaks on the transformed data in each of the measurements are within 4 percent of the actual values. The envelope of the data collected at 4.5 cm is different from the far-field measurements, but did not invalidate calcula-

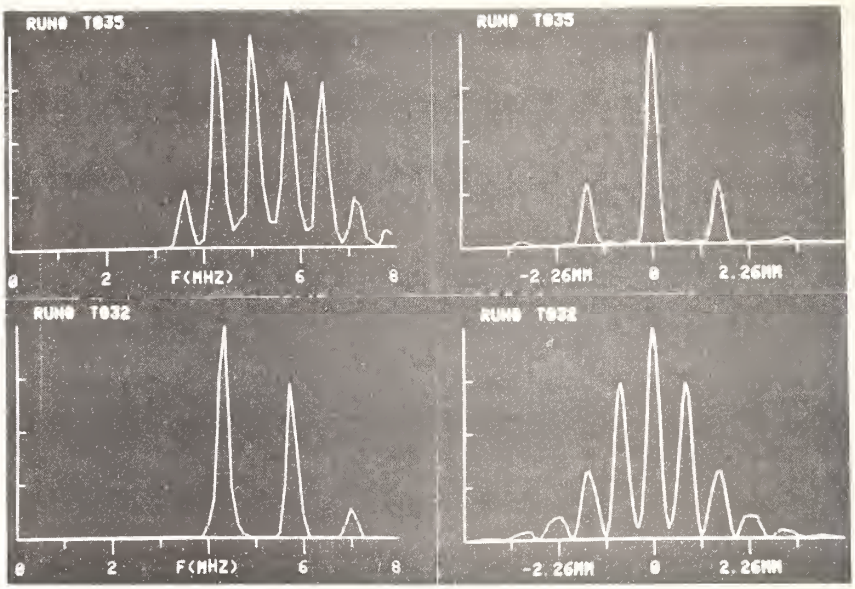

Fig. 1. Swept-Frequency Diffraction by Arrays. Measured values of scattered energy as a function of frequency are shown (left) on a linear scale with their corresponding Fourier transforms (right) also on a linear scale for array spacings of 1.52 mm (top) and 0.76 mm (bottom) at a transmitter range of 11.0 cm. The ultrasonically determined spacings were 1.55 mm and 0.78 mm respectively.

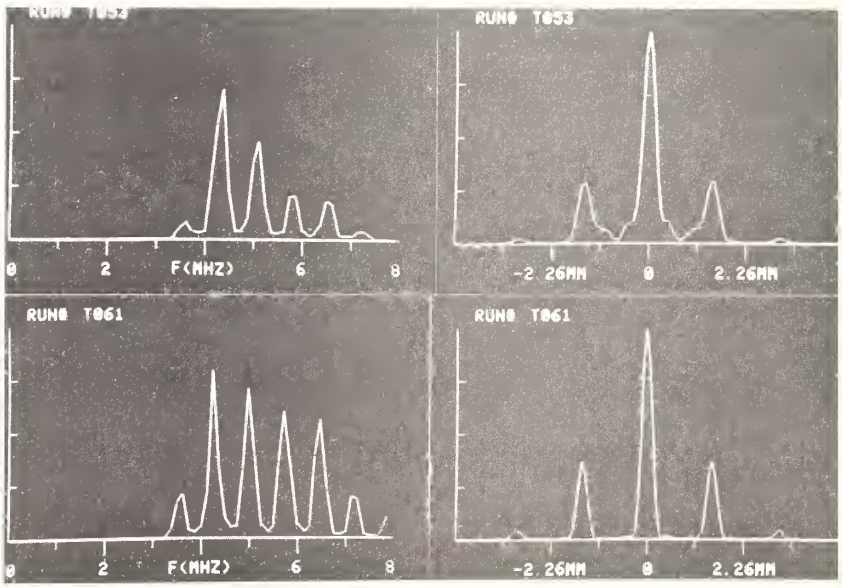

Fig. 2. Swept-Frequency Diffraction as a Function of Range. Measured curves of energy as a function of frequency are displayed (left) on a linear scale with corresponding Fourier transforms (right) also on a linear scale for transmitter ranges of 4.5 cm (top) and 11.5 cm (bottom) for an array spacing of 1.52 mm. The ultrasonically determined spacings were 1.48 mm at the far range and 1.55 mm at the near range.

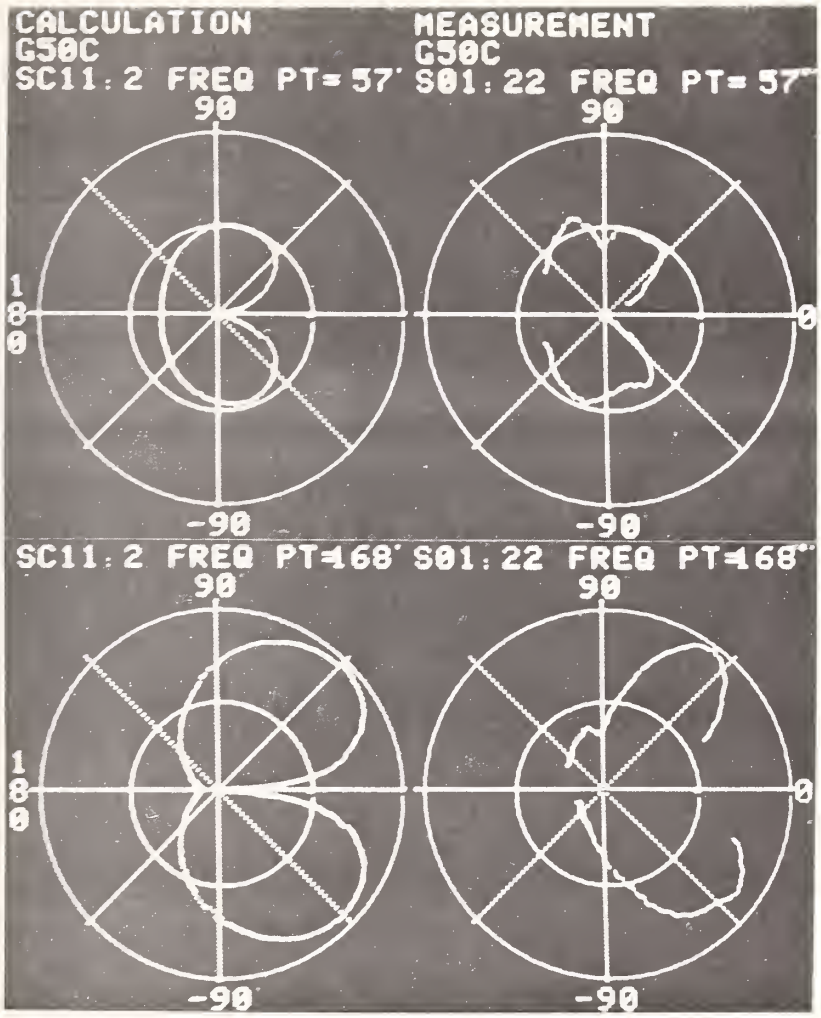

Fig. 3. Frequency-Dependent Angular Scattering by a Random Medium Model. Measurements of average intensity are shown (left) on a logarithmic scale along with calculated scattering (right) on the same scale for a frequency of 3.8 MHz (top) and 6.0 MHz (bottom). The measured data obtained from a suspension of particles demonstrates more forward scattering as frequency increases and compares well with computations of scattering from a cloud in which the average particle radius is 128 μm.

tions of spacings by Fourier inversion of the data.

Angle scans were carried out on three suspensions of different average size Sephadex[2] particles. Measurements of scattered ultrasound signal as a function of angle were averaged for each distribution of particle size. The averaged angle scan data is an estimate of the spectral power in wave number or reciprocal space of the variations in acoustic index of refraction.

Averages of ten angle scans for each of three particle size distributions were obtained. The transmitted main beam was subtracted from the average data and the resulting angular scattering data smoothed to remove artificial fluctuations arising from averaging only a finite number of sample functions. The final result was compared with calculations of scattered intensity using eq. (3) to determine average scattered intensity as a function of angle at two frequencies for the coarse grade of particles which had the largest average size (fig. 3). The averages for two other particle distributions show how off-axis scattering increases as average particle size decreases (fig. 4).

Enhanced optical transmittance images of five sample functions and the corresponding average log magnitude spectra were obtained from smears of three particle grades (fig. 5). A smoothed spatial frequency amplitude distribution was found by averaging the amplitudes along radii from which the nearest neighbor distances may be determined (table 1).

Pilot studies of acoustic scattering from human and pig liver tissue by angle scanning have been carried out (fig. 6). The data shows that there

[2]Trademark of Pharmacia Fine Chemicals.

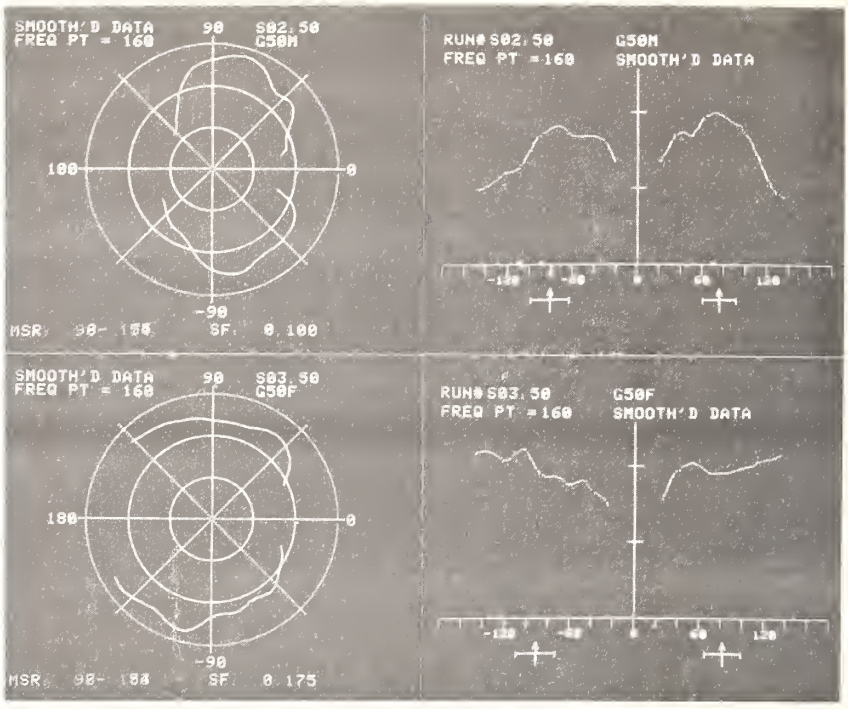

Fig. 4. Size-Dependent Angular Scattering by a Random Medium Model. The polar plots and corresponding Cartesian displays show average intensity on a linear scale at 5.9 MHz for distributions of scatterers with an average particle radius of 93 μm (top) and with an average radius of 84 μm (bottom). The increase in omnidirectional scattering for smaller scatterers is evident in both plots and also demonstrated by the mean scattering angle defined by arrows crossing standard deviation bars below the Cartesian plots.

Table 1. Nearest neighbor spacing determined by Fourier transform analysis of optical transmittance.

Particle distribution	Mean spacing (μm)	Spread of spacings (±1σ) (μm)
G50M	93.3	63.2 - 177.6
G50F	84.3	57.3 - 159.4

is significantly more scattered energy at small angles than in the backscattered mode. Scattering in the forward direction becomes greater as the frequency increases. Optical data obtained from these specimens shows the well-defined regular lobular structure of pig liver and the irregular structure of a post-necrotic cirrhotic human liver (fig. 7). The power spectra and their corresponding average radial distributions show the same trend of increased omnidirectional scattering from pig liver that the acoustic data demonstrate.

5. Discussion

The measured scattering from arrays of nylon cylinders yields element spacings that correspond well to actual values and shows the influence of near-field variations of transducer beams on the determination of scatterer spacing. The number of peaks in the transformed data indicates diffraction by integer multiples of the basic spacing and are a measure of the number of scatterers in the beam or the effective width of the common scattering volume which contains more array elements as the spacing decreases.

Diffraction-based measurements of array element spacing as a function of range from the transmitter show peaks that do not vary in position when the scatterers are in the near-field of the transducers. These measurements also support the utility of a model that employs the far-field assumption for inferring structure even when the far-field assumption is not strictly satisfied.

Acoustic scattering from Sephadex was measured using a wavelength that ranged from 2 to 30 times the particle diameters and corresponds to a transition region between point scattering and diffraction by individual spheres. This relationship of wavelength and particle size was chosen for its potential similarity to situations of interest in medical ultrasound. Differences in scattering due to particle size are still demonstrated by the analysis of both the acoustic and optical data. The acoustic data from the Sephadex experiments agrees with the predictions of the expression describing scattering from a cloud of particles.

For the coarse grade of particles, the computed results agree well with the experimental data. The mean value size parameter of 128 μm is well

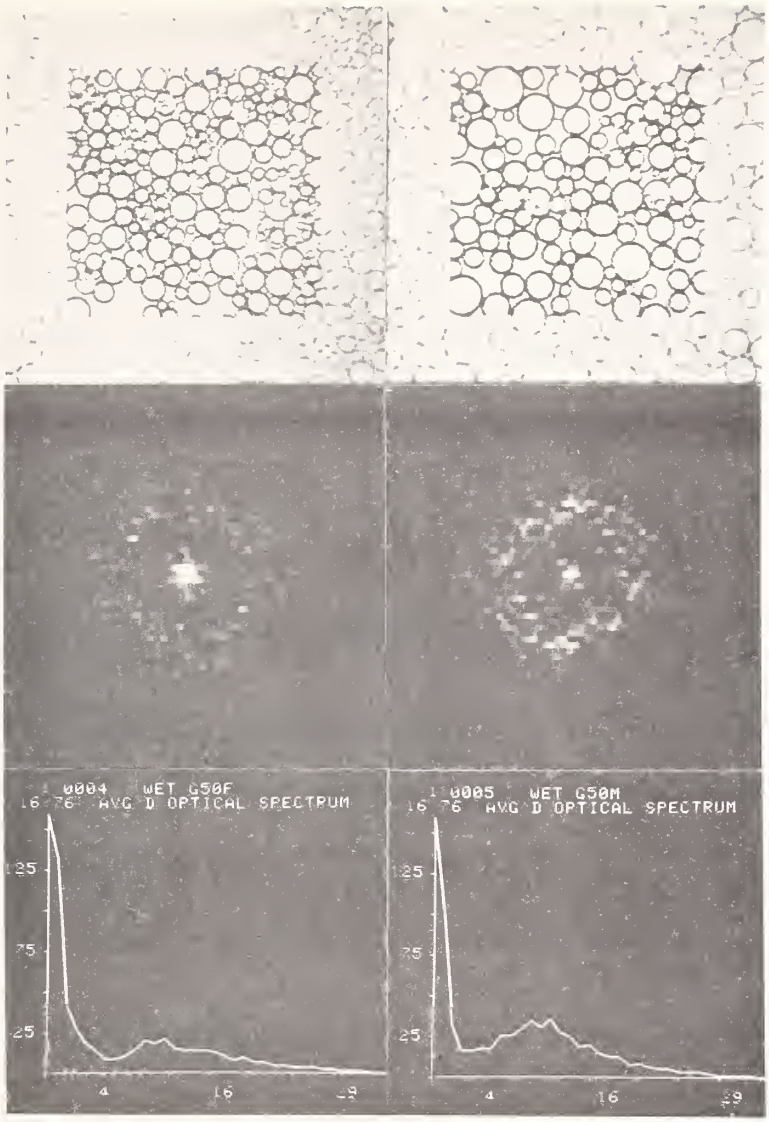

Fig. 5. Optical Image Analysis of Random Media Model. In (a) particles with an average size of 84 μm (left) and 93 μm are shown with the central field enhanced by amplitude mapping. The power spectra (b) obtained by averaging showed diffraction rings with an average radial distribution of energy (c) that is inversely proportional to scatterer size and consistent with the acoustic scattering results.

within the range of the manufacturer's specifications on sizes and is also confirmed by the optical determinations. Both experimental data and calculations show that the scattering becomes greater in the forward direction as frequency increases. Polar plots of average acoustic intensity as a function of scattering angle also show that a distribution of small particles scatters relatively more energy at larger angles than does a distribution of large particles.

These results are in agreement with theoretical predictions about scattering off-axis as a function of particle size, and support the swept-frequency studies in which small particles scattered more energy at high frequency than did large particles reported earlier [4]. The experiments are comparable because the Sephadex suspensions are isotropic so that angle scanning produces the same result as frequency scanning.

The acoustic scattering data was collected under conditions that reasonably approximate the plane wave, point receiver, and weak scattering assumptions employed in the theoretical development. The 170 microseconds between transmit and receive gates correspond to transducer distances of 12.6 cm from the center of the scattering volume. This distance normalized by the ratio, the square of transducer radius to the wavelength, is 10.9 and is well within the far-field resulting in a plane wave incident on the scattering volume. The distance also results

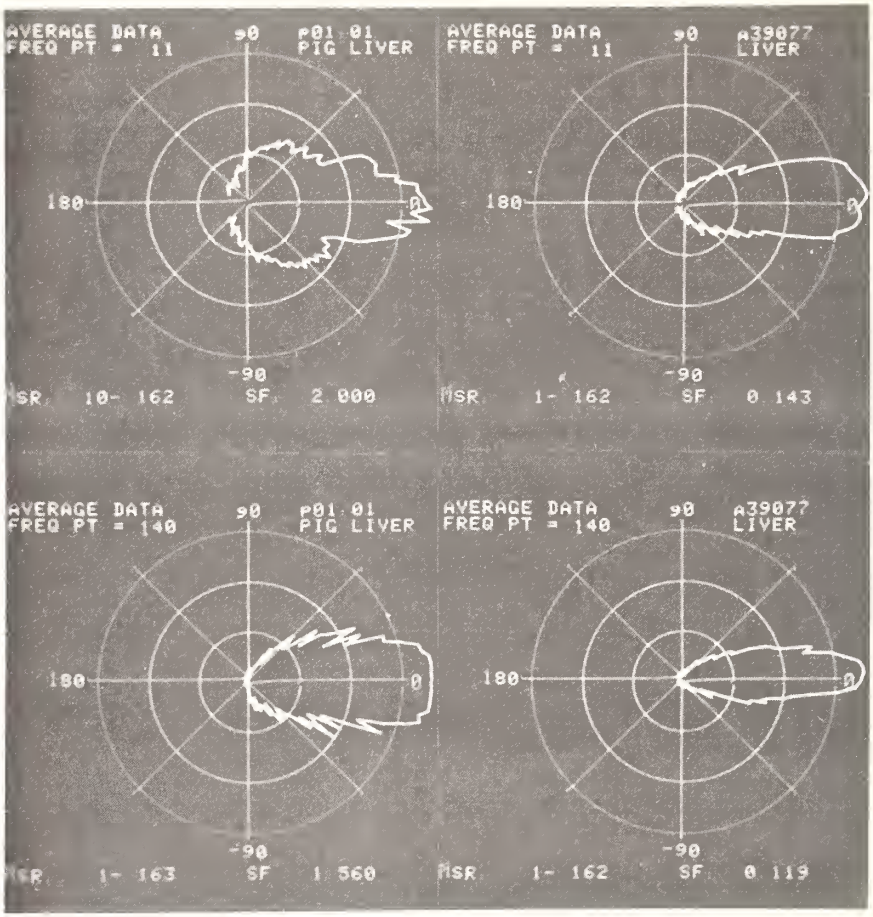

Fig. 6. Comparison of Average Angular Scattered Intensity From Normal Pig Liver and Cirrhotic Human Liver. Specimens studied at 3 MHz (upper panels) show that the normal pig liver scatters more omnidirectionally than cirrhotic human liver and that, as the frequency is increased to 6 MHz, the forward scattering component increases in both cases. This is consistent with scattering from collagen which is arranged in a smaller, more uniform matrix in the pig liver than in the cirrhotic human liver.

in a maximum phase variation of 16.4° across the face of the receiving transducer for a wave originating from a point at the center of the scattering volume and thus a point receiver approximation is justified.

The logarithmic compression of the received ultrasound signal near 0° scattering angle, needed to allow simultaneous demonstration of scattering signals at other angles, indicates that the assumption of weak, single scattering or the Born approximation is valid.

The polar plots do not demonstrate symmetric scattering about each side of the 0° scattering angle beam as anticipated from the isotropy assumption. A reason for this is that a slightly different scattering volume was sampled on each side of 0° due to error in concentricity of the transducer arms.

Optical characterization of a distribution of spheres shows a ring which agrees with theory. The good agreement between theory and final ring structures obtained by processing only five samples supports the notion that the particle distribution used for a random medium model is isotropic. Since the particles are closely packed, the spacings observed by light transmittance analysis are equal to particle size.

Parameters for the particle distributions derived from averages of radial lines in the two-dimensional log spectra are in excellent agreement with the values supplied by the manufacturer as well as being in qualitative agreement with analysis of acoustic scattering data.

The angle scan data from pig and human liver specimens demonstrate differences as a result of the different architecture of the tissues. The pig liver scatters more omnidirectionally than the human liver. At lower frequencies, the pig liver also shows a lobe structure indicative of local order in the lobular arrangement, while the human liver scattering, which is predominantly in the forward direction, results from larger, more irregular spacings. The increase in forward scattering at high frequencies as in the Sephadex ex-

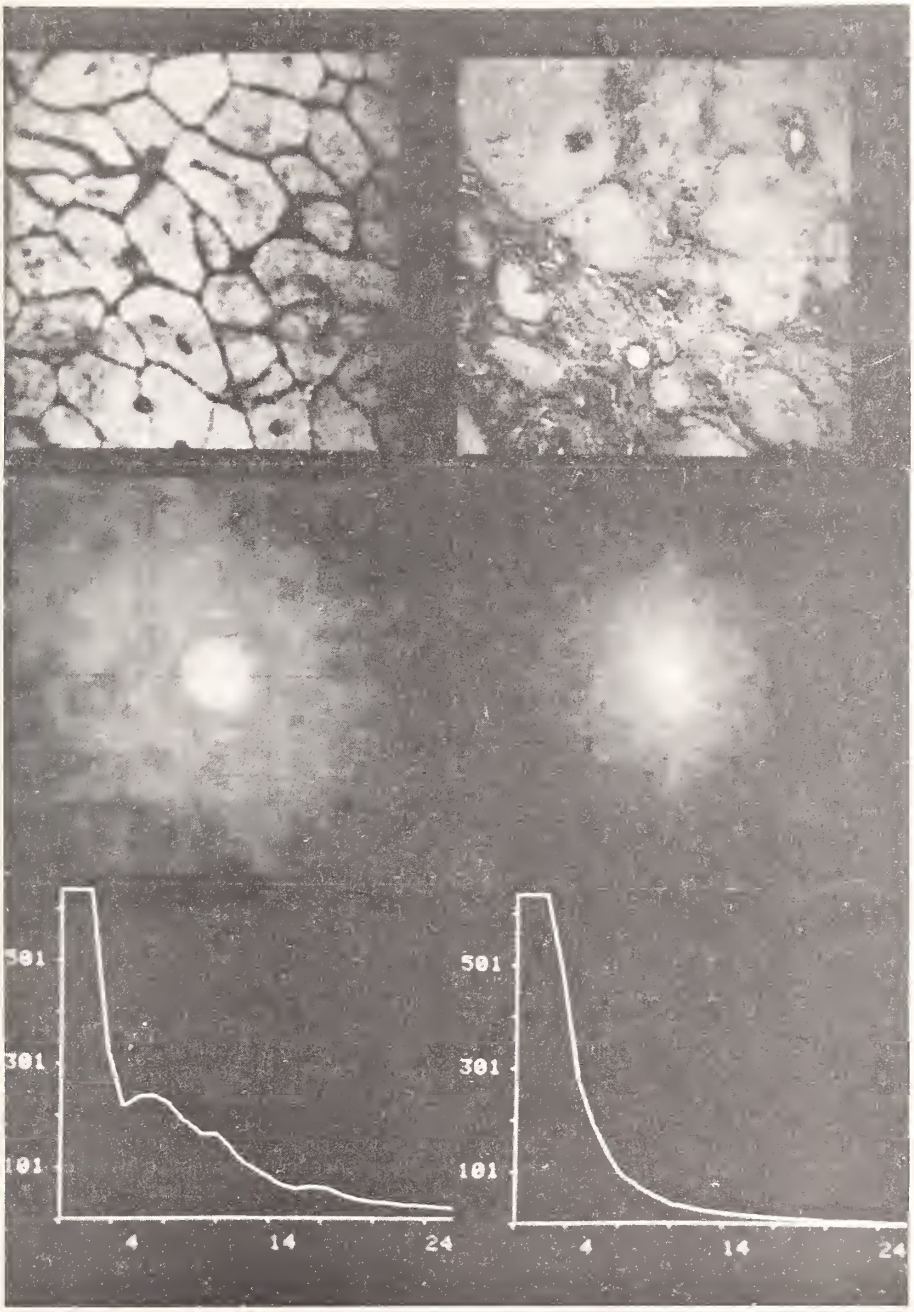

Fig. 7. Optical Image Analysis of Liver. In (a), normal pig liver (left) and cirrhotic human liver have been stained to show connective tissue as dark bands. The power spectra (b) obtained by averaging show that the pig liver produces a broader distribution of scattering than the human liver. The relatively isotropic patterns have been reduced to a one-dimensional form (c) by averaging radial lines at 1° increments to produce data comparable to ultrasound angular scattering when viewed as a Cartesian plot. The optical analysis demonstrates the same increased spread in scattering from pig liver that the acoustic patterns contain.

periments indicates that important scattering may take place from elements in the size range included in the Sephadex studies. The data also implies that backscattered energy, while easier to monitor in practical situations, represents only a small amount of tissue structure information. It remains to determine whether observed peaks in the scattering pattern are due to many randomly spaced scatterers in the tissue or a few large single scattering objects.

Further investigation is also required to determine the specific structural changes observed acoustically, correlate these results with histopathology, and establish the reproducibility of the results from these initial studies of liver specimens.

6. Conclusion

Experimental observation of acoustic diffraction by arrays using swept-frequency ultrasound have agreed well with theoretical predictions. The experiments indicate that near-field beam nonuniformities need not invalidate inference of scatterer spacing from a model employing a far-field approximation. However, more results are needed to bound limitations imposed on measurement of scattering by acoustic diffraction as a result of beam nonuniformities and misalignments.

The ultrasound angle scan data from Sephadex shows size-dependent scattering and agrees with theoretical predictions as well as with optical analysis. The Fourier analysis of optical data accurately confirms the particle size distribution information provided by the vendor and demonstrates a way optical images can be quantitatively analyzed to provide a reference for comparison with ultrasound data. The results obtained indicate the potential for remote probing with ultrasound to characterize a random medium from its scattering and the use of digitally processed optical data to confirm the results.

Preliminary data from swept-frequency and angle scan experiments with pig and diseased human liver tissue shows the importance of scattering at small angles and also that this technique may lead to a useful diagnostic tool. However, additional data is needed to characterize tissue and thus point the way to optimum parameters for clinical determinations of tissue structure from diffraction effects with ultrasound.

Acknowledgments

We wish to acknowledge important assistance in the conduct of this work by Edward E. Eyler, C. Robert Hoffman III, and Jeffrey Astheimer who developed computer programs, and Frank H. Slaymaker and Peter H. Helmers who designed major parts of the mechanical and electronic hardware used in these studies.

This work was supported by the National Science Foundation under grant #APR75-14890 and the National Heart and Lung Institute under grant #HL15016.

References

[1] Baum, G., Quantized Ultrasonography, in Recent Advances in Diagnostic Ultrasound, E. Rand, ed. (Charles C. Thomas, Publisher, Springfield, Ill., 1971).

[2] Chivers, R. C., Hill, R. R., and Nicholas, D., Frequency Dependence of Ultrasonic Backscattering Cross-Section: an Indicator of Tissue Structure Characteristics, in Proc. of the 2nd World Congress on Ultrasonics in Medicine, Rotterdam, The Netherlands, 4-8 June, 1973, M. deVlieger, D. N. White, and V. R. McCready, eds., pp. 300-303 (Excerpta Medica, Amsterdam, 1974).

[3] Heyser, R. C. and LeCroissette, D. H., A new ultrasonic imaging system using time delay spectrometry, Ultrasound in Medicine and Biology 1, (2), 119 (March 1974).

[4] Waag, R. C. and Lerner, R. M., Tissue Macro-Structure Determination with Swept-Frequency Ultrasound, in Proc. of 1973 Ultrasonics Symposium, Monterey, Calif., IEEE Cat. No. 73 CHO 807-8 SU 63-66, 5-7 November, 1973.

[5] Namery, J. and Lele, P. P., Ultrasonic Detection of Myocardial Infarction in Dog, in Proc. of 1972 Ultrasonics Symposium, Boston, Mass., IEEE Cat. No. 72 CHO 708-8 SU: 491-494, 4-7 October, 1972.

[6] Waag, R. C., Lerner, R. M., and Gramiak, R., Swept-Frequency Ultrasonic Determination of Tissue Macrostructure, in Ultrasonic Tissue Characterization, M. Linzer, ed., National Bureau of Standards Spec. Publ. 453, pp. 213-228 (U.S. Government Printing Office, Washington, D.C., 1976).

[7] Tatarskii, V. I., Wave Propagation in a Turbulent Medium (McGraw-Hill Book Company, New York, 1961).

[8] Lee, P. P. K., Waag, R. C., and Hunter, L. P., Swept-frequency diffraction of ultrasound by cylinders and arrays, J. Acoust. Soc. Am. 63 (2), 600-606 (1978).

[9] Morse, P. M. and Ingard, K. U., Theoretical Acoustics, Chapter 8, p. 439 (McGraw-Hill, Inc., New York, 1968).

[10] Goodman, J. W., Introduction to Fourier Optics (McGraw-Hill Book Company, New York, 1968).

[11] Azaroff, L. V. et al., X-Ray Diffraction (McGraw-Hill Book Company, New York, 1974).

[12] Slaymaker, F. H., Ultrssonic diffraction apparatus users manual, (Preliminary) Progress Report on Tissue Characterization with Ultrasound (NSF Project No. APR 75-14890), Appendix I, Dept. of Electrical Engineering, College of Engineering and Applied Science, Rochester, New York, June 1976. NTIS #PB267397/AS.

Reprinted from *Ultrasonic Tissue Characterization II*, M. Linzer, ed., National Bureau of Standards, Spec. Publ. 525 (U.S. Government Printing Office, Washington, D.C., 1979).

QUANTITATIVE MEASUREMENTS OF SCATTERING OF ULTRASOUND BY HEART AND LIVER

J. M. Reid and K. K. Shung

Institute of Applied Physiology and Medicine
and
Providence Medical Center
Seattle, Washington 98122, U.S.A.

Quantitative backscattering measurements have been made using the substitution method used to measure the scattering properties of blood previously. We have obtained preliminary experimental values for the backscattering coefficients of liver and myocardium, fully corrected for equipment and transducer parameters as well as attenuation of the scattering tissue. Results show that scattering for both liver and myocardium is an increasing function of frequency up to 10 MHz. This increase indicates that the tissue elements responsible for the scattering must be less than 30 micrometers in diameter. The level of scattering from liver tissue indicates that if it is isotropic scattering the scattering loss is large enough to account for about 28 percent of the total attenuation reported at 10 MHz frequency.

Key words: Absorption; attenuation; heart; liver; scattering; scattering cross-section.

1. Introduction

The recent interest in characterizing biological tissues through noninvasive ultrasonic means has resulted in investigations and reports on values of velocity, attenuation, impedance, and scattering and echo strength. The first three quantities are nearly always measured in a quantitative sense, the last two are usually measured in a relative sense. The last two quantities are sometimes spoken of interchangeably as if they were the same thing. However, echo strength is the result of the operation of a number of factors: 1) the absolute scattering strength of the tissues; 2) the absorption of the tissues (including the tissue that is doing the scattering); and 3) many equipment parameters.

Although it may appear to be expeditious to do characterization on the basis of echo amplitudes produced by existing equipment, we believe it preferable to obtain the data under conditions which allow the absolute scattering coefficients to be calculated independent of tissue absorption and equipment parameters. Knowledge of absolute scattering parameters is useful for the identification of mechanisms and the prediction of possible applications in medicine. An even more exciting use, however, is in the design of new equipment utilizing new approaches to tissue characterization which can generally only be done if the data obtained are independent of the taking equipment.

Quantitative backscattering measurements can be made using a substitution method which has already been used to measure the scattering properties of blood [1-4][1]. We have used this method to obtain preliminary experimental values for the scattering properties of liver and myocardium. Further more extensive studies on human tissues will be conducted. Animal tissues were used for convenience in adapting the system to solid tissues.

Results have been presented by Nicholas [5] on backscattering coefficients per solid angle for liver, spleen and brain. No details are given on the formalism used to derive the backscattering coefficient. Nicholas' values for liver are about an order of magnitude greater than our values, and at the higher frequencies would predict a scattering loss which equals the entire observed attenuation. Since this a relatively new field, we believe it essential to give as many details of the measurement and data reduction process as possible and, in this article, will present our complete procedure.

2. Method

The backscattering coefficient defined as power scattered per unit solid angle in the backward direction by a unit volume of scatterers was calculated by comparing the RMS value of the backscattered wave to that of a known reflected wave. The coefficient can be defined to be independent of the measuring system and the attenuation characteristics of the tissue [1,2].

Measurements were performed in a large water

[1]Figures in brackets indicate literature references at the end of this paper.

tank which was filled with normal saline solution. The temperature of the saline was kept at 18 °C ± 1 °C. The samples were fixed on a sample holder about 15 cm away from the transducer. Excised calf liver and heart were obtained immediately after the sacrifice of the animal and stored in normal saline solution at a temperature of 4 to 6 °C. Measurements were carried out within three days.

Five liver specimens and five heart specimens were used with each cut into sample regions which were examined so that only those samples free of gross connective tissue or blood vessel interface were used for the measurements to better define the bulk properties of each tissue type. The samples were 2 cm x 2 cm squares with a thickness of 3 to 5 cm. The liver samples were examined in a number of randomly chosen orientations so that 30 to 45 experimental values were calculated for each point on the results. In the measurements of myocardium samples, the direction of the sound beam was always perpendicular to the muscle fibers.

Ultrasonic transducers (Panametrics) with resonant frequencies at 3, 5 and 10 MHz and a diameter of 0.635 cm were used. Electronic equipment consisted of a gated burst generator, pulse echo receiver, and a controllable receiver gating circuit [2,3]. All time measurements were made on an oscilloscope and the output gated echo measured by a true RMS voltmeter. A calibrated attenuator, impedance matched to the receiver input circuit, was adjusted to obtain the same reference reading on the voltmeter for the reflected wave and the scattered wave.

The backscattering coefficient was calculated from the attenuator readings, equipment and equations expressing the received available power from targets located on the axis in the far field of a round piston transducer [1]. The received available power in the wave reflected from a plane interface can be written

$$\frac{P_r}{P_o} = \frac{E^2 A^2 \tau e^{-4\alpha_m R}}{R^2 T_p 4\lambda^2} k^2 \quad , \tag{1}$$

where P_r = received available electrical power (RMS)
P_o = transmitter electrical power (RMS)
E = transducer efficiency (a function of frequency)
A = transducer area
R = range from transducer to interface
T_p = pulse repetition period
τ = transmitted pulse length
λ = wavelength
α_m = pressure attenuation coefficient for propagation medium
k = amplitude reflection coefficient between propagating medium and reflector

In a similar manner, the available power in a wave scattered from a distribution of lossy scatterers, P_s, can be written [2]:

$$\frac{P_s}{P_o} = \frac{E^2 A^2 S^2 e^{-4\alpha_m R}}{8R^4 T_p \lambda^2 \alpha^2 c} \cdot \eta_d (e^{-2\alpha c t_1} - e^{-2\alpha c t_2})(e^{\alpha c \tau} - e^{-\alpha c \tau}) \tag{2}$$

where η_d = backscattering coefficient per unit solid angle, per cm^3
S = cross-sectional area of the sound beam, cm^2
α = attenuation coefficient of the scattering tissue
c = velocity of sound in the scattering tissue
R = range to surface of scattering tissue
t_1 = time from first surface echo to opening of receiver gate
t_2 = time from first surface echo to closing of receiver gate

Equation (2) neglects the front surface reflection of the sample since the cut specimens we employed did not include surface covering membranes, the usual source of such reflections. The terms in brackets are correction factors to account for the total attenuation losses of the scattering material. These losses include absorption of the sound in the scattering tissue between its surface and the region from which scattered echoes are gated into our receiver and measuring circuit, absorption of sound during the transmitted pulse and interaction factors which depend on the absorption of the wave during the duration of the receiver gate and the transmitted pulse. The scattering coefficient can be found by dividing eq. (2) by eq. (1) and solving for the coefficient. The resulting equation is:

$$\eta_d = \frac{P_s}{P_r} \frac{2k^2 R^2 \alpha^2 c\tau}{S(e^{-2\alpha c t_1} - e^{-2\alpha c t_2})(e^{\alpha c \tau} - e^{-\alpha c \tau})} \tag{3}$$

The ratio of P_s to P_r is obtained from the change of the input attenuator settings necessary to make the RMS readings of the pulse from the flat reflector equal the reading of the gated, scattered waves. Theoretically, this ratio should be expressed in terms of the open circuit transducer voltages due to the scattered and the reflected waves. When the attenuator is connected we read instead a loaded or closed circuit voltage. Since we use the same transducer and receiver impedance for the two waves, the loaded voltage is less than the open circuit voltage by a complex frequency-dependent factor which depends on the impedances in the circuit. This factor is the same for the scattered wave as for the reflected wave, however, and hence divides out when the ratio is taken. Therefore, the ratio is the same for the open-circuit as for the loaded condition. The other factors in eq. (3) can be obtained by direct measurement of apparatus dimensions, oscilloscope time settings and separate measurements of attenuation and velocity within the scattering tissue. In this investigation, these tissue properties were taken from the published literature [6-8]. The time lapse between the receiver gate and the tissue - saline surface (t_1) is in the order of 10 to 20 μm. Attenuation losses in this layer as well as losses in the sample volume are corrected for by use of eq. (3). The amplitude reflection coefficient between the saline and tissue surface was less than 0.1 and assumed negligible.

Figure 1 is the data collection sheet filled out by the experimenter at the time of measurement for one specimen at one frequency. The section of the sheet before the calibration run consists of equipment parameters. The calibration run allows

Date 4 MARCH, 1977

Data Collection Sheet for the Scattering Experiment

Sign K. K. SHUNG

Specimen: CALF MYOCAROIUM

Wave Frequency: 10 MHz Pulse Repetition Rate: 1 kHz

Temperature of Water Bath: 18 °C Pulse Width: 4 μs

Gate Width: 10 μs T_1: 10 μs

Transducer Position: 34 cm Reflector Position: 54 cm

Sample Position: 52.7 cm

Beam Width: 0.27 cm Beam Cross-Section: 0.057 cm^2

Calibration Run:

Reflector Position (cm)	Attenuator Reading (dB)
54	79
52	81.5
50	84.5
56	76.6
58	74.5

Reference on RMS Meter: 0.003 V, -8 dB

R(Distance between Transducer and Sample) = 15.4 cm -31.19 0.29

α(Attenuation Coefficient for Sample) = .1 Nepers/cm 1.68 -20.59

c(Velocity of Propagation) = 1.58 cm/second -29.19

DATA dB

1 11.5 2 10 3 11 4 9.5 5 10.5 6 14 7 17

8 9 9 8 10 10 11 9.5 12 15 13 17 14 15

15 11

REDUCED DATA SCATTERING COEFFICIENT cm^{-1}

1 0.017 2 0.023 3 0.015 4 0.011 5 0.014 6 0.03 7 0.06

8 0.01 9 0.008 10 0.012 11 0.011 12 0.038 13 0.06 14 0.038

15 0.015

Average:

Fig. 1. Sample data collection sheet. For each specimen at each frequency the data shown were recorded by the experimenter.

us to check for R^{-2} echo dependence, eq. (1), as proof of far-field conditions, and relates the attenuator reading at the surface of the sample to the attenuator reading at a reference position within the tank. Readings from the reference position are used to monitor system gain. The next four lines retain data which apply to this particular experiment. The distance, R, shown was calculated from the position of transducer and sample carriers shown at the top of the page and the use of corrections for the distance between the active surfaces of transducer and sample and the holder position. Attenuation coefficients and velocity of propagation (inadvertently recorded as cm/second rather than meters/second used in calculation) were obtained from the literature. The numbers shown at the right side of the figure were notes made during calculation in which various factors in eq. (3) were expressed in terms of dB. Under data we list the attenuator readings necessary to keep the RMS meter at its reference reading.

The result of final calculation of scattering coefficient, η_d, is shown at the bottom of the page.

3. Results and Discussion

The experimentally determined values of scattering coefficient are plotted in figures 2 and 3.

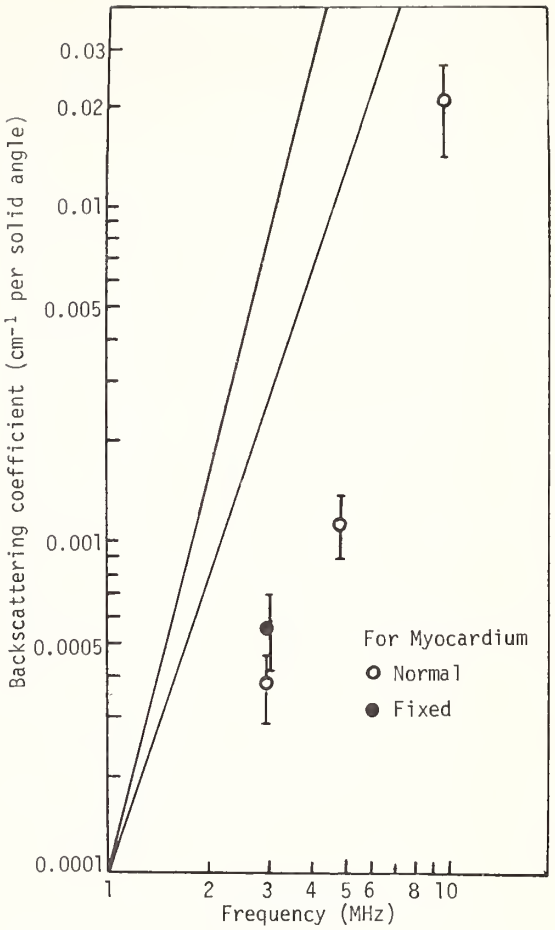

Fig. 2. Measured backscattering coefficient for the myocardium as a function of frequency. Experimental points are the average of 30 to 45 separate measurements on five or six samples. Bars indicate the standard deviation vs. frequency slopes for Rayleigh, fourth power scattering and for third power scattering.

One point using tissue fixed with 10 percent formalin is included for comparison. The data show that liver is a much stronger scatterer than heart tissue at the lower MHz frequencies. Also, the fixed tissue has a stronger scattering than the normal tissue in each case. The backscattering from both myocardium and liver increases with frequency. Figure 2 shows reference lines drawn through arbitrary points to give the attenuation slope for both fourth power (Rayleigh) and third power scattering. At the higher frequencies, the heart tissue appears to be approaching approximate fourth power dependence and the liver tissue less than a third power dependence. It must be recognized that the program is still in its early stages since only a few data points have been taken and positive conclusions, particularly with respect to frequency dependence, are not warranted. Scattering does appear to increase with frequency, however.

Since the scattering at 10 MHz is still increasing with frequency (fig. 2), it appears that the

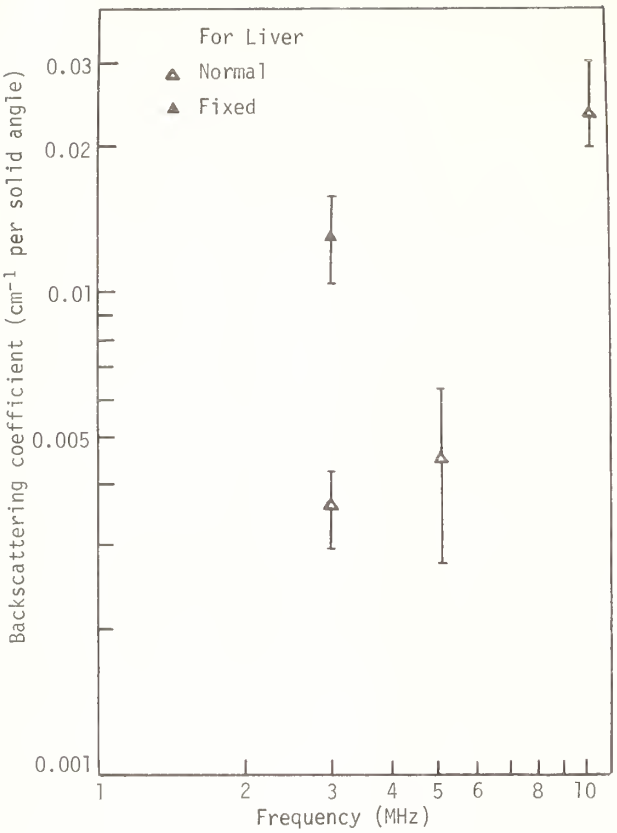

Fig. 3. Backscattering coefficient for liver tissue as a function of frequency.

structure responsible for producing the scattering must be smaller than the wavelength. For a spherical particle it is known that the circumference must be less than one wavelength, indicating that the diameter of such tissue elements in liver is less than 30 microns.

From these data, it is possible to estimate the contribution to attenuation caused by scattering alone. In cases where the angular dependence is known the total scattering loss, α_s, can be found from

$$\alpha_s = \int_{4\pi}^{\eta_d} (i,o)d\omega \quad , \qquad (4)$$

where ω = the solid angle
η_d = differential scattering coefficient
$\hat{i}$ = the incident direction of the wave
$\hat{o}$ = the direction of observation

As a first approximation, let us assume that the scattering from liver is isotropic, then,

$$\alpha_s = 4\pi\eta_{180^\circ}$$

At 10 MHz frequency the attenuation coefficient for liver due to scattering alone is then 0.3 neper/cm. This loss is about 28 percent of the total attenuation found in the literature [7][2].

This investigation has obtained experimental evidence that the scattering from within functionally homogenous tissue may be strong enough to influence the total attenuation. Since the scattering contribution is a strong function of frequency, we might expect that at a sufficiently high frequency the attenuation of some tissues or tumors might increase at a rate greater than the first power dependence found by previous investigators working at lower frequencies. If verified, such behavior could have great importance for tissue characterization, whether it be done using scattered waves or measurements of attenuation.

References

[1] Reid, J. M., The Scattering of Ultrasound by Tissues, in Ultrasonic Tissue Characterization, M. Linzer, ed., National Bureau of Standards Spec. Publ. 453, pp. 29-47 (U.S. Government Printing Office, Washington, D.C., 1976).

[2] Sigelmann, R. A. and Reid, J. M., The analysis and measurement of ultrasound backscattering from an ensemble of scatterers excited by sine wave bursts, J. Acoust. Soc. Am. 35, 1351 (1973).

[3] Shung, K. K., Sigelmann, R. A., and Reid, J. M., The scattering of ultrasound by blood, IEEE Trans. on Biomedical Engineering, BME-23, 6, 460 (1976).

[4] Shung, K. K., Sigelmann, R. A., and Reid, J. M., The Scattering of Ultrasound by Red Blood Cells, in Ultrasonic Tissue Characterization, M. Linzer, ed., National Bureau of Standards Spec. Publ. 453, pp. 207-212 (U.S. Government Printing Office, Washington, D.C., 1976).

[5] Nicholas, D., The Application of Acoustic Scattering Parameters to the Characterization of Human Soft Tissues, in 1976, IEEE Ultrasonic Symposium Proc., pp. 64-69 (1976), No. 76CH 1120-5SU.

[6] Wells, P. N. T., Physical Principles of Ultrasonic Diagnosis (Academic Press, London and New York, 1969).

[7] Pauly, H. and Schwan, H. P., Mechanism of absorption of ultrasound in liver, J. Acoust. Soc. Am. 50, 192 (1971).

[8] Yuhas, D. E., Mimbs, J. W., Miller, J. G., Weiss, A. N., and Sobel, B. E., Changes in Ultrasonic Attenuation Indicative of Regional Myocardial Infarction, in Ultrasonics in Medicine, D. White, ed., Vol. 3 (Plenum Press, New York, 1976).

[9] Gramiak, R., Hunter, L. P., Lee, P. P. K., Lerner, P. H., Schenk, E., and Waag, K. C., Diffraction Characterization of Tissue Using Ultrasound, in 1976, IEEE Ultrasonics Symposium Proc., pp. 60-63 (1976), No. 76CH 1120-5SU.

[2] It has to be noted this figure obtained was based on a very rough assumption. In reality, the scattering from liver is not isotropic as indicated by the experimental results of Gramiak et al. [9]. Our measurements do average η over many directions, so we feel the conclusions are warranted.

Reprinted from *Ultrasonic Tissue Characterization II*, M. Linzer, ed., National Bureau of Standards, Spec. Publ. 525 (U.S. Government Printing Office, Washington, D.C., 1979).

DEPENDENCE OF ULTRASOUND BACKSCATTER FROM HUMAN LIVER TISSUE ON FREQUENCY AND PROTEIN/LIPID COMPOSITION

M. Freese

Radionics Ltd.
Montreal, Quebec, Canada

E. A. Lyons

Winnipeg Health Sciences Center
Winnipeg, Manitoba, Canada

The dependence of ultrasonic volume backscatter on frequency, lipid and protein content in normal and fatty human (post-mortem) liver tissue was investigated with a view towards the possible development of a noninvasive quantitative diagnostic test for fatty liver. Mean values of the backscatter coefficient, its range and frequency dependence were determined for normal liver in the 1 to 5 MHz range and for fatty liver at frequencies of 2.25 and 3.56 MHz. The results indicate that frequencies below about 2 MHz should be avoided for quantitative measurements of the backscatter in liver. Although the measurements revealed considerable variation in the backscatter levels of normal liver, the backscatter levels in moderately and severely fatty liver were significantly greater than the normal range. Simple linear correlation of the backscatter magnitude with the lipid content for 21 samples (10 normal, 8 fatty, 1 cirrhotic, 2 other abnormal) yielded a value of 0.94, significant at the 1 percent level.

Key words: Backscatter frequency dependence; cirrhosis; composition-dependent scattering; fatty liver; stochastic scattering; tissue characterization; ultrasound attenuation; ultrasound diagnosis; ultrasonic tissue scattering.

1. Introduction

Quantitative data on the dependence of ultrasound scattering on the physical structure and composition of tissue is needed to understand the underlying scattering processes, to aid the development of optimum diagnostic scattering methods and to serve as a reference in clinical applications. From the standpoint of these objectives, specifically, the possible development of a noninvasive diagnostic test for fatty liver [1][1], this paper describes the results of a series of quantitative measurements of ultrasonic volume backscatter in the 1 to 5 MHz range for normal and fatty post-mortem human liver as a function of frequency and protein-lipid content. The results suggest that a noninvasive quantitative test for fatty liver based on the magnitude of the backscatter is feasible if the in vivo measurement problems can be overcome.

2. Methodology

The pulse echo technique and the calibration procedure employed for the backscatter measurements have been described in detail elsewhere [2]. Essentially, the received backscatter from the tissue is range gated, passed through either a square-law or linear envelope detector and integrated; time varied gain is employed to compensate for sample attenuation. The measurements are referenced to stainless steel ball bearing targets of known cross-section.

A. Backscatter Parameters

The parameters used to describe the backscattering are the average backscatter coefficient $\langle\Omega\rangle$ and the average "envelope" backscatter coefficient $\langle\Gamma\rangle$, the brackets denoting ensemble averaging. For monochromatic (CW) frequencies, $\langle\Omega\rangle$ is identical to the average backscatter cross-section per unit volume, while for pulses, the difference between $\langle\Omega\rangle$ and the corresponding CW value is dependent on the absorption coefficient--path length--pulse bandwidth product and the scatterer frequency responses [2,3]. (The maximum estimated error due to the finite pulse bandwidth was approximately 0.1 dB in these measurements.) The envelope backscatter coefficient $\langle\Gamma\rangle$ is proportional to the average magnitude of the backscatter signal but is normalized to be consistent with the statistical relation $\langle\Omega\rangle = \langle\Gamma^2\rangle$.

[1]Figures in brackets indicate literature references at the end of this paper.

B. Signal Processing

Stochastic signal process theoretical results were employed to determine appropriate thresholds for refining of the raw data. Scattering by the larger blood vessels in the liver poses a problem because its contribution tends to be largely extraneous to the scattering process of interest. To reduce this interference, the raw data were refined by rejecting individual measurements with values of the coefficient of variation $\gamma \geq 0.81$, the coefficient of variation being defined as $\gamma = (\langle \Gamma^2 \rangle - \langle \Gamma \rangle^2)^{\frac{1}{2}} / \langle \Gamma \rangle$. The presence of isolated large specular echoes tends to increase the expectation value of γ (= 0.52 for a random process described by a Rayleigh distribution [4]). Ordinarily, the probability of γ exceeding 0.81 is about 7 percent. The A-scan time averaging employed reduced this probability to 5 percent at 1.1 MHz decreasing to 0.5 percent at 3.56 MHz.

To further improve the averaging and avoid the long delay path required for far-field measurements, the measurements were performed in the near fields of the transducers. The measured values were then converted to equivalent far-field values using the experimental results obtained by Freese [5]; the same transducers were used in the present measurements[2]. The near- to far-field conversion factors ranged from + 1.4 and + 1.1 dB at 1.1 MHz to - 1.1 dB at 4.88 MHz.

Time varied gain based on running mean absorption estimates were employed during the measurements with appropriate corrections based on the measured absorptions being applied at the completion of the experiments [6].

C. Measurements

The ultrasonic measurements on the liver samples were conducted with two exceptions within one to three days post-mortem. The samples were removed from the cadaver prior to any postmortem infusion procedures, and were cut from the anterior portion of the liver extending below the ribs, with the backplane of the sample sliced roughly parallel to the external liver surface. With the samples immersed in physiological saline held at 20 °C and the ultrasonic beam incident perpendicularly on the external liver surface, the backscatter was measured at two depths extending from 0.6 cm to 1.8 cm, and from 1.2 cm to 2.4 cm below the surface, respectively. Four separate measurements were made at each depth. The total insonified volume averaged about 10 cm^3 per sample (5 cm^3 per sample in the case of the 1.1 MHz measurements).

The absorptions were measured by means of a substitution technique. To the extent possible, all of the measurements were carried out under double-blind conditions.

D. Diagnostics and Biochemical Assays

Subsequent to the ultrasonic measurements, the samples (nineteen male, six female) were classified on the basis of clinical and autopsy data as either normal or abnormal. The abnormal group (eight male, four female) was then further categorized according to the lipid content--fatty (seven male, two female) or nonfatty. One normal and one fatty sample were rejected because of technical problems. The lipid, protein, and moisture contents of the samples were determined by B. Guy Hunt Laboratories (Winnipeg) using standard chemical analytical methods.

[2]The conversion factors (as a function of transducer distance) were determined from scattering measurements on model media containing random scatterers whose dimensions were comparable to tissue cells. Corresponding data obtained for whitefish muscle tissue were generally found to be within 0.5 dB of the model media values.

3. Results and Discussion

The average lipid content and physical data for the normal samples (table 1) are in good agreement with generally accepted values [7]; however, the protein content appears to be about 20 percent low. Detailed data on the abnormal samples is given in table 2.

Table 1. Composition and physical characteristics of normal liver samples.[a]

Factor	Mean	Standard deviation
Total lipid (%)[b]	4.8	1.1
Protein (% nitrogen x 6.25)	14.6	2.1
Moisture (%)	77.5	2.8
Liver weight (g)	1680	280
Age of deceased (y)	55	26
Weight of deceased (kg)	67	9

[a]Eleven male, one female, ranging in age from 15 to 93 years.

[b]Estimated accurace of liqid analytical determination ± (0.1 (% lipid) + 1%).

A. Normal and Fatty Liver Tissue Ultrasound Attenuation

The attenuation was measured in eight of the normal samples, and yielded a mean value of 0.64 dB/cm/MHz for the frequency normalized absorption coefficient, α/f. Possibly reflecting a lower protein content, this value is about 10 percent lower than the mean value quoted by Wells [8] for the 3 to 5 MHz range. The average attenuation for the normal samples at the 2.25, 3.56 and 4.88 MHz frequencies were 1.5, 2.3 and 3.2 dB/cm, respectively.

In the case of the fatty livers, the absorptions were determined for all but the 7.7 percent lipid sample (table 2). Excluding the 45.6 percent lipid sample, which exhibited anomalously high absorption, the average value of α/f for the fatty livers was 0.86 dB/cm/MHz or about one third greater than for the normal livers.

The two extremely fatty samples (table 2) were rather interesting for, although similar in appearance, they had markedly different absorptions. The 35.5 percent lipid sample measured 2.74 dB/cm at 3.56 MHz (six replicates) which is only slightly more than in normal liver, while the 45.6 percent lipid sample measured a remarkable 14 dB/cm (three replicates). The reason for this anomalously high absorption is not certain but it seems to point to the possible presence of gas bubbles in the latter sample, despite the fact that the liver sample was obtained one day post-mortem. Also, un-

Table 2. Composition and clinical data for the abnormal samples.

Group	Total lipid %	Protein %	Moisture %	Clinical information sex	age y	height m	weight kg	history	Autopsy results Liver weight, g	Liver appearance
Fatty	7.7	16.0	72.2	M	--	1.63	52	alcoholism	1630	--
	9.0	14.0	71.1	M	26	1.70	69	-- (blood alcohol 150 mg)	1690	--
	11.4	11.4[a]	74.3	M	--	1.65	64	--	1940	--
	14.7	13.2	64.1	M	48	1.80	59	alcoholism	1900	pale yellowish alcoholic hepatitis, mod. fat infilt.
	14.9	13.2	71.2	M	54	--	--	--	--	--
	19.1	11.9	70.1	F	69	1.63	66	-- (blood alcohol 16 mg)	1600	pale
	35.5	10.6	52.5	M	60	1.82	84	--	3450	yellow
	45.6	8.4	44.4	M	50	1.68	117	alcoholism	5600	yellow, fatty
Nonfatty	3.6	18.1	79.8	M	64	1.74	82	cirrhosis	1730	yellow, firm nodular adv. cirrhosis
	3.7	15.2	79.6	F	91	1.56	40	diabetes (diet)	1220	--
	3.8	16.8	78	F	76	1.51	37	--	730	small

[a]Estimate.

like the 35.5 percent lipid sample, the 45.6 percent sample was buoyant in the 0.1 N saline solution.

B. Normal Liver Backscatter Coefficient, Range and Frequency Dependence

The backscatter coefficients and corresponding envelope backscatter coefficients for the normal samples are plotted as a function of frequency in figure 1(a) and (b). (A number of single data points are also included.) The ranges of the backscatter coefficients at each of the measurement frequencies are extremely broad. For example, at 2.25 mHz, $\langle\Omega\rangle$ varies from 0.17 to 2.9 mm^2/cm^3--a range of over 12 dB. With the exception of a single low value at 4.88 MHz, which may have been the result of a faulty measurement, the largest range is exhibited by the 1.1 MHz values. It is tempting to attribute this primarily to first-order diffraction effects [9,10] and to the greater statistical fluctuation at this frequency, but a more careful analysis of the measurements does not seem to support this view. While large fluctuations in the individual measurement values were observed in many of the samples, when the measurements were repeated on the same sample using slightly different aspect angles and insonified sites, the mean values seldom differed by more than 1 or 2 dB. Furthermore, if we take into account the dimensions of the blood vessels in terms of wavelength, the decrease of the highest $\langle\Omega\rangle$ values between 1.09 and 2.25 MHz is consistent with oblique incidence scattering by cylinders of corresponding radii in the transition region from Rayleigh to geometrical scattering (i.e., the vessels will tend to scatter specularly with increasing frequency). Since the larger blood vessels tend to radiate towards the liver surface, the oblique aspect angles would be more probable in our measurements resulting in an effective decrease in the backscatter at the higher frequencies. In contrast to the vessel orientations, the orientations of the liver lobule "fascia" appear essentially random over the extent of the insonified volumes. This would lead one to expect the ensemble averaged backscatter to be independent of aspect angle. In attempting to answer the question concerning the relative contributions of the liver lobules, blood vessels and other liver structures to the overall scattering process [11], our results would seem to indicate that scattering by the larger vessel inhomogeneities, if present in the insonified volume, will tend to dominate the backscatter below about 1.5 MHz.

The average frequency dependence of $\langle\Omega\rangle$ over the 2.25 to 3.56 MHz range is given by $f^{0.8}$(fig. 1(a)), decreasing to about f^0 in the 1.09 to 2.25 MHz interval, and increasing to $f^{1.5}$ between 3.56 and 4.88 MHz (if we exclude the 4.88 MHz value for the borderline sample). While there are too few values to provide more than a rough estimate of the frequency dependence in the latter two intervals, these values are in good agreement with those obtained by Nicholas [12] using spectral analysis. The relatively low frequency dependence observed illustrates the effect that the presence of even a relatively small number of "geometricl region" scatterers can have on the composite frequency dependence. For this reason the frequency dependence of diffuse volume backscatter may not be as useful a parameter for some tissue diagnostic applications as the magnitude, the angular dependence or the absorption.

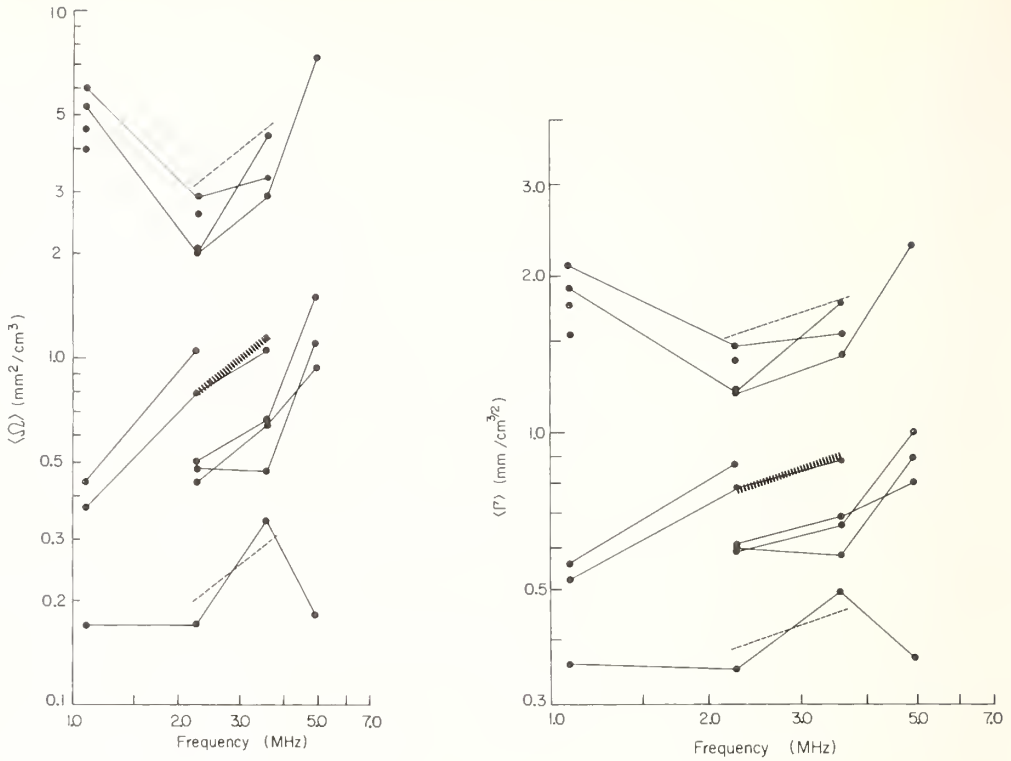

Fig. 1. (a) Backscatter coefficients as a function of frequency for samples of normal liver tissue. The logarithmic mean values of $\langle\Omega\rangle$ for the 2.25 and 3.56 MHz data are indicated by connecting heavy barred lines. The dashed lines correspond to ± 6 dB about the logarithmic means and bound essentially all of the measured values in this frequency range. The sample with the lowest backscatter coefficients suggests a borderline sample. Its moisture content of 81 percent was second highest of the normal samples.
(b) Corresponding envelope backscatter coefficients.

Similar comments apply to the envelope backscatter coefficient shown in figure 1(b) although the frequency dependence is only half as great (or less if the scattering process is inhomogeneous). The principal advantages of using $\langle\Gamma\rangle$ are that it simplifies the electronics requirements and is less sensitive to isolated large extraneous echoes thereby reducing the consequent error. For these reasons, we will consider mostly $\langle\Gamma\rangle$ instead of $\langle\Omega\rangle$ in the following paragraphs. However, to obtain an estimate of $\langle\Omega\rangle$ one need only compute $(1 + \gamma^2)\langle\Gamma\rangle^2$ using the average measured value of 0.6 for γ instead of the theoretical value of 0.52.

C. Backscatter Dependence on Lipid and Protein Content

Values of $\langle\Gamma\rangle$ were compared with the lipid and protein contents of both the normal and abnormal samples. Figure 2 shows the 2.25 MHz values of $\langle\Gamma\rangle$ as a function of the protein content (P) for normal samples. The value of the simple linear correlation coefficient $r_{\Gamma P} = 0.776$ and is significant at the 1 percent level (t-test assuming $r_{\Gamma P} = 0$; ten samples). Comparable results were obtained at the higher frequencies. This implies that in normal liver inherent differences in the protein content may result in $\langle\Gamma\rangle$ varying as much as 9 dB. (Conversely, taking the protein into account and assuming the scattering processes add in quadrature, the 12 dB range of the 2.25 MHz values in figure 1(a) and (b) can, in principle, be reduced by 4.5 dB.)

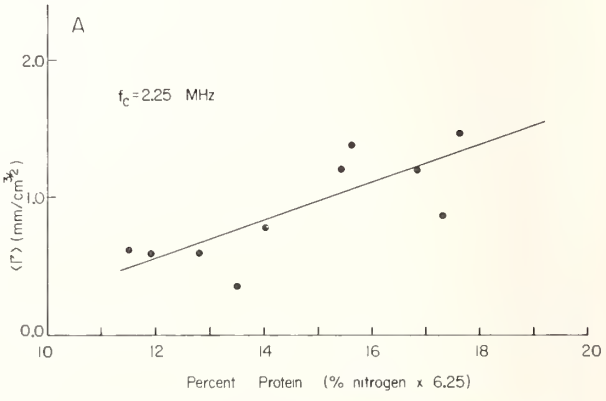

Fig. 2 Dependence of $\langle\Gamma\rangle$ on protein content in normal liver; the correlation coefficient $r_{\Gamma P} = 0.776$.

No significant correlation was observed at 1.1 MHz. This fact coupled with the previous observations would seem to indicate that frequencies below about 2 MHz should be avoided for quantitative measurements of volume backscatter from liver tissue.

In contrast to the correlation of the backscatter with protein content, the correlation of $\langle\Gamma\rangle$ with the lipid content of the normal samples was not significant. The presence of glycogen and other minor hepatic constituents (moisture tends to correlate inversely with lipid and protein) has been neglected but their contribution is not likely to be significant in normal liver.

The effect of the lipid becomes apparent in the fatty liver samples, which ranged from 7.7 to 45.6 percent lipid. The backscatter and lipid content (L) are highly correlated ($r_{\Gamma L}$ = 0.980 and 0.978 at 2.25 and 3.56 MHz, respectively) and suggest a roughly linear relationship between the two as shown in figure 3 for the 2.25 MHz values.

However, in view of the limited number of measurements and the possibility that the 45.6 percent lipid sample may have contained gas bubbles, the latter is probably at least partly due to coincidence since a linear dependence for a lipid content aoproaching 50 percent would seem unlikely.

The histological appearance of mildly and severely fatty livers are shown in figure 4(a) and (b). It can be seen from these pictures that the structural changes that occur in hepatic tissue with increasing lipid content span the spectrum from nearly normal to grossly abnormal. If we combine the two

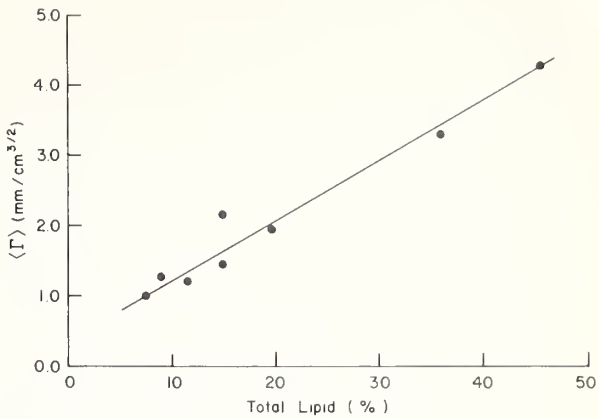

Fig. 3 Dependence of $\langle\Gamma\rangle$ on lipid content in fatty liver; the correlation coefficient $r_{\Gamma L}$ = 0.980; f_c = 2.25 MHz.

groups of samples and take the protein content into account, the multiple linear regression equation for $\langle\Gamma\rangle$ at 2.25 MHz becomes $\langle\Gamma\rangle = -1.4 + 0.10L + 0.12P$ with $r_{\Gamma,LP}$ = 0.966. This indicates that the effective scattering contributions by the protein and lipid (either directly or indirectly) are roughly comparable on a percentage weight basis, with the protein contributing about 40 percent more to $\langle\Omega\rangle$ at this frequency than the lipid for equal per-

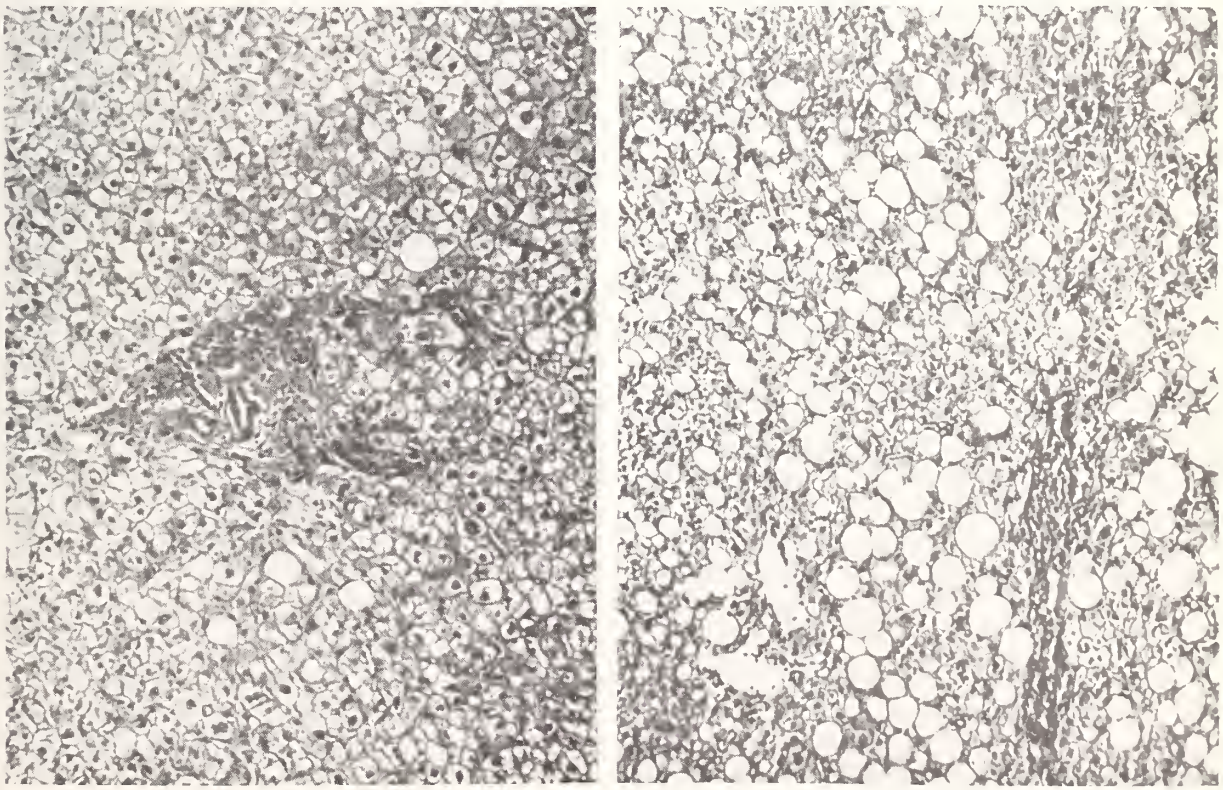

Fig. 4. (a) Mildly fatty liver in an alcoholic. Many of the hepatocytes contain large lipid globules (clear areas in the stained cytoplasm). Magnification 25X.
(b) Severe fatty liver in an alcoholic. The nuclei of the cells are displaced by large lipid globules; little cytoplasm remains. Magnification 25X.

centages of the two constituents. The corresponding result at 3.56 MHz was $\langle\Gamma\rangle = -1.9 + 0.10L + 0.17P$ with $r_{\Gamma,LP} = 0.939$. In this case, data was available for only eight normal and six fatty samples. Additional measurements will be needed to establish if the difference in the relative contributions implied by these two regressions (and therefore the frequency dependence of the normal and fatty samples) is significant.

For predictive purposes we require the percent lipid as a function of $\langle\Gamma\rangle$ and the percent protein. Moreover, the remaining abnormal nonfatty samples, listed in table 2, should also be included in the regression. The resultant linear regression equation obtained at 2.25 MHz was $L = 15.1 + 9.2\langle\Gamma\rangle - 1.2P$, with $r_{L,\Gamma P} = 0.971$. This regression with 18 degrees of freedom (21 samples) and F-test value = 157 is significant at the 1 percent level. Comparing it to the previous 2.25 MHz regression, the effect of the additional samples is seen to be minimal.

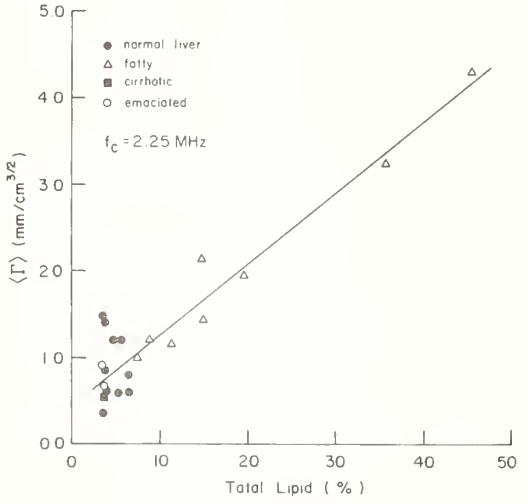

Fig. 5 Dependence of $\langle\Gamma\rangle$ on the lipid content for the combined group of normal and abnormal samples; the correlation coefficient $r_{\Gamma L} = 0.943$.

In potential diagnostic applications the percent protein would most likely not be available. The resultant simple two variable linear regression equation obtained, $L = -442 + 11.0\langle\Gamma\rangle$, is graphed in figure 5. The correlation coefficient $r_{L\Gamma} = 0.943$ is essentially the same as when the nonfatty abnormal samples were excluded. Figure 5 shows that the backscatter coefficients are substantially greater for the moderately and extremely fatty livers. The corresponding regression at 3.56 MHz, based on 17 samples, resulted in $L = -6.2 + 11.3\langle\Gamma\rangle$ and $r_{L\Gamma} = 0.914$. In view of the limited number of samples and the large weighting by the two extremely fatty livers, these regressions can only be considered preliminary. Nevertheless, they seem to suggest that a simple quantitative diagnostic test based on the magnitude of the backscatter is feasible in principle.

4. Summary

Experimental values of the volume backscatter coefficients and estimates of their distribution and frequency dependence were obtained for normal liver. These were discussed and compared from the point of view of the underlying scattering processes, the liver composition and potential diagnostic requirements. The results indicate that in the case of liver, frequencies under 2 MHz should be avoided for quantitative diagnostic backscatter measurements.

Significant correlations of the backscatter with protein content were observed in normal liver and with both protein and lipid content in abnormal fatty liver. In the case of the latter, regressions significant at the 1 percent level were obtained.

Acknowledgment

This work was supported in part by the Department of Environment, Freshwater Institute, Winnipeg, Canada.

References

[1] Wells, P. N. T., McCarthy, C. F., Ross, F. M. G., and Read, A. E. A., Comparison of A-scan and compound B-scan ultrasonography in the diagnosis of liver disease, Br. J. Radiol. 42, 818-823 (1969).

[2] Freese, M. and Hamid, M. A. K., Lipid Content Determination in Whole Fish Using Ultrasonic Pulse Backscatter, 1974 Ultrasonics Symp. Proc., IEEE Cat. #74 CHO-896 15U, 69-76 (1974).

[3] Freese, M., Quantitative diagnostic measurements of ultrasound tissue scattering (in preparation).

[4] Ol'shevskii, V. V., Characteristics of Sea Reverberation (Consultants Bureau, New York, 1967).

[5] Freese, M., Comparison of Near- and Far-Field Measurements of Diffuse Ultrasonic Tissue Volume Backscatter, 1975 Ultrasonics Symp. Proc., IEEE Cat. #75 CHO-994 45U, 33-36 (1975).

[6] Freese, M. and Lyons, E. A., Ultrasonic backscatter from human liver tissue; its dependence on frequency and protein/lipid composition, J. Clin. Ultrasound (in press).

[7] Schiff, L., ed., Diseases of the Liver, 3rd ed. (Lippencott Co., New York, 1969).

[8] Wells, P. N. T., Physical Principles of Ultrasonic Diagnosis (Academic Press, London and New York, 1969).

[9] Nicholas, D. and Hill, C. R., Acoustic Bragg diffraction from human tissues, Nature 257, 305 (1975).

[10] Lele, P. P., Mansfield, A. B., Murphy, A. I., Namery, J., and Senapati, N., Tissue Characterization by Ultrasonic Frequency-Dependent Attenuation and Scattering, in Ultrasonic Tissue Characterization, M. Linzer, ed., National Bureau of Standards, Spec. Publ. 453, pp. 167-196 (U.S. Government Printing Office, Washington, D.C., 1976).

[11] Gramiak, R., Hunter, L. P., Lee, P. P. K., Lerner, R. M., Schenk, E., and Waag, R. C., Diffraction Characterization of Tissue Using Ultrasound, 1976 Ultrasonics Symp. Proc., IEEE Cat. #76 CH1120-5SU, 60-63 (1976).

[12] Nicholas, D., The Application of Acoustic Scattering Parameters to the Characterization of Human Soft Tissues, 1976 Ultrasonics Symp. Proc., IEEE Cat. #76 CH1120-5SU, 64-69 (1976).

Reprinted from *Ultrasonic Tissue Characterization II*, M. Linzer, ed., National Bureau of Standards, Spec. Publ. 525 (U.S. Government Printing Office, Washington, D.C., 1979).

ULTRASOUND BACKSCATTERING FROM BLOOD: HEMATOCRIT AND ERYTHROCYTE AGGREGATION DEPENDENCE

M. Hanss and M. Boynard

Laboratoire de Biophysique
UER Expérimentale de Médecine et de Biologie
74, rue Marcel Cachin - 93000 Bobigny

and

UER Biomédicale des Saints-Peres
45, rue des Saints-Peres - 75006 Paris

The ultrasound back-scattering of blood has been shown to be increased when the erythrocytes sedimentation rate is high. Moreover, in this case, temporal fluctuations of the back-scattered intensity have been also demonstrated. To explain these results, a simplified theory of ultrasound back-scattering by blood is presented. The model of the blood structure used is: the erythrocytes are associated to form spherical transient aggregates having the same cell number, m. The acoustic wave is scattered by these clusters called "scattering units." The scattered intensity is calculated for one scattering unit taking a spherical elastic model, then for a blood unit volume, when the hemotocrit H is very low. It is found that the back-scattered intensity is proportional to H and to m. When H is not negligible, a simplified statistical theory is proposed. The main result is that the back-scattered intensity is still proportional to m but that it passes through a maximum value when H get near 0.3. An explicit relation between the mean relative value of the intensity fluctuation, H and m is given. Therefore, the aggregation state of blood can in principle be determined through ultrasound scattering studies. Further theoretical developments are in progress so as to take into account the distribution of the number of erythrocytes in each kinetic units and the variation of this number with H.

Key words: Blood erythrocytes aggregation; blood hemotocrit; ultrasound back-scattering from blood.

When an ultrasound echographic probe is placed on top of a vertical cylindrical tube filled with blood, it has been found that the echo pattern of the sedimenting blood varies according to its sedimentation rate [1][1]. For high sedimentation rate samples, the mean back-scattered intensity is larger; furthermore the echo amplitude at a given depth in the erythrocyte column presents characteristic temporal fluctuations. We wish to present a simple theoretical approach in order to explain these phenomena. Though the scattering of ultrasound by blood is increasingly used in clinical medicine, the fundamental data on this property are very scarce, and mainly due to Reid and co-workers [2-5]. Fluctuations (temporal and spatial) in the echo amplitude have also been reported by Atkinson and Berry [6]. However, none of these studies can give a straightforward explanation of our experimental results.

[1]Figures in brackets indicate literature references at the end of this paper.

Blood Model

The red blood cell (RBC) concentration is usually defined by the hematocrit H, that is, the time average of the RBC volume fraction in a given blood volume. For a normal blood sample, H is rather large ($H \simeq 0.45$) so that the RBC interact each with the other. We will describe these interactions by assuming that m RBC are mechanically correlated during a period τ_c larger than the ultrasound pulse, giving rise to a transient aggregate which we assume to be spherical, with radius A; this dimension could be thought of as a correlation length. We will also suppose that each aggregate has the same number m of RBC. The ultrasound wave is scattered by these aggregates which therefore will be called the scattering units (S.U.).

If ν is the number of S.U. per unit volume and v_h the RBC volume, the usual hematocrit number H is given by:

$$H = m v_h \nu \qquad (1)$$

However we are interested in the volume fraction of the S.U. and not the static hematocrit H. We will introduce a "dynamic" hematocrit number H' as follows:

$$H' = \nu v'_{su}$$

where v'_{su} is the excluded volume of the S.U. (fig. 1) which takes into account the S.U. volume, v_{su}, and the trapped plasma between the S.U.:

$$v'_{su} = v_{su} \cdot p_{su}$$

where p_{su} is a dimensionless number greater than or equal to 1. The volume of one S.U. must also take into account the trapped plasma inside the S.U.:

$$v_{su} = m v_h p_h$$

where p_h is another dimensionless quantity greater than or equal to 1. If the RBC were perfectly packed without free volume for the plasma, p_{su} and p_h would be equal to 1. For an imperfect packing, they are greater than 1. The dynamic hematocrit H' is greater than H because in the course of their motions the RBC's and S.U.'s carry with them a fraction of the plasma. Its value is:

$$H' = m\nu v_h p_h p_h \qquad (2)$$

Using this model, the S.U. radius is given by:

$$A = \left(\frac{3}{4\pi} m v_h p_h\right)^{1/3} \qquad (3)$$

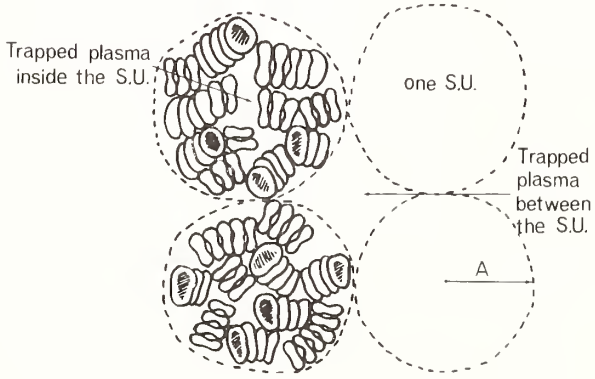

Fig. 1. Blood model used, showing the transient spherical aggregation (scattering unit S.U.).

Ultrasound Back-Scattering by One S.U.

Let i_o be the incident wave intensity per unit area of a spherical scattering center, with radius A smaller than the wavelength. The scattered intensity per unit solid angle in the direction θ is i_D. The detecting solid angle being $d\Omega$, the differential scattering cross-section is:

$$d\sigma = \frac{i_D}{i_o} d\Omega$$

In back-scattering experiments, the angles θ and ϕ values are 180° and 90° respectively (fig. 2). The detecting solid angle depends on the probe surface S and the distance x between the probe and the S.U. One can take into account these parameters by introducing a geometrical factor $g(x) = S/x^2$.

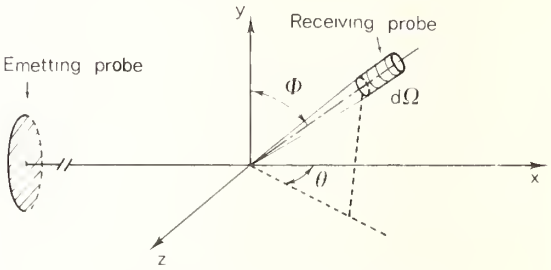

Fig. 2. Scattering coordinates.

We can only measure intensities emitted and received by the probe, I_o and I_D. They differ from i_o and i_D because of the attenuation of the incident and scattered beams by the medium between the probe and the S.U. They also differ because the ultrasonic field varies with distance. We can lump all these factors in a general function of the distance x, G(x) so that one can write

$$I_D = \frac{d\sigma}{d\Omega} I_o G(x) \qquad (4)$$

The factor G(x) is not essential in our final results. It could be determined by a substitution method as described, for instance, by Sigelmann and Reid [3].

The differential scattering cross-section is known for some simple models [7]. Using the results for an elastic sphere, the back-scattered intensity is finally:

$$I_D = I_o G(x) \frac{\omega^4 A^6}{9 c_o^4} \left[\left(1 - \frac{c_o^2 \rho_o}{c^2 \rho}\right) + 3\left(\frac{\rho - \rho_o}{2\rho + \rho_o}\right)\right]^2 \qquad (5)$$

$$I_D = I_o G(x) \frac{\omega^4}{c_o^4} A^6 K$$

where c and c_o are the sound wave velocities in the S.U. and the plasma respectively, and ρ and ρ_o the corresponding densities. We assume that the S.U. coefficients, c and ρ, are identical to the RBC coefficients, c_h and ρ_h.

Back-Scattering by Whole Blood

The scattering of dense particle medium is a complex theoretical problem which has already been treated by Twersky [8-10] and applied by Shung, Sigelmann and Reid [4,5]. The following simplified approach can be used. Let $s' = q_{su} s$ be the functional diametral area of one S.U.,

where s is the diametral area of one S.U. and q_{su} is a dimensionless number, usually greater than 1, and which is characteristic of the S.U. packing. For a spherical S.U. one has: $s' = q_{su}\pi A^2$.

We are interested by the intensity $I_{\Delta x}$ scattered by a cylindrical volume element having the same axis as the ultrasonic wave with height Δx and base area S at a distance x from the probe (fig. 3).

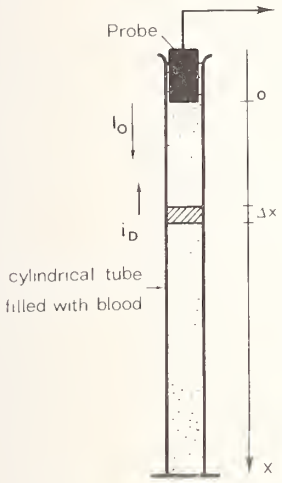

Fig. 3. Simplified diagram of the sedimentation tube with the echographic probe.

We will consider in this volume an elementary slab (S, 4A) defined by the two sections with distances (x + 2A) and (x - 2A). The maximum number of S.U. which can exist in this slab is 2N = 2S/s'; we will call N the number of sites, each composed of two cells, which can be occupied by 0 or 1 or 2 S.U.

Figure 4 shows a simplified slab with 7 sites occupied in such a way that the ensemble average of the hematocrit is 4/7. Eq. (5) only applies to the sites "f"; for the other ones, eq. (5) indicates that the scattered intensity is zero.

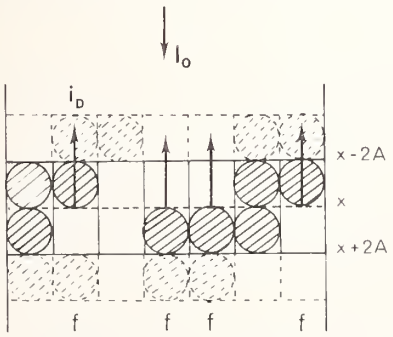

Fig. 4. Statistical model. The slab (x - 2A, x + 2A) has 7 sites with an occupation probability of 4/7. Only the "f" emplacements have a favorable configuration for backscattering.

By a simple calculation in order to find the probability that a given site is in a favorable configuration (as regards back-scattering), it can easily be shown that the number of sites, N_f, which have a favorable configuration in an elementary slab 2A is:

$$N_f = NH'(1 - H') \qquad (6)$$

Assuming that I_o and I_D do not depend on x in the volume Δx (this point is justified by the low values of the attenuation and reflexion coefficients in blood), each slab 2A back-scatters with the intensity:

$$I_{2A} = NH'(1 - H')I_D \qquad (7)$$

As there are $\Delta x/2A$ elementary slabs in the interrogated volume (Δx, S), one has:

$$\frac{I_{\Delta x}}{\Delta x} = \frac{NH'}{2A}(1 - H')I_D$$

This expression can be further transformed by replacing N by S/s' and H' by $p_{su}p_hH$, using eq. (5) for I_D. As we have used an impenetrable spheres model with a cubic packing, the factor p_{su}/q_{su} is equal to 3/2. Finally one obtains:

$$\frac{I_{\Delta x}}{\Delta x} = \left(\frac{3}{4\pi}\right)^2 \frac{SI_o\omega^4}{c_o^4} G(x)Kmv_h p_h^2 H(1 - p_h p_{su} H) \qquad (8)$$

In this derivation we have added the individual intensities and not the wave amplitudes, thus ignoring the interference problem. This is justified in a first approach because the distribution of the scatterers in the interrogated volume is random.

Back-Scattering Fluctuations

Examination of eq. (8) shows that the only fluctuating quantities are H or H' (the packing factors do not fluctuate as we have assumed a spherical model for the aggregates. It is also assumed in the model that m is constant. For an elementary variation dH' of H' in a slab (2A), the scattered intensity will vary according to eq. (7):

$$dI_{2A} = I_D N(1 - 2H')dH'$$

The relative mean quadratic fluctuation F_{2A} is defined as follows:

$$F_{2A} = \frac{\langle (dI_{2A})^2 \rangle^{1/2}}{\langle I_{2A} \rangle}$$

and can be written:

$$F_{2A} = \frac{\langle (1 - 2H')^2 \rangle^{1/2}}{\langle H'(1 - H') \rangle} \langle (dH')^2 \rangle^{1/2}$$

$$F_{2A} = a\langle (dH')^2 \rangle^{1/2}$$

If one transforms dH' into dν, one obtains:

$$F_{2A} = a v_h p_h p_{su}^m \langle d\nu^2 \rangle^{1/2}$$

As in the initial model the site occupancy probabilities are independent, the S.U. distribution obeys Boltzmann statistics and $\langle (d\nu)^2 \rangle^{1/2}$ is given by [11]:

$$\langle (d\nu)^2 \rangle^{1/2} = \frac{\langle \nu \rangle^{1/2}}{(2AS)^{1/2}}$$

Therefore F_{2A} can be written:

$$F_{2A} = a(2ASv_h p_h p_{su}^m)^{1/2} \langle H' \rangle^{1/2}$$

The corresponding fluctuation coefficient for the blood column Δx is $F_{\Delta x}$:

$$F_{\Delta x} = \frac{\langle (dI_{\Delta x})^2 \rangle^{1/2}}{\langle I_{\Delta x} \rangle}$$

Assuming independent fluctuations for the $\Delta x/2A$ elementary slabs in Δx, the total fluctuation is given by:

$$F_{\Delta x} = \left(\frac{2A}{\Delta x}\right)^{1/2} F_{2A}$$

or:

$$F_{\Delta x} = \left(\frac{36}{\pi^2} v_h p_h p_{su}^3 S^3\right)^{1/6} \quad (9)$$

$$\frac{\langle H' \rangle^{1/2} \langle (1 - 2H')^2 \rangle^{1/2}}{\langle H'(1 - H') \rangle} \frac{m^{1/6}}{\Delta x^{1/2}}$$

This relation shows that the standard deviation of the fluctuations, given by $F_{\Delta x} \langle I_{\Delta x} \rangle$, is proportional to $m^{7/6} . \Delta x^{1/2}$.

Discussion

In our model, the interactions between RBC lead to monodisperse spherical aggregates. Indeed, microscopic observations show a reversible aggregation in normal and pathological blood [12]. Our picture may be oversimplified, as these transient aggregates are polydispersed in dimension and shape. We feel however that introducing polydispersity function would not change our treatment fundamentally.

Equation (8) is very similar to a previous result obtained by Shung et al. [4] using Twersky's theory [8-10]. However, as this theory predicts that the back-scattering goes through a maximum for H = 0.50, Shung et al. introduced an empirical fitting constant as their experimental results showed a maximum for hematocrit values between 0.25 and 0.30

We have plotted on figure 5 their experimental results and a theoretical curve obtained by using eq. (8) and the following values:

ω = $2 \pi 5.2\ 10^6\ s^{-1}$
ρ_o = 1.078; ρ = 1.223
c_o = 1550 m s^{-1}; c = 1610 m s^{-1}
G(x) = 1 (negligible attenuation)
m = 2 (slight aggregation)
p_{su} = 1
v_h = 10^{-10} cm^3
p_h = 2

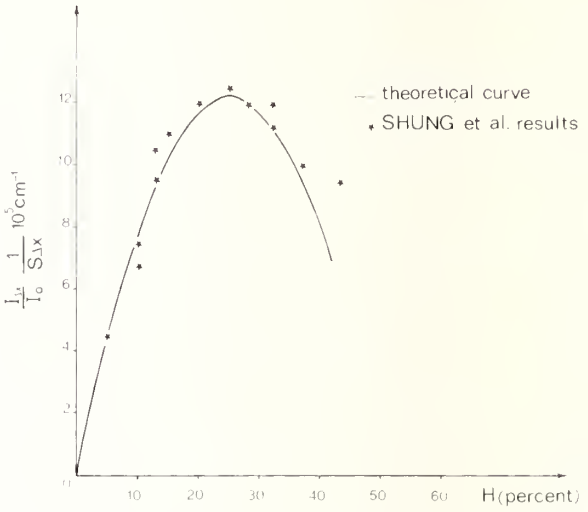

Fig. 5. Back scattering of whole blood as a function of hematocrit: correlation between the experimental results of Shung et al. [4,5] and theoretical values calculated according to eq. (8).

Shung et al.'s scattering coefficient α is identical to:

$$\frac{I_{\Delta x}}{I_o} \frac{I}{S\Delta x} .$$

The quantitative agreement between the two results seems satisfactory, our treatment can directly explain the experimental results of Shung et al. [4,5].

The aggregation dependence of the scattered intensity by whole blood is also shown in eq. (8) and has recently been demonstrated by Shung and Reid [13].

In order to derive the fluctuation coefficient, it has been assumed that the probability of finding a S.U. in a given elementary volume is proportional to the S.U. number concentration and independent of the occupation state of the neighbouring elementary volumes. This would be the case for pure Brownian motion. However, as has already been pointed out by Atkinson and Berry [6], the thermal diffusion of RBC's is much too slow (10^8 s) to travel one wavelength.

Two other mechanisms could be postulated. The first one is convection streams which break apart, associate, rotate and translate the aggregates, so that the occupancy of a given elementary volume fluctuates to and fro in the occupation probability. The second explanation can be found in the dissociation-association kinetic of the S.U. In that case it is m which would fluctuate. Further ex-

periments are needed in order to assess the respective importance of the mechanisms.

Summary

The ultrasound back-scattering of blood has been shown to be increased when the erythrocyte sedimentation rate is high (fig. 1). Moreover, in this case, temporal fluctuations of the back-scattered intensity have also been demonstrated. In order to explain these results, a simplified theory of ultrasound back-scattering by blood is presented.

The following model of the blood structure is used: the erythrocytes are associated to form spherical transient aggregates having the same cell number, m. The acoustic wave is scattered by these clusters called "scattering units".

The scattered intensity is calculated for one kinetic unit taking a spherical elastic model, then for a blood unit volume, when the hematocrit H is very low. It is found that the back-scattered intensity is proportional to H and to m.

When H is not negligible, a simplified statistical theory is proposed. The main result is that the back-scattered intensity is still proportional to m but that it passes through a maximum value when H gets near 0.3.

An explicit relation between the mean relative value of the intensity fluctuation, H and m is given.

Therefore, the aggregation state of blood can in principle be determined through ultrasound scattering studies. Further theoretical developments are in progress so as to take into account the distribution of the number of erythrocytes in each kinetic unit and the variation of this number with H.

References

[1] Hanss, M., Boynard, M., and Perrin, J. Erythrocyte sedimentation by an echographic method, Biomedicine 25 (3), 81 (1976).

[2] Reid, J. M., Sigelmann, R. A., Nasser, M. G., and Baker, D. W., The Scattering of Ultrasound by Human Blood. Proceedings of the 8th International Conference in Medicine and Biological Engineering (1969).

[3] Sigelmann, R. A. and Reid, J. M. Analysis and measurement of ultra-sound backscattering from an ensemble of scatterers excited by sine wave bursts, J. Acoust. Soc. Am. 53, 1351-1355 (1973).

[4] Shung, K. K., Sigelmann, R. A., and Reid, J. M., The scattering of ultrasound by red blood cells, Applied Radiology 77 (Jan., Feb. 1976).

[5] Shung, K. P., Sigelmann, R. A., and Reid, J. M., The scattering of ultrasound by blood, I.E.E.E. trans. on biomed. Engin. BME 23 (6), 460 (1976).

[6] Atkinson, P. and Berry, M. V., Random noise in ultrasonic echoes diffracted by blood, J. Phys. Math. Nucl. 7 (11), 1293-1302 (1974).

[7] Morse, P. M. and Ingard, K. U., Theoretical Acoustics (McGraw Hill, New York, 1968).

[8] Twersky, V., On scattering of waves by random distribution: I. Free space scatterer formalism, J. Math. Phys. 3, 700 (1962).

[9] Twersky, V., On scattering of waves by random distribution: II. Two space scatterer formalism, J. Math. Phys. 3, 724 (1962).

[10] Twersky, V., Acoustic bulk parameters of random volume distributions of small scatterers, J. Acoust. Soc. Am. 36, 1314 (1964).

[11] Landau-Lifchitz, Statistical Physics (Mir ed., Moscow, 1967).

[12] Schmid-Schonbein, M., Gallasch, G., Gosen, J. V., Volger, E., and Klose, M. J., Red cell aggregation in blood flow, Klin. Wschr. 54, 149 (1976).

[13] Shung, K. K. and Reid, J. M., Ultrasonic detection of erythrocyte aggregation, 29th ACEMB Sheraton-Boston, Boston, Massachusetts, 6-10 November 1976.

CHAPTER 6

TUMOR DOPPLER SIGNATURES

Reprinted from *Ultrasonic Tissue Characterization II*, M. Linzer, ed., National Bureau of Standards, Spec. Publ. 525 (U.S. Government Printing Office, Washington, D.C., 1979).

TUMOUR DETECTION BY ULTRASONIC DOPPLER BLOOD-FLOW SIGNALS

P. N. T. Wells, M. Halliwell, R. A. Mountford,
R. Skidmore, A. J. Webb and J. P. Woodcock

Bristol General Hospital and Bristol Royal Infirmary
Bristol, United Kingdom

An in situ cancer is avascular and harmless. Vascularisation is necessary before a tumour is potentially capable of rapid growth. Distinctive continuous-wave ultrasonic Doppler signals have been obtained transcutaneously from malignant breast tumours. Similar signals have been detected from abdominal malignancy, by means of a pulsed Doppler. These signals may form the basis of a practicable method of screening for breast cancer, and of improving the accuracy of cancer diagnosis.

Key words: Blood flow; breast cancer; diagnosis; Doppler; screening; ultrasonics.

1. Tumour Blood Flow

A single aberrant cell is almost certainly the origin of every solid malignant tumour. This cell divides to form a colony of malignant cells, called an in situ cancer. An in situ cancer is avascular and harmless, and cannot grow beyond the volume limited by diffusion of nutrients and wastes. The event which converts an in situ cancer into a "tumour" is apparently the release by the malignant cells of a diffusable chemical substance, called the "tumour angiogenesis factor" [1][1]. Once the tumour is vascularised it is potentially capable of rapid growth. The blood flow in normal tissue like that of the breast is in the range 10 to 30 ml min^{-1} kg^{-1} [2]. The blood flow in lymphomas is about 380 ml min^{-1} kg^{-1}, in differentiated tumours, 140 ml min^{-1} kg^{-1}, and in anaplastic tumours, 110 ml min^{-1} kg^{-1} [3].

The possibility that changes in blood flow might be used to detect malignant tumours is discussed in this paper, and some preliminary results are presented. Most of the experimental work was done with breast lesions, because of their accessibility and the potential importance of the method in screening for breast cancer.

The blood vessels which serve the breast are illustrated in figure 1. The mass of a typical female breast is about 0.3 kg. Assuming that the three main arteries each serve one third of the breast, the normal flow rate in each artery would be around 1 to 4 ml min^{-1}. A malignant tumour with diameter of 20 mm would require a flow rate of about 0.5 to 1.5 ml min^{-1}. Therefore, in an individual, there might be a significant difference between the flow in an artery supplying a tumour and part of the breast, and the flow in the corresponding artery serving the other normal breast. There is at present no non-invasive method of measuring blood flow volume which would enable this

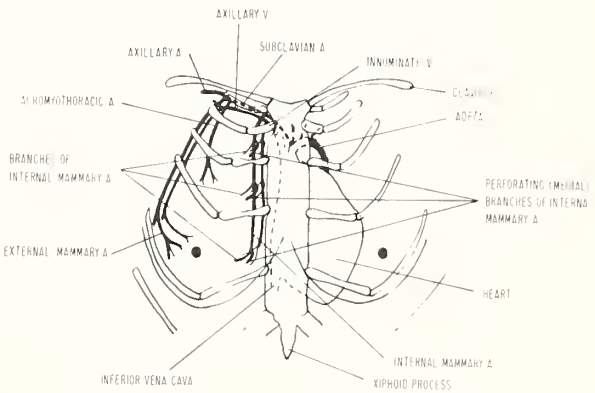

Fig. 1. Principal blood vessels serving the right breast.

to be tested. It may be that a change might occur in the pulsatility index of the flow [4], but this would be difficult to establish since every pair of arteries (serving the two breasts) would need to be studied.

In biomedicine, liquid flow through small ducts has previously been recognised in backscattered ultrasonic Doppler frequency-shifted signals [5] in two situations. The first of these is in the placenta [6] and the second, in the fetal lung during breathing [7]. Recently it has been reported that characteristic blood flow signals are associated with neovascular flow in malignant tumours [8] and additional data are presented in this paper.

2. Breast Investigations

Breasts were examined as illustrated in figure 2. A regular continuous-wave ultrasonic Doppler blood-flow detector [5] was used. The hand-held probe had a diameter of about 10 mm, and contained two separate 8 MHz transducers, one for transmitting and one for receiving. The transducers were

[1]Figures in brackets indicate literature references at the end of this paper.

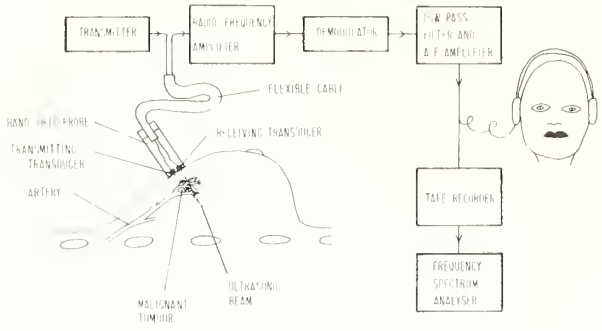

Fig. 2. Method of obtaining ultrasonic Ooppler blood-flow signals from the breast.

aligned so that the volume sensitive to motion extended axially beyond the end of the probe. For each patient, the Ooppler signals obtained from over the lesion were compared with those from the corresponding site on the opposite breast. Both breasts of each normal individual were thoroughly explored to search for Ooppler signals which were asymmetrical and characteristic of neither normal arterial nor venous flow.

The results are summarised in table 1. Sonograms of the signals recorded from a normal mammary artery, a malignant breast tumour, and tissues at the corresponding site in a normal breast, are shown in figure 3.

Table 1. Ultrasonic Doppler signals obtained from breast in various clinical conditions.

Confirmed diagnosis[a]	Number of patients with neovascularisation signals		
	None	Weak	Strong
Normal	2	0	0
Mastitis	1	0	0
Mammary duct papillomatosis	1	0	0
Mammary duct ectasia	2	0	0
Benign mammary dysplasia	2	1	0
Cyst	1	2	0
Fibroadenoma	0	1	0
Lymphoma	0	0	1
Carcinoma	0	0	2

[a]Number of patients = 16.

3. Investigations of Other Tumours

Signals apparently associated with malignant neovascularisation have been detected in the abdomen. Two-dimensional scanning was used to locate a pancreatic tumour. The ultrasonic beam of the scanner probe was directed through the tumour. The probe was then connected to a 2 MHz pulsed Ooppler [5]. Blood flow signals were detected when the Doppler was range-gated into the tumour.

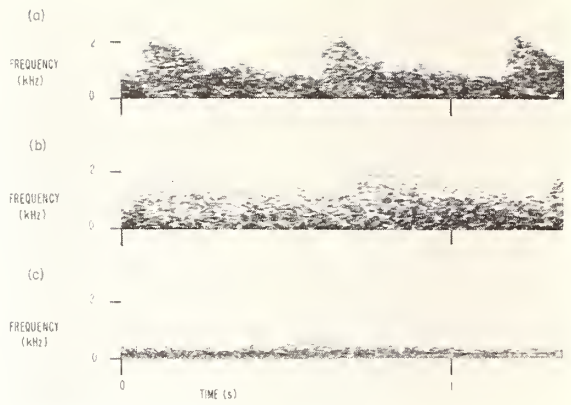

Fig. 3. Sonograms of ultrasonic Ooppler blood-flow signals obtained from the breast. (a) Normal individual: branch of internal mammary artery; (b) malignant tumour; and (c) flow at site corresponding to (b) in other breast of the same patient.

4. Oiscussion

A. Breast Cancer

Breast cancer is the most common malignancy in Western women. In the United Kingdom, breast cancer affects at least 80 in 100,000 females; it kills 1 in 50 women, 1 in 75 women between the ages of 35 and 60 years, and 1 in 3,500 females of all ages every year. Breast cancer is the main cause of all deaths among women between the ages of 40 and 44. Extrapolating from 1973 U.S. data [9], the present economic cost of breast cancer in the United Kingdom is in the order of $40 million per year (and $200 million per year in the United States).

Earlier diagnosis and treatment of breast cancer might improve the survival time of the patient [10]. If the cancer is removed whilst it is still in situ, the patient is cured. The next step in the natural progress of the disease is when the growing cancer begins to invade the surrounding tissue. For a time, the cancer cells remain localised. If diagnosed and treated at this stage, the 5-year survival rate is around 85 percent. If untreated, the cancer metastases, with regional involvement of the lymph nodes which drain the breast, and the 5-year survival rate falls to about 53 percent. If left untreated, metastases occur in more distant parts of the body. This advanced cancer is virtually incurable, although the time taken for the patient to die is variable.

The treatment of patients with early breast cancer is more successful than that of those in whom the disease is advanced. Breast cancer is usually discovered when the patient herself feels a lump. Even in a "suitable" breast, the smallest lump which can be detected by manual palpation is not much less than 10 mm in diameter [11]. The risk of the presence of distant metastases from a tumour with a doubling time of 1.5 months increases from 22 percent when its diameter is 1 mm, to 43 percent, when it is 10 mm. Once a lump has been discovered in a breast, present diagnostic procedures are already adequate, although there may be

disagreement about the best course of treatment if the lump is a malignant tumour. The possibility exists, however, that diagnosis of pre-symptomatic lesions by an effective screening procedure might lead to a reduction in breast cancer mortality as a result of earlier treatment.

Mammography, either conventional or xeroradiographic, seems to be the best contemporary method of detecting early breast cancer [12]. Unfortunately, however, mammography as a screening procedure confers no benefit on women who are well and under the age of 50 [13]. In these women only 19 percent of cancers would not have been detected without mammography, and so the benefit (which has to be set against the risk of radiation-induced cancer as a consequence of mamography [14]) is small. Even if technical developments were to result in a reduction in x-ray exposure to an acceptable level, the logistics of interpreting the vast number of mammograms which would be obtained in a screening programme pose apparently insoluble problems of manpower, boredom and expense.

Thermography has been used to study breast tumours [15] but initial enthusiasm for the method has declined. Thus, in a series [16] of 2523 volunteers, 1 patient out of 4 who developed cancer within 18 months of the examination was detected by thermography; 344 had abnormal or suspicious scans, but no abnormality. These and other results are so poor that the method (at least when used alone) seems to have no role in screening for breast cancer.

Conventional two-dimensional pulse-echo ultrasonography is capable of producing images of the breast of quite high resolution [17-20]. Unfortunately, the normal breast is a complex irregular structure, the recognition without prior knowledge of small tumours is very unreliable, and there seems to be no way of automating the analysis of the vast number of scans which would result from even only a modest screening programme. The results reported in the present paper indicate that characteristic Doppler signals may be a cancer-specific ultrasonic tissue signature. They might form the basis of a practicable breast cancer screening method.

B. Other Tumours

Cancer-specific Doppler signals could have an important place in the interpretation of the inadequate data which sometimes results from conventional diagnostic tests such as radiography, echography, scintigraphy, and computerised tomography. These opportunities, which are quite distinct from screening, include, for example, the differentiation of small solid and cystic renal lesions, and the differentiation of ophthalmic tumours and organised haematomas.

References

[1] Folkman, J. and Cotran, R., Relation of Vascular Proliferation to Tumor Growth, in International Review of Experimental Pathology, C. W. Richter and N. A. Epstein, eds., Vol. 16, pp. 207-48 (Academic Press, New York, 1976).

[2] Woodcock, J. P., Theory and Practice of Blood Flow Measurement (Butterworths, London, 1975).

[3] Mäntyla, M., Kuikka, J., and Rekonen, A., Regional blood flow in human tumours with special reference to the effect of radiotherapy, Br. J. Radiol. 49, 335-8 (1976).

[4] Woodcock, J. P., The Significance of Changes in the Velocity/Time Waveform in Occlusive Arterial Disease of the Leg in Ultrasonics in Medicine, L. Filipczyński, ed., pp. 243-50 (Polish Scientific Publishers, Warsaw, 1970).

[5] Wells, P. N. T., Biomedical Ultrasonics (Academic Press, London, 1977).

[6] Hunt, K. M., Placental localization using the Doptone foetal pulse detector, J. Obstet. Gynaec. Br. Commonw. 76, 144-7 (1969).

[7] Boyce, E. S., Dawes, G. S., Gough, J. D., and Poore, E. D., Doppler ultrasound method for detecting human fetal breathing in utero, Br. Med. J. 2, 17-8 (1976).

[8] Wells, P. N. T., Halliwell, M., Skidmore, R., Webb, A. J., and Woodcock, J. P., Tumour detection by ultrasonic Doppler blood-flow signals, Ultrasonics (to be published).

[9] Scitovsky, A. A. and McCall, N., Economic Impact of Breast Cancer in Frontiers of Radiation Therapy and Oncology, J. M. Vaeth, ed., Vol. 11, pp. 90-101 (Karger, Basel, 1976).

[10] Brinkley, D. and Haybittle, J. L., A 15-year follow-up study of patients treated for carcinoma of the breast, Br. J. Radiol. 41 215-21 (1968).

[11] Slack, N. H., Blumenson, L. E., and Bross, I. D. J., Therapeutic implications from a mathematical model characterizing the course of breast cancer, Cancer, N.Y. 24, 960-71 (1969).

[12] Feig, S. A., Shaker, G. S., Schwartz, G. F., Patchefsky, A., Libshitz, H. I., Edeiken, J., Nerlinger, R., Curley, R. F., and Wallace, J. D., Thermography, mammography and clinical examination in breast cancer screening, Radiology 122, 123-7 (1977).

[13] Strax, P., Venet, L., and Shapiro, S., Value of mammography in reduction of mortality from breast cancer in mass screening, Am. J. Roentg. 117, 686-9 (1973).

[14] _____, Radiation-Induced Breast Cancer, Br. Med. J. 1, 191-2 (1977).

[15] Williams, K. L., Lloyd Williams, F. J., and Handley, R. S., Infra-red thermometers in the diagnosis of breast disease, Lancet 2, 1378-81 (1961).

[16] Hitchcock, C. R., Hickok, D. F., Soucheray, J., Moulton, T., and Baker, R. C., Thermography in mass screening for occult breast disease, J. Am. Med. Ass. 204, 419-22 (1968).

[17] Wells, P. N. T. and Evans, K. T., An immersion scanner for two-dimensional ultrasonic examination of the human breast, Ultrasonics 6, 220-8 (1968).

[18] Jellins, J., Kossoff, G., Reeve, T. S., and Barraclough, B. H., Ultrasonic gray scale visualization of breast disease, Ultrasound Med. Biol. 1, 393-404 (1975).

[19] Baum, G., Ultrasound mammography, Radiology 122, 199-205 (1977).

[20] Kobayaski, T., Gray-scale echography for breast disease, Radiology 122, 207-14 (1977).

CHAPTER 7

PROPAGATION THROUGH BONE AND SKULL

Reprinted from *Ultrasonic Tissue Characterization II*, M. Linzer, ed., National Bureau of Standards, Spec. Publ. 525 (U.S. Government Printing Office, Washington, D.C., 1979).

A THEORY RELATING SONIC VELOCITY TO MINERAL CONTENT IN BONE

Sidney Lees

Forsyth Dental Center
Boston, Massachusetts 02115, U.S.A.

and

Carel L. Davidson

University of Amsterdam
Amsterdam, The Netherlands

Bony tissues consist primarily of mineral hydroxyapatite (HAP) crystallites embedded in a matrix of a much softer material, collagen. Currey and others suggested that bone is a two-phase composite, like mineral filled plastics, but the known laws of mixtures give at best a crude approximation of the observed elastic properties of bone. We have investigated the problem by measuring the ultrasonic velocity in mineral filled particulate composites as a function of the mineral concentration.

It was found that the ultrasonic velocity can be predicted for some mineral filled plastics by applying the Reuss formalism to the longitudinal elastic modulus, indicating that these are families of Reuss solids in some sense. Other mineral filled plastics do not seem to obey this rule, the ultrasonic velocity being greater than predicted. Bone appears to belong to this latter class of particulate composites.

The literature indicates that in certain situations the mineral filler affects the plastic matrix, giving the plastic constituent a higher modulus. A maximum longitudinal modulus is ultimately attained so that two Reuss formalism bounds can be obtained, the lower one calculated from the modulus of the unfilled plastic, the upper using the maximum modulus. The ultrasonic velocities of a system of fluorapatite (FAP) filled epoxy was found to lie between such bounds.

Currey and his successors assumed bone collagen has the same elastic properties as tendon collagen and that these are invariant with respect to contained HAP. The literature shows the contrary, that bone collagen, even when demineralized, is more highly cross linked than any other collagen. Moreover, the literature indicates that HAP crystallites are chemically bonded to the collagen molecules.

It is postulated that bone collagen is stiffened because HAP crystallites form on the intermolecular cross links, encasing them and making their effective lengths very short. It is shown that the sonic velocity for bone can be bounded by two Reuss formalism curves in the same manner as for FAP epoxy.

Key words: Bone; collagen; crosslinking modification; curvelinking; hydroxyapatite; sonic velocity.

1. Bony Tissues

Bony tissues are essentially a mineral, hydroxyapatite (HAP), embedded in an organic matrix, mostly collagen. HAP is an hexagonal crystallite which in bone and dentin is usually less than 100 nm in any dimension. The shape and size distribution of the crystallite in bone has been studied for many years with inconclusive results, except that they are small. Certain x-ray diffraction studies indicate the crystallites are needlelike, others that they are platelets. Electron micrographs show platelets, but the needle form is not thereby excluded. There is reason to believe both forms are present depending on the site of formation. There is also a strong contention that a significant fraction of the mineral is amorphous [1][1].

Collagen is a generic term for a class of protein that make up much of the body tissue. Bone collagen differs from other collagens in the body because it is so insoluble, indicating a high degree of intermolecular cross linking. The organic part of bone constitutes about 65 percent by volume of the tissue of which 95 percent is collagen. The mineral occupies 35 percent of the volume. Since collagen is such an important body constituent, its chemistry has been studied intensively for many years and is

[1]Figures in brackets indicate literature references at the end of this paper.

still a major field of biochemistry. Very recently the sonic and elastic properties of some types of collagen have begun to be studied because of the need to determine the presence of collagen in tissues and to identify its extent.

All collagens are highly structured materials in a multilevel hierarchal order. The molecular weight of the basic collagen molecule, defined as tropocollagen, is approximately 300,000 daltons, which is a very large molecule even in organic chemistry. The molecule is much like a piece of spaghetti having a wet diameter of 1.5 mm and a length of about 300 nm. It is difficult to draw to scale and all figures in this paper are purely schematic. As noted, bone collagen differs from other body tissue collagens by an extensive network of intermolecular cross links that render it insoluble in even the most potent of solvents. On the other hand, tendon collagen is reported to be mostly lacking in intermolecular bonds but having many hydrogen bonded intramolecular links, so that it can be dissolved and reconstituted readily. While other tissues like arteries and joints calcify, there is reason to think that the special structural characteristics of bone collagen cause it to calcify in a unique manner [2].

2. Two Phase Mineral-Filled Plastic Composites

It is the contention of this paper that the mechanical properties of bone can only be understood in the light of the chemical interrelationship between the mineral crystallites and bone collagen. Previously Currey [3], Welch [4] and Katz [5] have considered bone to be a mechanically mixed two phase mineral-filled polymer composite. Their concept yields a crude representation of the variation of elastic modulus with mineral content, but the detailed correlation is not good. Currey [6] even suggested that the crystallites are much longer than observed in order to attribute a fibrous mineral structure to bone to account for the observed elastic and strength properties.

We believe that the difficulties of our predecessors are due to several causes. The elastic modulus of collagen is not well known and there has been no distinction among the various types. Previous investigators used estimates for tendon fibers rather than bone collagen. Except for Mason's [7] sonic velocity measurement on kangaroo tail tendon fibers, the estimates of the elastic modulus were based on low strain rate tests. Secondly, there was no attempt to examine the chemical structure of collagen or the effect of the structure on the properties of bone. Collagen was considered a structureless homogeneous isotropic continuum and the short range order of body tissue collagen was ignored. Thirdly, there is little understanding even at this date how the HAP crystallites are laid down despite a long and intensive investigation over many years by many investigators. Fourth, the estimates of the elastic modulus of bone have been mostly those obtained by standard stress-strain testers. Bone is viscoelastic. Strain rates and the magnitude of the strain in conventional stress-strain testing causes hysteresis and often permanent distortion. In this paper we use only ultrasonic velocity measurements where the amplitude of displacement is of the order of an angstrom and the period is much less than any relaxation time of the medium.

3. Ultrasonic Measurements

It was the availability of measurements of the ultrasonic velocity of several hard tissues that led to the elastic theory presented here. Conventional procedures for measuring elastic properties are difficult because bone is a viscoelastic material and the data must include the rate of change of strain as well as the strain itself. Moreover, the sample is significantly affected by the test process, so that repeated tests are not consistent. Such a situation requires further interpretation to make sense of the data which is particularly difficult where the material (bone) varies widely due to its biological origin. Ultrasonic velocity measurements, on the other hand, can be repeatedly performed on the same sample with an uncertainty that depends mostly on the measurement technique and not on the sample. The contribution of biological variation can be treated separately apart from the measurement process.

There is a need to relate the elastic properties obtained at high strain rates with the more conventional techniques. Papadakis [8] has designed and tested an infrasonic resonator for testing plastics at about one hertz but which he says can be increased to 1000 hertz. It will be useful to find the sonic velocity measurements in bone at these low frequencies, but the limitations imposed by the inhomogeneities of biological material will require considerable modification of the Papadakis equipment.

4. Rule of Mixtures

It is reasonable to consider bone to be a two-phase mineral-filled composite as Currey did, but it is necessary to know the relationship by which the elastic properties of the composite can be calculated from those of the constituents. A number of rules of mixtures have been proposed for estimating the elastic moduli of the composite but each has limited applicability. Generally they work reasonably well when the properties of the two constituents are nearly alike but when there is a tenfold or greater ratio in density, the mixing rules do not seem to apply.

A number of mineral filled plastics were studied to determine a relationship between longitudinal sonic velocity and mineral content. The first series included tungsten-filled vinyl, crystabolite-filled polymethylmethacrylate, and crystabolite-filled epoxy. It was discovered that one of the known mixing rules did apply. Reuss postulated an expression of the form:

$$\frac{1}{K} = \frac{v_1}{K_1} + \frac{v_2}{K_2} \qquad (1)$$

where v_1 = volume fraction of the plastic constituent
v_2 = volume fraction of the mineral constituent = $1 - v_1$
K = elastic modulus of composite
K_1, K_2 = elastic moduli of constituents.

In this application the longitudinal modulus was used rather than the bulk and shear moduli which was Reuss's intention. Since

$$K = k + 4/3\ \mu \qquad (2)$$

where k = bulk modulus and μ = shear modulus, another value for the longitudinal modulus can be calculated from Reuss's expression applied first to the bulk modulus and then to the shear modulus, but it will be quite different from the value yielded by eq. (1) for the longitudinal modulus directly inserted. Consequently, the expression in eq. (1) is designated the Reuss formalism.

The sonic velocity is calculated as usual from the relation:

$$c = K/\rho \qquad (3)$$

where $\rho = v_1\rho_1 + \rho_2 v_2$ and ρ = density.

Figures 1, 2 and 3 taken from Lees and Davidson [9] show how well Reuss's formalism applies to these examples. It is not obvious why and we do not have an explanation. It is characteristic of these figures that the sonic velocity decreased, or at best does not increase much, as the mineral content increases on the left hand side of the curve, even though calculations show the longitudinal modulus of the composite is increasing. It was found that the density in this regime increases much more rapidly than the elastic modulus. When v_1 is large and K_2 is ten times K_1 the first term on the right side of eq. (1) dominates.

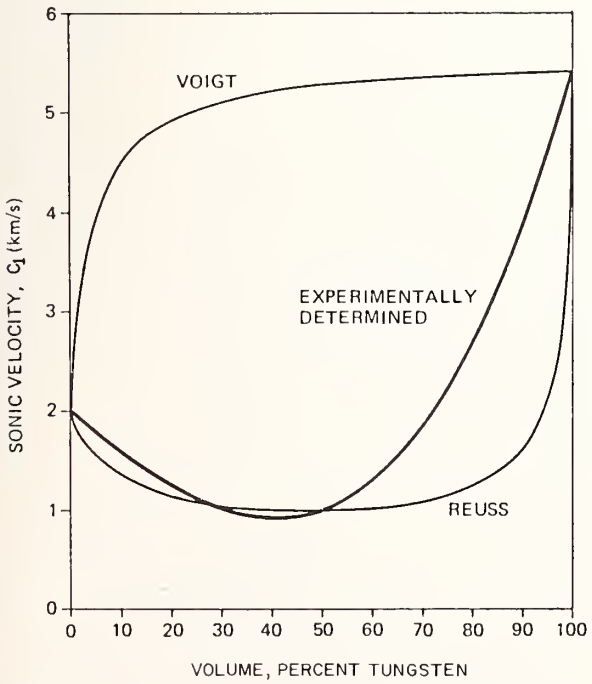

Fig. 1. Voigt-Ruess bounds for vinyl-tungsten composite system with experimentally determined curve (from Lees and Davidson [9]).

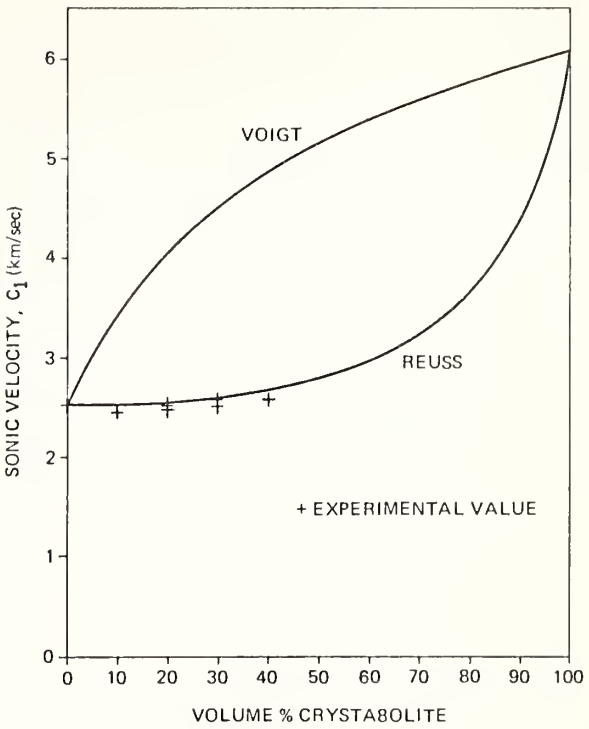

Fig. 2. Polymethylmethacrylate-crystabolite system (from Lees and Davidson [9]).

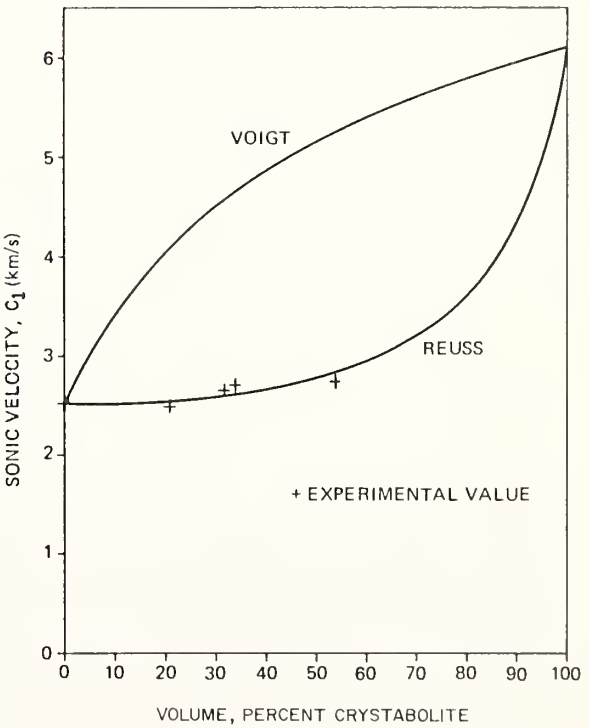

Fig. 3. Epoxy-crystabolite composite system (from Lees and Davidson [9]).

5. Modified Conditions for Rule of Mixtures

As the investigation proceeded a new kind of mineral-filled plastic, fluorapatite-filled epoxy, was found which apparently does not follow Reuss's formalism. Fluorapatite (FAP) closely resembles HAP but unlike HAP it can be obtained in large crystals. Powdered FAP is much more crystalline and well behaved crystallographically than HAP. Both FAP and HAP are surface active materials. In figure 4, the lower curve shows the variation of sonic velocity of the composite with mineral content when the longitudinal modulus of the unfilled plastic is taken as the value of K_1. It may be observed that all the measured values are above the lower curve and that there is some scatter among them.

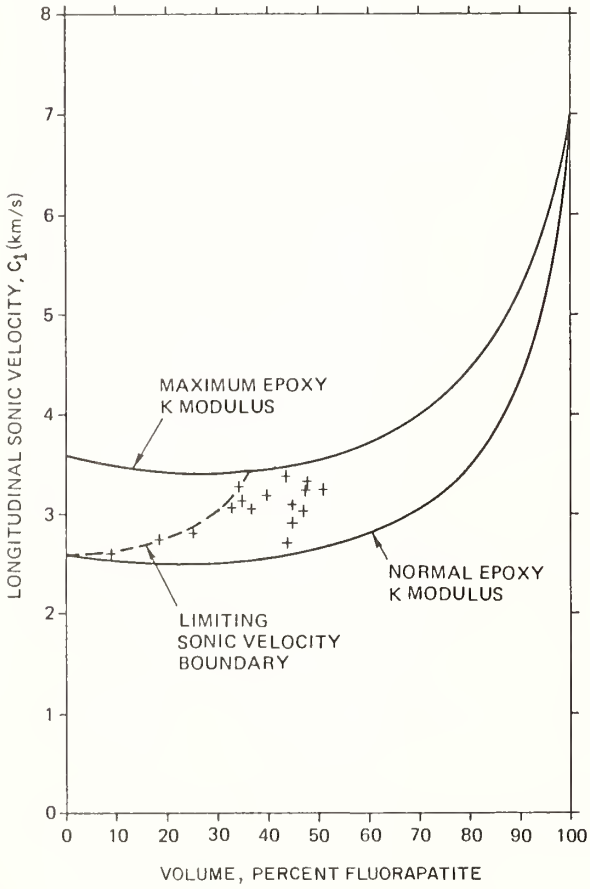

Fig. 4. Epoxy-fluorapatite composite system (from Lees and Davidson [9]).

The only difference between the situations of figures 3 and 4 is the replacement of one mineral filler by another. It must be concluded that sometimes the filler can influence the mechanical behavior of the plastic matrix. Now it is well known that polymers become stiffer as the cross linking density increases so it is inferred that FAP must cause the epoxy to increase the cross linking density. A similar situation was described by Kumins [10] who found that titanium dioxide causes an increase in cross linking density in epoxy, apparently by a factor of ten when about 3 volume percent titanium dioxide was added. Burhans et al. [11] showed a strong dependence of the elastic moduli on the maximum cross link length, so that either an increased cross linking density, or a decreased maximum cross link length, or both can increase the elastic moduli.

In order to see how this could be applied to the FAP-epoxy composite system, the maximum value for the compressive modulus reported by Burhans et al. was used as a basis for estimating the corresponding maximum value for the longitudinal modulus. A new Reuss curve was calculated using the higher modulus. When plotted on figure 4 it provided an upper bound, so that all the experimentally determined velocities fell between two Reuss curves. This is interpreted to mean that FAP can affect the cross linking density of the matrix. The scattered values of the ultrasonic velocity indicates a variability in the cross linking density from one experiment to the next. The samples were not always prepared the same way and the changed conditions could possibly modify the influence of the filler. For example, the samples were compressed, after mixing, in an attempt to achieve higher mineral content. This caused a gray exudate to ooze from the mold, the gray color being attributed to the very fine FAP particles. But these fine particles are most likely to have maximum influence on cross linking density because of their increased surface area.

6. Structure of Collagen

It is now possible to study ultrasonic wave propagation in bone with these two concepts in mind. First, that for a specific two phase mineral-filled polymer the longitudinal modulus of the composite can be found from the Reuss formalism and, second, the longitudinal modulus of the matrix can be affected by the presence of the filler.

While collagen is a polymer and bone may be considered a two-phase mineral-filled polymer, bone is not formed by starting with a mix of mineral and monomer. Collagen is laid down first and then it becomes mineralized when the HAP crystallites are deposited. When bone is demineralized the collagen matrix can be recovered as a rubbery solid having the form and shape of the original bone. However, when collagen is removed the mineral structure left behind is a weak solid that easily crumbles into a powder. It must be concluded that the collagen forms a continuous medium but the mineral does not. The mineral fills voids in the collagen.

Collagen has been studied for many years and much is now understood about its chemistry and ultrastructure but many unresolved problems remain such as the three-dimensional order, the chemical character of the intermolecular cross links and the location of the cross links (Ramachandran [13], Gallop and Paz [14], Veis [15]). Collagen exhibits many levels of order terminating in a fibrous structure. The successive levels of organization can be understood with the aid of figure 5a from Lees and Davidson [2]. The smallest element is the α-helix which spontaneously combines in triplets to form a

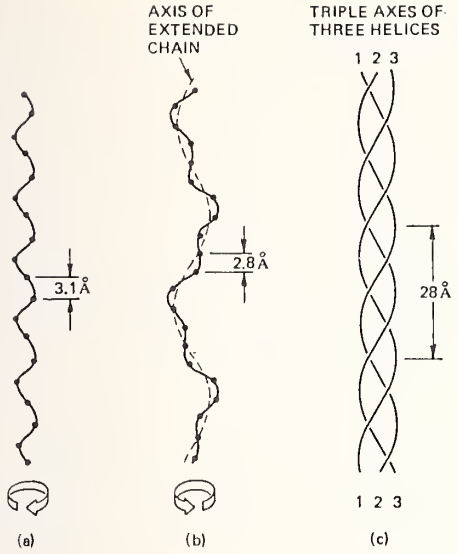

(a) The α-helix is left handed. Each spot is a residue and repeat length is 3.1 Å.
(b) The α-helix is twisted into a right handed helix which reduces repeat length between residues to 2.8 Å and the repeat of the supercoil is 10 times residue length, or 28 Å.
(c) Three α-helices are threaded to form a single tropocollagen (TC) unit. (Adapted from Glimcher and Krane, 1968 [12]).

Fig. 5a. The tropocollagen unit (from Lees and Davidson [2]).

superhelix molecule, the tropocollagen (TC) unit. In turn TC forms microfibril ropes, which in their turn form three-dimensional fibrils. Fibrils join to form fibers seen in tendon.

1. The basic element, the α-helix chain, has a molecular weight of about 100,000 and several types have been identified depending on the amino acid composition. The α_1 chain has 1052 amino residues of which 1011 are in triplet sets where the first term is glycine. The N terminus has 16 nonhelical residues beginning with an amino (NH_2) group while the C end has 25 nonhelical residues terminating in a COOH group. Gallop and Paz [14] as well as Hulmes et al. [16] show the residue map. It is the triplet with first term glycine that defines the characteristic pattern through all subsequent hierarchal levels.

2. Three α-helices are wound into a superhelix about 300 nm long, 1.5 nm diameter (wet) and a molecular weight of about 300,000 (Ramachandran). This is the basic molecule, the TC unit. In experiments, the α-helix spontaneously links up to form collageneous materials which have important industrial and medical uses but the product is not the ordered collagen of bone and tissue. It does demonstrate that the hydrogen bonded state between the α-helices is stable and the basis for interaction between TC units in the higher levels of structure.

3. TC units join in sets that exhibit "quarter staggering" in tissue as illustrated in figure 5b, based on a submolecular length of 67 nm or 234 residues, the D-length (Hodge [17]). A TC unit is 4.4 D units long and packs into a structure exhibiting a repeated 0.6 D unit gap between TC ends. It is a requirement of Hodge's scheme that no two quarter stagger gaps can be adjacent, which imposes a severe restriction on the three-dimensional structure that has not yet been resolved (Segrest and Cunningham [18]).

4. The nonhelical chains at each end of the TC unit and some of the adjacent glycine coded triplets are probably the links between molecule ends but may also serve to link helices within a single molecule, i.e., the inter and intramolecular links are similar. However, many of the intramolecular links must be hydrogen bonds, while much of the intermolecular links between parallel molecules must be chains covalently bonded as side chains to residues in the backbone of the molecule.

5. A number of three-dimensional structures have been proposed for the microfibrils, fibrils and fibers. We use Smith's five strand rope of TC units [19] as modified by Miller and Parry [20]. It is shown in figure 5c as Smith proposed the model with a 67 nm axial stagger, 72° aximuthal displacement between axes of nearest neighbors and 43 nm hole between colinear TC units. It incorporates a repeating pattern after 5 x 67 nm and a helix with a five-fold

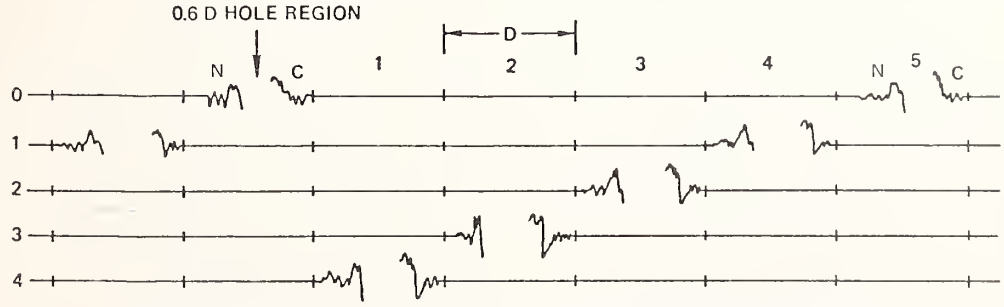

N END = 16 RESIDUE LONG NONHELICAL END + TRANSITION HELICAL REGION
C END = 25 RESIDUE LONG NONHELICAL END + TRANSITION HELICAL REGION
D = REPEAT LENGTH OF 234 RESIDUES
(Adapted from Gallop and Paz, 1975 [14])

Fig. 5b. "Quarter" staggering scheme (from Lees and Davidson [2]).

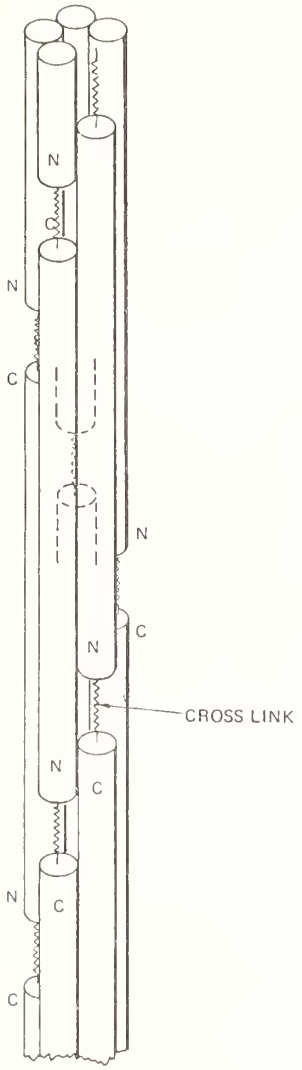

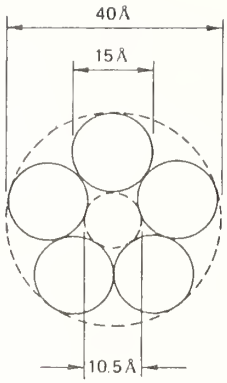

Fig. 5c. Smith's five stranded rope model for the microfibril (from Lees and Davidson [2]).

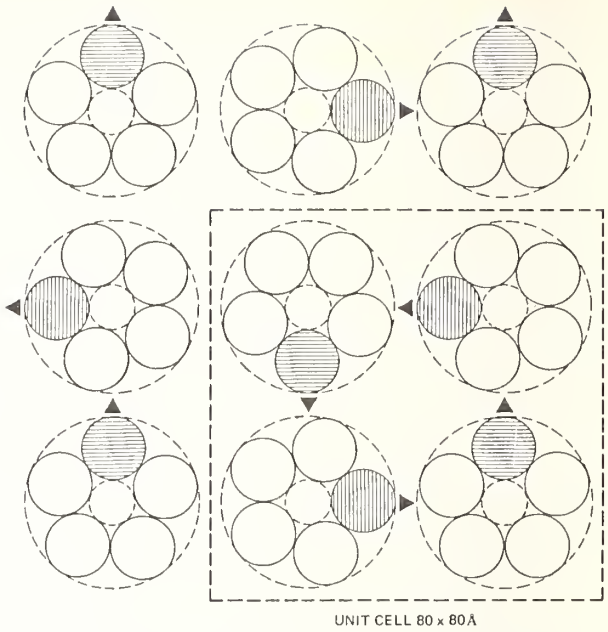

Fig. 5d. Miller and Parry model of the structure and packing of a fibril (from Lees and Davidson [2]).

screw axis (five subunits per screw turn characterized by the holes). The pentagonal unit is 4 nm in diameter when the wet TC unit is 1.5 nm diameter and the lumen is 1.1 nm.

6. Miller and Parry indicated that the five-strand rope must be twisted to produce a four-fold symmetrical supercoil, where the holes are now 90° apart, but there is still a pentagonal packing of the strands. The colinear TC units are inclined about 2.5° to the rope axis to accommodate the twist.

7. Miller and Parry have deduced a fibril packing structure based on a square or tetragonal cell of four microfibrils as in figure 5d. While Miller and Parry did not say so, the pattern of successive helical structures suggests that the microfibrils are coiled about each other while maintaining the four unit cell.

On the basis of this description, the ultra-structure of collagen can be schematically represented as in figure 6 where the microfibrils

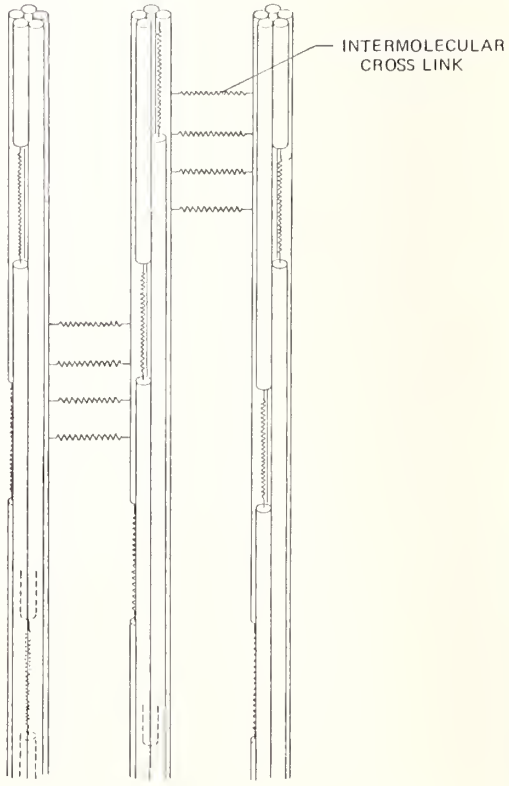

Fig. 6. Schematic representation of the ultra-structure of collagen showing intermolecular cross links.

are tied together with cross links of organic chains. The TC units are probably very stiff along their major axis. Enemoto and Krimm [21] calculated a value for the Young's modulus of a very similar molecule, polyglycine II, which they found to be 41 GPa, a value far in excess of any reported value for collagen or even for bone (26 GPa). Polyglycine II has a triple helix hydrogen bonded molecule and closely resembles collagen in its structure (Ramachandran [13]). The Young's modulus for TC is probably about the same value, which indicates that the collagen structure is more yielding than the TC units because the cross links are softer. Moreover, the long skinny TC units must bend quite easily unless they are severely restrained, which makes collagen tissue softer than its component molecules.

7. Mineralization of Bone

As the tissue mineralizes, HAP crystallites begin to fill the voids in the quarter stagger gaps, between microfibrils and between fibrils. The loci are inferred because they have been sited definitely only between fibrils (White et al. [1]). It is our contention that the crystallites form on the cross links until they grow to a size that fills the voids. It is implied that the crystallites start with the cross links as the nucleating seeds, which further implies that the stereochemistry of the organic chain must be favorable to the hexagonal habit of HAP. There is no accepted theory to explain how crystallites form and grow in tissue but some workers indicate that the process is mediated by a sequence of chemical stages rather than precipitating from a saturated solution. Whatever the process it entails a mineralization of the organic cross links until the crystallite encases the links. In figure 7 a schematic representation of the mineralized microfibrils shows the crystallites embedding the cross links and effectively shortening them. There is a cross link from one microfibril to a crystallite and its continuation on the other side connects the crystallite to a second microfibril. The connections are made to TC units in the strands of the microfibrils, hence to side chains of the residues on the α-helix.

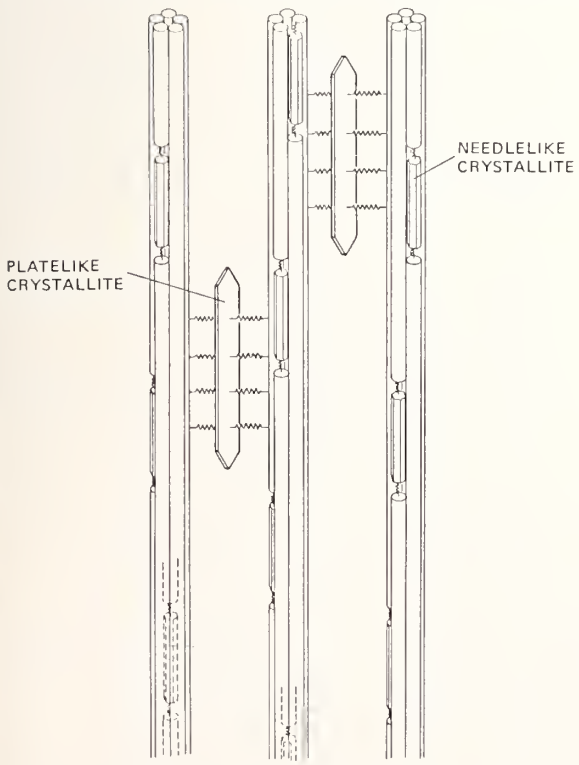

Fig. 7. Schematic representation of mineralized bone collagen showing crystallites embedding the cross links.

The effect of mineralization in bone is to shorten the cross links and thereby increase the longitudinal modulus of the matrix. There may well be additional cross links formed at the same time or prior to mineralization, but the cross linking is most likely mediated by a different chemical process than that for mineralization. The stiffening of the collagen matrix need not necessarily be associated with a greater cross linking density.

8. Ultrasonic Velocity of Mineralized Tissues

In order to apply the theory it has been necessary to estimate the equivalent isotropic sonic velocity for hard tissues. Since bone and dentin are anisotropic the estimates are not well based and the ultimate test and evaluation of this theory requires a better way to find the isotropic velocity equivalent. Alternatively, it may be possible to extend the theory to deal with the anisotropy as Yoon and Katz [22] are attempting to do but the theory is still incomplete.

Figure 8 shows representative values for the longitudinal sonic velocity of bone, dentin and enamel. There are four bone values, one for normal bovine bone by Lang [23], and three by Abendschein and Hyatt [24]. The latter include one normal human bone and two of lower density from ill people. It is interesting that the normal human and normal bovine bone values coincide despite the quite different methods for making the measurements.

Unlike the mineral filled composites we do not yet have good values for the elastic properties of the constituents of bone, particularly bone collagen. Several Reuss curves were calculated based on the different published estimates for the elastic modulus of collagen, usually the Young's modulus which was converted to the longitudinal modulus by assuming Poisson's ratio to be 0.35 (Katz [5]).

Three Reuss curves are shown in figure 8. The lowest bound is based on the longitudinal modulus suggested by Currey [3] and Katz [5], 3.75 GPa. The intermediate bound is calculated from Mason's value [7] measured ultrasonically on kangaroo tail tendon. The upper bound was obtained by using Reuss's formalism backward on the sonic velocity and density of normal bone.

It can be seen from figure 7 that the intermediate and upper curves bound the experimental data, much like the two bounding curves in figure 4. The lowest bound is based on a value of longitudinal modulus based on low strain rate test data, a technique that characteristically

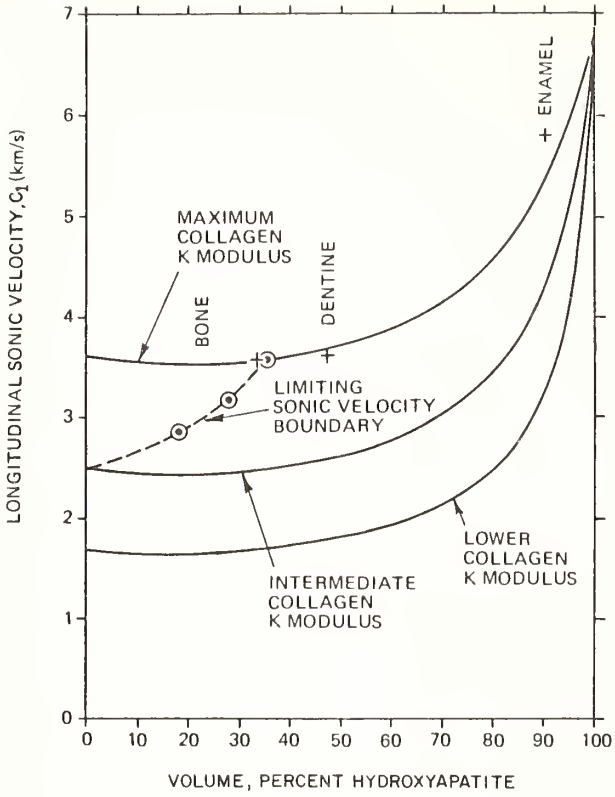

Fig. 8. Ultrasonic velocity in mineralized tissues (from Lees and Davidson [2]).

yields low values compared to ultrasonic measurement techniques.

The data represented in figure 8 can only be regarded as indicative and not definitive. In particular the value of enamel cannot be taken as properly a member of this class of materials because it is not a collageneous tissue. Enamel is formed by a totally different process than that for bone and dentin. The HAP content of enamel is so high that the mineral component of eq. (1) dominates, which will be true for a comparable mineralized collageneous tissue. However, the theory developed here shows that it is unlikely to have so much mineralization in bony tissues.

Acknowledgment

S. L. is pleased to acknowledge support from NSF Grant GH-42515 and National Institute of Dental Research, NIH, Research Grant Number RO1-DE-3992. Some of the experimental data was obtained while at the Department of Materials Science, University of Amsterdam with funds from the National Science Foundation and the University of Amsterdam.

Note added in proof:

The authors have recently learned that some of the concepts presented here were surmised by McCutchen [25]. In his paper he says "I suggest that collagen is the prime tension carrier in bone, and that bone's stiffness modulus is much greater than isolated collagen because intimate association with the mineral raises the collagen's tensile stiffness."

References

[1] White, S. W., Hulmes, D. J. S., Miller, A., and Timmins, P. A., Collagen-mineral axial relationship in calcified turkey leg tendon by x-ray and neutron diffraction, Nature 266, 421-425 (1977).

[2] Lees, S. and Davidson, C. L., The role of collagen in the elastic properties of calcified tissues, J. Biomech. 10, 475-486 (1977).

[3] Currey, J. D., Three analogies to explain the mechanical properties of bone, Biorheology 2, 1-10 (1964).

[4] Welch, P. O., The composite structure of bone and its response to mechanical stress, in Recent Advances in Engineering Science, A. C. Eringer, ed., Vol. 5, pp. 245-262 (Gordon and Breach,

[5] Katz, J. L., Hard tissue as a composite material - I. Bounds on the elastic behavior, J. Biomech. 4, 455-473 (1971).

[6] Currey, J. D., The relationship between the stiffness and the mineral content of bone, J. Biomech. 2, 477-480 (1969).

[7] Mason, P., Viscoelasticity and structure of keratin and collagen, Kolloid, Z., A. Polymere 202, 139-147 (1966).

[8] Papadakis, E. P., Balanced resonator for infrasonic measurement of Young's modulus and damping in flexure, J. Test and Eval. 1, 126-132 (1973).

[9] Lees, S. and Davidson, C. L., Ultrasonic measurement of some mineral-filled plastics, IEEE Trans. Sonics and Ultrasonics SU-24, 222-225 (1977).

[10] Kumins, C. A., Long range effects of polymer pigment interaction in the solid state, J. Paint Technology Engineering 37, Pt. 1, pp. 1314-1336 (1965).

[11] Burhans, A. S., Pitt, C. F., Sellers, R. F., and Smith, S. G., High performance epoxy resin systems for fiber-reinforced composites. Prelim. Paper, 21st Annual Mtg. Reinforced Plastics Division, Soc. Plastics Ind. (1965).

[12] Glimcher, M. J. and Krane, S. M., in Treatise on Collagen, B. S. Gould, ed., Vol. 2 (Academic Press, New York, 1968).

[13] Ramachandran, C. N., in Treatise on Collagen, C. N. Ramachandran, ed., Vol. 1, Chap. 3 (Academic Press, New York, 1967).

[14] Gallop, P. M. and Paz, M. A., Posttranlational protein modifications with special

attention to collagen and elastin, Physiol. Rev. 55, 418-487 (1975).

[15] Veis, A., Collagen Biosynthesis, in CRC Critical Reviews in Biochemistry, Vol. 2, p. 443 (The Chemical Rubber Co., Cleveland, Ohio, 1974).

[16] Hulmes, D. J. S., Miller, A., Parry, D. A. D., Piez, K. A., and Woodhead-Galloway, J. W., Analysis of the primary structure of collagen for the origin of molecular packing, J. Mol. Biol. 79, 137-148 (1973).

[17] Hodge, A. J., in Treatise on Collagen, C. N. Ramachandran, ed., Vol. 1, Chap. 4 (Academic Press, New York, 1967).

[18] Segrest, J. P. and Cunningham, L. W., Unit figril models derived from the molecular topography of collagen, Biopoly. 12, 825-834 (1973).

[19] Smith, J. W., Molecular pattern in native collagen, Nature 219, 157-158 (1968).

[20] Miller, A. and Parry, D. A. D., Structure and packing of microfibrils in collagen, J. Mol. Biol. 75, 441-447 (1973).

[21] Enemeto, S. and Krimm, S., Elastic moduli of helical polypeptide chain structures, Biophys. J. 2, 317-325 (1962).

[22] Yoon, H. S. and Katz, J. K., Ultrasonic wave propagation in human cortical bone, J. Biomech. 9, I. Theoretical considerations for hexagonal sysmmetry 407-412; II. Measurements of elastic properties and microhardness 459-464 (1976).

[23] Lang, S. B., On the anisotropic elastic coefficients of bone and results on fresh and dried bovine bones. IEEE Trans. Biomed. Engineering 17, 101-105 (1970).

[24] Abendschein, W. and Hyatt, G. W., Ultrasonics and selected physical properties of bone, Clin. Orthop. 69, 294-301 (1970).

[25] McCutchen, C. W., Do mineral crystals stiffen bone by straitjacketing its collagen? J. Theor. Biol. 51, 51-58 (1975).

Reprinted from *Ultrasonic Tissue Characterization II*, M. Linzer, ed., National Bureau of Standards, Spec. Publ. 525 (U.S. Government Printing Office, Washington, D.C., 1979).

ULTRASONIC PROPERTIES AND MICROTEXTURE OF HUMAN CORTICAL BONE

Hyo Sub Yoon and J. Lawrence Katz

Center for Biomedical Engineering
Rensselaer Polytechnic Institute
Troy, New York 12181, U.S.A.

The wave propagation in human cortical bone (dried) was investigated, using an ultrasonic pulse transmission method at room temperature. Firstly, it has been found that the symmetry of human cortical bone is consistent with the hexagonal system, based on the ultrasonic velocity measurement and microscopic observations. The five independent elastic stiffnesscs were determined at 5 MHz, and they are (in GPa): c_{11} = 23.4 ± 0.31, c_{33} = 32.5 ± 0.44, c_{44} = 8.71 ± 0.13, c_{12} = 9.06 ± 0.38, c_{13} = 9.11 ± 0.55.

Secondly, this study shows that bone filters and polarizes ultrasonic waves. Thirdly, since, in a piezoelectric medium such as bone, the wave propagation (or elastic stiffnesses) is modified by the piezoelectric coupling, the piezoelectric contribution or "stiffening" was calculated for bone, employing the piezoelectric and dielectric constants of bone reported in the literature. Compared with the corresponding values of two well-known piezoelectric materials, α-quartz (single crystal) and "poled" barium titanate ceramic (polycrystalline), it has been found that the piezoelectric "stiffening" in bone is negligible. Finally, the sound velocities were measured over the frequency range of 1 to 5 MHz for the transverse mode and of 2 to 10 MHz for the longitudinal mode. For all the eight independent modes the ultrasonic velocities are found to increase with increasing frequency, implying that bone is viscoelastic even at these high frequencies.

Key words: Anisotropy; dispersion; elasticity; human bone; microhardness; microstructure; piezoelectricity; thermodynamics; ultrasound; viscoelasticity; wave propagation.

1. Introduction

The material symmetry is an important concept for interpreting and analyzing the structure-property relationships of a material, from both theoretical and practical points of view. This is especially true when one has to deal with many tensorial properties of a multiphase-composite material such as bones and teeth. The maximum use of symmetry elements in the medium simplifies the analysis enormously and provides a clearer physical picture for any phenomenon than otherwise.

It is known that bone has a remarkably well organized structure, consisting mainly of the protein (collagen, not well crystallized), the inorganic phases (crystalline hydroxyapatite and possibly a type of amorphous calcium phosphate) and a fluid phase (*in vivo*). Therefore, one can expect that several crystal-physical phenomena occur in bone. It has, in fact, been reported that bone is both pyroelectric (first-rank tensor) and piezoelectric (third-rank tensor). When employing ultrasonic waves of low strain levels much less than 10^{-6}, as in diagnostic ultrasound, one must take into account these interactions between thermal and electrical properties, and between elastic and electrical properties, respectively. In other words, it is necessary to regard bone as a thermodynamic system. However, the situation becomes more complicated for a more realistic case than the above idealized one because bone appears to be viscoelastic even at ultrasonic frequencies.

It is now clear from the above information that one cannot treat each physical or thermodynamic property independent of the others, as has been done in the past, *e.g.*, [1,2][1]. Instead, one should start with a simple situation when studying bone, then move to a more complex model by adding one or more independent variables, as was followed in the present investigation on human compact bone. For this purpose it is convenient to assign hierarchal levels of structural organization to bone, that is, molecular, ultrastructural, microscopic and macroscopic. The wavelengths of ultrasound employed (3.7 x 10^{-1} to 2.2 mm) are of the order of magnitude appropriate to the microscopic level. This is the level at which conventional metallographic techniques are best suited to study the microstructure or microtexture of bone. Note that the microtexture of human bone is different from

[1]Figures in brackets indicate literature references at the end of this paper.

that of bovine, canine, or any other mammalian bone.

The simplest situation for ultrasonic studies of bone is one in which temperature (room) and frequency (5 MHz) are kept constant. This circumstance corresponds very closely to the situation of plane wave propagation in an elastic medium and yields a set of elastic stiffnesses for bone. As the next step, the piezoelectric contribution was considered for the ultrasonic wave propagation in bone. So far, bone has been treated as an elastic dielectric. In order to determine the existence of a frequency dependence or dispersion of the ultrasonic velocities at room temperature, the sound velocities were measured over the frequency range of 1 to 5 MHz for the transverse mode and of 2 to 10 MHz for the longitudinal mode. These results are important when it is necessary to accurately delineate ultrasonic paths, as in ultrasonic encephalography, monitoring of fracture healing, and other medical and dental diagnoses since the attenuation of ultrasonic waves in calcified tissue is substantially larger than that in soft tissue.

2. Theoretical Background: The Thermodynamics of Bone

In order to derive the relationships between the mechanical, electrical and thermal properties of bone, i.e. to establish the thermodynamic aspects of bone, let us, following Voigt [3], introduce a thermodynamic potential per unit volume, Ξ, as a function of ten independent variables: stress T_μ, electric field strength E_i and entropy σ, combined with the appropriate coefficients, elastic stiffness $c_{\mu\nu}$, dielectric permittivity ε_{ij}, specific heat C, piezoelectric stress constant $e_{i\mu}$, thermal stress coefficient q_μ pyroelectric constant p_i and absolute temperature θ. Thus:

$$\Xi = -\frac{1}{2} c_{\mu\nu}^{E,\sigma} S_\mu S_\nu + \frac{1}{2} \varepsilon_{ij}^{S,\sigma} E_i E_j + \frac{1}{2} \frac{\theta}{C^{S,E}} \sigma^2 \qquad (1)$$

$$+ e_{i\mu}^{\sigma} E_i S_\mu + \frac{\theta\, q_\mu^E}{C^E} S_\mu \sigma + \frac{\theta\, p_i^S}{C^S} E_i \sigma,$$

where summation over repeated indices is implied, and i,j = 1, 2, 3; μ, ν = 1, 2, . . ., 6. A superscript indicates the quantity to be kept constant. Here magnetic effects are not included in eq. (1) because they are usually very small compared to electric effects. Also, bone is treated as an anisotropic linear elastic solid, i.e. as a linear elastic dielectric, rather than as either metallic, ferromagnetic, or ferroelectric solids. That is, for simplicity the viscoelastic properties are considered separately.

Since the propagation of ultrasonic waves through a medium is an adiabatic process (isentropic), eq. (1) is simplified to

$$\Xi = -\frac{1}{2} c_{\mu\nu}^{E,\sigma} S_\mu S_\nu + \frac{1}{2} \varepsilon_{ij}^{S,\sigma} E_i E_j + e_{i\mu}^{\sigma} E_i S_\mu \qquad (2)$$

Differentiation of eq. (2) with respect to S_μ and E_i, respectively, gives the well-known equations of state (or constitutive equations) for a piezoelectric medium:

$$-\left(\frac{\partial \Xi}{\partial S_\mu}\right)_{E,\sigma} \equiv T_\mu = c_{\mu\nu}^{E,\sigma} S_\nu - e_{i\mu}^{\sigma} E_i \qquad (3)$$

$$\left(\frac{\partial \Xi}{\partial E_i}\right)_{T,\sigma} \equiv D_i = e_{i\mu}^{\sigma} S_\mu + \varepsilon_{ij}^{S,\sigma} E_j \qquad (4)$$

which now define stress T_μ and electric displacement D_i. Note that the coefficients on the leading diagonal represent the principal effects while the off-diagonal coefficients (equal to each other) measure the coupled effects.

For the pulsed ultrasonic measurements of thickness vibration, the elastic stiffness appropriate for the vibration would properly be designated as

$$c_{\mu\nu}^{D_n, E_t, \sigma},$$

meaning that the normal component of the electric displacement and the transverse components of the electric field are constant (usually zero). By combining Newton's second law of motion with the constitutive eqs. (3) and (4) and substituting plane wave solutions u_j (= $U_j \exp i(\omega t - \vec{k}\cdot\vec{x})$) for the medium of density ρ, it may be shown that:

$$\rho \frac{\partial^2 u_i}{\partial t^2} = c_{ijk\ell}^{D_n, E_t, \sigma} \frac{\partial^2 u_k}{\partial x_j \partial x_\ell}, \qquad (5)$$

where:

$$c_{ijk\ell}^{D_n, E_t, \sigma} = c_{\mu\nu}^{D_n, E_t, \sigma} = c_{\mu\nu}^{E,\sigma} + \frac{e_{m\mu}^{\sigma} e_{m\nu}^{\sigma}}{\varepsilon_{mm}^{S,\sigma}} \qquad (6)$$

with m being fixed.

Note that the directions i, n, m are parallel to one another, and that

$$c_{\mu\nu}^{D_n, E_t, \sigma}$$

is, in general, different from $c_{\mu\nu}^{D,\sigma}$ which is given by:

$$c_{\mu\nu}^{D,\sigma} = c_{\mu\nu}^{E,\sigma} + \frac{e_{i\mu}^{\sigma} e_{j\nu}^{\sigma}}{\varepsilon_{ij}^{S,\sigma}}. \qquad (7)$$

For more details the reader is referred to references [4-6].

3. Experimental Procedure

A. Specimen preparation

Bone samples were cut with a band saw out of the right femoral mid-diaphysis from the cadaver of a 57-year-old male who died of gastric adenocarcinoma. Two well-oriented specimens in the shape of a rectangular parallelepiped (0.5461 cm x 0.8933 cm x 0.6233 cm for $X_1X_2X_3$ cut and 0.4750 cm x 0.5641 cm x 0.7645 cm for 45° cut), were then cut using an Isomet low speed saw with a diamond blade 10.16 cm diameter and 0.03048 cm thick. Distilled water was used as the lubricant

and coolant during cutting. The specimens were oriented using a straight surface in the medial quadrant, which is always parallel to the bone axis (X_3 axis) in any femur, taking the X_1 axis along the radial direction and the X_2 axis perpendicular to both, thus forming a right-handed rectangular coordinate system. The lateral quadrant of the mid-diaphysis was selected for obtaining the specimens because, for this particular bone, this quadrant was macroscopically more uniform than was the rest of the cross section.

Conventional metallographic techniques were then employed for grinding and polishing the specimens. In order to prepare a pair of parallel surfaces for ultrasonic measurements, the specimen, mounted on a parallel-face device with double-stick tape, was ground under a flow of cooling water, with an AB Handimet Grinder on which a 600 grit silicon carbide paper strip was pasted. This was followed by polishing with 0.3 μm alumina slurry on a 20.32 cm diameter bronze wheel covered with wool broadcloth. Each time after grinding and polishing, the specimen was cleaned in an ultrasonic cleaner for 3 minutes. The orientation of a specimen was checked by microscopic observation of osteon arrangement in the transverse cross section.

Each specimen, wrapped with soft tissue papers, was dried very slowly to avoid undesirable results such as cracks and distortions. This was done by keeping the specimen in a glass vial whose plastic lid was tightly closed, for a day, followed by placing it first in a desiccator for 10 days, and subsequently in a vacuum oven at 24 °C and 533 Pa for 4 days. Finally, the specimen was dried in a vacuum line equipped with both a mechanical pump and a diffusion pump at room temperature for 3 days. Before proceeding with the ultrasonic velocity measurements, the moisture content of the specimen was stabilized by keeping it in air until changes in the specimen's dimensions were recorded as less than 0.1 percent.

B. Micrographs and microhardness measurements

From the same mid-diaphysis of human bone, another cylindrical specimen 0.5 cm long was prepared in the identical manner as described before. This specimen was used both for obtaining micrographs (75X) of the transverse cross section and for Vickers (HV) microhardness measurements, employing a Bausch & Lomb Metallograph and a Kentron Tester, respectively. A typical microstructure of the transverse cross section is shown in figure 1a. Compare it with that of young bovine bone shown in figure 1b. The hardness of the bone specimen was measured with a 200 g load at locations equally spaced radially on the four quadrants: anterior, posterior, lateral and medial. Care was taken to make all indentations away from Haversian canals or lacunae.

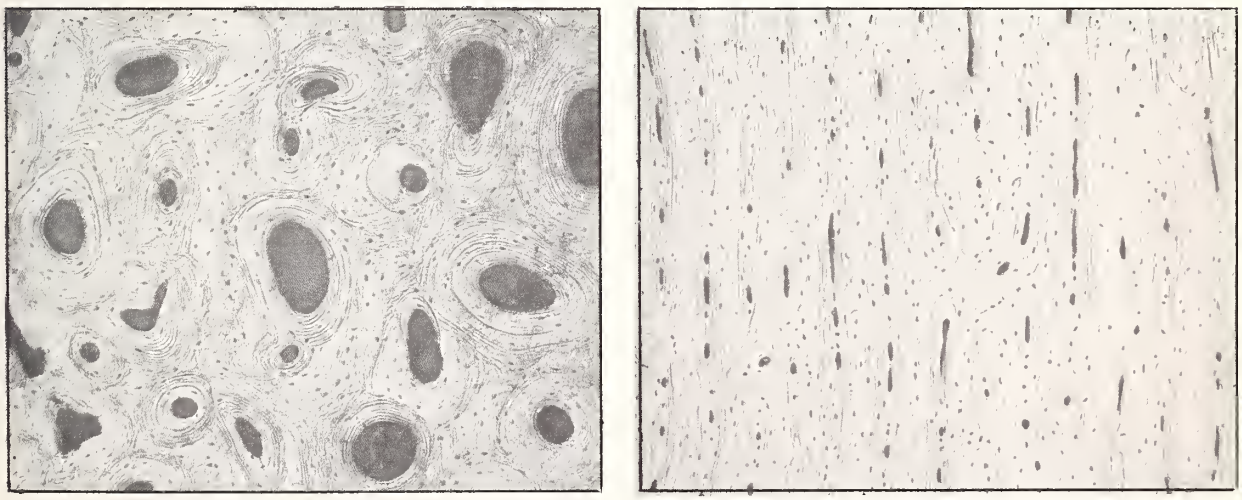

(a) HUMAN (b) BOVINE

Fig. 1. Microstructures of human and bovine demora, 75X (transverse cross section), (a) human and (b) bovine.

C. Ultrasonic setup and measurements

A block diagram for the pulse through-transmission technique is shown in figure 2. For each frequency step, a pair of PZT-5A piezoelectric transducers (chromium-gold plated on both faces) was used to transmit and receive the ultrasonic pulses. For the specimen holder, a pair of parallel faces of aluminum buffer disc was prepared by hand-grinding it on 400- and 600-grit silicon carbide paper strips, as explained previously, and by polishing with a 3 μm diamond compound; the disc was cleaned ultrasonically after each step. The transducer was cemented on one face of the buffer disc with salol (melting point 43 °C), the other face being in contact with a face of the specimen during the transit-time measurements. No coupling medium was used

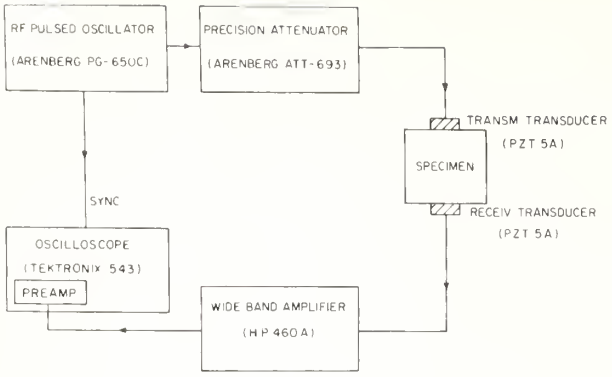

Fig. 2. Block diagram of pulse transmission method.

between the buffer disc and the specimen surface since dried bone is porous and the specimen volume was very small. Instead, the acoustic coupling was formed by lightly pressing down the upper part of the specimen holder with a screw. For more details see reference [7].

Pulse transit (or delay) times in the specimen were measured from the shift of the pulse positions as observed on the horizontal axis of the oscilloscope with and without the specimen between the aluminum alloy buffer discs. The horizontal (time) axis of the oscilloscope was calibrated with a Time-Mark Generator 180A. The accuracy of the pulse transmission method was checked by measuring the transit times both of AT cut quartz oscillator plates of known frequencies, and a beryl single crystal whose values were determined previously by Yoon and Newnham [8] using a pulse superposition method [9].

4. Experimental Results and Discussion

A. The homogeneity and microtextural symmetry of human cortical bone

Figure 3 shows that the bone is "intrinsically" homogeneous within the limit of experimental errors along the radial direction on the four quadrants. Weaver [10] has also observed a wide zone of mid-cortical bone of uniform hardness for autopsy and surgical bone specimens. Kallieris' results [11] show no significant differences in hardness between fresh human bones of various structural designs in different layers of compact bones. These findings justify somewhat the use of small specimens for measurements of the physical or mechanical properties of bone.

Rauber [12] and Dempster and Liddicoat [13] have shown that bone has different physical and mechanical properties along and perpendicular to its long axis. Therefore, the symmetry (or pseudosymmetry) of the microstructural texture of bone may be either orthorhombic, tetragonal, trigonal, or hexagonal. Since bone is an opaque, microstructural composite, neither optical nor single crystalline x-ray diffraction techniques can be employed to determine its full textural symmetry. An ultrasonic wave propagation method can provide information about both the symmetry and the elastic (and viscoelastic) properties of either crystalline or non-crystalline materials. The microstructure on the transverse cross section of bone shows a pseudo-hexagonal close-

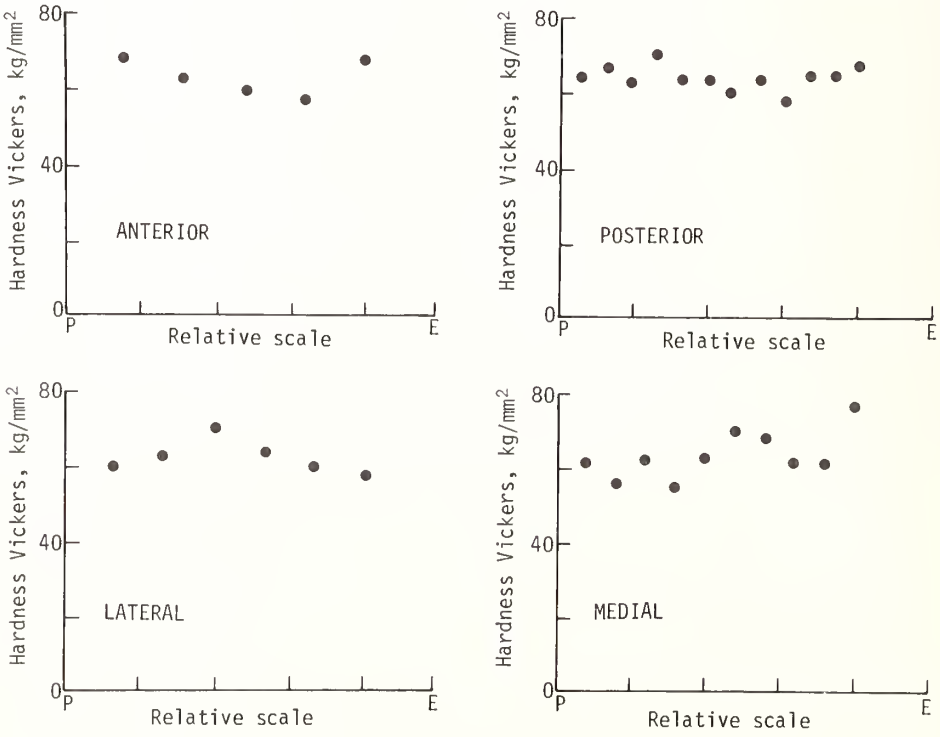

Fig. 3. Microhardness (Vickers Hardness) of human femur (dried). P = periosteum and E = endosteum.

packing of Haversian systems or osteons. Previously, Katz [14] and Katz and Ukraincik [15] suggested that the arrangements of osteons and interstitial lamellae could be considered to be pseudo-hexagonal. Thus, the tetragonal and trigonal systems can be eliminated. The ultrasonic measurements have shown that c_{11} and c_{22} or c_{44} and c_{55} are equal to each other, thereby leaving only hexagonal symmetry as appropriate for bone.

B. The elastic stiffness of bone

Table 1 shows the ultrasonic velocities together with their standard deviations at room temperature and 5 MHz along various directions in the human femur specimens. The eight independent velocity measurements provide four internal cross-checks. For comparison the corresponding sound velocities in a Durango fluorapatite single crystal [16] are included. From these velocities and the independently measured mass density ρ, the elastic stiffnesses of bone were calculated, as shown in table 2 where the pseudo-single crystal elastic stiffnesses of hydroxyapatite (HAP) [15], enamel and dentin [17] are included, in addition to the elastic stiffnesses of fluorapatite (FAP) [16]. Note in the case of the mineralized tissues that the stiffnesses, in general, increase with the amount of apatite.

Table 1. Sound velocities in human compact bone and fluorapatite crystal at room temperature.

Mode	Propagation direction, $\tilde{N}$	Displacement direction, $\tilde{U}$	Sound velocity (km/s) Fluorapatite[a]	Human femur (dried)
αL	[001]	[001]	7.586	4.18 ± 0.03
αT	[001]	[100] or [010]	3.635	2.16 ± 0.01
γL	[100]	[100]	6.842	3.55 ± 0.02
γT_h	[100]	[010]	3.978	1.98 ± 0.01
γT_3	[100]	[001]	3.638	2.17 ± 0.02
45L	$\left[\frac{1}{\sqrt{2}}\ 0\ \frac{1}{\sqrt{2}}\right]$	$\sim\left[\frac{1}{\sqrt{2}}\ 0\ \frac{1}{\sqrt{2}}\right]$	7.020	3.86 ± 0.03
$45T_h$	$\left[\frac{1}{\sqrt{2}}\ 0\ \frac{1}{\sqrt{2}}\right]$	[0 -1 0]	3.811	2.06 ± 0.01
$45T_v$	$\left[\frac{1}{\sqrt{2}}\ 0\ \frac{1}{\sqrt{2}}\right]$	$\sim\left[-\frac{1}{\sqrt{2}}\ 0\ \frac{1}{\sqrt{2}}\right]$	4.033	2.24 ± 0.02

[a] See reference [16].

Table 2. Elastic stiffnesses of calcified tissues and apatite single crystals at room temperature.

$c_{\mu\nu}$ (GPa)	Fluorapatite [16]	Hydroxyapatite [15]	Enamel [17]	Dentin [17]	Bone (dried)
c_{11}	150.5	137	115	37.0	23.4 ± 0.31
c_{33}	185.0	172	125	39.0	32.5 ± 0.44
c_{44}	42.51	39.6	22.8	5.70	8.71 ± 0.13
c_{12}	48.8	42.5	42.4	16.6	9.06 ± 0.38
c_{13}	62.2	54.9	30.0	8.7	9.11 ± 0.55
ρ(g/cm^3)	3.2147	3.17	2.9	2.2	1.86

In figure 4 are plotted the elastic stiffnesses of bone as a function of angle ϕ from the X_3 axis. This shows how the elastic stiffnesses are interrelated to the orientation in a plane parallel to the X_3 axis. In other words, the longitudinal modes αL, 45L and γL are related,

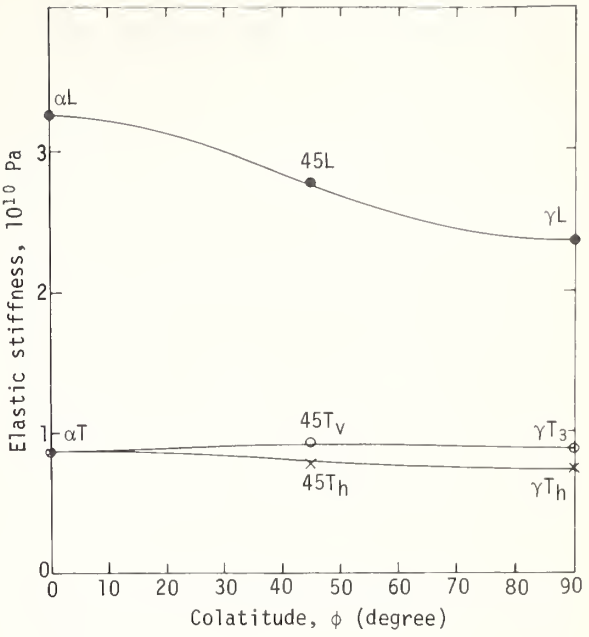

Fig. 4. Angular dependence of the elastic stiffnesses of human bone.

while the degenerate transverse mode αT along the bone axis (X_3) is separated out into the two branches, $45T_v \rightarrow \gamma T_3$ and $45T_h \rightarrow \gamma T_h$.

In a hexagonal medium there exists, in general, three pure mode directions (α, β, γ) along each of which one purely longitudinal and two purely transverse modes of propagation occur, forming a mutually orthogonal set. Of these the α and γ directions (see table 1) are known from the symmetry of the hexagonal medium. The β direction, which lies on a conical surface between the X_3 axis and its perpendicular, is given in terms of the elastic stiffnesses of the material. It has been found that no β direction exists in bone. It may be that in bone the structural arrangement of the collagen fibrils and fibers and the osteons may not allow any direction of high symmetry for the β pure mode. This can explain the observed phenomena that bone polarizes and filters the ultrasonic waves.

C. The piezoelectric "stiffening"

Following Fukada and Yasuda [18] and Fukada [19], point group 6[3] was chosen as the piezoelectric class of symmetry for bone, which is also consistent with the pyroelectric measurements on bovine bone by Lang [1]. In table 3 is summarized the piezoelectric contribution to the elastic stiffnesses of bone, except for the two

[3] While it is true that bone does not exhibit crystalline symmetry in the usual sense, as would be demonstrated by x-ray diffraction analysis, 6 is the appropriate point symmetry to describe the microstructural level of the organization of bone in that it is consistent both with the morphological observations and with the ultrasonic data within the precision of the measurements.

Table 3. Piezoelectric corrections to elastic stiffnesses of bone.

Mode	$c_{\mu\nu}^{D_n,E_t,\sigma}$	$\frac{c_{\mu\nu}^{D_n,E_t,\sigma} - c_{\mu\nu}^{E,\sigma}}{c_{\mu\nu}^{E,\sigma}}$
αL	$c_{33}^E + \frac{e_{33}^2}{\varepsilon_{33}}$	1.9×10^{-8}
αT	c_{44}^E	0
γL	c_{11}^E	0
γT_h	c_{66}^E	0
γT_3	$c_{44}^E + \frac{e_{15}^2}{\varepsilon_{11}}$	3.9×10^{-7}
$45T_h$	$\frac{1}{2}\left(c_{44}^E + c_{66}^E + \frac{e_{14}^2}{\varepsilon_{11} + \varepsilon_{33}}\right)$	2.3×10^{-6}

mixed modes (45L and $45T_v$), employing the piezoelectric constants for horse femur [19] and the permittivities of bovine bone by Gundjian and Chen [20] with the correction for frequency dependence following Liboff and Shamos [21]. Note that the piezoelectric "stiffening" in bone is very small and may therefore be neglected within the experimental errors. Table 4 compares the values

$$\left(c_{\mu\nu}^{D,\sigma} - c_{\mu\nu}^{E,\sigma}\right)/c_{\mu\nu}^{E,\sigma}$$

of the typical piezoelectric materials α-quartz and polarized barium titanate ceramic, with the corresponding values of bone (see 2. Theoretical background).

Table 4. Comparison of the piezoelectric contribution to the elastic stiffnesses of bone, α-quartz and and $BaTiO_3$ ceramic.

$$\left(c_{\mu\nu}^{D,\sigma} - c_{\mu\nu}^{E,\sigma}\right)/c_{\mu\nu}^{E,\sigma}$$

μν	Bone (room temp.) Point group, 6 (x 10^{-7})	α-Quartz (20 °C) Point group, 32 (x 10^{-2})	$BaTiO_3$ ceramic (25 °C) Point group, 6 mm (x 10^{-2})
11	0.18	0.86	0.93
33	0.19	0	17.0
44	82.0	0.072	28.0
12	0.46	-11.0	2.0
13	0.56	0	- 8.4
14	---	- 0.99	---
66	0	1.9	0

D. The frequency dependence of ultrasonic velocities

Figure 5 shows how the eight sound velocities in dried human bone change with frequency at room temperature. In all cases the ultrasonic velocities are found to increase with increasing frequency. All the transverse modes exhibit almost

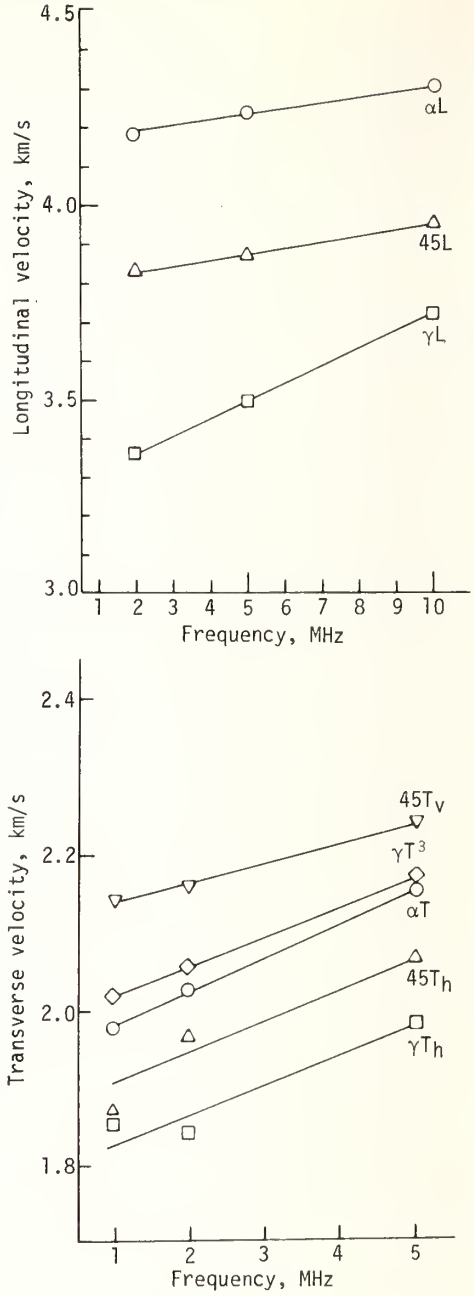

Fig. 5. Frequency dependence of sound velocities in human bone (dried).

similar dispersion behavior, while one of the longitudinal modes (γL) has a steeper slope than the rest of modes.

Brillouin [22] summarizes the explanations of the geometric dispersion due to a periodic or discrete lattice, which were originated by Cauchy and refined by Powell and Kelvin. This book also includes Brillouin's own research on the subject. More recently, Sutherland and Lingle [23] reported the geometric dispersion of acoustic waves by an elastic-elastic composite of tungsten wires embedded in an aluminum matrix over the incident frequency range of 0.63 to 8.57 MHz. They also

reported the existence of pass- and forbidden-bands, in addition to the shift of the incident frequency upon propagating through the material. In their case the phase velocity always decreases with increasing frequency within each pass band.

For a linear viscoelastic solid, e.g., polymethyl methacrylate, Asay, Lamberson and Guenther [24] reported on the viscoelastic dispersion of ultrasonic waves, in which the phase velocity increases with increasing frequency and approaches a plateau. These results can be explained by relaxation phenomenon of "molecular" units (see Gross [25]).

As mentioned earlier, bone is a hierarchal composite on many levels of structure. Of principal concern here is the microstructural level of organization. In this case the osteons behave as stiff hollow elastic fibers ensheathed by a compliant viscoelastic material, mainly collagen and protein polysaccharides.

It is clear that much additional data are needed with respect to ultrasonic attenuation in bone over a wide frequency range as well as spectral analysis of both transmitted and reflected pulses. In addition it would be valuable to perform studies on synthetic composites of collagen and hydroxyapatite in various combinations in order to obtain dispersion data from controlled composites. Still from the modelling described above, it is reasonable at present to explain the dispersion of the phase velocities in human compact bone in terms of its viscoelastic components.

Acknowledgment

Contribution No. 94 from the Laboratory for Crystallographic Biophysics; this work was supported by US PHS through NIDR Grant No. 5T1-DE-117-14.

References

[1] Lang, S. B., Pyroelectric effect in bone and tendon, Nature 212, 704-705 (1966).

[2] Lang, S. B., Ultrasonic method for measuring elastic coefficients of bone and results on fresh and dried bovine bones, IEEE Trans. Bio-Med. Engng. 17, 101-105 (1970).

[3] Voigt, W., Lehrbuch der Kristallphysik (B. G. Teubner, Leipzig, 1910); reprinted with an additional appendix, 1928 (Johnson Reprint Corp., New York, 1966).

[4] Cady, W. G., Piezoelectricity (Dover Publications, New York, 1964).

[5] Yoon, H. S. and Katz, J. L., Ultrasonic wave propagation in human cortical bone - I. Theoretical considerations for hexagonal symmetry, J. Biomech. 9, 407-412 (1976).

[6] Yoon, H. S. and Katz, J. L., Ultrasonic wave propagation in human cortical bone - III. Piezoelectric contribution, J. Biomech. 9, 537-540 (1976).

[7] Yoon, H. S. and Katz, J. L., Ultrasonic wave propagation in human cortical bone - II. Measurements of elastic properties and microhardness, J. Biomech. 9, 459-464 (1976).

[8] Yoon, H. S. and Newnham, R. E., The elastic properties of beryl, Acta Cryst. A29, 507-509 (1973).

[9] McSkimin, H. J., Pulse superposition method for measuring ultrasonic wave velocities in solids, J. Acoust. Soc. Am. 33, 12-16 (1961).

[10] Weaver, J. K., The microscopic hardness of bone, J. Bone Joint Surg. 48A, 273-288 (1966).

[11] Kallieris, D., Härtemessungen an frischen menschlichen Knochen, Z. Rechtsmed. 68, 164-170 (1971).

[12] Rauber, A. A., Elasticität und Festigkeit der Knochen (Engelmann, Leipzig, 1876).

[13] Dempster, W. T. and Liddicoat, R. T., Compact bone as a non-isotropic material, Am. J. Anat. 91, 331-362 (1952).

[14] Katz, J. L., Anisotropic elastic properties of calcified tissues, IADR Program and Abstracts of Papers, p. 71, Abstract No. 73 (1971) (49th General Session, Intern. Assoc. Dent. Res., Chicago, Illinois).

[15] Katz, J. L. and Ukraincik, K., On the anisotropic elastic properties of hydroxyapatite, J. Biomech. 4, 221-227 (1971).

[16] Yoon, H. S. and Newnham, R. E., Elastic properties of fluorapatite, Am. Mineral. 54, 1193-1197 (1969); Yoon, H. S., Elastic properties of fluorapatite and beryl, Ph.D. Thesis (Pennsylvania State University, University Park, PA, 1971).

[17] Lees, S. and Rollins, F. R., Jr., Anisotropy in hard dental tissues, J. Biomech. 5, 557-566 (1972).

[18] Fukada, E. and Yasuda, I., Piezoelectric effects in collagen, Jap. J. Appl. Phys. 3, 117-121 (1964).

[19] Fukada, E., Mechanical deformation and electrical polarization in biological substances, Biorheology 5, 199-208 (1968).

[20] Gundjian, A. and Chen, L. L., Standardization and Interpretation of the Electromechanical Properties of Bone, IEEE Trans. Biomed. Engng. 21, 177-182 (1974).

[21] Liboff, A. R. and Shamos, M. H., Solid State Physics of Bone, in Biological Mineralization, I. Zipkin, ed., Chap. 14, pp. 335-395 (Wiley, New York, 1973).

[22] Brillouin, L. Wave Propagation in Periodic Structures (Dover Publications, New York, 1953).

[23] Sutherland, H. J. and Lingle, R., Geometric dispersion of acoustic waves by a fibrous composite, J. Composite Mater. 6, 490-502 (1972).

[24] Asay, J. R., Lamberson, D. L., and Guenther, A. H., Pressure and temperature dependence of the acoustic velocities in polymethylmethacrylate, J. Appl. Phys. 40, 1768-1783 (1969).

[25] Gross, B., Mathematical Structure of the Theories of Viscoelasticity (Hermann & Cie., Paris, 1953).

Reprinted from *Ultrasonic Tissue Characterization II*, M. Linzer, ed., National Bureau of Standards, Spec. Publ. 525 (U.S. Government Printing Office, Washington, D.C., 1979).

ATTENUATION AND DISPERSION OF ULTRASOUND IN CANCELLOUS BONE

James E. Barger

Bolt Beranek and Newman Inc.
Cambridge, Massachusetts 02138

Measurements of the insertion loss and insertion phase shift for ultrasound transmitted through sections of cancellous bone from human skull are reported as functions of frequency over the range extending from 0.3 MHz to 3.0 MHz. The frequency dependence of insertion loss and of phase speed are both found to be caused principally by scattering of sound by the blood and fat filled interstices in the bone matrix. Independent scattering measurements made at all observation angles confirm the scattering phenomenon. It is concluded that both the high attenuation and the significant dispersion at frequencies above about 1 MHz will limit the ability to characterize brain tissue by its backscatter at these high frequencies. Also, most reported sound speeds in cancellous bone have been calculated from the time-of-flight of broad-band pulses, and are therefore group speeds. These group speeds will exceed the phase speeds by about 15 percent in magnitude.

Key words: Attenuation; dispersion; skull bone; sound speed; ultrasound.

1. Introduction

The objective of this research was to measure, as a continuous function of frequency in the range extending from 250 kHz to 2.5 MHz, both the insertion loss and the phase speed of ultrasound in cancellous bone. These measurements are especially important as design data for ultrasound systems that are to characterize tissue through skull bone, which comprises two outer tables of ivory bone and an inner layer of cancellous bone, called diploe. This diploe layer is known to contribute most of the ultrasonic attenuation, as well as pulse waveform distortions, at diagnostic system frequencies [1][1].

Successful tissue characterization involves frequency spectrum analysis, over a rather broad band of frequency, of the sound scattered by a range-gated segment of tissue [2]. The attenuation that occurs when scattered sound is transmitted through diploe can change the spectrum in the band in which signal amplitude exceeds noise amplitude by an amount sufficient to permit spectrum identification. Also, the pulse waveform distortions owing to frequency-dependent sound speed, also called dispersion, can substantially reduce the range resolution of the broadband scattered sound.

The experiments reported in this paper were all performed on cancellous bone samples obtained by removing the ivory tables from a 9.5-mm thick section of human skull that had been fixed for about six months in buffered formalin.

The experimental apparatus is described schematically in figure 1. A pulse generator applies a broadband, high-voltage pulse to a focused transducer. This transducer generates at its focus a pulse having a peak pressure of about eight bars and a bandwidth (defined at 10 dB down points) of about 300 kHz to 2.5 MHz. The pulse is captured and digitized at 20 MHz and subsequently transmitted to a PDP11/40 computer for spectral analysis.

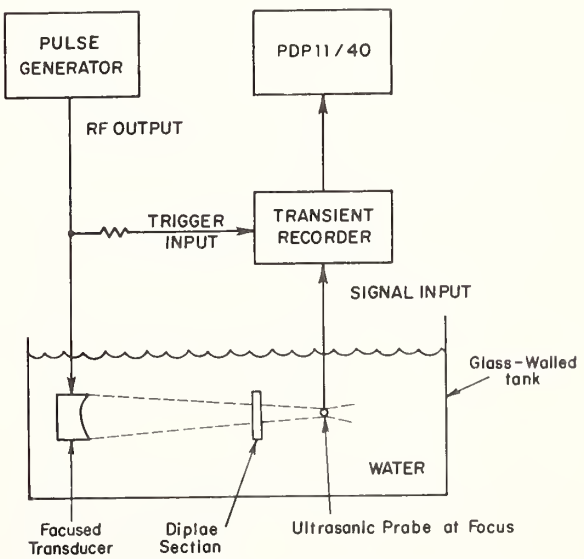

Fig. 1. Schematic diagram of experimental apparatus for measuring insertion loss and phase through bone samples.

The ultrasonic waveforms are measured at the focus of the transducer with a small piezoelectric

[1]Figures in brackets indicate literature references at the end of this paper.

disc probe 3 mm in diameter and 0.3 mm thick. The disc is positioned with its major response axis collinear with the axis of the ultrasonic beam. The disc diameter is equal to the diameter of the sound beam at about its 6-dB down points, so that the probe output voltage is proportional to the sound pressure averaged over the sound beam.

The insertion loss and phase of the diploe sample are functions of the Fourier coefficients T(f) of the pulse at the focus beyond the diploe sample and of the Fourier coefficients S(f) of the pulse also measured at the focus, but without the diploe sample. The insertion loss in dB and the insertion phase angle are defined in eq. (1). Both functions are calculated at 19.5-kHz intervals of frequency by the computer.

$$IL \equiv -20 \log |T/S| \qquad (1)$$

$$\phi \equiv \arg T - \arg S \ .$$

The phase speed of sound, c_1, in the diploe sample can be calculated from the frequency ratio of the insertion phase angle, $\phi/f = \phi'$. The insertion phase angle is the increase in phase of sound transmitted through the diploe layer less the increase in phase of sound transmitted through a water layer having the same thickness, h, as the diploe layer. This increase is expressed in eq. (2), where ϕ is the phase angle in degrees and c_0 is the phase speed of sound in water.

$$\phi = 360 \ f \ h \ (c_1^{-1} - c_0^{-1}) \ . \qquad (2)$$

Solving for the phase speed in diploe, we have

$$c_1 = c_0(1 + \phi' \ c_0/360h)^{-1} \ . \qquad (3)$$

If the phase speed c_1 is a function of frequency, which it will be if ϕ' is not constant, the transmission is said to be dispersive.

2. Experimental Results

A. Insertion Loss

The insertion loss for a 4-mm thick sample of diploe as a function of frequency is shown on figure 2. These data show very little loss at 0.3 MHz, with a sharply increasing loss between 0.7 and about 1.3 MHz. At higher frequencies, loss increases more slowly with increasing frequency, reaching about 40 dB at 2 MHz.

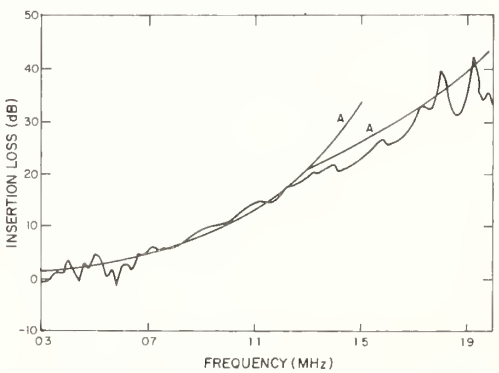

Fig. 2. Insertion loss of a 4-mm thick sample of diploe compared with calculated loss due to scattering and to absorption (A).

B. Phase Speed

The insertion phase angle for a 4-mm thick diploe sample is shown as a function of frequency on figure 3. We see that the phase angle does not increase linearly with frequency. Three different values of phase angle are noted at three different frequencies. The phase-frequency ratios ϕ' are used together with eq. (3) to calculate the phase speeds at the three different frequencies. The results at 0.5 MHz and 1.5 MHz are c_1 = 2190 m/s and c_1 = 2530 m/s. Similar data on the 4-mm thick diploe sample at 3.5 MHz showed c_1 = 2800 m/s [3]. This tangent is sketched on figure 3, where it is seen to match with the data for frequencies above 2 MHz.

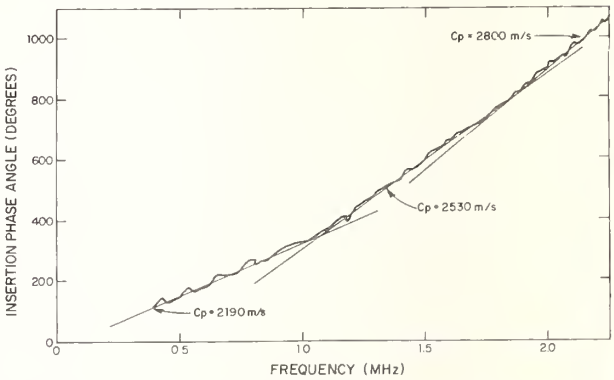

Fig. 3. Insertion phase shift of a 4-mm thick sample of diploe showing three tangent regions of different group speed c_g.

C. Scattered Sound

The insertion-loss measurement apparatus was modified, as follows, to measure the sound scattered by the diploe layer. A 6-mm diameter core was cut from the skull sample and positioned coaxially at the focus. The probe was then scanned around a 9-cm radius circle centered on the focus and including the incident sound axis. The sound pressure levels at 9 cm relative to the sound pressure level at the focus are shown on figure 4 as a function of observation angle. The narrow beam directed back towards the source is sound reflected from the outer table. The small increase in sound pressure level at 180° is the transmitted sound. Sound reaching the probe at all other angles has been scattered by the skull core.

3. Discussion of Results

A. Insertion Loss

The insertion loss is shown on figure 2 to be a rapidly increasing function of frequency. The scattered sound shown on figure 4 is approximately omnidirectional. Both of these experimental facts lead us to suspect that sound is being scattered by the fat- and blood-filled interstices in the spongy bone matrix. Omnidirectional scattering is caused by small discontinuities in the bulk modu-

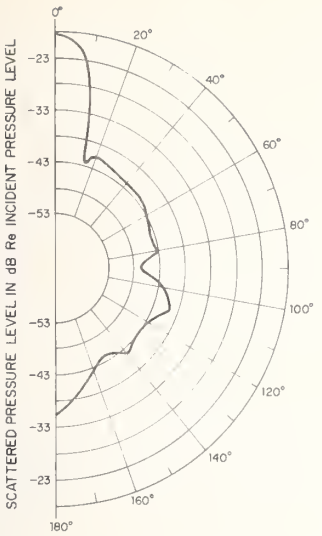

Fig. 4. Sound pressure levels measured 9 cm from a core of diploe caused by 20-μs pulses of 1-MHz sound incident from the direction of 0 degrees.

lus of the medium. If the average bulk modulus of diploe is represented by B_o and the bulk modulus of the material in the interstices by B, we can write the scattering cross-sectional area σ of a single interstice having volume V [4] as

$$\sigma = 4\pi^3\lambda^{-4}V^2(B-B_o/B_o)^2 \quad . \tag{4}$$

We consider a plane wave having intensity I incident upon a layer of diploe that is ℓ units thick and having lateral area A. The total power, W_s, scattered out of this slice having volume $A\ell$ is the sum of power scattered by all N interstices therein:

$$W_s = I\sum_{j=o}^{N} \sigma_j = I\ 4\pi^3\lambda^{-4}(\Delta B/B_o)^2 \sum_{j}^{N} V_j^2 \quad . \tag{5}$$

We simplify the expression for scattered power by observing that the volume of the slice $A\ell$ is equal to the total volume of scatterers $N\overline{V}$, where the average volume is

$$\overline{V} = N^{-1} \sum_{j}^{N} V_j \ .$$

We define also the normalized variance β of the interstitial volumes.

$$\beta \equiv \overline{V^2}/\overline{V}^2 \tag{6}$$

Combining eq. (5) with eq. (6), upon defining the product AI as the power, W_i, incident upon the slice, we have the following result for the ratio of power scattered from the slice to power incident upon the slice.

$$W_s/W_i = 4\pi^3\lambda^{-4}\beta\ \overline{V}\ (\Delta B/B_o)^2\ell \tag{7}$$

Equation 7 is equal to the product $\alpha\ell$, where α is the intensity attenuation coefficient, because the power balance for the power, W_t, transmitted through a thin slice is $W_t = W_i - W_s$.

$$W_t/W_i = 1 - W_s/W_i = e^{-\alpha\ell} \simeq 1 - \alpha\ell \tag{8}$$

Dividing by incident power W_i and equating to the definition of attenuation coefficient, we have the desired equality.

The average bulk modulus of the diploe sample was calculated from measured mass density and sound speed. The result was $B_o = \rho_o c_o^2 = 7.81\cdot10^{10}$ μbar. The bulk modulus of the interstitial contents was taken to resemble blood, $B = \rho c^2 = 2.54\cdot10^{10}$ μbar. The average interstitial volume was calculated from the average diameter d of the interstices, namely, 0.6 mm. The probability density distribution for interstice volumes is not known, but we will assume it to be a Rayleigh distribution, for which $\beta = 4/\pi$.

When these quantities are substituted into eq. (7), we have for the attenuation due to scattering

$$IL/\ell\ (dB/cm) = 4.34\alpha = 13.2\ F^4 \ , \tag{9}$$

where F is frequency in MHz.

The fundamental result, eq. (4), is valid only for scattering elements that have diameters smaller than about one-third wavelength. For our sample, then, valid results occur at frequencies less than 1.3 MHz. At higher frequencies, the scattering law saturates and changes to a frequency-squared increase [4]. Therefore, the complete analytical representation of scattering is given by eq. (10).

$$\begin{aligned} IL/\ell\ (dB/cm) &= 13.2\ F^4 \qquad F<F_o \\ &= 13.2\ F_o^2F^2 \quad F>F_o \ , \end{aligned} \tag{10}$$

where $F_o(MHz) = (c_1/3d)\ 10^{-6}$.

In addition to attenuation by scattering, there is attenuation by absorption. A typical value of the pressure attenuation coefficient in bone is 1.5 nepers/cm at 1 MHz [5]. The associated insertion loss per cm is $IL/\ell = 13.2F$. The total attenuation, namely, the sum of absorption and scattering attenuation, is plotted on figure 2 for a 4-mm thick section. The agreement is very good between the experimental and the theoretical values of loss, indicating general accuracy of the scattering theory.

B. Sound Power Balance

The sound power balance used to obtain eq. (10) can be checked with the data shown on figure 4. The incident sound power, W_i, is given in terms of the incident sound intensity, I, and the radius, a, of the focus, $W_i = \pi a^2\ I$. The reflected sound power, W_r, is given in terms of the reflected half-beamwidth, θ, and the reflected intensity, I_r, measured at distance r_o, $W_r = \pi(r_o\sin\theta)^2\ I_r$. The scattered sound power, W_s, is given in terms of the scattered sound intensity, I_s, measured at distance r_o, $W_s = 4\pi r_o^2\ I_s$.

The sound power balance requires power incident, W_i, to equal the power scattered, W_s, plus power reflected, W_r, plus power absorbed, W_a. We observed in the preceding section that attenuation by absorption is equal to attenuation by scattering at a frequency of 1 MHz. The scatter data on figure 4 are for this frequency, so we take W_a =

W_s. Dividing both sides of the power balance by the incident power, W_i, we have eq. (11).

$$\frac{W_s+W_r+W_a}{W_i} = 8(r_o/a)^2(I_s/I_i) + (r_o\sin\theta/a)^2(I_r/I_i) \quad . \tag{11}$$

The value of r_o is 9 cm, the value of θ is about 5° (at 3-dB down point), and the focal radius is 2 mm. The value of I_s/I_i is equal to $10^{-4.3} = 5.0 \cdot 10^{-5}$ and the value of I_r/I_i is equal to $10^{-1.9} = 1.2 \cdot 10^{-2}$, because the reflected pressure is 19 dB less than the incident pressure and the average scattered pressure is 43 dB less than the incident pressure. Substitution of all parameters into eq. (11) gives the result $(W_s+W_r+W_a)/W_i = 0.994$. Since a value of 1.0 confirms the hypothesis, this result is very good, and the sound power is accurately accounted for by reflection, scattering, and absorption. The transmitted power was neglected, since it is scarcely more intense than the forward-scattered sound.

C. Sound Speed

The phase speed, c_p, is defined in terms of the wavenumber, k: $c_p = \omega/k$. This is the speed that an observer of an harmonic wave would travel in order to see a constant wave pressure. The group speed, c_g, is defined also in terms of the wavenumber: $c_g = d\omega/dk$. This is the speed that an observer of a "packet" of sound energy, having by necessity a finite bandwidth, would travel in order to see a constant wave pressure. The two speeds are different whenever the medium is dispersive or whenever k is not a linear function of frequency. We see clearly from the data on figure 3 that sound propagation in diploe is dispersive. This result is consistent with our finding that attenuation is due mainly to scattering, for sound propagation is then dispersive [6].

Experimental measurements of sound speed in bone, including diploe, have almost universally used the time-of-flight of a sound impulse from which to calculate sound speed. This method yields the group speed, although experimenters have not generally noted this. Their results cannot properly be compared with measurements of phase speed in diploe, unless the difference is accounted for.

The definition of group speed yields eq. (12), which expresses the group speed in terms of phase speed.

$$c_g = c_p \left[1 - \frac{f}{c_p}\frac{dc_p}{df}\right]^{-1} \quad . \tag{12}$$

The phase speed calculation from our data on the 4-mm skull sample (fig. 3 and ref. [3]) are plotted on figure 5. We see that a simple frequency-power law fits the experimental data quite well, according to $c_p \sim f^n$, where n = 0.131. In this case eq. (12) gives

$$c_g = c_p(1 - n)^{-1} = 1.15\ c_p \quad .$$

This calculated group speed is plotted on figure 5 together with the experimental values of phase speed.

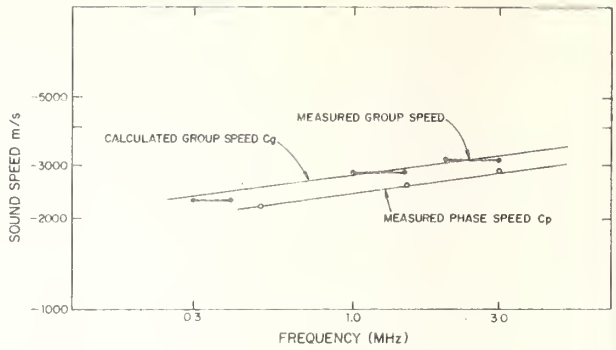

Fig. 5. Measured values of phase speed and group speed in diploe shown with group speed calculated from the phase speed.

The sound speed of the 4-mm diploe sample was measured by the time-of-flight method, using three pulses containing most of their energy between 0.3 to 0.4 MHz, 1.0 to 1.5 MHz, and 2.0 to 3.0 MHz [3]. These measurements give the group speed, and the values are plotted also in figure 5. It can be seen that the measured values of group speed are higher than measured values of phase speed, and that they agree rather well with the calculated values.

D. Use of Focused Beam

A focused beam was used to make the measurements reported herein because only in this way can a narrow beam be generated several transducer-diameters away from the transducer. The scattering of sound by the bone adversely affects the beam shape at the focus only if a parameter $\beta = \sqrt{\pi\ \overline{\mu^2}}\ k^2 aL$ exceeds unity [7]. The mean square deviation of the index of refraction is $\overline{\mu^2}$, the average diameter of a scatterer is a, and the distance traversed by the sound beam is L. For the 4 mm thick diploe sample, the value of the parameter β is only about 0.01, so that no sensible beam distortion or phase aberration is caused at the focus by the scattering in the diploe layer.

4. Conclusions

We conclude that scattering of diagnostic ultrasound by the blood- and fat-filled interstices in diploe dominates sound attenuation at frequencies above about 0.7 MHz and also introduces dispersion.

The detrimental effects of large diploe attenuation can be largely avoided by using interrogation pulses that contain no frequency components greater than about 0.7 MHz. Attenuation due to scattering in the diploe studied equals the attenuation due to absorption at 1 MHz and exceeds it at higher frequences.

The detrimental effects due to diploe dispersion are confined only to the higher frequency range, where scattering dominates attenuation. Therefore, if low-frequency pulses are used, there will be little dispersion. If, however, high frequencies are necessary to obtain trans-skull tissue characteristics by spectral analysis, dispersion can significantly reduce range resolution. For example, if a pulse contained energy in the band from 0.5 to 2.0 MHz, and was transmitted through a 6-mm thick diploe layer, the depth

smearing in the brain due to dispersion would be 0.73 mm, but the nominal depth resolution of the same 1.5-MHz bandwidth pulse in an undispersive water-like medium is 0.5 mm.

We find that almost all reported sound speeds in bone have been obtained by the time-of-flight pulse method and are, therefore, actually group speed. There is no evidence that sound propagation in ivory bone is dispersive, so these data are equivalent to phase speed. Since we find sound propagation in diploe to be dispersive, most published sound speed values in diploe will be higher than correct values for phase speed.

References

[1] White, D. N., Clark, J. M., Curry, G. R., and Stevenson, R. J., The Effects of the Skull Upon the Spatial and Temporal Distribution of a Generated and Reflected Ultrasound Beam (Ultramedison, Kingston, Ontario, 1976).

[2] Lizzi, F. L. and Laviola, M. A., Ultrasonic Spectral Investigations for Tissue Characterization in Ultrasound in Medicine, Denis White and Palph Barnes, eds., Vol. II, pp. 427-39 (Plenum Press, New York, 1976).

[3] Fry, F. J. and Barger, J. E., Acoustical properties of human skull, to be published in J. Acoust. Soc. Amer.

[4] Mason, W. P. and McSkimin, H. J., Attenuation and scattering of high frequency sound waves in metals and glasses, J. Acoust. Soc. Amer. 19, 472 (1947).

[5] Goldman, D. E. and Hueter, T. F., Tabular data of the velocity and absorption of high frequency sound in mammalian tissue, J. Acoust. Soc. Amer. 28, 35-37 (1956).

[6] Howe, M. S., Wave propagation in random media, J. Fluid Mech. 45, 769-83 (1971).

[7] Chernov, L. A., Wave Propagation in a Random Medium (Dover Publications, Inc., New York, 1967).

Reprinted from *Ultrasonic Tissue Characterization II*, M. Linzer, ed., National Bureau of Standards, Spec. Publ. 525 (U.S. Government Printing Office, Washington, D.C., 1979).

TRANSKULL TRANSMISSION OF AXISYMMETRIC FOCUSED ULTRASONIC BEAMS IN THE 0.5 TO 1 MHZ FREQUENCY RANGE: IMPLICATIONS FOR BRAIN TISSUE VISUALIZATION, INTERROGATION, AND THERAPY

F. J. Fry

Ultrasound Research Laboratories of the
Indianapolis Center for Advanced Research
Indianapolis, Indiana 46202, U.S.A.

In order for ultrasound to become a practical clinical technique for diagnosis of many intracerebral diseases in the adult human, it has been necessary to answer questions concerning insertion loss of skull, temporal and spatial characteristics of beams operating in the 0.5 to 1.0 MHz range (the requisite frequency is a function of the particular adult skull) have a maximum single pass skull insertion loss of nearly 10 dB (20 dB for a pulse echo system) which can be handled with present techniques to provide adequate signal strength from normal and pathological features of brain. In this frequency range, for skulls in our studies, the appropriately selected frequency is unchanged after double pass skull transmission, the 6 dB beam width is increased by a maximum of 40 percent and the beam focus is shifted laterally by a maximum of 3 mm. Resolution of string targets or live brain targets has been demonstrated to be in the 2 to 3 mm range at 1 MHz and at 0.5 MHz it appears that 4 to 6 mm resolution can be achieved.

A high intensity focused ultrasonic beam (1 MHz) has been transmitted through an excised adult skull and used to produce a focal thermal flaw in lucite. This simulation test indicates that the induction of transkull focal lesions in live adult brain may now be possible.

Key words: Axisymmetric; beams; focal thermal flaw; skull transmission; ultrasound.

1. Introduction

In the adult human skull the diploe layer is a dominant factor in determining the magnitude of insertion loss for a transmitted ultrasonic beam. Insertion loss characteristics for human skull as a function of frequency have been documented in the literature [1-4][1] but only recently has the acoustic character of the specific skull layers been more clearly defined [5]. These measurements indicate that frequencies less than 0.5 MHz are necessary to have a single pass insertion loss less than 10 dB for some adult human skulls. Skulls we have studied with a loss of this magnitude at a given frequency will transmit an ultrasonic signal of this same frequency with minimal temporal distortion. For infants, the skull insertion loss at ordinarily used diagnostic frequencies (2.25 MHz) is less than 20 dB since there is essentially no diploe layer. Since the two-way insertion loss is twice the one-way loss in a pulse echo regime, the 20 dB maximum skull insertion loss (at the appropriate frequency) is not a serious impediment to pulse echo visualization and interrogation of brain features. Preservation of temporal coherence in the wave is also an important feature and this can be achieved when the appropriate ultrasonic frequency range is selected.

Use of an axisymmetric focused beam in previous studies indicated that preservation of the beam spatial focal character was achieved in a qualitative sense and that the maximum lateral displacement of the beam was of the order of 3 mm. Studies with phased array systems indicated a need for phase compensation at the receiver array to correct for local skull thickness variations which change the arrival time of the waves at the receiver elements [6-8]. Such variations also lead to variable insertion losses over the skull.

This report covers studies in which low intensity axisymmetric focused ultrasonic beams suitable for diagnostic medicine have been transmitted through excised adult human skull sections. The beams have been studied for their temporal and spatial preservation as well as displacement after skull transmission. Transkull B-scan presentations of physical targets and live human brain indicate considerable potential for clinical diagnostic medicine.

[1]Figures in brackets indicate literature references at the end of this paper.

No previous literature seems to exist which indicates the possibility of transmitting an intense focused ultrasound beam through an adult human skull which would be capable of producing focal lesions in brain. A series of experiments reported here shows that a high intensity focused ultrasonic beam of a frequency appropriate for a given skull can be transmitted through the excised adult human skull and produce a thermal focal "lesion" in lucite [9]. Previous studies show that lucite, in the physical model sense used here, can simulate live brain tissue [10].

2. Materials and Methods

Measurement of frequency dependent attenuation loss in skull was made with a system described elsewhere [5]. A schematic diagram of the essential components is shown in figure 1.

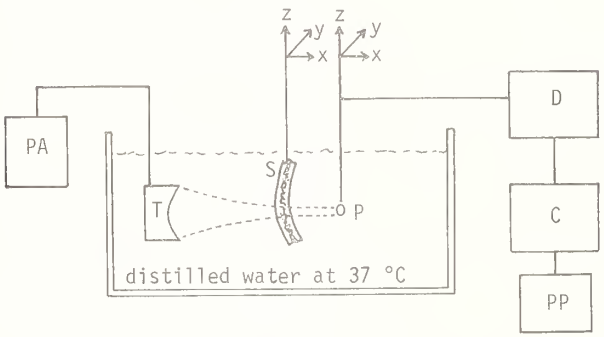

Fig. 1. Schematic diagram for skull insertion loss measurements as a function of frequency.
PA = pulser
T = focused transducer
S = skull (formalin fixed)
P = probe
D = digitizer (8 bit 100 MHz Biomation 8100)
C = computer (PDP-11/45)
PP = printer/ploter (Versatec 1100)
x-y-z = (3 orthogonal) motion coordinate system

Sound from the transducer passes through the skull section under study and is received on a 3 mm diameter ferroelectric probe (10 MHz fundamental resonance). The acoustic signal from the probe is analyzed by an FFT (Fast Fourier Transform) method in the skull and non-skull case, and the difference of the Fourier coefficients at each frequency is taken as the insertion loss at that frequency.

Measurements of beam configuration and displacement after skull transmission were made by moving the probe in a direction perpendicular to the sound transmission axis. The skull is also mounted on a coordinate system so that it can be moved in 3 orthogonal directions. Rotational axes are also provided so that the central ray of the transducer can be angulated with respect to the skull surface.

B-scans of physical models or patients were made with the apparatus shown schematically in figure 2. This apparatus provides a mechanically driven linear scan path. Such a path is very limiting for scans involving skull since it is important to approximately follow the skull contour so that the central transducer ray is normal to the skull surface for minimal insertion loss. In order to have minimal beam displacement, this normal angulation configuration should be preserved.

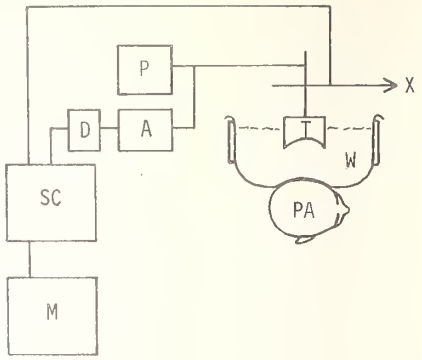

Fig. 2. Schematic diagram for B-scan imaging.
PA = patient
T = tranceiver
W = water bath
X = mechanically driven linear motion
P = pulser
A = amplifier
D = detector
SC = scan converter
M = monitor

For the high intensity focused beam study involving production of thermal "lesions" in lucite (lucite used here as a brain simulation target) the system configuration is shown in figure 3. A 1 MHz high power transducer [11] with a 6 dB down (ultrasound intensity) beam diameter of 2.2 mm was used for this part of the study. The skulls used were obtained from

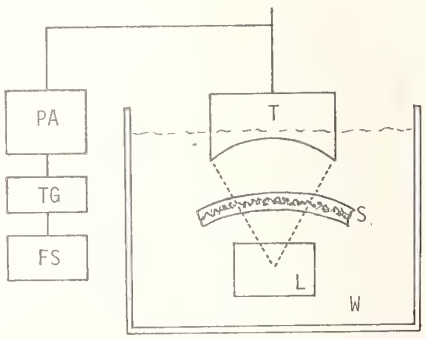

Fig. 3. Schematic diagram for high power transkull test.
T = high power focused transducer
S = skull (formalin fixed)
L = lucite block (2 inch x 2 inch x 2 inch)
W = temperature-controlled water bath
PA = power amplifier (1 kW)
TG = timing gate
FS = frequency source

patients at autopsy and were immediately placed in Ringer's solution and stored in the refrigerator. By the time the experiments reported here were conducted, the skulls had been placed in formalin and stored at room temperature. The storage procedure has been shown to provide the necessary conditions for long-term stability of the acoustical properties of skull starting from the fresh excised state properties [12].

3. Results

One particular adult human skull has been selected from a group used in the preparation of an extensive manuscript [5] on acoustic properties of skull to illustrate the frequency filtering properties of adult skull having a diploe layer. Figure 4 shows the free field probe received waveform transmitted from a focused transducer with a damped resonant frequency of 2.5 MHz. When the skull is inserted between the transducer and the probe the signal strength is greatly attenuated, as will be described later, and the dominant transmitted frequency is 0.56 MHz. When a 0.5 MHz frequency damped pulse is transmitted through the skull, reflected from a glass plate and passed again through the skull, the received waveform recorded from the original transducer is shown on figure 5. The double pass transmission loss is 10 dB for this skull. Use of ultrasonic frequencies in this range (0.5 MHz) is an advantage because of the temporal coherence preservation.

Spatial aspects of beam displacement and distortion after skull transmission for a 0.5 MHz focused beam is demonstrated on figure 6. These beam aspects have been studied with skull-to-probe distances from 2 to 10 cm, which is the range needed for brain target delineation in the intact skull case with the live patient. In these two adult skulls the maximum beam dis-

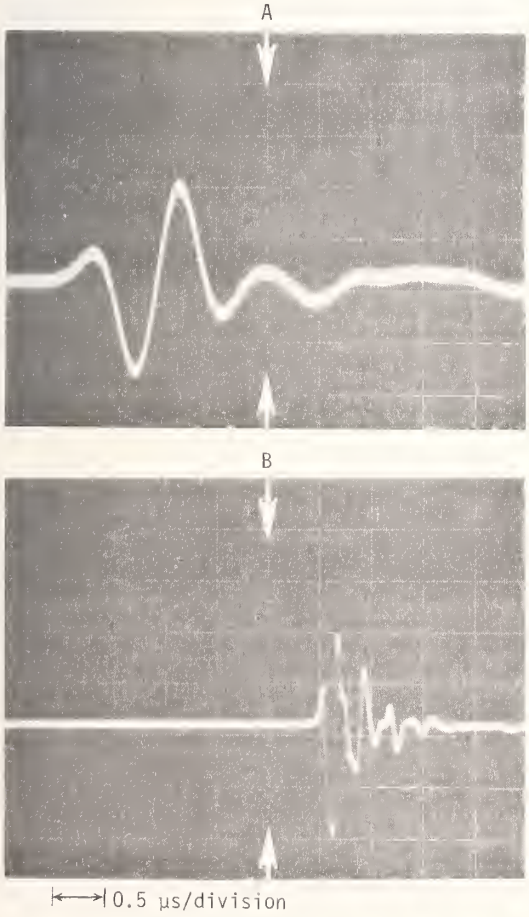

Fig. 4. Probe received waveforms (using setup shown on fig. 1 with an oscilloscope connected in fromt of D).
B = without skull (2.5 MHz)
A = with intervening skull (skull filtering permits 0.56 MHz transmission)

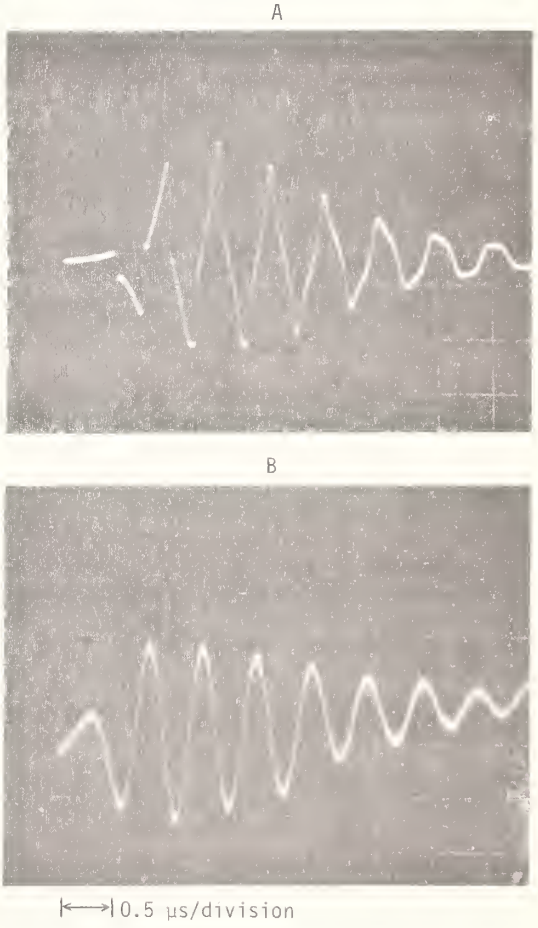

Fig. 5. Transceiver waveforms after reflection from glass plate (using setup shown on fig. 1 with an oscilloscope connected in front of D).
A = without skull (0.5 MHz, distortion is due to the electrical driving network)
B = after skull transmission (0.5 MHz, skull has filtered out the high frequency components in the A waveform but the 0.5 MHz fundamental has been preserved.

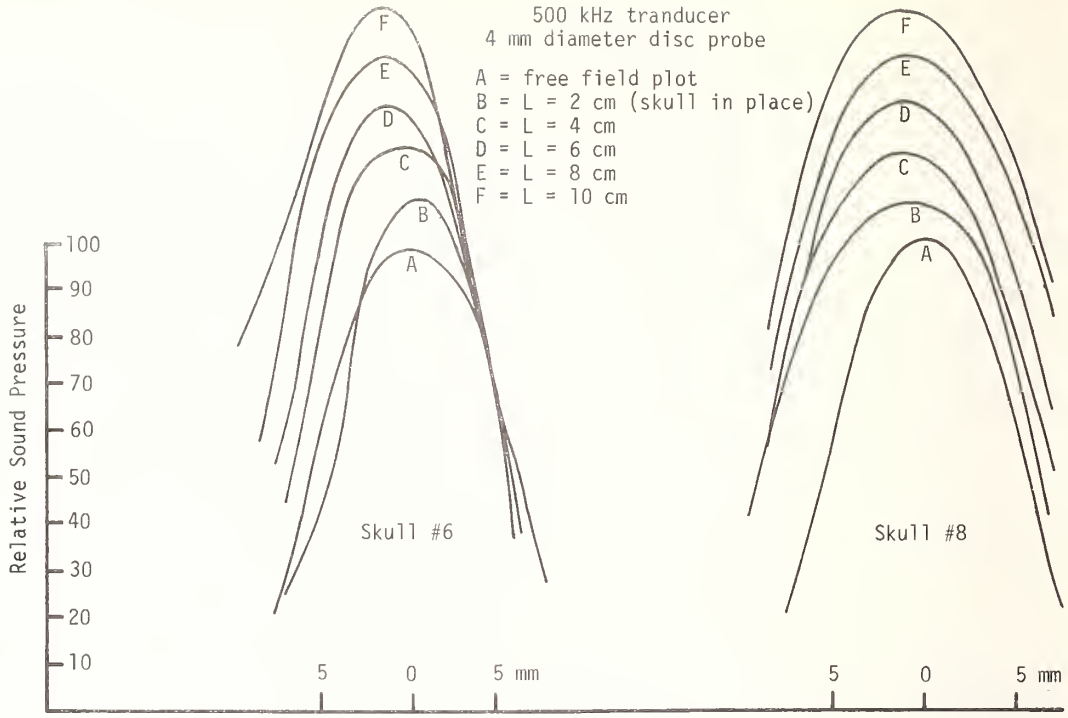

Fig. 6. Beam distortion and displacement after single pass skull transmission as a function of probe-to-skull distance (L) for a fixed transducer-to-probe distance (20 cm). Lateral beam plots and beam displacement obtained by moving the probe for the field plots (using setup shown on fig. 1 with oscilloscope connected in front of D to display the receiving probe output as a function of space coordinate). Insertion loss variations for skulls 6 and 8 were within ± 0.1 dB of the mean insertion loss value for all skull-to-probe distances L. Curves for each L distance are shown vertically displaced on the graph for reading convenience.

placement from the free field condition is 2.5 mm for any probe-to-skull position, and the maximum insertion loss variations for the same range were within ± 0.1 dB of the mean value for all axial distances studied. These studies also show that the 6 dB beam width is increased by a maximum of 40 percent. Other studies show [5] that when a focused transceiver is used with the probe as a target, the 6 dB beam widths decrease in all cases over the 6 dB beam widths in the single pass transmission case with the probe as receiver.

On the basis of temporal and spatial coherence and beam displacement, a 0.5 MHz frequency is appropriate for adult human skulls. The insertion loss characteristic as a function of frequency for adult human skull, shown on figure 7, indicates the desirability of this frequency (0.5 MHz) from a system sensitivity viewpoint if skull insertion loss is to be minimized. Given these indicators for using 0.5 MHz ultrasonic frequency for transskull visualization and interrogation of brain, the important remaining aspect is resolution. Within the scope of these studies, using a very preliminary transceiver prototype (0.5 MHz) and no signal processing to provide image enhancement, the scan of a string target without intervening skull is shown on figure 8. Although the image quality is not ideal, it can be seen that targets spaced 5 mm apart in real space can be resolved. Note also that range resolution has not been optimized since this prototype transceiver is not highly damped.

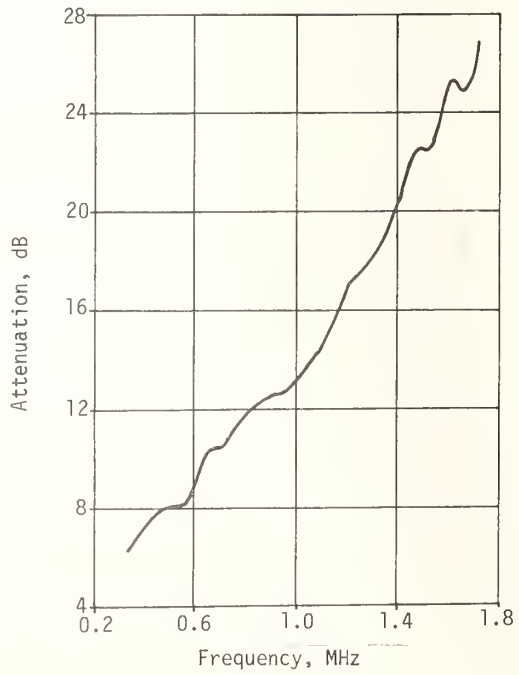

Fig. 7. Insertion loss as a function of frequency for single pass skull transmission (skull 6 section - formalin fixed).

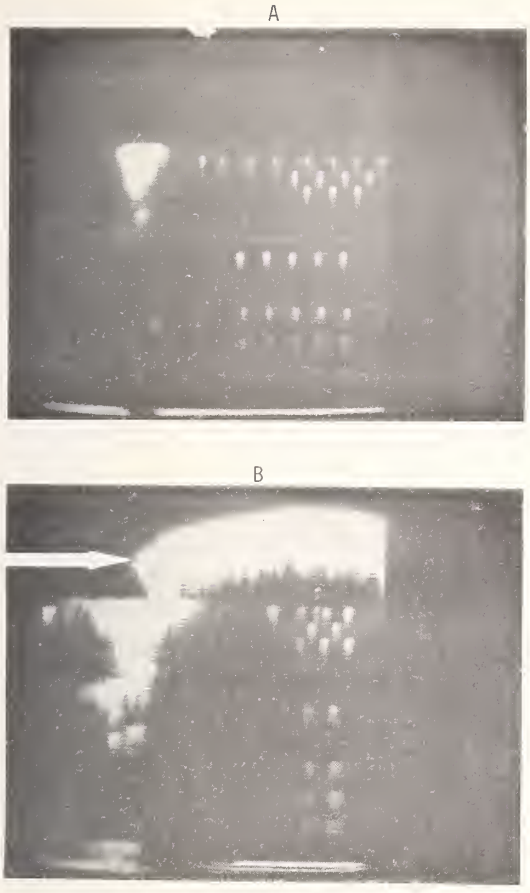

Fig. 8. Monofilament nylon string target (0.01 inch string diameter) with 0.5 MHz focused transducer visualized with system shown on fig. 2.
A = without skull lowest set of 3 x 5 array has strings 1 cm apart on centers.
B = with skull

This resolution will be improved with a larger aperture angle, and with appropriate signal processing this resolution will be apparent over a wide dynamic range of signal strengths. When the skull is interposed there are targets which show evidence of lateral resolution similar to that in the non-skull case. Note that because of this scanning system's inability to follow the skull contour not all strings can be visualized. A scan mode in which the scanning transducer axis is maintained perpendicular to the skull surface at the point of passage of the central ray of the focused beam will resolve this problem.

Our studies include a transkull visualization of a glioblastoma in a live adult patient in which an x-ray transaxial tomographic scan was also made. Results of these scans are shown on figure 9. In this case the skull insertion loss was small enough so that a 1 MHz focused transceiver could be used (this unit is somewhat more optimal than the 0.5 MHz prototype). The tumor tissue was verified by pathological examination at the time of surgery. The computerized axial

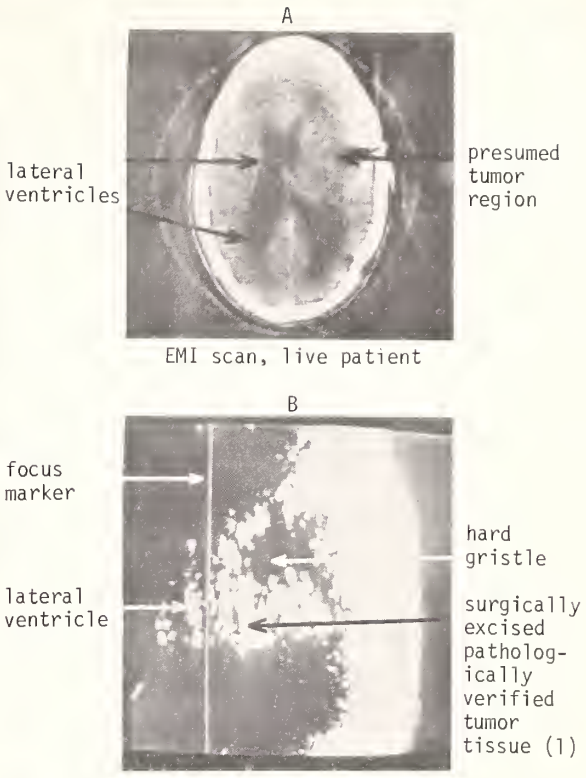

Fig. 9. B-scan of live human patient brain tumor compared to CAT (computerized axial tomography) scan. These scans are of a horizontal section through the brain. The ultrasound scans were made with the system shown on fig. 2.
A = CAT scan
B = ultrasonic scan

tomographic scan showed presumed evidence of a tumor on normal brain structural grounds (ventricular outlines and displacement), but not on a tissue density difference basis. The ultrasound scan clearly shows tissue differentiation. The linear motion scan mode used does not follow the skull contour so that the patient-transceiver angle was selected to permit best viewing over the tumor region. Spatial resolution of some targets in the lateral direction is 2 mm and in the longitudinal direction is 3 mm. It is anticipated that resolution using an appropriate 0.5 MHz transceiver will be no worse than twice these dimensions.

The above material is relevant to ultrasonic regimes for transkull diagnostic purposes and as such uses ultrasonic intensities appropriate to that usage (low milliwatt average intensity range). The subsequent material covers experiments demonstrating transmission through excised adult human skull of intense ultrasonic focal beams suitable for such interactions as focal lesion production in brain.

For this study, the high power transducer was used to produce focal thermal "lesions" in the lucite block brain tissue simulator [10]. These lesions were first produced with no skull intervening in the acoustic path. The human skull section was then inserted in the acoustic path

and focal lesions were produced of a size similar to those produced in the non-skull case. A number of focal thermal lesions were produced at various distances from the lucite surface (typically 2 cm deep). The skull intervening beam plot compared to the free field case is shown on figure 10. The single pass insertion loss was 12 dB for this skull at the 1 MHz operating frequency of the transducer. More extensive coverage of this work is provided in other material [9].

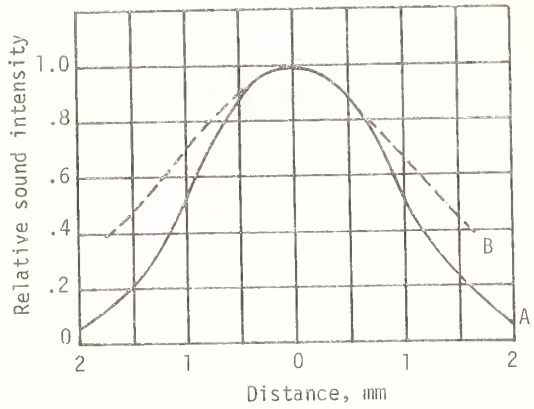

Fig. 10. Lateral beam plot obtained with high intensity focused ultrasonic transducer, with and without intervening skull. Measurements made with systems shown on fig. 1.
A = without skull
B = with skull, the beam axis was shifted 2 mm laterally from the free field position (A) and the insertion loss was 12 dB so no direct intensity comparisons should be made from this figure.

4. Conclusion

This work has shown that for ultrasound to have a significant impact in medicine for diagnosis and/or therapeutics of brain disorders, it is necessary to use ultrasonic frequencies in the 0.5 to 1.0 MHz range. In this range, the single pass insertion losses can be held to a maximum of 10 to 12 dB and the temporal coherence of the wave can be maintained. It has also been shown that the focused beam configuration can be maintained after skull transmission so that the advantages of resolution and intensity gain can be utilized. In diagnosis, these advantages lead to excellent pictorial images of brain structures and ability to perform tissue interrogation on temporarily undisturbed waves due to skull transmission. For potential therapeutics in brain, these ultrasonic techniques offer the possibility of transkull ablation of tumor tissue or other tissues such as that involved for focal epilepsy and modification of blood-brain barrier for enhancing chemotherapeutics of tumor therapy or other brain disorders.

When appropriate ultrasonic frequencies and focal beams are used, it seems apparent that a significant impact can now be made in brain diagnosis and possibly therapeutics with ultrasonic devices and techniques.

Acknowledgments

Work reported here was supported by NIH Grant No. NO1-NS-3-2319, NSF Grant No. APR75-14487 and The Indianapolis Center for Advanced Research.

References

[1] Heuter, T. F., Cavlieri, A., Langmuir, B., Butkus, W., Kyrazia, D., Ballantine, H. T. and Bolt, R. H., The Detection of Intracranial Tumors by Use of Ultrasound, Quarterly Progress Report, Acoustics Laboratory, Massachusetts Institute of Technology, Cambridge, Mass., pp. 38-46, July/September (1951).

[2] Goldman, D. E. and Hueter, T. F., Tublar data of the velocity and absorption of high frequency sound in mammalian tissue, J. Acoust. Soc. Amer. 28 (1), 35-37 (1956).

[3] Martin, B. and McElhaney, J. F., The Acoustic Properties of Human Skull Bones, in Biomedical Material Research, Vol. 5, pp. 325-333 (John Wiley & Sons, Inc., New York, 1971).

[4] Smith, J. W., Phillips, D. J., von Ramm, O. T. and Thurstone, F. L., Real Time B-Mode Echo-Encephalography, in Ultrasound in Medicine, Vol. 2, D. White, ed., pp. 373-381 (Plenum Press, New York, 1976).

[5] Fry, F. J. and Barger, J. E., Acoustical Properties of Human Skull (submitted to J. Acoust. Soc. Amer., 1977).

[6] Phillips, D. J., Smith, S. W., von Ramm, O. T. and Thurstone, F. L., A Phase Compensation Technique for B-Mode Echo-encephalography, in Ultrasound in Medicine, D. White, ed., Vol. 1, pp. 345-404 (Plenum Press, New York, 1975).

[7] Smith, S. W., Mitter, E. B., von Ramm, O. T., and Thurstone, F. L., Signal Processing Techniques for Improving B-Mode Echo-encephalography, in Ultrasound in Medicine, D. White, ed., Vol. 1, pp. 405-414 (Plenum Press, New York, 1975).

[8] Phillips, D. J., Smith, W. W., von Ramm, O. T., and Thurstone, F. L., Sampled Aperture Techniques Applied to B-Mode Echo-encephalography, in Acoustical Holography, N. Booth, ed., Vol.6, pp. 103-120 (Plenum Press, New York, 1975).

[9] Fry, F. J., Transkull Transmission of an Intense Focused Ultrasonic Beam, Ultrasound Med. Biol. 3 (2,3), 179-184 (1977).

[10] Lele, P. P., Irradiation of plastics with focused ultrasound: a simple method for evaluation of dosage factors in neurological applications, J. Acoust. Soc. Amer., 34 (4), 412-420 (1962).

[11] Fry, F. J., Heimburger, R. F., Gibbons, L. V., and Eggleton, R. C., Ultrasound for Visualization and Modification of Brain Tissue, I.E.E.E. Trans. Sonics and Ultrasonics SU-17 (3), 165-169 (1970).

[12] White, D. N., Clark, J. M., Curry, G. R., and Stevenson, R. J., The Effects of the Skull Upon the Spatial and Temporal Distribution of a Generated and Reflected Ultrasonic Beam, available from Ultramedison, Box 763, Kingston, Ontario, Canada (1976).

Reprinted from *Ultrasonic Tissue Characterization II*, M. Linzer, ed., National Bureau of Standards, Spec. Publ. 525 (U.S. Government Printing Office, Washington, D.C., 1979).

SOME ADVANCES IN ACOUSTIC IMAGING THROUGH SKULL

S. W. Smith

Food and Drug Administration
Rockville, Maryland 20852, U.S.A.

D. J. Phillips

Center for Biomedical Engineering
University of Washington
Seattle, Washington 98105, U.S.A.

O. T. von Ramm and F. L. Thurstone

Department of Biomedical Engineering
Duke University
Durham, North Carolina 27706, U.S.A.

Previous attempts to image the adult brain through the skull using diagnostic ultrasound have resulted in images of poor lateral resolution and limited dynamic range. The skull can be modeled as an acoustic lens whose attenuation increases rapidly above 1 MHz and whose thickness variations introduce phase aberrations on the order of several wavelengths across the transducer aperture. Statistical analysis of skull thickness data indicate that an electronic sector scanner using a 1 MHz linear array transducer is less sensitive to these effects of the skull than traditional pulse echo systems operating at higher frequencies. Representative ultrasound tomograms of the brain are shown. In addition, water tank experiments are described in which the skull phase aberration, $\phi(x)$, was measured on line and removed by incorporating a compensating phase variation, $-\phi(x)$, into the transmit and receive timing of a digitally controlled real time phased array imaging system. Preliminary results show that the lateral resolution of the imaging system is restored in both the transmit and receive modes.

Key words: Brain scanning; echoencephalography; neurology; phase compensation.

1. Introduction

Since the initial development of B-mode ultrasonography, there have been many attempts (Fry et al. [1][1]; Brinker and Taveras [2]) to produce high quality cross-sectional images of the brain through the intact adult skull. Real time B-mode echoencephalography was initially demonstrated by Somer in 1968 using phased array techniques. Despite these efforts, B-mode echoencephalography is seldom used clinically because of the poor quality of the images obtained with current techniques. One reason for the immediate widespread application of computerized tomography in the head has been the failure of B-mode ultrasonic imaging of the brain. The intervening presence of the skull results in poor signal to noise ratio, limited dynamic range and reduced lateral resolution.

Three characteristics of skull bone are responsible for poor quality brain images: (1) substantial attenuation of diagnostic ultrasound by the skull bone; (2) rapid increase of that attenuation with the frequency of ultrasound; and (3) the variation of thickness of the inner table of the skull. In order to optimize B-mode ultrasound images of the brain, these aberrating effects of the skull bone must be overcome. By a proper choice of transducer frequency, aperture size, image format, and the use of effective signal processing techniques, significant improvement may be achieved in ultrasound tomograms of the brain. In this manuscript these three problems of acoustic imaging through the skull will be examined. In addition one promising technique will be described in which the effects of phase variations due to the skull have been removed by a phase compensation process implemented with the real time, swept focus, phased array imaging system under current evaluation at Duke University (von Ramm and Thurstone [3]).

[1]Figures in brackets indicate literature references at the end of this paper.

2. Ultrasound Attenuation of the Skull

A propagating ultrasonic pulse is strongly attenuated after two passages through the skull by such phenomena as diffractive scattering, mode conversion, absorption, and the impedance mismatch at the skull-brain interface (White [4]). Previous measurements (Hueter [5]; Smith et al. [11]; Fry et al. [6]) indicate that the attenuation of ultrasound by the skull is strongly frequency dependent increasing from approximately 10 to 20 dB/cm at 1 MHz to 50 to 60 dB/cm at 2 MHz.

In figure 1 the solid curve shows skull attenuation data from Hueter [5] normalized to a 1 cm thickness. The dashed line shows similar data which we obtained from a preserved segment of the adult skull. The data indicate that a 2 MHz signal is attenuated approximately 50 dB/cm of travel through skull bone. The attenuation at 1 MHz is approximately 12 dB/cm. Much of the energy lost from the interrogating pulse returns to the imaging system as unwanted acoustic noise.

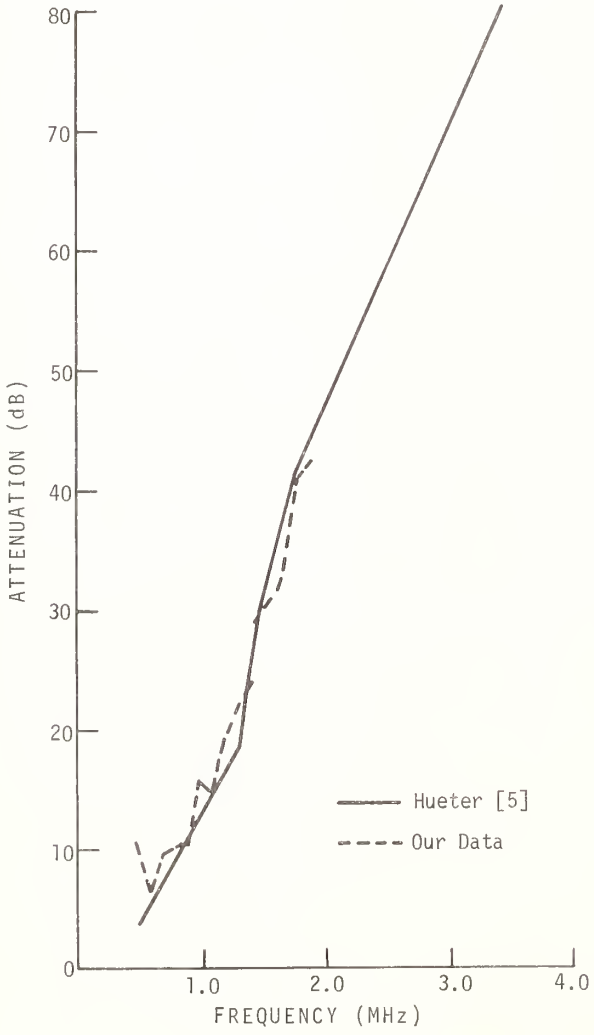

Fig. 1. Attenuation of skull bone versus frequency.

Such a high background reduces the signal to noise ratio, obscuring low level echo information and restricting the useful dynamic range of the imaging system. The result is usually a high contrast B-mode image of the brain in which only the strong specular echoes are displayed. From the figure it can be seen that using a 1 MHz transducer substantially reduces the problem of high attenuation due to the skull.

The rapid increase of attenuation with frequency also degrades the lateral resolution of a B-mode imaging system (Smith et al. [11]). For a typical broadband diagnostic transducer, the ultrasonic pulse contains significant amounts of energy above and below the center-frequency. After two passes through an adult skull the high frequency content of the pulse has been significantly reduced relative to the low frequency components. The center frequency of the ultrasound is effectively shifted to a lower frequency. For a fixed transducer aperture, such a frequency shift will result in degraded lateral resolution. Our experience with linear array transducers and broadband piston transducers has indicated that an interrogating 2 MHz pulse will show a center frequency of approximately .8 MHz after two passes through the temporal region of an adult skull. This results in more than a twofold loss in resolution capability in the lateral dimensions. A 1 MHz ultrasonic pulse is also shifted to approximately .8 MHz but the resultant loss of resolution is not as significant since the original transducer aperture will normally be larger at 1 MHz. For acoustic imaging through the skull, a 1 MHz transducer would appear to be a reasonable compromise considering the requirements of system resolution, adequate sensitivity and transducer size.

3. Thickness Variation of the Skull Bone

Of equal importance is a consideration of the effects of the thickness variation of the skull bone on image quality. In the temporal and parietal areas of the skull where most neurological ultrasound examinations are made, the inner table of the skull bone undergoes variation in thickness on the order of 1 to 2 mm. It has been shown that phase variations are introduced across the transducer aperture when acoustic energy propagates through such a section of skull (Phillips et al. [8]). Figure 2 (Phillips et al. [8]) shows two elements of a one dimensional transducer array simultaneously transmitting an acoustic pulse through a section of skull. (An analogous situation would apply in the receive mode.) Since the acoustic velocity differs between bone and soft tissue, variations in skull thickness will produce relative changes in the phases of the acoustic wavelets emerging from the inner table of the skull. The velocity of sound has been reported to be approximately 3050 m/s in skull bone (Martin and McElhaney [9]) while the velocity in brain has been measured to be approximately 1540 m/s (Wells [10]). The phase variation $\Delta\phi$ can be described by

$$\Delta\phi = 2\pi f\left(\frac{\Delta y}{C_S} - \frac{\Delta y}{C_B}\right) \qquad (1)$$

where Δy is the thickness variations of the skull bone; C_S is the velocity of sound in the skull

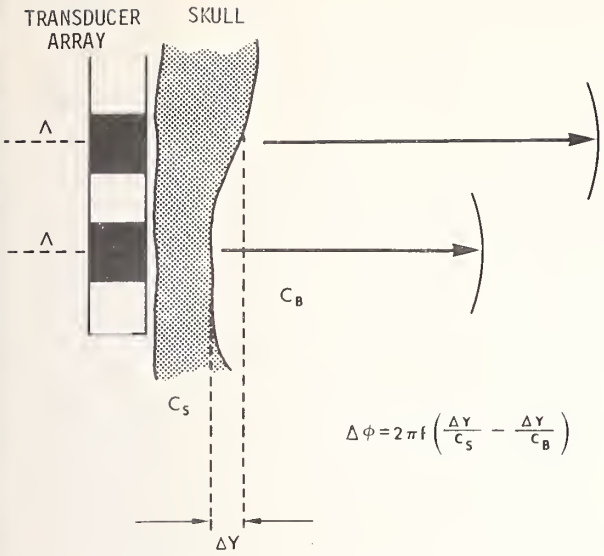

Fig. 2. Phase aberrations introduced by the presence of skull.

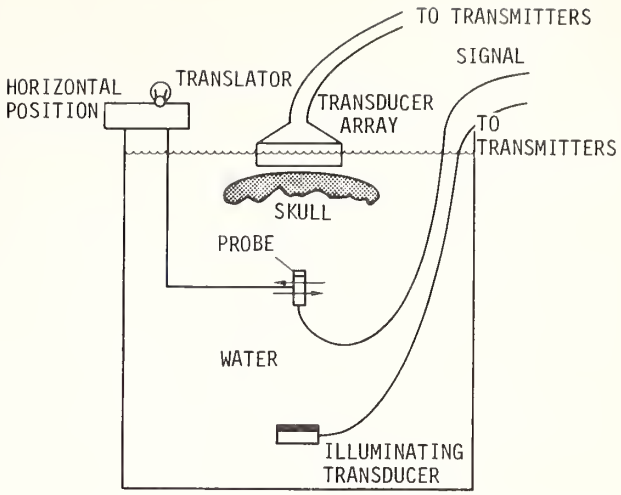

Fig. 3. Measurement system for transducer field plots.

bone and C_B is the velocity of sound in brain.

Based on the attenuation data and skull thickness variation, the skull bone can be modeled as an attenuating plate of varying thickness positioned in front of the transducer array. The validity of this model has been demonstrated by studies of acoustic transmission through skull flaps performed in a water tank environment with a linear array transducer (Phillips et al. [8]). Acoustic field plots, experimentally measured through skull, were compared with calculated field plots using thickness data from the same skulls. If the proposed model of the skull is valid as a first order approximation, then the character of the calculated plots should correlate closely with the experimental field measurements. Sections of skull from the temporal region were frozen upon removal, thawed before experimental use and then continuously stored in water. A diagram of the experimental arrangement is shown in figure 3. The multielement array measured 24 mm in length and consists of 16, equally-spaced, transducer elements. Each element is 0.35 mm in width and 14 mm in elevation. The center frequency was experimentally measured to be 1.8 MHz in water. The linear array was placed just under the surface of the water with the skull flap positioned in close proximity. Independent control of the transmit timing delay for each element was provided by continuously variable, mono-stable multivibrators whose outputs were directly coupled into the solid state transmitter pulsers. The acoustic field patterns of the array were recorded using a small transducer probe which could resolve small spatial variations of acoustic pressure. A Helix transducer probe measuring 0.46 mm in diameter was used for this purpose. The acoustic pressure was displayed on a cathode ray tube and recorded on photographic film as a function of the lateral position of the translated field probe.

The Helix probe was then moved aside and a simple piston transducer 12.5 mm in diameter was used as an illuminating transducer which provided a smooth acoustic wavefront incident at the inner table of the skull. The relative arrival times of the acoustic energy were recorded at the individual array elements. The arrival time or phase variations are directly related to the variations in thickness of the skull across the transducer aperture. As a theoretical check of the proposed model of skull bone, computer simulations of acoustic field pressure were constructed using the relative phase shifts of the acoustic pulses which had traveled through the skull to the individual array elements.

Figure 4 compares the experimental and calculated acoustic field plots which are used to evaluate the ultrasound beam character. Relative acoustic pressure was normalized to the spatial maximum of each scan and plotted as a function of lateral position. The extent of the lateral translation is 25 mm. The element transmit delays were set for a 10 cm Gaussian focus, and the experimental field plot was recorded in the focal plane.

The upper plot shows the measured acoustic pressure at a range of 10 cm without the presence of a skull flap; the middle plot shows the measured acoustic pressure when the adult skull is placed in front of the linear array. Of particular interest is an azimuthal shift of the main lobe to the right and the broad main lobe beamwidth. The bottom plot shows the computer calculation where the experimentally measured arrival times were incorporated into the transmit timing sequence to simulate the acoustic field pattern. In each simulation a transmit pulse character was specified along with an attenuation factor for each element to more accurately represent the experimental situation. However, the amplitude variations across the transducer aperture appeared to be of little significance for thickness variations on the order of ultrasonic wavelengths. If the proposed model of the skull is valid as a first order approximation, then the character of the simulation should correlate closely with the acoustic field plot obtained experimentally. The computer simulation shows an azimuthal shift of 4.9 mm to the

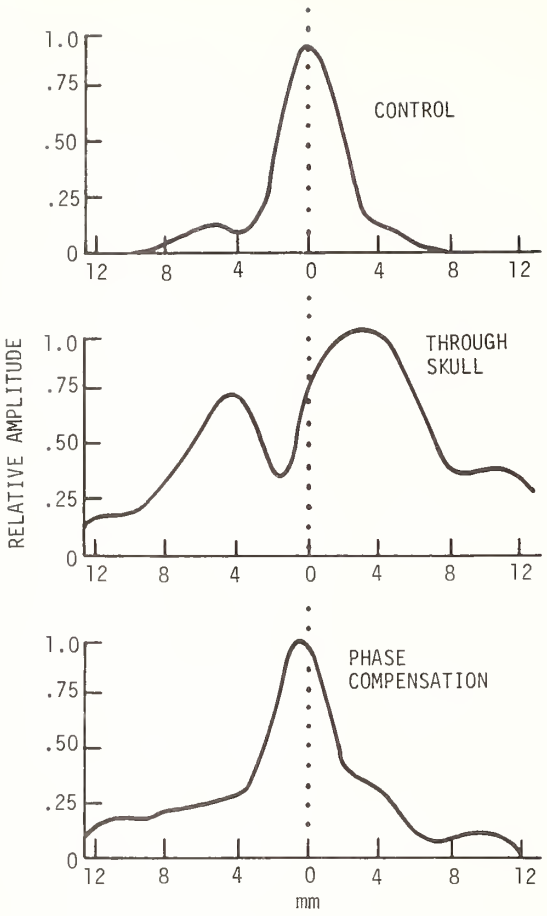

Fig. 4. Comparison of experimental versus calculated transducer field plots through the skull.

right compared with the 5.0 mm shift in the experimental plot. The 6 dB beamwidths in both plots are noted to be 7.0 mm. The overall geometrical similarities lend considerable support to the proposed first order model of the skull.

4. Resolution Limitations in the Presence of Phase Variations

One should now consider what is the extent of image degradation due to skull thickness variation in B-mode echoencephalography. As has been briefly discussed in a previous publication (Smith et al. [7]), the skull thickness itself and hence the phase across a one-dimensional transducer can be written as an n^{th} order polynomial:

$$\phi = A + B_x + C_x^2 + D_x^3 + E_x^4 + \ldots . \qquad (2)$$

where ϕ is the phase variation and x is the location on the skull or transducer. Thus the phase variation due to the skull can be described as the sum of a mean phase shift, a linear phase variation and higher order terms. On the average the magnitude of the coefficients will decrease with higher orders, i.e., the finer grain variations will have smaller amplitudes than, for instance, the linear thickness variation of the skull across the transducer. It is also evident that the thickness variations of the skull will have less significance for imaging systems using longer wavelengths.

The mean thickness and the 1st order thickness variation of the skull make up the first two terms of the phase polynomial. The mean thickness of the skull with its acoustic velocity of 3050 m/s results in a range shift in an individual A-mode or B-mode line. A linear thickness variation of the skull results in a refraction of an A-mode or B-mode line according to Snell's law. A range shift or an azimuthal shift does not alter the beam width of a transducer. Hence, these effects do not degrade the resolution of an A-mode line or individual line of a B-mode image. However, for a linear B-scan or a compound B-scan, a linear skull phase variation which changes as a transducer is moved across the skull can cause distortions and misregistration in both the range and lateral dimensions. A phased array sector scanner as described by Somer [11] or Thurstone and von Ramm [12] produces a B-scan image in real time through a single fixed spot on the skull. Targets comprising such a sector image are shifted uniformly in range and azimuth by the first two terms of the phase polynomial and consequently there is no image distortion.

Second and higher order skull phase variations across the transducer aperture act like an undesired lens and degrade the lateral resolution of a single A-mode line and every type of B-mode scanner. The more random the phase variations, the more disrupted is the diffraction pattern of the transducer. In fact, an upper limit can be put on the resolution capability of conventional imaging through a phase aberrating medium (Goodman [13]). If Δ is the average linear dimension of the transducer over which the phase aberration is constant to within, say, one radian, then the resolution capability of the system is approximately that of a diffraction limited system with an effective transducer aperture, D_{eff}, related to Δ by

$$D_{eff} = \frac{F}{F - \rho} \Delta \qquad (3)$$

where F is the distance from the transducer to its focal point, and ρ is the distance from the transducer to the aberrating medium. Transducer apertures of size greater than D_{eff} collect more energy but have no greater resolution capability. Note that the most severe resolution limitation occurs for $\rho \approx 0$. that is, when the perturbing medium is directly adjacent to the transducer in which case $D_{eff} = \Delta$. Thus, a contact scanner, no matter what its aperture size, is limited to the same resolution as a transducer of size Δ. Long path, focussed, mechanical water bath scanners such as have been described by Fry et al. [1] and Thurstone et al. [14] can maintain larger effective apertures, since the transducer is sufficiently removed from the head so that the surface area of the skull subtended by the beam is very small and the relative phase variation is less significant. However, these mechanical scanners must move over the surface of the skull making them susceptible to registration errors due to refraction effects

from linear phase variations as explained above. Tomograms from a contact electronic sector scanner suffer no distortions from linear phase variations. Therefore, if much of the thickness variation of the skull is a linear variation, an electronic sector scanner will be able to maintain much of its normal resolution capability.

One should now consider how large the thickness variation or phase variation is in the skull in the areas most commonly used for acoustic windows.

For a conventional imaging system, the amount of deviation of $\phi(x)$ from the constant value A, in eq. (2), will be a good predictor of how badly the image resolution will be degraded by phase aberrations.

Fried [15] has considered this question for astronomical imaging, wherein the changing refractive index of the moving air causes a phase aberration affecting optical telescopes. One function which can be used to predict resolution limitation is the root mean square phase variation, normalized to aperture size plotted as a function of aperture size.

$$R = \left\{ < \frac{1}{D} \int_{-D/2}^{D/2} \left[\phi(x) - \overline{\phi(x)} \right]^2 dx > \right\}^{\frac{1}{2}} \qquad (4)$$

$< >$ is an ensemble average, $\overline{\phi(x)}$ is the mean phase across the aperture, and $\phi(x)$ is the phase shift due to the skull at some point, x, within the aperture. To examine this function, phase variations were measured for the 16 elements of a linear array which are separated by 1.5 mm. Sets of readings were taken at 10 different positions in the temporal regions from an adult skull and a pediatric skull. The measurements were made by recording the time of flight of an acoustic pulse as it propagates through the skull and arrives at the elements of the linear array.

For a given aperture size, the mean phase was first determined, and then the squares of the deviations were calculated for each element within that aperture. The sum of the squares was taken and then normalized to the aperture size. This was done for every possible aperture of elements within one set of measurements e.g., for an aperture size of eight elements there are nine possible apertures within each 16 element array. The procedure was performed for each of the ten sets of measurements; a final ensemble average was made, and the square root was taken.

Figure 5 shows the result of the calculations for two frequencies. The root mean square phase variation is plotted in terms of radians versus aperture size for 1.8 MHz and 1 MHz. The function is monotonically increasing at least up to an aperture size of 24 mm. It will level off at some larger size since the maximum thickness variations of the bone are not more than a couple of millimeters.

Fried [16] chooses the criterion that for root mean square (rms) phase variations of 1 radian ($\lambda/2\pi$), the resolution capability has reached an upper limit no matter what the aperture size. Increasing the aperture dimension beyond this point, increases the phase variation so rapidly that many elements on the aperture are always out of phase. From figure 5, the phase variation is

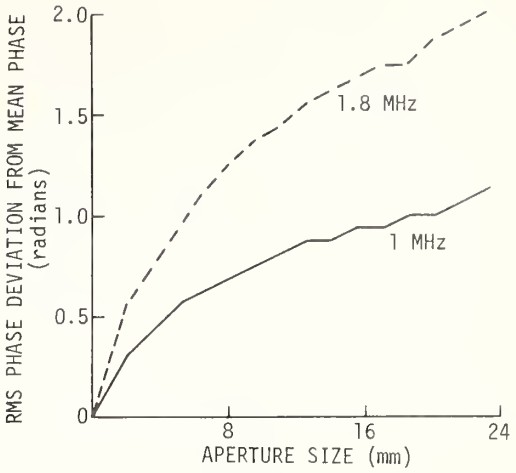

Fig. 5. Root mean square skull phase deviation from mean phase shift versus aperture size.

one radian for an aperture of 6 mm at 1.8 MHz. Therefore, the maximum effective aperture for a conventional contact ultrasonic scanner at 1.8 MHz is 6 mm, i.e., a numerical aperture of 7.3 wavelengths (ratio of aperture size to wavelength) and a resolution capability of 7.8 degrees using the Rayleigh criterion. At 1 MHz the rms phase variation reaches one radian for an aperture size of 18 mm. Therefore, the maximum effective aperture for a conventional contact ultrasonic scanner at 1 MHz is 18 mm or a numerical aperture of 12.2 wavelengths and a resolution capability of 4.6 degrees. One concludes then that in the presence of such skull variations a conventional contact B-scanner can achieve a larger useful numerical aperture and hence better lateral resolution at 1 MHz than at 1.8 MHz.

At this point it would be interesting to make another set of calculations which would be applicable to an electronic sector scanner using a contact transducer. It has been mentioned that such an imaging system is insensitive to linear phase variations across its aperture. Consequently, the relevant function to be calculated is the rms phase deviation, R_L, from the phase slope for a given aperture size; i.e., the deviation from

$$\phi_L(x) = A + Bx \; . \qquad (5)$$

Following the same line of thought as above, we now calculate

$$R_L = \left\{ < \frac{1}{D} \int_{-D/2}^{D/2} \left[\phi(x) - \overline{\phi_L(x)} \right]^2 dx > \right\}^{\frac{1}{2}} \qquad (6)$$

where $\overline{\phi_L(x)}$ is the slope of the phase data for a given aperture size. In this series of calculations, using the same data as above, the slope and intercept were determined by the least squares methods, and the calculations proceeded as above. Figure 6 shows the results to be as expected. For an electronic sector scanner at 1.8 MHz, the rms phase variation reaches a critical value of

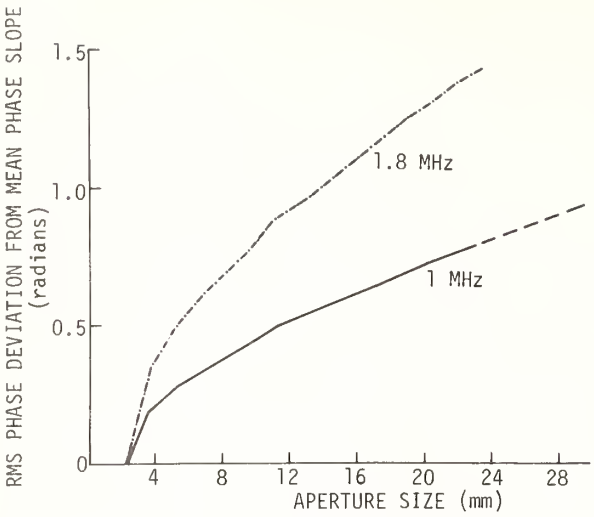

Fig. 6. Root mean square skull phase deviation from phase slope versus aperture size.

one radian at an aperture size of approximately 14 mm. Therefore, on the average, the maximum effective aperture size will be 14 mm or 17 wavelengths and the resolution capability will be 3.4 degrees.

Now at 1 MHz, the rms phase variation for a sector scanner never reaches one radian for the aperture data which we measured. If we extrapolate this curve, we find that it will reach one radian near 1.25 inches or 32 mm. This corresponds to a maximum effective numerical aperture of 21 wavelengths and a resolution capability of 2.7 degrees.

These calculations, based on limited data, have yielded consistent results. For the one-dimensional skull data analyzed here, a 1 MHz transducer can achieve a larger effective numerical aperture and hence better lateral resolution than can a transducer operating at a higher frequency. The considerations of the increasing attenuation with frequency of ultrasound by the skull lend added support to the choice of a 1 MHz transducer for transkull imaging. In addition since a phased array sector scanner is insensitive to linear phase variations due to the skull, such a system would offer advantages in maintaining its resolution capability over conventional B-scanners.

A representative image is shown in figure 7 using the real time phased array B-scan system with a 1 MHz, 31 mm linear array transducer. A horizontal ultrasound tomogram through the skull of a 45 year old female is compared to an anatomical cross-section (Roberts and Hanaway [17]). As indicated, one can see the far skull, the mid-cerebral fissure, the posterior areas of the lateral ventricles, mid-line structures and echoes from the sylvian fissure. The corpus callosum appears as the relatively echo free band between the mid-cerebral fissure and the posterior areas of the lateral ventricles. Images of similar quality along with real time

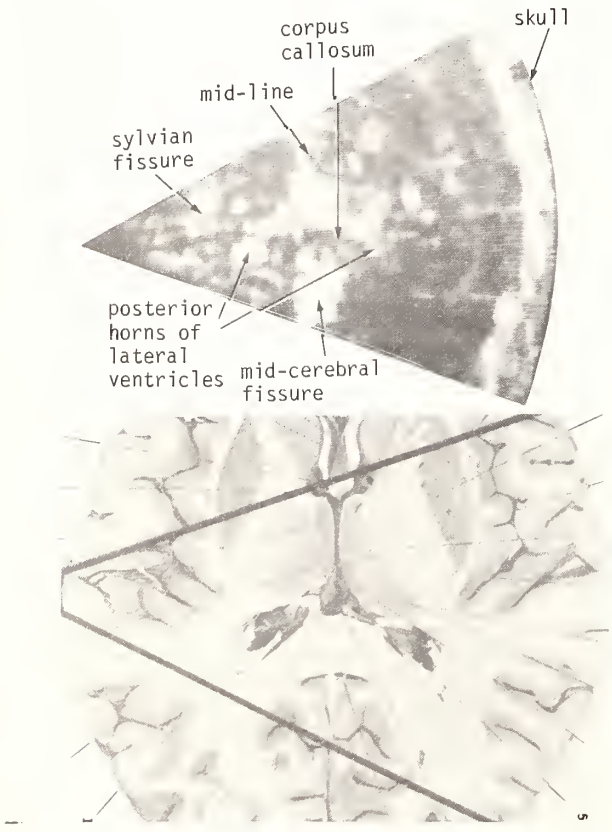

Fig. 7. Horizontal cross sectional ultrasound image of brain through adult skull compared to anatomical brain section.

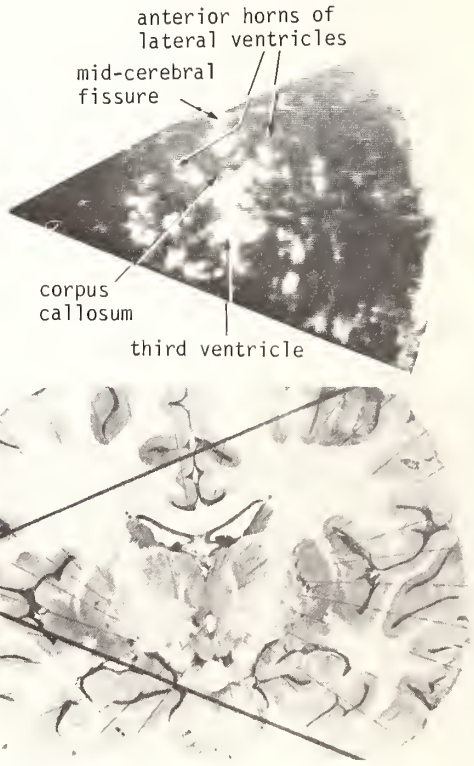

Fig. 8. Coronal cross sectional ultrasound image of brain through skull compared to anatomical brain section.

display or pulsating cephalic blood vessels have been obtained in both horizontal and coronal sections.

Figure 8 shows a coronal scan in a ten year old normal female taken slightly posterior to the pinna of the ear. In this view the far skull, the mid-cerebral fissure, the anterior horns of the lateral ventricles, the third ventricle and the near side sylvian fissure are visualized. Furthermore, the corpus callosum is again seen as a relatively echo-free band above the anterior portions of the lateral ventricles. In this view the posterior cerebral arteries are consistently seen as pulsating echoes in the lower portion of the scan on both sides of the mid-line. In addition, the branch of the middle cerebral artery is also seen quite frequently in the area of the sylvian fissure.

5. Resolution Improvement via Phase Compensation

Having arrived at an improved transducer configuration to overcome partially the attenuation and phase aberration effects of the skull, signal processing techniques have been used in preliminary experiments to remove more completely the effects of skull thickness variations in a phased array imaging system.

Perhaps the most logical signal processing method is to measure the phase variation $\phi(x)$ of the aberrating-medium before an image is made, determine a compensating phase variation, $-\phi(x)$, and then add such a phase compensation to the imaging system in the form of an acoustic lens. Independent control over each element of the transducer array in transmit and receive modes provided a method to produce any desired wavefront response within the limitations imposed by element size and spacing with respect to the wavelength of ultrasound used. Such a process has long been recommended to compensate for lens aberrations in optical telescopes (Tsujiuchi [18]).

Recently several groups have reported construction of large sampled aperture telescopes whose mirror elements will move to compensate for the time varying phase aberrations of the turbulent atmosphere in real time (Muller and Buffington [19]; Hardy et al. [20]).

Figure 9 illustrates the basic principle of the phase compensation technique in an electronic phased array scanner (Phillips et al. [8]). Five representative elements of the transducer array are chosen with a section of skull placed in front of them. Part A shows the phase aberrated wavefronts emerging from a variable thickness skull when the elements are phased to produce a focussed wavefront in a medium of constant acoustic velocity. In B, an acoustic wavefront provided by another source passes from the inner table of the skull to the transducer elements. Knowledge of the spatial character of the incident wavefront and the arrival times at each transducer element allows for the determination of the relative changes in skull thickness in front of the elements comprising the aperture. When these relative phase variations are incorporated into the transmit timing as shown in C, the emergent wavefronts exhibit a restored phase character similar to that originally intended.

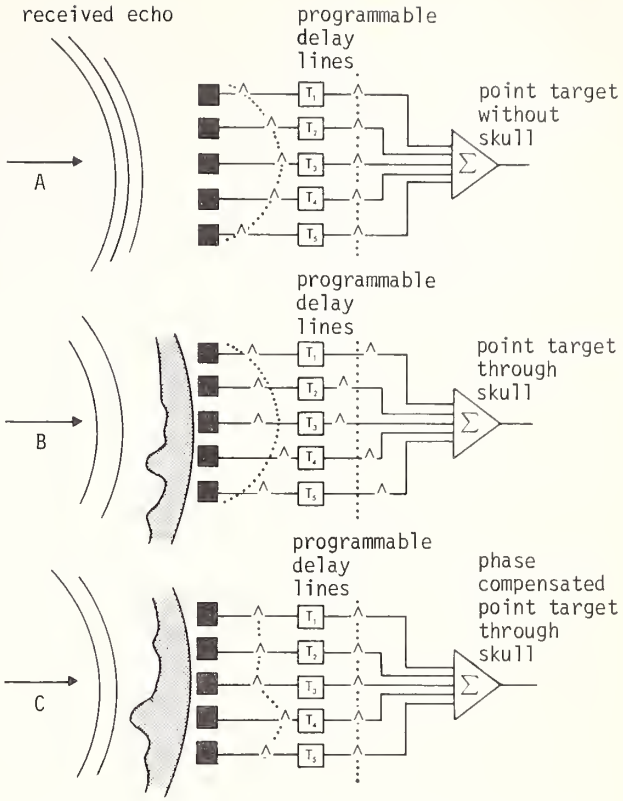

Fig. 9. Principle of the phase compensation technique.

The following experiment using the equipment configuration of figure 3 is presented to illustrate preliminary findings (Phillips et al. [8]) utilizing phase compensation. As shown in figure 10a the control field plot was recorded at a range of 10 cm when the transducer elements were phased for a 10 cm focus and the skull removed. The 6 dB beamwidth was experimentally measured to be 4.5 mm compared with a calculated 4.3 beamwidth for the diffraction limited aperture. Figure 10b shows the beam plot with the adult skull positioned between the array and field probe. The 6 dB beamwidth was increased to 14.0 mm, and a main lobe refraction of 3.0 mm to the right is also apparent. The relative phase changes as a function of skull position in front of the linear array were measured, and the phase compensated beam profile is shown in figure 10c. Although the acoustic beam is attenuated due to a single transmission through skull bone, the phase character due to variations in skull thickness is restored. The refracted lobe was returned to within 0.5 mm of the axis defined in the control, and the 6 dB beamwidth was significantly improved and measured to be 4.5 cm. Although the foregoing studies were performed for the transmit mode in a direction normal to the face of the transducer, it was hoped that similar improvements could be realized when the ultrasound pulse was electronically steered and focussed in the receive mode.

The next step was to perform phase compensation studies for the transmit-receive mode in the water tank environment through a

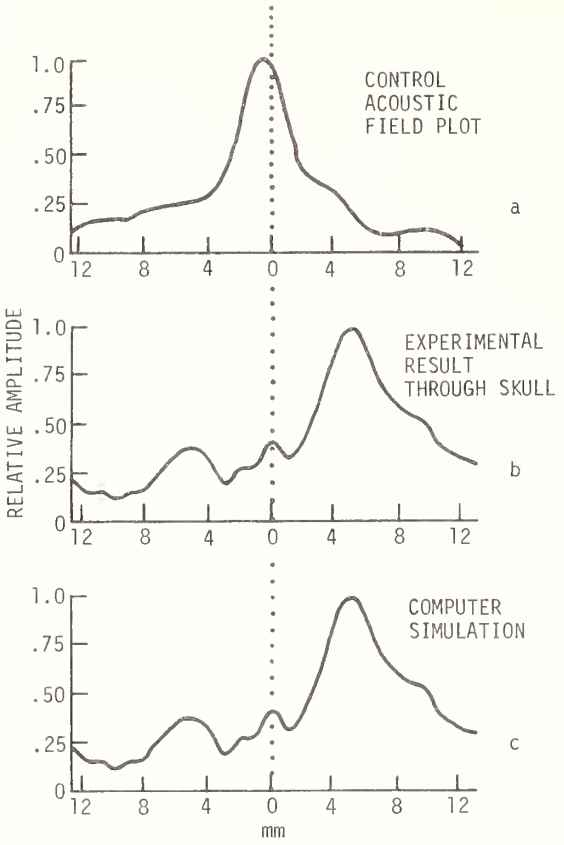

Fig. 10. Acoustic field plots demonstrating phase compensation in the transmit mode.

preserved skull segment. A phased array B-scan system capable of 2 to 4 mm resolution in range and azimuth throughout a 15 cm field of view was used (von Ramm and Thurstone [3]). A 31 mm, 1 MHz, linear array was used to minimize the effects of skull attenuation and reduce the relative phase variation across the transducer as has been described above. To implement the phase compensation technique, pulses from the array passed through the skull and were reflected by a wire target located at a range of 7 cm. Notwithstanding the aberrated character of the initial transmitted pulse, the echoes from the wire target return to the skull as spherical waves since the wire approximates a line reflector of infinitesimal size.

Figure 11 illustrates the process of phase compensation. Part A in figure 11 shows the received echoes for five representative channels. The returning echoes arrive at individual elements of the array according to the spherical character of the incident wavefront. Since the programmable delay lines are sequenced to provide a focus for all points throughout the object volume of interest, the electronic pulses corresponding to the received echoes emerge from the delay lines at identical times as shown to the right. In part B a skull sample was placed in front of the linear array. Due to the aberrating nature of the skull the emerging wavefront no longer resembles a diverging spherical wave. Since the delay times are sequenced for a focus in a homogeneous medium it is not surprising that

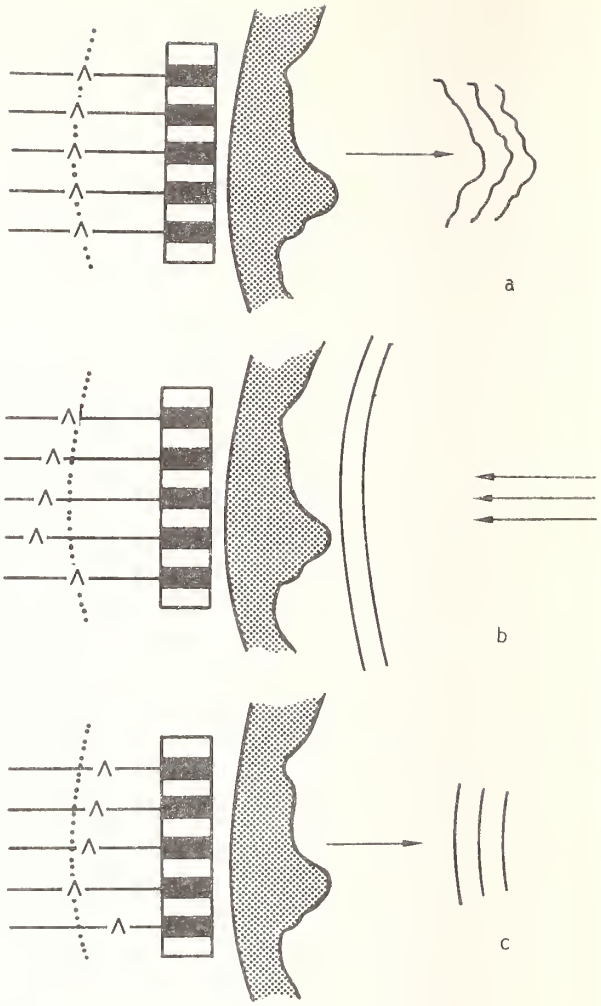

Fig. 11. Principle of phase compensation technique in the receive mode.

the outputs from the delay lines are unable to provide phase coherence for an echo returning from a point target when the skull is interposed. In part C the received echoes from the same point target through the skull flap are restored to phase coherence by adjusting the delays of each delay line under software control, so that all outputs arrive in time coincidence with that of one channel chosen as reference. This procedure removes the timing errors caused when imaging through skull of varying thickness or composition.

Results are shown in the images of figure 12. Each image was made with the gain and reject controls set for optimum resolution. The left hand control image shows the ultrasound image of a line target used to produce the illuminating wavefront and a series of strings of variable spacing (5 mm to 10 mm) without the presence of a skull. The center image shows clearly the degraded resolution in the image of the same targets through a section of bone from the temporal area of the skull. The right hand image shows a significant restoration of image resolution for the line target and the strings in the center of the field of view. Decreased off-axis sensitivity

CONTROL THROUGH SKULL THROUGH SKULL WITH PHASE COMPENSATION

Fig. 12. Resolution targets through skull using phase compensation.

through the skull as the critical angle was approached was responsible for the target dropout at the edges of the field of view. The phase compensation technique clearly reduced the spot size of the targets imaged through the skull, thus restoring much of the azimuthal resolution of the system.

Implementation of the phase compensation technique in a clinical environment will be more complex since additional procedures and techniques must be utilized for ease of clinical use. Of basic importance is the necessity of producing a smooth acoustic wavefront incident at the inner table, within a live, intact head. One can speculate that the pineal gland which is calcified in most adults or the relatively planar structures of the third ventricle or the far side of the skull may serve as adequate reflectors to use to measure the phase variation of the inner table of the skull.

The results presented here are still preliminary. It is difficult to predict how much improvement will be necessary in lateral resolution and target dynamic range before B-mode images of cephalic structures routinely provide information of diagnostic value. However, the improvements presented here are encouraging and may lead to new techniques of acoustic imaging of cephalic structures having acceptable resolution for diagnostic evaluation.

Acknowledgments

This work was supported by USPHS grants HL-12715, HL-14228, HS-01613, and by the Food and Drug Administration, Bureau of Radiological Health.

References

[1] Fry, F. J., Eggleton, R. C., and Heimburger, R. F., Transkull Visualization of Brain Using Ultrasound: An Experimental Study, in Ultrasonics in Medicine, M. de Vlieger, D. N. White, and V. R. McCready, eds., pp. 97-103 (American Elsevier Publishing Company, Inc., New York, 1974).

[2] Brinker, R. A. and Taveras, J. M., Ultrasound cross-sectional pictures of the head, Acta. Radiol. Diag. 5, 745-753 (1966).

[3] Von Ramm, O. T. and Thurstone, F. L., Cardiac imaging using a phased array ultrasound system I: system design, Circulation 53 (2), 258-262 (1976).

[4] White, D. N., Ultrasonic Echo-encephalography. Medical Ultrasonic Laboratory, Kingston, Ontario, Queen's University, 1970.

[5] Hueter, T. F., Messung der Ultraschallabsorption in menschlichen Schädelknochen und ihre Abhängigkeit von der Frequenz, Naturwissenschaften 39, 21-22 (1952).

[6] Fry, F. J., Barger, J. E., and Sanghivi, N. T., Acoustic Properties of Human Skull Bone. (Proceedings of the World Federation of Ultrasound in Medicine and Biology), in Ultrasound in Medicine, D. N. White and R. Brown, eds., Vol. 3, p. 2095 (Plenum Press, New York, 1977).

[7] Smith, S. W., Phillips, D. J., von Ramm, O. T., and Thurstone, F. L., Real Time B-mode Echoencephalography, in Ultrasound in Medicine, D. N. White, ed., Vol. II, pp. 373-382 (Plenum Press, New York, 1976).

[8] Phillips, D. J., Smith, S. W., von Ramm, O. T., and Thurstone, F. L., Sampled Aperture Techniques Applied to B-mode Echoencephalography, in Acoustical Holography, N. Booth, ed., Vol. 6, pp. 106-119 (Plenum Press, New York, 1975).

[9] Martin, B. and McElhaney, J. N., The Acoustic properties of human skull bone, J. Biomed Mater. Res. 5, 325-333 (1971).

[10] Wells, P. N. T., Physical Principles of Ultrasonic Diagnosis (Academic Press, New York, 1969).

[11] Somer, J. C., Electronic sector scanning for ultrasonic diagnosis, Ultrasonics 6, 153-159 (1968).

[12] Thurstone, F. L. and von Ramm, O. T. A New Ultrasound Imaging Technique Employing Two-Dimensional Electronic Beam Steering, in Acoustical Holography, P. S. Green, ed., Vol. 5, pp. 249-250 (Plenum Press, New York, 1974).

[13] Goodman, J. W., Huntley, W. H. Jr., Jackson, D. W., and Lehman, M., Wavefront-Reconstruction Imaging Through Random Media, Applied Physics Lett. 8, 311-313 (1966).

[14] Thurstone, F. L., Kjosnes, N. I., and McKinney, W. M., Ultrasonic scanning of biologic tissue by a new technique, Science 149, 302-303 (1965).

[15] Fried, D. L., Optical resolution through a randomly inhomogeneous medium for very long and very short exposures, J. Opt. Soc. Amer. 56, 1372-1379 (1966).

[16] Fried, D. L., Statistics of a geometric representation of a wavefront distortion, J. Opt. Soc. Amer. 55, 1427-1435 (1965).

[17] Roberts, M. and Hanaway, J., Atlas of the Human Brain in Section, pp. 22-47 (Lea and Feiberger, Philadelphia, 1970).

[18] Tsujiuchi, J., Correction of Optical Images of Compensation of Aberrations and by Spatial Frequency Filtering, in Progress in Optics, II, E. Wolf, ed., pp. 133-182 (John Wiley and Sons, New York, 1963).

[19] Muller, R. A. and Buffington, A., Real time correction of atmospherically degraded telescope images through image sharpening, J. Opt. Soc. Amer. 64, 1200-1210 (1974).

[20] Hardy, J. W., Feibleib, J., and Wyant, J. C., Real Time Phase Correction of Optical Imaging Systems, in Digest of Optical Propagation Through Turbulence (abstract only). July 9-11, 1974, Boulder, Colorado, ThB1-1-ThB1-4.

Chapter 8

IMAGE RECONSTRUCTION

Reprinted from *Ultrasonic Tissue Characterization II*, M. Linzer, ed., National Bureau of Standards, Spec. Publ. 525 (U.S. Government Printing Office, Washington, D.C., 1979).

CHARACTERIZATION OF IN VIVO BREAST TISSUE BY ULTRASONIC TIME-OF-FLIGHT COMPUTED TOMOGRAPHY

G. H. Glover

General Electric Company
Medical Systems Division
Applied Science and Diagnostic Imaging Lab
Milwaukee, Wisconsin 53201, U.S.A.

The use of ultrasonic time-of-flight (TOF) computed tomography for characterization of tissue in live breasts is reported. Quantitative distributions of the refractive index within a tomogram of the specimen were obtained by reconstruction from 5 MHz TOF projection data. Fifteen breast cancer patients and five asymptomatic volunteers were scanned during the clinical feasibility study. The results indicate that young, dense breasts have wide variation in the refractive index distributions. In older subjects, however, various lesions are found to have distinctive indices. Histograms of the reconstructions show differences between pathological and normal breasts.

Key words: Breast cancer; computerized tomography; mammography; time-of-flight; tissue characterization; ultrasonic imaging; ultrasound.

1. Introduction

Ultrasonic energy potentially provides an attractive modality for mass screening programs in breast cancer detection. Its advantage is particularly evident in light of the recent publicity concerning suspected hazards of radiographic procedures. It is, therefore, of interest to characterize quantitatively the ultrasonic properties of breast tissue, with an eye towards differentiation of various neoplasms and breast parenchyma. A useful vehicle for this purpose (and perhaps for mass screening as well) is computerized time-of-flight (TOF) tomography.

TOF tomography was first published by Greenleaf et al. [1][1] in 1975. Since then, several other workers [2,3] have published reports on other aspects of this technology. In this technique, the speed of propagation of an ultrasonic wave is accurately measured along many uniformly sampled paths through the specimen (see fig. 1). The data are obtained from measurements of the time delay for reception of a short pulse traversing the path. In the parallel-scan geometry shown in figure 1, the set of values corresponding to a given angle relative to the specimen collectively form one TOF projection (or view). Other projections are then obtained by rotating the scanner relative to the specimen. A two-dimensional refractive index distribution is then obtained from the projection data by computerized image reconstruction techniques [4]. The result-

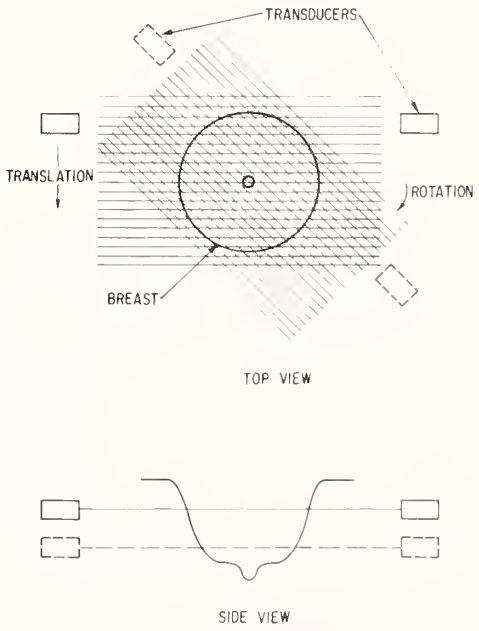

Fig. 1. Geometry of scanner. A single pair of transducers are translated in 1 mm steps to form one projection. One hundred projections are obtained by rotation of the scanner through 180 degrees. Other slices are acquired with the scanner lowered relative to the breast (side view).

[1]Figures in brackets indicate literature references at the end of this paper.

ing images are displayed as an array of square pixels, each of which represents the local speed of propagation supported by the tissue. The process is very much analogous to x-ray computed tomography methods.

The speed of propagation of an ultrasound wave depends upon the elasticity and mass density of the propagating medium. Thus, the TOF reconstructions directly provide quantitative, localized information about significant mechanical properties of the bulk tissue. (By contrast, echo amplitude is a very complicated function of interfacial and bulk tissue ultrasonic characteristics, as well as of geometry.) The propagation velocity has been found to vary by several percent in various types of soft tissue [5]. In this paper, velocity measurements of tissue structure in in vivo breasts are presented and analyzed with the aid of histograms. In the following section, the experimental technique is described.

2. Experiment

A. Technique

Only a brief description is given here as the details have been presented elsewhere [3,6]. The scanner used in the study is shown in figure 2. A transmitter and a receiver transducer (Panametrics, 5 MHz) were rigidly mounted on a carriage which could be translated by a stepping motor. Samples were acquired at 1 mm intervals (163 samples/projection). The tank was mounted under a canvas sling supported by a metal and wooden structure so that the subject lay prone with the breast immersed in the water of the inner tank. Thus, horizontal slices 5 mm thick transaxial to the breast were obtained as shown in figure 1. After the first projection was acquired, additional projections were measured as the tank was rotated through 180 degrees in 1.8 degree steps by a second motor. The TOF data (n seconds of delay) were stored on digital cassette tape for later reconstruction.

Fig. 2. Scanner mechanism mounted in wooden frame. Both tanks are water filled. The breast is immersed in inner tank, which is isolated for electrical precaution.

The reconstructions were obtained using the convolution algorithm [4]. The original reconstruction utilized time-sharing software and were displayed in a 57 x 57 matrix format [6]. For the present work, the images were re-reconstructed in a 64 x 64 matrix representing 12 x 12 cm with a minicomputer. Reconstruction time was about 60 seconds using conventional FORTRAN coding.

The velocity values v are given in CTU values, defined as [6]

$$CTU = \frac{v - v_0}{v_0} \times 1000, \qquad (1)$$

where v_0 is the velocity of propagation in the water (at about 34 °C). Thus, +10 CTU corresponds to a velocity 1 percent greater than for water.

The clinical study was performed at the Albany Medical College. Fifteen symptomatic patients and five asymptomatic volunteers were scanned. Mammograms and clinical reports for the patients were available before the scans to help localize the region of interest. Generally, three slices 1 cm apart for the pathological breast and one slice of the contralateral breast were acquired. After the TOF scans, biopsies were performed on the suspicious breasts. These results were then made available for comparison with the reconstructions. A thorough historical comparison would have been desirable, but was outside the scope of this study.

B. Results

Figures 3 and 4 show typical reconstructions of breasts having lesions. In these pictures, high velocities are depicted as black. Figure 3 shows a right breast (age 53) containing a large (benign) fibroadenoma. The CTU values for the lesion are 20-28, while the mammory fat (white areas) has CTU values of about -60. The left breast depicted on figure 4 (age 44) contains infiltrating ductal carcinoma with CTU numbers 40-45. The mammory fat has CTU values similar to those in figure 3.

The streaking artifacts in these pictures derive from patient motion during the long scan time required to obtain the data (about 9 minutes/slice). As a result, the pictures are much noisier (standard deviation, $\sigma \simeq 10$ CTU in the water bath) than the intrinsic velocity resolution of the system determined with a stationary phantom ($\sigma \simeq 2$ CTU). Nevertheless, the reconstructions are of sufficient accuracy to characterize the large-mass lesions studied here.

Table 1 presents a summary of the CTU values for several types of lesions as well as fat and asymp-

Table 1. Summary of CTU values for several types of lesions, fat and asymptomatic breast parenchyma.

	CTU numbers
Symptomatic patients (ages 33 to 85)	
mammary fat	-50 to -70
normal parenchyma	0 to 15
fibroadenoma/fibrocystic disease (benign)	12 to 30
carcinoma	40 to 60
inflammatory skin thickening	40 to 65
Asymptomatic subjects (ages 24 to 29)	
fibrotic mammary glands, ducts	8 to 60

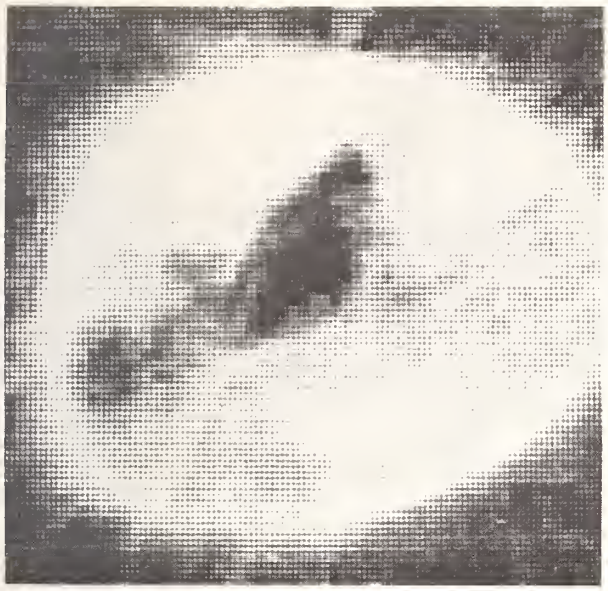

Fig. 3. Reconstruction of breast with large fibroadenoma (black region).

Fig. 4. Reconstruction showing infiltrating ductal carcinoma (lower quadrant) and inflammatory carcinoma central region.

tomatic (presumed normal) breast parenchyma. In the older patients, the CTU values were found to be distinctive for fat, normal parenchyma, fibrotic tissue, and carcinoma. Malignant lesions and inflammatory skin thickening due to the presence of an internal malignant neoplasm have characteristic CTU numbers greater than 40, while benign lesions (fibrocystic disease, fibroadenoma) have CTU values less than 30. However, the CTU values for the dense breasts of the younger asymptomatic subjects span the entire range. It is, therefore, impossible to differentiate solely on the basis of CTU value neoplastic tissue from normal fibrotic parenchyma in such cases.

In several slices wherein the lesion did not completely fill the 5 mm axial slice thickness, the CTU values were less than the bulk numbers in the table. These partial volume effects arise because the component of transmitted signal which arrives earlier due to traversal through the high velocity lesion ultimately becomes too low in amplitude to be detected relative to the signal components which exclude the lesion. The transition is not perfectly sharp due to refraction and tissue dependent attenuation effects. Excluding such cases, however, there were no counter-examples to the CTU values classifications in the table.

3. Statistical Analysis

A rudimentary statistical analysis of the reconstructions was performed by computing the histograms and cumulative distribution functions. For this purpose, a program was developed which searched the matrix for the edge of the breast, fit an arbitrary ellipse to the boundary points by regression, and calculated the histogram for those elements within the ellipse. The class interval was chosen as 3 CTU numbers in computing the histograms. The results were normalized to remove variations in specimen size. Figure 5 shows histograms for a young, asymptomatic subject. Note that the two normal breasts have similar tissue distributions. This was not always the case, although generally the skew and kurtosis of the histograms were similar. The distributions are peaked near CTU = 0 and contain considerable fibrotic tissue with high CTU numbers. The variations in the histograms for different young subjects were quite wide. This is illustrated by plotting the (inverse) cumulative probability function.

$$\emptyset_j = \sum_{i=j}^{N} f_i \qquad (2)$$

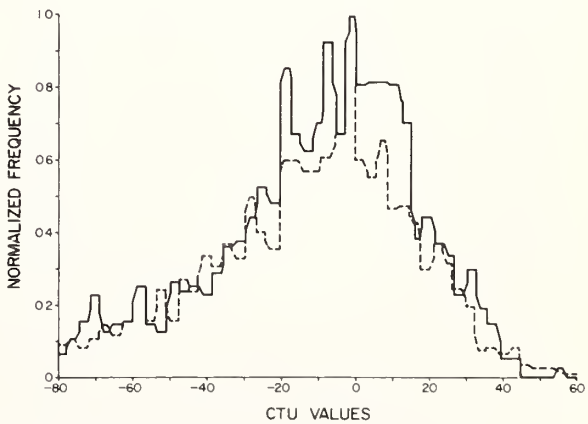

Fig. 5. Histograms of right (solid) and left (dashed) breasts of 24 year old asymptomatic subject. The distributions are very similar and centered near CTU = 0. Considerable fibrotic structure is evident from the peak position and area under the high valued tails.

where f_i is the frequency for the i^{th} CTU value. Curves for three of the subjects are shown in figure 6. As may be seen, the curves span a large range of CTU values.

Fig. 6. Inverse cumulative probability function for three normal, young subjects. The zero asymptotes (which reflect peak CTU values) show wide variation.

Figure 7 shows histograms for a 58 year old patient with carcinoma in the right breast and a normal left breast. Note that the peak for the normal histogram has shifted position to low negative values relative to figure 5. This reflects the atrophy of glandular structure (high CTU) and

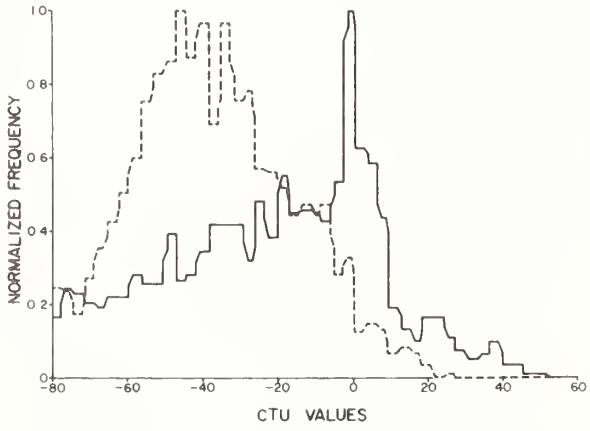

Fig. 7. Histograms of 58 year old patient with carcinoma in right breast (solid) and normal (dashed) left breast. The normal distribution is peaked near CTU = -40, indicating atrophy of the glandular tissue and replacement by fat. The kurtosis and skew of the histogram for the pathological breast are markedly dissimilar to the normal one.

replacement by fat (low CTU) in the post-menopausal breast. Although not enough data is available from this study, undoubtedly the peak position is a decreasing function of age [7]. The histogram for the pathological breast has markedly dissimilar shape (skew and kurtosis) and extends to higher CTU values. The carcinoma is contained in the high valued region. (The peak near zero probably represents some water being included in the histogram by the algorithm.) Figure 8 shows examples of cumulative distribution plots

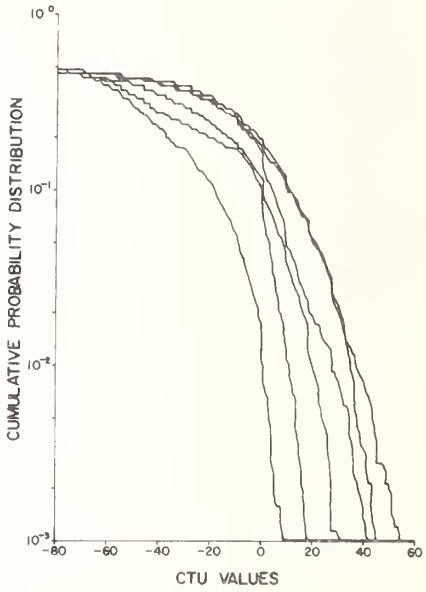

Fig. 8. Inverse cumulation probability function for a representative sampling of the older patients. The zero asymptotic values can be roughly correlated with tissue type. - - - = normal, ... = fibroceptic/ adenoma, _____ = carcinoma.

for older normal breasts, and breasts containing fibrotic and carcinoma tissue. In general, figures 6 and 8 tend to reflect the results of all the scans summarized in table 1.

4. Discussion

Human female breasts are constituted of time varying fractions of various components. It appears plausible that each of these components (parenchyma, glands, fat, etc.) have ultrasonic properties which are relatively similar between different subjects. Indeed, the wide variation in average and peak CTU numbers observed for young dense breasts probably represents an incomplete analysis of the volumetric fractions of glandular tissue, fat, and ducts present in any given subject. In any case, a single number representing velocity values averaged over the volume of a breast [7] is probably too simplistic to be representative of the breast.

The symptomatic subjects examined in this study were chosen to have large, unambiguous lesions in order to acquire data on the various tissue components. These data, however, represent a statistically insignificant number of cases on which to

base any absolute conclusions. In fact, a larger data base will probably show wider variation in values than was found in this study. Nevertheless, the present results suggest a distinction between normal and neoplastic tissue which is encouraging for mammographic application.

There are potentially several methods of utilizing the TOF data in cancer detection suggested by the histograms. When available, histograms of the contralateral breast provide a reference which could form part of a comparative basis. Alternatively or additionally, a reference base which depends on age and other variables can be accumulated. Besides the histograms, which present a volumetric picture of the constitutive elements, the individual pixel values, rates of change, and geometry can be searched for characteristic patterns. Application of such speculation, however, must await the acquisition of more massive amounts of data.

Acknowledgments

The clinical data was acquired with the help of R. W. Sponzo, M.D., his staff and colleagues at the Albany Medical College.

References

[1] Greenleaf, J. F. et al., Algebraic Reconstruction of Spatial Distributions of Acoustic Velocities in Tissue from their Time of Flight Profiles, in Acoustic Holography, W. Booth, ed., Vol. VI, pp. 71-89 (Pergamon Press, New York, 1975).

[2] Carson, P. L., Oughton, T. V., and Hendee, W. R., Ultrasonic Transaxial Tomography by Reconstruction, in Ultrasound in Medicine, D. White and R. Barns, eds., Vol. II, pp. 341-350 (Plenum Press, New York, 1976).

[3] Glover, G. H. and Sharp, J. C., Reconstruction of Ultrasound Propagation Speed Distributions in Soft Tissue: Time-Of-Flight Tomography, IEEE Trans. Sonics and Ultrasonics SU-24, 229-234 (1977).

[4] Gordon, R. and Herman, G. T., Three dimensional reconstruction from projections: a review of algorithms, Internat. Rev. Cytology 38, 111-151 (1974).

[5] See, e.g., Wells, P. N. T., Review: absorption and dispersion of ultrasound in biological tissue, Ultrasound in Med. and Biol. 1, 369-376 (1975).

[6] Glover, G. H., Computerized time-of-flight ultrasonic tomography for breast examination, Ultrasound in Med. and Biol. (in press).

[7] Kossoff, G., Fry, E. K., and Jellins, J., Average velocity of ultrasound in the human female breast, J. Acoust. Soc. Am. 53, 1730-1736 (1973).

Reprinted from *Ultrasonic Tissue Characterization II*, M. Linzer, ed., National Bureau of Standards, Spec. Publ. 525 (U.S. Government Printing Office, Washington, D.C., 1979).

VARIATION OF ACOUSTIC SPEED WITH TEMPERATURE IN VARIOUS EXCISED HUMAN TISSUES STUDIED BY ULTRASOUND COMPUTERIZED TOMOGRAPHY

B. Rajagopalan, J. F. Greenleaf, P. J. Thomas,
S. A. Johnson, and R. C. Bahn

Biodynamics Research Unit
Departments of Physiology and Biophysics, and
Department of Pathology and Anatomy
Mayo Clinic and Mayo Foundation
Rochester, Minnesota 55901, U.S.A.

Variation of acoustic speed as a function of temperature was measured in fresh excised human liver, psoas muscle, spleen, spinal cord, kidney and fat, parenchyma and muscles associated with female breasts. Tissues were encased in rubber finger cots and suspended in a temperature controlled water bath. A prototype clinical ultrasound breast scanner was used to obtain data required to reconstruct distributions of acoustic speed within two-dimensional planes through the tissue specimens over a temperature range of 20 to 40 °C. Quantitative images (printer listings of acoustic speed) of 64 x 64 pixels were used to obtain averages of up to 16 speed measurements within the image of each tissue. The acoustic speed in most tissues increased monotonically with temperature following the behavior of water. Acoustic speed of fat showed an anomalous decrease in acoustic speed around 34 °C suggesting possible phase transition.

Key words: Aperture synthesis; computed tomography; Doppler; fluid flow; high resolution; reconstruction; temperature reconstruction; ultrasound.

1. Introduction

Historically, production of images by ultrasound scanning has been done by displaying either the pulse echo reflected from an object (B-scan) or by displaying the attenuated signal (C-scans) transmitted by an object [1][1]. These modalities, although useful, give only a qualitative mapping of tissue interfaces and geometries. Images representing quantitative distributions of basic mechanical tissue properties as characterized by ultrasound scattering cross section, impedance [2,3] and acoustic speed [4] may be intrinsically more valuable than the qualitative images representing tissue borders and geometries. A quantitative imaging modality would eliminate operator-dependent variations one often finds in the qualitative imaging modalities. Ultrasound computerized tomography [4] is one such imaging modality by which the distribution of one fundamental mechanical parameter, i.e., acoustic speed, in a tissue can be studied.

The purpose of this report is to describe methods and initial results of applying computerized tomography to the problem of obtaining quantitative images representing the distribution of acoustic speed and the effect of temperature on these values for tissues from various parts of the body, especially the human breast. The knowledge of temperature coefficients of acoustic speed in tissues may be useful in estimating the temperature change in a region of tissue occurring due to external causes such as ultrasonic heating or drugs. Since various disease processes alter tissue temperature, the temperature coefficients may also be helpful in the interpretation of computerized tomography images of live tissues.

The reconstruction problem in ultrasound computerized tomography has been described elsewhere [4] and will not be described in detail here. A good introduction to the basic mathematics of computerized tomography and a general overview of the analytical and iterative algorithms can be found in the review articles by Gordon and Herman [5] and Brooks and Dichiro [6]. The convolution reconstruction algorithm for the divergent beam geometry was first derived by Lakshminarayanan [7] and later a mathematically rigorous treatment of the same problem leading to identical results was given by Herman and his coworkers [8]. This divergent beam convolution reconstruction algorithm is used exclusively for all the reconstruction images in this paper.

2. Experimental Arrangement

In ultrasound computerized tomography the profile data consist of measurements of time-of-

[1]Figures in brackets indicate literature references at the end of this paper.

flight of an acoustic pulse through the sample along different rays or directions. The data are obtained by divergent beam scanning with a single pair of transducers one on each side of the region of interest. The schematic of the data collection geometry is shown in figure 1. The scan angle is α and is incremented at 0.15° intervals using a stepping motor. After the scan the ultrasound transmitter-receiver arm is rotated to a new θ position and another scan is initiated. Thus, for each θ position there is one profile of time-of-flight data. One hundred twenty profiles separated in view by 3° increments are gathered over the 360° range.

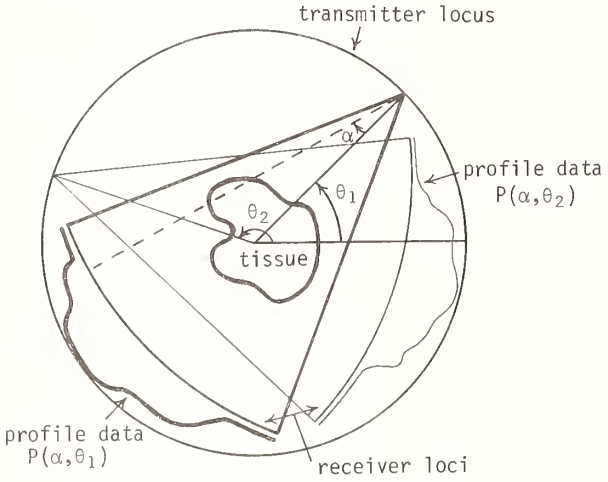

Fig. 1. Data collection geometry for ultrasound tomography. θ_1 and θ_2 are the angles made by the central ray in the scan with x-axis for two different scans. Profile data $P(\alpha,\theta_1)$ is gathered by rotating the receiver-transmitter arm about an axis passing through the apex of the sector and perpendicular to the plane of the figure. Thus, the receiver loci are arcs. The transmitter mounted at the axis of the scan describes a circle as profile data from different views (θ) are gathered.

The schematic of the experimental arrangement for collecting computerized tomography data is shown in figure 2. The system is driven by an Interdata 7/32 minicomputer which controls the height and rotation angle (θ) of the scanner arm and collects the time-of-flight data from the digital output of the time-of-flight (TOF) clock and control box. This TOF clock and control box is interfaced to the digital I-O of the minicomputer and upon a command from the computer collects time-of-flight data, outputs the data, steps the scanner arm to the next orientation in the scan and repeats this process until one profile of data are collected. At the end of the scan the scanner arm is rotated to the new θ position by a command from the minicomputer and the process of collecting profile data resumed by a trigger to the TOF clock and control box. These time-of-flight profiles representing propagation delay of acoustic pulses along many rays through the tissue under examination are input to the reconstruction programs to obtain quantitative distributions of

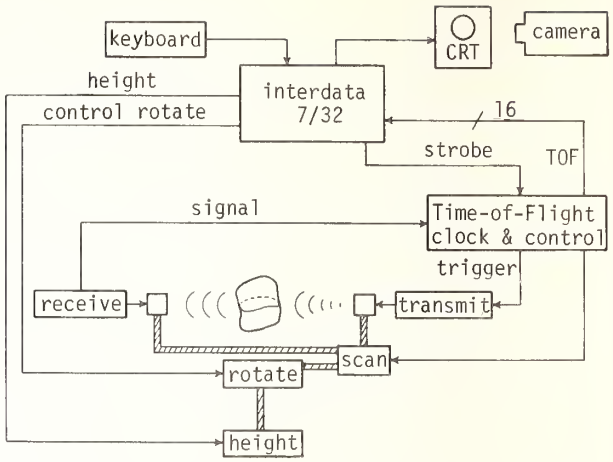

Fig. 2. Ultrasound computed tomography system: Data collection and control. Computer controls transmit-delay-and position. Time-of-flight of signal is measured with a 16-bit 100 MHz clock and counter which is read by the computer at up to 400 points along a scan profile, each point separated by 0.15°. One hundred views each containing 400 samples and each sample containing eight channels of 16-bit time-of-flight data can be obtained in a period of 2.5 minutes.

acoustic speed in the transverse plane through the tissue.

3. Reconstruction Algorithm

The mathematical steps to arrive at the reconstruction picture from the set of profile data are given in this section without attempting to derive any of them. These steps known as the reconstruction algorithm are treated extensively in the literature and the derivation for divergent beam geometry starting from Radon transform [9] can be found in the reference mentioned earlier [8].

The raw data of each profile consist of time measurements (in seconds x 10^{-8}) at each increment along the arc of the scan. The data for the 20 or more points closest to each end of the profile are the time-of-flight for sound through water, and never vary by more than one unit (10^{-8} s) from the lowest to the highest. The average of the first few points is subtracted from each point of the profile and the differences $P(j,\theta)$ represent the profile data for reconstruction. Here θ is the angle made by the central ray of the scan with x-axis (arbitrarily chosen) and $j = -n \ldots -1, 0, 1, \ldots +n$ indexes the angles of the $2n+1$ individual rays of the scan with $j = 0$ at the center of the scan. For each rotation angle θ the profile data are reduced by the cosines of the angles of the individual rays from the center line.

$$P(j,\theta) \text{ modified} = P^*(j,\theta) = P(j,\theta) \cos(j\epsilon) \qquad (1)$$

where ϵ is the constant angular increment in the scanning motion (0.15°). The modified profile

$P^*(j,\theta)$ is convolved with a kernel to give the convolved modified profile $C(k,\theta)$, i.e.,

$$C(k,\theta) = \sum_{i=k_{min}}^{k_{max}} A_i \, P^*(i-k,\theta) \qquad (2)$$

The kernel is given by

$$A_0 = \left(\frac{1}{4}\right) D\varepsilon \qquad (3)$$

$$A_i = 0 \text{ for even } i \text{ and } i = 0$$

$$A_i = \frac{-\varepsilon D}{r^2} \sin^2(i\varepsilon) \text{ for odd } i$$

where D is the distance from the axis of rotation for the scanning motion to the axis of rotation for rotate motion and k_{min} and k_{max} indicate the lower and upper limits of the scan. Finally, the back-projection is formed, along the lines of the acoustic rays, converging at the axis of scan motion, with the back-projected $C(k,\theta)$ weighted with inverse square of the relative distance of the point from the axis of the scan to distance D. Thus, for each time-of-flight profile at an angle θ the matrix $f(x,y)$ forming the reconstructed picture is incremented by

$$\Delta f(x,y)_\theta = \frac{\varepsilon}{2} C(k,\theta) \frac{D^2}{r^2} \qquad (4)$$

where r = distance of the point (x,y) from the axis of the scan. $C(k,\theta)$ is interpolated if no ray goes through the point (x,y). The sum of all the back-projected $\Delta f(x,y)_\theta$ for all θ values yields the reconstructed image at (x,y).

$$f(x,y) = \sum_{\text{sum over } \theta} \frac{\varepsilon}{2} C(k,\theta) \frac{D^2}{r^2} \qquad (5)$$

When the back-projection is finished, the value for each pixel will be the increase or decrease in time per centimeter at that point, compared with water. The time-of-flight for water (in the same units, calculated from the measured time and known distance, and verified by the known velocity of sound in water for the particular temperature) is then added to the value of each pixel, and the reciprocal of the sum is scaled to give the final result in meters per second. The reconstructed digital images represented by a matrix of 64 x 64 pixels can be displayed in gray scale in a Ramtek display system.

4. Experimental Results and Discussion

The accuracy with which the acoustic speed can be determined using ultrasound computerized tomography is demonstrated in figure 3 in the high correlation of our data with the literature value (10) for 2.5 percent salt solution. Thin rubber finger cots filled with saline served as the test object. The agreement of the literature values with the experimental results over the entire temperature range is within ± 0.3 percent. Since the reconstructed image is a matrix giving the acoustic speed in each pixel (pixel size ≃ 1.5 mm^2) mean and root mean square deviation of the

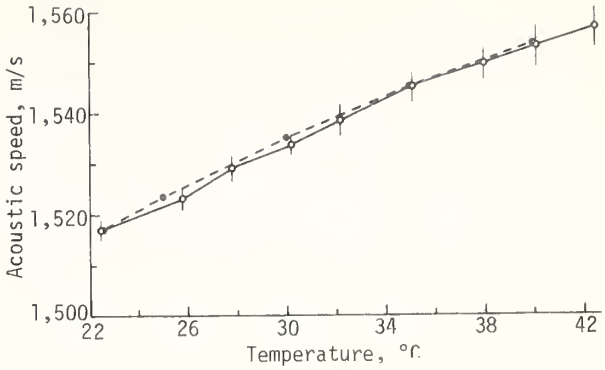

Fig. 3. Comparison of acoustic speed in 2.5 percent salt solution (2.5 g salt in 100 cm^3 of water), as determined by ultrasound computerized tomography, with the literature values. The literature values have an accuracy of ± 4 cm/s. Acoustic speed values were taken as the average of 20 samples in the reconstructed image.
∘Ultrasound computerized tomograph data
•Millero, F. J. and Kubinski, T., J. Acoust. Soc. Am. 57, 312 (1975).

acoustic speed are easily determined by analyzing the quantitative distribution of acoustic speed in the image. Similar statistical analysis was done on the reconstruction images of all the tissues that were studied and reported in this paper.

Tissues were obtained and selected by a pathologist as being representative of selected tissue types. Samples of tissue acquired were about 2 to 3 centimeter square and 5 centimeter long and were suspended in a bath of normal saline. Reference objects such as finger cots filled with saline of known concentrations were also suspended with the tissues. Later in the study the tissues were packed into finger cots under normal saline and suspended in the water bath. This procedure simplified the tissue handling considerably and the effect of finger cots on the quantitative results was found to be negligible.

The temperature of the water bath was increased in increments of about 2 °C and the tissues were allowed to equilibrate with the bath water prior to each new scan. The temperature of the bath was controlled ± 0.1 °C and experiments were done over a range of approximately 22 to 42 °C.

The ultrasound computerized tomography images for the acoustic speeds in spleen, kidney, liver, spinal cord and psoas muscle at two different temperatures are displayed in figure 4. Since the two pictures are displayed in the same gray scale any increase in the acoustic speed with temperature is seen as an increase in the brightness of the corresponding regions of the image. The water background is brighter in the image for 33.2 °C for the same reason. Figure 5 gives a similar picture for breast tissues at temperatures 14 °C and 41 °C. Because of the very large temperature change, the corresponding changes in the acoustic speeds are seen strikingly in this picture. The water background goes from dark to bright and the image of salt solution gets brighter at the higher temperature. Images of the breast fat which were brighter than the water

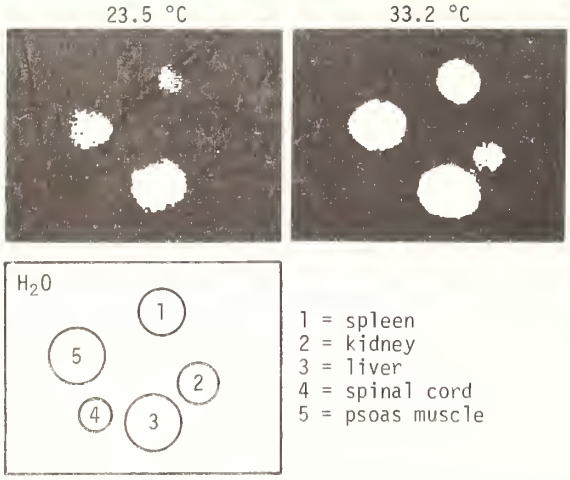

Fig. 4. Ultrasound computerized tomography images of acoustic speed distribution in various tissues, in vitro, at two different different temperatures. Same gray scale used for both the pictures. Higher acoustic speed is displayed brighter. Reconstruction size is 15 cm square. Tissues were encased in rubber finger cots to prevent solutes from diffusing into or out of the tissues. Tissues were unfixed and maintained at 10 to 14 °C until used some 12 to 24 hours after autopsy. (Reproduced with permission from Greenleaf, et al., Proceedings of the Vth International Conference on Information Processing in Medical Imaging (in press).)

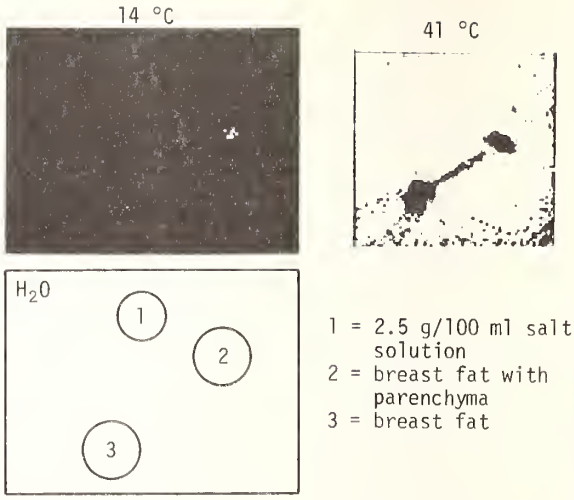

Fig. 5. Ultrasound computerized tomography pictures of acoustic speed distributions in breast tissues, in vitro, at two different temperatures. Reconstruction size is 15 cm square. Fat exhibits acoustic speed higher than water at 14 °C and lower than water at 41 °C.

background at the lower temperature become darker at the higher temperature since the acoustic speed in the breast fat has decreased with increasing temperature. The dark streak from fat to fat in the picture for 41 °C is an artifact caused by the lens effect of the cylindrically shaped tissue. The increase in the acoustic speed in parenchyma with temperature is also seen from this picture.

Results of the statistical analysis of the reconstruction images giving the mean and standard deviation of the acoustic speeds at various temperatures in all the tissues studied are given in tables 1 and 2. These data are graphically illustrated in figures 6, 7, and 8. From figure 6 it is clear that the tissues liver, psoas muscle, spleen, spinal cord and kidney have higher acoustic speeds than water and their temperature variations are similar to that of water. The breast muscle and parenchymal tissue are about 3 percent higher in acoustic speed than normal saline. Their temperature behavior is also very similar

Table 1. Temperature variation of acoustic speed in excised human breast tissues.

Tissue	Temperature 22.5 °C	25.8 °C	27.8 °C	30.2 °C	32.2 °C	35.1 °C	38.0 °C	40.1 °C	42.5 °C
Salt finger (2.5%)	1516.7[a] (2.1)[b]	1523.2 (2.1)	1529 (2.6)	1533.6 (2.1)	1538.4 (2.8)	1544.8 (3.1)	1549.6 (3)	1552.8 (4.2)	1556.5 (3.8)
Fat breast	1480.7 (2.5)	1466.9 (9.9)	1472.1 (9.8)	1477.4 (9.9)	1478.1 (11.4)	1436.3 (15.6)	1435.6 (18.4)	1438.7 (18.1)	1441.8 (17.5)
Fat with parenchyma	1494.7 (4.1)	1487.5 (5.5)	1491.5 (5.5)	1497.8 (5.7)	1500.9 (6.2)	1471.3 (9.7)	1471.3 (13.1)	1474.2 (13.4)	1475.9 (12.8)
Parenchyma	1539.4 (4.5)	1545.7 (4.0)	1551 (4.6)	1558.1 (3.9)	1562.1 (4.1)	1564.5 (7.6)	1564.3 (6.4)	1569.6 (6.3)	1571.9 (6.4)
Muscle	1543.1 (5.2)	1551.4 (6.2)	1554.2 (6.5)	1562.4 (7.1)	1565.5 (6.4)	1566.9 (4.5)	1570.7 (6.9)	1574.6 (6.7)	1579.5 (5.4)
Background (normal saline)	1504.0 (3.2)	1512.5 (3.6)	1519.2 (2.8)	1523.7 (2.5)	1528.4 (2.4)	1535.4 (4.0)	1539.1 (2.9)	1541.9 (3.0)	1546.4 (2.8)

[a] Velocity, m/s.
[b] Standard deviation.

Table 2. Temperature variation of acoustic speed in selected excised human tissues.

Tissue	Temperature 17.0 °C	22.0 °C	23.5 °C	26.2 °C	30.2 °C	33.2 °C	35.2 °C	37.2 °C	39.0 °C	40.8 °C
Liver	1547.0[a]	1555.5	1563.1	1564.6	1571.1	1573.5	1575.3	1578.1	1580.0	1581.7
	(2.5)[b]	(1.8)	(3.0)	(2.8)	(2.5)	(1.8)	(2.5)	(2.9)	(2.2)	(1.5)
Kidney	1508.5	1523.8	1536.1	1536.3	1545.2	1551.4	1555.8	1560.2	1562.6	1564.3
	(4.3)	(4.6)	(2.1)	(5.2)	(2.7)	(1.4)	(1.8)	(1.8)	(1.2)	(0.9)
Spleen	1528.0	1538.8	1544.3	1549.1	1556.4	1561.9	1546.0	1567.1	1569.3	1573.0
	(1.8)	(1.8)	(1.8)	(1.6)	(2.0)	(1.7)	(2.1)	(2.3)	(2.6)	(2.1)
Psoas muscle	1542.5	1459.5	1554.8	1560.2	1566.4	1571.6	1573.5	1575.6	1577.6	1580.3
	(3.0)	(3.0)	(1.1)	(1.7)	(2.2)	(1.8)	(1.8)	(1.1)	(2.1)	(1.8)
Spinal cord	1509.0	1523.0	1523.0	1526.0	1532.6	1538.0	1538.0	1542.4	1543.8	1456.5
	(4.5)	(4.6)	(5.3)	(3.0)	(3.2)	(2.6)	(3.5)	(3.3)	(3.0)	(2.0)

[a] Velocity, m/s.
[b] Standard deviation.

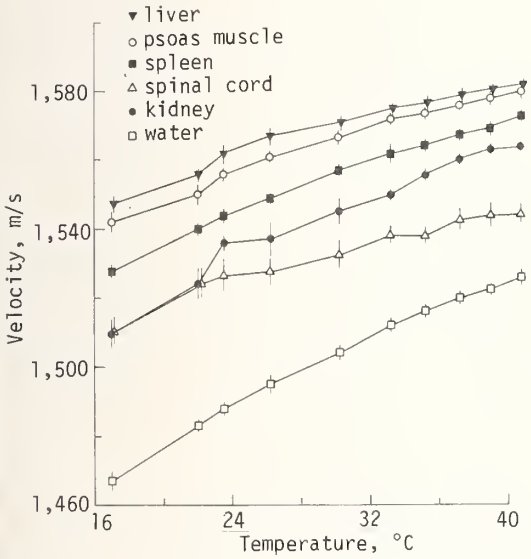

Fig. 6. Variation of velocity of sound with temperature in various tissues. Ultrasound computerized tomography data. Values are averages of about 15 values taken in the visually defined center of respective tissue samples within the image. Bars are ± RMSD.

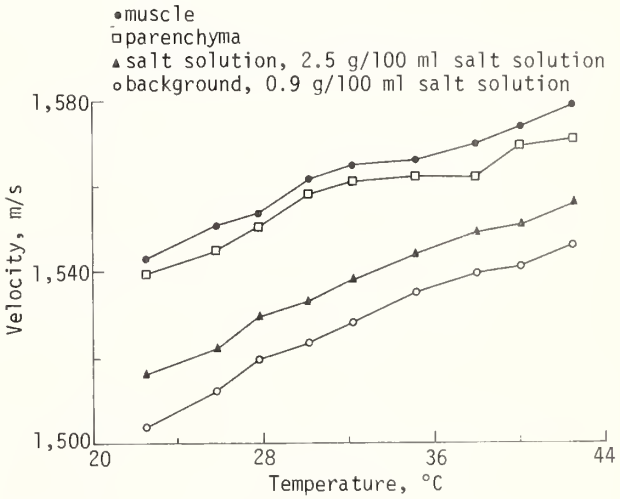

Fig. 7. Variation of acoustic speed within pectoralis muscle and normal parenchyma of breast. Values obtained in the manner described in figure 6.

to that of saline or water as seen in figure 7. However, breast fat and parenchymatous fat have acoustic speeds below that of normal saline and show a complex behavior with temperature as illustrated in figure 8. Initially the acoustic speed increases slowly with temperature and around 35 °C decreases markedly and then increases with a small slope of about 1 meter per second per °C. Similar decrease but much less pronounced is seen around 27 °C also. A plot of the variation of the temperature coefficient versus temperature for fat and muscle shown in figure 9 illustrates the strikingly different temperature behavior of fat. This complex behavior is suggestive of possible phase transitions just below the body temperature (37 °C). Hoyer and Nolle [11] studied the behavior of nematic and cholesteric liquid crystals near the isotropic to liquid crystal transition by measuring the propagation constants of ultrasonic waves. Their study indicates that the acoustic speed goes through a minimum at the temperature of the phase transition. Dyro and Edmonds [12] investigated ultrasonic dispersion in cholesteryl esters and their results show that the acoustic speed exhibits markedly different behavior around the phase transition. Though the fat sample in the present study is not a homogeneous, "clean", one-component system, the possibility of a phase transition of some kind cannot be excluded. More detailed studies using different physical chemistry techniques such as differential scanning calorimetry may shed some light into the anomalous temperature behavior of the breast fat.

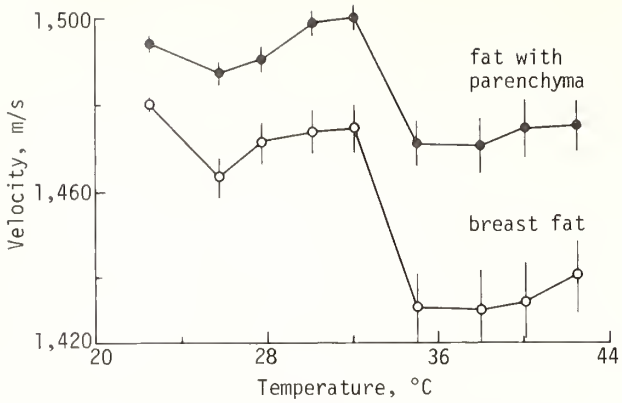

Fig. 8. Variation of acoustic speed in normal breast fat. Slope of alteration in acoustic speed with temperature is negative for fat in certain regions of temperature. Vertical shift in curves is apparently due to presence of parenchyma which has temperature dependence much like water (see fig. 7).

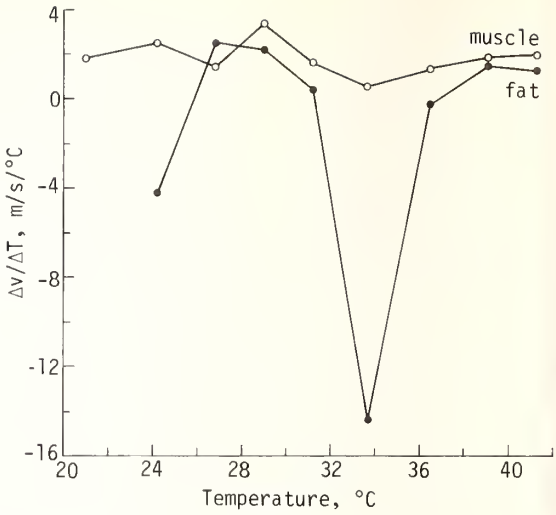

Fig. 9. Variation of temperature coefficient of acoustic speed with temperature in pectoralis muscle and in fat from breast. Negative temperature dependence of fat in certain regions of water is visualized by plotting slope of figure 8.

Alterations of temperature within various tissues can be expected under various inflammatory processes such as infections. It is also well known that certain carcinomas are associated with a high temperature due to their increased metabolism. Knowledge about the temperature variations of acoustic speed in diseased tissues and in normal tissues should be valuable in future studies of acoustic speed distributions within patients whose tissues are undergoing various disease processes. Computerized ultrasound tomography may provide the possibility of quantitatively measuring acoustic speed in breast tissues in vivo.

Acknowledgments

The support from Dr. Earl H. Wood, Dr. Erik L. Ritman, and the staff of the Biodynamics Research Unit, Mayo Clinic, is appreciated. This research was supported by Grants HL-07111, HL-00170, HL-00060, RR-00007, HL-04664, NIH-HT-4-2904 from the National Institutes of Health, United States Public Health Service, and NCI-CB-64041 from the National Cancer Institute.

References

[1] Green, P. S., Schaefer, L. F., Jones, E. D., and Suarez, J. R., A New High-Performance Ultrasonic Camera, in Acoustical Holography, Vol. 5, pp. 493-503 (Plenum Press, New York, 1973).

[2] Jones, J. P., Impediography: A New Ultrasonic Technique for Non-Destructive Testing and Medical Diagnosis, in Ultrasonics International (1973), Conference Proceedings, p. 214 (PIC Science and Technology Press, U.K., 1974).

[3] Kak, A. C. and Frye, F. J., Acoustic Impedance Profiling: An Analytical and Physical Model Study, in Ultrasound Tissue Characterization, M. Linzer, ed., National Bureau of Standards Spec. Pub. 453, p. 231 (U.S. Government Printing Office, Washington, D.C., 1976).

[4] Greenleaf, J. F. and Johnson, S. A., Algebraic Reconstruction of Spatial Distributions of Refractive Index and Attenuation in Tissues from Time-Of-Flight and Amplitude Profiles, in Ultrasonic Tissue Characterizations, M. Linzer, ed., National Bureau of Standards Spec. Pub. 453, pp. 109-119 (U.S. Government Printing Office, Washington, D.C., 1976).

[5] Gordon, R. and Herman, G. T., Three-dimensional reconstruction from projections: A review of algorithms, International Review of Cytology 38, 111-151 (1974).

[6] Brooks, R. A. and Di Chiro, G., Principles of computer assisted tomography (CAT) in radiographic and radioisotopic imaging, Phys. Med. Biol. 21, 689-732 (1976).

[7] Lakshminarayanan, A. V., Reconstruction from Divergent Ray Data. Department of Computer Science, State University of New York at Buffalo, Technical Report 92 (1975).

[8] Herman, G. T., Lakshminarayanan, A. V., and Naparstek, A., Convolution reconstruction techniques for divergent beams, Comput. Biol. Med. 6, 259-271 (1976).

[9] Radon, J., Ueber die Bestimmung von Funktion durch ihre Integralwerte Langs gewisser Mannigfaltigkeiten, Berichte Saechsische Akademie der Wissenschaften 69, 262 (1917).

[10] Millero, F. J. and Kubinski, T., Speed of sound in seawater as a function of temperature and salinity at 1 atmosphere, J. Acoust. Soc. Am. 57, 312-319 (1975).

[11] Hoyer, W. A. and Nolle, A. W., Behavior of liquid crystal compounds near the isotropic-anisotropic transition, J. Chem. Phys. 24, 803-811 (1956).

[12] Dyro, J. F. and Edmonds, P. D., Ultrasonic absorption and dispersion in cholesteryl esters, Mol. Cryst. Liq. Cryst. 25, 175-193 (1974).

Reprinted from *Ultrasonic Tissue Characterization II*, M. Linzer, ed., National Bureau of Standards, Spec. Publ. 525 (U.S. Government Printing Office, Washington, D.C., 1979).

HIGH SPATIAL RESOLUTION ULTRASONIC MEASUREMENT TECHNIQUES FOR CHARACTERIZATION OF STATIC AND MOVING TISSUES

Steven A. Johnson, James F. Greenleaf, and B. Rajagopalan

Biodynamics Research Unit
Department of Physiology and Biophysics
Mayo Foundation
Rochester, Minnesota 55901, U.S.A.

Robert C. Bahn

Department of Pathology
Mayo Clinic and Mayo Foundation
Rochester, Minnesota 55901, U.S.A.

Brent Baxter

Department of Computer Science
University of Utah
Salt Lake City, Utah 84112, U.S.A.

Douglas Christensen

Departments of Bioengineering and Electrical Engineering
University of Utah
Salt Lake City, Utah 84112, U.S.A.

Clinical and pathology-based arguments are presented for the need for higher resolution ultrasound images. The theoretical foundation and experimental characteristics of a high resolution, sampled aperture, reflection technique termed "synthetic focus" imaging are given. It is shown by theory and simulation that such synthetic focus images may be corrected for attenuation and refraction effects and thereby approach one-half wavelength resolution. The similarity between synthetic focus and seismic migration techniques is discussed. An example of a high resolution, seismic processed (i.e., migrated) image obtained from real data at medical ultrasound frequencies is shown. Synthetic focus imaging theory is extended to moving coordinate systems and the effect of Doppler shift effects on echo pulse shape is discussed. A generalized wide aperture Doppler imaging theory is presented which suggests further improvements in signal-to-noise ratio, spatial resolution and flow velocity over narrow aperture systems is possible. A new computed tomographic flow measurement and reconstruction technique based on transmission measurements is presented. This technique permits imaging the three flow velocity components and temperature of homogeneous fluids in a three-dimensional domain.

Key words: Aperture synthesis; computed tomography; Doppler; fluid flow; high resolution; reconstruction; temperature reconstruction; ultrasound.

1. Introduction

This paper presents theoretical and experimental evidence that useful measurements of tissue characteristics with limiting spatial resolutions of about one-half wavelength are possible in static and moving media (e.g., tissues). This paper has three objectives: First, to present the case for striving for higher resolution images of tissue parameters, second, to describe the theoretical and experimental techniques whereby such high resolution images may be obtained and, third, to report progress toward obtaining such high resolution images.

2. The Case for Seeking Higher Resolution Images

A. Higher Resolution Images of Static Tissues

The first goal or purpose of this paper is in part philosophical, yet is demonstrable, and calls attention to an important area of investigation (improved resolution) where future research progress can be made. It can be argued that reliable tissue characterization requires attention to at least three independent requirements: First, choosing an adequate set of tissue dependent acoustic parameters to be measured; second, measuring the parameters with accuracy and precision in some set of regions in the tissue; and third, making this measurement region as small as possible and as densely arranged or packed as possible (i.e., forming an image).

The third requirement is not always necessary to gain some information on tissue type but its inclusion improves the certainty of characterization. Certainly, it is clear that an early diagnosis of a disease state (such as cancer) is enhanced by detection of smaller masses made possible by higher resolution and better tissue identification. In some cases the tissue type may well be primarily determined by the morphology and pattern of its structure and the change in pattern of the surrounding tissue [1,2][1]. This has its analog in microscopic pathologic techniques where both stain (acoustic tissue characterization parameter is its analog) and pattern are important in tissue typing or characterization.

In the long range, the improvement of resolution may be the most important objective for future research progress. At present, the primary attempt to detect small focal processes such as cancers, abscesses, infarcts of less than 0.5 to 1 cm in diameter is difficult and may not be justified economically. However, often more fundamental than the focal lesion itself, regardless of its size, is the state of the tissue surrounding circumscribed lesions. The pattern of the adjacent tissue plays a crucial role in the identification of specific diseases by supplying the physician with information concerning the local context of the process under consideration.

Compared to tumor nodules, the structures of the surrounding "normal" tissues are relatively delicate. Their patterns are essentially determined by the dimensions of the fibrous and vascular framework of an organ. It would be desirable to image such delicate patterns associated with the tertiary branching of major arteries of the heart, brain, kidneys, and lungs, the bronchial tree, the biliary ducts of the liver and the ductular system of the breast. Since vascular or ductal systems at the level of tertiary branching involve tubular structures approximately 0.5 to 1.0 mm in diameter, this objective fixes the upper limit of useful picture element size at about 0.25 to 0.5 mm. From a practical point of view, this level of resolution would provide at least 20 resolutable picture elements (pixels) over an area 2.5 millimeters in diameter. Such an area would correspond roughly to the cross-sectional area of the lumen and portions of the wall of a coronary artery.

In this manner, imaging studies can eventually become focused upon pathogenesis, prevention, and early detection of disease rather than upon the diagnosis of gross advanced lesions.

B. The Case for Seeking High Resolution Images of Moving Tissues

The velocity of moving tissue may be obtained by two general methods. First, by a differential method in which velocity is computed from images of the location of the tissue at two separate times separated by a short time interval (this could be done by comparing two separate real-time B-scans of the heart, for example), and second, by direct methods which make use of alterations in frequency or phase in the received ultrasound signals. Examples of images produced by this latter method are the familiar pulsed Doppler B-scan technique [3] and the new fluid velocity vector reconstruction technique developed by Johnson et al. [4].

Images produced by the first or differential method have application in understanding moving solid tissues such as the heart and circulatory system and their components (e.g., valves, vessel walls, etc.). Any improvement in the spatial and temporal resolution of methods for imaging these moving structures would produce a corresponding improvement in imaging the velocity of these structures at high spatial resolution. The effort which has been and now is being made in the field of x-ray angiography [5] is an indication of the potential contribution which such high spatial and temporal ultrasound imaging methods could make to health care.

Images produced by the direct velocity imaging techniques (based on frequency or phase shift techniques) have application in measuring the velocity of fluid produced or modified by tissues (e.g., air in the respiratory system, urine, etc.) or the velocity of fluid tissues (e.g., the blood). The well-known Doppler technique (a reflection method) measures the velocity of scattering centers (e.g., the red and white cells) in the blood. The new velocity vector reconstruction method (a transmission method) measures the velocity of the carrier (i.e., the plasma) of the scattering centers or a combination of the velocity of the two constitutive components. Thus, the two methods are complementary. The ability to obtain images at high spatial and temporal resolution of blood flows promises to be of great value for several reasons. First, it may be argued that since the x-ray angiographic method is of proven worth, then any competitive ultrasound techniques would also be valuable. Second, the new pulsed Doppler systems now in development or use, although of limited to moderate imaging capability, are proving to be of great value [6]. For example, the SRI-built carotid scanner, now undergoing clinical trials at Mayo, is proving the value of its Doppler flow measuring features (the scanner has real-time B-scan capability also) [7]. Third, ultrasound procedures are noninvasive and have no demonstrable cumulative toxic effect when power and energy levels are controlled. Fourth, ultrasound procedures are painless and usually can be completed quickly.

[1]Figures in brackets indicate literature references at the end of this paper.

3. Imaging Methods for Static Media

A new high resolution reflection imaging mode has been developed in the Mayo laboratory to image or characterize tissue structures in the body where a full 360 degree data collection geometry is precluded by the ribs, the spine, and other body structures [7,8]. This new mode is termed synthetic focus imaging [7].

The mathematics for synthetic aperture imaging may be derived by reference to figure 1. Let P_k define a measure of the probability for acoustic amplitude scattering or reflection toward the detector aperture from picture element k when illumination from each transmitter element in the

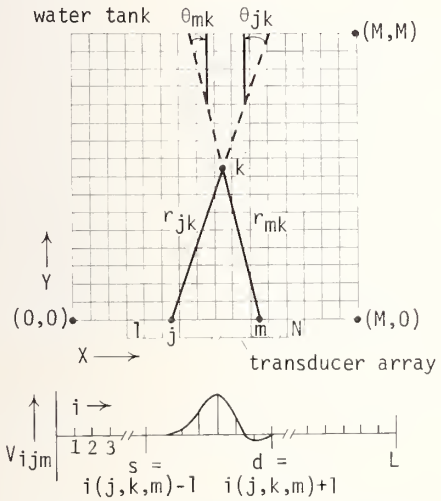

Fig. 1. Geometry for derivated of equations for ultrasonic imaging by generalized synthetic aperture methods. A transducer array with N elements is in acoustic contact with a water tank. Positions in the tank are described by coordinate system XY. A typical ray path is shown for energy transmitted by the m^{th} transducer and scattered by picture element k into the j^{th} transducer. Here r_{jk} and r_{mk} are the distances from j to k and from m to k, respectively. Angle θ_{jk} is measured from r_{jk} to the Y axis counterclockwise. V_{ijm} is the voltage sample from the j^{th} transducer at time after transmission of the signal by the m^{th} transducer. Here s and d are start and end times of a time interval 2w which contains the echo from k at its midpoint. Time L is greater than the maximum time associated with all paths defined by j, m, and k. (Reproduced with permission from [7].)

array aperture, measured at picture element k, is normalized. The probability for energy scattering is the square of P_k. For the case of a very narrow pulse of ultrasonic energy, P_k is given by

$$P_k = \sum_{m=1}^{N} \sum_{j=1}^{N} \sum_{i=t-w}^{t+w} V_{i,j,m} R_{j,k} T_{k,m} K_{t-1} \quad (1)$$

where $V_{i,j,m}$ is the i^{th} voltage sample from the j^{th} array element when the m^{th} array element was used as the transmitter. $R_{j,k}$ is the receiver-range azimuth illumination normalization factor between the k^{th} picture element and the j^{th} array element. Thus, $R_{j,k}$ is independent of time, but is an approximate function of some power of the magnitude of $\vec{r}_{j,k}$ (where $\vec{r}_{j,k}$ is the vector from array element j to picture element k) and of the cosine of the angle between $\vec{r}_{j,k}$ and $\vec{n}_j$ (the unit vector normal to array element j). Thus, $R_{j,k}$ may be written

$$R_{j,k} = \left[\exp\left(\int_k^j \alpha(s)ds\right)\right]\left[\int_k^j ds\right]^q \left[\vec{n}_j \cdot \vec{S}_{k,j}\right]^{-1} \quad (2)$$

where α is the attenuation coefficient along the ray path connecting k and j, q is a rational number from 0.5 for cylindral waves to 1.0 for spherical waves, and $\vec{S}_{k,j}$ is the unit tanget vector at j of the ray which passes from k to j. $T_{k,m}$ is the corresponding transmitter function between the k^{th} pixel and m^{th} array (transmitter) element. Thus, $R_{j,k}$ and $T_{k,m}$ affect the energy normalizations referred to in the definition of P_k. N is the number of array elements. The factor K_{t-i} is a kernel function for performing convolution or cross correlation operations on the raw data $V_{i,j,m}$. If $V_{i,j,m}$ is of the appropriate pre-transmitted form or post-received processed form, then K_{t-i} may be of the form of a delta function $\delta_{o,t-i} = \delta_{t,i}$. The limits $t \pm w$ are related to the transmitter pulsewidth t_w which is less than some arbitrary bracketing interval t_B which contains the transmitted pulse of width t_w.

Then,

$$t = \left(\int_m^k \frac{ds}{U(s)} + \int_k^j \frac{ds}{U(s)}\right)\frac{1}{\Delta t} \quad , \quad (3)$$

$$w = t_w/2\Delta t \quad (4)$$

where Δt is the sampling interval time between successive samples in the digitized signal, and u is the effective velocity of sound in the insonified medium. The two line integrals are taken along the rays connecting transmitter m to k and k to receiver j respectively.

An important modification to the synthetic focus equations above would change the sum over i to allow for refraction or bending of acoustic rays. The effect of this bending is manifest in shifts in the values of s and d compared to that obtained by computing the round trip pulse time in a homogeneous medium. This effect is illustrated in figure 2. The value of t would be replaced by the correct round trip time computed using curved rays obtained from ray tracing techniques [9,10]. The coordinate system set up by the intersection of rays and wavefronts and the corresponsing slight shift in round trip (a few percent) will allow a low spatial resolution perturbation correction to be made to the basic homogeneous media round trip time equations.

Another useful modification to the basic synthetic-focusing scheme presented above would

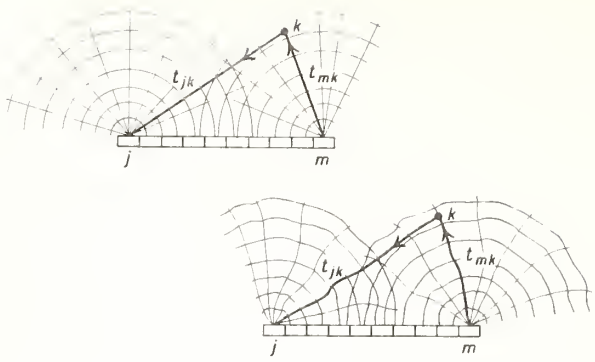

Fig. 2. Orthogonal coordinate systems for describing ray paths from transducer elements in constant (left) and variable (right) refractive index media. On the left the ray paths between each transducer element and receiver element are segments of straight lines. The lines of equal time of propagation are circles. On the right the ray path and equal time lines are from transmitter element m to scattering site k and the time t_{jk} from k to receiver element j is shown as a heavy line. (Reproduced with permission from [9]).

be to replace $V_{i,j,m}$ with the output of a hardware or software correlator, allowing transmission not only of pulses of energy, but arbitrary waveforms as well. This may be a faster method for obtaining the optimum resolution waveforms than performing the inner products in software using the kernel K_{t-i} as indicated by equation (1).

Figure 3 shows the similarities between the x-ray computer assisted tomography and synthetic focus ultrasound algorithms. It is seen that back projection in both instances can be thought of as a line integral in data space:

1) In the x-ray case the reconstructed value at each pixel in the tomogram is obtained by integration along a unique path in the convolved data space. The convolved data space is composed of the collected projection profiles convolved with a kernel function. The curved path associated with each pixel is a sine wave modified in phase and amplitude for the special case of parallel ray projections, hence, the name "sinogram" space for this representation of the data.

2) In the ultrasound synthetic focus method, the image value at each pixel in the tomogram is obtained by integration along a unique path, also in a convolved data space. The values in the convolved data space can be obtained by either transmitting the required waveform or by digital processing or equalization of the received data. In the case of a homogeneous material in the object space, e.g., water, the set of echoes from each receiver element for a fixed transmitter position falls on a hyperbolic curve in data space. The synthetic focus algorithm reconstructs the scattering amplitude at each pixel by integration along the hyperbolic curve which is unique to that pixel.

Back projection, as just described, may be termed "pixel driven" because the value at each pixel is computed to completion before a value is

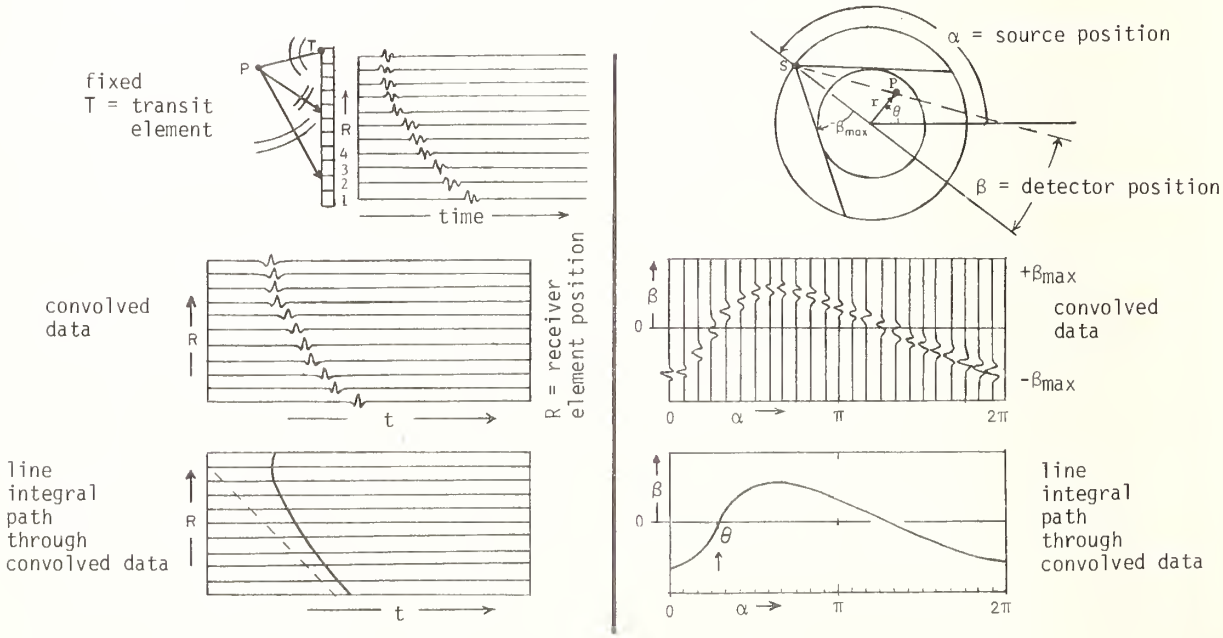

Fig. 3. Illustration of the similarity between "back projection" reconstruction in the x-ray case and echo mode synthetic focus image formation with ultrasound.
Left panel - Reflection Ultrasound Data Space - Pixel driven synthetic focus algorithm generates a unique hyperbolic curve along which "back projection" algorithm performs a line integral for the data value at each pixel value.
Right panel - Transmission X-ray Data Space - Pixel driven convolution algorithm generates unique sine wave like curve along which "back projection" algorithm performs a line integral for the data value at each pixel value.

assigned to a new pixel. The line integration along curves in data space is assigned to each pixel in this mode of computation.

An alternative conceptualization of back projection is possible in which each data point in data space is used to influence the value of all pixels in the image space before a new data point is processed. This formulation may be termed "profile driven" back projection for the reasons just given, or termed "smear and add" back projection because the pixels which are influenced most by each data point are located on or near a curve in image space. The "smear" may refer to convolution. In the x-ray case, the "smear and add" occurs back along the original x-ray path which produced the data value at the detector. This is a very strong intuitive reason for the term "back projection". In the ultrasound case, the back projection in the image space occurs along an ellipse (not a hyperbole) for each data space. The ellipse, of course, represents the locus of points of equal transmitter-receiver pair round trip time. The superposition of the set of values along all ellipses for all such transducer pairs constitutes the final ultrasound scatter amplitude image in an analogous manner to the formation of an x-ray convolution algorithm image by the sum of all back projected convolved projections. This viewpoint is further explained in figure 4.

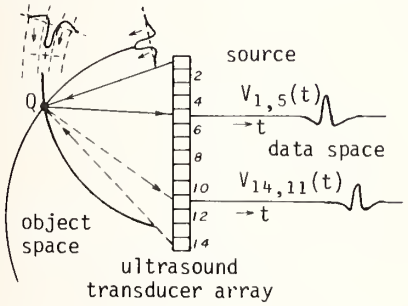

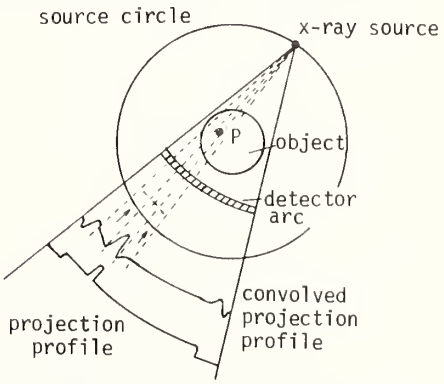

Fig. 4. Illustration of the ultrasound analog of back projection of a convolved projection profile.

The left figure shows the signal voltage $V_{1,5}(t)$ received on element 5 when transmitting from element 1 as a function of time. Also shown is the voltage $V_{14,11}(t)$ for receiver 11 and transmitter 14. For simplicity, it is assumed that the object space contains only one scattering point Q. The data $V_{i,j}(t)$ is assumed to be ready for back projection. The right figure shows an x-ray source and object with a dense point at P which produces the sharply peaked projection profile. Reconstruction of the object is achieved by back projection of the convolved profiles for all source positions around 360°. In the ultrasound case, the receiver echo data is projected along ellipses in the object space (note that this is equivalent to summing along a set of hyperbolae in the data space). As in the x-ray case, back projection of non-negative unconvolved raw projection profile data does not give optimum resolution but instead gives the true object convolved with a blurring function. The effect of the blurring function may be nearly removed (deconvolved) if the projection profiles are first convolved with a deblurring kernel. Such kernels usually have a strong central maxima with symmetric heavily damped bipolar side lobes. In the ultrasound case maximum resolution (the Rayleigh limit and even much better) is achieved when the impulse response of a single scatterer is made to look like such a kernel in the data space.

A. Diffraction Considerations

Although no diffraction theory has been used in the derivation of the synthetic focus equations, it is still true that images obtained from their application are very nearly diffraction limited (at least qualitatively and quantitatively in some cases). The reason for this, perhaps surprising, result lies in the use of an extremum ray path time between the scattering center (image point) and transducer element in the synthetic focus method. These ray paths are often identical to, or very nearly equal to, the characteristic solution lines to the wave equation (the wave equation includes diffraction effects). Thus, although some energy travels by diffracted paths, a large fraction usually will travel by the extremum paths used by the synthetic focus method.

B. Comparison With Seismic Methods

Many similarities exist between the synthetic focus ultrasound algorithm developed by Johnson et al. [7] and classical seismic migration methods [11]. One similarity is in the method of collecting data. Both migration and synthetic focus methods use the concept of separate source or transmitting points and geophone or receiving points respectively. This is illustrated in figure 5 for the case of a linear geophone and circular synthetic focus ultrasound arrays.

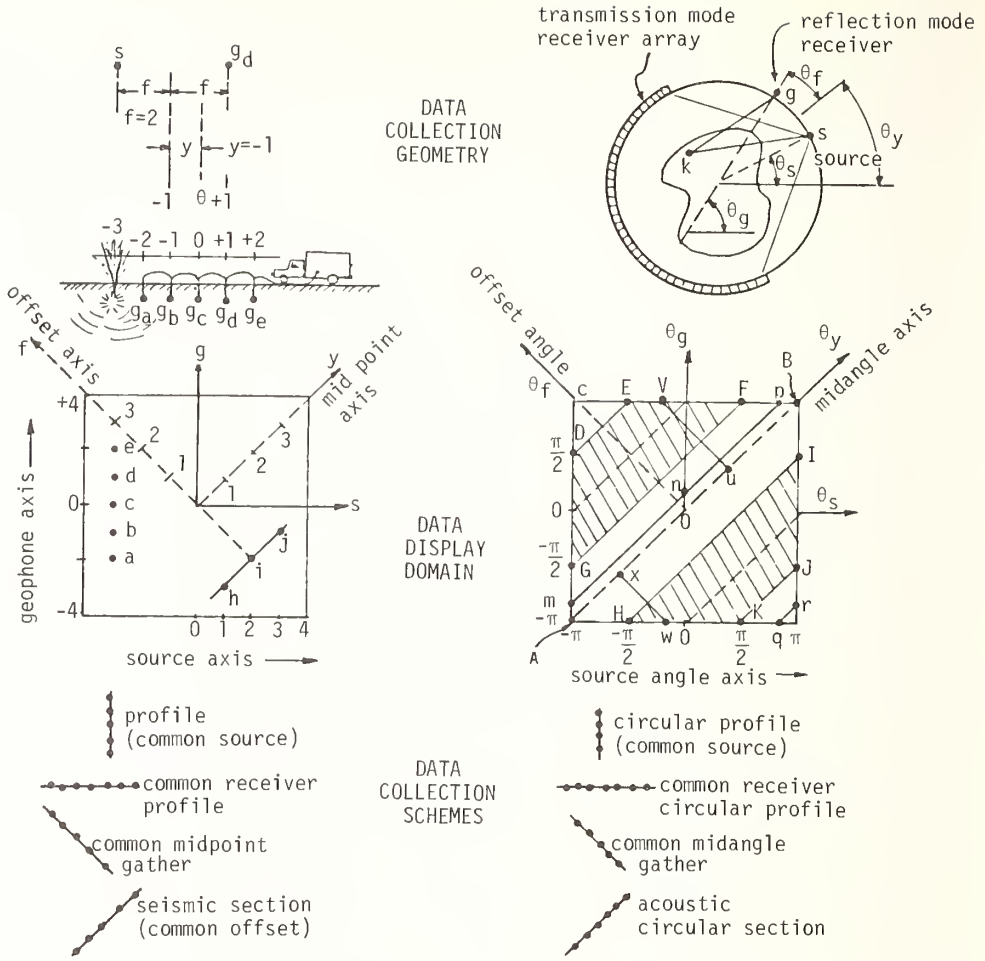

Fig. 5. Illustration of the similarities between classical seismic data collection with linear geophone arrays and ultrasound imaging with circular transducer arrays. The left most column of figures illustrates the major parameters used to describe seismic data collection in one-dimensional, i.e., linear, arrangements of source positions (shot point = s) and receivers (geophone = g). The right most column of figures illustrates how the circumgerence of a circular arrangement of sources and receivers may be described in terms of the analogous parameters in the left column. The shot position s is replaced by source angle θ_s and geophone position g is replaced by the receiver angle θ_g.

In the top most left figure, typical source s is located at position -3 and typical geophone g_d is located at position +1 (arbitrary units). The mid point of the (s,g_d) pair is at position -1 and is defined as the mid point y (i.e., y = -1). The separation of s and g_d from the midpoint is -2 and +2 respectively and is defined as the offset f (f for "offset"). Note f is positive when g is on the positive side of the midpoint.

Also shown is a typical seismic data collection geometry with a source (dynamite blast) located at -3 and geophones at -2, -1, 0, 1, 2. This particular source-receiver combination is plotted as points a, b, c, d, e on the g-s plane. Point d at (-3,1) in the g-s plane, represents time history data for a source at -3 and a geophone at +1. The midpoint and offset coordinates (-1,2) of data point d can be found from its projection onto the midpoint and offset axes respectively. The directions of straight line sets of data points at angles of 0, 45°, 90°, and 135° to the s-axis have important properties and are given characteristic names. A vertical line is a profile and corresponds to a data point with a common source (the usual mode of seismic collection). A horizontal line is a common receiver profile (rarely used), a line at 45° is a seismic section (common offset) and is often obtained by rearrangement of multiple profiles. A seismic section is also commonly generated by towing a geophone at a fixed separation behind a source in the ocean. A line at 135° is called a common midpoint gather.

The top most drawing on the right shows how the concepts described in the left column can be applied to circular geometries. The

Fig. 5. (continued)

linear parameters s, g, y, and f have their angular analogues, θ_s, θ_g, θ_y, and θ_f respectively.

The s-g plane, which extends to infinity on all sides, is replaced by a finite and bounded θ_s-θ_g plane (bounded by $\pm \pi$). The θ_s-θ_g plane provides a convenient means for displaying the data collected for x-ray or ultrasound transmission computed reconstruction tomography. In the top right figure, a circular receiving array covering 180° is shown opposite the source s. Transmission data collected by this array is contained in the trapazoids DEFG and HIJK. Reflection data for s coincident with g is found on the line AOB. Reflection data for the receiver offset from the source line AOB. Reflection data for the receiver offset from the source as shown is found along lines mnp and qu. (This is one line mnpqr when the periodic nature of the data space is considered).

The direction of straight line data sets in the θ_s, θ_g plane can be given analogous names as those defined in the s-g plane. These data sets are shown at the bottom of the right column (i.e., circular profile, common receiver circular profile, common midangle gather, and acoustic circular sections).

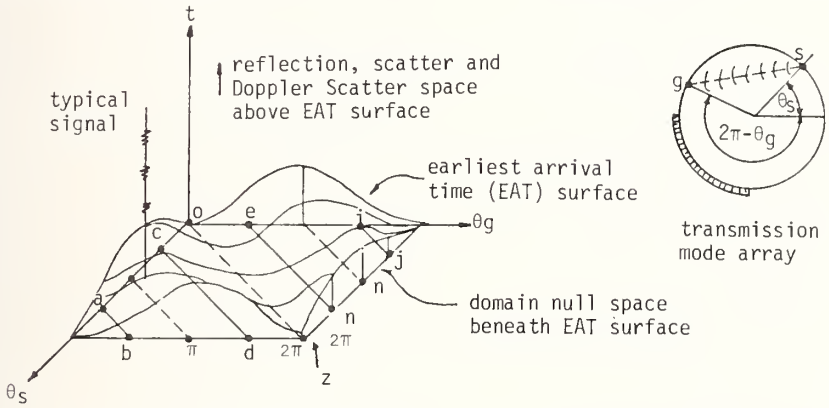

Fig. 6. Illustration of the mathematical properties of acoustic data collected from source-receiver pairs on a circular boundary. The time dependent voltage of the signal received by receiver g is plotted as an amplitude (fourth amplitude dimension not shown) vs., θ_s, θ_g, and time t. The coordinates θ_s, θ_g are source and receiver positions as defined by the drawing at the right. For any two points s and g on the circumference, there exists an earliest arrival time (EAT) for acoustic energy to propagate from s to g. This time is zero if s is coincident with g but is maximum (or near maximum for non-homogenous substances) when s and g are on opposite ends of a diameter. Thus, for times t less than EAT, the values in the range (not the domain) of (θ_s, θ_g, t) are zero (no signal has as yet arrived). Thus, the EAT value assigned to each pair (θ_s, θ_g) defines a surface below which all values in the same range are zero. This surface is called the EAT surface. The region above the 0-z axis (i.e., the $\theta_s = \theta_g$ line) provides maximum time separation of echoes from most neighboring points and provides maximum Doppler shifts for fluid flows. The region above areas abcd and ehij corresponds to receiver positions nearly opposite from the source and are used for computed tomographic (i.e., C.T.) transmission data collection. A maximum arrival time (MAT) surface (not shown) also can be drawn for which all points above this surface correspond to multiple reflections or multiple scattering events, or both.

The similarity between linear array seismic methods and synthetic focus medical ultrasound methods exists for both linear and circular scanning geometries. Circular geometries are found in x-ray computed tomographic reconstruction instruments and in their ultrasound counterparts developed at Mayo Clinic by Greenleaf and Johnson [12]. This similarity is explored and developed in figure 5 and its legend. Many of the important features of transmission mode reconstruction imaging such as "sinogram" space, or transformation from fan beam to parallel beam geometries, can be analyzed with the aid of the well-known seismic s-g plane data representation (s-g means source and geophone pair location for each data record).

The nature of the s-g data domain representation in circular geometries can be extended to include the time variable. An explanation of the features of this three-dimensional data domain is given in figure 6. There it is shown that the domain can be partitioned into two regions by a surface which corresponds to the earliest arrival time of an acoustic pulse or signal. The distance between a point P on this surface and the s-g plane corresponds (nearly inversely proportionally) to the "merit" of the echo spatial resolution information contained in the signal associated with the point P (i.e., a receiver opposite a source can have no or little echo information).

The synthetic focus method reported by Johnson et al. [7], according to the seismic nomenclature,

collects a profile for each transmitter position. The side looking radars or side looking synthetic aperture radars can be classified in seismic terms as producing one zero-offset section per flight path. It is well-known that superior focused (i.e., "migrated") seismic images can be obtained by the use of multiple profiles rather than by the use of one zero-offset section [11]. Thus, our synthetic focus method should produce images superior to those produced by literal adaptation of side looking radar or synthetic aperture techniques to medical imaging.

Also, in radar technology, refraction (i.e., normal moveout corrections) are not usually, if ever, made (but should be for medical imaging).

4. Imaging in Moving Media

A. General Considerations

Imaging in the presence of moving media requires that certain changes be made to the basic image forming equations for both reflection and transmission modes of imaging. We will show that consideration of these requirements provides not only a method for imaging structures embedded in the moving media (points in the moving media) but also methods for imaging the velocity distribution of the moving media itself.

The equations of synthetic focusing can be adapted to the case of moving media by using the time of travel associated with the ray paths which have been bent by the moving media. Thus, the expression for the time t of travel must be replaced by an expression containing the velocity of the media. For the case where the velocity of the media is small compared to the acoustic speed, this may be written as (by modifying equation 3)

$$t = \int_m^k \frac{1}{u}\left(1 - \frac{\vec{V}\cdot\vec{T}}{u}\right) ds + \int_k^j \frac{1}{u}\left(1 - \frac{\vec{V}\cdot\vec{T}}{u}\right) ds \quad (5)$$

Here, u is acoustic speed, $\vec{V}$ is fluid velocity, and $\vec{T}$ is a unit tanget vector along the ray path connecting k to the transducer elements m or j. A more exact expression for t, in the case when $\vec{V}$ is not very small in comparison to u, has been given by Johnson and others [10,13]. In addition to time shifts, a moving media also produces a compression or expansion of the shape of a waveform. When more exact imaging is required, the effect of this stretching may be removed by use of an appropriate compensating algorithm as is now shown. Let $g(y) = b \cdot h(t-t_o)$ be the received synthetic focus waveform for $\vec{V} = 0$. Here, b is the scattering strength and h is the transmitted waveform (for simplicity, the frequency dependence of the scattering process is assumed to be found in $H(\cdot)$). Let an upper case letter represent the Fourier transform of a corresponding lower case letter. Then, the corresponding expression in frequency space is $G(f) = b \cdot \exp(-2i\pi f t_o)H(f)$.

The Doppler frequency shift due to motion of the media has the effect of replacing f by $(f + \Delta f)$. Here, Δf is given by $\Delta f = f\,\vec{V}\cdot(\vec{T}_R + \vec{T}_S)/u$, where $\vec{V}$ is the velocity of the flow and where $\vec{T}_R$ and $\vec{T}_S$ are the unit tanget vectors from the scattering center in the flow to the receiver and transmitter (source) respectively. For $|V|/u \ll 1$, the effect of this frequency shift changes the form of G(f) to $G_D(f)$ given by $G_D(f) = b \cdot \exp(-2\pi f t_o)H(1 - \beta)(f)$ where $\beta f = \Delta f$. The corresponding time functions are given by

$$g_D(t) = (b/|1 - \beta|)h((t - t_o)/(1 - \beta)). \quad (6)$$

Thus, movement of a scattering center toward a source and receiver produces a shortening of pulse width and an increase in pulse amplitude.

B. Synthetic Focus Doppler Imaging

The principle of synthetic focusing may be applied to Doppler velocity imaging to improve the spatial and velocity resolution and to capture more of the Doppler scattered signal (by the use of a larger receiving aperture) and thereby increasing the signal-to-noise ratio in the final velocity image. Simply increasing the aperture of a single transducer may not improve Doppler resolution and signal-to-noise ratio because the Doppler shift will not be constant over the large aperture. A method is needed which will make use of the different Doppler shifts on a large sampled aperture.

For simplicity, a method suitable for flows restricted to a plane will be given first. It is assumed that the transmitting and receiving transducers are also restricted to this plane and are located on part of, or on the complete, circumference of a circle. Assume that the transmitter produces a narrow beam of pulsed-energy which constitutes a cord of this circle. Let the velocity of the flow at each point along the cord be $\vec{V}(q)$. Let $\vec{T}_s(q)$ and $\vec{T}_j(q)$ be the unit tanget vectors from the scattering center q to the transmitter source s and receiver j respectively. The use of time gates to achieve spatial resolution is assumed. Then the Doppler shift Δf is given by $(f/u)\vec{V}\cdot(\vec{T}_s + \vec{T}_j)$. This may be written as $\Delta f(q) = (f/u(q))\,[(\cos\theta_t + \cos\theta_j)V_x + (\sin\theta t + \sin\theta_j)V_y]q$. Then this constitutes a set of simultaneous equations in V_x and V_y. This set is usually over determined since the set can be spanned with only two independent values of θj, but the over-determination provides for better signal-to-noise level. The above equation may also be written as

$$\Delta f(q)_j = [f/u(q)]\;(|\vec{V}(q)|)\;[\cos(\vec{V},\vec{T}_s) + \cos(\vec{V},\vec{T}_j)],\; j = 1,2... \quad (7)$$

Note that the first term is a frequency bias and the second term has a period of 2π in θ_j. The direction of the flow $\vec{V}$ and its magnitude may be found from this set of equation by several schemes:

1) The Fourier transform of the above equation may be taken with respect to angle $(\vec{V},\vec{T}_j)$. The square root of the sum of the squares of sin and cos terms with period 2π is equal to $(|V|f/u)$ while the angle $(\vec{V},\vec{T}_S)$ is proportional to the arc tangent of the ratio of these terms.

2) A least squares fit of a phase shifted cosine function can be made to the data. This least squares technique can also be applied to three-dimensional flows and two-dimensional detectors. The velocity V can then be obtained.

These two schemes and the theory presented up to this point assume that a unique value of Δf may be obtained for each point q and detector j.

This is not exactly true because in practice, the frequency measure is broadened due to: 1) noise, 2) ambiguity due to range gating, and 3) turbulence in the flow. In most or many cases, the broadening may be tolerated by the use of offset frequency quadrature Doppler detection schemes which produce an output voltage whose mean is proportional to the mean Doppler shift of a broadened signal [3].

C. Flow Reconstruction by Acoustic Transmission

We have previously suggested that fluid flow within a measurement region may be determined by transmitting and receiving acoustic energy through the measurement region along a plurality of rays such that each volume element is transversed by a set of rays having components in each direction for which flow components are to be reconstructed [10]. The propagation time of the acoustic energy along the plurality of rays constitutes the only measurements required by this method which has now been verified for flows with velocities small compared to the speed of sound [4]. Since this method is analogous to computed reconstruction tomography methods and has been reported elsewhere, the corresponding theory is not reported here.

D. Synergistic Flow Reconstruction

It is clear that both transmission reconstruction and Doppler methods could be applied simultaneously with sufficient parallel data collection and processing capability. Such an approach, combining larger apertures and both imaging modes, although perhaps impractical at this time, has several theoretical advantages: 1) greater signal-to-noise ratios, 2) greater spatial and velocity resolutions, 3) the transmission reconstruction mode can provide refractive index information for correction of the Doppler imaging mode, and 4) drag velocity might be calculated from the difference between the Doppler mode velocity image (scattering center velocity) transmission mode velocity image. These principles could be applied to statistically steady-state flow using one Doppler channel and one transmission channel by time multiplex methods.

5. Computer Simulation and Experimental Studies

An example of the resolution capability of the synthetic focus technique is demonstrated in figure 7. This figure is very significant because it presents experimental evidence that resolution of less than one-half wavelength (at the center frequency of a pulse) can be obtained with ultrasound; at 3 MHz this corresponds to 0.25 mm. It is expected that, when synthetic focusing, refractive index reconstruction and other ultrasound imaging modalities are combined, a synergistic union will result. Thus, each mode will not only add its own form of new information but will also help remove some of the limitations of other forms of imaging. For example, knowledge of refractive index can correct for defocusing effects in echo imaging mode [9,11].

Thus, a major limitation to applying the complete capabilities of the synthetic focus technique to complex tissues can be solved by the synergistic treatment of the problem of refraction of ultrasound. Consequently, an iterative correction of refraction has been developed. This ray tracing technique has also been approached from established geophysical seismic imaging theory. The corrections used by seismologists to unscramble their seismographic results indicate the feasibility of this approach. An example of the order of improvement attending images originally collected by synthetic focus methods, when seismic image correction techniques are used, is given in figure 8. This image is significant because it represents (to our knowledge) the first application of seismic wave migration techniques to real ultrasound data. This image has been presented in an earlier paper [9].

In these images presented in figures 7 and 8, no attempt has been made to accurately control the waveform of the echo from a single point to maximize resolution. Although, the right-hand

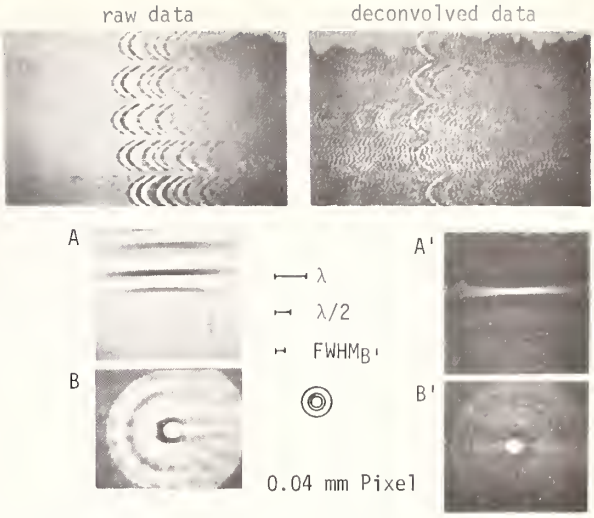

Fig. 7 Synthetic focus images of a nylon thread from data taken from one view angle and from multiple view angles. The top left image represents the raw data from 26 receiver elements for each of five transmitters. Left image A is the corresponding synthesized image. The lower left image B is obtained from simulating the effect of many such 32 element arrays on a circle or radius corresponding to geometry of image A. Top right is the result of deconvolving the ray data of top left with impulse response of the system. Middle right A and lower right are images synthesized from deconvolved data and corresponding to A and B, respectively. The labeled line segments and circles in the center are the relative wavelength of sound drawn to the same scale as the reconstructed images. Note that the full width at half maximum of the peak in image B' (FWHM$_{B'}$) is less than one-half wavelength ($\lambda/2$) while that in image B is larger and more nearly $\lambda/2$. Each picture element is .04 mm square. The resonant frequency of the transducer elements is about 3 MHz. (Reproduced with permission from Johnson et al., Digital Processing of Biomedical Images, 1976, pp. 203-226.)

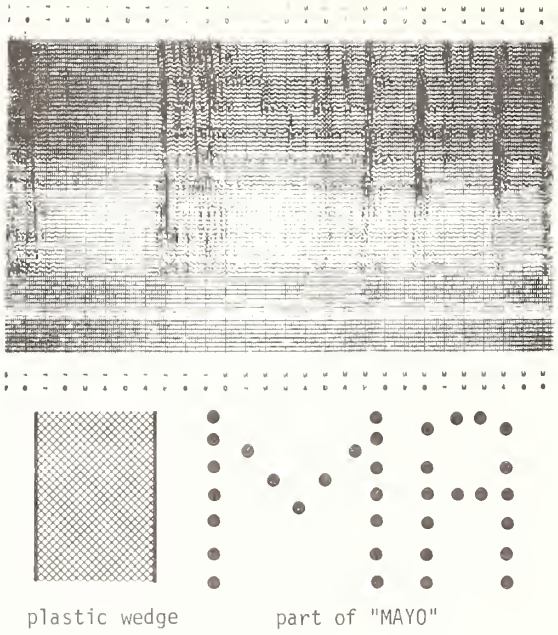

Fig. 8 Refraction corrected synthetic focus image. The bottom portion of figure shows a plastic wedge and pattern of nylon threads which spell "Mayo", however, only the "MA" portion is visible in the figure. An array of 32 transducer elements is located to the left but is not shown. Sonic waves produced by the array refract through the wedge, reflect or scatter from the threads, pass back through the wedge and are then received by the array. No recognizable image was produced when the corresponding data was processed with a simple synthetic focus algorithm which assumed constant speed of the ultrasound waves. The out-of-focus image produced by this simple algorithm is not shown here.

The image at the top is the result of application of a geophysical data processing algorithm which corrects for refraction without prior information of the presence of the wedge. This is accomplished by "wave front migration" techniques which determine the effective refractive index layer by layer as the algorithm works itself away from the array. Such algorithms work for layered materials but could be extended to structures found in the human body. The center frequency of the damped burst transmitted from the array is 3 MHz. The target is the same one reported in Volume 6 of Acoustical Holography by S. A. Johnson et al. [7].

side of figure 7 shows the image produced by a deconvolution process which satisfies only the general requirements. Therefore, a computer simulation study was undertaken to investigate the maximum 2-D resolution limit which can be obtained with a signal constrained to have no frequency components greater than an upper frequency limit f_m. This transmitted kernel signal h(t) was chosen to have a frequency distribution given by $H(f) = H_0|f|$ for $|f| \leq f_m$ and $H(f) = 0$ for $|f| > f_m$. This function is the well-known Ramachandran Lakshminaraynan kernel [15]. A data collection geometry of a 12 cm radius ring of 120 common transmitter and receiver positions equally spaced on 360 degrees was simulated. Imaging was confined within a concentric 7 cm circle. The value of f_m was set at 1 MHz and the simulated received echo signals were sampled at 100 ns intervals. The simulated received echo signals were back projected along ellipses in the image space as per figure 4. The 2-D point response function (2-D PRF) was found not to differ significantly between points near the center and edge of the 7 cm radius imaging region. Various (time) frequency filtered versions of the above kernel were tried also. Only slight improvement in 2-D PRF was observed with some kernels but reduction in 2-D side lobe response could be obtained with an attendant slight loss in resolution with other kernels. Some of the results of these studies are presented in figure 9.

Since the experimental image obtained by application of the new transmission mode fluid temperature and vector velocity technique have been published in more detail previously [4], only one example reconstruction is presented here. Figure 10 shows reconstructions of fluid flows made in the refractive index reconstruction breast scanner at Mayo Clinic. Applications of these techniques, for example, for measurement and reconstruction of tissue temperatures during hyperthermia cancer therapy have been reported elsewhere [16].

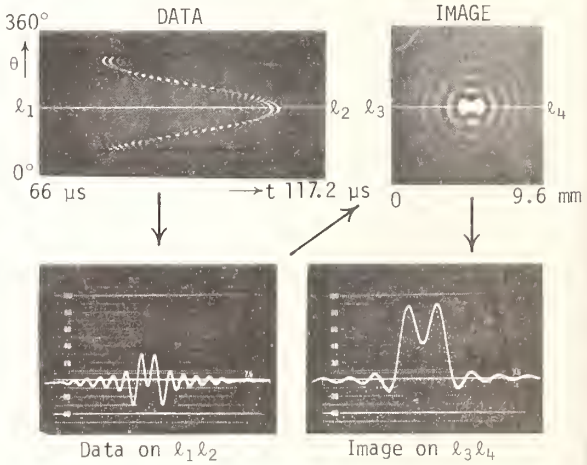

Fig. 9 Illustration of simulated data and corresponding synthetic focus resolution test. Top left: gray scale plot of received data for two scattering centers separated by 1/2 wavelength (measured at the maximum frequency limit of transmitted kernel). The amplitude for 120 views on 360° vs time is shown. Bottom left: amplitude plot of above data along brightened line l_1l_2. Top right - 0 mm by 9.6 mm synthetic focus image (64 by 64 pixels) from these data. Bottom right: amplitude plot along the white line l_3l_4 in the above image demonstrating the resolution of the two point targets. In the gray scale images above, gray = zero, black = negative, and white = positive amplitudes.

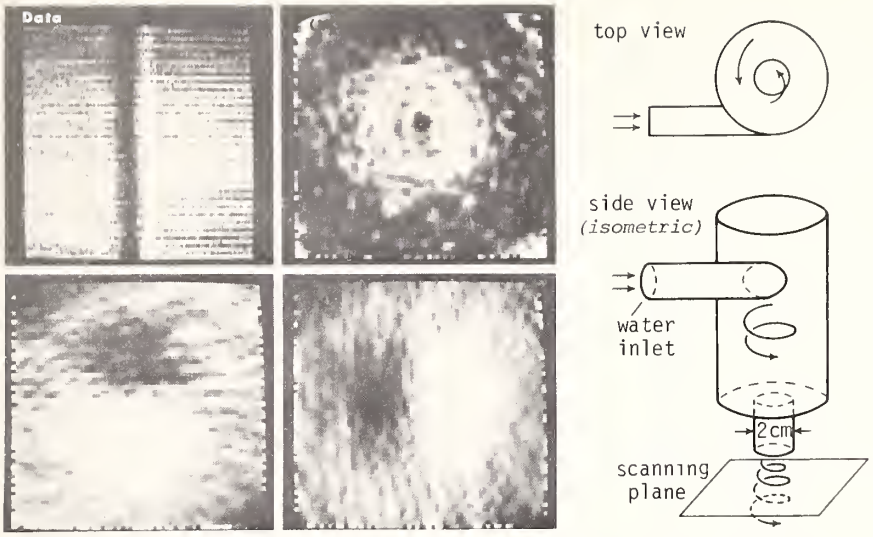

Fig. 10. Experimental data and reconstruction of vector components of fluid vortex. Top left shows experimental data and is an image of the difference between the time of arrival with flow and without flow (fast arrival = white, no change gray, slow = black) vs. scan position (left to right) vs. angle of view (top to bottom). Top right shows reconstructed planar fluid speed $(V_x^2 + V_y^2)^{1/2}$, black is zero, white is positive. Bottom left shows x component of velocity V_x. Bottom right shows y component of velocity V_y. In V_x and V_y, black is negative, gray is zero and white is positive. Reconstruced flow is maximum (73 cm/s) at a radium of 0.62 cm. Reconstructions are 64 pixels per side. Geometry of vortex scanning plane, and vortex generator are shown in top and side views in right margin. (Reproduced with permission from Greenleaf et al., Quantitative Imaging from Transmission Ultrasound (in press).)

6. Conclusion

We suggest that instruments capable of producing higher resolution images of specific ultrasound tissue parameters would provide a valuable service in clinical applications. Wide aperture techniques are known which can provide this high resolution. To be successfully applied in the human body, these wide aperture techniques must be modified to compensate for refraction and possibly, in some cases, also diffraction effects. Candidate techniques can be found in the synthetic focusing methods developed in our laboratory and in analogous geophysical or seismic methods. These techniques can provide resolution of one-half wavelength in homogeneous, isotropic media. It seems reasonable that this degree of resolution may be approached in the body by use of wide apertures and improved refraction and absorption compensating algorithms. Improvement of resolution from one wavelength to one-half wavelength is difficult because knowledge of the spatial and temporal history of the transmitted and received waveform is necessary for application of these algorithms. This knowledge may, in principle, be obtained with the proper transducer design and scanner geometry. Our computer simulation and laboratory experiments provide encouragement and evidence that resolutions of about one to one-half wavelength should be feasible in some applications. We further predict that efforts to design economical scanners to provide this resolution will be a fruitful research and development endeavor. We believe such endeavors will rely heavily upon the use of high speed digital data processing methods and sophisticated mechanically and electronically scanned apertures with large solid angles.

Acknowledgment

The support from Dr. Earl H. Wood, Dr. Erik Ritman, and the staff of the Biodynamics Research Unit, Mayo Clinic, is appreciated. The refraction corrected image of the "MA" shown in figure 9 was computed using seismic migration techniques with the help of John Farr, of Houston, Texas, and his help is greatly appreciated. This research was supported by Grants HL-00170, HL-00060, RR-00007, HL-04664, NIH-HT-42904 from the National Institutes of Health, United States Public Health Service; NCI-CB-64041 from the National Cancer Institute.

References

[1] Wolfe, J. N., Risk for breast cancer development determined by mammographic parenchymal pattern, Cancer 37, 2486-2492 (1976).

[2] Wolfe, J. N., Breast patterns as an index of risk for developing breast cancer, Am. J. Roentgenol. 126, 1130-1139 (1976).

[3] Woodcook, J. P., Development of the ultrasonic flowmeter, Ultrasound in Medicine and Biology 2, 11-18 (1975).

[4] Johnson, S. A., Greenleaf, J. F., Tanaka, M., and Flandro, G., Reconstructing three-dimensional temperature and fluid velocity vector fields from acoustic transmission measurements. Instrument Society of America Transactions, March 1977 (in press).

[5] Sandler, H. and Rasmussen, D., Angiographic analysis of heart geometry, in Roentgen-, Cine-, and Videodensitometry, Paul H. Heintzen, ed., pp. 212-223 (Georg Thieme Verlag, Stuttgart, 1971).

[6] Cardiovascular applications of ultrasound. Proceedings of an International Symposium held at Janssen Pharmaceutics, Beerse, Belgium, May 29-30, 1973. Robert S. Reneman, ed. (American Elsevier Publishing Company, Inc., New York, 1974).

[7] Johnson, S. A., Greenleaf, J. F., Duck, F. A., Chu, A., Samayoa, W. F., and Gilbert, B. K., Digital Computer Simulation Study of a Real-Time Collection, Postprocessing Synthetic Focusing Ultrasound Cardiac Camera, in Acoustical Holography, Newell Booth, ed., Vol. 6, pp. 193-211 (Plenum Press, New York, 1975).

[8] Duck, F., Johnson, S. A., Greenleaf, J. F., and Samayoa, W., Digital image focusing in the near field of a sampled acoustic aperture, Ultrasonics, 83-88 (March, 1977).

[9] Johnson, S. A., Greenleaf, J. F., Bahn, R. C., Samayoa, W. F., Duck, F., Hansen, C., Tanaka, M., and Lent, A., Reconstruction of three-dimensional ultrasound tissue properties from transmission and other data. American College of Radiology Conference on Computerized Tomography and Radiology, St. Louis, Missouri, April 25-28, 1976, pp. 149-162.

[10] Johnson, S. A., Greenleaf, J. F., Samayoa, W. F., Duck, F. A., and Sjostrand, J., Reconstruction of three-dimensional velocity fields and other parameters by acoustic ray tracing. 1975 Ultrasonics Symposium Proceedings, IEEE Cat. #75 CHO 994-4SU.

[11] Claerbout, J. F., Fundamentals of Geophysical Data Processing with Applications to Petroleum Prospecting (McGraw-Hill, New York, 1976).

[12] Greenleaf, J. F., and Johnson, S. A., Algebraic Reconstruction of Spatial Distributions of Refractive Index and Attenuation in Tissues from Time-of-Flight and Amplitude Profiles, in Ultrasonic Tissue Characterization, M. Linzer, ed., National Bureau of Standards Spec. Publ. 453, pp. 109-119, October, 1976. (U.S. Government Printing Office, Washington, D.C., 1976).

[13] White, R. W., Acoustic ray tracing in moving inhomogeneous fluids, Acoustical Society of America 53 (6), 1700-1703 (1973).

[14] Brooks, Rodney A. and Di Chiro, Giovanni, Principles of computer assisted tomography (CAT) in radiographic and radioisotopic imaging, Phys. Med. Biol. 21 (5), 689-732 (1976).

[15] Ramachandran, G. N., and Lakshminarayanan, A. V., Three-dimensional reconstruction from radiographs and electron micrographs: application of convolutions instead of Fourier transforms, Proc. Natl. Acad. Sci., U.S. 68 (9), 2236-2240 (1971).

[16] Johnson, S. A., Greenleaf, J. F., Rajagopalan, B., Christensen, D. A., and Baxter, B., Nonintrusive acoustic temperature tomography for measurement of microwave and ultrasound-induced hyperthermia. Workshop on Electromagnetics and Cancer, 1977 IEEE-MTTS International Microwave Symposium, June 24, 1977. (Submitted to the Journal of Bioengineering.)

Reprinted from *Ultrasonic Tissue Characterization II*, M. Linzer, ed., National Bureau of Standards, Spec. Publ. 525 (U.S. Government Printing Office, Washington, D.C., 1979).

MAPPING TRUE ULTRASONIC BACKSCATTER AND ATTENUATION DISTRIBUTION IN TISSUE - A DIGITAL RECONSTRUCTION APPROACH

F. A. Duck and C. R. Hill

Physics Division, Institute of Cancer Research
Clifton Avenue, Sutton, Surrey, United Kingdom

The back-scattered intensity from any location in an ultrasonically irradiated medium is dependent upon both the local back-scattering cross-section and the attenuation by the overlying medium. An iterative digital reconstruction technique has been investigated which is capable of mapping quantitatively and separately the distributions of attenuation coefficient and back-scatter cross-section using multiple pulse-echo data. Such a technique will enable tissue to be characterised on the basis of these two separate acoustic parameters. A description of the technique is given, together with results from simulation studies leading to an improved processing technique. The potential and limitations of the method are discussed.

Key words: Attenuation; back-scattering cross-section; digital reconstruction; iterative; ultrasound.

1. Introduction

A major deficiency of currently used pulse-echo techniques for tissue characterisation and imaging is their failure to give truly quantitative measurements of tissue-specific acoustic parameters. The problem arises since the observed time-dependent echo amplitudes result from two sets of unknown quantities. These are back-scattering cross-sections of the interrogated volumes and attenuation coefficients of the volume in the transmission path. In conventional B-Scan practice it is usual to emphasise the use of back-scattering cross-section as the useful tissue characterisation parameter, and suppress, or compensate for, the amplitude changes due to the tissue attenuation. This latter is done in two ways. In the first place, a time-gain-compensation (TGC) amplifier is used which compensates for attenuation under the assumption that attenuation, if not uniform, varies in a way which is identical irrespective of transducer position and orientation. The precise form of the attenuation versus time (or depth) variation is often under operator control. Secondly, compound scanning techniques are used which result in an evening-out of the shadowing effects of overlying tissue layers, with any given TGC function. Automatic methods have been developed for adaptive gain compensation (McDicken et al. [1][1]; De Clercq et al. [2]). These have shown that some improvement in gain compensation can be obtained, and presumably the TGC function generated could be used diagnostically. However such techniques are designed to operate on multiple pulse-echo data taken from a particular orientation, assume uniform back-scattering and have an operating time constant of several seconds. In contrast, the method we have developed, and which is described below, generates separately two-dimensional maps of attenuation coefficient and back-scattering cross-section, from multiple orientated pulse-echo data which may be gathered very rapidly for subsequent processing. The two clear incentives for investigating this technique are:

1) It provides a quantitative map of acoustic attenuation coefficients which may be used diagnostically for tissue characterisation.

2) It provides a correctly attenuation-compensated B-Scan, a map which can now be correctly referred to as a back-scatter map.

[1]Figures in brackets indicate literature references at the end of this paper.

2. The Method

As noted above little or no diagnostic information from local attenuation variations is available when compound B-Scanning is used. In simple scanning, however, regions which differ significantly from the expected local attenuation will, by virtue of the pre-set TGC used throughout the scan, result in modified signal levels from regions beyond them. For example a local, dense athero-sclerotic lesion will cast a shadow below it, and a fluid filled cyst of low attenuation will result in increased amplitude signals from tissue beyond it since the gain is over-compensating for attenuation losses. Such signs are used clinically for diagnosis but only under those circumstances where the local effects are clear. The basic concepts are shown simply in diagrammatic form in figure 1, which shows images of a localised increase in attenuation (at A) in a uniform scattering medium. A simple linear scan results in an

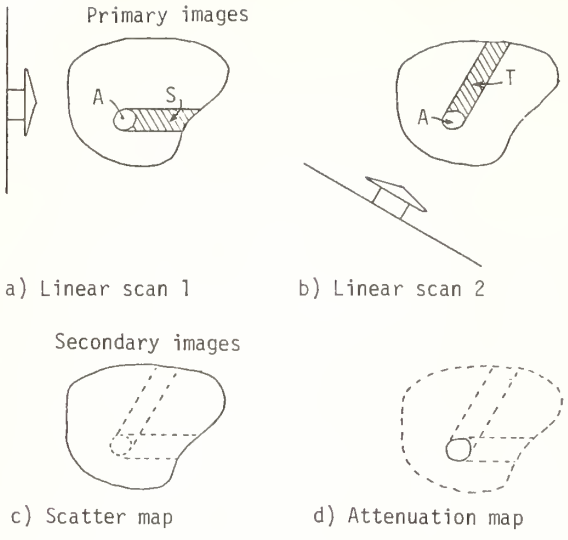

Fig. 1. The generation of separate maps of back-scatter cross-section and attenuation coefficient from multiple pulse echo data. A local increase in attenuation at A within a scattering medium casts shadows S and T in simple linear scan images (a) and (b). The combination of these by peak detection gives a first guess at a scatter map (c). The differences as between this and a, b are used to generate d, the attenuation coefficient map and correct c.

image (fig. 1a) in which a shadow (S) is cast through the image behind the local attenuating site. In this simple case it would normally be assumed that there was indeed a locally high attenuation at A. However, an identical image could have been generated if there was an elongated region of low back-scatter cross-section which was coincident with the shadow region S. These two situations can be easily distinguished by carrying out a second simple linear scan at a new angle (θ) (fig. 1b). Now the region which was in shadow (S) is imaged clearly and there is a new shadow (T). Combining the two simple scans gives a compounds scan (fig. 1c) which may destroy the attenuation information. Comparing the simple and compound scans enables the true attenuation map to be inferred.

In general of course, all tissue layers will cast an acoustic shadow on tissue layers behind them to a greater or lesser extent, and the real situation is additionally complicated because the scattering characteristics of the medium vary. However, as seen below, account can be taken of both sets of parameters simultaneously.

The physical situation described is in many ways conceptually similar to the problem handled in axial tomography, and whose computed solutions are exploited widely in clinical medicine for the reconstruction of x-ray attenuation coefficients from transmitted x-ray intensities. Here the problem of the reconstruction in 3 dimensions of a parameter map from a set of 2-dimensional profiles is reduced to that of the reconstruction of a set of parallel, 2-dimensional distributions of the parameter from related 1-dimensional profiles. Such transmission imaging techniques have been investigated in ultrasound for the reconstruction of acoustic attenuation from transmitted pulse amplitudes (Greenleaf et al. [3]) and for the reconstruction of acoustic refractive indices from transmitted pulse times-of-flight (Greenleaf et al. [4]). The analytic description for this problem was formulated by Radon [5] and a range of computational techniques, based on this analysis or on the use of iterative techniques, have been reported (e.g., Gordon et al. [6]). In transmission imaging the reduction in intensity (or shadow) in the transmitted energy can be measured directly. In the present situation however this reduced intensity signal cannot be measured directly but is re-radiated with a strength depending upon the local back-scatter cross-section. A new set of unknown quantities is therefore introduced. Although the values of these back-scattered cross-sections are unknown their related positions in space are known since the position and orientation of the transducer and time delay can be measured.

3. Theory

The mathematical formulation of the problem is designed to establish a set of simultaneous equations based upon an assumed model; the equations may then be solved iteratively by computational techniques. At present there is no equivalent formulation to that of Radon for the reconstruction of distributions of parameters from transmitted profiles. Indeed it may well be that if there were it would not be of direct use computationally because of the necessary assumptions made in the model.

The back-scattered intensity I_r received from any position r in an ultrasonically irradiated field, can be given as

$$I_r = I_{ref} \cdot A(r) \cdot \exp\left(-2 \int_0^r \alpha_x dx\right) \cdot \sigma_r / r^2 \qquad (1)$$

where A(r) is a factor depending upon the beam geometry;

r = the distance of the scattering target from the acoustic centre of the transducer;
α = the local attenuation coefficient; and
σ = the local back-scattering cross-section per unit volume per steradian.

In logarithmic forms this becomes

$$\ln\left(\frac{I_r}{I_{ref}}\right) = \ln\left(\frac{A(r)}{r^2}\right) - 2\int_0^r \alpha_x dx + \ln(\sigma_r) \qquad (2)$$

In order that the situation is amenable to a digital solution the region to be imaged can be modelled as a rectangular grid of n elements, within each of which α and σ_r are constant, with the only changes being at the boundaries of the elements. This geometry is illustrated in figure 2. In addition it is assumed that there are no losses from absorption and scattering processes outside the region to be imaged. Then, for any image element within this set, eq. (2) can be rewritten as

$$\ln\left(\frac{I_r}{I_{ref}}\right) = K_r - 2\sum_{n=1}^{n} \alpha_n W_n + \ln(\sigma_r) \qquad (3)$$

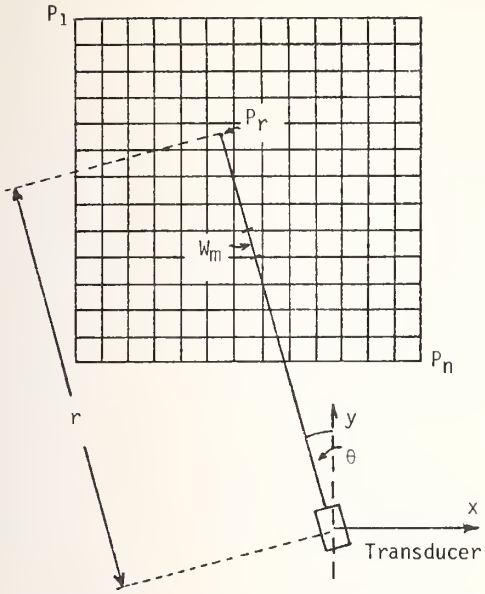

Fig. 2. Image grid geometry. The image consists of n cells $P_1 \ldots P_n$. Each cell P_r has associated with it acoustic parameters of attenuation coefficient α_i and back-scatter cross-section, $\sigma_i W_m$ is the ray/cell intersection length.

where K_r is a potentially known geometric factor, and where W_i, i = 1...n, are a set of geometric weighting factors related to the image grid and beam geometry. If ray geometry is assumed then W_i is the length of intersection of the ray with the image element P_i. In general $W_i = 0$ for many i.

If a multiplicity of measurements I_r are made from a number of directions then eq. (3) extends to a set of simultaneous equations in which α_i, i = 1...n and σ_i, i = 1...n are the unknowns. One characteristic of this set of equations is that it is sparse since, as pointed out above, many values of W_i are zero. A digital iterative technique is suited to the solution since it can handle such large sets of equations under conditions where exact solutions may be multiple, or not exist at all. As pointed out above, such techniques have already been used highly successfully in medicine for the reconstruction of the distribution of x-ray attenuation coefficients from transmitted profiles and in radiation emission tomography.

4. Computational Procedure and Results

As presented, the problem is closer to that posed in emission than in transmission tomography. In the former case the isotopic distribution is to be mapped in the presence of attenuation. In general however the techniques described in emission tomography either ignore the effect of attenuation or compensate for it simply by comparing opposed views. In general no serious attempt is made to generate attenuation maps for diagnostic use. Clearly, our formulation set out above allows for the computation of both back-scatter cross-sections and attenuation coefficients simultaneously. The successful implementation of this approach is described later.

A variety of iterative approaches are available and are under investigation. The technique which at present appears most promising and has been investigated most fully generates the (n + 1)th value of attenuation coefficient from the nth value α_i^n by

$$\alpha_i^{n+1} = \alpha_i^n \left(1 + \frac{e \cdot W_i}{\Sigma(W_K^2) + c^2}\right) \qquad (4)$$

where e is the difference between the data value from any location and the predicted value from the current image arrays, and c is a weighting factor for the back-scatter cross-section. (W_K^2) is summed only over the image elements in the beam up to the position related to the data value used. Similarly, the (n + 1)th value of σ_i is generated from the nth value using eq. (5)

$$\alpha_i^{n+1} = \alpha_i^n \left(1 + \frac{e \cdot c}{\Sigma(W_K^2) + c^2}\right) \qquad (5)$$

These expressions are similar to those used by Gordon et al. [7] in the transmission reconstruction algorithms ART.

The program set up to investigate this approach can receive either simulated or real data. Simulation enables up to 10 circular fields of specified radius, position and acoustic properties to be used. Figure 3 shows a reconstructed image using simulated data from a cylindrical scattering region containing smaller cylindrical regions of increased attenuation. The larger region is of 12 mm radius and has an attenuation coefficient of

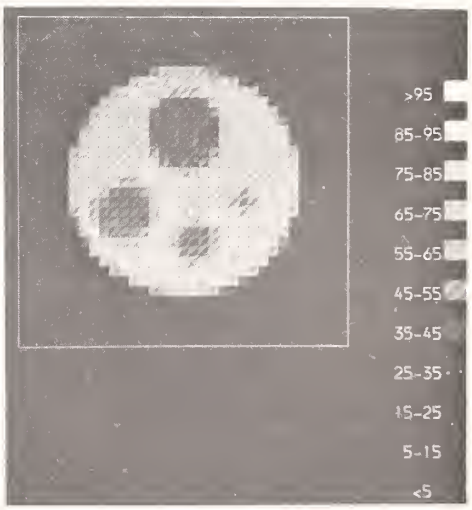

Fig. 3. Reconstructed attenuation coefficient map from simulated data after 4 cycles. The image is on a 33 x 33 matrix of 1 mm square cells. The object was a cylindrical region 12 mm diameter, attenuation coefficient 0.2 neper cm^{-1} including 4 regions 4, 3, 2, 1 mm diameter, attenuation coefficient 0.1 neper cm^{-1}. Data was from 10 linear scans with pulse spacing 0.5 mm. The associated scatter field was uniform.

0.2 neper cm^{-1}. The smaller regions have radii 4, 3, 2, and 1 mm and attenuation coefficients of 0.1 neper cm^{-1}. The image shown was generated after 4 iterative cycles, i.e. after all the data had been used 4 times. The convergence and numerical accuracy of the computation is indicated in figure 4. The attenuation coefficient values in pixels along column 18 are plotted for the second, fourth and sixth iterative cycles. There is little alteration in the values from the third to the fifth cycle and the solution clearly is converging to values which are numerically correct.

Such rapid convergence to a low noise image is dependent very largely upon the choice of iterative procedure used. In particular it has been found that the most rapid convergence has been from a primary scatter map generated from all the data either averaged or peak detected, with a primary attenuation map set to zero. Convergence did occur from a primary scatter map generated from a single linear scan, but was very slow and oscillatory in pattern. The sequence of iterative corrections has also been observed to alter the noise characteristics of the final image. Several sequence orders have been investigated including sequencing along a pulse train, in a forward or re-

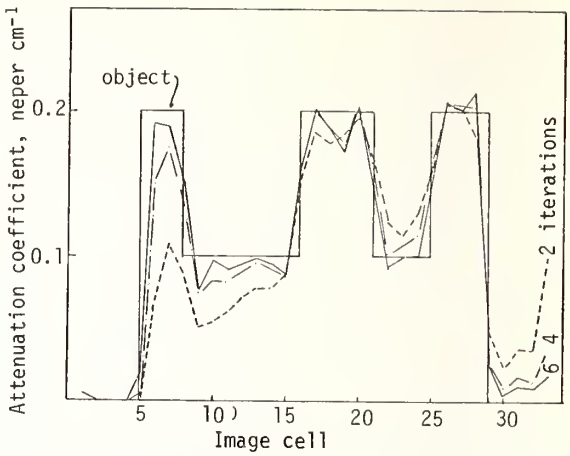

Fig. 4. The convergence of attenuation values along column 18 of figure 3 after 2, 4 and 6 cycles compared with the simulated object values. The starting assumption was $\alpha = 0$ everywhere. Pulses taken in sequence and pulse values in reverse sequence.

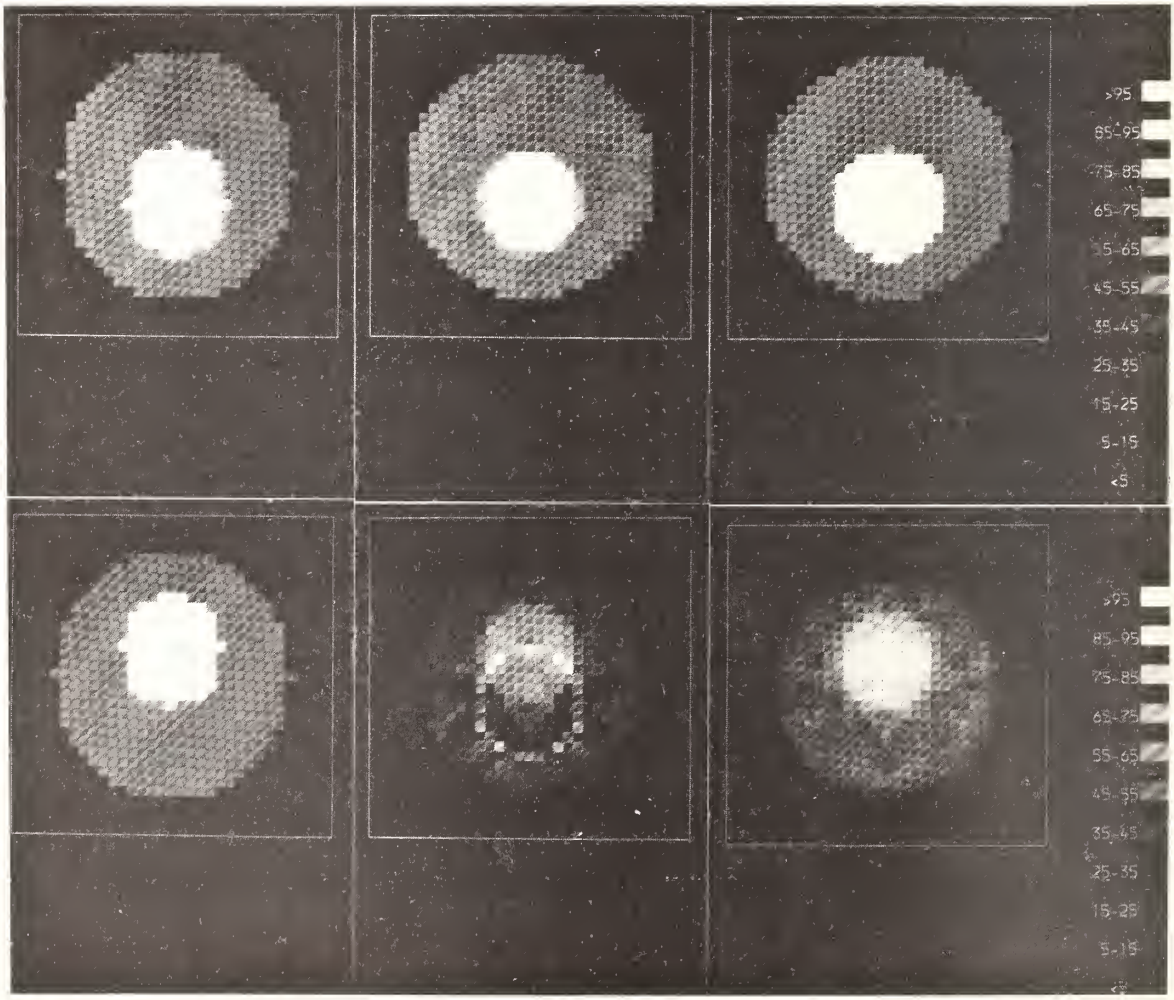

Fig. 5. Reconstructed maps of backscatter cross-section (upper) and attenuation coefficient (lower) from overlapping regions. The objects are shown on the left. The reconstructed maps with high threshold are shown in the center. An edge artifact appears in the attenuation map. Low threshold images (right) are less noisy and show suppression of the artifact.

verse direction, and changing order in which pulses are used. An additional weighting not included in eqs. (4) and (5) has also been used which improved convergence, to compensate for the fact that pixel values close to the transducer are modified more often than those at a distance along a sampled pulse.

Abrupt changes in the scatter level have been found to result in edge artifacts occurring in the attenuating field. This is illustrated in figure 5, which shows reconstruction of a 3-component simulated field with overlapping regions of altered σ and α. A ring artifact in the attenuation plot is clearly evident, associated with the perimeter of the small scattering region. However, when a threshold is introduced to limit the conditions under which eqs. (4) and (5) operate (as in fig. 5, right) the edge artifact is suppressed. It is clear that in tissue it is unlikely that such an abrupt change will occur but such a threshold also enables a control to be kept on the effect of highly directional spectral reflections.

5. Discussion

A convergent iterative computational procedure has been developed to solve the set of equations describing quantitatively the back-scatter of sound from a distributed scattering and attenuating medium. It has been shown that, under simulation conditions, accurate reconstructed maps of both back-scatter and attenuation distributions can be obtained. Some problems posed by the application of the techniques to real data have already been investigated. Since an iterative procedure is being used, it is possible to include controls which limit the range of application within the iterative process to include only those which are deemed to force the process to converge effectively. It is clear however that the success of the application in tissue will depend upon the extent of validity of some of the assumptions used in the model, and this is yet to be evaluated. Anisotropy in σ or α, position errors caused by refractions and the effects of a finite beam width and diffraction errors must all place some ultimate limitation on the method. Within these limitations however the techniques offer the potential of a quantitative imaging of back-scatter cross-section and attenuation coefficients from pulse-echo data.

6. References

[1] McDicken, W. N., Evans, D. H., and Robertson, D. A. R., Automatic sensitivity control in diagnostic ultrasonics, Ultrasonics 12, 173-176 (1974).

[2] DeClercq, A. and Maginness, M. G. Adaptive Gain Control for Dynamic Ultrasound Imaging, in IEEE Ultrasonics Symposium Proceedings pp. 59-63 (1975).

[3] Greenleaf, J. F., Johnson, S. A., Lee, S. L., Herman, G. T., and Wood, E. H., Algebraic Reconstruction of Spatial Distributions of Acoustic Absorption within Tissue from Their Two-Dimensional Acoustic Projections, in Acoustical Holography, P. S. Green ed., vol. 5., p. 591 (Plenum Press, New York, 1974).

[4] Greenleaf, J. F. and Johnson, S. A., Algebraic Reconstruction of Spatial Distributions of Refractive Index and Attenuation in Tissues from Time-of-Flight and Profiles, in Ultrasonic Tissue Characterisation, M. Linzer ed., National Bureau of Standards Spec. Publ. 453, p. 109 (U.S. Government Printing Office, Washington, D.C., 1976).

[5] Radon, J., Über die Bestimmung von Funktionen durch ihre Integralwerte längs gewisser Mannigfaltigkeiten. (On the determination of functions from their integrals along certain manifolds.) Berichte Sächsische Akademie der Wissenschaften (Leipzig), Mathematische-Physische Klasse 69, 262-277 (1917).

[6] Gordon, R. and Herman, G. T., Three-dimensional reconstruction from projections: a review of algorithms, International Review of Cytology 38, 111-151 (1974).

[7] Gordon, R., A tutorial on ART, IEEE Trans. Nuc. Sci., NS-21, 78-93 (1974).

CHAPTER 9

SIGNAL PROCESSING AND PATTERN RECOGNITION

Reprinted from *Ultrasonic Tissue Characterization II*, M. Linzer, ed., National Bureau of Standards, Spec. Publ. 525 (U.S. Government Printing Office, Washington, D.C., 1979).

A COMPREHENSIVE ULTRASONIC TISSUE ANALYSIS SYSTEM

M. Linzer, S. I. Parks, S. J. Norton,
F. P. Higgins[1], D. R. Dietz[2], and R. W. Shideler

National Measurement Laboratory
National Bureau of Standards
Washington, D.C. 20234

and

T. H. Shawker and J. L. Doppman

Clinical Center
National Institutes of Health
Bethesda, Maryland 20014

A progress report on the development of a comprehensive system for ultrasonic tissue characterization is presented. Major elements of the program include computerized tomography studies, particularly for breast cancer detection; opto-acoustic visualization of ultrasonic fields, for testing of new imaging schemes, studies of propagation through inhomogeneous media, in vitro measurements, and transducer calibration; electronic focusing, especially annular array imaging; sensitivity enhancement, using digital signal averaging and pulse compression techniques; computer and chirp waveform techniques for compensation of frequency-dependent attenuation; the SonoChromascope, a digital device for real-time acquisition, processing, and display of B-scan images; and computer-based image processing.

Key words: Annular array; breast cancer; chirp signals; imaging; opto-acoustic; pulse compression; sensitivity; signal averaging; signal processing; tissue characterization; tomography; transducers; ultrasonics.

I. INTRODUCTION

This paper reports on the progress of a Comprehensive Ultrasonic Tissue Analysis System (CUTAS) which is being developed by the Signal Processing and Imaging Group, Center for Materials Science, NBS, and clinically-evaluated by the Department of Diagnostic Radiology, Clinical Center, NIH. Three principal areas are being emphasized in this work:

1. Computerized tomography studies, particularly for breast imaging,
2. Optical visualization of ultrasonic fields.
3. General purpose clinical studies.

II. COMPUTERIZED TOMOGRAPHY STUDIES

Major emphasis to date has been the development of backprojection algorithms for reconstruction of cross-sectional images of reflectivity using a circular array of transducer elements enclosing the object. Three basic modes of data acquisition and image reconstruction were analyzed (fig. 1): (1) the same element serves as transmitter and receiver and data is backprojected along circular paths centered at the element; (2) distinct transmitter and receiver with fixed separation and backprojection along elliptical paths with the elements at the foci; and (3) distinct transmitter and receiver with varying separations and backprojection along corresponding elliptical paths. Point spread functions (PSF's) were evaluated for narrowband, wideband, and an analytically-derived optimum pulse which yields the best sidelobe response and a mainlobe width equal to one-third of the

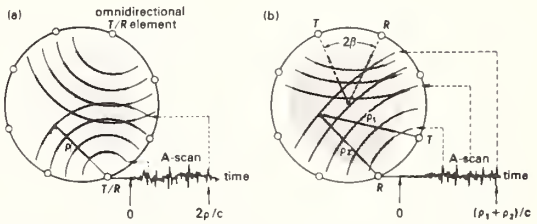

Fig. 1. (a) Operation of circular array with same element serving as transmitter and receiver. Each point in the A-scan is the sume of echoes arising from scatterers along a circular arc centered at the active element. (b) Operation of circular array with separate transmitter and receiver elements. Each point in the A-scan is the sum of echoes arising from points lying along an elliptical arc whose foci are the transmitter and receiver.

[1]Present address: Western Electric Company, Princeton, New Jersey
[2]Present address: McDonnell Douglas Corporation, St. Louis, Missouri

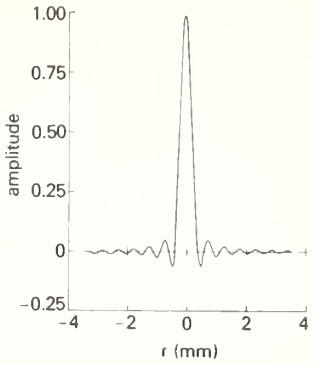

Fig. 2. Point spread function obtained by back-projecting an analytically-derived optimum pulse along circular paths in image space.

wavelength corresponding to the cut-off frequency of the pulse (fig. 2). When backprojection is performed along elliptical paths, corresponding to two separate elements, the mainlobe of the PSF was shown to be broadened by a factor proportional to the cosine of half the angle subtending the two elements at the center of the array. This behavior places a practical restriction of about 45° on the angular separation of the elements. Computer simulations confirmed the salient properties predicted by the analytically-derived PSF's. The characteristics of the PSF's were calculated as a function of the number of array elements, the position of the reflecting point within the object, and the shape of the pulse.

The backprojection analysis has been extended to three-dimensional reconstructions (using spherical transducer arrays) and to incorporate corrections for velocity inhomogeneities in the medium. Work in progress includes the development of a perturbation approach for correcting velocity images and algorithms for frequency-dependent time-gain compensation. A prototype breast scanner is now under construction and will be used to evaluate these various developments in ultrasound tomography.

III. OPTICAL VISUALIZATION OF ULTRASONIC FIELDS

A major laboratory facility for reconstruction and optical visualization of ultrasonic fields has been developed. The system is based on the use of a Michelson interferometric system which is capable of measuring the displacement of a thin metallized 150 mm diameter pellicle immersed in water. Major advances of the NBS development over previous designs include measurement of both the amplitude and phase of the displacement, and absolute calibration of the displacement to approximately one percent accuracy.

This capability of measuring the complex ultrasound field over a large aperture, coupled with computer acquisition and analysis of the experimental data, has provided us with a powerful research tool for visualization and reconstruction of ultrasonic wavefronts. In our initial work, the ultrasonic field of a transducer was measured at the plane of the pellicle placed near the transducer face. The exact (plane wave) solution was used to reconstruct the field at other planes, including that of the transducer face. The ultrasonic wavefronts at other planes were also measured and compared to the calculated values. Both narrowband (gated-cw) and wideband (pulsed) waveforms were used to excite the transducer. Computerized holographic reconstructions of several model targets were also made. An example of a reconstructed plane in the field of a pulsed transducer is shown in figure 3. Other planned

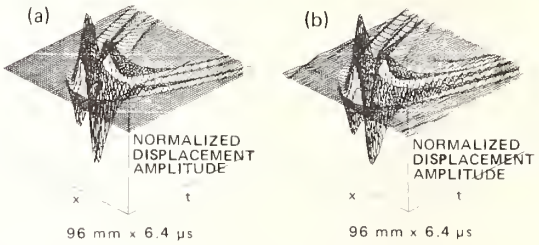

Fig. 3. (a) Computer reconstruction of a propagating wideband pulse at 100 mm (far-field) from transducer face. Reconstruction was based on measurement of the time-dependence of the amplitude and phase of the pulse in a near-field plane. (b) Actual measurement of pulse at 100 mm plane.

uses of the system include studies of new ultrasonic imaging schemes, measurements of ultrasonic parameters of tissue in vitro, and examination of ultrasonic propagation through inhomogeneous media.

IV. GENERAL-PURPOSE CLINICAL STUDIES

A general-purpose clinical scanner is now under active development (fig. 4). Major components of the system include annular array focusing for improving resolution; sensitivity enhancement techniques using A- and B-scan averaging, chirp-radar approaches and focusing; first-order corrections for frequency-dependent attenuation in the medium; and improved signal processing approaches combining the real-time acquisition, processing, and display capability of the Sono-Chromascope with computer post-processing. To date, our approach has been to evaluate each component separately as it is developed. Eventually, we expect to integrate these various elements into a unified facility for clinical ultrasound examinations.

A. Annular Array

1. Expanding-Aperture Annular Array

A dynamically-focused annular array system for contact B-scanning has been developed (fig. 5). The design is based on a constant F-number approach, whereby, at short focal lengths, the aperture is expanded in proportion to the focal length. This approach allows the use of wider array elements, thus increasing the sensitivity of the system and reducing radial-mode coupling. Other major advantages include a substantial reduction in the delays and refocusing rates required for the lens synthesis with a corresponding reduction in the electronic complexity of the system. The initial design employs an array,

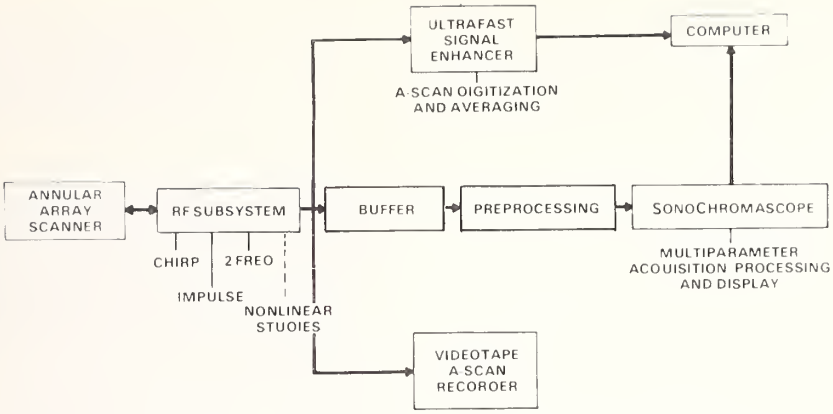

Fig. 4. Block diagram of general purpose clinical ultrasound system.

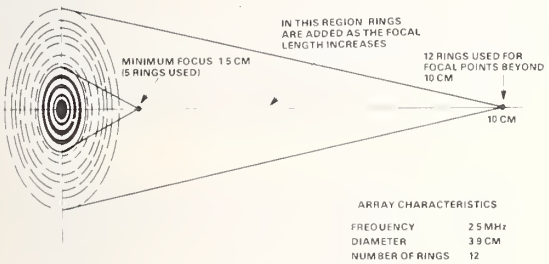

Fig. 5. Operation of the expanding-aperture array with dynamic focusing on receive.

operating at 2.25 MHz, with four annuli active at the near focal length of 1.5 cm. As the focal length increases, the array expands to a maximum of twelve rings, with 4.0 cm outer diameter, for focal lengths greater than 12 cm. A single, tapped delay line with 1 μs total duration provides the time delays for focusing on receive. A continuously-variable point or line focus is provided on transmit. Experimental measurements vides the time delays for focusing on receive. A continuously-variable point or line focus is provided on transmit. Experimental measurements of the focusing properties of the system have been made. Some of these results are shown in figures 6 and 7. Clinical evaluation of the annular array scanner is now underway.

(a) (b)

Fig. 6. B-scans of AIUM test object with a single fixed-focus transducer (a) and with the dynamically-focused annular array (b).

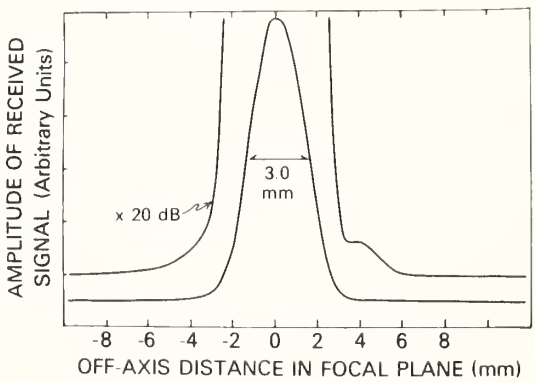

Fig. 7. Measured response of the annular array focused at 10 cm on transmit and receive.

2. Wideband Annular Array Response

Theoretical studies of the effect of bandwidth on the focal plane response of a circular lens and annular array were carried out. Particular emphasis was placed on lens systems operating at approximately 50 percent bandwidth, typical of those used in ultrasound imaging. An analytical model of the focal plane response of both the circular lens and annulus, driven by an impulse, was developed. The wideband response was then calculated by convolving the impulse response with the driving function. For a circular lens, the beam width in the focal plane, as well as the position and height of the sidelobes, was analyzed as a function of bandwidth and aperture weighting. The wide bandwidth model of an annulus was used to calculate the response of an annular array. A detailed comparison was made of this model with the experimentally-measured response of an array, operating at 2.25 MHz with 40 percent bandwidth (fig. 8).

B. Ultrafast Signal Averaging and Pulse Compression Techniques

A signal averager and pulse compression system has been developed for sensitivity enhancement in ultrasonic diagnosis. Potential applications include the use of transducers which are ineffi-

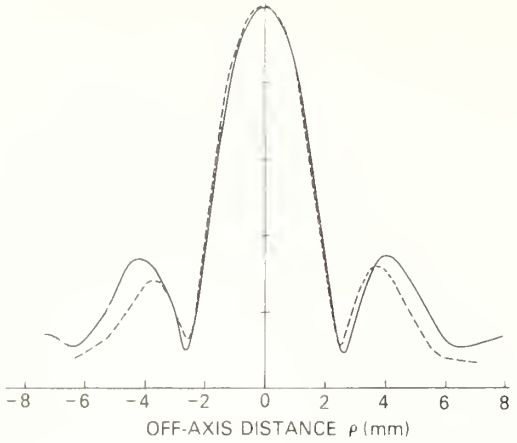

Fig. 8. Field pattern at 10 cm generated by a 0.4 diameter piston transmitter and a thin, 1.4 cm diameter, annulus receiver. The solid line is the calculated response and the dashed line is the measured response.

cient but otherwise have very desirable features (e.g., point and line sources, polymer transducers, CdS phase-insensitive transducers); higher frequency operation for improved pattern recognition and increased resolution; detection of small reflections; examination of obese patients; and penetration through skull and bone. These systems also make it possible to reduce peak power while keeping average power, and hence sensitivity, constant.

1. Signal Averager

The signal averager is capable of real-time (unbuffered) averaging at 50 MHz rates. To our knowledge, this device is the fastest digital averaging device in existence. Major features include 4K 24-bit words, 12.5 kHz maximum repetition rate, computer interface, 6-digit cursor readout of signal amplitude, region of interest expansion (up to a factor of 16), 3-digit settability of sample rate, internal/external trigger, internal delay, segmented memory capability (full, halves, quadrants, octants), plug-in ADC's (4 bit, 50 MHz; 8 bit, 20 MHz), ADC resolution enhancement (via ordered dither), display normalization and semi-real time display at high frequencies. The sensitivity-enhancement capability of the averager was demonstrated on a PZT line source and on a number of highly-attenuating biomaterials, including human tibia (fig. 9), and a fiber composite (fig. 10) used in synthetic implants.

2. Pulse Compression

The pulse compression circuit incorporates a surface acoustic wave (SAW) "chirp" filter. Pulse compression ratios of 30:1 and 8:1 have been obtained in the case of 8 MHz and 3 MHz filter bandwidths, respectively. An example of both an expanded and compressed (8:1 compression ratio) echo from a human heart in vivo is shown in figure 11. The chirp system was also used to compensate for frequency-dependent attenuation in the medium by modulating the amplitude of the

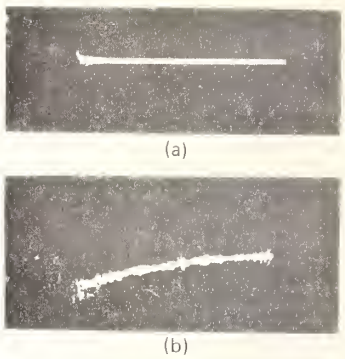

Fig. 9. Ultrasonic reflection from posterior cortex of tibia; (a) no averaging; (b) after averaging for 2^{15} scans.

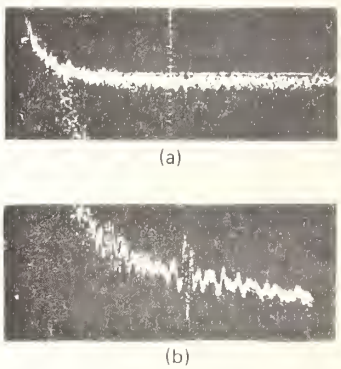

Fig. 10. Backwall reflection from 5 cm thick fiber composite: (a) no averaging; (b) after averaging for 2^{15} scans.

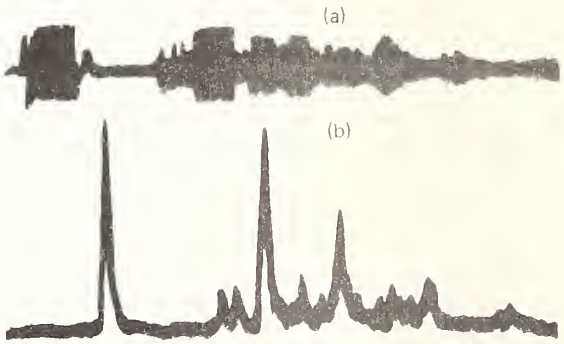

Fig. 11. Preamplified echo from a human heart in vivo. The initial transient is the clipped transmission pulse; the remaining echoes are from tissue: (a) expanded pulse; (b) pulse after 8:1 compression.

expanded stimulus pulse as a function of time. Since the frequency of this pulse was also time-dependent, the strongly-attenuated frequencies were enhanced. This approach has important implications for improving range resolution and for tissue characterization and is now under detailed investigation.

C. SonoChromascope

The SonoChromascope (fig. 12) is a state-of-the-art device for the digital acquisition, processing, recording, and display of ultrasonic B-scan images.

Fig. 12. Clinical ultrasound examination using the SonoChromascope.

Acquisition algorithms include a choice of log or linear detection; recording the minimum and/or maximum echo for each pass through a pixel (thus, for example, providing a measure of scattering anisotropy); unconditionally writing the last value; and summing with normalization (thereby improving sensitivity). A combination of up to four different algorithms may be applied simultaneously to produce different spatially-congruent images during the same B-scan.

After acquisition, the image or images are displayed on two color-TV monitors. Images in complementary colors may be overlaid to permit visual discrimination of subtle differences. A variety of thresholding and display modes, augmented by a lightpen, permit semiquantitative measurements of ultrasound echo intensity. To use the lightpen, the operator "paints in" the area of interest. As he does so, the average image intensity (or intensities) and the area painted in are displayed on digital readouts.

If more sophisticated processing or storage is required, the data may be transferred to a minicomputer. Processed or stored images may be returned to the SonoChromascope for display.

Spatial and amplitude resolution depend upon the acquisition mode. For example, in the "unconditional write" mode, the word size is 8 bits and the picture contains 480 x 480 pixels; in the sum mode, the word size is 14 bits and there are 480 x 240 pixels.

The SonoChromascope is presently interfaced to a commercial B-scan system, from which it receives the rf or log-detected A-scan signal and appropriate information about transducer position. It is now undergoing clinical evaluation.

V. SUMMARY

A major effort is now underway in developing a comprehensive system for ultrasonic tissue characterization. The program encompasses imaging, including electronic focusing and computerized tomography; sensitivity enhancement; measurement of tissue parameters in vitro; studies of ultrasound propagation through inhomogeneous media; computer and chirp techniques for compensation of frequency-dependent attenuation; real-time digital processing and display techniques; and computer-based image processing. Several of these developments have already been completed, and, where appropriate, are undergoing clinical testing. Complete descriptions of this work will be published shortly.

Reprinted from *Ultrasonic Tissue Characterization II*, M. Linzer, ed., National Bureau of Standards, Spec. Publ. 525 (U.S. Government Printing Office, Washington, D.C., 1979).

THEORETICAL ANALYSIS OF INSTANTANEOUS POWER SPECTRA AS APPLIED TO SPECTRA-COLOR ULTRASONOGRAPHY

W. D. Jennings, E. Holasek, and E. W. Purnell

Department of Surgery, Division of Ophthalmology
School of Medicine
Case Western Reserve University
Cleveland, Ohio 44106, U.S.A.

Spectra-color ultrasonography (SCU), a technique for two-dimensional (B-mode) display of ultrasonic spectral data, has been analyzed theoretically. The analysis includes the use of an instantaneous power spectrum calculated from broadband gated echo spectra produced by an analog spectrum analyzer. The results of the analysis indicate that additional signal processing factors must be added to the SCU system as it was originally designed. With the inclusion of these modifications, the SCU scan represents a true low resolution instantaneous spectral analysis of ultrasonic echo waveforms. An experiment was performed to test the theoretical equations we have developed relating SCU to an instantaneous spectral analysis. The comparison of the SCU signals and the computed SCU equivalent based on an instantaneous power spectrum is presented.

Key words: Instantaneous power spectra: Color-coded B-scan; spectra-color ultrasonography (SCU); spectrum analysis; ultrasonic spectroscopy.

1. Introduction

Several years ago we developed spectra-color ultrasonography (SCU) which was originally designed as an approximate spectroscopic technique to display two-dimensional (B-mode) spectroscopic information from a sector scanned tissue segment [1,2][1]. Originally, the SCU image was formed by first passing a broadband B-scan ultrasonic echo train through a voltage tuned filter set at three different center frequencies (bandpass positions). Each of the three resultant filtered B-scans was then assigned a color (red, green or blue). The three colored B-scans were then superimposed to form a single frequency-dependent color coded B-scan display. The final colored B-mode image displayed frequency-dependent properties of the tissue being scanned, though the precise meaning of the display was not apparent.

The subject of this presentation is an analysis of the SCU process in terms of an instantaneous power spectrum. An instantaneous power spectrum is a time dependent spectral decomposition of a signal. The conventional Fourier Power Spectrum of a signal is defined by an integral of the signal over all time, and thus, is independent of time. An instantaneous power spectrum, however, is a function of both time and frequency. It is the dual functionality of instantaneous power spectra that makes them applicable to signals that originate from spatially distributed sources with varying spectral content, such as ultrasonic echo waveforms.

Several definitions of an instantaneous power spectrum have been devised. We began our work on instantaneous power spectra by attempting to adapt a particular instantaneous power spectrum, the one defined by Chester Page [3], to spectra-color ultrasonography. During our investigations, experimental evidence led us to the conclusion that for spectra-color ultrasonography to represent a true instantaneous power spectrum, it is appropriate to use Morris Levin's modification of Page's definition of an instantaneous power spectrum, rather than Page's original definition. This paper is an account of those investigations.

2. Theory

Essential to the analysis of spectra-color ultrasonography, is the concept of an instantaneous power spectrum. We began with the approach of Chester Page [3] which we will briefly review here. For any time domain signal g(t)[2], the running Fourier transform of g(t) is defined as

$$G_t(\omega) = \int_{-\infty}^{t} g(x)e^{-j\omega x}dx \quad . \qquad (1)$$

[1]Figures in brackets indicate literature references at the end of this paper.

[2]In our case, g(t) is the receiving transducer voltage corresponding to the instantaneous acoustic pressure on the transducer face.

That is, $G_t(\omega)$ is the Fourier transform of the semi-infinite signal g(x) taken from x = -∞ to x = t. Note here that x is a dummy variable, allowing us to use the time variable t as the trailing edge of the gate on g(t). The instantaneous power spectrum of g(t) can then be defined as

$$\rho(t,\omega) = \frac{\partial}{\partial t} \left| G_t(\omega) \right|^2 \quad . \tag{2}$$

Page also shows that $\rho(t,\omega)$ can be represented by

$$\rho(t,\omega) = 2g(t)\mathrm{Re}\left[e^{j\omega t} \int_{-\infty}^{t} g(x)e^{-j\omega x}dx \right] \quad . \tag{3}$$

Using eq. (3) as a starting point, we have analyzed SCU as follows: In the original SCU implementation, the signal g(t) was passed through a voltage tuned filter set at three different bandpass positions. In the frequency domain, the i^{th} filter can be described by some function $C_i(\omega)$. In general, $C_i(\omega)$ is a complex function, including phase delays introduced by the filter as a function of frequency. The time domain representation of the filter will be designated by $c_i(t)$, which is also complex in general. The function $c_i(t)$, is the inverse Fourier transform of $C_i(\omega)$, and is the impulse response of the filter

$$c_i(t) = \frac{1}{2\pi} \int_{-\infty}^{\infty} C_i(\omega)e^{j\omega t}d\omega \quad . \tag{4}$$

Thus, the filtered signal can be described in the time domain by

$$S_i(t) = \mathrm{Re}\left[c_i(t) * g(t) \right] \quad . \tag{5}$$

What we would like to display is the band-limited instantaneous power spectrum of the signal. That is, the desired display is

$$J_i(t) = \int_{-\infty}^{\infty} \rho(t,\omega)C_i(\omega)d\omega \quad . \tag{6}$$

$J_i(t)$ is the instantaneous power (as defined by Page) of the signal g(t) in the frequency band described by $C_i(\omega)$. Substituting eq. (3) into eq. (6) and rearranging we get

$$J_i(t) = 2g(t) \int_{-\infty}^{\infty} C_i(\omega)\mathrm{Re}\left[e^{j\omega t} \int_{-\infty}^{t} g(x)e^{-j\omega x}dx \right] d\omega \quad . \tag{7}$$

If we assume at this point that the filter function $C_i(\omega)$ is a real valued function, rather than complex, we can write

$$J_i(t) = 2g(t)\mathrm{Re}\left[\int_{-\infty}^{\infty} C_i(\omega)e^{j\omega t} \int_{-\infty}^{t} g(x)e^{-j\omega x}dx d\omega \right]$$

or (8)

$$J_i(t) = 2g(t)\mathrm{Re}\left[\int_{-\infty}^{\infty} \int_{-\infty}^{t} C_i(\omega)e^{j\omega t} g(x)e^{-j\omega x}dx d\omega \right] \quad .$$

By combining the exponential terms, and interchanging the order of integration we get

$$J_i(t) = 2g(t)\mathrm{Re}\left[\int_{-\infty}^{t} \int_{-\infty}^{\infty} C_i(\omega)g(x)e^{j\omega(t-x)}d\omega dx \right] \tag{9}$$

or

$$J_i(t) = 2g(t)\mathrm{Re}\left[\int_{-\infty}^{t} g(x) \int_{-\infty}^{\infty} C_i(\omega)e^{j\omega(t-x)}d\omega dx \right] . \tag{10}$$

By use of eq. (4), eq. (10) becomes

$$J_i(t) = 4\pi g(t)\mathrm{Re}\left[\int_{-\infty}^{t} g(x)c_i(t-x)dx \right] \quad . \tag{11}$$

For a filter that is causal in the time domain ($c_i(t) = 0$ for $t < 0$), eq. (11) becomes

$$J_i(t) = 4\pi g(t)\mathrm{Re}\left[\int_{-\infty}^{\infty} g(x)c_i(t-x)dx \right] \quad . \tag{12}$$

The integral in eq. (12) is the convolution integral for g(t) and $c_i(t)$. Using the notation of eq. (5), eq. (12) becomes

$$J_i(t) = 4\pi g(t)S_i(t) \quad . \tag{13}$$

Thus, we come to the conclusion that for SCU to represent a true color coded low resolution instantaneous spectral analysis we must modify the original system in two ways:

(1) The filters used must have filter functions that are real in the frequency domain, or be modified so as to be effectively real.

(2) The filtered waveforms must be multiplied by the broadband signal before video processing and display.

3. Experimental Approach

We have tested the theory by comparing $J_i(t)$ calculated by eq. (6) with $J_i(t)$ defined by eq. (13), which mathematically represents the modified SCU system.

Calculation of $J_i(t)$ by eq. (6) requires measurement of the filter functions $C_i(\omega)$. We used three fixed filters with 1.6 MHz bandwidths centered at 7, 9, and 11 MHz. The fixed filters replaced the voltage tuned filter used in earlier implementations of spectra-color ultrasonography. The spectrum of the ultrasonic echo from a glass block was used as a reference spectrum, and the spectrum of the signal passed through each filter was recorded. The filtered spectra and reference are shown in figure 1. The spectra are plotted from 5 to 15 MHz. A 5 MHz crystal controlled oscillator was used to provide a frequency marker for accurate spectral measurements. All spectra were recorded by our automated data acquisition

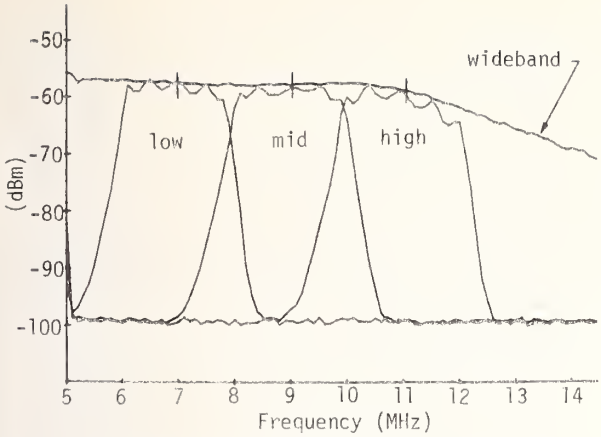

Fig. 1. Wideband reference spectrum and spectra of the low, middle and high bandpass filtered reference signals.

system [4] controlled by a programmable calculator.

A natural sponge was used as the target material because of its stability and similarity to human tissue in acoustical properties. The instantaneous power spectrum, $\rho(t,\omega)$ required by eq. (6), was calculated by eq. (2). To produce the semi-infinite signal $g_t(x)$ we constructed a programmable gating system. Using the crystal controlled 5 MHz source as a clock, the gate could be automatically varied in length in 200 nanosecond increments. Power spectra $|G_t(\omega)|^2$ of the signal gated at increasing lengths were recorded. The value of $(\partial/\partial_t)|G_t(\omega)|^2$ was calculated by subtracting spectra of gated signals of increasing length to approximate the differential. $J_i(t)$ was then calculated as the summation of $C_i(\omega) \cdot (\partial/\partial_t)|G_t(\omega)|^2$ over all frequencies to approximate the integral in eq. (6).

To determine $J_i(t)$ by eq. (13), the filtered signal, $S_i(t)$, was multiplied by the broadband signal, g(t), using a double balanced modulator. A broadband pulse amplifier was used to bring the level of g(t) into the operating range (approximately one volt) of the modulator. The modulator provided bipolar multiplication of the two signals, as shown in figure 2. The multiplied signal for each of the three bandpass filters is shown in figure 3.

For each filter, an appropriate precision delay line was added to the broadband signal before multiplication in the modulator. The delay lines

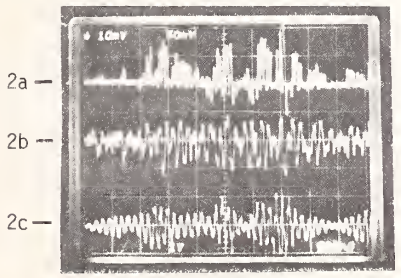

Fig. 2. Analog signal multiplication for the middle frequency band. a) multiplied signal, J(t); b) wideband signal, g(t); c) filtered waveform, $S_i(t)$.

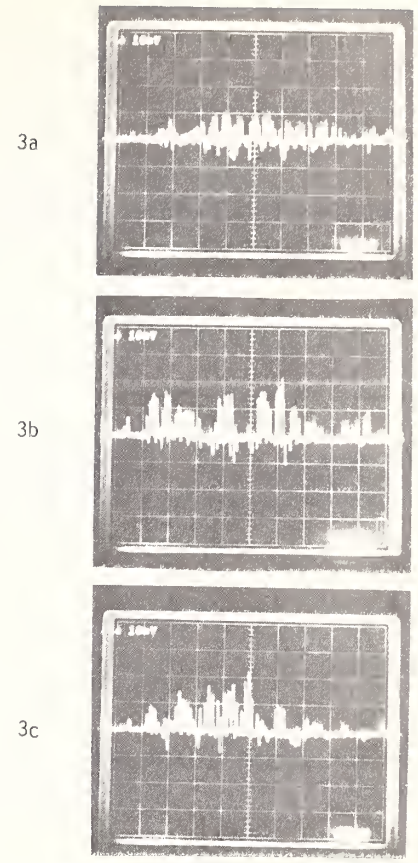

Fig. 3. Analog multiplied signals, $J_i(t)$ for the three frequency bands. a) high frequency band; b) middle frequency band; c) low frequency band.

were necessary to compensate for the group delay through the filters. Group delays were approximately 1 microsecond, but were different for each filter. Thus, the requirement that the filter functions be real was approximately satisfied.

4. Results and Discussion

Figures 4a, 4b, and 4c, show $J_i(t)$ calculated by eq. (6), and $J_i(t)$ determined by the signal multiplication described in eq. (13) for the three filters. The time resolution of the calculated signals is one point every 200 nanoseconds, while the analog multiplied $J_i(t)$ is a continuous function of time. The calculated $J_i(t)$ represents the average of $J_i(t)$ over the 200 nanosecond interval.

Noise in the system was reduced by averaging in the case of the calculated $J_i(t)$. The plots shown in figure 4, represent an average of 40 scans through the 5 microsecond section of sponge. Figure 5 shows the individual scans before averaging, and figure 6 shows plots of the averaged signals. The noise becomes progressively higher with deeper signal penetration, as shown in figure 5. This effect is due to the internal noise of the spectrum analyzer. The signal to noise ratio of the spectrum analyzer was constant for all signal levels, since the spectrum analyzer was used in the logarithmic mode. Thus, for higher signal levels

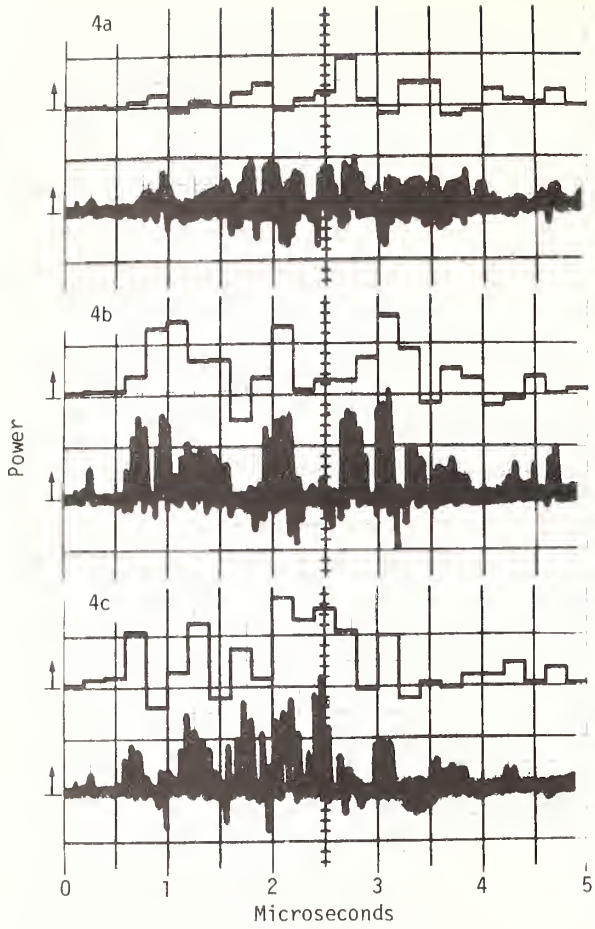

Fig. 4. Comparison of $J_i(t)$ calculated by eq. (6) (upper trace) with the multiplied $J_i(t)$ defined by eq. (13) (lower trace) for the three filters. a) high frequency signals; b) middle frequency signals; c) low frequency signals.

(longer gates) the absolute noise level increased. This resulted in a decreased signal to noise ratio for the differential power spectrum of higher level signals.

It is interesting to note that the time resolution of the multiplied signal $J_i(t)$ is better than the resolution of the broadband signal $g(t)$ and significantly better than the resolution of the filtered signals, $S_i(t)$ used in the original SCU implementation (see fig. 2). This is interpreted as a result of having increased the information bandwidth of the broadband signal $g(t)$ by the bandwidth of the filtered waveform $S_i(t)$ in the multiplied signal $J_i(t)$.

We can also observe that agreement between the calculated $J_i(t)$ and the analog multiplied $J_i(t)$ progressively improves as we go from the high frequency band to the low frequency band. This trend is probably due to the fact that the assumption of a real filter function is better justified for the low frequency filter than for the high frequency filter. The time delay error which was approximately constant for the three filters, is most disruptive to the high bandpass filter, because of the shorter repeat period of the filtered signal.

The results of this experiment show only fair agreement between the band limited instantaneous power calculated by eq. (6), and the band limited instantaneous power produced according to eq. (13). This result demands that we reexamine the assumptions made in the theoretical analysis. The first assumption of a real valued filter function is reasonably valid because of the broadband delay line compensation for the group delay through the filters. The appearance of predominately positive signals in the multiplied waveforms indicates that the filtered and broadband waveforms are largely in phase, though the filters have some dispersive effects. The second assumption was that the filter is causal in the time domain. This assumption also appears valid for passive filters. However, close examination reveals that the two assumptions above are mutually exclusive. That is, if a filter function is real valued in the frequency domain, it must be noncausal in the time domain. This is true

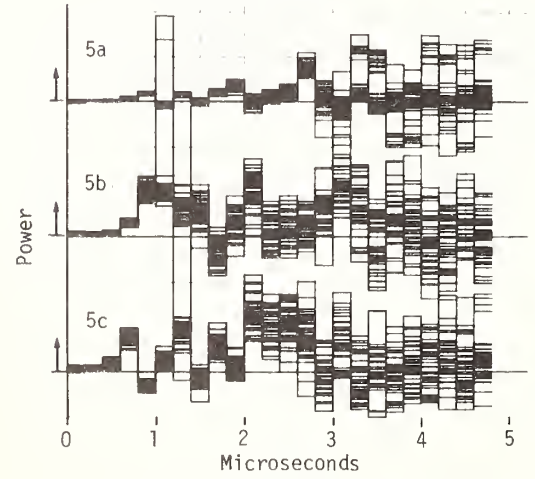

Fig. 5. Individual calculator plots of $J_i(t)$ for 40 scans through the sponge. a) high frequency band; b) middle frequency band; c) low frequency band.

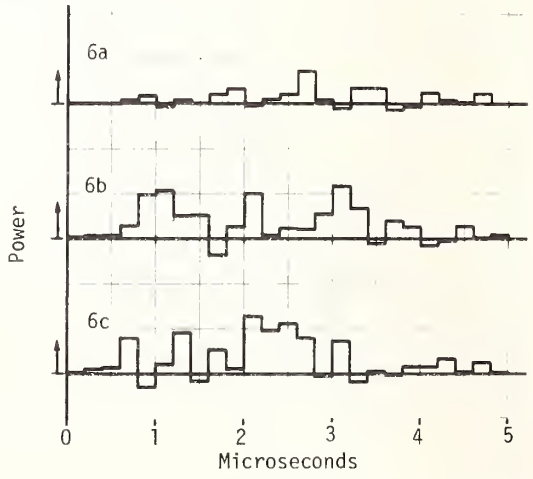

Fig. 6. Calculator plot of the average $J_i(t)$ for the 40 scans in figure 5. a) high frequency band; b) middle frequency band; c) low frequency band.

because a real valued function, when transformed by eq. (4), must have a real part (the integral of the cosine terms) that is an even function of time. An even function of time must be noncausal. Hence, the transition from eq. (12) to eq. (13) is not valid.

5. Time Reversal Symmetry

From the above discussion, it appears impossible to display Page's instantaneous power spectrum by simple signal filtering and broadband multiplication. The restriction to non-causal filters required by eq. (8) introduces a contribution to the instantaneous power from the signal at future times. The time reversal symmetry of the filter function in the time domain means that eq. (13) corresponds to an average of Page's instantaneous power and a similar instantaneous power with the time scale reversed (i.e., a signal taken from ∞ to time t). An instantaneous power spectrum of this type has been introduced by Morris Levin [5].

Levin defines an instantaneous power spectrum analogous to Page's except with the added property of time reversal symmetry. According to Levin, the symmetric instantaneous power spectrum is given by

$$\rho_s(t,\omega) = \frac{1}{2}\frac{\partial}{\partial t}\left[|G_t(\omega)|^2 - |G_t^+(\omega)|^2\right] \tag{14}$$

where

$$G_t(\omega) = \int_{-\infty}^{t} g(x)e^{-j\omega x}dx \tag{15}$$

and

$$G_t^+(\omega) = \int_{t}^{\infty} g(x)e^{-j\omega x}dx \quad . \tag{16}$$

Levin also shows that $\rho_s(t,\omega)$ is given by

$$\rho_s(t,\omega) = g(t)\mathrm{Re}\left[G(\omega)e^{j\omega t}\right] \tag{17}$$

where

$$G(\omega) = \int_{-\infty}^{\infty} g(t)e^{-j\omega t}dt \quad . \tag{18}$$

$G(\omega)$ is simply the frequency spectrum of the complete waveform g(t). By analogy to eq. (6) above, we redefine the band limited instantaneous power $J_i(t)$ (for Levin's spectrum) to be

$$J_i(t) = \int_{-\infty}^{\infty} \rho_s(t,\omega)C_i(\omega)d\omega \tag{19}$$

where $C_i(\omega)$ is defined as before. Substituting eq. (17) into eq. (19) gives

$$J_i(t) = \int_{-\infty}^{\infty} g(t)\mathrm{Re}\left[e^{j\omega t}G(\omega)\right]C_i(\omega)d\omega \quad . \tag{20}$$

Again, assuming $C_i(\omega)$ is real valued rather than complex, eq. (20) becomes

$$J_i(t) = g(t)\mathrm{Re}\left[\int_{-\infty}^{\infty} G(\omega)C_i(\omega)e^{j\omega t}d\omega\right] \quad . \tag{21}$$

The integral in eq. (21) is the inverse Fourier transform of the product $G(\omega)C_i(\omega)$, and hence becomes the convolution of the two corresponding time domain signals

$$J_i(t) = 2\pi g(t)\mathrm{Re}\left[g(t)*c_i(t)\right] \tag{22}$$

or

$$J_i(t) = 2\pi g(t)S_i(t) \tag{23}$$

where $S_i(t)$ is defined by eq. (5). No assumption of causality of $c_i(t)$ is required in the derivation of eq. (23) because of the time reversal symmetry of Levin's instantaneous power spectrum.

Thus the two modifications of the SCU system stated above (broadband delay and signal multiplication) produce a band limited instantaneous power corresponding to Levin's instantaneous power spectrum, rather than Page's spectrum as initially intended.

6. Conclusions

The analysis we have presented indicates that spectra-color ultrasonography should be modified in two ways. First, the filters used must have real filter functions in the frequency domain, including compensation for the time delays through the filter. Second, the appropriate signals to color code and display are the products of the filtered signals with the broadband echo waveform, rather than the simple filtered waveforms.

With these two modifications in effect, SCU represents a true low resolution instantaneous spectral analysis of ultrasonic echoes corresponding to the instantaneous power spectrum of Morris Levin. In addition, the time resolution of the new system exceeds that of the broadband signal.

Acknowledgments

This work was supported in part by National Institute of Health Grant #EY 00224-15 and The Ohio Lions Research Foundation.

References

[1] Holasek, E., Gans, L. A., Purnell, E. W., and Sokollu, A., A method for spectra-color B-scan ultrasonography, J. Clinical Ultrasound, 3, 175-178 (1975).

[2] Purnell, E. W., Sokollu, A., Holasek, E., and Cappaert, W. E., Clinical spectra-color ultrasonography, J. Clinical Ultrasound, 3, 187-189 (1975).

[3] Page, C. H., Instantaneous power spectra, J. Applied Physics, 23, 103-106 (1952).

[4] Holasek, E., Jennings, W. D., Sokollu, A., and Purnell, E. W., Recognition of Tissue Patterns by Ultrasonic Spectroscopy, Ultrasonic Symposium Proceedings, IEEE Cat. #73 CH 0807-8SU, 73-76 (1973).

[5] Levin, M. J., Instantaneous Spectra and Ambiguity Functions, IEEE Transactions Information Theory, Vol. IT-10, 95-97, (1964).

Reprinted from *Ultrasonic Tissue Characterization II*, M. Linzer, ed., National Bureau of Standards, Spec. Publ. 525 (U.S. Government Printing Office, Washington, D.C., 1979).

IDENTIFICATION OF TISSUE PARAMETERS BY DIGITAL PROCESSING OF REAL-TIME ULTRASONIC CLINICAL CARDIAC DATA

L. Joynt, D. Boyle, H. Rakowski, R. Popp, and W. Beaver

Center for Integrated Electronics in Medicine
and Division of Cardiology
Stanford University
Stanford, California 94305, U.S.A.

A study to assess the feasibility of obtaining diagnostically useful tissue characterization information by digitally processing clinical cardiac data is described. Normal subjects, myocardial infarction, IHSS, and amyloid patients were studied. The data acquisition system used to record data from a real-time scanner is also described. Significant changes in the RF signals and frequency spectra as the heart moves were noted over very short time intervals, indicating the need for a dynamic tissue characterization measure. Wide variation in the spectral characteristics of the signals from the normal population were found. Behavior of the spectra for the MI patient data were noted which differentiated them from the other subjects.

Key words: Clinical cardiac data; Fast Fourier Transform; digital processing; frequency spectra; in vivo; microprocessor-controlled data acquisition; myocardial infarction; real-time; tissue characterization; ultrasound diagnosis.

1. Introduction

The possibility of obtaining diagnostic information by processing clinical ultrasound data from cardiac patients is explored in this paper. Lele et al. [1][1] and Yuhas et al. [2] have differentiated between normal and ischemic or infarcted heart muscle in vitro on the basis of measurements of acoustic attenuation. Extension of these methods to clinical ultrasound examinations is complicated by factors including cardiac motion, intervening tissue, and the angle of incidence of the ultrasound beam to the interrogated tissue [3]. The most direct approach to exploring the effects of these difficulties in the clinical environment is to interface to an instrument in clinical use. Coupling a real-time scanner to a high-speed data acquisition system makes it possible to obtain information on the dynamic state of the heart. A preliminary study on a limited number of patients and normal subjects was done in order to assess the feasibility of deriving diagnostically useful information about the type and state of cardiac tissue by digital processing of clinically acquired data.

2. Data Acquisition

A. The Data Acquisition System

The design of the data collection system for this project is based on a number of considerations. In order to eliminate possible information loss due to the detection process, the rf signal is digitized for off-line computer processing. Experience with an earlier version of the data system had shown that large changes occur in signals recorded at 100 ms intervals. Accordingly, the current version was designed to record as continuously as feasible so that these changes could be observed in more detail. Thus, large quantities of data must be recorded at a very high rate. A compromise solution, trading off the speed of semiconductor memory for the low cost of tape memory by using both high and low speed semiconductor memory to buffer the input to a magnetic tape drive, is used in the present system. A Biomation 8100 Transient Recorder is used as the A/D converter and high speed buffer. The data is then transferred to a large slow speed buffer, consisting of 32 kilobytes of microcomputer memory, which stores data from a number of scan lines for subsequent recording on a magnetic tape drive having a transfer rate of 30 kilobytes/second. This device provides mass storage and convenient input to a computer for later processing.

The data acquisition performance of the system is determined by the limitations of the digital hardware and by the characteristics of the scanner. When the Varian real-time sector scanner is used as the signal source, data may be acquired from any one cursor-selected scan line every 600 microseconds or from the sequence of scan lines comprising a frame every 30 milliseconds. The rf signal is digitized at 20 MHz so that about 100 microseconds or 7 cm of data can be stored in the transient recorder's 2048 word memory. Only those samples actually corresponding to the area of interest are transferred to the microcomputer memory buffer. The total time to re-

[1]Figures in brackets indicate literature references at the end of this paper.

cord data from one scan line is under 2 milliseconds. Thus, a substantial portion of a frame can be digitized at real-time rates. The system also includes the option to record a sequence of lines at 30 ms intervals in order to cover a complete cardiac cycle in one buffer. When the data buffer is filled the recording process is interrupted for a few seconds while the data is transferred to magnetic tape.

Data acquisition is triggered at a pre-selected point of the cardiac cycle. A simultaneous Polaroid picture can be obtained. If more than one buffer is required, subsequent buffers also begin at the selected point of the cardiac cycle.

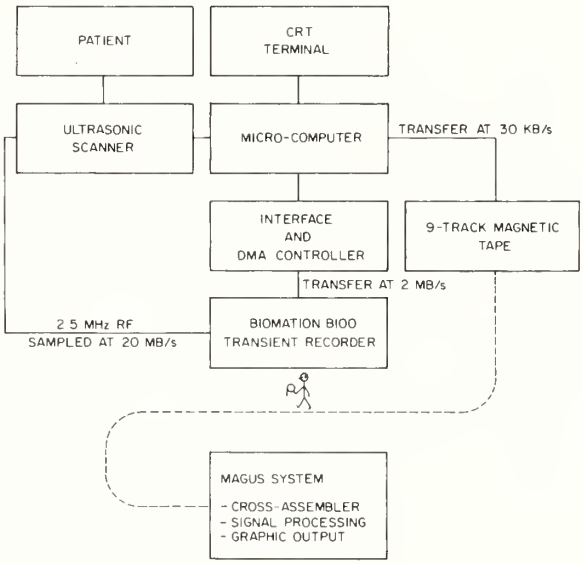

Fig. 1. Block diagram of the data acquisition system. The RF signal is sampled at 20 MHz, filling up the transient recorder buffer at 20 Megabytes/second, transferred to microcomputer memory at 2 Megabytes/second, and transferred to magnetic tape at 30 kilobytes/second.

The data system has been designed to be easy to use in a clinical environment. The operator can interact with the microcomputer software system to specify the data-taking procedure. Information about the portion of the frame to be digitized is stored in a table and written on the tape along with the data for use in processing. Comments can be added from the operator's CRT terminal to record additional information about the tissue under study.

B. Data Acquisition Procedure

A variety of patients with different myocardial pathologies were chosen to exhibit various degrees of focal or diffuse replacement of normal myocardium. Included were patients with transmural myocardial infarction (2), idiopathic hypertrophic subaortic stenosis (IHSS) (3), and cardiac amyloidosis (1). Three normal subjects were studied as controls.

Consideration of changes in the echoes due to motion and muscle contraction during the cardiac cycle is particularly important in a clinical study of cardiac patients. In order to study these changes single scan lines through the septum and posterior wall of the left ventricle were recorded at 2 ms and 30 ms intervals. Data-taking was synchronized with the patient's electrocardiogram to commence at end systole and end diastole. In the patients with myocardial infarction, the area of infarction was identified as an akinetic left ventricular segment corresponding to the region denoted by Q waves on the electrocardiogram. Data was collected from this segment and compared to normally contracting segments in the same patient. In the patients with IHSS, the region of asymmetric septal hypertrophy could easily be identified and often has an abnormal ground-glass appearance when viewed in the real-time image [4]. Again, comparison was made with adjacent areas of normal myocardial appearance and thickness and with the posterior left ventricular wall. In the patient with diffuse myocardial involvement with cardiac amyloidosis, representative areas of interventricular septum and posterior left ventricular free wall were studied.

3. Data Analysis

The recorded ultrasonic data was processed on an HP21MX minicomputer. Fourier transforms of each recorded data trace were computed using the Fast Fourier Transform (FFT) algorithm. By taking the Fourier transform of a single echo, one obtains information about the overlying tissue through which the acoustic pulse has passed, while the Fourier transform over an interval containing several echoes gives information about the spatial structure of the tissue through interference effects. Periodicities of the spectral peaks due to constructive interference between scatterers spaced by a distance d will be spaced by $\Delta f = c/2d$, where c is the acoustic velocity.

The system impulse response of the Varian scanner is illustrated in figure 2. The limited bandwidth, from about 1.8 to 2.9 MHz, has implications for both kinds of tissue information sought. In vitro studies by other workers [1-8] have shown that differences in frequency-dependent attenuation between normal and ischemic or infarcted heart tissue are small over this range. Only periodicities corresponding to spatial separations larger than .75 mm will appear in this narrow bandwidth. Thus the available tissue characterization information would be derived from observing shifts in the overall shape of the spectrum.

A primary interest was to note the effects of cardiac motion on the spectra of returned echoes. We tried to assess changes in the spectra as a function of time in order to see possible differences in the spectra corresponding to the anatomic differences between the normal and diseased heart muscle. Figures 3 through 7 show examples of the data processing sequence for the long axis view of the septum at end diastole for one patient in each of the groups studied.

4. Results

Substantial changes in the RF signals returned from the heart and their spectra were observed over time intervals short compared to the cardiac cycle. Data recorded at 2 ms intervals appeared to adequately represent the dynamically varying signal, whereas data recorded at 30 ms changed abruptly and apparently randomly between traces. Figures 8 and 9 demonstrate this effect. A dynamic characterization of heart tissue is probably indicated since parameter measurements derived from the frequency

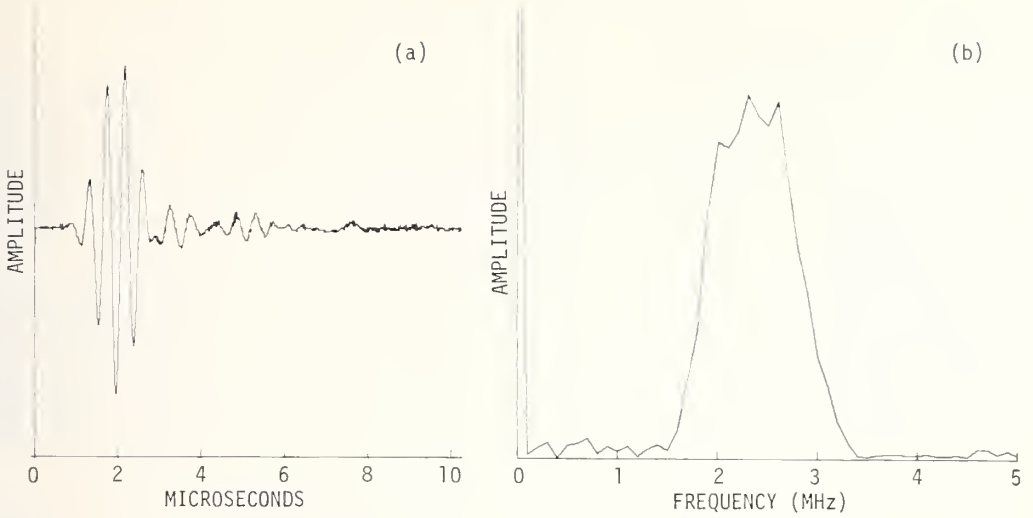

Fig. 2. a) Impulse response of Varian Real-time Sector Scanner measured by recording a single echo returned from the front side of a Lucite block in a water tank. This echo was digitized at 100 MHz. b) 1024 point FFT of impulse response.

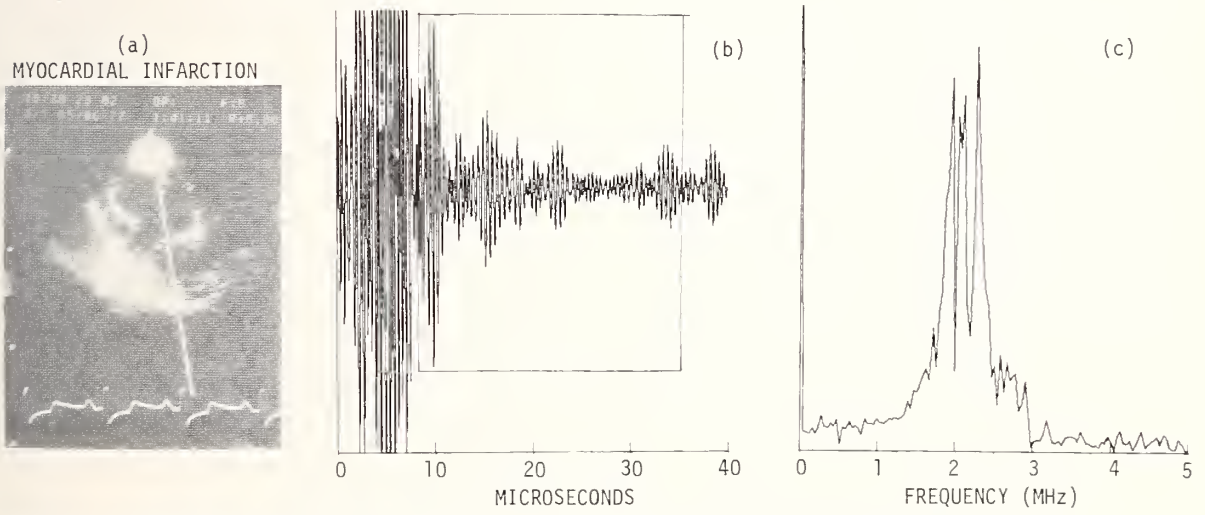

Fig. 3. a) Photograph of the scanner image. The rf signal was recorded along the scan line indicated by the bright cursor line on the image. b) The recorded rf trace is synchronized to the desired point in ECG and to the picture of the scanner image. The operator chooses the origin of the time scale. Here, echoes from the septum were recorded. c) 512 point FFT. The portion of the rf trace used in the FFT is outlined in figure b.

spectrum at one instant of time may not adequately describe the same tissue 30 milliseconds later.

The first, second, and third central moments were used to characterize the spectrum of each tissue sample, permitting study of changes in the shape of the spectrum. Differential frequency-dependent attenuation, as indicated by a shift in the first moment, for normal versus damaged myocardium was not observed. In fact, attenuation/centimeter appeared to be constant across the frequency range involved. It is likely that frequency dependent effects are overshadowed by the effects of imaging a tissue volume deep within the body, due to overlying tissue, diffraction spreading of the beam, and orientation of the tissue to the ultrasound beam. There was a wide range of normal spectral moments which overlapped those of the diseased patients. Disappointingly, the IHSS tissue, which presents a different appearance on the scanner image, was not distinguishable from the normal by the shape of the Fourier spectra. A comparison of normal and IHSS tissue spectra is depicted in figure 10. The myocardial infarction (MI) patients were set apart from the others by much less fluctuation in their spectral mean and variance curves (fig. 11). This implies that the tissue is moving or contracting less than normal tissue which correlates well with the observed image on the real-time display. There

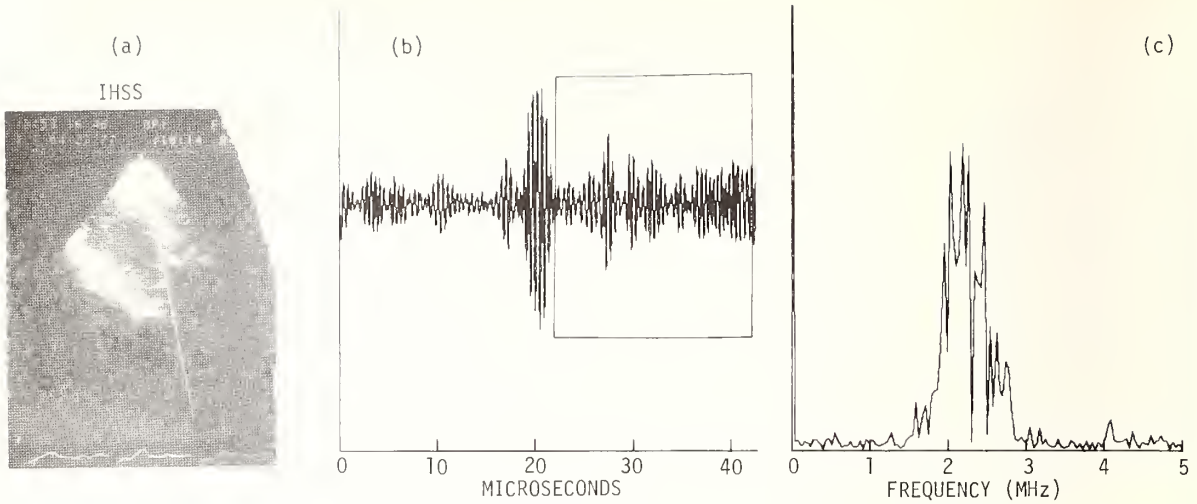

Fig. 4. a) Photograph of scanner image. b) Recorded rf signal from selected scan line. c) 512 point FFT.

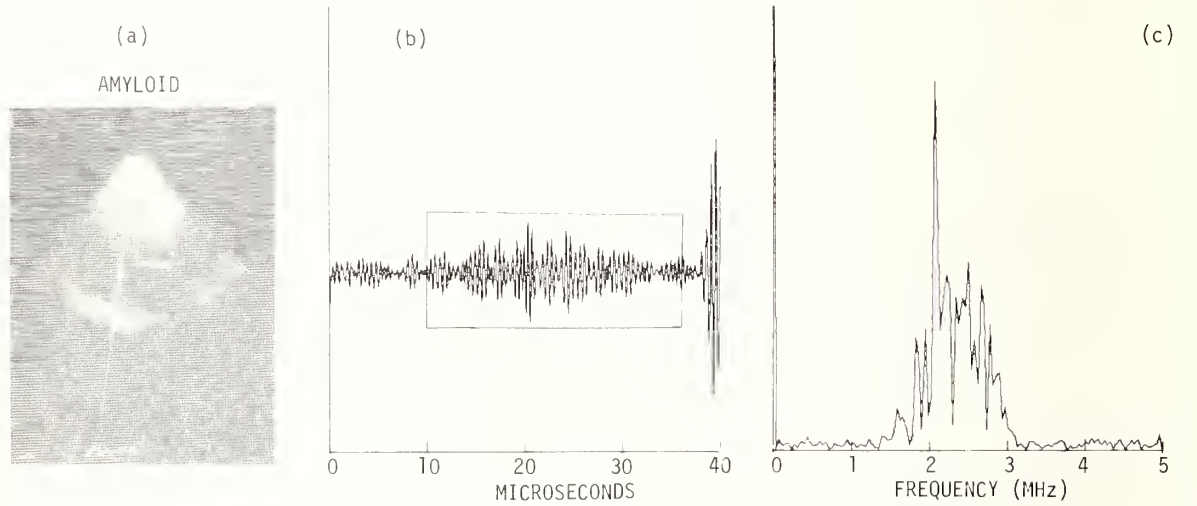

Fig. 5. a) Photograph of scanner image. b) Recorded rf signal from selected scan line. c) 512 point FFT.

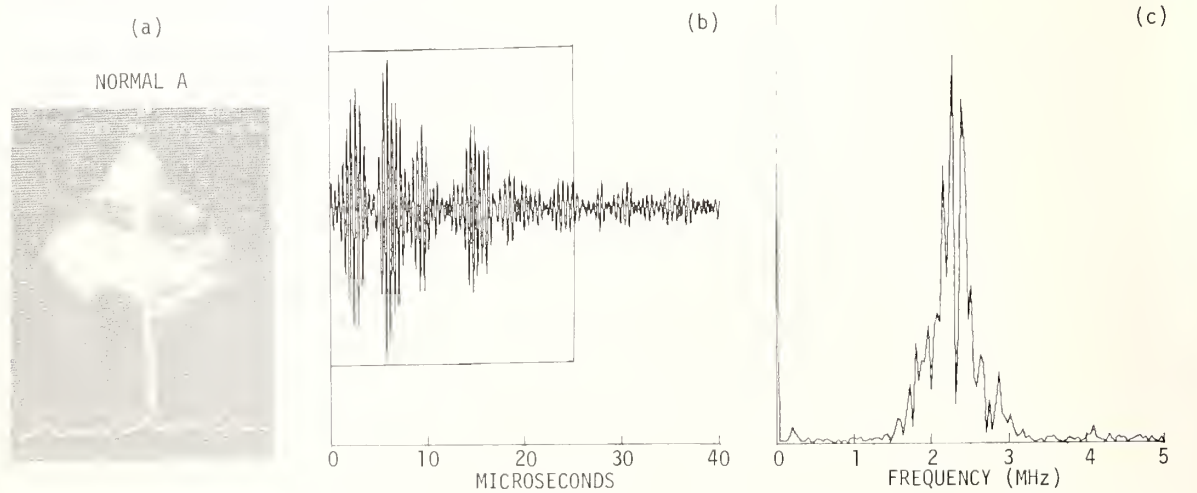

Fig. 6. a) Photograph of scanner image. b) Recorded rf signal from selected scan line. c) 512 point FFT.

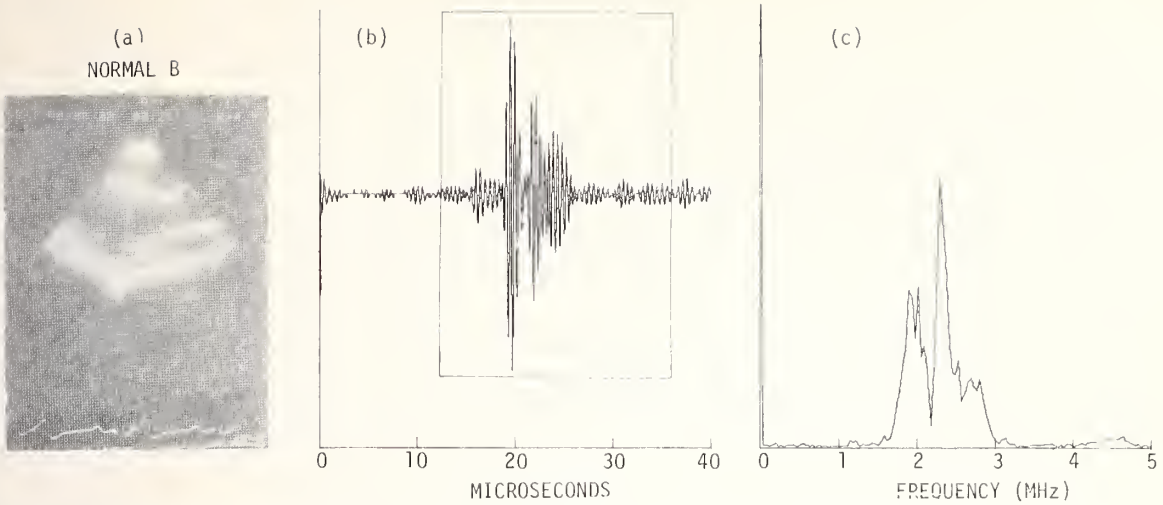

Fig. 7. a) Photograph of scanner image. b) Recorded rf signal from selected scan line. c) 512 point FFT.

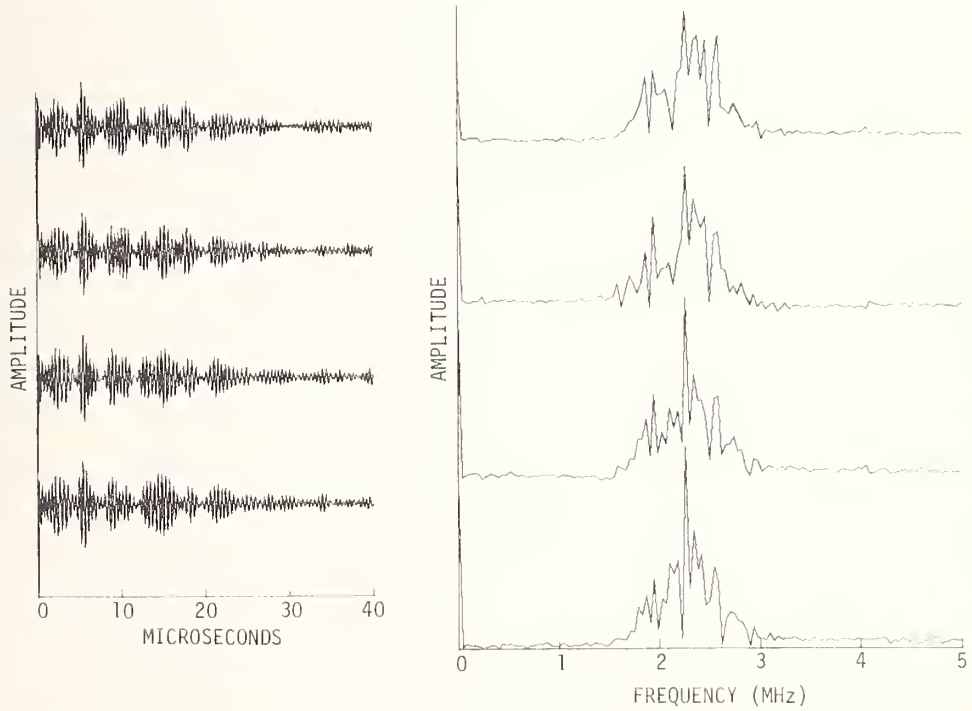

Fig. 8. a) Sequence of rf echo traces from normal septum. Signals were recorded at 2 ms intervals. Bottom trace occurred first in time. b) FFT spectra of signals in a.

was also a spectral shift of approximately 100 kHz in the means of the spectra between the long axis and short axis views for the MI data. This is likely due to a more tangential view of the tissue in short axis, demonstrating the substantial effect of orientation to the ultrasound beam.

5. Conclusions

Straightforward application of methods [1,2,8] which have differentiated between normal and ischemic or infarcted myocardium in vitro to in vivo data derived from current clinical instruments is not likely to be successful due to the triple whammy of limited bandwidth, overlying tissue, and cardiac motion. Spectrum skewing due to broad frequency interference effects and analysis of the time sequence of spectral changes may show some utility. The substantial changes in the rf and frequency spectra over very short time intervals lead to speculation that they reflect the state of contraction of cardiac muscle as well as changes in geometry. The data acquisition system described in this paper represents a significant advance in the state

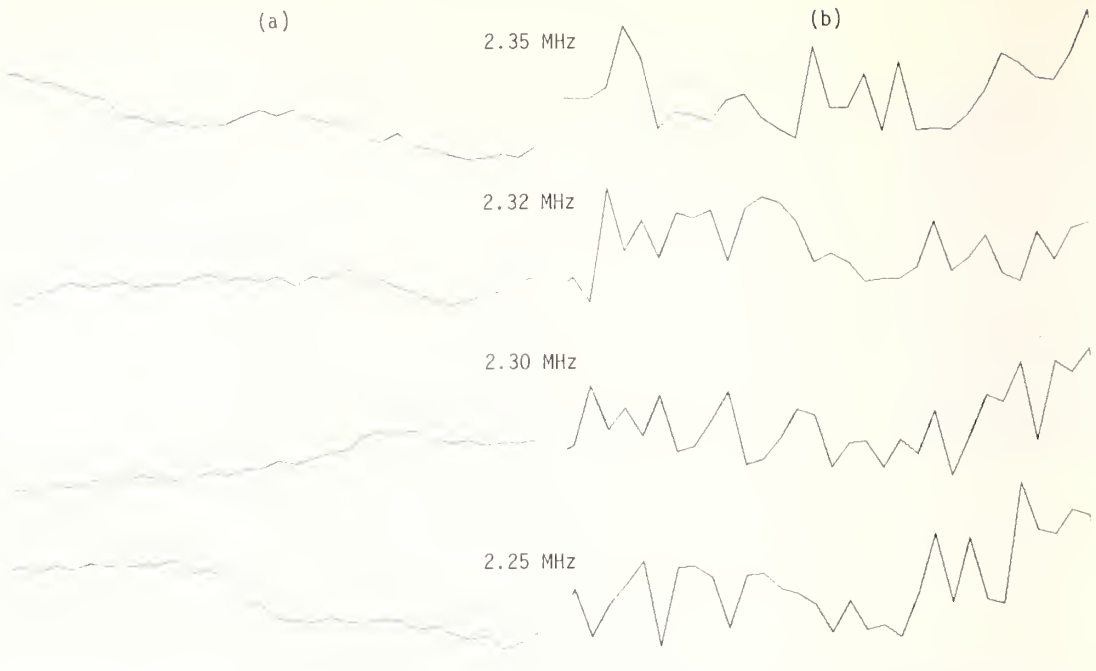

Fig. 9. a) Four frequency components of the FFT of normal septum data recorded at 2 ms intervals. Each component is plotted as a function of time. b) Same four frequency components plotted as a function of time for data recorded at 30 ms intervals.

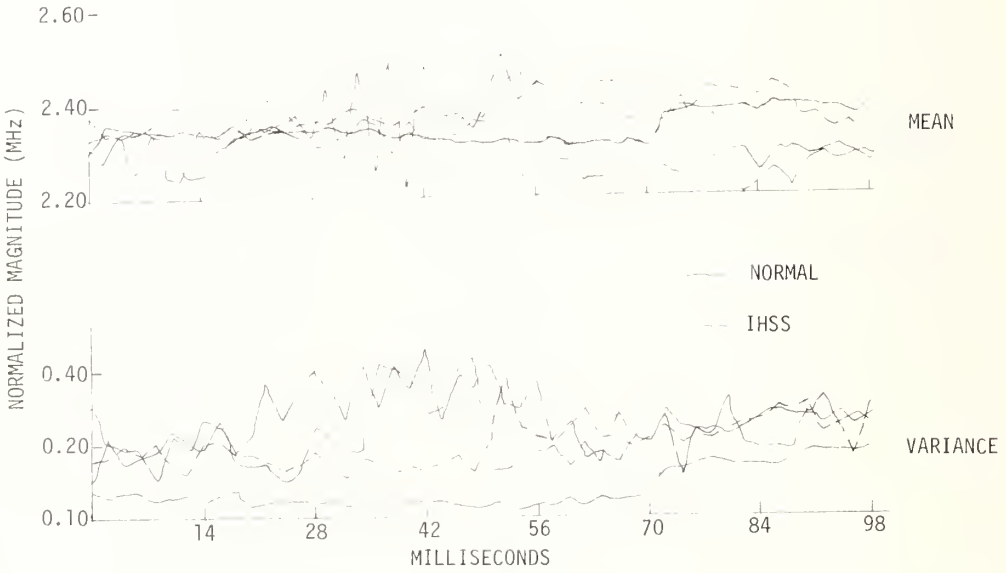

Fig. 10. Comparison of mean and variance of spectra of normal and IHSS spetal tissue. Moments are plotted as a function, 2 ms per point.

of the art of the digital recording of ultrasound rf in terms of flexibility and ease of use as well as in the kind of data it makes available.

Acknowledgment

This work was supported by the U.S. Department of Health, Education, and Welfare under grant GM-17940.

References

[1] Lele, P. P., Mansfield, A. B., Murphy, A. I., Namery, J., and Senapti, N., Tissue Characterization by Ultrasonic Frequency-Dependent Attenuation and Scattering, in Ultrasonic Tissue Characterization, M. Linzer, ed., National Bureau of Standards Spec. Publ. 453, pp. 167-196 (U.S. Government Printing Office, Washing-

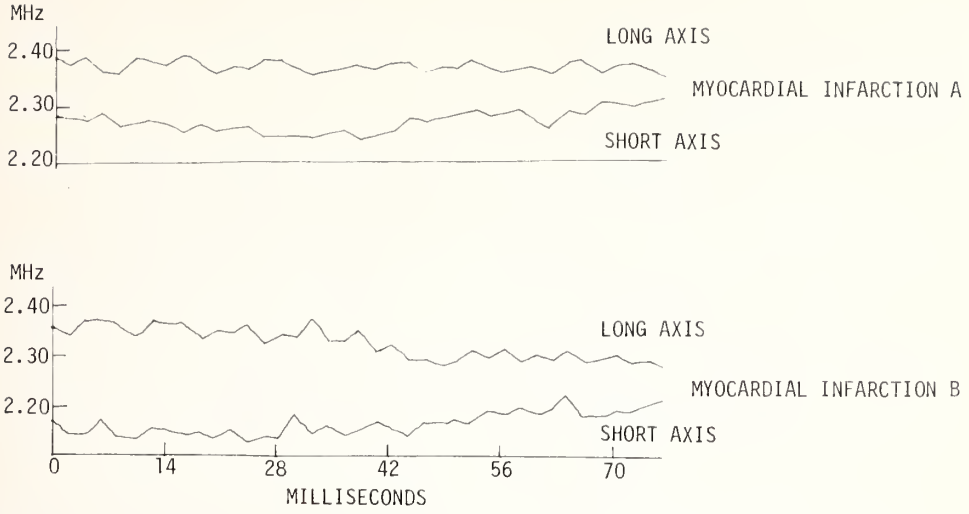

Fig. 11. Means of the spectra of data from two infarcted spetums. Data is plotted at 2 millisecond/point for the long and short axis views for both patients.

ton, D.C., 1976).

[2] Yuhas, D. E., Mimb, J. N., Miller, J. G., Wiess, A. N., and Sobel, B. E., Changes in Ultrasonic Attenuation Indicative of Regional Myocardial Infarction in Ultrasound in Medicine, D. White, ed., Vol. 3 (Plenum Press, New York, 1977).

[3] Chivers, R. C. and Hill, C. R., A spectral approach to ultrasonic scattering from human tissue: methods, objective and backscattering measurements, Phys. Med. Biol. 20 (5), 799-815 (1975).

[4] Rossen, R. M., Goodman, D. J., Ingam, R. E., and Popp, R. L., Echocardiographic criteria in the diagnosis of idiopathic hypertrophic subaortic stenosis, Circulation 50, 747-751 (Oct. 1974).

[5] Cooley, J. W. and Tukey, J. W., An algorithm for the machine calculation of complex Fourier series, Math. Computation 19, 297-301 (1965).

[6] Oppenheim, A. V. and Schaefer, R. V., Digital Signal Processing (Prentice-Hall, Inc., Englewood Cliffs, N. J., 1975).

[7] Crawford, F., Waves (McGraw-Hill, New York, 1968).

[8] Namery, J. and Lele, P. P., Ultrasonic Detection of Myocardial Infarction in Dog, in Proceedings of 1974 Ultrasonic Symposium, p. 491 (IEEE Cat. No. 72 CHO 7088 SU, 1974).

[9] Mohammed, A. and Smith, R. G., Data Windowing in Spectral Analysis, DREA Report 75/2, Defense Research Establishment Atlantic, Dartmouth, N. S., Research and Development Branch, Department of National Defense, Canada.

[10] Fields, S. and Dunn, F., Correlation of echographic visualizability of tissue with biological composition and physiological state, J. Acoust. Soc. Am. 54, 809-811 (1973).

Reprinted from *Ultrasonic Tissue Characterization II*, M. Linzer, ed., National Bureau of Standards, Spec. Publ. 525 (U.S. Government Printing Office, Washington, D.C., 1979).

DYNAMIC AUTOCORRELATION ANALYSIS OF A-SCANS IN VIVO

J. C. Gore,[1] S. Leeman,[1] C. Metreweli,[2] N. J. Plessner,[1] and K. Willson[1]

[1] Department of Medical Physics
[2] Department of Diagnostic Radiology
Royal Postgraduate Medical School
Hammersmith Hospital, London, England

A realistic tissue model has been analysed to indicate the information that may be derived from autocorrelation studies of in vivo A-scan echograms, as well as to show some of the limitations of such techniques. Although many of these difficulties are not easily overcome when considering single, or even averaged, realisations of the autocorrelation function (ACF), an analysis of the time course of the ACF is less subject to such objections.

Several potentially useful clinical applications of such temporal changes are being investigated. These include measurements of echoes from within heart muscle throughout the cardiac cycle as a possible indicator of cardiac disease; similar variations in echoes from the stomach wall during gastric emptying are demonstrated, and a relationship to contractile state is postulated.

Results are also presented which indicate that the perfusion of tissues with blood may be assessed by this technique, and, on a different physiological time scale, changes in the placenta throughout pregnancy have been investigated. The technique is being extended to the study of the response of malignant tumours to treatment.

Key words: A-scan; correlation analysis; temporal changes.

1. Introduction

Tissue characterisation may be defined as the attempt to establish what quantitative parameters, other than range information, may be extracted from ultrasound probing of human tissue; the quantities derived should reflect intrinsic tissue properties and in particular its physiological state, be useful diagnostically, or for pre- and post-operative assessment, or for monitoring response to treatment. The attempt is not necessarily restricted to an ultrasound technique, but this modality is particularly attractive, not only for the usual reasons, but also because it provides the facility for receiving and analysing a signal from a reasonably localised region of tissue, as well as providing images to enable that region to be accurately placed. Clearly, only physical properties of tissue, or their possible change with time, are amenable to detection--often micro-structural features are of interest, but other possibilites (e.g., temperature measurement) are certainly not excluded.

Isolated echo structure may be probed in tissue characterisation analyses [1-3][3], even though the extracting of purely physical, as opposed to geometrical, data is more complicated than may appear at first sight [3]. Here we will restrict ourselves, as have many others, to the scattered low-level signals from a region of tissue, and perform what may be termed tissue characterisation by "echo ensemble" analysis. The extent to which these two methods are complementary is not known at present, but it may be noted that both are implicit in qualitative attempts to extract diagnostically useful data from grey-scale images.

2. Some Theoretical Ideas

A conceptual basis for the empirical approach may be laid from theoretical considerations, just as the impedance mismatch concept simplifies the interpretation of much of conventional ultrasound scanning.

The tissue model adopted here comprises an in-

[3] Figures in brackets indicate literature references at the end of this paper.

homogeneous medium, with local density and compressibility fluctuations generating the ultrasound scattering. In this context, the aim of tissue characterisation by echo ensemble analysis is to uncover the three-dimensional spatial, and even temporal, distribution of these fluctuations; while the hope of the technique is that all, or preferably some, of the information is sufficient to establish unambiguously the state of the tissue.

A convenient starting point is the wave equation for ultrasound propagation in a medium with stationary inhomogeneities of the type described above [4].

$$\nabla^2 p - \frac{1}{c_0^2}\frac{\partial^2 p}{\partial t^2} = \frac{1}{c_0^2}\gamma(\underline{r})\frac{\partial^2 p}{\partial t^2} + \nabla_0\left[\mu(\underline{r})\nabla p\right] \qquad (1)$$

where $p(\underline{r},t)$ is the acoustic pressure at location $\underline{r}$ and time t;
$\mu(\underline{r})$ is the density fluctuation,

$$\mu = (\rho - \rho_0)/\rho$$

with ρ_0 the mean, and $\rho(\underline{r})$ the exact local density;
$\gamma(\underline{r})$ is the compressibility fluctuation,

$$\gamma = (\kappa - \kappa_0)/\kappa_0$$

with κ_0 the mean, and $\kappa(\underline{r})$ the exact local compressibility.

c_0 is the mean velocity,

$$c_0^2 = (\rho_0\kappa_0)^{-1} .$$

The right-hand side of eq. (1) is conventionally called the source term, since it is easily demonstrated [5] to be a "source" of waves, and it describes the interaction of the medium with the ultrasound field. The source term depends on both the fluctuations in the medium and the local, instantaneous value of the pressure wave, as it must do if it is to describe a scattering situation. The tissue model described by eq. (1) may be shown [5], to contain that of Waag and Lerner [6] as a special case. Since the scattering is known to be weak, both γ and μ may be taken to be small quantities. Any scattering calculation requires the initial conditions to be clearly specified, and we have adopted an initial pulse p_{in} incident along the Z-direction, of the form:

$$p_{in}(\underline{r},t) = a(z - c_0 t)b(h)\exp\{i(k_0 z - \omega_0 t)\} \qquad (2)$$

where a is the (axial) pulse shape, b is the beam profile, h is the spatial coordinate transverse to Z, k_0 is the carrier wave vector amplitude, and $\omega_0 = c_0 k_0$. Eq. (2) is a good approximation to pulses from diagnostic machines over much of the range of interest.

For weak scattering, and for weakly focused incident fields, the far-field final result [7] shows that the back-scattered pressure amplitude is generated by the pulse-smoothed density/compressibility fluctuations in the medium. The power spectrum, of the backscattered echoes (with boundary effects neglected), is given by:

$$|p_s(\omega)|^2 \propto \omega^4 \left|A\left(\frac{\omega}{c_0} - k_0\right)\right|^2 \left|\Gamma\left(\frac{2\omega}{c_0}\right)\right|^2 \qquad (3)$$

where A is the Fourier transform of the axial pulse shape, ω^4 represents a "Rayleigh" factor, and the effect of the medium is contained only in the structure factor,

$$\Gamma = \Gamma_\gamma - \Gamma_\mu$$

with

$$\Gamma_\mu(\kappa) = \frac{1}{2\pi}\int_{-\infty}^{\infty} \langle\bar{\mu}\rangle e^{ikz} dz$$

$$\langle\bar{\mu}\rangle = \int_0^\infty dh \int_0^{2\pi} d\theta h b(h)\mu(h,\theta,z)$$

and similarly for Γ_γ. θ is the angle variable in the cylindrical polar coordinates (h,θ,Z) used in the calculation. The Z-integration may be extended to infinite limits, since the fluctuations are presumed to vanish outside the (finite) scattering volume. The structure factor Γ is the spatial frequency spectrum of the beam-profile smoothed tissue structure, and it is seen that, for the backscattering case, the density and compressibility fluctuations contribute equally, but with different phase. At other scattering angles the two types of fluctuations will contribute with differently varying magnitudes, and they may be regarded as two different types of scattering element: the one (compressibility) scattering as an acoustic monopole, and the other (density) behaving as an acoustic dipole. This behaviour may be deduced from the form of the source term in eq. (1), or more directly, from straightforward physical arguments [5]. Since the relative importance of the two types of scattering element varies with direction, different observers employing a fixed-angle scattering technique may obtain apparently conflicting results from the same tissue. In general, at least six independent one-dimensional experimental functions would have to be measured in order to reconstruct both γ and μ from the data, and since this would seem to be impracticable, it is emphasized that, for the characterization of anisotropic tissues by fewer independent functions, it is essential to specify internal tissue landmarks with respect to which scanning planes and directions may be fixed. If not, intercomparison of results between different workers, and the repeatability of a single investigator's findings, cannot be established.

Quite apart from difficulties inherent in trying to quantitate the effect of overlying tissues and interfaces, the above calculation shows that pulse shape, beam profile, and carrier frequency are important quantities which fundamentally influence the scattered pressure power spectrum, and which must be specified or, better, deconvoluted from the data. Moreover, in regions where the incident pulse is sharply focused ($|\nabla p_{in}|$ large), scattering from the density fluctuations becomes more prominent; this may well prescribe a suitable technique for mapping the density and compressibility scattering elements individually, if so desired. In addition, the measured backscattering is further modified by the transfer properties of the receiver [8], but

all these "system" artifacts are measurable, and should be prescribed, if not specifically allowed for.

Pulse smoothing implies a certain loss of fine detail: scattering experiments do not indicate the tissue micro-structure ($<<\lambda$) as such. It is quite clear from the above that measured pressure power spectra from the same tissue may differ with different transducer apertures and excitations, but it is also worth emphasizing that, in principle, the same backscattered power spectrum may be seen from different tissues, with different density and compressibility fluctuations, provided that Γ_γ-Γ_μ remains the same. This merely underlines the fact that, even for isotropic media, a single backscattering experiment is in general insufficient to characterize tissue unambiguously. Fortunately, in practice, the situation may be less complicated as there is some indication that, for most tissues, only the compressibility (i.e., elasticity) fluctuations are of importance for the production of echoes [9].

3. Method

As indicated in eq. (3), by measuring the power spectrum of echoes, the structure factor, Γ, may in principle be determined over a limited band of spatial frequencies to within an accuracy set only by noise and the uncertainty in knowledge of $|A|$. However, we have chosen to explore the use of the time-domain autocorrelation function (ACF) of echo amplitudes; as well as being easier to calculate, the ACF contains all the information included in the power spectrum, and although the errors inherent in its estimation differ from those in power spectrum calculations, it seems likely that on-line ACF measurement may be at least as suitable for "in vivo" tissue characterization in real time as Fourier methods. The desired autocorrelation function is given by

$$c(\tau) = \int_{-\infty}^{\infty} p(t)p(t+\tau)dt$$

where $p(t)$ = the backscattered acoustic pressure amplitude at time t.

From eq. (3), it can be shown that

$$c(\tau) \propto \beta(\tau) * \xi(\tau)$$

where * denotes convolution,

$\beta(\tau)$ = the ACF of $\langle\gamma\rangle - \langle\mu\rangle$ and is an indicator of tissue structure.

$\xi(\tau)$ = the ACF of the second derivative of the impulse response of the pulse-echo system [8].

The convolution with the system function, ξ, limits the information available unless steps are taken to remove its influence, but such further processing has not yet been attempted by us.

The equipment used in these studies is a Nuclear Enterprises NE 4102 Diasonograph, operated with weakly focused transducers centred on 2.5 MHz, with total system bandwidth approximately 1½ MHz. Signals from the A-scan receiver are at present recorded photographically from an oscilloscope, and the echo envelope is then digitised with a sonic pen (SAC Graf Pen), interfaced to a HP 2100A computer via a Tektronix 4010 visual display unit. With this arrangement effective sampling rates of up to 15 MHz are achieved, although at present it is more usual to sample echoes from a region $\sim$ 2 cm in extent at a rate of 7½ MHz, consistent with providing estimates of the ACF at lag intervals corresponding to 100 μm of tissue.

The discrete, normalised ACF, c_j', is estimated from N echo samples, P_i, using the unbiased estimator [10],

$$c_j' = c_j / c_0$$

$$c_j = \frac{1}{N} \sum_{i=1}^{N-j} P_i - \bar{P}_{i,M} \; P_{i+j} - \bar{P}_{i+j,M}$$

where

$$\bar{P}_{i,M} = \frac{1}{(2M+1)} \sum_{i-M}^{i+M} P_i$$

is the running mean of the echo amplitude. The moving average is calculated over a distance that is sufficiently large not to influence the fine structure of the ACF estimate but which filters spurious low frequency fluctuations and strengthens stationarity. Such detrending is performed typically over intervals of $\sim$ 1 cm.

4. Data Analysis

In general, the entire ACF must be considered when characterizing a single train of echoes, but one or more particular features of each ACF may be extracted in order to summarise quantitatively any given set of echo samples. For example, the positions (and to a lesser extent the shapes) of peaks within the ACF indicate distances over which there exists structural coherence; prominent and regular peaks indicate a regular arrangement of scattering sites. The mean number of crossings, moments of the function, or curve fitting techniques using small numbers of parameters, may each be used to describe, concisely, essential details of an estimated ACF, but the method of feature extraction chosen will depend on the particular application.

In order to overcome some of the objections that have been indicated above against the use of single realisations of echo characteristics in one dimension, the analysis has been restricted to situations where the tissue investigated has been found to be isotropic, or where only the changes with time of echo characteristics are deemed to be clinically useful. In this way, by following the time course of echo features, each tissue acts as its own internal standard and less reliance need be placed on the values of individual, single measurements. Time-plots of echo features such as those described above depict changes in scattering structure, whilst polar phase diagrams are useful when the change is periodic. Cross correlation of the ACFs realized at different times are calculated to yield information about changes, relative to a chosen reference time, and examples are given below.

In analysing echoes in this fashion, the ACF features to be emphasized have often to be chosen arbitrarily, and caution has to be exercised when attaching significance to any particular one.

There are some reliable guidelines that may be derived by standard techniques to suggest which ACF values may be regarded as spurious, but a final decision as to the significance (or otherwise) of any derived result can be made only on the basis of clinical, in vivo investigations. However, as an interim indicator of our awareness of artifactual correlations, the results given below are marked with the 95 percent confidence limits (σ) for an autocorrelation function generated with N data points from a random process [11],

$$\sigma = \frac{1}{N} \pm 2/\sqrt{N} \ .$$

5. Results

There are several clinical problems which may be explored by using temporal characteristics of the ACFs of echoes to indicate changes within tissues and three classes may be distinguished.

First, there are cyclic events in which echo characteristics alter in synchronism with some physiologically significant, repetitive process, such as respiration, or with the cardiac cycle, whose phase is easily monitored on the electrocardiograph (ECG). It is, for example, reasonable to suppose that myocardial activity will be associated with a redistribution of scattering centres in the tissue, since it necessarily involves changes in both its elastic state and density. The time course of scattered echoes from within the left ventricular posterior wall is easily followed in the conventional mitral valve echogram scanning direction. Figure 1 depicts the ACFs measured from a normal heart in end-systole and end-diastole, showing typical changes from one phase to the other. The interpretation of this in

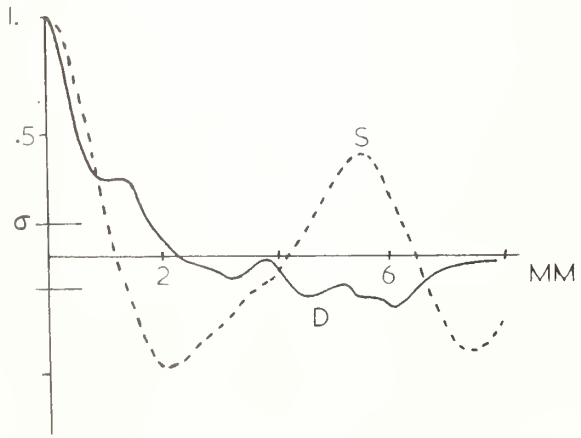

Fig. 1. The ACFs of echoes from the left ventricular posterior wall of a normal heart, measured in end-systole (S) and end-diastole (D).

terms of alterations in muscle fibre dimensions or elastic state remains to be confirmed, whilst the degree of change in disease remains to be established, but the possibility clearly exists of measuring in vivo characteristics which may be related to myocardial contractility.

The flow of blood in the systemic circulation is also directly coupled with cardiac events. Following the notion that the perfusion of certain organs with blood proceeds in synchronism with the heart's action, the possibility of identifying poorly perfused transplanted kidneys is under investigation. Figure 2 indicates how echoes from the anterior region of the upper pole of a viable kidney, investigated some months after successful transplantation, change with time. The obvious changes between phases, and the reversion in the subsequent cycle, is suggestive of a cyclic, cardiac-synchronised structural reorganisation within the kidney. This approach to the quantitation of echo characteristics may also be applicable to other organs, such as the liver and placenta, and possibly to tumours.

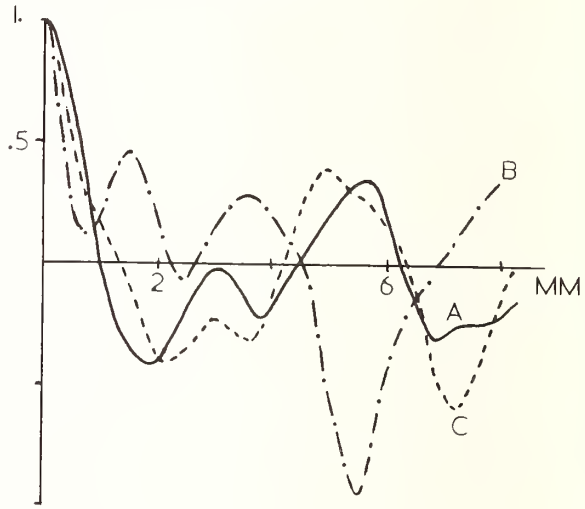

Fig. 2. Characterisation of echoes from cortex of transplanted kidney at different times. Three autocorrelations were measured, at (cardiac) end-diastole, end-systole, and the subsequent end-diastole. Curve A is the cross-correlation of the first diastolic ACF with itself, curve B is the cross-correlation of the first diastolic and systolic ACFs, whilst curve C is the cross-correlation of the two diastolic functions, and shows a reversion back to the original state in synchronism with the heart.

A different cyclic process with less regular period is the muscular activity associated with gastric emptying. The contraction of the stomach wall in normal digestion (which may be monitored over cycles with periods of approximately 20 seconds with conventional M- and B-scan techniques) [12] produces changes in echo characteristics not dissimilar to those associated with myocardial contraction, and this lends support to our interpretation of the origin of heart wall echo changes. Thus, a similar model, viz., contraction of muscle elements causing changes to their acoustic scattering properties, may be employed to interpret the results of both cardiac and gastric measurements. ACFs of echoes from the anterior stomach wall are shown in figure 3, and cross correlations of the ACFs from different phases in figure 4: the position of the first principal minimum is plotted as a rotating phasor in figure 5.

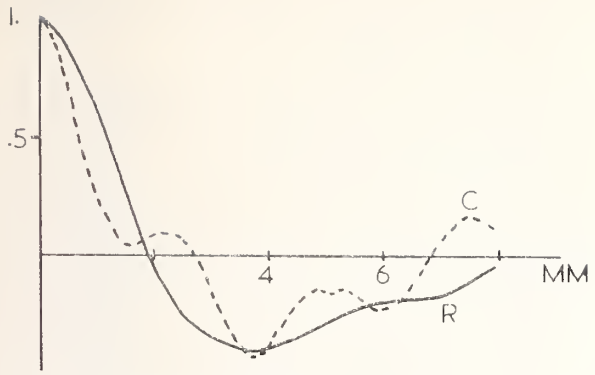

Fig. 3. The ACFs of echoes from the anterior stomach wall, contracted (C) and relaxed (R).

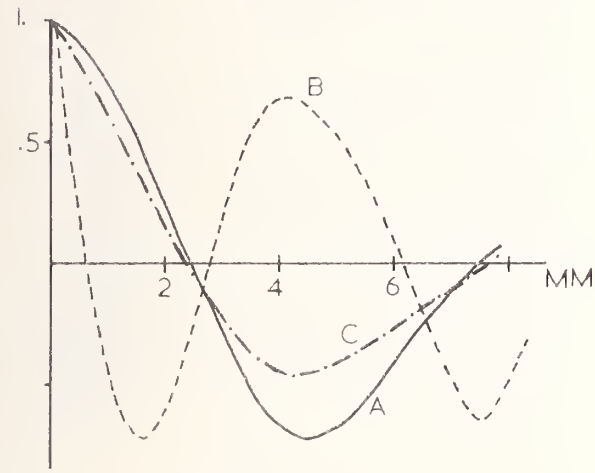

Fig. 4. Characteristics of echoes from stomach wall at different times. The ACF at time 0 is cross-correlated with itself (A), with the ACF at a time ∿ 4 seconds later when the stomach is contracted (B), and with the ACF at a time ∿ 8 seconds after contraction, when the muscle has again relaxed (C). These events were chosen by reference to the stomach M-scan. Note the general shape of the cross-correlation function does not change but the first minimum moves with contraction.

A second class of time change being investigated is the alteration in scattering characteristics of tissues with age or maturity, and of particular interest are changes in the placenta throughout pregnancy. Ageing placentas present different grey scale B-scan appearances: cross-correlation of ACFs obtained at different stages of normal pregnancy are shown in figure 6. This technique may also reveal differences between normal and insufficient placentas of the same maturity.

A third class of application is the monitoring of structural changes in tumours during and after treatment. Such changes have already been observed in B-scan images of irradiated malignant tumours and in vivo ultrasonic tissue characterization using the techniques outlined above may provide a clinically useful method of assessing tumour kinetics [13].

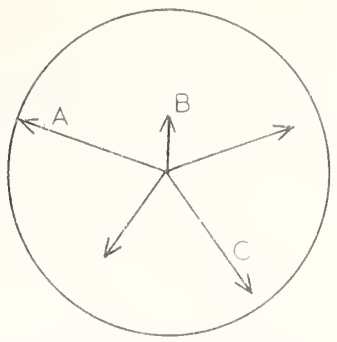

Fig. 5. Phasor diagram showing locus of the position of the first minimum of the function produced by cross-correlating the ACFs of echoes from stomach wall measured at different times (as in fig. 5). Total cycle time ∿ 20 seconds. The radius of the circle corresponds to a correlation lag of 4.8 mm.

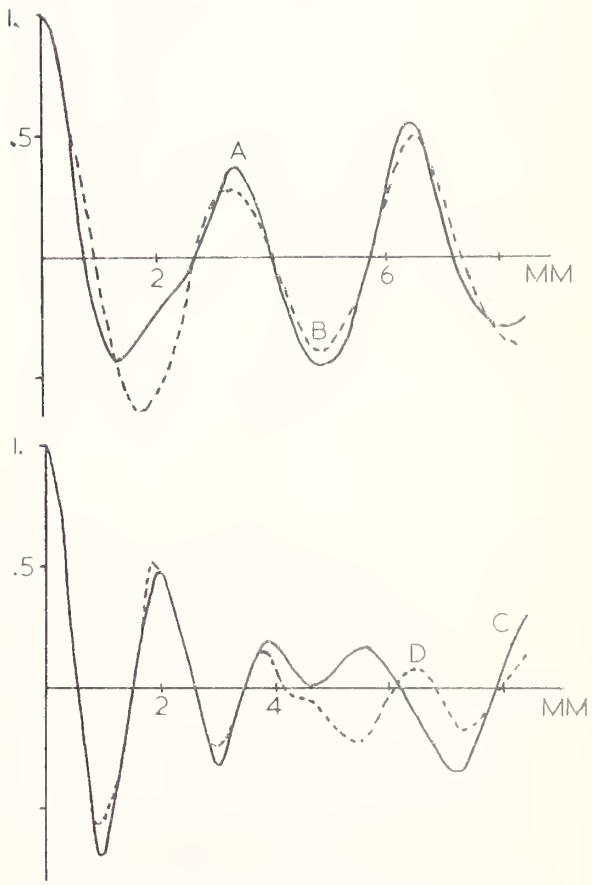

Fig. 6. Characteristics of echoes from placenta at different stages of pregnancy. ACFs were obtained at 15, 24, 38 and 41 weeks, and each of these ACFs was cross-correlated with the 15 week ACF to produce curves A, B, C and D respectively. There appears to be little change between 15 and 24 weeks, or between 38 and 41 weeks, whereas there is a clear change between 24 and 38 weeks.

6. Conclusions

The use of single autocorrelation functions to characterize complex, three-dimensional scattering media may be severely limited because different tissues may realise similar results. Many of the objections raised against the use of one-dimensional techniques, however, are overcome if the time course of events is followed and only changes in echo characteristics are regarded as significant. Whilst the ACF summarises the information contained in a single train of echoes, the cross correlation of sequentially produced ACFs summarises dynamic features of scattering. New diagnostic information may possibly be derived from a study of cyclic changes in gastric and cardiac muscle, and in other organs blood perfusion may be assessed. Changes in the nature of tissues with age or treatment may have important significance which, as yet, we are unable to evaluate.

A limited number of patients and volunteers have so far been investigated with this "dynamic" technique, and it is impossible to unequivocally claim success in any particular application; but there is equally no cause to reject the original concept that echo ACFs reveal changes in the physiological state of tissues. The influence of factors such as tissue movement or anisotropy and the relative merits of different transducers and methods of signal processing will have to be carefully evaluated, and the optimal choice of echo ACF features to be extracted remains uncertain. Despite the problems, there is every reason to hope that dynamic tissue characterization is an appropriate path to obtaining information of genuine clinical utility.

Acknowledgements

We gratefully acknowledge Mr. George Hooker's help with the analysis of data, and thank Dr. E. W. Emery for his useful discussions and comments. S. L. is in receipt of a Wellcome Fellowship.

References

[1] Lizzi, F., Katz, L., St. Louis, L., and Coleman, D. J., Applications of Spectral Analysis in Medical Ultrasonography, Ultrasonics, 77-80, March 1976.

[2] Trier, H. G., Decker, D., Reuter, R., Epple, E., Lepper, R. D., and Nagel, M., Frequency-modulated Portions of the Time-amplitude Ultrasonogram of Models, in Proceedings of the Second European Congress on Ultrasonics in Medicine, pp. 121-128 (Excerpta Medica, Amsterdam-Oxford, 1975).

[3] Gore, J. C. and Leeman, S., Echo structure in medical ultrasonic pulse-echo scanning, Phys. Med. Biol. 22 (3), 431-443 (1977).

[4] Morse, P. M. and Ingard, K. N., Theoretical Acoustics (McGraw-Hill, New York, 1968).

[5] Leeman, S., Simple Physical Ideas on Ultrasound Pulse Scattering from Tissue, R.P.M.S. Medical Physics Reports, US76/3 (1976). (Available by request only)

[6] Waag, R. C. and Lerner, R. M., in Ultrasonics Symposium Proceedings, I.E.E.E. Cat. 73, CHO 807-850.

[7] Gore, J. C. and Leeman, S., Ultrasonic backscattering from human tissue: A realistic model, Phys. Med. Biol. 22 (2), 317-326 (1977).

[8] Gore, J. C. and Leeman, S., New Criteria for the Assessment of the Resolution of Ultrasonic Scanners, in Ultrasonics in Medicine, E. Kazner, M. de Vlieger, H. R. Muller, and V. R. McCready, eds., pp. 197-203 (Excerpta Medica, Amsterdam, 1975).

[9] Fields, S. and Dunn, F., J. Acoust. Soc. Am. 54, 809-813 (1973).

[10] Jenkins, G. M. and Watts, D. G., Spectral Analysis and its Applications (Holden-Day, San Francisco, 1968).

[11] Chatfield, C., The Analysis of Time Series: Theory and Practice, Chap. 4 (Chapman and Hall, London, 1975).

[12] Bateman, D. N., Leeman, S., Metreweli, C., and Willson, K., A noninvasive technique for gastric motility measurement, Brit. J. Radiol. 50, 526-527 (1977).

[13] Leeman, S., Badcock, P. C., Gore, J. C., Plessner, N. J., and Willson, K., Ultrasonic Backscattering Assessment of Tumour Response to Treatment, presented to Tumour Ultrasound 77, International Conference, London, 1977. (Copy available by request.)

Reprinted from *Ultrasonic Tissue Characterization II*, M. Linzer, ed., National Bureau of Standards, Spec. Publ. 525 (U.S. Government Printing Office, Washington, D.C., 1979).

COMPUTER SPECTRAL ANALYSIS OF ULTRASONIC A MODE ECHOES

D. E. Robinson

Ultrasonics Institute
Sydney, Australia

Tissue attenuation as a function of frequency measured by the effect on the power density spectrum of the echo off glass shadowed by the tissue sample is shown to give results comparable to those published previously. A method of measuring attenuation within tissue by comparison of the scattered echoes from shallow and deep scatterers is investigated and shown to have limitations. An assessment of properties of the scatterers from investigation of the spectral properties of the echoes from a scattering region is suggested.

Key words: Acoustic; computer processing; digital acquisition; digital signal processing; pulse-echo techniques; spectrum analysis; ultrasonics.

1. Introduction

At present the bulk of tissue characterisation by ultrasound in clinical practice is done by qualitative examination of the grey scale B Mode echogram. The current work is directed to deriving quantitative characterisation data by spectral analysis of 180° backscattered echoes, or ultrasonic A Mode, following the approach of Lizzi [1][1].

2. Measuring Equipment

The transducer beam pattern requires to be narrow to give good spatial resolution and with a well behaved spectrum to avoid complications in spectral analysis techniques [2]. This is achieved in the focal zone of a focussed transducer of aperture 65 mm and curvature 35 cm and usable frequency range from 1.5 to 4 MHz. The 20 dB echo beamwidth at the focus is 6.7 mm.

The receiver amplifier gain is variable in 1 dB steps allowing an input dynamic range of 100 dB without overload. Receiver gain variation is used instead of transmitter power control as it is found that due to non-linearities in the transmitter, the transducer or the medium, significant changes in echo wave shape occur with changes in transmitter power. The signals are digitised at 10 MHz sampling rate using an 8 bit Biomation 8100 waveform recorder interfaced to an Interdata Model 85 computer. The computer and an interactive signal processing program have been described elsewhere [3].

The spectrum used here is the square magnitude of the Discrete Fourier Transform (DFT) of the echo signal or Power Density Spectrum. All spectra shown in this paper have been interpolated as described by Rabiner et al. [4] by extending the set of 128 or 256 recorded time samples with zero-valued samples up to a total signal length of 1024 before computing the DFT. Comparisons between spectra are made by calculating the logarithm of the ratio of the spectra (log ratio) and observing the ordinate at 2.5 MHz in dB and the slope in dB/MHz. The log ratio for point and plane target echoes remain within 3 dB and the slope within 2 dB/MHz for distances from the transducer focus of ± 30 mm.

A B-Mode display of the examined tissue is provided for A mode beam position selection and guidance. An example of input data and corresponding B mode display is shown in figure 1.

3. Experimental Techniques

First the echo from a thick glass block at the focus with no intervening tissue is recorded, and regarded as the impulse response of the system. The tissue specimen is then placed in a polyethylene bag in front of the glass block and echoes from a series of 30 adjacent beam positions at 3 mm intervals were recorded from three locations; from the glass block behind the tissue and from shallow and deep within the examined tissue. In each case the transducer was moved so that the echoes were recorded from the focal area of the transducer beam. In the case of the scattered echoes, a region was selected which did not have large discrete echoes on the B Mode scan.

4. Signal Processing

When measuring the spectrum of a statistical signal, some form of averaging is required to obtain a smooth and stable spectral estimate [5]. This can be done in the spatial domain by translating the beam axis as described by Lizzi [1] and adding the spectra corresponding to a number of adjacent lines of sight to obtain an average spectrum. This has the effect of reducing the amplitude of ripples in the spectrum.

[1]Figures in brackets indicate literature references at the end of this paper.

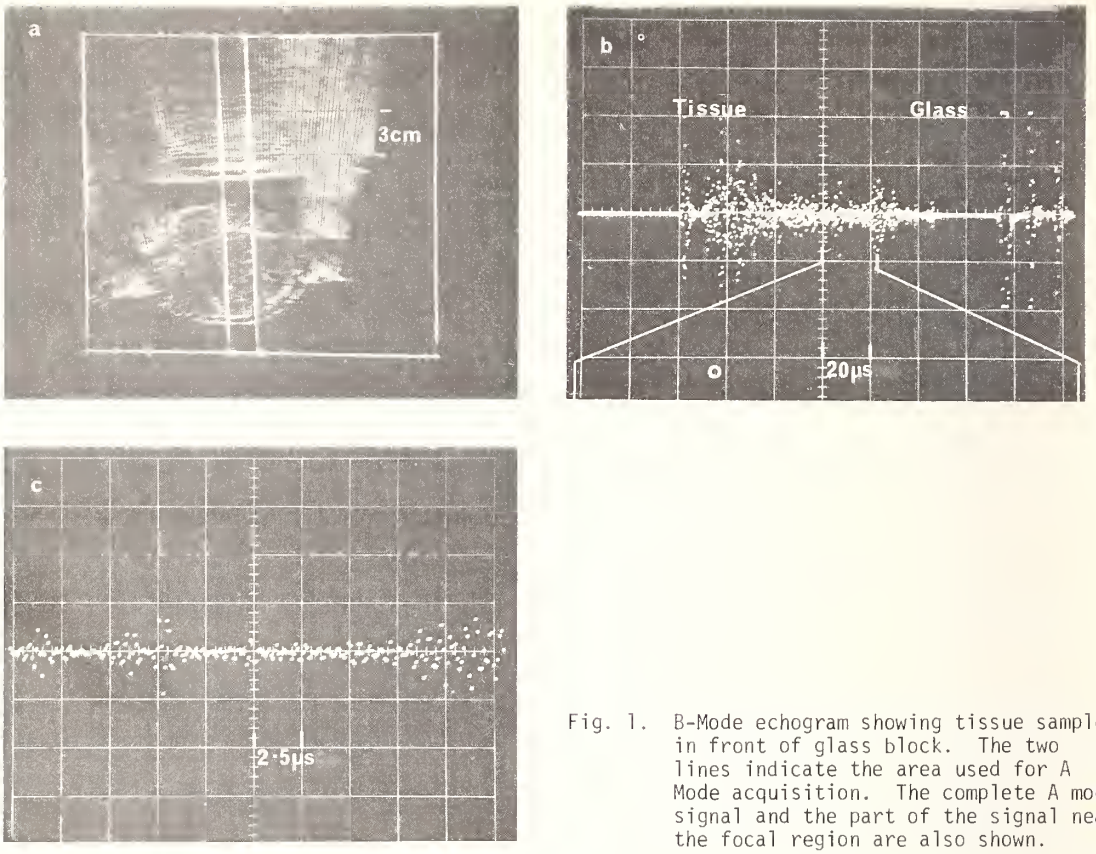

Fig. 1. B-Mode echogram showing tissue sample in front of glass block. The two lines indicate the area used for A Mode acquisition. The complete A mode signal and the part of the signal near the focal region are also shown.

It should be noted that the "fine structure" in the spectrum of individual echo signals may be a function, not of the statistical nature of the sample, nor of the local tissue structure, but simply of the length of the time window. For instance, given a signal $x(t)$ with transform $X(f)$ and spectrum $X(F)^2$ the sum of two identical shifted signals $x(t) + x(t - \tau)$ has a spectrum $2X(f)^2 (1 + \cos w\tau)$. The factor $(1 + \cos w\tau)$ gives rise to "wiggles" in the measured spectrum which are not directly related to local tissue "structure" but are merely phase effects between widely spaced echoes. Figure 2a and 2b show the spectra for a single echo and two identical echoes separated by 5 mm. This effect is reduced by windowing in the autocorrelation domain, or lag windowing. The autocorrelation function is the Inverse Fourier Transform of the Power Density Spectrum. The Autocorrelation functions of the single echo and two identical echoes spaced at 5 mm (66 sample intervals) are shown in figure 2c and 2d. Also shown in figure 2d is a Hamming window in the Autocorrelation (lag) domain suitable for removing the effect of widely spaced echoes. Multiplication by the window function has the effect of removing contributions to the Autocorrelation function of lags greater than 32 sample intervals (2.5 mm) and leaving only the contributions from closely spaced echoes. The smoothed Power Density Spectrum obtained by re-transforming the weighted Autocorrelation function into the frequency domain is shown in figure 2e. The effect of this procedure on tissue echoes is shown in figure 3 where the original time sample of scattered echo data is windowed with a Hamming window of length 128 (corresponding to 10 mm of tissue). The lag windows are of length 64, 32 and 16 samples increments corresponding to correlation lengths of 5, 2.5 and 1.25 mm and thus limiting the effect on the spectrum to structures of these sizes.

In the analysis of the echoes off glass no time windowing or spectral smoothing is necessary since we are dealing with only deterministic single echo waveforms and not statistical signals. The power density spectra of the echo off glass with and without shadowing by the tissue were calculated, and the log ratio formed. A typical set of results is shown in figure 4. The log ratio is a measure of the attenuation due to the tissue as a function of frequency. The values are only significant for frequencies contained in the original power density spectrum of the unshadowed glass echo. A line of best fit was computed on a least total weighted squared error basis with the weighting function being the original power density spectrum values for the echo off glass at the focus.

The parameters of the line $y = ax + b$ where y is the best fit to the log ratio value and x the frequency value are given by:

$$a = \frac{\sum_i W_i \sum_i x_i y_i W_i - \sum_i x_i W_i \sum_i y_i W_i}{\sum_i W_i \sum_i x_i^2 W_i - \left[\sum_i x_i W_i\right]^2}$$

$$\text{and } b = \frac{\sum_i y_i W_i}{\sum_i W_i} - \frac{\sum_i x_i W_i}{\sum_i W_i} \cdot a$$

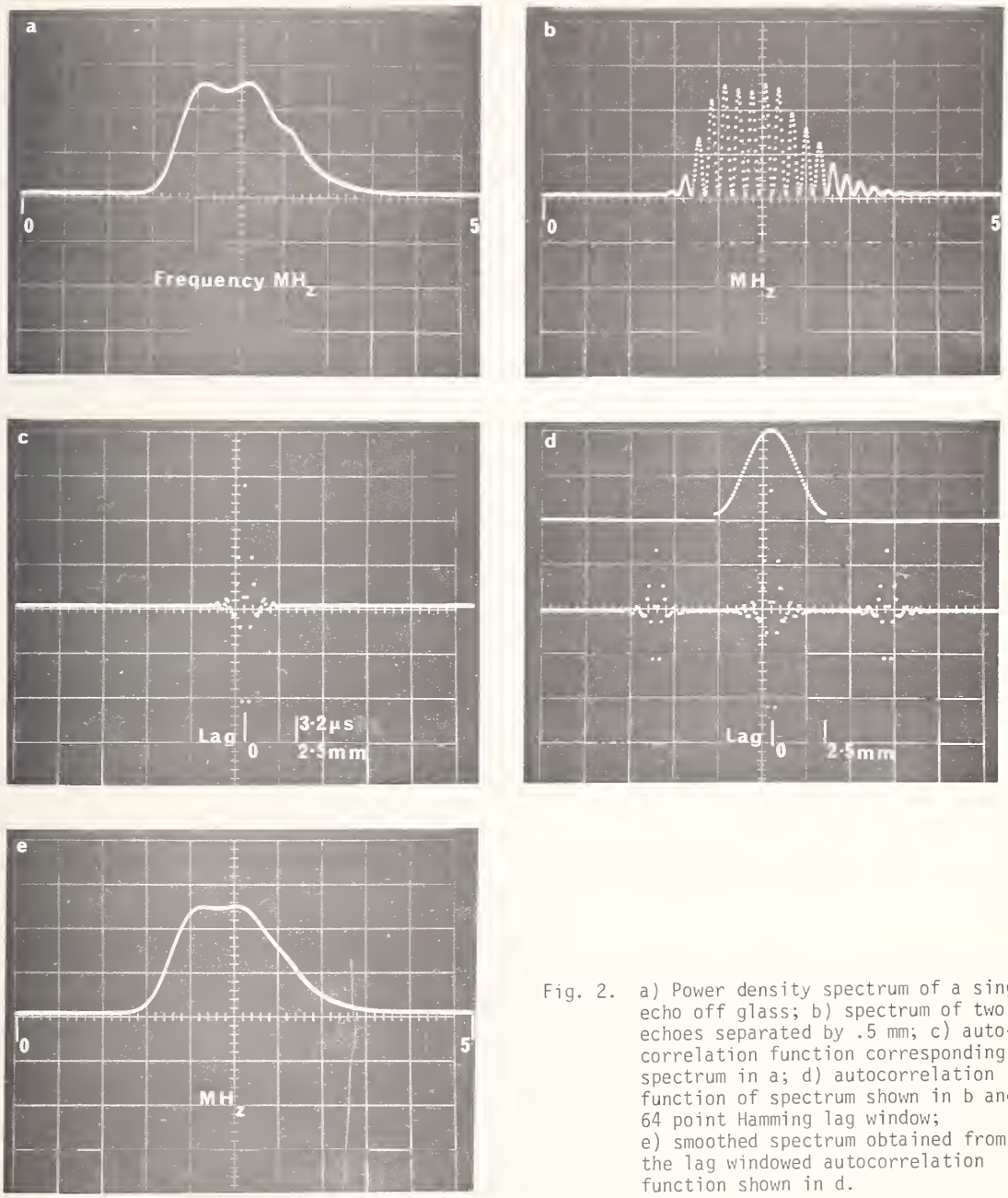

Fig. 2. a) Power density spectrum of a single echo off glass; b) spectrum of two echoes separated by .5 mm; c) autocorrelation function corresponding to spectrum in a; d) autocorrelation function of spectrum shown in b and 64 point Hamming lag window; e) smoothed spectrum obtained from the lag windowed autocorrelation function shown in d.

where the x_i, y_i and W_i are the values of the frequency, log ratio and weighting function for the successive frequency samples.

For echoes from scatterers within the tissue the echo signal was windowed using a time window of length 128 samples or 10 mm and the spectrum was smoothed by a lag window of 64 lags corresponding to 5 mm. The log ratio between deep and shallow echo spectra was formed and the weighted best fit line calculated as before. A typical result is shown in figure 5.

5. Results

Being initial experiments readily available animal material was used. The material was skeletal beef muscle along and across the fibre direction and calf liver. The results are shown in table 1.

The log ratio curve, indicating tissue attenuation was approximately linear within the pass band for all tissue samples using the shadowed glass approach. For this reason more confidence is placed in the determination of attenuation slope by this

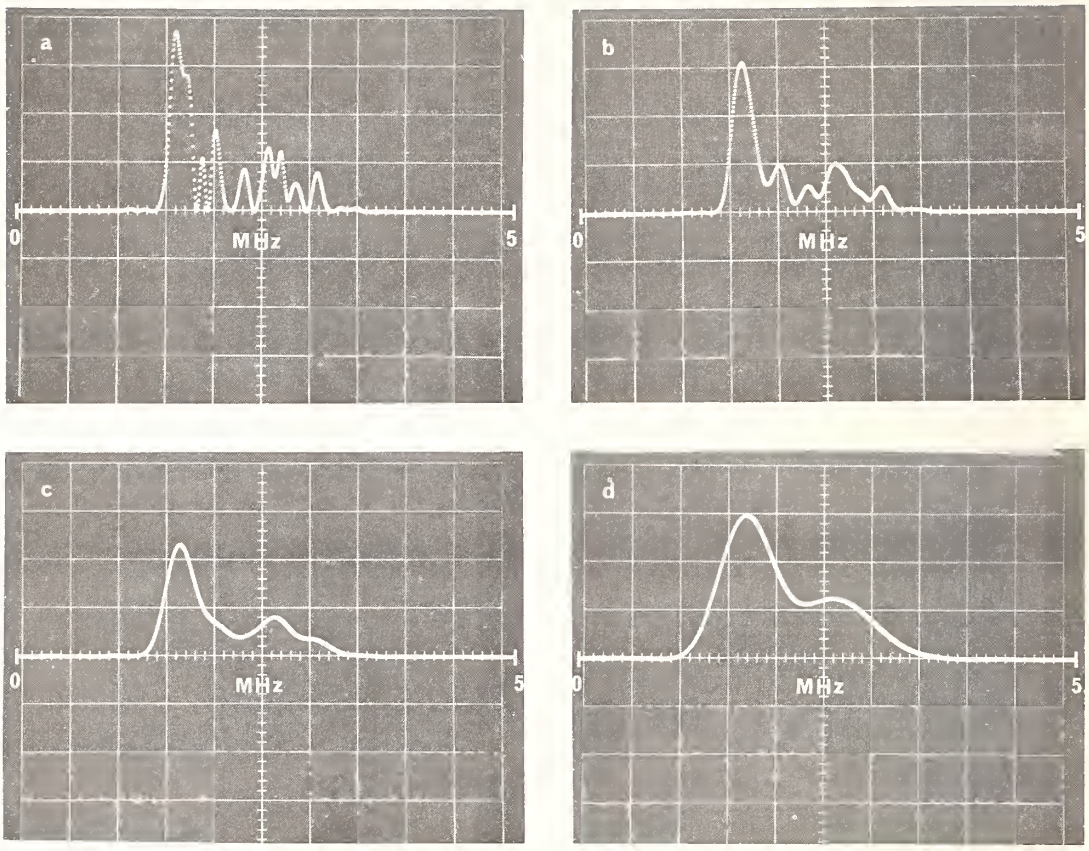

Fig. 3. Effect of lag windowing on echo spectrum. A single line of data was windowed with a 1 cm Hamming window and the spectrum a) smoothed with a Hamming lag window of b) 5 mm, c) 2.5 mm and d) 1.25 mm.

Table 1. Tissue attenuation determined by the shadowed glass method and by the scattered echo comparison method.

Tissue	Quoted atten. (Wells [6]) dB/cm MHz		Shadowed glass Slope dB/cm MHz	Shadowed glass Atten. at 2.5 MHz dB/cm	Scattered Slope dB/cm MHz	Scattered Atten. at 2.5 MHz dB/cm
Muscle along fibres	1.3		1.5	4.9	1.2	5.8
Muscle across fibres	3.3	(1)	.65	1.5	.28	2.8
		(2)	.78	1.8	.15	1.7
Liver	.94	(1)	.82	2.2	.72	3.0
		(2)	.73	3.1	.53	4.2

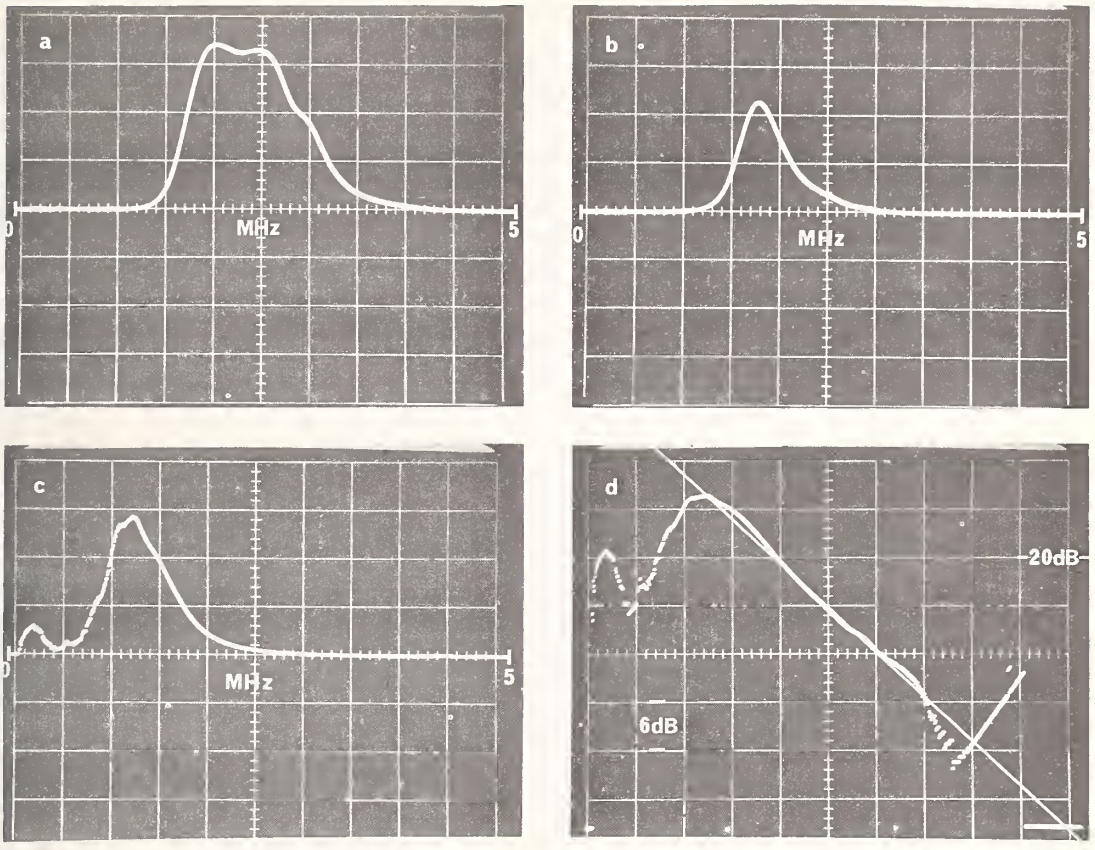

Fig. 4. Results of shadowed glass measurement on muscle across fibre direction showing a) unshadowed and b) shadowed spectra, c) ratio of spectra and d) log ratio with weighted best fit line superimposed. Note that the ripple amplitude is small in the linear region.

method. The values attenuation versus frequency in dB/cm MHz were in reasonable agreement with previously published values for the muscle along the fibres and for liver. The values for muscle across the fibres were similar to the other values but not in agreement with Wells [6]. The log ratio curves for the scattered echo measurements all showed significant ripples, indicating that some phasing effects still remain. The values for liver and muscle along the fibres agreed reasonably well with the shadowed glass method, but the muscle along fibres gave widely different results.

6. Discussion

It is obvious that further work is needed before the scattered echo comparison method will be useful for attenuation determination. The shadowed glass method appears to give repeatable results but is not suitable for clinical examinations.

The current approach in scattered echo analysis is to average in the power spectral domain with the aim of reducing the ripples in the spectrum to obtain a smooth and stable spectral estimate. It appears that an alternative approach is to average in another domain to obtain a stable estimate of the underlying spectral ripple, which is a measure of the "structure" of the echo signal. Two obvious candidates are the Autocorrelation and the cepstral domains. This structure can be postulated from the same model of distributed discrete point scatterers that is used to justify the single frequency scattering versus angle approach to tissue characterisation.

References

[1] Lizzi, F., Katz, L., St. Louis, L., and Coleman, D. J., Applications of spectral analysis in medical ultrasonography, Ultrasonics 14, 77-80 (1976).

[2] Robinson, D. E. and Williams, B. G., Computer Analysis of Ultrasonic Pulse Echo Signals, in Ultrasound in Medicine and Biology, D. White and R. E. Brown, eds., p. 1443 (Plenum Press, New York 1977).

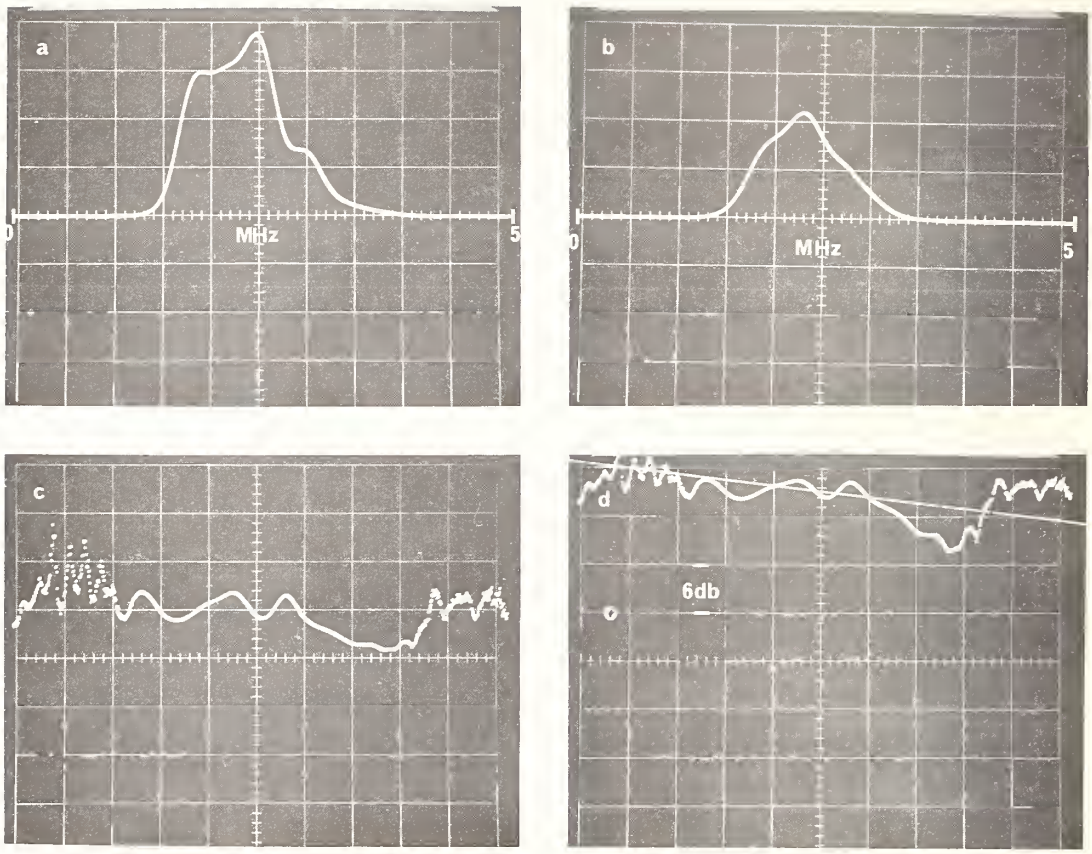

Fig. 5. Results of scattered measurement showing a) shallow and b) deep echo spectra, c) the ratio and d) log ratio with best fit line superimposed. Note the large ripple content of the log ratio.

[3] Robinson, D. E., Williams, B. G., and Horn, P. R., Digital acquisition and interactive processing of ultrasonic echoes, Ultrasound in Med. & Biol. 2, 199-212 (1976).

[4] Rabiner, L. R., Gold, B., and McGonegal, C. A., An Approach to the Approximation Problem for Nonrecursive Digital Filters, in IEEE Trans. Audio Electroacoustics, AV-18, 83-106 (1970).

[5] Jenkins, G. M. and Watts, D. G., Spectral Analysis and its Application, p. 209 (Holder-Day 1968).

[6] Wells, P. N. T., Physical Principles of Ultrasonic Diagnosis. Academy Press 1969.

Reprinted from *Ultrasonic Tissue Characterization II*, M. Linzer, ed., National Bureau of Standards, Spec. Publ. 525 (U.S. Government Printing Office, Washington, D.C., 1979).

CEPSTRAL SIGNAL PROCESSING FOR TISSUE SIGNATURE ANALYSIS

J. Fraser and G. S. Kino

Stanford University
Stanford, California 94305, U.S.A.

J. Birnholz

Harvard Medical School
Boston, Massachusetts 02115, U.S.A.

The reflected signal received by an ultrasonic transducer is modeled as a convolution of a transducer response with a reflection function for the target region. Cepstral analysis translates that signal into a domain where those components interact additively rather than through convolution and where separation can be accomplished with simple bandpass filtering operations. The cepstral transform of the pulse echo signal also provides direct access to any periodic behavior of reflectors arising from their spacing. As an example of these capabilities, the technique is used experimentally to describe the characteristic spacing of macrostructural reflecting elements in the pig liver in vitro and to determine the frequency dependent attenuation behavior of normal human liver in vivo.

Key words: Attenuation; B-scan; cepstrum; computer; convolution; de-convolution; liver; power spectrum; signal processing; tissue characterization; tissue parameters; ultrasound.

1. Introduction

We describe in this paper preliminary experiments with new types of non-linear signal processing used for eliminating certain types of signal distortion in conventional acoustic imaging systems which preclude unambiguous identification of specific tissue features.

An acoustic propagation path through a tissue region can be treated as a one-dimensional array of reflectors. While each individual reflector may be expected to replicate the time characteristics of a self convolved transducer impulse response (assuming an impulsive excitation), that pulse form is altered or distorted during propagation by the frequency dependent attenuation processes of the medium intervening between reflector and transducer. Previous studies have indicated that tissue specific information is derived from both attenuation properties of the region, as well as the distribution and backscatter features of the individual reflectors [1][1]. Therefore, an effective signal processing scheme must provide a means of eliminating the transducer response and separating frequency dependent attenuation effects from target signal components. Our approach has been to take advantage of certain properties of the cepstrum, or Fourier transform, of the signal log power spectrum [2]. The rationale for this choice derives from previous uses in comparable signal processing tasks: (1) homomorphic deconvolution of speech and music waveforms for improved recording fidelity [3]; (2) dereverberation enhancement of seismic data [4]; and (3) recognition and characterization of flaw configuration in nondestructive testing [5]. This method has not been applied to medical diagnostic ultrasound previously.

2. Analysis of the Return Echoes

We consider first what occurs when a signal is incident on body tissue. We will mainly be interested in the situation in which we observe a reflected signal with the same transducer used to illuminate the tissue. Techniques for looking at off axis reflections can, in principle, provide a great deal more information. But, in practice, they are extremely difficult to employ without the use of arrays of transducers to carry out repeatable measurements of this kind. Even with the use of arrays of transducers, because of the distortions along the body path to an organ of interest, the problems are very severe in terms of repeatability. In that case, it is probably better to concentrate on the development of imaging systems first, then process the images in some detail. Thus, the method described here is entirely devoted to the use of a single transducer operating in a reflection mode.

The signal received by a reflection mode system can be considered to arise from a one-dimensional reflection function R of distance z along the beam path R(z). In the far field of a plane transducer,

[1]Figures in brackets indicate literature references at the end of this paper.

or the focal zone of a focused transducer, the phase fronts are roughly planar and normal to the beam. Under these conditions, it can be shown by perturbation theory that R(z) is the weighted sum across the beam of the component along the beam of the gradient of the acoustic impedance of the tissue. That is, if the beam pattern is P(r), and the impedance is Z(r,z) which varies slightly around an average value of Z_0,

$$R(z) \propto \frac{1}{Z_0} \int_0^\infty 2\pi r dr P(r) \hat{z} \cdot \nabla \{Z(r,z)\} \quad . \qquad (1)$$

We wish to work in the time domain, using R(t), where, with V the acoustic velocity in tissue

$$t = 2z/V \qquad (2)$$

since the time required is for a round trip. Any information about R(t) which can be obtained will be related to changes of impedance in the tissue, and, hence, may be of use in tissue characterization.

A region of tissue is interrogated by passing a pulse A(t) of ultrasound through it and observing the return signal S(t). S(t) is given by the convolution of A(t) and R(t):

$$S(t) = \int A(\tau)\, R(t - \tau) dt \qquad (3)$$

which can be represented symbolically as

$$S(t) = A(t) * R(t). \qquad (4)$$

We do not necessarily seek to recover R(t) exactly, but rather to derive statistical information about it. We are interested in knowing the distribution sizes of the objects response for the reflected signal, and how regularly they are spaced in the tissue. We may also be interested in the evolution of A(t) as the pulse passes through tissue with frequency dependent attenuation.

Since the autocorrelation function responds to structures with strong peaks, it could be considered a possible processing technique to extract structure information from S(t). However, it can be shown that the autocorrelation of two convolved functions is the convolution of their autocorrelations. Using ★ to represent correlation,

$$S(t) \bigstar S(t) = \big(A(t) \bigstar A(t)\big) * \big(R(t) \bigstar R(t)\big) \quad . \qquad (5)$$

Since A(t) is an oscillatory function, $A(t) \bigstar A(t)$ is also, and the autocorrelation of R is confused by the convolution. The best that can be done in this case is to recover the envelope of the autocorrelation. A convenient technique for this purpose is to find the envelope of the analytic function associated with the autocorrelation by taking the Fourier transform, zeroing negative frequency components, and taking the magnitude of the inverse transform [6]. Since the autocorrelation is normally performed by inverse transforming the power spectrum, very little additional effort is needed. One merely zeros the negative frequencies in the power spectrum.

An example of a typical ultrasound echo is shown in figure 1. This echo represents the return from a pig liver, using a 3.5 MHz transducer. A pattern of multiple echoes is evident, but not readily quantifiable. The envelope of the autocorrelation of this signal is shown in figure 2. Several peaks are discernable, but none is dominant. A more sophisticated technique is sought.

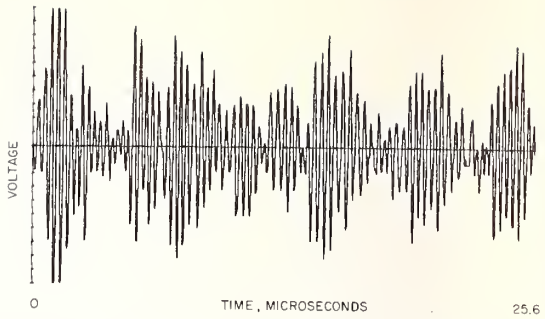

Fig. 1. The recorded ultrasonic echo from a section of fresh pig liver, in vitro, using a nominally 3.5 MHz transducer. This represents 1.9 cm of tissue.

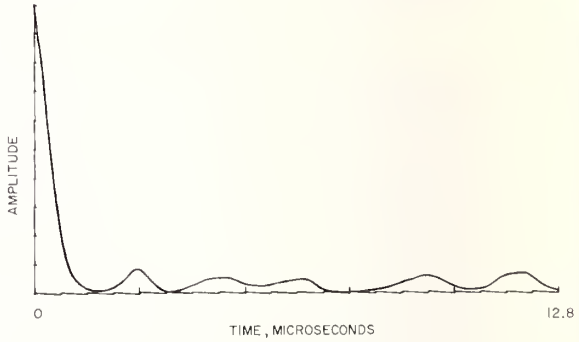

Fig. 2. The envelope of the autocorrelation function of the signal in figure 1.

3. The Inversion Process

In tissue signature analysis, responses from the tissue are weighted by the form of the transducer response. In addition, there is distortion due to the tissues on the way to the organ of interest. So a process is desired which, given S(t), can separate A(t) and R(t). Under ideal conditions, if one of two convolved functions is known, the other may be found. Deconvolution is performed by Fourier transforming, inverse filtering, and inverse Fourier transforming.

If eq. (4) is Fourier transformed, the convolution leads to a product, and rearranging gives:

$$R(\omega) = \frac{\bar{S}(\omega)}{\bar{A}(\omega)} \quad . \qquad (6)$$

Several factors prevent the use of this formal inversion process in the present case. The presence of finite noise in the recorded signal means that $\bar{S}(\omega)$ is not known exactly. In addition, as the ultrasonic transducer responses are band-limited, $\bar{A}(\omega)$ becomes vanishingly small in the same frequency ranges where $\bar{S}(\omega)$ is dominated by noise, so the noise has a disproportionate influence on the recovery of $\bar{R}(\omega)$. Finally, since the signal has prop propagated through a tissue of unknown and frequency dependent attenuation, $\bar{A}(\omega)$ is not known. A different approach is, therefore needed.

4. Homomorphic Processing

We have used so-called homomorphic processing, or cepstral analysis, for this purpose. At the present time, we have by no means developed this type of processing to its limit, but we have made a start on techniques employing it and our intention is to develop the techniques further.

The basic idea behind homomorphic processing is to turn a nonlinear process into a linear process.

Consider the convolution to the signal from the transducer A(t) with the tissue response R(t) in the time domain

$$S(t) = A(t) * R(t) \tag{7}$$

In the frequency domain, the two components derived from these signals are

$$\bar{S}(\omega) = \bar{A}(\omega) \cdot \bar{R}(\omega) \tag{8}$$

A product form is also obtained for the power spectrum

$$|\bar{S}(\omega)|^2 = |A(\omega)|^2 \cdot |R(\omega)|^2 \tag{9}$$

By taking the logarithm of $|\bar{S}(\omega)|^2$, the multiplication is converted to a sum. This enables normal linear signal processing techniques to be used.

Let

$$\hat{S}(\omega) = \log|\bar{S}(\omega)|^2 \tag{10}$$

$$\hat{A}(\omega) = \log|\bar{A}(\omega)|^2 \tag{11}$$

$$\hat{R}(\omega) = \log|\bar{R}(\omega)|^2 , \tag{12}$$

then

$$\hat{S}(\omega) = \hat{A}(\omega) + \hat{R}(\omega) . \tag{13}$$

Finally, if we take the Fourier transform of $\hat{S}(\omega)$ defined as $\hat{S}(t)$, we can write

$$\hat{S}(t) = \hat{A}(t) + \hat{R}(t) \tag{14}$$

$\hat{S}(t)$ is called the cepstrum of S(t). The notation is used to distinguish it from S(t). Figures 3, 4, and 5 demonstrate the convolution of a simulated transducer impulse response with an impulse pair, and the additive property of the log power spectra and cepstra.

We note that in the log power spectrum domain the system is linear and subject to all the rules and techniques of linear filtering. Such filtering may be accomplished by taking one more Fourier transform, yielding the cepstrum of the

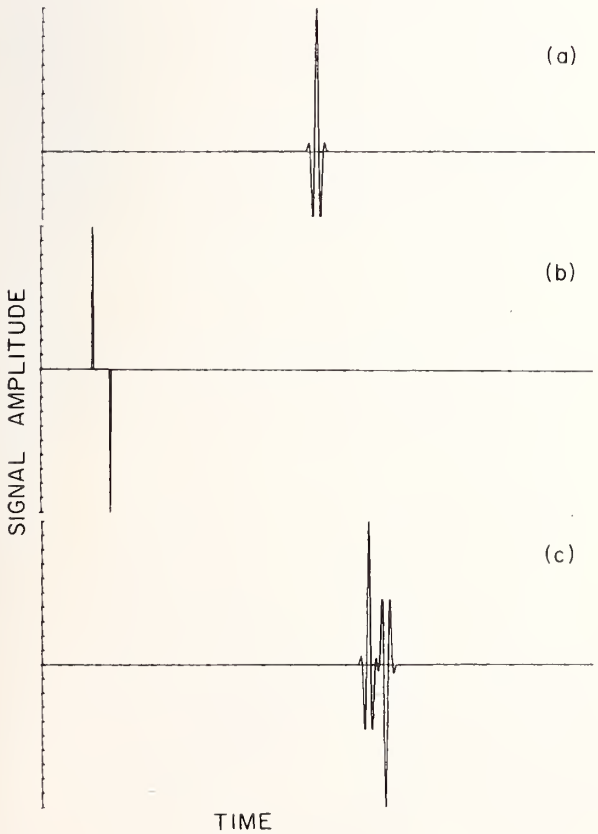

Fig. 3. (a) A simulated transducer impulse response of the form $e^{-\pi(t/8)^2} \cos 2\pi(t/8)$.
(b) An impulse pair with spacing 16.
(c) The convolution of (a) and (b).

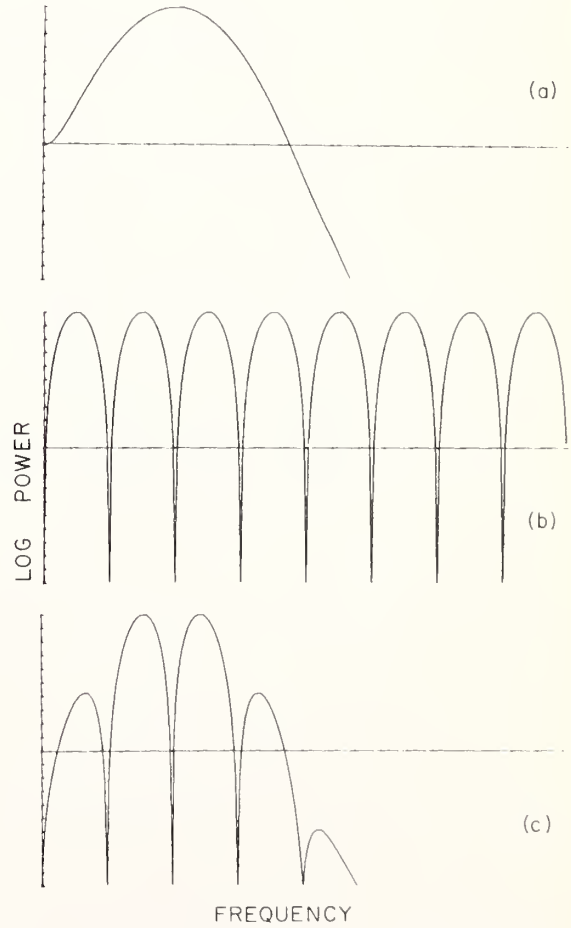

Fig. 4. The log power spectra of figure 2(a), (b), and (c) respectively.

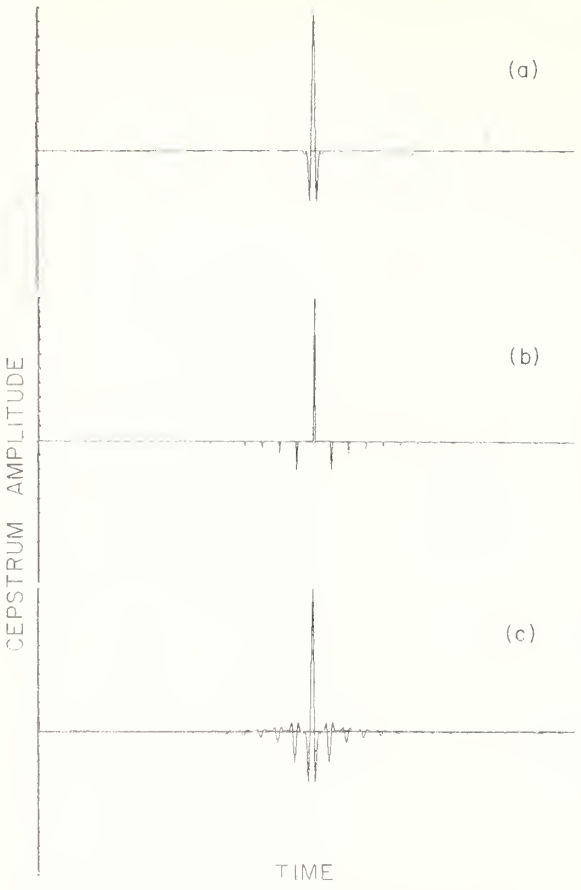

Fig. 5. The cepstra of figure 3(a), (b), and (c) respectively.

original signal. Filtering may then be performed by multiplying the cepstrum by a weighting function to select a desired portion, then reversing as many processing steps as necessary to reach a useful and recognizable domain. Since information was lost in taking the power spectrum complete inversion is not possible. This restriction is removed by the use of the complex cepstrum, in which the real logarithm of the power spectrum is replaced by the complex logarithm of the complex spectrum. However, this technique, which has been demonstrated in seismographic and speech processing applications, is much more difficult to use in practice. If, instead, we reconstruct the signals from the real cepstrum, we obtain the correlation function of the original signals, or of the tissue impedance variations.

5. Possible Applications

Filtering in the cepstrum domain is useful only if the cepstra of the two components fall in different regions of the domain. The spectrum of a broadband transducer impulse response can be close to a Gaussian response in frequency. So its logarithm is close to a parabolic response in frequency, and cepstrum is a relatively narrow pulse centered at the origin, which has a time width of the same order as the original impulse. This effect can be seen in figures 3(a) and 5(a). The cepstrum of the reflection pattern is not known and varies from tissue to tissue.

Some examples of the cepstra of impulse trains can yield insight into what may happen in tissue, and suggest features which will be meaningful. Two impulses with separation t will yield a string of impulses with separation t and of strength decaying fairly rapidly toward zero away from the origin, as seen in figures 3(b) and 5(b). If more than two impulses exist with the same spaces, the cepstrum is similar, but with a slower decay rate. This is depicted in figure 6. Figure 6 also demonstrates a problem which often arises in the digital implementation of the cepstrum. When the logarithm of the power spectrum is taken, the nonlinear process generates harmonics in the time domain which can cause aliasing in the cepstrum, even though the original spectrum bandwidth was well within the Nyquist bandwidth of the sampling process. In general, any repetitive pattern in a signal will lead to a peak at a time equal to that spacing in the spectrum, as well as lesser peaks at multiples of that spacing. The cepstrum itself may not be easy to interpret for ultrasound echoes from tissue unless the tissue has a fairly simple and distinct structure. But the decay rate of the cepstrum is related to the spacings and numbers of periodic reflections in the tissue, and hence, may be useful for tissue characterization.

If the minimum spacing between strong reflections in the tissue is somewhat greater than the wavelength of the interrogating sound, all information about the periodicities of reflections will be separated from the information about the character of an individual reflection in the cepstrum. In this case, it should be possible to filter the cepstrum and recover the average of the power spectral densities of the individual reflections from a region of tissue. This should be a good

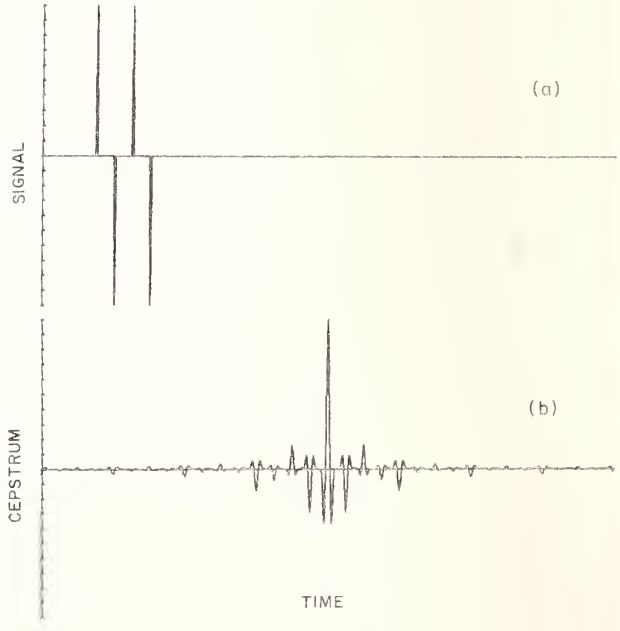

Fig. 6. (a) Four impulses with spacing 16.
(b) The cepstrum of the convolution of the impulse response of 3(a), with the impulse train of 6(a).

approximation to the spectrum of the transmitted ultrasound pulse as it passes through the region of tissue within an unknown constant. If such a calculation is carried out on signals from two succeeding regions of tissue along the line of sight, the difference between them will contain information about the frequency dependence of the attenuation of ultrasound in the tissue between these two regions.

6. Experimental Techniques

A surplus B-scan imaging system, loaned by the Radiology Department of the Stanford University Medical Center, was obtained, originally as a means of positioning the ultrasound transducers and generating images for identification of the source of echoes to be processed. It was found that the pulse generator and receiving amplifier of the system, a Picker, were of excellent quality. Also, a depth marker was available, which could be used to select a portion of a trace. By tapping a small amount of the received signal with a high impedance isolation transformer at a low impedance point in the receiver, a high quality radio frequency signal was obtained without compromising either the operation or safety of the existing B-scan system. The tapped R-F signal was further amplified and monitored by an oscilloscope and a Biomation 8100 transient recorder, which was set to record when armed by a pushbutton accessible to the operator of the B-scan system. A PDP11/10 minicomputer was used to store the digitized R-F signals from the transient recorder on a magnetic disc, and later to read the stored records and process them as desired. In practice, the operator manipulated the transducer until the beam passed through the desired area, using the B-scan image, if desired; then placed the depth marker at the beginning of the region of interest, checked the signal on the oscilloscope, and initiated recording with the pushbutton. This was found to be quite fast and convenient. The system is depicted schematically in figure 7.

After some experimentation, it was decided to standardize the format of recorded data in order to simplify the signal processing programs. A sample rate of 20 MHz was chosen, giving a usable signal bandwidth of 10 MHz. Record length was standardized at 512 samples, which represented 25.6 μs, or about 1.9 cm of tissue. This was found to be long enough for most purposes, but a provision was made to store four consecutive records if desired, representing 7.7 cm of tissue. Fourier transforms could be calculated on 512 point records in 10 seconds, and cepstra in 23 seconds, fast enough for interactive studies on the effects of various types of filtering.

Two types of experiments have been run to collect data for various purposes. In the first type, the scanning arm of the B-scan system is not used. The transducer is fixed in a water tank, suspended from a micrometer adjustable frame. The transducer's beam could be aligned to reflect from the water surface for transducer characterization and reference purposes, on targets suspended from a rotatable mount, or on tissue samples pinned to a sponge on the bottom of the tank. In the second mode, the scanning arm was used and identification of tissues was made using the images formed.

Single reflections from the surface of the water tank were used to obtain data on the efficiency and spectral characteristics of both purchased and fabricated transducers, and to verify the structure of the cepstrum of a transducer impulse response. Impulse responses and cepstra for two commercial transducers are shown in figures 8 and 9. A transducer was then aimed at the rotating mount, and a fixture holding three 1.1 mm diameter rods side by side in the beam at a spacing of 2.5 mm was attached, as shown in figure 10. The array of rods was rotated from perpendicular to the beam to parallel, and on to perpendicular again, and the reflections recorded at five degree increments in angle to provide reflections of various spacings. The envelope of these cepstra is plotted as a function of angle in figure 11. The sinusoidal dependence of spacing on angle can be clearly seen. The short spacing is seen best on one side of 90°, and the long spacing on the

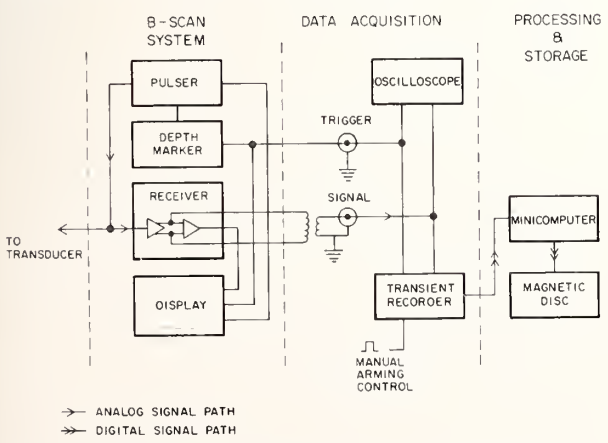

Fig. 7. A schematic diagram of the system used to obtain, store, and process ultrasonic echoes.

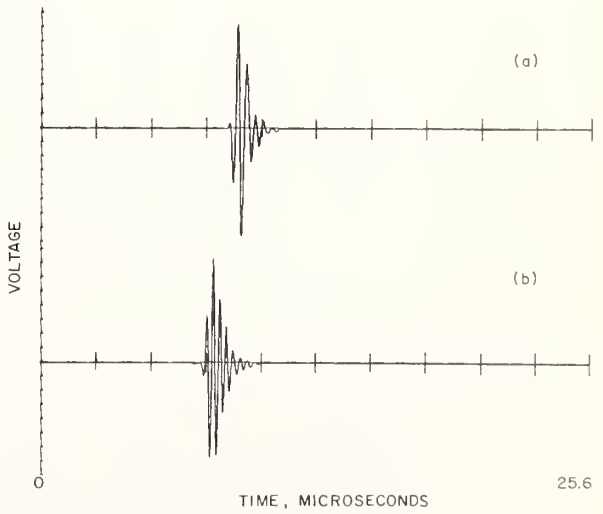

Fig. 8. (a) Impulse response of a commercial 2.25 MHz transducer.
(b) Impulse response of a commercial 3.5 MHz transducer.

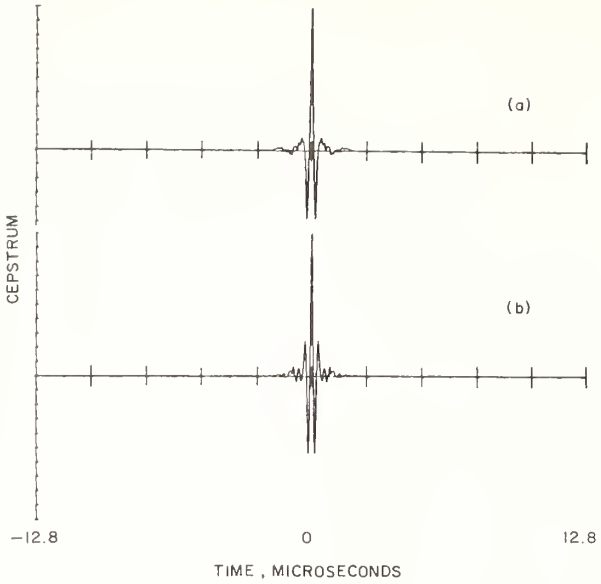

Fig. 9. (a), (b) Cepstra of the impulse responses of 8(a) and (b) respectively.

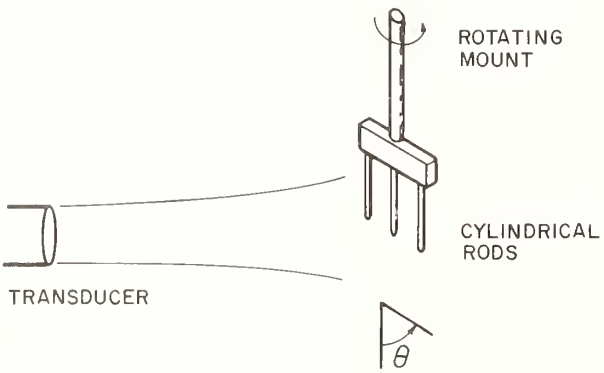

Fig. 10. Schematic diagram of a scheme to produce three identical echoes with variable spacing. Three 1.1 mm diameter steel rods are mounted 2.5 mm apart center to center.

other because a slight misalignment of the rods caused the reflections to be unequal in strength and to depend on angle. At angles where the separation between the reflections is comparable to the pulse width (that is, about .5 μs), interference can be seen to occur between the peak representing the pulse shape and that representing the periodicity.

In order to demonstrate the ability of the cepstrum to detect a periodic structure in biological tissue, a particularly simple sample was chosen: pig liver. Pig liver is a large organ, readily available in a fairly fresh state, and having a characteristic and simple period structure [8]. Our sample was several centimeters thick, and was observed to have an internal structure consisting largely of spherical lobules of fairly uniform size, about 2 mm in diameter. Several echoes were recorded from various parts of the liver, using a 3.5 MHz focused transducer in the water tank. The best of the cepstra recovered is shown in figure

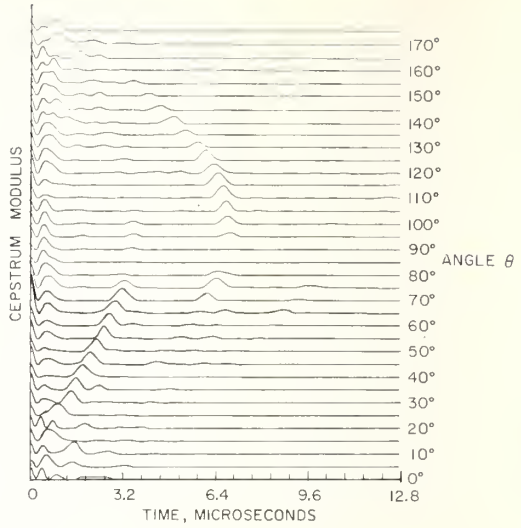

Fig. 11. Moduli of cepstra recovered from the scheme of figure 10, as a function of angle.

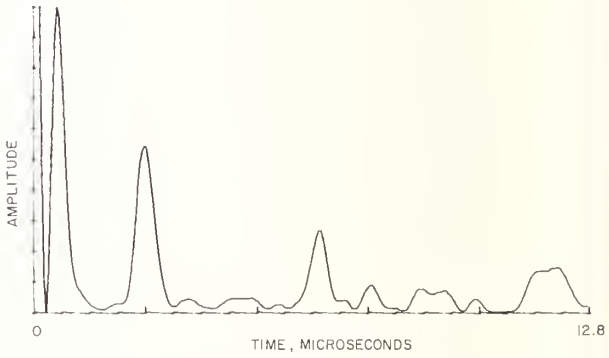

Fig. 12. The modulus of the cepstrum of the signal shown in figure 1.

12. The signal from which it was derived was shown in figure 1. The strong peak at 2.5 μs corresponds to a spacing of 1.9 mm between reflectors, which corresponds well with the observed size of the lobules. Other cepstra were not always so simple.

Cepstra were also calculated for signals from various regions of human livers from autopsies, as well as from thigh muscles and the area of the liver, in vivo. The details of the structure of both the power spectrum and the cepstrum were found to vary markedly among the samples, and even between two consecutive 5 mm long regions of single records. Some cepstra showed substantial single peaks; some did not. The decay rates of the cepstra varied substantially also. We conclude that the tissues studied are sufficiently inhomogeneous to prevent easy interpretation of these results. A broad statistical study of a large number of signals documented as to the location and possible pathology of the tissue, original transducer response, and thickness of intervening tissue, will be needed to prove the usefulness, or lack thereof, of such techniques.

7. Attenuation Estimation

Since the cepstrum is the Fourier transform of the log power spectrum, low pass filtering, or smoothing, of the log power spectrum may be done by multiplying the cepstrum by a window function which leaves short time responses untouched and eliminates long time values. The resultant gated signal may then be Fourier transformed to the frequency domain again. If the variations in the spectrum are due to reflections with relatively large spacing tissue, and, hence, are rapid compared to the finite bandwidth of the incident beam of sound, the rapidly varying spectral components can be filtered out, leaving a good approximation to the log power spectrum of the incident beam distorted by the average attenuation in the tissue. If such an approximation is made for two consecutive regions of tissue along the same ultrasonic beam path, the difference between them should exhibit the frequency dependence of the attenuation of ultrasound through the path between them. Such a calculation does not require as strong an assumption about the variations in the log power spectrum due to the tissue reflections. There may be slow variations; if they are the same in the two regions of tissue, their difference will be zero. Since slow variations in the log power spectrum arise from structure fine compared to the ultrasonic pulse length, the success or failure of this technique to predict a plausible frequency dependence for the attenuation of ultrasound will give a measure of the similarity of the structure of the two regions of tissue on the scale of the ultrasonic pulse length.

Since the advantage of this technique would be its ability to measure attenuation in vivo non-invasively, it was applied to the data recorded in vivo. This procedure is illustrated in figures 13 and 14. First the data is windowed to the proper length and Fourier transformed, and log power and spectra obtained. The signal to noise ratio has been artifically decreased to 20 dB to de-emphasize the random spectral components outside the useful bandwidth of the transducer, 1 to 3 MHz. The cepstra are then computed and low pass filtered with a sine-squared window, which closely approximates a Gaussian window, but completely cuts off long time components. Fourier transforming again yields the smoothed log power spectrum. Subtracting one such spectrum from the other and dividing by the path length between them yields a curve which, over the useful bandwidth of the transducer, estimates the frequency dependence of the loss over that path. The absolute loss is not estimated here, although with attention to time-gain control settings and assumption of equal reflection amplitudes in the two regions, it could be. In this example in which the signals were taken from two regions about 1 cm long and 2 cm apart in the area of the liver of a person with a presumed normal liver, the estimated loss follows fairly well a linear frequency dependence, although with a coefficient of 0.8 dB/cm MHz, slightly lower than the previously reported in in vitro value [9].

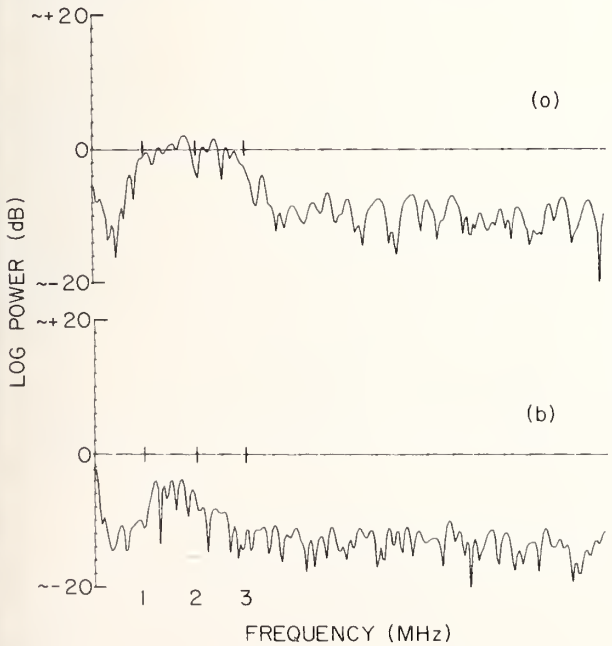

Fig. 13. (a) and (b), log power spectra from two consecutive 1 cm long regions of in vivo human liver tissue with 2 cm center spacing, recorded with a 2.25 MHz transducer.

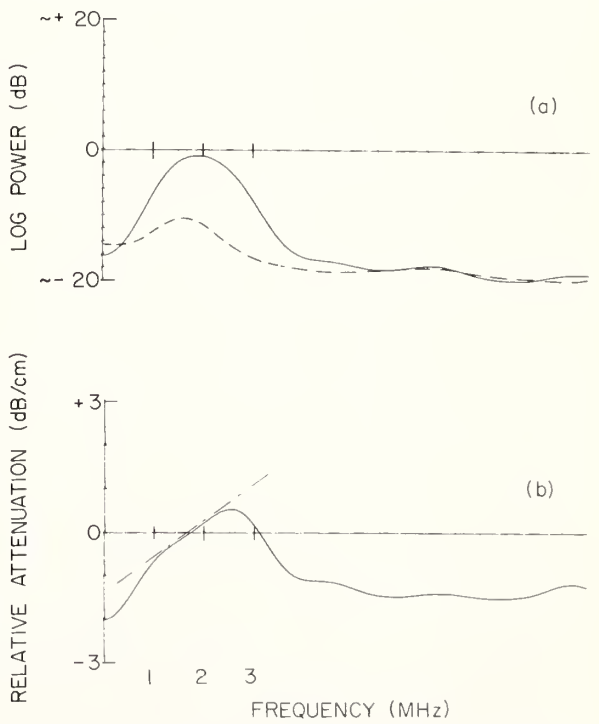

Fig. 14. (a) Solid line, the cepstrally smoothed log power spectrum derived from that of figure 13(a). Dashed line, the same function of the spectrum of figure 13(b).
(b) Solid line, the difference between the two smoothed spectra, divided by the path length. Dashed line, the slope of the attenuation in the frequency range where both spectra are above noise. This slope is .8 dB/cm.

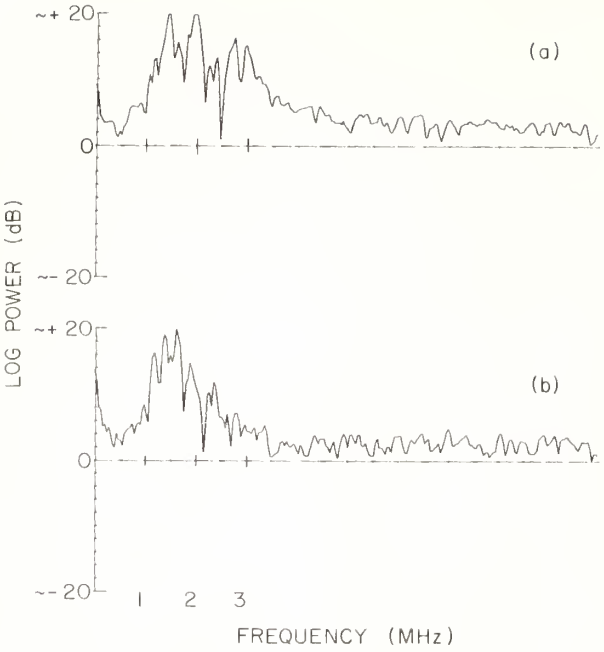

Fig. 15. Log power spectra analogous to those of figure 13, but from a different region of the liver.

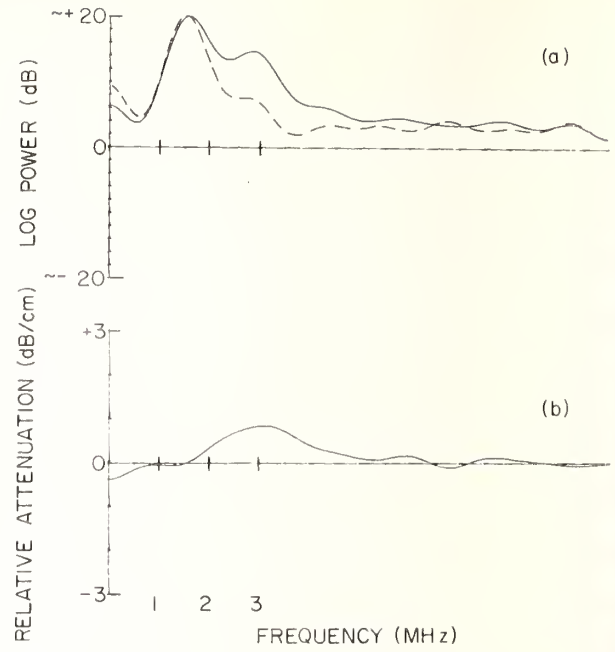

Fig. 16. (a) Smoothed log power spectra from those of figure 15.
(b) Attenuation estimated from figure 16(a). No estimate is possible in this case.

An interesting phenomenon has been found in the two in vivo livers and the one in vitro liver studied with this technique so far. In many of the log power spectra calculated, there is a deep notch, representing an absence of reflection at frequencies varying from 2.4 to 2.7 MHz. This notch has been seen with both focused and unfocused transducers of both 2.25 and 3.5 MHz center frequency. This phenomenon violates the conditions under which one can get a good estimate of attenuation. It occurs only once in the useful bandwidth of the transducers used, and so cannot be considered rapidly varying. Its frequency varies enough from region to region that it does not cancel when two spectra are subtracted. The very deep notch is almost, but not quite, removed by the smoothing operation. Since the attenuation calculation takes the difference between two similar functions, it is sensitive to the small error which remains. An example of this problem is shown in figures 15 and 16. Such a phenomenon probably arises because most of the reflections in a region are coming from a single type of structure: one with a constant size of a fraction of a millimeter. Measurements over a broader bandwidth could determine more exactly what type of structure this is. If it could be identified, there might be clinically useful information available.

8. Conclusions

From this limited study, we conclude that:

(a) Cepstral analysis, by converting ultrasonic signals from a domain in which the output is the convolution of an impulse response with a reflection function to a domain in which it is a sum, allows the separation of information about the distribution of spacings between reflectors from information about the incident impulse.

(b) Two potentially useful parameters for tissue characterization in vivo are the form of the cepstrum of ultrasound echoes from tissue, which can identify periodicities in the tissue; and attenuation coefficient estimation by cepstral smoothing of log power spectra.

A lack of consistency from one region to another within a tissue suggests considerable variability in the tissue. Further work, utilizing statistical studies on large data bases, will be required to verify the usefulness of these techniques. Cepstral analysis should prove useful, since averaging over similar samples will enhance the tissue-dependent information. This is in marked contrast to the power spectral domain, where averaging over similar samples tends to eliminate tissue-dependent information and approximate the power spectrum of the measuring system.

Acknowledgments

The work reported in this paper was supported in part by the National Science Foundation under Grant No. ENG 75-18681, and in part by the Kaiser Foundation.

References

[1] Several of these studies are reviewed in: Dunn, F., Ultrasonics Attenuation, Absorption, and Velocity in Tissues and Organs; and, Reid, J.M., The Scattering of Ultrasound by Tissues, in Ultrasonic Tissue Characterization. M. Linzer, ed., National Bureau of Standards Spec. Publ. 453, pp. 21-28 and 29-47 (U.S. Government Printing Office, Washington, D.C., 1976).

[2] Bogert, B. P., Healy, M. J. R., and Tukey, J. W., The Frequency Analysis of Time Series for Echoes: Cepstrum, Pseudo-Autocovariance, Cross-Cepstrum, and Saphe Cracking, in Proc. Sym. Time Series Analysis, M. Rosenblatt, ed., pp. 209-243 (John Wiley and Sons, Inc., New York, 1963).

[3] Stockham, T. C., Jr., Restoration of Old Acoustic Recordings by Means of Digital Signal Processing, Preprint, 41st Convention, Audio Engineering Society, New York, October 1971.

[4] Ulrych, T. J., Application of homomorphic deconvolution to seismology, Geophysics 36 (4), 650-660 (August 1971).

[5] Adaptive Nonlinear Signal Processing for Characterization of Ultrasonic NDE Waveforms, Task 2: Measurement of Subsurface Fatigue Crack Size, in Technical Report AFML-TR-76-44, April 1976, Section 6.4, p. 54.

[6] Bracewell, R., The Fourier Transform and Its Application, pp. 269-271 (McGraw-Hill, New York, 1965).

[7] Oppenheim, A. V. and Schafer, R. W., Digital Signal Processing Chap. 10, pp. 480-531 (Prentice-Hall, Inc., Princeton, 1975).

[8] Lele, P. P., Mansfield, A. B., Murphy, A. I., Namery, J., and Senapati, N., Tissue Characterization by Ultrasonic Frequency Dependent Attenuation and Scattering, in Ultrasonic Tissue Characterization, M. Linzer, ed., National Bureau of Standards Spec. Publ. 453, pp. 167-196 (U.S. Government Printing Office, Washington, D.C., 1976).

[9] Goldman, D. E. and Heuter, T. F., Tabular data of the velocity and absorption of high frequency sound in mammalian tissues, J. Acoust. Soc. Am. 28, 35 (1956).

Reprinted from *Ultrasonic Tissue Characterization II*, M. Linzer, ed., National Bureau of Standards, Spec. Publ. 525 (U.S. Government Printing Office, Washington, D.C., 1979).

RECOGNITION OF PATTERNS IN ULTRASONIC SECTIONAL PICTURES OF THE PROSTATE FOR TUMOR DIAGNOSIS

W. von Seelen,[1] A. Gaca,[2] E. Loch,[2] W. Scheiding,[3] and G. Wessels[2]

[1]Institut für Zoologie
Arbeitsgruppe III (Biophysik)
D-6500 Mainz, Federal Republic of Germany

[2]Deutsche Klinik für Diagnostik
D-6200 Wiesbaden, Federal Republic of Germany

[3]Battelle Institut e.V.
D-600 Frankfurt/M., Federal Republic of Germany

We examined the prostate with ultrasonics to diagnose tumorous alterations of the organ. We scanned directly from the abdominal wall through the filled bladder (transvesical). The research is aimed at: 1) improvement and mathematical preparation of the ultrasonic pictures to assist the physician in his diagnosis; and 2) ascertainment of significant parameters which allow the classes "normal prostate," "adenoma" and "carcinoma" to be distinguished in screening examinations. The results show that with ultrasonics, adenomas and carcinomas are recognizable in 96 percent of the examined patients and can be differentiated from normal prostate tissue. The palpation finding was used as a reference in most cases.

Key words: Pattern recognition; prostate tumors; ultrasound.

1. Introduction

Carcinoma of the prostate ranges third in cancer mortality in the Federal Republic of Germany. Besides the subjective rectal palpation findings which give the physician signs of organic alterations, it is useful to look for other examination methods.

The aim of this investigation is to analyze the value of the ultrasonic scan for differential diagnosis and treatment control of tumor diseases and to check in establishing preclinic findings the possibility of a screening procedure allowing a quick separation between suspect and non-suspect cases in large groups of patients.

The apparatus available for the methodical part of the investigations are two ultrasonic scanners: Combison II Kretz (Compound-Scanner) Vidoson, Siemens (Realtime-Scanner) as well as a computer (PDP 11/34). The apparatus is shown schematically in figure 1. This study includes both examinations in vivo and some examinations in vitro. Transvesical representation of the prostate was chosen for in vivo examination. The ultrasonic pictures are taken from above the organ by scanning in sections of 3 mm; the angle at which the sound waves enter is either $\alpha = 15°$ or $\alpha = 20°$ from the vertical.

Figure 2 shows the position of the organ as well as the direction of entry of the sound used to produce the pictures discussed below. The frequencies are 2.25 MHz and 4 MHz. Linear scanning is used to cover the area of the organ with a slightly altered angle of entry for the forward and reverse runs. The B pictures gained in this way are recorded on a video tape which serves as mass storage. For the computer analysis the video signal can be digitized by a specially developed interface and read into a 512 x 512 matrix; a region of interest can be marked out within the picture. In addition, it is possible to feed the non-demodulated HF signal or the A signal into the PDP 11 computer. Two control techniques were employed in the analysis of the ultrasonic pictures: comparison with the urologists' palpation findings and in vitro examinations of dissection material taken during operations.

The ultrasonic pictures reproduce the geometrical arrangement and form of the density gradients in the tissue which are situated perpendicular to the direction of the sound. Since not enough is known about the reflecting properties of the various tissues, the picture features for the different picture classes cannot be defined exactly a priori. The study was therefore carried out in the following stages:

1. Definition of a limited learning sample which can be diagnosed as certainly as possible with the palpation findings and histological controls.
2. Determination of as many apparently significant features as possible.
3. Generation of an adaptive classifier which begins with a fixed initial weighting of the features. This weighting is changed in the course of the classification of the learning sample so as to eliminate errors. In this way the physician

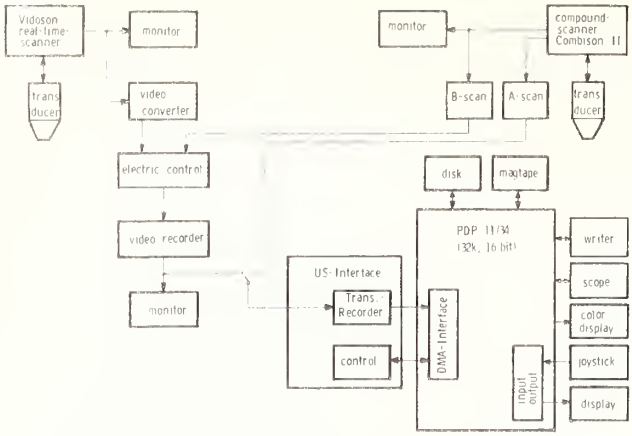

Fig. 1. Flow chart of apparatus for producing and analyzing the ultrasonic pictures.

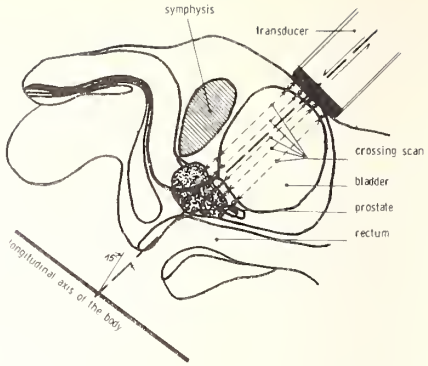

Fig. 2. Method of transvesical scanning the organ.

Fig. 3. Ultrasonic picture of a normal prostate.

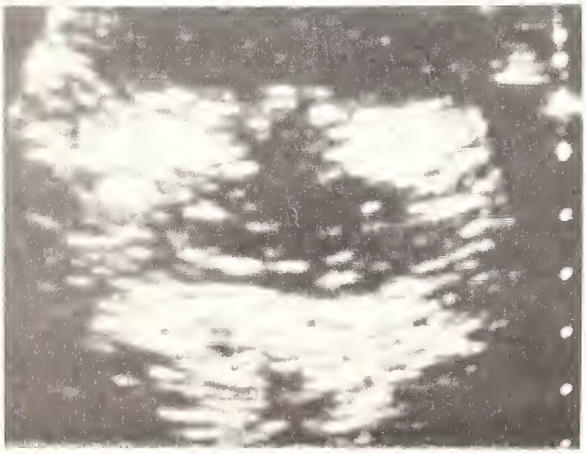

Fig. 4. Ultrasonic picture of an adenomatous prostate.

Fig. 5. Ultrasonic picture of a carcinomatous prostate.

supervises the determination of features and class limits.

4. Ascertainment of the validity of the individual features to determine a precise set of distinguishing features which does not involve too difficult or costly application. The criterion for validity is provided by the alteration in detection rate for the relevant feature.

Figures 3, 4 and 5 each show one representative of the classes normal, adenomatous and carcinomatous respectively. While the normal organ's interior is characteristically largely echo free, the adenoma appears highly structured. The carcinoma in the right half causes a "shadow" which penetrates the capsule areas. Other features of the pictures will be discussed below.

2. Preprocessing of the Pictures

Preprocessing the pictures is intended to allow the doctor to make the most certain possible diagnosis. For this it is necessary to eliminate disturbances and distortions in the picture and to create the possibility of accentuating features relevant to suspected cases, if this is required. To this end the operations described below were im-

plemented on the digital computer and then first tested by subjecting them to the same classification procedure as the original pictures. The following operations were carried out on the pictures (for different numbers of patients in each case).

a. Definition of a "region of interest." This operation consists in limiting the organ area on the screen and reducing the amount of data taken over in the computer from the picture to 128 x 128 picture points (8 bits per point) which thus refer to the region of interest. This limitation of the picture is carried out by the physician treating the case.

b. Standardizing the intensity of the picture. The space dependent intensity of the picture $x(r,s)$ in the B scan picture varies a great deal from patient to patient (age, corpulence, etc.) and also depends on the amplification of the experimental device. Therefore, parameters dependent on intensity should only be used in the diagnosis when $x(r,s)$ is divided by the mean value $\overline{x(r,s)}$ determined in a defined organ area. The resulting picture is the basis for several computer operations.

c. Inverse filtering. To eliminate the loss in lateral focus due to the form $H_k(r,s)$ of the sound beam as far as possible, the values ascertained under water for this space dependent coupling were used to determine the filter characteristic value $H_i(r,s)$. The conditions for the realization of $H_i(r,s)$

$$\underline{\underline{F}}(H_k(r,s)) \cdot \underline{\underline{F}}(H_i(r,s)) = 1$$

were replaced by

$$\underline{\underline{F}}(H_k(r,s)) \cdot \frac{1}{1 + \underline{\underline{F}}(H_i^*(r,s))} = 1$$

for numerical reasons. $\underline{\underline{F}}$ characterizes the Fourier transform according to the two space coordinates r,s. Figure 6a shows the sectional picture of a 0.5 mm thick wire in the tank of water as well as its filtered representation with improved radial focus.

d. Symmetrical filtering. The convolution of the picture $X(r,s)$ with any optional symmetrical, and thus phase free transmission function $H(r,s)$ allows a far-reaching alteration of the pictures, when one varies the parameters m_1, m_2, B_1, B_2 in

$$Y(r,s) = X(r,s) * H(r,s)$$

with

$$H(r,s) = Um_1 e^{-(r^2+s^2)/B_1^2} - Um_2 e^{-(r^2+s^2)/B_2^2}$$

Two phase free band pass filters with different mean frequencies Um_1 and Um_2 were realized for $m_1B_1 = m_2B_2$ and $B_2 > B_1$. Figures 6b (F) and 6c (G) show the result of the operation for $Um_2 > Um_1$. The classes can be better distinguished in the filtered version of the picture (F, Um_1) than in the original picture (cf. Section 4). The second filter operation (G) is interpreted so that the picture amplitude is approximately proportional to the gradient of the intensity in the original picture. This variable has to be taken into consideration at the boundary of carcinomas.

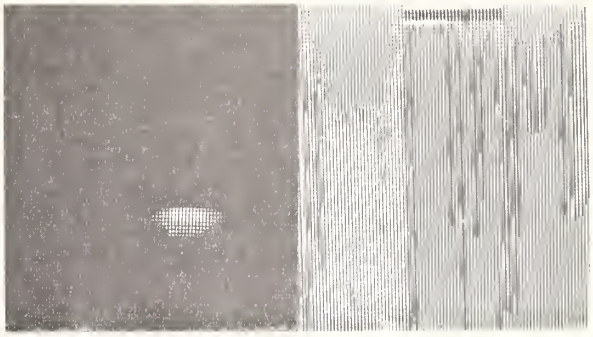

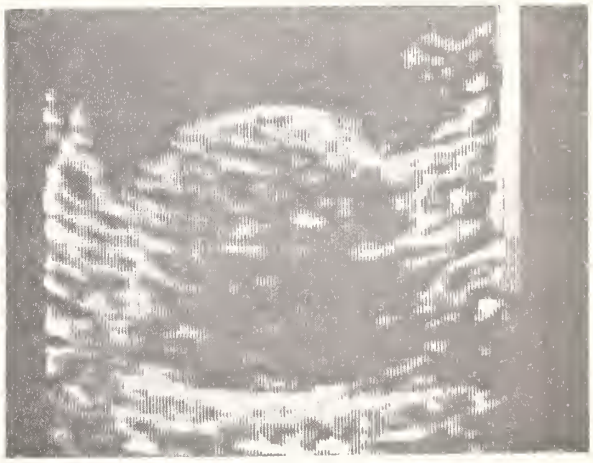

(b)

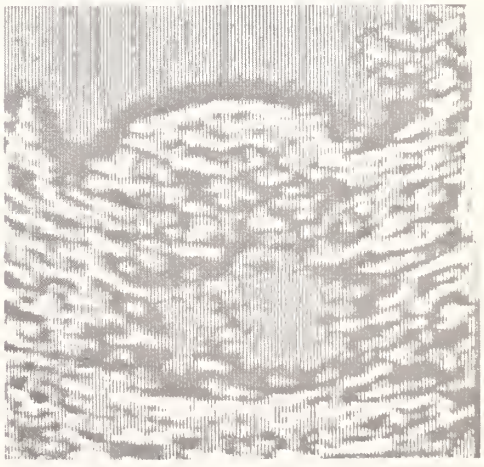

(c)

Fig. 6. Sectional picture of a wire before and after inverse filtering (a); band pass filtered sectional picture of a carcinomatous organ with Um_1 (F) (b); and Um_2 (G) (c).

e. Phase dependent filters. It is easier to judge the pictures, if the function H(r,s) is not symmetric, i.e.:

$$H(r,s) = Um_1 e^{-(r^2+s^2)/B_1^{*2}} - Um_2 e^{-((r-r_0)^2+(s-s_0)^2)/B_2^2}$$

with $B_1^* << B_1$. In this case the Fourier transform F (H(r,s)) is complex and a phase shift exists. In this way a picture is produced which is interpreted as pseudo three-dimensional when viewed. If H(r,s) characterizes a differentiating space filter combined with a nonlinear characteristic curve, then the same effect occurs together with an accentuation of the intensity modulation. Figure 7 shows two examples for different H(r,s) (paper in preparation). All filter operations, insofar as they are linear, can be combined to one operation.

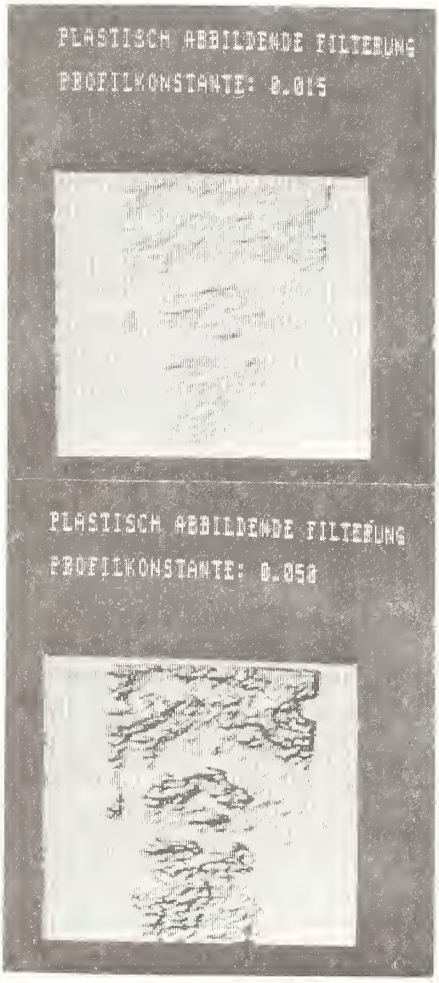

Fig. 7. Filtering with asymmetrical functions H(r,s).

f. Equidensities. It is easier to analyze the weak modulations in the area of the organ more exactly when the low pass filtered original picture is provided with lines of equal intensity. Figure 8 shows an example with an increased number of picture points.

Fig. 8. Carcinomatous prostate represented in equidensities in a low pass filtered sectional picture.

It depends on the problem in question which of the procedures described is best suited for the physician's diagnosis. Only the F and G pictures have been tested with the classification procedure (cf. Section 4).

3. Feature Extraction

The problem of feature extraction has to be solved in two ways. The reference vectors are determined on the basis of the physician's palpation findings and the vectors $\underline{x}_i$ are obtained from the ultrasonic pictures. The palpation finding takes into consideration size, consistency, surface state and simple form parameters [1-5][1]. The analysis of the ultrasonic picture refers to global and local features which in the first phase are still partly obtained by visual scrutiny of the screen picture. Should these features prove to be effective in distinguishing classes, the procedure will be completely automated.

In particular, the following features are quantified:

1. Longitudinal diameter of the organ.
2. Rise in the base of the bladder.
3. Local gaps in the capsule.
4. Coarse parallel fibrous structure in the interior of the organ.
5. Fine fibrous structure in the interior.

The automatic determination of features 4 and 5 by multiple correlation of the picture with texture pictures in which the form of the elements is optional (e.g., elliptical) but their location is statistical, is being implemented at present.

After the picture has been transferred from the video recorder to the computer, the following parameters are extracted according to the definition of the region of interest:

6. Surface of the sectional picture Fg.
7. Autocorrelation $\phi_{xx}(o,o)$
8. The standardized signal power in the region of interest, i.e., $\phi_{xx}(o,o)/\overline{x(r,s)}^2$.

[1]Figures in brackets indicate literature references at the end of this paper.

9. The amplitude density distribution $p(x(r,s))$ with the relevant first three moments or central moments respectively

$$E(x(r,s)), \quad E(x(r,s) - \overline{x(r,s)})^2,$$

$$E(x(r,s) - \overline{x(r,s)})^3.$$

10. Curve of the autocorrelation function along a line through the suspect zones $\phi_{x_r x_r}(r')$.
11. Coherence width and relative extremes of the autocorrelation function $\phi_{xx}(r)$ along a line through suspect zones.
12. Power and energy above a threshold or within an amplitude window respectively. This operation has so far only been implemented on 60 statistically selected patients.

In order to include local form parameters in the consideration, the features 6 through 11 were determined in the original picture and in two filtered pictures (F,G) and classified separately. In this way the efficiency of the filtering in distinguishing these features was tested. The effect of picture standardization and parameter 12 have so far only been studied on 60 patients. The vaidity of all the parameters mentioned is being tested with an adaptive classifier.

4. Classification

If $\underline{y}_i$ is a feature vector, then classification consists in the division of feature space by class limits so that

$$D_i(\underline{y}) \geq D_j(\underline{y}) \qquad i,j = 1,2, \ldots m, \; i \neq j$$

when $\underline{y}_i$ is correctly classified; D is a discriminating function [6]. In this project an adaptive linear classifier was chosen at first with

$$D_i(\underline{y}_i) = \sum_{k=1}^{n} {}^{k}y_i \, {}^{k}W_i + {}^{n+1}W_i$$

The variable ${}^{k}W_i$ designates the kth component of the reference vector $\underline{W}_i$ which is generated in ρ steps with the aid of a learning sample according to the rule

$\underline{W}_{i,\delta+1} = \underline{W}_{i,\delta}$ if $\underline{y}_i$ was correctly classified

and

$\underline{W}_{i,\delta+1} = \underline{W}_{i,\delta} + C_\delta \cdot \underline{y}_{i,\delta}$ if $\underline{y}_i$ was incorrectly

classified with

$$C_\delta = \operatorname{sign}\left[\frac{\underline{W}_{i,\delta} \cdot \underline{y}^T_{i,\delta}}{\underline{y}_{i,\delta} \cdot \underline{y}^T_{i,\delta}}\right] .$$

In the case of a Gaussian distortion of the features, the decision rule minimizes the quadratic distance between the reference vector and the vector to be classified. The decisions on a correct or incorrect classification in the adaptive process described above are based on the physician's palpation findings. After generation of the reference vector, the pictures were classified in stages. First, the set of features 1 through 5 was applied (Part I), then the parameters 6 through 11 for the original pictures as well as two filtered versions of the picture (Part II) and then parameter 12 on intensity standardized pictures for 60 patients. A classification on the basis of the complete featureset (I + II + III) will be realized if feature 12 is determined for all patients. The class-specific reference-vectors were established with 25 patients per class in the first stage of the project. Therefore the following number of patients can be considered as a test data set.

Part I. After taking palpation findings from 500 patients, the parameters 1 through 5 (Section 3) were extracted and the classes normal (N) and suspect (adenomatous (A), carcinomous (C)) distinguished. The physician's diagnoses were:

a) 97 patients normal
b) 324 patients adenomatous or carcinomatous
c) 79 patients nonspecifically suspect (prostatitis, congestion etc.).

If P(N/A + C) characterizes the probability that a patient classed as normal nevertheless has an adenoma or carcinoma (false negative) one obtains the following results for false classification. In the case of unequivocal diagnosis:

P(N/A + C) = 3.2 % (false negative)
P(A + C/N) = 7.4 % (false positive)

If the nonspecific suspect cases are also taken into consideration then P(N/A + C) = 7.2 percent. The increase in error due to group c can be further lowered with more precise examination. If the total number of false classifications is considered, the probability of error is 3.9 percent. In the 3 group problem the mean error rate increases to 8 percent.

Part II. The classification of the pictures from 198 patients according to the features 6 through 11 resulted in a mean error of 11.9 percent for the 2 group problem (normal/not normal) with the original pictures and 10 percent for the filtered version F and 14 percent for the filtered version G. First results are now available for studying the weighting of the individual features and altered decision strategies but the analysis has not been completed.

Part III. Using feature 12 presupposes standardizing the picture intensity. In a set of 60 patients selected statistically the rate of error for the 2 group problem was 0 percent. The mean error for the 3 group problem was 7 percent and P(C/N + A) = 0 percent. This study is at present being extended to the whole group of patients (500). An improvement in the classification can be expected.

As the features in the three classification experiments are at least partially independent from each other, it is to be expected that the rate of error can be reduced with a combined set of features. The systematic study of these combinations, which are intended to attain a better feature vector with a few easily calculable components has not yet been completed.

The further studies are concerned with ascertaining a histologically tested learning sample, determining the sharpest distinguishing parameter and obtaining a classifier which takes the statistical parameters of the features into consideration.

References

[1] Gaca, A., Loch, E. G., Scheiding, U., von Seelen, W., and Wessels, G., Ultraschalluntersuchungen der Prostata zur Erkennung von Tumorerkrankungen. Report BF-R-62.991-3 (1977) Bundesministerium für Forschung, Bonn, Kennedy-Allee. (This report contains a comprehensive list of the relevant literature.)

[2] King, W., Kiemeyer, W., Mark, R., Boyce, W. H., and McKinney, W. M., Current status of prostatic echography, J. Amer. Med. Ass. 226 (4), (1973).

[3] Takahashi, H. and Ouchi, T., Ultrasonic diagnosis in the field of urology. First Report, Japanese Medical Ultrasonics, pp. 7-10, Tokyo, (1963).

[4] Takahashi, H., and Ouchi, T., Ultrasonic diagnosis in the field of urology. Second Report, Japanese Medical Ultrasonics, pp. 35-37, Tokyo, (1964).

[5] Watanabe, H., Igari, D., Tanahashi, Y., Hasada, K., and Saitoh, M., Diagnostic application of ultrasonography to the prostate, Invest. Urol. 8, 548-559 (1971).

[6] Fu, K. S., Digital Pattern Recognition (Springer-Verlag, Berlin 1976).

Reprinted from *Ultrasonic Tissue Characterization II*, M. Linzer, ed., National Bureau of Standards, Spec. Publ. 525 (U.S. Government Printing Office, Washington, D.C., 1979).

RECENT DEVELOPMENTS IN OBTAINING HISTOPATHOLOGICAL INFORMATION FROM ULTRASOUND TISSUE SIGNATURES

K. Preston, Jr.,[1] M. J. Czerwinski,[1] M. L. Skolnik,[2] and D. E. Leb[3]

[1]Department of Electrical Engineering
Carnegie-Mellon University
Pittsburgh, Pennsylvania 15213, U.S.A.

[2]Ultrasound Laboratory
University of Pittsburgh Medical Center
Pittsburgh, Pennsylvania 15213, U.S.A.

[3]Department of Medicine
University of Pittsburgh
Pittsburgh, Pennsylvania 15261 U.S.A.

Statistical, signal-analytic techniques may be applied to ultrasonic pulse-echoes received from organs of the human body. Simultaneous tissue biopsies of these organs may be sectioned, stained, and measured by the computerized optical microscope using various image-analytic techniques. This paper reports some preliminary work along these lines as related to the kidney and liver.

Key words: Picture processing; signal analysis; ultrasound.

1. Introduction

In the 1950s Wild and Reid [1][1] noticed that there appeared to be a correlation between the properties of the A-scan in mammography and the histopathology of breast tissue in human subjects. Later Fry [2] compared the histopathology of animal tissue (feline and porcine) with the B-scan echogram. More recently Mountford and Wells [3], using digitized A-scans from both normal and cirrhotic subjects, found that specific signal parameters (amplitude, rise time, etc.) correlated with liver pathology. Ossoinig [4], Fields et al. [5], and Taylor and Milan [6] made further observations of B-scan texture, amplitudes and positions of the peaks in the demodulated A-scan, and A-scan amplitude probability distribution functions ("histograms"), respectively.

The advent of high-speed digitizers and inexpensive digital computers has now opened this field to many new investigations. One of these investigations was commenced by the authors under a grant from the National Science Foundation (APR75-08154) in mid-1975. A preliminary report was presented by Preston[7] at the first meeting of this international seminar at Gaithersburgh in 1975. The Carnegie-Mellon University program is being conducted along the lines of a project in classical pattern recognition in distinction to a project in biological modeling. The work is being conducted on both humans and animals in vivo in cooperation with the Departments of Radiology, Renology, and Pathology of the University of Pittsburgh Health Center. Each subject, or more specifically, the target organ within the subject, is considered to reside in Signal Space. This space is interrogated in three ways. A standard B-scan is made using commercial equipment (Picker Echoview) and, at the same time, several A-scans are digitized using a special-purpose, digitizing system (Stahl Research Labs.). Finally, in addition to the ultrasonogram and the digitally recorded A-scan, a tissue biopsy is made of the organ under examination. These interrogations furnish information which constitutes what we term "Data Space."

A visual diagnosis is made from the ultrasonogram by the staff of the Ultrasound Laboratory and is combined with the histopathological diagnosis carried out by the Department of Pathology. This furnishes information on disease type and severity. At the same time a numerical analysis is performed on the digitized A-scan using the statistical methods described below. These various methods of analysis of the information in Data Space provide us with numerical information which is contained in Measurement Space. These measurements, taken over a population of patients, are then processed in a supervised fashion (correlation of measurements with predetermined disease types) using a standard discriminant function software package (University of California BMDO7M) to generate points in Classification Space. Finally, images of the tissue biopsy are digitized by the Biomedical Image Processing Group at Jet Propulsion Laboratory and analyzed using the Biomedical Image Processing Unit of the Department of Radiation Health at the University of

[1]Figures in brackets indicate literature references at the end of this paper.

Pittsburgh. The balance of this paper discusses A-scan digitizations, A-scan analysis, image digitization and processing, and reports results to date in these areas.

2. Materials and Methods

The ultrasound digitizer is the basic unit used for digitizing A-scans. The digitizer (Stahl Research Labs. model 4036) is a complete digitizing system rather than a simple analog/digital converter. Its block diagram is shown in figure 1. The unit requires only two inputs, namely a synchronizing or gating signal and the analog waveform to be digitized and stored. The digitizer runs under control of an internal 15 megahertz clock. Burst length and skip burst values are entered using digiswitches on the control panel of the model 4036. When a synchronizing pulse is received, the digitizer proceeds to sample and digitize the input data at a 15 megahertz rate until the number of words stored equals the burst length. The unit then begins counting additional synchronizing pulses until the count has reached the number set for the skip burst. When this count has been reached, the next synchronizing pulse causes another burst to be digitized. This continues until the 4096 word memory is full (each word is one 8-bit byte). At the present time we are using a burst length of 128 which corresponds to 8.5 microseconds of recorded signal over which the pulse-echoes are received from about 0.65 centimeter of tissue.

The digitizer incorporates a modem and complete memory teletype (Texas Instruments model 700) having twin digital cassettes each of which is capable of storing 250,000 words of digitized A-scan data. When the user desires to transmit data to a remote computer, the modem is interfaced via the telephone system, a dial-up connection is made, and the digital cassettes are activated and transfer their data via the communication link. In our present program the computer used is a Digital Equipment Corporation PDP10 model KA at Carnegie-Mellon University.

In all experiments to date, the A-scan is digitized directly from the output of the radio frequency (rf) amplifier. The unit employed for both pulsing the transducer and amplifying the A-scan is a Panametrics model 5055 custom-modified to provide bandwidth to 20 MHz. In our experiments we have used the model 5055 at its full gain setting (60 dB) and with full bandwidth with the interval damping resistor set to 250 ohms. The organs of interest have been the liver and kidney for which we obtain signal levels at the output of the model 5055 rf amplifier ranging from a few tens to a few hundreds of millivolts. (The least significant digit of the digitizer corresponds to approximately 8 millivolts.)

The transducer utilized is a Panametrics custom-made biopsy transducer whose characteristics have been measured by the Acoustics Branch, National Bureau of Standards, and are presented in figure 2. As can be seen, the resonant frequency is close to 4 MHz with a 25 percent 3 dB bandwidth.

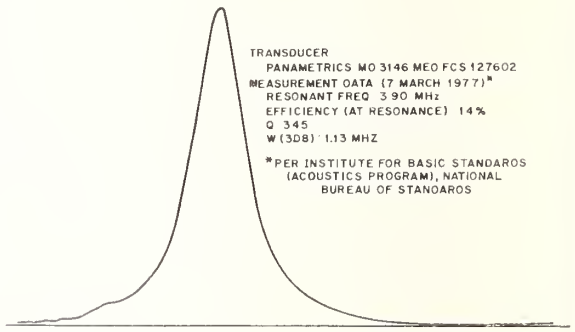

Fig. 2. Transducer 1-way frequency response as determined by the National Bureau of Standards.

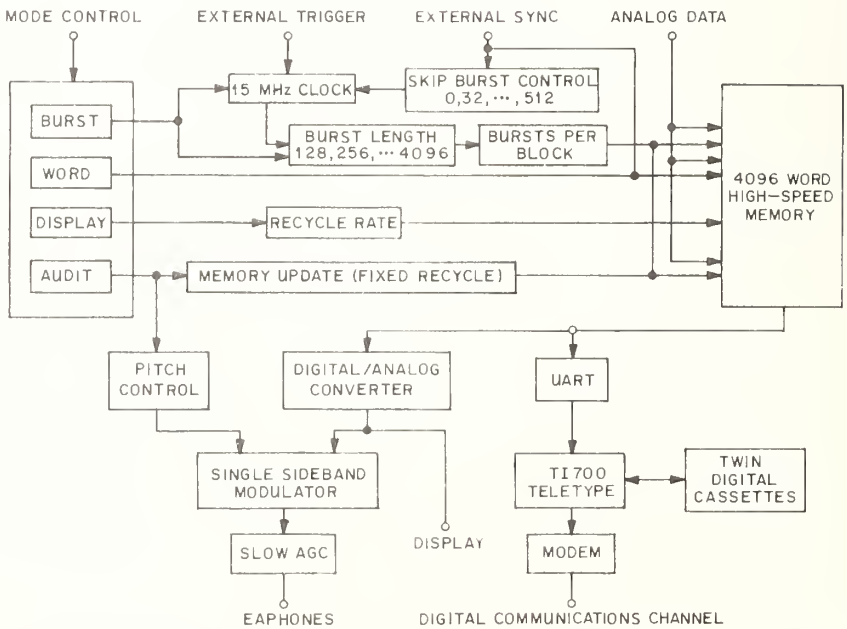

Fig. 1. Block diagram showing the three modes of operation of the Stahl Research Laboratory model 4036 digitizer.

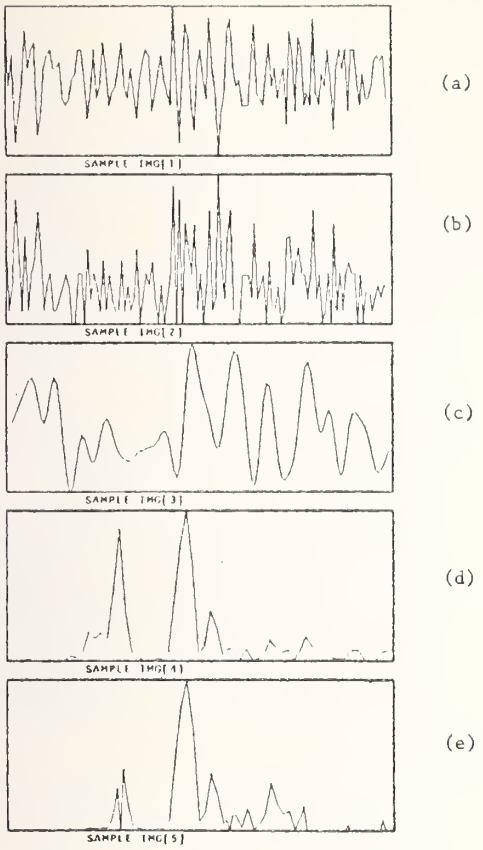

Fig. 3. Five signal regimes for the normal liver: (a) normalized rf waveform; (b) rectified; (c) video; (d) frequency spectrum; (e) deconvolved spectrum. Here time samples are taken each 100 ns with the frequency domain covering 0 to 5 MHz in 0.08 MHz intervals.

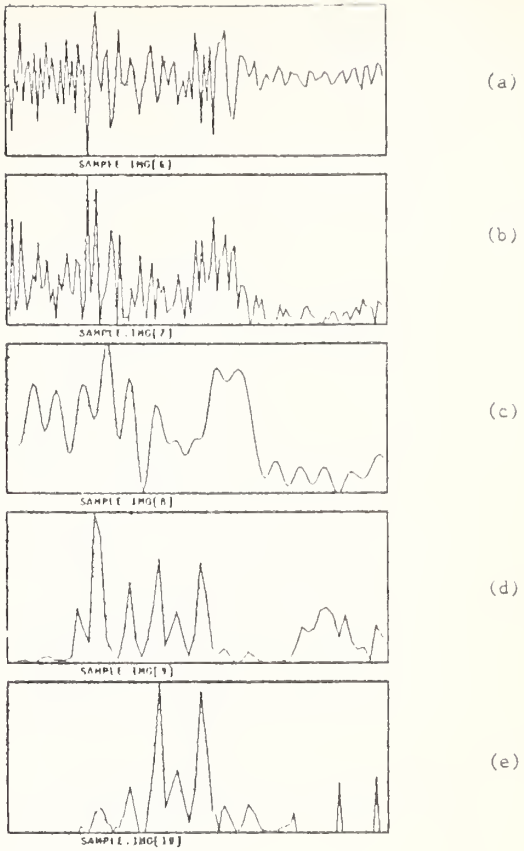

Fig. 4. The five signal regimes in the same order as in figure 7 for the normal kidney.

3. A-Scan Analysis

Five signal regimes (see figs. 3 and 4) are used in the analysis of the waveform: (1) Direct rf waveform, (2) Rectified rf waveform, (3) Video waveform (the rf envelope), (4) The rf Wiener spectrum, (5) The selectively deconvolved rf Wiener spectrum. For regime (5) the frequency spectrum of the transmitted signal is used to normalize the spectrum of the received A-scan, except at those frequencies where the uncertainty in determining the transmitted spectrum is large. Computationally, the selectively deconvolved spectrum $D(\omega)$ is given by

$$D(\omega) = \frac{S_i(\omega)}{S_p(\omega)}\left(\frac{1}{1 + c^2}\right) + S_i(\omega)\left(\frac{c^2}{1 + c^2}\right)$$

where $S_i(\omega)$ is the spectrum of the direct rf signal, $S_p(\omega)$ is the spectrum of the transmitted signal from which the A-scan echoes are produced, and quantity c is the coefficient of variation of the transmitted pulsed (taken over an ensemble of transmitted (pulses). This quantity is in itself a function of the frequency ω.

Figure 5 shows a computer generated graph of four sequential pulse echoes from a phantom consisting of a multiplicity of polyethylene disks immersed in water. This figure shows the graphical plot (above) and (below) a graytone M-scan rendition. The slight shift in pulse position which is evident in the M-scan output is an artifact due to synchronization problems. The pulse consists of about four cycles at the resonant frequency of the transducer and is, therefore, about one microsecond in duration. Figure 6 shows the Wiener spectra of the same four pulses presented in figure 5.

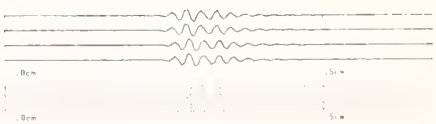

Fig. 5. Digitally produced A-scan plots and M-mode graphs of pulse-echoes reflected from a plane surface.

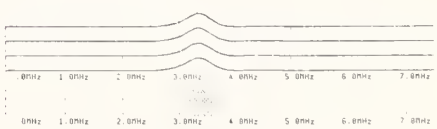

Fig. 6. The frequency spectra corresponding to the pulse-echoes shown in figure 9.

Using a burst length of 128 words, the full memory holds 32 bursts. We are currently employing two settings of skip burst, namely, 0 and 256. At a skip burst setting of 0 the entire recording takes place during 32 pulses which, with the Picker Echoview running at a PRF of 1 kHz, takes 32 milliseconds. The skip burst setting of 256 lengthens the recording interval to 8 seconds. A comparison of recordings taken at the two skip burst settings provides a measure of signal stationarity (see figs. 7 through 14).

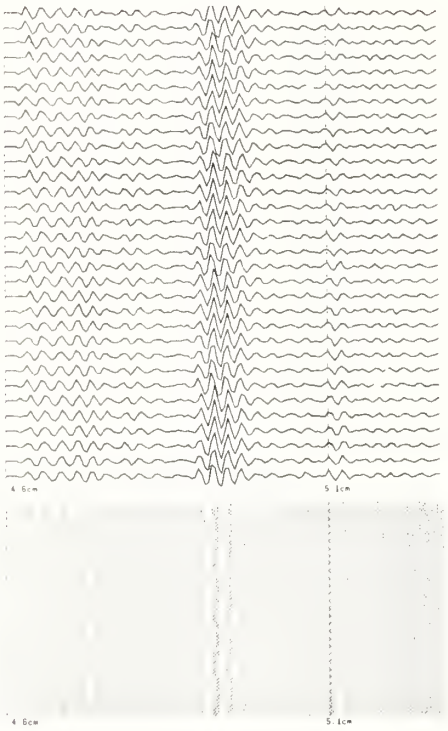

Fig. 7. Thirty-two pulse-echoes obtained from a normal region of the human kidney in vivo. Echo separation is a 0.001 second.

Observation of figures 12 and 14, which were taken at the skip burst 256 setting, indicate that long-term stability of the frequency spectrum does not exist. This observation raises some doubt as to the validity of spectral measurements which have been previously reported in the literature for use in tissue identification. Most researchers using spectral signatures have neither considered nor even discussed short-term versus long-term stability problems. In using the A-scan as a tissue signature, these researchers must remember that all observations in vivo are of a dynamic system. Even with held inspiration, the organ in the patient is moving throughout the cardiac cycle and, in typical clinical ultrasound laboratories using scanners with hand-held transducers, further movement is introduced through the inability of the ultrasonographer to hold the transducer steady.

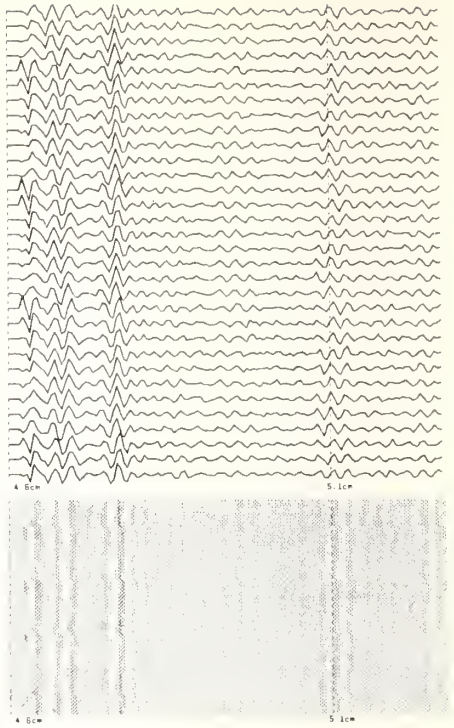

Fig. 8. Thirty-two pulse-echoes obtained from a carcinomic region of the same kidney ensonified in preparing the data shown in figure 11. Pulse-to-pulse separation is 0.001 second.

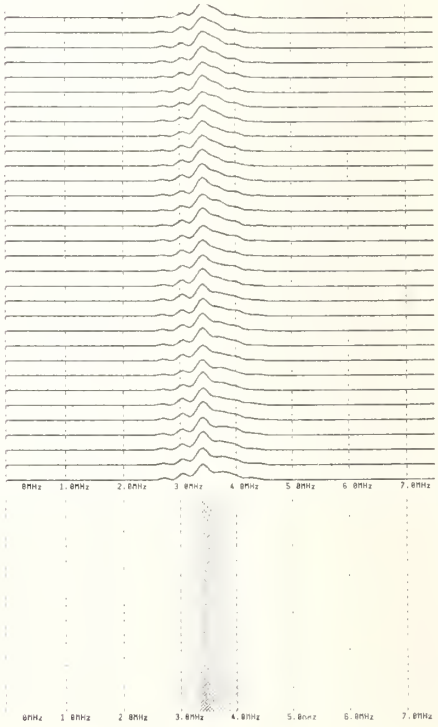

Fig. 9. The thirty-two frequency spectra corresponding to the A-scans shown in figure 11.

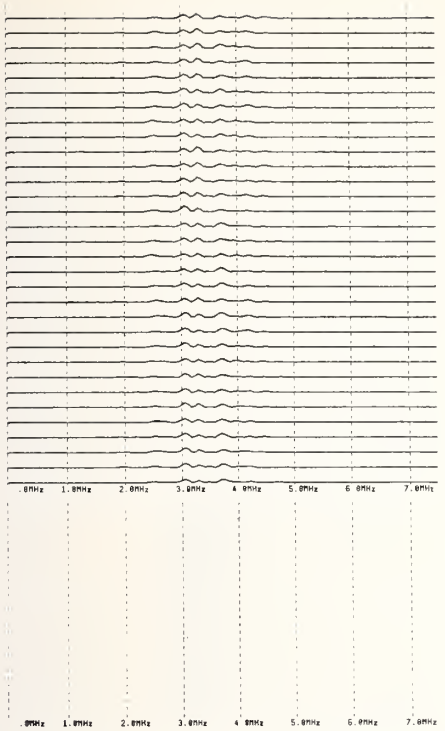

Fig. 10. The thirty-two frequency spectra corresponding to the A-scans shown in figure 12.

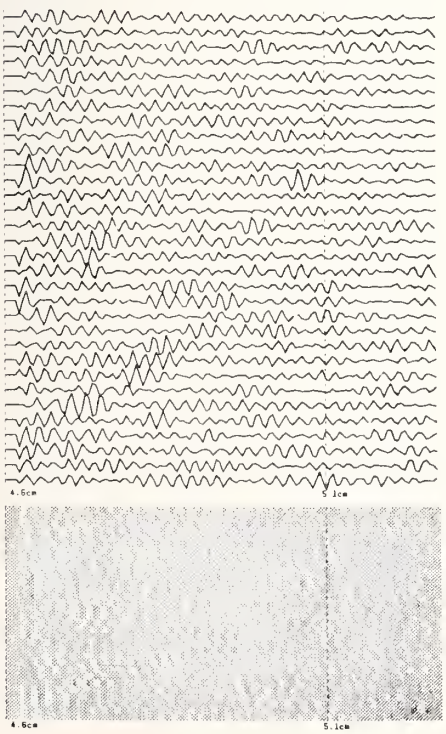

Fig. 11. Thirty-two pulse-echoes obtained on a long-term basis from a normal region of the same kidney ensonified in preparing the data shown in figure 11. Pulse-to-pulse separation is 0.25 second.

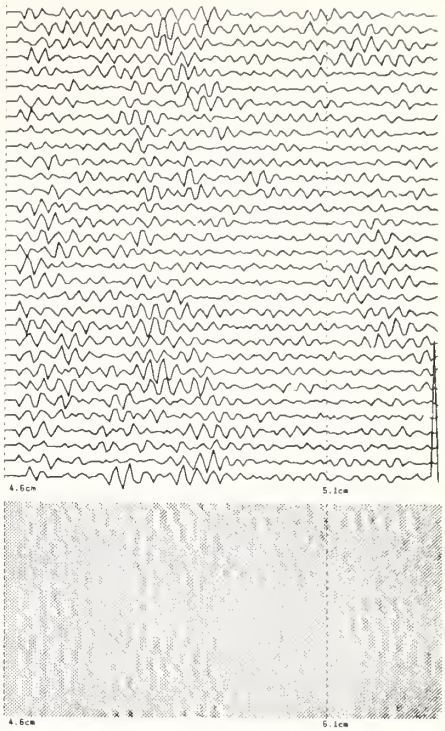

Fig. 12. Thirty-two pulse-echoes obtained from a carcinomic region of the same kidney, again with a pulse-to-pulse separation of 0.25 second.

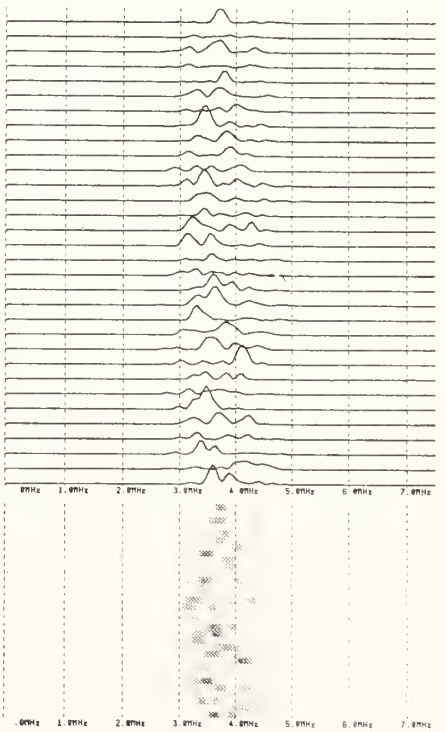

Fig. 13. The thirty-two frequency spectra corresponding to the A-scans shown in figure 16.

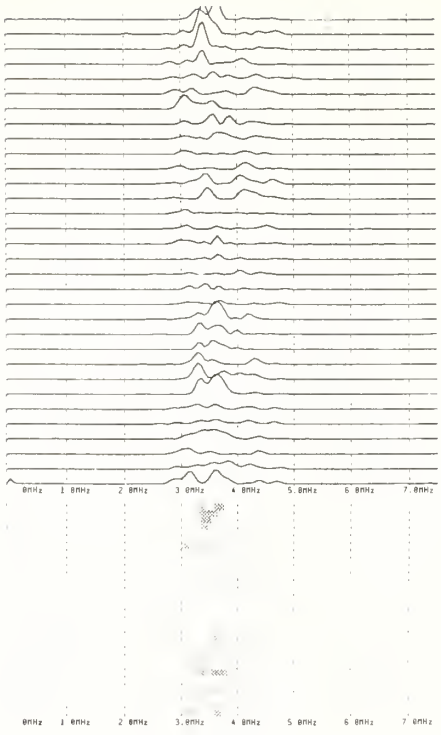

Fig. 14. The thirty-two frequency spectra corresponding to the A-scans shown in figure 16.

4. Data Reduction

In the early 1970s Mountford and Wells [3,8,9] described their work in the quantitative analysis of A-scans taken from normal and cirrhotic livers. Initially their data was obtained from oscilloscope photographs of the rf A-scan obtained from the subcoastal examination of supine patients through the anterior abdominal wall (the same physiological approach taken in our own work). Thirty A-scan oscillograms were recorded per patient over a population of 30 normal and 13 cirrhotics using an ultrasonic frequency of 1.5 MHz (with an unrecorded bandwidth). One hundred data points were recorded for each A-scan over a time-span of 65 microseconds which corresponds to approximately 4.8 centimeters of tissue (digitizations started at approximately 5 centimeters beyond the anterior abdominal wall). Measures were made which related to signal amplitude, the rate of change of signal amplitude, frequencies, rise-times, fall-times, peak-to-peak amplitudes, etc. The most significant of these measures in separating the normal from the cirrhotic liver (using Student's t-test) are tabulated below.

Measure	t-test
Rate of mean amplitude decay	1.28
Mean echo amplitude at intercept	12.38
Mean echo amplitude at mid-point	13.31
Mean trough-to-peak rise-time	4.20
Mean peak-to-trough fall-time	2.39
Mean trough-to-peak amplitude	2.07
Total number of troughs	3.55
Total number of peaks	3.59

As can be seen the most successful measure is the mean echo amplitude at the mid-point of the time-window. The associated t-test value indicates an extremely high success rate in separating normals from cirrhotics over this particular patient population. Other significant measures are the mean rise-time and the total number of peaks and troughs. It is somewhat surprising, since these measures directly relate to the frequency of the signal, that the authors state that "(the) restricted bandwidth of the system used in the present study appears to prejudice the possible use of frequency spectrum analysis as a diagnostic index."

Subsequent to the above-reported experiment the authors modified their experimental approach, discarded photographic recording of the A-scan, and developed equipment for real-time digitization. In their second experiment 100 time-samples were extracted per patient the sampling interval being 0.1 microsecond (corresponding to a tissue span of 2 centimeters). The initiation point of their digitizations was 6.5 centimeters beyond the anterior abdominal wall. Ten normals and three cirrhotics were examined with 180 A-scans recorded in interrupted quiet respiration and an additional 180 A-scans recorded at held maximal inspiration (except for cirrhotics in which recordings were made only at held maximal inspiration). In the second experiment the only measures reported were the rate of mean echo amplitude decay and the mean echo amplitude and intercept. The frequency utilized was 1.67 MHz and it can be inferred from the authors' discussion that the pulse duration was approximately 3 microseconds. The sampling aperture was 12 ns with digitization at 6-bits. Because of the small sample size the t-test was not calculated, but it was found, as before, that the mean echo amplitude at mid-point (for held maximal inspiration) could successfully be used to separate normals from cirrhotics. Interestingly, the data spread in this experiment appears to be far greater than in the initial experiment indicating that the earlier low error rate values may be subject to question. After these first two experiments were conducted, no further investigations apparently have been carried out.

Our own analysis has gone beyond that of Mountford and Wells in that there is equal emphasis on both frequency-domain analysis and time-series analysis. The analysis has been carried out according to traditional statistical lines (see, for example, Wilks [10]). This approach also appears to have been taken by Decker et al. [11] at the University of Bonn, in the analysis of A-scans taken from the eye. In our own work we consider each of the five regimes of our data as a tissue signature and, for each A-scan recording for each subject, make the same statistical measures. The signature is represented as follows:

$$\text{Signature} = f(x_i) \qquad i = 1,\ldots,128$$

The function f may represent any one of the five signal regimes. In other words, it may be either the rf recording, the rectified rf, the envelope of the rf, or the Wiener spectrum or deconvolved Wiener spectrum of the rf.

Measures With Respect to the Argument

Eight measures are made with respect to the argument x. Before making these measures the function is normalized in the following manner:

$$\sum_i f(x_i) = 1$$

This normalization is applied to both time-series and frequency-domain data and can be thought of as a normalization to a standard acoustic pressure for the time-series data and to a standard acoustic power for the frequency-domain data. After normalization summations are carried out over four "bins" of the data points as follows:

$$N^{th}\ \text{Bin} = \sum_{i \in N} f(x_i) \qquad \begin{array}{l} N = 1 : i = 0\text{-}15 \\ N = 2 : i = 16\text{-}31 \\ N = 3 : i = 32\text{-}47 \\ N = 4 : i = 48\text{-}63 \end{array}$$

This produces the first 4 measures for each regime. Next the moments of f are calculated as follows:

$$N^{th}\ \text{Moment} = \sum_i \left(x_i - x_o\right)^N f(x_i) \qquad N = 2,3,4$$

$$x_o = \sum_i x_i f(x_i)$$

The above equations produce 8 measures with respect to the argument x. Next the statistical properties of the values of f are computed. A histogram or probability density function of the values of f is calculated and called $p(y_j)$ where p is the likelihood that f has the value y_j. The probability density function is normalized to 0 mean and unit variance as follows:

$$\sum_j y_j(y_j) = 0 \qquad \sum_j y_j^2 p(y_j) = 1$$

This normalization once again insures that arbitrary settings in acoustic amplification and on received power levels do not effect the results. (Note that, in contradistinction to the experiments by Mountford and Wells, we do not operate a system which has open-loop control on the transmitted and received signal levels but, rather, operate in an arbitrary level mode). Once the function p has been computed, we record its third and fourth moment which, of course, are proportional to the skew and kurtosis of this function, respectively.

Then the co-occurrence matrix or diagram is generated, i.e., $p(y_j,y_k)$ which is the likelihood that two adjacent values of f have precisely the values y_j and y_k. This function is two-dimensional and may be represented using a scatter plot of the values y_j and y_k as is shown in figure 15. As can be seen from figure 15, an ellipse may be fitted to the data from which we compute eigenvectors (the major and minor axes), eigenangle (the angle made to the y_j axis), and the eigenvolume (area of the ellipse).

Finally, the 3-gram is computed. Since there are only 128 values of f, a three-dimensional scattergram is sparsely filled from a statistical point of view so that, rather than fitting a three-dimensional ellipsoid, an 8-bin histogram is computed with the values of f inarized with respect to a threshold equal to the mean value of f so that the bins of the histogram are given by

$$(y_j,y_k,y_\ell) = 000,000,\ldots,111$$

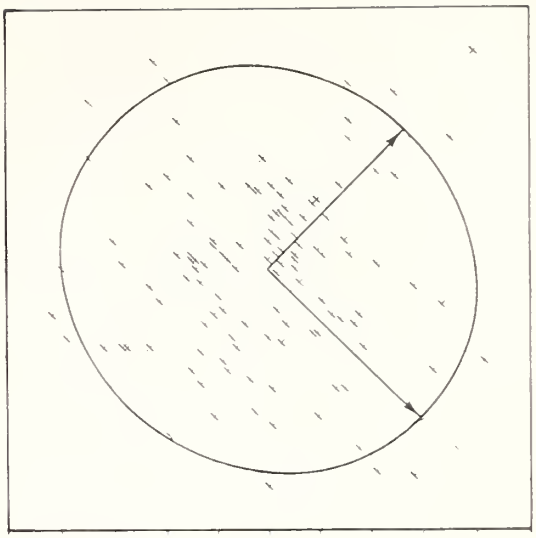

Fig. 15. The di-gram (scatter plot) corresponding to a single A-scan taken from a normal liver using 5-bit digitization over 28 points taken at 100 ns intervals.

The range of this binary 3-gram is then entered as the final measurement. This leads to 8 measures with respect to the argument x, 2 measures related to first order probability, 3 measures related to second order probability, and 1 measure of third order probability. Since all of these measures are computed for each of the five data regimes, a total of 14 measures are made per regime, leading to 70 measurements per A-scan.

5. Biopsy Tissue Image Analysis

As mentioned in Section 1, biopsied tissue is being prepared not only for visual examination but also computer analysis. Using standard 4 μm thick tissue slices stained with hematoxylin-eosin and mounted on microscope slides, the Automatic Light Microscope Scanner (ALMS) at the Jet Propulsion Laboratory produces 512 x 512 pixel (picture point) digitizations of the previously ensonified sample as shown in figures 16 and 17. Each image field is approximately 0.5 millimeter square selected so that a statistically sufficient number of various tissue cell types are displayed. A software system, called AUTOPIC, was written incorporating cellular logic commands for image analysis in the Cartesian tessellation patterned after the hexagonal parallel pattern transforms of Golay [12]. These transforms have been found useful by Preston [13,14] in the analysis of images of human white blood cells, chest x-rays, ophthalmological ultrasonograms, etc. Using AUTOPIC applied to the images shown in figures 16 and 17 normal cell nuclei and inflammatory cell nuclei were located (figs. 18 and 19) using a command sequence which caused the analysis flow-charted in figure 20 to be carried out. Since an increase of inflammatory cells (called "microcytes" in fig. 20) is an indicator of disease, this analysis provides an index of histopathology which may be correlated with the A-scan measures to determine the relevance of these measures in assaying disease entities.

Fig. 16. Computer generated graytone image of a 0.5 x 0.5 mm region in an eosin-hematoxylin stained tissue section from a normal rabbit kidney.

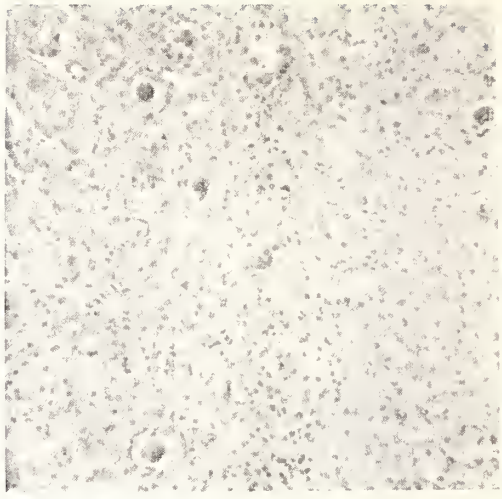

Fig. 17. Graytone image (0.5 x 0.5 mm) of pyelonephritic rabbit kidney tissue.

Fig. 18. Computer analysis of the normal rabbit kidney tissue image shown in figure 16 showing an overlay of white squares and white circles to indicate nuclei classified as microcytes and macrocytes, respectively.

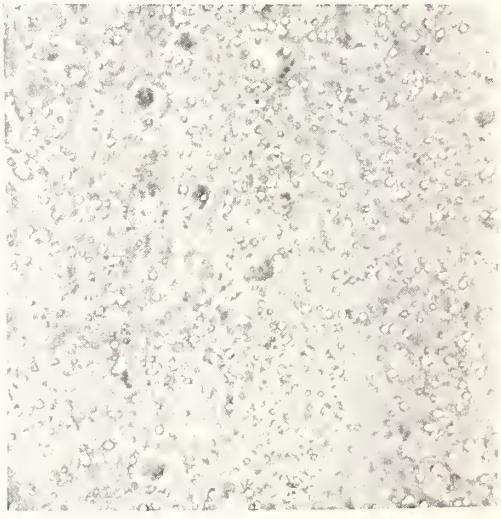

Fig. 19. Computer analysis of the pyelonephritic rabbit kidney tissue image (fig. 17) showing a microcytes and macrocytes as in figure 18.

6. Results

Most of the program to date has been allocated to both the construction and calibration of hardware and to the development of a software system for both the computation and graphical display of the data gathered. In this paper we report on our first human biopsy patient, a female aged 64 years, whose pathology was a large carcinoma of the kidney. By observation of the B-scan the region to be digitized is readily located. Using the equipment described in Section 2, the A-scans given in figures 7 through 14 were recorded.

Thirty-two of these A-scans were of normal kidney tissue and 32 of the carcinoma. Using the short-term data given in figures 7 through 10, all 70 measures were examined for the 64 recordings and the two measures most useful in differentiating normal and pathological tissue were found to be the second moment with respect to the argument x where x was selected in the frequency-domain and the contents of the second bin (or quartile) of the rectified time-

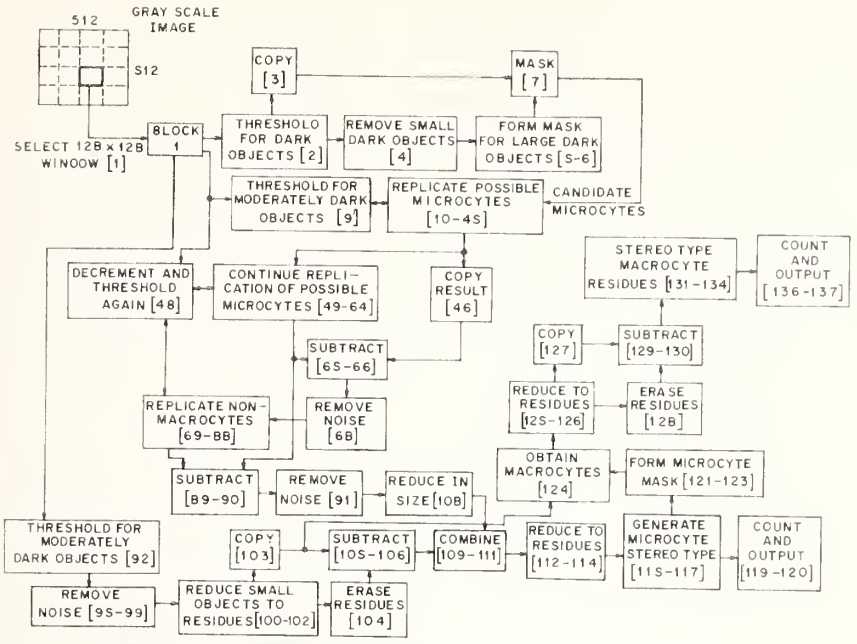

Fig. 20. Block flow chart of the image analysis program carried out in the digital computer analysis of the tissue images shown in figures 16 and 17.

series. Scatter plots of these measures are shown in figure 21 for the 32 A-scans of both the normal kidney and the abnormal kidney under short-term conditions. The Mahalanobis Distance was taken as a measure of separability and indicates a high degree of confidence in telling these two types of tissues apart. However, when the A-scan data taken under long-term conditions (figs. 11 through 14) were utilized, the Mahalanobis Distance indicated somewhat worse differentiation between the two types of tissue (fig. 22) typifying the effects of the dynamic variability of the A-scan.

The other experiment which is reported here involved the introduction of pyelonephritis in the animal kidney and the comparative analysis of A-scan data and histologic data derived from images of biopsies of the ensonified tissue. The animal model selected was the rabbit.

The disease was introduced unilaterally. At the acute stage, four weeks after introduction of the disease, the kidneys (both normal and abnormal) were operatively exposed and 128 A-scans were recorded for each organ via a 6 cm water bath coupler suggested by Dr. Goans of the Oak Ridge National Laboratory. This avoided signal corruption by intervening tissue.

Results of the A-scan analysis (for animal R06) are shown in figure 23, which is a scattergram of the data on 256 A-scans taken in groups of 32 in 8 second intervals over several minutes using the two best computer measures for separating normal from abnormal. The Mahalanobis Distance is 3.2 and the classification success rate is 98 percent. Similar results (100% classification) were obtained for the tissue image analysis (fig. 24) using a single measure, i.e., the count of microcyte density in the four 0.25 x 0.25 mm regions shown in figures 17 and 19. Pictorial and A-scan data taken from six other animals is now being analyzed.

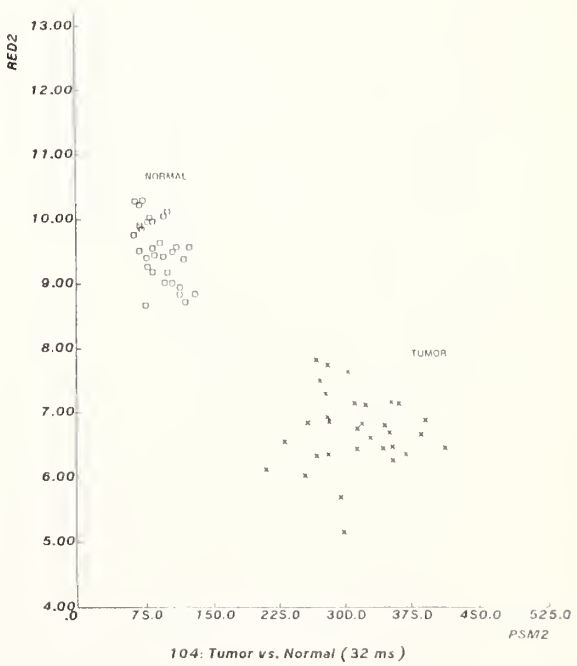

Fig. 21. Scatter plot of 64 points in a 2-coordinate space representing the best measures for differentiating ultrasonic pulse echoes from those received from carcinomic human kidney tissue in vivo. The coordinates are the variance of the power spectrum (PSM2) and the second quartile sum of the rectified waveform (RED2). The plot is derived from the short-term data shown in figures 7-10.

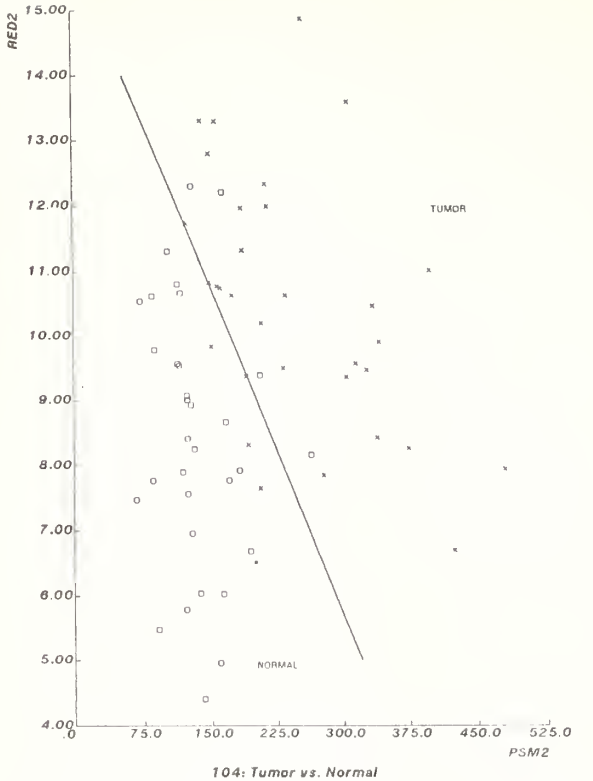

Fig. 22. Scatter plot similar to figure 23 using data extracted from figures 11-14 showing A-scan information gathered in the long-term (8 seconds). Dynamic variance of the data causes the classification success to drop to 87 percent for normal human kidney tissue and to 91 percent for carcinomic human kidney tissue.

Fig. 23. Scatter plot of 256 points using the two measures which were found to be best for distinguishing ultrasonic echoes from normal and pyelonephritic rabbit kidney in vivo. These measures are the fourth moment of the power spectrum (PSD4) and the variance (second moment) of the rectified signal data histogram. Classification success for this long-term data is 100 percent for normal tissue; 93 percent for pyelonephritic.

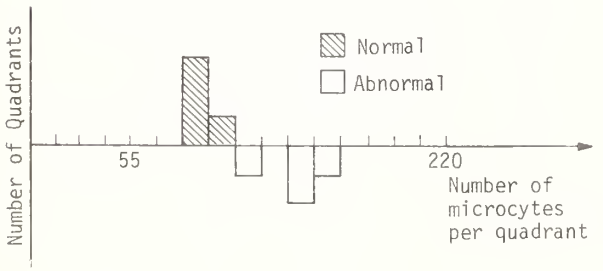

Fig. 24. Histogram based on the microcyte count per quadrant (0.25 x 25 mm) in figures 18 and 19 showing 100 percent success in computerized differentiation between normal and pyelonephritic rabbit kidney tissue images. The microcyte count is indicative of inflammation and is significantly higher in pyelonephritis.

7. Acknowledgements

In addition to the workers and colleagues acknowledged in the text, the authors would like to acknowledge the work of Dr. Niel Wald, Chairman of the Department of Radiation Health, University of Pittsburgh and the staff of his Biomedical Image Processing Group, Jet Propulsion Laboratories for assistance in image analysis and recording; Dr. Donald Eitzen, Ultrasonic Standard Group, National Engineering Laboratory, National Bureau of Standards, and his staff for performing the calibration of our tranducer; Dr. Frank Fry, Ultrasound Research Laboratories, Indianapolis Center for Advanced Research, and his students for calibration of the beam pattern of the transducer and measurements of its performance using phantoms; Drs. Andrew Dekker, Denis Borochovitz, Jeffrey D. Hubbard, University of Pittsburgh Health Center, for visual reading and reporting on tissue section pathology; Dr. Terrance Matzuk, consultant, for providing ultrasound interface electronics; Mr. Gilbert Arnold, Mellon Institute, and his staff for providing the illustrations; Mrs. Tanya Rogers, Department of Electrical Engineering, Carnegie-Mellon University for typing the manuscript.

References

[1] Wild, J. J. and Reid, J. M., Application of echo ranging techniques to the determination of structure of biological tissue, Science 115, 226 (1952).

[2] Fry, E., Okuyama, D., and Fry, F. J., Ultrasonic differentiation of normal liver structure as a function of age and species, Proc. 6th Intern'l. Cong. on Acoustics, Tokyo (1968).

[3] Mountford, R. A. et al., Ultrasonic liver scanning: automatic A-scan analysis, Physics in Medicine and Biology 17, 559-569 (1973).

[4] Ossoinig, K. C., Quantitative echography - the basis of tissue differentiation, J. Clin. Ultrasound 1, 190 (1973).

[5] Fields, S. and Dunn, F., Correlation of echographic visualizability of tissue with biological composition and physiological state, J. Acoust. Soc. Amer. 54, 809 (1973).

[6] Taylor, K. J. W. and Milan, J., Digital A-Scan Analysis in the Diagnosis of Chronic Splenic Enlargement, in Ultrasonic Tissue Characterization, M. Linzer, ed., National Bureau of Standards Special Publication 453, pp. 71-80 (U.S. Government Printing Office, Washington, D.C., 1976).

[7] Preston, K., Jr., Use of Pattern Recognition for Signal Processing in Ultrasonic Histopathology, in Ultrasonic Tissue Characterization, M. Linzer, ed., National Bureau of Standards Special Publication 453, pp. 51-60 (U.S. Government Printing Office, Washington, D.C., 1976).

[8] Mountford, R. A. and Wells, P. N. T., Ultrasonic liver scanning: the quantitative analysis of the normal A-scan, Physics in Medicine and Biology 17, 14-24 (1972a).

[9] Mountford, R. A. and Wells, P. N. T., Ultrasonic liver scanning: the A-scan in cirrhosis, Physics in Medicine and Biology 17, 261-269 (1972b).

[10] Wilks, W., Mathematical Statistics, Wiley (1963).

[11] Decker, D., Epple, E., Leiss, W., and Nagel, M., Digital computer analysis of time-amplitude ultrasonograms from the human eye, J. Clin. Ultrasound 1 (2), 150 (1973).

[12] Golay, M. J. E., Hexagonal parallel pattern transforms, IEEE Trans. Comput. C-18, 733 (1969).

[13] Preston, K., Jr. and Onoe, M., Digital Processing of Biomedical Images, Plenum Press (1976).

[14] Preston, K., Jr., Application of the Golay Transform to Image Analysis, in Digital Image Processing and Analysis, l'Institute de Recherche d'Informatique et d'Automatique, Paris (1976).

CHAPTER 10

TISSUE VIABILITY AND TISSUE PHANTOMS

Reprinted from *Ultrasonic Tissue Characterization II*, M. Linzer, ed., National Bureau of Standards, Spec. Publ. 525 (U.S. Government Printing Office, Washington, D.C., 1979).

DAMAGE AND DEATH IN TISSUES AND ASSOCIATED CHANGES IN THEIR MECHANICAL PROPERTIES

L. Weiss

Roswell Park Memorial Institute
Buffalo, New York 14263, U.S.A.

Mechanical effects of tissue damage associated with artefactual change during examination, and that developing naturally during tumor development, have been demonstrated by a quantitated cell detachment test. Although the precise relationship between this semi-destructive test of tissue properties and ultrasonic, nondestructive tests is uncertain, it appears feasible to consider the following points in studies of the interaction of ultrasound with tissue specimens: a) thin specimens should be examined quickly to avoid anoxic and hypoxic damage; b) note must be made of the heterogeneities within solid tumors, particularly those produced by necrosis; c) degenerative changes in a tumor and surrounding non-malignant tissues may act as image-enhancers.

Key words: Cell detachment; mechanical properties; tissue damage; tissue death.

1. Introduction

The interactions of ultrasound with tissues, depends in a sense on their mechanical properties. In this presentation, two facets of tissue damage will be examined from a mechanical viewpoint. The first is a consideration of the hypoxia which results and its possible artefactual effects, when pieces of tissue are examined. The second is a consideration of the mechanical heterogeneity in and around solid cancers.

The mechanical properties of tissues depend partially on the properties of their individual cells and partially on the properties of the material lying between them, in much the same way as the properties of a brick wall depends on the properties of the bricks, the mortar and the bonds between them. Tissue properties may be measured by nondestructive techniques, such as those involving ultrasound, or by destructive techniques which result in reduction of the tissue into either subcellular dimensions, or into its component living cells. The release of living cells from tissues have been studied, particularly solid cancers, as part of a program on the mechanisms of metastasis [1-3][1]. In this work, quite sensitive quantitative techniques have been developed to measure cell detachment, which is dependent on the strength of the intercellular material. In tissues, the intercellular material represents a modification of the extramembranous, peripheral regions of cells which is rich in glycoproteins.

[1]Figures in brackets indicate literature references at the end of this paper.

2. Cell Detachment from Tissues

Cylinders are punched from tissues using a 13 gauge (~ 2 mm) trocar and cannula, and these are then divided into 1 or 2 mm lengths over a scale, under magnification. Two such cylinders are placed into each of a number of screw-capped, glass vials, 4.5 cm long and 1.3 cm diameter, containing 2 ml of cold Hanks' balanced saline solution. These operations, which take 20 to 30 minutes, are all done in solutions at 4 °C to minimize metabolic differences.

The vials are clamped onto a reciprocating shaker, making 275 oscillations per minute, with an excursion of 4.5 cm, for 40 minutes, at room temperature (25 °C). In some experiments, tissue cylinders were shaken for 10 minutes only. After shaking, 0.25 ml of 10 percent buffered formaldehyde is added to each vial and mixed by gentle inversion. When present, the macroscopic remains of the cylinders rapidly settle to the bottoms of the vials, and the released cells and cell clusters in the supernatant fluid are counted in a Fuchs-Rosenthal chamber, and their diameters measured with an image-splitting eyepiece (Vickers-A.E.I., England) at a final magnification of X300. It has previously been demonstrated that the described formaldehyde-fixation does not affect these two numerical determinations.

An estimate of the volume of tissue liberated by shaking was obtained from the product of the cube of the mean "particle" radius and the mean number of such cell units. Volume functions of this type are used for purposes of comparison.

Small pieces of tissue were fixed in formalin and subsequently examined in 4 μm stained sections. Aliquots of liberated cells are centrifuged onto

slides (Cytospin: Shandon-Elliott, England), and morphologically characterized after reaction with Wright's stain. A full description of the technique and its use is given elsewhere [4].

The cell detachment test described here is non-destructive as far as the component cells of a tissue are concerned, and their viscoelastic properties must play a role in cell detachment. However, assuming that the plane of detachment lies within the cell periphery/intercellular region, then the tests are destructive for this tissue component in the sense that they are essentially concerned with obtaining a "yield-point". In contrast, the ultrasonic techniques discussed here are completely non-destructive. Thus, although the precise relationship of the two techniques is problematical and the results are expected to be somewhat different in general terms it would be expected that changes in tissues detected by one procedure might well be reflected in the other. Proposed work will hopefully clarify this relationship, which at present is simply presented as a working hypothesis.

3. Examination Artefacts

In determining parameters of the interactions of ultrasound with tissues, the tissues themselves are held in a tank of fluid in the ultrasonic beam, for varying periods of time. From many biologically oriented studies, it is well-known that unless the fluid is of physiologic tonicity and pH, and that unless the tissues themselves are well-oxygenated, tissue damage will occur. The relevant question is, how much artefactual alteration will be produced in the ultrasound/tissue interaction by this damage?

From a practical viewpoint, it is unnecessary to investigate the effects of unphysiologic fluids on the interactions, because many solutions are available which maintain optimal conditions of ionic strength and constitution, pH *etc.* [5]. However, one outstanding problem is the possibility of inadequate tissue oxygenation, and the consequences of it. In the case of isolated tissue slices, Warburg [6] showed that their limiting thickness in cm (H) for O_2 consumption, where D is the diffusion coefficient, A is the rate of respiration of the tissue (ml O_2 uptake/ml tissue/minute), and $[O_2]$ is the oxygen concentration in the atmosphere surrounding the tissue, then:

$$H = (8 \cdot D \cdot [O_2]/A)^{\frac{1}{2}} .$$

Thus, in pure oxygen, the maximum thickness of tissue permitting the passive penetration of O_2 to its center is 0.47 mm. In air ($[O_2]$ = 21 percent) the corresponding maximal thickness of tissue is only 0.21 mm. Similar considerations have to be taken into account in determining the depth of fluid covering examined tissues. Studies on the kinetics of gas diffusion in cell culture systems by McLimans *et al.* [7] have demonstrated that as predicted by Fick's Law, the passive diffusion of oxygen through unstirred fluid to actively metabolizing tissues is very sensitive to the depth of fluid, and that in the case of isolated liver cells covered by only 1.6 mm of physiologic saline, the total initial equilibrated concentration of oxygen will be exhausted in only 1280 seconds, normal biologic syntheses will be impaired and, if left under these conditions, the cells will die.

In order to get a feeling for tissue-oxygenation under the conditions in which ultrasonic tissue characterization experiments will be made, freshly isolated cylinders of rat liver 1 cm in diameter and 0.5 cm in length, were obtained from exsanguinated rats. These were then placed in a beaker containing 100 ml Hanks' balanced saline solution, a commonly used mammalian "physiologic" solution, buffered at pH 7.2, and maintained at 37 °C. The pO_2 was measured at various depths in the liver cylinder determined with a micrometer, with oxygen ultramicroelectrodes having a tip diameter of 15 µm. The electrode has been described elsewhere [8]. It was shown that in the five minutes required to start measurements after removal of the liver cylinders, the oxygen tensions at depths of 1 to 2.5 mm were near zero, and at a depth of 0.5 mm, they were approximately 60 mmHg. These measurements compare with mean values for the liver in the unanesthetized, spontaneously respiring rat of 20 to 30 mmHg [9]. Thus, there is good reason for considering the effects of hypoxia in ultrasonic experiments, since in most of these, comparatively thick pieces of tissues are used.

It has been shown that lysosomal changes in rat hepatic parenchymal cells are induced by subjecting animals to hypoxia [10]. It has also been shown that activation of lysosomes with release of lysosomal enzymes into the tissues can cause massive tissue degradation [11] within hours, and changes detectable by cell detachment tests on cellular monolayers, within 2 minutes [12].

In order to determine if the treatment of the 1 cm diameter cylinders leading to anoxia or hypoxia resulted in analogous changes, shaking-tests of the type described earlier were made on this material. After incubation in Hanks' solution at 37 °C for periods up to 2 hours, plugs were cut from the 1 cm cylinders, and the volumes of cells released at the different times, from the outermost 1 mm regions near to the cut surface and the innermost 2 mm thick regions at the center of the 5 mm thick cylinder were compared. The results shown in table 1 indicate that greater ($.02 > p > .01$) volumes of parenchymal cells are released from the inner anoxic region at the center of liver cylinders than from the outer parts. During the experiments, detectable amounts of protein and acid phosphatase (a lysosomal hydrolase) are released into the medium, but this facet of the experiments needs developing.

It should be noted that examination of standard histologic preparations of the liver revealed no clear-cut evidence of damage after 2 hours incubation, and would not have permitted predictions of the detachment experiments. It is of interest that Hueter, in experiments cited by Dunn [13] was unable to detect changes in the ultrasonic absorption coefficient of liver, measured over the range of 1 to 6 MHz, until 9 hours after death, when it progressively decreased. It is difficult to compare these experiments with those reported here, since Hueter's were made at 25 °C (c.f. 37°) and the tissue was maintained at 10 °C between measurements, and it is well-known that reduction in temperature retards post-mortem change. Future work will hopefully clarify the correlation between changes detected by the shaking test and ultrasound.

If degenerative, autolytic changes due to lysosomal mobilization prove to be an inconvenience

Table 1. Release of liver parenchymal cells.

Incubation time (minutes)	Sites	Numbers of cells released (x1000) ± SE (n)	Unit diameters (μm) ± SE (n)	Comparative volumes released Inner : Outer
		Experiment 1		
30	Inner	57 ± 7.3 (13)	10.5 ± 0.14 (161)	1 : 1.8
30	Outer	37 ± 4.9 (16)	10.0 ± 0.13 (110)	
60	Inner	20 ± 3.5 (14)	10.0 ± 0.15 (131)	1 : 1.4
60	Outer	15 ± 1.5 (13)	9.9 ± 0.13 (107)	
120	Inner	16 ± 0.7 (8)	10.5 ± 0.39 (100)	1 : 1.5
120	Outer	12 ± 1.9 (12)	10.0 ± 0.27 (105)	
		Experiment 2		
30	Inner	16 ± 2.8 (8)	10.0 ± 0.11 (102)	1 : 1.9
30	Outer	10 ± 2.7 (9)	9.5 ± 0.11 (94)	
60	Inner	15 ± 4.0 (6)	9.6 ± 0.13 (136)	1 : 1.2
60	Outer	13 ± 3.4 (6)	9.4 ± 0.08 (154)	
120	Inner	13 ± 1.9 (9)	9.9 ± 0.09 (111)	1 : 1.5
120	Outer	10 ± 2.4 (8)	9.4 ± 0.12 (98)	

in ultrasonic measurements, it is worthy of note that the analogous changes observed in vitro [11, 12] were inhibited and/or retarded by adding small quantities (c. 10 μg/ml) of hydrocortisone hexisuccinate to the medium.

4. Mechanical Heterogeneity in Tumors

The essence of the successful treatments of cancer is early diagnosis. In the breast for example it can be seen (fig. 1) that depending on the clinical type [14], the probability of metastasis varies considerably with the size of the cancer at the time of diagnosis. In the most malignant (Type A) the slowest rate of increased probability of metastasis, where therapeutic intervention would be most effective, is in lesions of 1 to 7 mm diameter. In the least malignant (Type B), there is an increased probability of metastasis from 22 to 36 percent, as the lesion increases in diameter from 1 to 5 mm. It is therefore pertinent to ask whether changes in or around a cancer as it develops can so modify the mechanical properties of the cancer itself or the surrounding nonmalignant tissues, that the image of the tumor is enhanced and/or changes in the surrounding tissues effectively increase the "lesion" size.

From previous considerations of examination of artefacts, the question arises of whether various tissue interactions caused by, or resulting in degenerative change in a solid cancer could fill this role of "image enhancer". Cell death, or necrosis is a salient feature of many solid cancers. One contributory cause of this is that blood vessels entering or leaving cancers from their peripheries, tend to be occluded by tissue pressures associated with growth, leading to vascular stasis and thrombosis. The inward diffusion of nutrients, and the outward diffusion of metabolic products becomes inadequate, and tissue death results. There are other contributory causes of necrosis in and around tumors; including cell and humorally mediated cytotoxicity associated with inflammatory change, but the end result is the same. In a cancer with

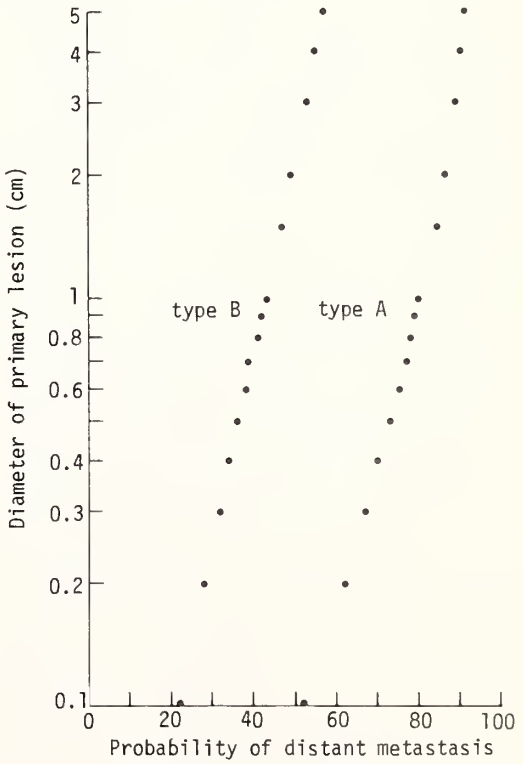

Fig. 1. The probability of distant metastases in breast cancers of types A and B, of different size at the time of diagnosis.

well-developed necrosis, the necrotic material liquefies and the lesion becomes cystic. The different absorptive properties of the liquefied and solid regions lead to image enhancement--as is well-recognized on a macroscopic scale, and represents an example of the heterogeneity of tumors [15].

Much previous work has not taken into account the heterogeneity of normal, and particularly pathologic tissues. This heterogeneity may be due to normal anatomic structures such as large blood vessels, fascial planes etc., or to local pathological situations such as necrosis, cyst formation, cellular inflitrations, tissue edema etc. Very few pathologic lesions consist of a "pure" tissue type, and for this reason average, integrated interaction data collected from a large volume of tissue may be inappropriate for tissue signature studies. In any general consideration of ultrasonic tissue characterization it is mandatory to consider not only the macroscopic or average features of lesions, but also their individual "microscopic" components. By "microscopic", a region of a lesion is implied which has the dimensions of the narrowest ultrasonic beam used for tissue characterization experiments. With this in mind, the mechanical properties of different regions of the same tumor, and the nonmalignant tissues around it have been determined by the cell detachment technique, on Walker 256 "carcinosarcomas" transplanted in livers of rats.

A. Effect of Site Within Tumor

Cystic, subcutaneous Walker 256 tumors were selected, with necrotic centers of approximately 3 cm mean diameter, and with wall thicknesses of 2 to 5 mm of "healthy" cancerous tissue. The release of cells from the inner and outer 1 mm lengths of cylinders taken radially through the cyst walls are shown in table 2. In the two representative examples shown, 3 and 6 times greater volumes of tumor were released from the inner, juxta-necrotic regions of the cyst walls than from their outer parts.

B. Effects of Necrotic Extract on Tumor Cell Release

The subcutaneous tumors from which material was obtained fell into two groups. The first were roughly spherical, with diameters of approximately 1 cm, and contained minimal, friable necrotic cores. The second group, were roughly egg-shaped with diameters of approximately 4 cm and 6 cm in the short and long axes respectively, and were largely necrotic, with healthy cancerous "rims" varying from 2 to 4 mm in depth.

Table 2. Tumor cells released from inner and outer parts of walls of subcutaneous cystic Walker 256 tumors.

"Cell"-release (X 1000) ± SE (n)		Mean size µm ± SE (n)		Volume ratio
Inner 1 mm	Outer 1 mm	Inner 1 mm	Outer 1 mm	Inner/Outer
202 ± 65 (9)	77 ± 12 (9)	77 ± 3.5 (99)	74 ± 3.1 (99)	3:1
90 ± 26 (9)	36 ± 8.2 (10)	110 ± 3.3 (100)	83 ± 3.5 (100)	6:1

Cylinders obtained from the peripheral regions of the tumors were first incubated with 1/10 dilutions of necrotic extracts in HBSS for 20 minutes at 37 °C and then shaken for 10 minutes at room temperature (24 °C). The representative results of 6 separate experiments with 3 separate batches of necrotic extract are summarized in table 3. In the case of the 1 cm diameter tumors, 8 to 11 times greater volume of tumor was released after exposure to necrotic material than in the appropriate controls. In the case of the largely necrotic tumors, it is seen that pretreatment with necrotic extract produced no significant increase in the volume of tumor released by shaking, compared with controls.

C. Effects of Tumor on Surrounding "Normal" Tissues

Following the direct injection of Walker ascites cells (10^7 cells in 0.2 ml HBSS) into the liver, tumors of approximately 1 cm diameter grew within 10 days. The tumors and the surrounding liver were bisected, and cylinders of liver were removed at its junction with the tumor, and at 0.5 and 1.0 cm from this interface. The results of 10 separate experiments, together with release data from 2 normal livers are given in table 4. It is shown that a greater volume of parenchymal cells are released from tumor-bearing than normal livers. In addition the closer the normal liver samples are to the tumor interface, the more readily are cells detached from them.

Table 3. Tumor cylinders incubated with necrotic extract for 20 minutes at 37 °C; then shaken for 10 minutes.

Tumors	Experimental (E)		Control (C)		Volume ratio E:C
	Numbers released (X 1000) ± SE (n)	Clump diameter (µm) ± SE (n)	Numbers released (X 1000) ± SE (n)	Clump diameter (µm) ± SE (n)	
c. 1 cm	171 ± 56 (17)	57 ± 2.0 (100)	245 ± 16 (17)	23 ± 0.3 (100)	10:1
> 4 cm	376 ± 56 (10)	23 ± 1.0 (199)	477 ± 61 (10)	21 ± 0.6 (197)	1.0:1

Table 4. Release of "normal" liver parenchymal cells surrounding tumors as function of distance from tumor interface.

Distance from tumor edge	Numbers released (X 1000) ± SE (n)	Clump size (μm) ± SE (n)	Volume ratio (cf. normal)
0 cm	324 ± 16 (65)	42 ± 0.6 (510)	4.1:1
0.5 cm	256 ± 20 (36)	43 ± 0.6 (306)	3.7:1
1.0 cm	224 ± 17 (19)	38 ± 0.5 (204)	2.3:1
Normal liver	350 ± 16 (84)	25 ± 0.2 (400)	1.0

D. Effects of Necrotic Extract on Liver Cell Release

Standard tissue cylinders were obtained from the livers of normal rats. These were incubated for 20 minutes at 37 °C, in either 10 percent necrotic extract in HBSS, or in BSA control solutions. The cylinders were shaken for either 10 or 40 minutes. Representative results of 4 separate experiments given in table 5 show that after 10 minutes shaking, 3 times greater volume of cells were released from liver cylinders pretreated with necrotic extract than from the control series; after 40 minutes shaking, the ratios of extract-treated to controls increased to 50:1.

The results of experiments (A) through (D) show clear-cut differences in the mechanical properties of different parts of the same tumor, and in the tissues surrounding them. The changes appear to be related to the presence and diffusion of necrotic material. If the increased detachment patterns is due to liberated lysosomal enzymes in which the necrotic material is rich, then it must be remembered that some of these may be contributed by macrophages and polymorphs [16] which are frequently found in association with tumors and necrotic tissues.

5. Conclusions

If these results, based on cell detachment, are indicative of changes detectable by ultrasound, and studies presently underway will hopefully clarify this, then three positive suggestions come from this work:

A. Attention must be given to the microenvironmental conditions under which specimens are maintained while being examined, and the time spent on examination must be minimized.

B. It is not enough to determine the characteristics of whole tumors; individual regions must be characterized and identified at a "microscopic level".

C. Changes consequent to degeneration, occurring in a cancer, and in the nonmalignant tissues surrounding it, may enhance its detection by ultrasound by creating new differentials within these tissues.

Acknowledgments

My thanks are due to Dr. H. Bicher and Mr. L. D'Agostino, Department of Radiotherapy for making measurements of oxygen-tension, and to Ms. J. Holmes, D. Lombardo and Mr. D. Graham for their technical assistance.

This work was partially supported by Grants #PDT-14 from the American Cancer Society Inc. and CA-17609 from the National Institutes of Health.

Table 5. Release of parenchymal cells from normal liver ± necrotic extract.

Time shaken	Experimental (E) Numbers released (X 1000) ± SE (n)	Experimental (E) Clump diameter (μm) ± SE (n)	Controls (C) Numbers released (X 1000) ± SE (n)	Controls (C) Clump diameter (μm) ± SE (n)	Volume ratio E:C
10 m	88 ± 4.4 (10)	31 ± 1.2 (137)	60 ± 3.5 (9)	19 ± 0.9 (127)	3:1
40 m	250 ± 4.9 (10)	51.3 ± 2.9 (100)	40 ± 4.8 (10)	25.6 ± 1.6 (100)	50:1

References

[1] Weiss, L., The Cell Periphery, Metastasis and other Contact Phenomena (N. Holland Press, Amsterdam, 1967).

[2] Weiss, L., ed., Fundamental Aspects of Metastasis (North-Holland/American Elsevier, 1976).

[3] Weiss, L., Cell detachment and metastasis, Gann (1977a) (in press).

[4] Weiss, L., Tumor necrosis and cell detachment, Internat. J. Cancer (1977b) (in press).

[5] Altman, P. L. and Katz, D. D., eds., Cell Biology, p. 61 et seq., F.A.S.E.B., Bethesda, Maryland (1976).

[6] Warburg, O., Über den Stattwechsel der Tumoren (Springer, Berlin, 1956).

[7] McLimans, W. F., Crouse, E. J., Tunnah, K. B., and Moore, G. E., Kinetics of gas

diffusion in mammalian cell culture systems. 1. Experimental, Biotech. Bioeng. 10, 725-740 (1968).

[8] Cater, D. B., Silver, I. A., and Wilson, G. M., Apparatus and technique for the quantitative measurement of oxygen tension in living tissues, Proc. Roy. Soc. Lond. (Series B) 151, 256-276 (1959/1960).

[9] Gornandt, L. and Kessler, M., PO_2 Histograms in Regenerating Liver Tissue, in Oxygen in Tissues, M. Kessler, D. F. Birnley, L. C. Clark, D. W. Lubbers, I. A. Silver, and J. Strauss, eds., p. 288 (Urban & Schwarzenberg, München-Berlin-Wien, 1973).

[10] Ericsson, J. L. E., Mechanism of Cellular Autophagy, in Lysosomes in Biology and Pathology, J. T. Dingle and H. B. Fell, eds., Vol. 2, pp. 345-394 (North-Holland, Amsterdam, 1969).

[11] Fell, H. B. and Weiss, L., The effect of antiserum, alone and with hydrocortisone, on foetal mouse bones in culture, J. Exptl. Med. 121, 551-560 (1965).

[12] Weiss, L., Studies on cellular adhesion in tissue culture. VIII. Some effects of antisera on cell detachment. Exptl. Cell Res. 37, 540-551 (1965).

[13] Dunn, F., Ultrasonic Absorption by Biological Materials, in Ultrasonic Energy, E. Kelly, ed., pp. 51-65 (Univ. of Illinois Press, Urbana, 1965).

[14] Slack, N. H., Blumenson, L. E., and Bross, I. D. J., Therapeutic implications from a mathematical model characterizing the course of breast cancer, Cancer 24, 960-971 (1969).

[15] Blumenson, L. E. (1972) Cited by L. Weiss, Some Patho-biological Considerations of Breast Cancer by Ultrasonic Holography, in Ultrasonic imaging and holography, G. W. Stroke, W. E. Kock, Y. Kikuchi, and J. Tsujinchi, pp. 567-585 (Plenum Press, New York, 1974).

[16] Davies, P. and Allison, A. C., The Secretion of Lysosomal Enzymes, in Lysosomes in Biology and Pathology, J. T. Dingle and R. T. Dean, eds., Vol. 5, pp. 61-98 (North-Holland, Amsterdam, 1976).

Reprinted from *Ultrasonic Tissue Characterization II*, M. Linzer, ed., National Bureau of Standards, Spec. Publ. 525 (U.S. Government Printing Office, Washington, D.C., 1979).

A HUMAN ABDOMINAL TISSUE PHANTOM

P. D. Edmonds, Z. Reyes, D. B. Parkinson

Stanford Research Institute International
Menlo Park, California 94025, U.S.A.

R. A. Filly

University of California Medical Center
San Francisco, California 94122, U.S.A.

H. Busey

Picker Corporation
Northford, Connecticut 06472, U.S.A.

The objective of this work was to determine the feasibility of constructing a phantom that would simulate human abdominal tissues when interrogated by advanced B-scan diagnostic ultrasound equipment operating at 2.25 and 3.5 MHz. Satisfactory results were obtained with gelatin based components having dispersed scatterers and embedded sponge, plastic tubes and rubber bulbs filled with saline solution. Stability of the gelatin was achieved by addition of a stabilizing agent, a preservative and impervious coatings to prevent water evaporation.

Key words: Gelatin; human abdominal tissues; phantom.

In the course of producing and installing ultrasonic diagnostic equipment, a need arises for a phantom object with stable acoustic properties, that will generate displays suitable for optimizing the adjustment of various pre-set equipment levels, particularly in the grey-scale circuitry. The need extends beyond the concerns of a single company because there is a lack of basic standardization in the industry. The general availability of a suitable phantom would improve uniformity of displays obtained with different ultrasonic imaging systems.

This paper describes the evolution of a phantom object intended to simulate many of the ultrasonic properties of human abdominal tissue when imaged by a Picker Echoview System 80L Laminograph. Figure 1 is an abdominal B-scan showing the variety of textures to be simulated.

The design specification called for:

- attenuation coefficient at 2.25 MHz = 1.7 ± 0.1 dB/cm;
- velocity of propagation at 22 °C (72 °F) = 1540 ± 50 m/s;
- simulation of fine and coarse texture of normal and pathological liver, as well as the specular reflection of capsular interfaces and blood vessels, cysts with or without sediment, and abdominal aorta, utilizing the full range of grey levels;
- density = 1.05 ± 0.1 g/cm^3;
- mechanical stability up to 65 °C (150 °F);
- flexible exterior surface permitting limited sector scanning;
- abrasion resistant surface in the presence of mineral oil and aqueous gels.

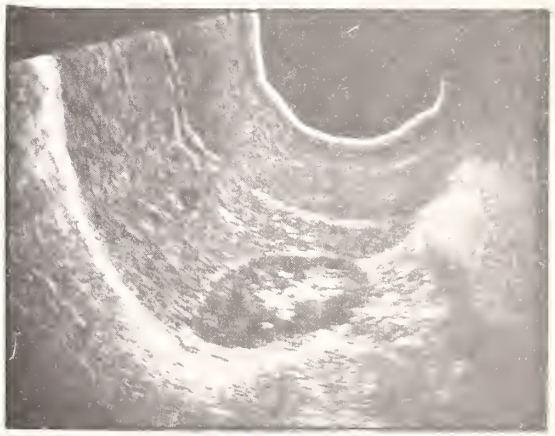

Fig. 1. Human abdominal B-scan showing variety of textures to be simulated.

Less importance was attached to reproducing specific organ geometries or spatial relationships.

Initial work focused on the selection of a base material. Classes of materials considered were room temperature vulcanizing (RTV) silicone rubbers, "ρc" rubbers, gelatin gels, 3M® percussion pads and "Hydron®" polymer. In order to simulate "texture", it would be necessary to incorporate scattering centers in the base material. Hence, some part of the overall attenuation coefficient, A, of an acceptable simulating material would be attributable to scattering and the residual absorption coefficient, α, of the base

material without scattering had to be correspondingly less than the desired overall attenuation coefficient: $\alpha = A - \alpha_s$, where α_s is the attenuation per centimeter due to scattering.

Measured absorption coefficients and propagation velocities of the candidate base materials are given in table 1. The absorption data were obtained by the substitution method and the velocity data by the pulse travel time method [1][1]. The techniques of sample preparation as described in the notes may have influenced the data. It is evident that only RTV 602 and gelatin had sufficiently low absorption coefficients to permit additional attenuation due to scattering without exceeding the specified overall attenuation coefficient. Both these materials had disadvantages. The velocity of RTV compounds is only two thirds of the desired figure. The gelatin is liable to drastic changes of dimensions and properties as water evaporates from the gel.

Table 1. Measured material properties at 2.25 MHz, 22 °C.

Material	Absorption coefficient (dB cm^{-1})	Propagation velocity	Notes
General Electric			
RTV 602	1.34 ± 0.2	980 ± 10	a
RTV 615	2.55 ± 0.3	980 ± 10	b
Goodrich			
#35080 "pc" rubber	2.84 ± 0.11	1546 ± 3	c
3M® percussion pad, style 3290	1.7 ± 0.2	1490 ± 10	d
"Hydron® ", dry	16 ± 2	2050 ± 12	e
"Hydron® ", wet	13 ± 2	1950 ± 12	f
10% gelatin/water	<0.5		g
+ 1% chrome alum	<0.1	1539 ± 10	h
Specification	<1.7 ± 0.1	1540 ± 50	

[a] 0.25% SRC05 catalyst; cured 48 hours at room temperature.

[b] 10% 615B catalyst; cured 48 hours at room temperature.

[c] Sample formed from uncured rubber stock by milling and molding for 45 minutes at 6.6 kg/m^2 and 150 °C.

[d] Measured as received in sheet form.

[e] The sample from Hydron, Inc. (2-hydroxy ethyl methacrylate polymer in water) was dried and then molded at 175 °C under pressure. This produced a hard, brittle, opaque cylinder which was immersed in distilled water to swell and soften. The resultant swelling was irregular. Internal bubbles and interfaces became visible. The attenuation was greater than 10 dB/cm at 2.25 MHz, 22 °C. This sample was then recovered by dissolving in ethanol; the solution was placed in a dessicator in the presence of ethanol and dried over a period of 2 months to yield a translucent 1/8 inch thick disc. The "dry" sample was this disc equilibrated with air.

[f] A portion of the disc was cut and immersed in distilled water for 24 hours. It became opaque white and evidently different from contact lens material. This was the "wet" sample.

[g] Photographic gelatin swollen in water and softened by heating. Diluted to 10% solution in distilled water; 0.1% sodium benzoate added as a preservative. Softening point 25 °C (77 °F).

[h] 1% chrome alum added as a stabilizer. Softening point > 95 °C (203 °F).

[1] Figures in brackets indicate literature references at the end of this paper.

Consideration was given to accepting a base material (such as RTV) with a velocity outside the specified range, and scaling the sizes of phantom components so that the travel times of pulsed signals would correspond to those in the organs being simulated. However, this approach was judged inherently unacceptable and it was anticipated that a base material could be found or formulated with the desired combination of properties. Also the RTV silicone rubber was believed to suffer from long term instability of acoustic properties [2]. In retrospect, it seems probable that the same precautions to combat instability that are described below for gelatin-based compounds would be applicable to RTV silicones in applications where scaling sizes might be acceptable.

Gelatin gels were considered suitable for subsidiary experiments in which various scattering materials were dispersed in the gelatin before molding; the objective was to produce a fine textured image and the specified attenuation coefficient. From both laboratory measurements and imaging, with the controls on the diagnostic equipment set for abdominal imaging, it was found that a 1 percent dispersion of a cellulose fiber or a 0.05 percent dispersion of glass microspheres in 10 percent gelatin in water produced the desired results. The cellulose fiber had an average fiber length of 70 to 140 μm; the glass microspheres ranged from 10 to 250 μm in diameter.

The next objective was to identify materials which, when embedded in gelatin, would simulate the acoustic aspects of abdominal organs. Trial and evaluation led to a selection of materials each of which was embedded separately in a gelatin block containing scatterers. These blocks could then be stacked in various sequences and coupled with mineral oil for trial imaging.

Figure 2 illustrates the various inclusions imaged at 3.5 MHz. The top block contains the base scattering material consisting of 1 percent cellulose fiber in 10 percent gelatin in water. A gelatin filled natural sponge is placed near the left edge.

The middle layer contains a soft rubber bulb filled with saline solution to simulate a large cyst or fluid filled organ. The bright spot in the center of the bulb is an artifact caused apparently by a focusing action. The right side of the center layer contains a natural sponge filled with the gelatin containing scatterers, which might be used to simulate metastatic liver disease.

The lowest level contains a variety of tubing. The parallel lines display the 1/8 inch wall of a soft rubber tube filled with clear gelatin. The upper wall is seen near the junction between the blocks and the lower wall in the center of the block. This is offered as an example of the resolution available at a depth of 14 cm through

Fig. 2. Phantom components imaged at 3.5 MHz.

the various phantom components. At the lower right, some cross sectional images of tubes compare favorably with normal images of the portal vein or abdominal aorta. The tubes are polyolefine shrink tubing 5/16 inch o.d. with 0.02 inch wall and clear vinyl tubing 7/16 inch diameter with 1/16 inch wall. These phantom components were scanned at both 2.25 MHz and 3.5 MHz with improvements in resolution at the higher frequency corresponding to that found in biological tissue. Figure 3 shows an image at 2.25 MHz with resolution clearly inferior to that of figure 2.

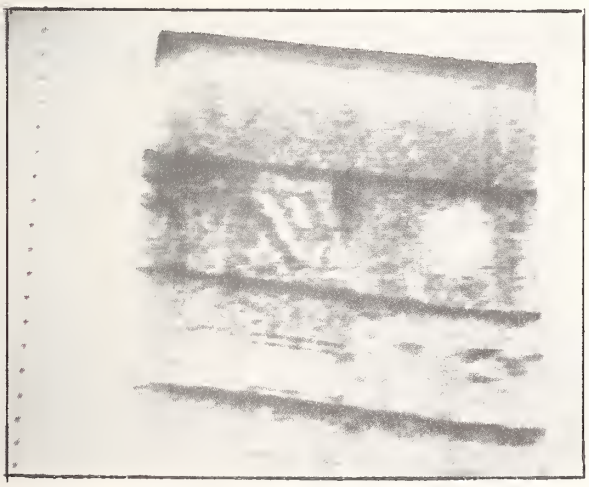

Fig. 3. Phantom components imaged at 2.25 MHz.

The echo discontinuities and interfaces between layers should be eliminated when a continuously molded phantom is produced rather than the individual blocks shown here.

Gelatin gels were originally considered undesirable as the base material because of their obvious instability under heat and evaporation of water and their susceptibility to degradation while nourishing mold organisms. However, the addition of chrome alum as a thermal stabilizer and sodium benzoate as a preservative eliminated two of these undesirable features. The problem of evaporation of water is not so easily solved if it is required that the propagation velocity remain in the range 1540 ± 50 m/s. Two solutions appear possible: a substantial fraction of the water can be replaced by hydrophilic compounds that have at least as high a boiling point as water and preferably higher. Table 2 shows some results of this approach; all the velocities are too high. Alternatively, samples can be coated to prevent the water from evaporating; this approach was undertaken.

Table 2. Velocities at 2.25 MHz, 22 °C.

Composition	Velocity (m/s)
10% gelatin, 89% water 1% chrome alum	1539 ± 10
10% gelatin, 20% water 70% glycerol	1900
10% gelatin, 20% water 67% glycerol, 3% PEG 200	1900
10% gelatin, 45% water 45% PEG 600	1770
10% gelatin, 20% water 60% PEG[a] 200, 10% sorbitol	1749
10% gelatin, 45% water 45% PEG 200	1746
10% gelatin, 45% water 45% DEG	1717
10% gelatin, 20% water 70% DEG[b]	1703
10% gelatin, 30% water 60% carbitol	1644

[a] PEG = Polyethylene glycol
[b] DEG = Diethylene glycol

First the base material was slightly modified by inclusion of 5 percent polyethylene glycol 200 in the formulation, to provide compatibility with the first of five coatings that were applied to the test blocks of gelatin. Then, successive coatings of a butadiene-acrylic rubber, a mixture of this rubber with paraffin, and two coats of a mixture of the same rubber with polyvinyl acetate were applied. By grading the coatings in this manner, good adhesion and acoustic contact between coatings was obtained, while providing the desired properties in succession. The paraffin prevented water evaporation, and the polyvinyl acetate provided the tough flexible exterior surface. Water evaporation through this coated specimen has been reduced to 0.25 percent per day with the specimen open to air. It is expected that a practical phantom would be enclosed in a protective case, within which the humidity can be somewhat controlled as long as a reservoir of water is replenished. Consequently, the problem of water evaporation is considered to be under control, although further improvements in coating formulations are under study.

In conclusion, specific combinations of materials have been identified to make possible the construction of a phantom object to simulate many of the acoustic characteristics of human abdominal tissue. Such a phantom should aid in the standardization of operating conditions of ultrasonic diagnostic equipment.

Acknowledgments

The authors wish to acknowledge the invaluable assistance of William Mullen in performing acoustical measurements, Marie Comas and Irving Illing in preparing test samples, and Linda McKay, Cheryl Wilson and Diane Eskelson in scanning the many test components.

The work reported in this paper was carried out on behalf of the Picker Corporation.

References

[1] McSkimin, H. J., Ultrasonic Methods for Measurement, in Physical Acoustics, W. P. Mason, ed., Vol. IA, pp. 271-334 (Van Nostrand, New York, 1965).

[2] Private communication at WFUMB Workshop, August 1976.

Reprinted from *Ultrasonic Tissue Characterization II*, M. Linzer, ed., National Bureau of Standards, Spec. Publ. 525 (U.S. Government Printing Office, Washington, D.C., 1979).

TISSUE SIMULATORS FOR DIAGNOSTIC ULTRASOUND

Reginald C. Eggleton and James A. Whitcomb

Ultrasound Research Laboratories of
The Indianapolis Center for Advanced Research, Inc.
Indianapolis, Indiana 46202, U.S.A.

Factors are presented related to the design, construction and use of phantoms to replace human patients or subjects in the development, testing, clinical training and promotion of ultrasonic diagnostic equipment. Materials are described which match the acoustic properties of tissue. Realistic echograms can be obtained by scanning properly configured phantoms using such materials.

The phantoms may be simple geometric test patterns, sections of human torso or complete human torsos simulating dynamic cardiovascular and respiratory movements to evaluate the real-time systems.

Key words: Training phantoms; tissue signature; tissue simulators; ultrasonic phantoms.

1. Introduction

Tissue simulators or phantoms, as they are sometimes called, may be utilized in the field of medical ultrasound for purposes of quantitatively and qualitatively evaluating the performance of diagnostic or therapeutic equipment. They may also be used for purposes of training. Yet another application is basic study of the interaction of sound with tissues for purposes of improving existing diagnostic criteria, understanding the mechanisms of acoustic image formation and for devising new diagnostic methods.

The design and construction of realistic ultrasonic phantoms to substitute for human patients or subjects during the early training of technicians and physicians is based upon knowledge from several diverse fields of study. The anatomy of the phantom must be correct with respect to the details visualized by ultrasound. Landmark features used by ultrasonographers to orient and identify the scan planes must be accurately represented. The acoustic properties of biological materials important to the appearance of the image must be catalogued for the tissues that will be represented in the phantoms. A knowledge of materials that can be used in the construction of the phantoms is necessary. It is essential to know how to control various acoustic properties such as attenuation, scattering, speed of sound, impedance, etc. Likewise it is necessary to have a knowledge of the chemistry of the materials to select components which will give the phantoms adequate stability and a useful life.

A knowledge of fabricating techniques required in the construction of the phantoms is also necessary. The methods for casting and welding of phantom materials to obtain the shapes and contours necessary to adequately model the human anatomy are also required. It is also desirable to have the necessary artistic ability to create an aesthetically acceptable model which will have the feel and appearance of the structures it purports to represent.

2. Materials and Methods

Hydrocolloid gels are ideally suited for construction of ultrasound tissue phantoms because of the flexibility and control over acoustic parameters and the stability with respect to time. There are two hydrocolloid systems which are particularly suitable for this application; one which is reversible, and the other irreversible. A combination of the two allows great flexibility in fabricating techniques.

Irreversible Hydrocolloid - Alginic acid was first prepared and analyzed by Stanford in 1886 [1][1] who established it as a weak organic acid that readily forms salts and bases. Nelson and Cretcher [2] hydrolyzed alginic acid to obtain the salt of D-mannuronic acid. X-ray and chemical evidence suggest that alginic acid is a high molecular weight polymer made up of D-mannuronic acid. Several different methods indicate that the commercial sodium alginates have a molecular weight between 3200 and 200,000 and a degree of polymerization from 0.180 to 0.930. Recent evidence has been obtained showing that the polymer molecule is entirely linear, consisting of linked mannuronic acid units and $\alpha\ell(1\rightarrow4)$ linked glutamic acid units [3-5]. Models constructed from x-ray diffraction data indicate that the D-mannuronic acid units are in the C-1 chair configuration, whereas the ℓ-glutamic acid units are in the 1-C configuration [6];

[1]Figures in brackets indicate literature references at the end of this paper.

thus algin is a copolymer and not simply a mixture of mannuronic acid and gluronan.

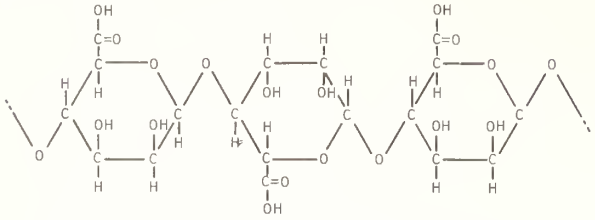

The copolymers are linked together with an alternating composition. The statistical description of the structure of algin is best obtained by assuming that the copolymer is formed according to the penultimate-unit theory of addition copolymerization [7].

Water soluble salts of alginic acid include those of alkaline metals, ammonia and low molecular weight amines. Sodium alginate is the most common salt and is readily available. Solutions can be made in either hot or cold water. Alginates dissolve most easily when sifted into water and vigorously agitated. High speed stirring and gradual addition of solid increases the rate of dissolution. Facilitation of the process can be achieved by wetting the alginate with ethanol or glycerol or other water-miscible liquid before it is added to the water. With a good dispersion the alginate dissolution should be completed in a few minutes.

The properties of alginate solutions can be changed readily to provide either slow, fast or intermediate types of flow [8]. Algin solutions are strongly influenced by covalent ions such as calcium which increase the viscosity and lower the flow properties, with little change in the acoustic properties. Alginates show increasing non-Newtonian flow characteristics with increased degree of polymerization and substitution of calcium for sodium [9], and become thixotropic at low levels of calcium. The effect of this ion in causing increased viscosity is more pronounced in alginates with higher D-mannuronic acid content [10]. The viscosity of sodium alginate solutions can be depressed by using sodium with potassium salts. The high viscosity alginate can attain a viscosity of at least 2000 cps at a concentration of 1 percent in water, whereas a low viscosity product will have a viscosity of less than 10 cps at the same concentration as a function of molecular weight. Algin solutions behave like other fluids in their dependence of viscosity on temperature and may decrease approximately 2.5 percent per °C with increasing temperature. The viscosity of water soluble algin salts changes only slightly as a function of changes in pH, in the range of 4 to 10.

The cross-linking created by the substitution of calcium for sodium renders the alginate insoluble. When the insoluble salt is formed by the reaction of the sodium alginate in solution with a calcium salt, for example, the calcium ion may replace the sodium ions in two adjacent molecules to produce a cross-linking between the two molecules. As the reaction progresses, a cross-linked molecular complex or polymer network forms. Such a network constitutes the micelles structure of the gel. Solutions of sodium alginate are stable for long periods at room temperature but, like other polysaccharides, are depolymerized in the presence of a number of autoxidizable substances such as phenolic compounds. Sodium alginates tend to retard the growth of many microorganisms or are passive with respect to others. Although the algin is resistant to the attack of microorganisms, its solutions are subject to some bacterial action during prolonged storage. Agents such as Zepharin chloride can be added in small quantities to further decrease the bacterial growth. Small amounts of calcium increase the stability of sodium alginate solutions.

Pure algins in water form gels having excellent optical clarity. By altering the formulation, gels can be varied in texture from those which are soft and exhibit flow characteristics to those which are tough and elastic. This range of properties exhibits little effect on the acoustic impedance or acoustic velocity characteristics of the material. As a result, algin gels are ideally suited to tissue simulation in that structures can be molded and the attenuation and scattering properties can be independently controlled.

In general, the gels are formed by the gradual and uniform release of either calcium or hydrogen ions, or a combination of the two throughout the algin solution. The setting time can be controlled by the addition of a limited amount of a compound such as phosphate or polyphosphate that is capable of combining with calcium. Frequently calcium sulphate and a phosphate buffer are combined to control the gelation rate of the alginate solutions.

The acoustic properties of the gel are determined largely by the water. Two percent sodium alginate solution is the usual concentration in combination with small quantities of salts. The acoustic velocity using the phase method [13] is approximately 1550 meters per second at 37 °C; the density of the 2 percent gel is approximately 1.04 grams per cubic centimeter, thus the acoustic impedance falls in the center of the plot of tissue characteristics (see figure 5). The attenuation for the gel without the scatterers incorporated is approximately 0.5 dB cm^{-1} MHz^{-1}.

Reversible Hydrocolloid - An organic hydrophilic colloid of polysaccharide can also be utilized for construction of acoustic test objects. A commonly available form utilizes the sulphuric ester of a linear polymer of galactose. This material undergoes a reversible reaction, sol $\rightleftarrows$ gel, under the influence of temperature changes.

In the gel state the binding forces are secondary forces, e.g., dipole interactions or van der Waals forces. When the concentration of the dispersed phase in the hydrocolloid is of the proper amount, the sol can be changed to a semisolid gel when the temperature is decreased below the critical point ($\sim$ 110°F). The gelation is complete at approximately 100°F. In this process the dispersed phase agglomerates to form chain fibrils, referred to as "micelles." The process continues until a three-dimensional matrix is formed with much branching and intermeshing of the micelles to form a "brush heap" structure. The intermeshing and weak binding forces contribute strength to the structure. The interstices of this structure are filled with water; the water predominantly contributes to the acoustic properties of the gel. It will be noted upon warming that the sol state is again attained but the temperature must be maintained at 120°F for a period of time be-

fore liquefaction is achieved. The temperature lag between gelation and liquefaction is described as a hysteresis phenomenon.

In the gel state the structure exhibits both elastic and viscous properties. If the gel is deformed it requires time to recover. Likewise, if the gel loses water, it will tend to absorb water approaching the initial state. The strength of the gel is decreased at elevated temperatures, but can be substantially increased with the addition of a small amount of borax. The borax accomplishes this by increasing the interaction of the micelle framework. The borax also increases the viscosity in the sol state. The addition of absorbers and scatterers also increases the viscosity, as well as adding to the strength of the gel. A suitable composition would consist of water (83.5 percent), polysaccharide (14.2 percent), potassium sulphate (2 percent) and borax (0.2 percent). The potassium sulphate is introduced to minimize the amount of syneresis as well as imbibition. The introduction of soluble salts into the gel adjusts the osmotic pressure of the dispersion medium and thus helps to stabilize the system. The polysaccharide frequently used is extracted from seaweed and is a linear polymer of galactose, shown below.

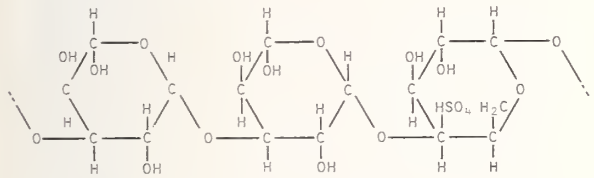

The acoustic properties of the gel with embedded scatterers and absorbers closely match those of tissue. The specific acoustic properties can be adjusted by varying the composition of the gel.

The choice of whether to use the reversible or irreversible hydrocolloid will be dictated by the fabrication requirements. For example, an inclusion within a simulated organ could be constructed from an irreversible hydrocolloid and then later cast in the reversible hydrocolloid so that the temperature of the embedding material would not affect the shape of the inclusion. One obvious advantage of the reversible hydrocolloid during the development phase is that the materials can be re-used, and it is therefore more economical, but once the design has been established, this advantage disappears.

The acoustic properties of the reversible polysaccharide hydrocolloid gels are: density - 1.044 g/cm^3; velocity of sound - 1,540 m/s; attenuation - 0.4 dB cm^{-1} MHz^{-1}. These values are remarkably close to those measured for the irreversible hydrocolloid and for tissue.

Test objects utilizing this material were constructed in which various concentrations of scatterers were incorporated as layers. Because there is no difference in the characteristic acoustic impedance across interfaces, the only reflection produced is due to the scattering (no specular reflection is obtained). Figure 1 shows two test objects developed to display a wide dynamic range of backscattering targets. The relative concentration of scatterers is indicated for each level, and ranges from 0.1 to 100 as marked on the test object.

Silastic Phantoms - A tissue simulator not

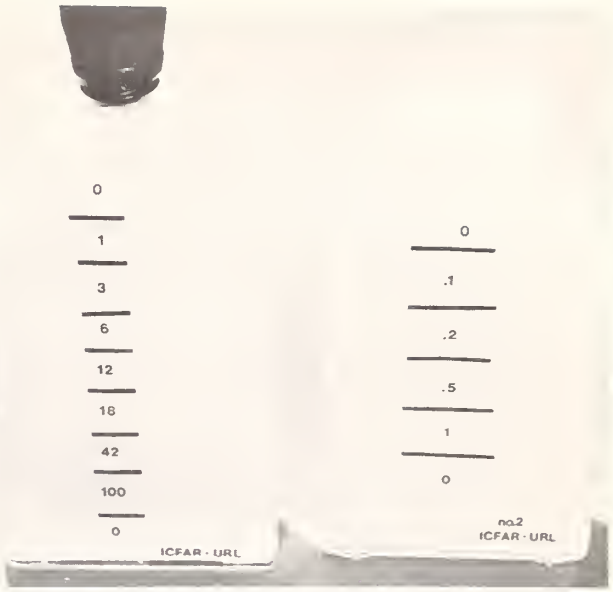

Fig. 1. Scattering test objects are constructed with Dextran spheres dispersed in a reversible hydrocolloid (polysaccharide). The relative concentration ranges from 0.1 to 100 as marked to produce a range of scattering intensities. To scan the test object the transducer is placed against a thin plastic window at the top of the device.

previously described in a publication was submitted to the AIUM Standards Committee in 1970 [12]. This silastic device contained both interfaces of graded reflectivity and scattering sources. The test block was constructed as indicated in figure 2 using silicone rubber (RTV 3110) and a silicone

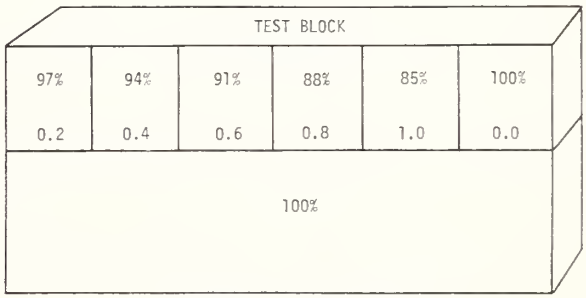

COMPOSITION OF TEST SPECIMEN

Composition of mixture Silicone rubber RTV 3110	Silicone fluid DE200-20cs	Density g/cm^3 ρ	Sound velocity at 37.0 °C m/s × 10^{-3} C	Characteristic impedance rayl × 10^{-5} Z
100 %	0 %	1.129	0.960	1.084
97	3	1.124	0.962	1.082
94	6	1.120	0.964	1.080
91	9	1.115	0.967	1.078
88	12	1.110	0.969	1.076
85	15	1.105	0.971	1.073
	100	0.971	0.975	0.947

Fig. 2. The tissue simulator shown schematically above was constructed using mixtures of silastic and fluid to achieve a range of impedance differences across an interface.

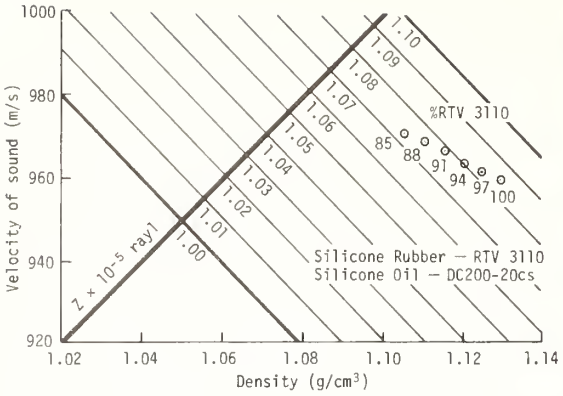

Fig. 3. Materials exhibiting a range of acoustic impedances are achieved by varying the ratio of a two-component plastic system where the individual components have different acoustic properties. In this instance, silicone rubber and silicone fluid are mixed to vary the acoustic impedance over a 1 percent range. These components are then assembled in a test block to provide interfaces of varying reflectivity

fluid (DC200-20CS). This mixture provided a range of acoustic impedances (fig. 3). Suspended in the silicone fluid were particles whose mean diameter was 7 μm. These particles represented a source of acoustic scattering, thus an ultrasound B-mode scan of the test block revealed the interface between silastic blocks of various composition and scattering which occurs in the bulk medium (fig. 4). Panels A, B, C and D show the test block at four gain levels 40, 30, 20 and 10 dB. An adjustment was then made to the visualization system which sacrifices sensitivity for higher longitudinal resolution, better signal-to-noise ratio and dynamic range compression, but displays the weak specular reflectors at the interfaces with good "gray scale" and resolution, but without displaying the scatterers. Panel E shows the effect of optimizing the system response for visualizing the interfaces within the test block. The response curve was adjusted to give an output of 1 volt for an interface with 1.0 percent difference in acoustic impedance (minimum detectable brightness on the display). The echoes from the scatterers then fell below 0.1 volt level. This is an example of the way in which the test object can be used to standardize the equipment performance so as to optimize the display of a particular type of target, organ or condition.

Plastisol Phantoms - Phantoms constructed of plastisol are more suitable for basic studies on the interaction of sound and tissue because of their inherent stability and the precision with which the characteristic acoustic impedance, velocity and density can be controlled to achieve precise acoustic properties. Because of its relatively high attenuation it is not ideally suited for construction of training phantoms where properties and distances of 15 to 20 cm are required.

By using various plasticizers and by adjusting the resin/plasticizer ratio, it is possible to modify the characteristic acoustic impedance of the system throughout the range of soft tissue structures. The acoustic properties of a system

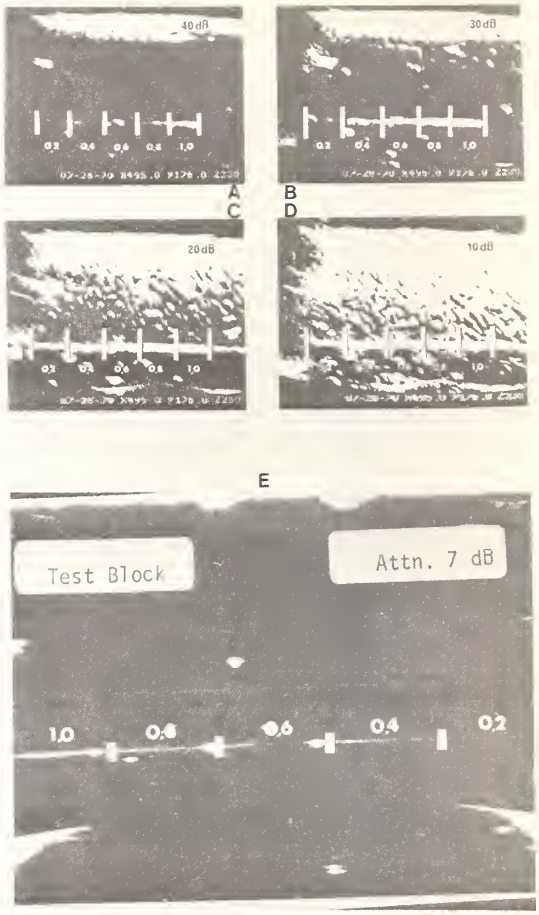

Fig. 4. Ultrasonic scan (at various sensitivities) of test block shows low intensity specular reflections at interfaces and scattering from particles in the bulk material.

using epoxy soya plasticizer are shown in figure 5. Also plotted are a number of tissue characteristics for reference. It will be noted that it is possible to match the impedance, velocity or density of most any tissue and that the other parameters will be nearly equivalent. The attenuation of this plastisol system is higher than tissue and ranges from about 2 dB cm^{-1} MHz^{-1} to 4 dB cm^{-1} MHz^{-1} for the materials shown in figure 6.

Analysis of the frequency characteristics is achieved by making measurements with a range of transducers operating in a pulsed mode. A Fast Fourier Transform (FFT) for displaying the frequency spectrum of the pulse transmitted through the specimen is compared with the spectrum obtained for a pulse transmitted through water [13]. Figure 7 shows the normalized frequency response for both the reference and sample waveforms. Amplitude comparison between the reference and sample transformed responses yields the normalized attenuation as a function of frequency, as shown in figure 8. Additional transducers may be utilized to extend the frequency range. Phase comparisons between the reference and sample responses give the phase velocity, as plotted in figure 9.

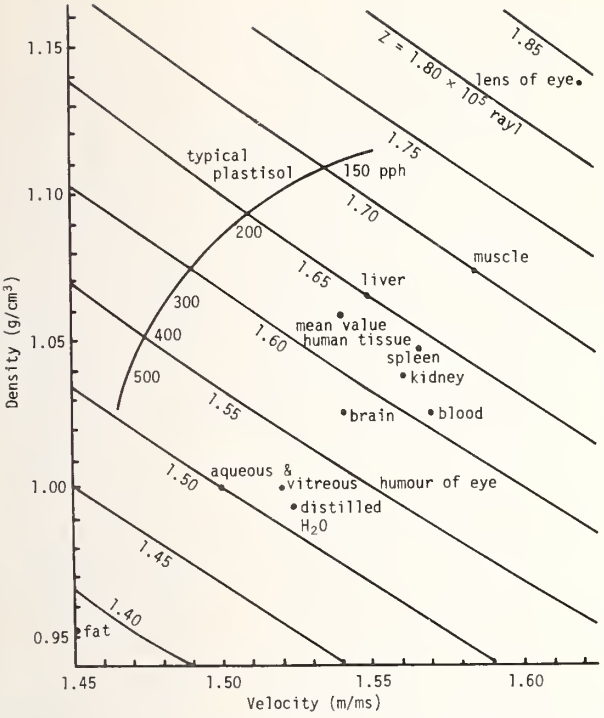

Fig. 5. Acoustic properties of a plastisol system in which the resin/plasticizer ratio is adjusted to match the impedance of biological materials.

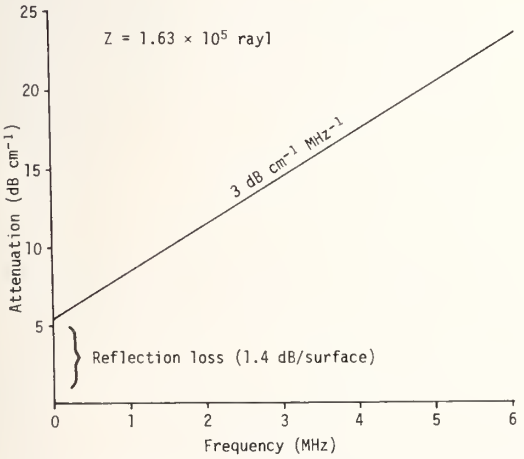

Fig. 6. The normalized attenuation as a function of frequency is shown for two plastisol samples having impedances of 1.52 and 1.63 x 10^5 Rayl respectively. Note that the former closely matches the impedance of water so that the reflection losses at the interface are minimal. In the second specimen, the reflection losses average 1.4 dB per surface. Inasmuch as most normal soft tissue has a much lower attenuation rate than that shown for these two samples, materials of this type would be utilized to represent highly attenuating pathological states such as those commonly found in breast tumors.

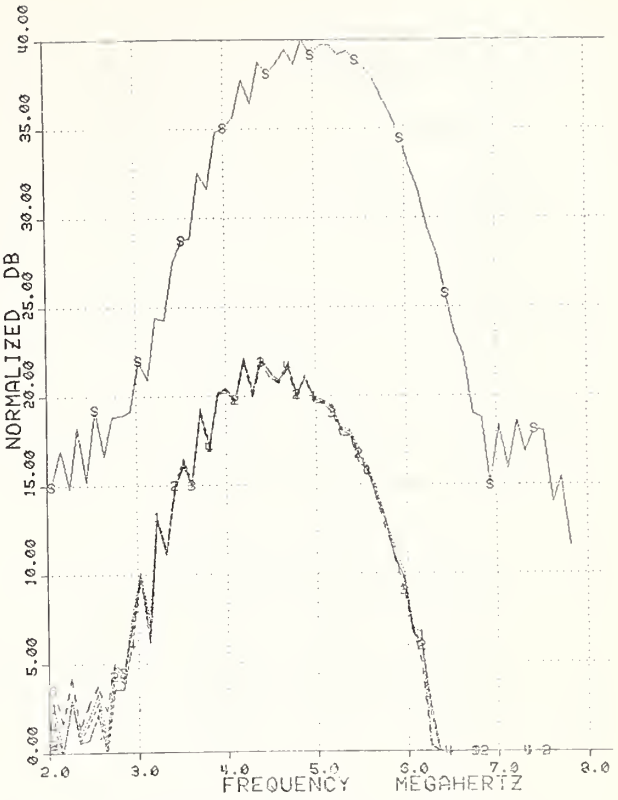

Fig. 7. The method for evaluating tissue simulators includes measurement of the frequency response characteristics of the specimen using a computer-generated Fourier transform of the pulse propagated through the specimen. The S201 sample used here is from the epoxy soya plastisol family having an acoustic impedance of about 1.56 x 10^5 Rayl. The upper curve, "S", is the reference response without the sample. Below it are four sample responses for four closely spaced points on the sample. The signal-to-noise ratio for this run is such that the data in the 3 to 6 MHz range is valid, with the best accuracy assumed around 4.2 MHz, the frequency of maximum sample signal amplitude. The sample and reference responses may be compared both in magnitude and phase. Magnitude comparison yields the sample attenuation (see fig. 8) while phase comparison gives the sample phase velocity (see fig. 9).

Scatterers - The vast majority of echoes obtained by scanning a patient are from scatterers rather than specular reflectors. These scatterers produce echoes which are not individually resolved but add constructively when they are in phase to produce a spot on the display. To duplicate this phenomenon in tissue phantoms, it is necessary to embed small scatterers (like the cells in tissue) whose dimensions are small compared to the wavelength of the sound. Spherical scatterers adequately represent cells whose geometry is essentially spherical, but elongated scatterers are required to represent tissues in which

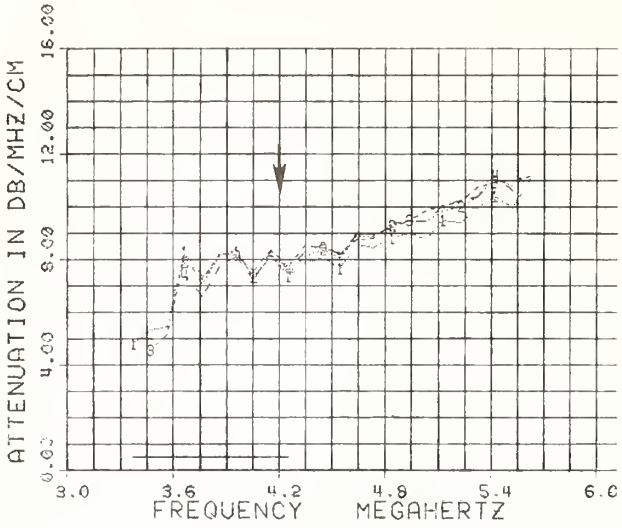

Fig. 8. The attenuation, normalized in the customary manner, for the Fast Fourier Transform responses given in figure 7, is given here. Only data in the assumed valid data range of 3 to 6 MHz is presented; however, the variation in attenuation seen here is still partly due to the low signal amplitudes near 3 and 6 MHz. The solid bar at the bottom of the plot indicates the range of frequencies over which a least squares curve fit was performed on the attenuation (in dB) vs. frequency data. The arrow is on the frequency of maximum amplitude, as described in figure 7.

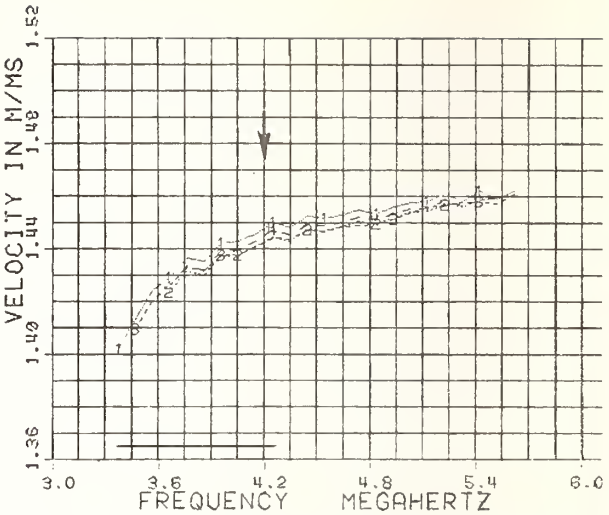

Fig. 9. The phase velocity of the sample examined in figures 7 and 8 is presented here. This phase velocity is defined by the equation

$$C_s = \frac{1}{(1/C_r + d\phi/df)(1/2\pi t)}$$

where C_r is the velocity of the reference medium, t is the thickness through which the acoustic pulse travels in the sample, and $d\phi/df$ is the slope of the phase angle vs. frequency data. This latter value is determined by the least squares technique over the range of frequencies indicated by the solid bar at the bottom of the plot. The arrow is on the frequency of maximum amplitude, as described in figure 7. For comparison, the group velocity, that is, the velocity of the pulse containing all frequencies as shown by the Fourier transform of figure 7, for this sample is 1.558 m/ms.

the cellular makeup is other than spherical, like in muscle, for example.

Small plastic microspheres are available in a variety of material types which can be embedded in the acoustic medium to produce scattering. The particles come in a variety of sizes. In general the particle size should approximate the dimensions of the scatterers of tissue, if the frequency dependence of scattering is important.

One of the common sources is the Dextran particles (Sigma Chemical Company, for example) used in Sephadex columns. This type of particle tends to imbibe water, thus the dimension in the dry state will be different than the dimension in the aqueous medium. Particles can be sized by putting the powder through graded sieves. Waag et al. [14] have used three grades, each of which contains a wide range of sizes. There may be occasions when the range of sizes would be desirable in simulating tissue. It is characteristic of tissues to have rather uniform cellular dimensions.

Grade	Size
G50M	86 - 257 μm
G50F	34 - 137 μm
G50SF	17 - 68 μm

The uniformity of unscreened microspheres compared with screened microspheres is shown in figure 10. A uniform population of microspheres may be used to study the frequency dependence of scattering and will simulate tissues having spherical cells. The range of frequencies for the transition from Rayleigh to Bragg scattering is very broad if the distribution of microspheres as shown in figure 10A is used in a tissue phantom, but is abrupt with scatterers in figure 10B. This point will be further developed later (see fig. 14).

Acrylic microspheres are available as a dental repair material. These microspheres can also be sifted through graded sieves to obtain uniform size distribution. In some instances the more intense scattering provided by the acrylic microspheres is desirable. Further, the dimensional stability is very much greater, therefore, for applications in which dimensional stability is crucial, the acrylic microsphere should be considered.

Another source of microspherical particles is Teflon microspheres, which are similar to the acrylic microspheres in terms of scattering, strength and dimensional stability. Both the Teflon and acrylic microspheres may need to be mixed with a wetting agent, such as alcohol, to promote suspension. Since these spheres are denser than water, they tend to settle out faster than the Dextran.

(A)

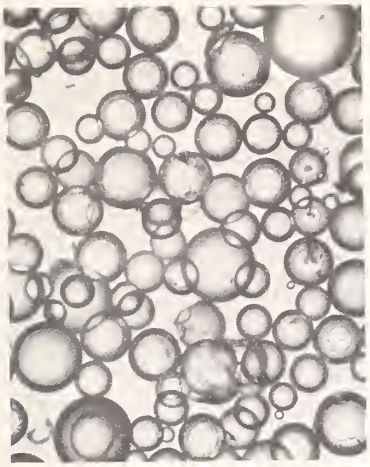

(B)

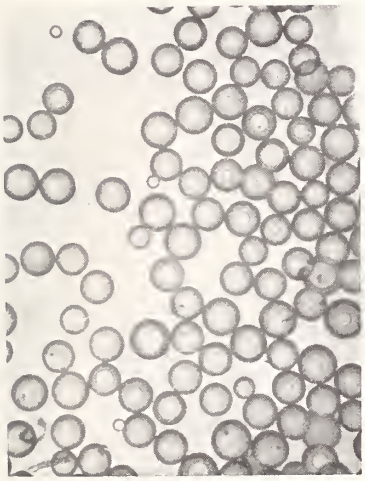

Fig. 10. The Sephadex column packing spheres are useful sources of acoustic scatterers and are available in three size ranges; however, each of the size ranges has a spectrum of scatterer sizes. The photograph on the left shows the distribution of sizes obtained for the medium range. The photograph on the right shows the 20 μm sizes selected by a screening process.

Hollow glass microspheres show the greatest difference in impedance compared with the medium (fig. 11A). The glass microspheres are lower in density than water and tend to float.

Between these four spherical scatterers with their various acoustic properties, it is possible to simulate many different tissue conditions. Scatterers are added to the medium in a concentration of approximately 1 percent per unit volume. For Dextran this gives a backscattering characteristic equivalent to a highly reflecting tissue. In many cases less than 1 percent is adequate to mimic the desired tissue.

The angular dependence of scattering can reveal information on the orientation of asymmetrical scatterers. It is therefore important to include such sources in the test target that are aligned in a specific direction. Targets containing such

(A)

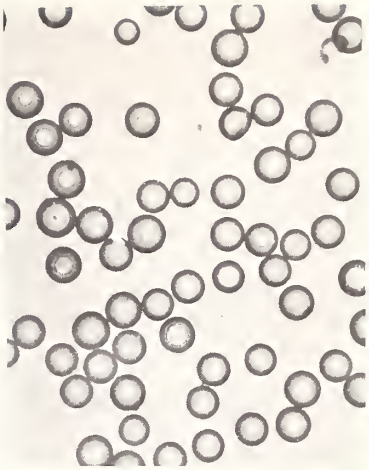

(B)

Fig. 11. Scattering particles consist of cellulose acetate filaments or plastic spheres. The acetate fibers are 5 μm in diameter and 0.1 mm in length, and the spheres shown in the photograph are approximately 10 μm in diameter, but other sizes can readily be obtained by putting the random spheres through screens of the appropriate size mesh. Alignment of the fibers is achieved by flowing the medium prior to curing. The number of scatterers per unit volume, the size of the scatterers, the difference in acoustic index of refraction of the scatterers compared with the embedding medium, the form factor, the diameter/length ratio and the degree of order are all factors which influence the statistical distribution of scattering.

scatterers will exhibit angular dependence of scattering more like that of muscle.

Rod-like scatterers can be obtained by using flocking, which is a cellulose acetate material (see fig. 11B). The flocking is an acetate filament and is available in various size ranges. Alignment of the rods can be achieved by causing the material to flow, then gelling the substrate before diffusion reorients the rods. The rods exhibit an angular dependence of scattering when

they are all aligned in the same direction. Flocking is available in a variety of size ranges, but typical dimensions are 15 micrometers by 1 millimeter.

Attenuators - The attenuation of the hydrocolloid materials is low and comparable to water. The addition of scatterers increases the attenuation, but this may still be below the level needed to simulate many tissues; therefore, it is necessary to add a substance to further increase the attenuation without increasing the scattering properties. A substance to achieve this property would be any insoluble powder whose particle size is very small compared with the wavelength of the examining beam. Numerous powders will fulfill this requirement. Among those used is diatomaceous earth, talcum powder, powdered chalk, graphite, lamp black, etc. We have used diatomaceous earth for this principally because of its availability. The powder is mixed with the scattering spheres and hydrocolloid until the desired attenuation has been achieved. Using this technique the scattering and attenuation can be adjusted independently over some range of acoustic characteristics.

Fabrication Techniques - Organs can readily be molded by using natural organs or models of natural organs. Any of several molding techniques is suitable, including gel molds. The positive replica of the organ is cast in the gel and the mold is partially opened. The replica is extracted by deforming the gel mold.

The surface of the mold may be covered with glycerin or other suitable parting agent and the warm sol solution is poured into the mold. Sprues can be provided to carry away gas as the gas in the mold is displaced by the sol.

If the organ is to represent a kidney, for instance, it would be desirable to cast the organ in several stages to build up a structure which simulates the internal architecture of the kidney. In this case the core is held in place by struts while the cortex is being cast in the mold. Afterwards, the struts are removed and the void is filled with sol, using a syringe. The completed kidney is then encapsulated in a film to minimize evaporation and add stability and convenience of handling. The film can be applied by dipping or by sealing the material with such as a thin polyethylene over the surface of the organ and heat sealing the edges. The very thin polyethylene is easily stretched over the organ and if the procedure is carefully done, it is possible to avoid inclusion of air between the skin and the kidney. The thickness of the skin will determine the specular reflection from the surface of the organ.

Specular reflectors can also be generated by casting smooth interfaces between materials having different acoustic impedances and scatterers are introduced by mixing plastic microspheres or rods in the compound before the heat treating (solvation). The plastic microspheres should be of a size which is very small compared to the wavelength and comparable in dimensions to cells in tissue, i.e., in the order of 10 micrometers in diameter. The material of the microsphere could be chosen so that it will not be affected by the embedding material. In order to avoid introducing gas bubbles into the mixture it is necessary to wet the microspheres with a small quantity of liquid which is miscible with the plasticizer and which does not interfere with its properties, such as alcohol.

3. Classification of Tissue Simulators

As noted in the Introduction there are three major applications for tissue simulators, or phantoms: 1) a training device to be used in place of human subjects; 2) a device for evaluating the performance of ultrasonic visualization systems; and 3) a model for studying the basic interactions between sound and tissue.

Each of the three areas of application imposes design requirements on the construction of tissue simulators. The training device should yield realistic echograms when scanned with conventional diagnostic equipment so that the trainee can learn scanning techniques and the interpretation of echograms. The training device should also be fabricated to include both normal and abnormal anatomy (fig. 12) illustrating the diagnostic criteria. The phantom should contain all of the necessary landmarks and reference points used by ultrasonographers in their diagnostic protocol. The dimensions of the training device should hold a 1:1 correspondence with the dimensions of the structures represented, therefore, the attenuation in the tissue simulator should correspond closely with the attenuation experienced in the corresponding human anatomy.

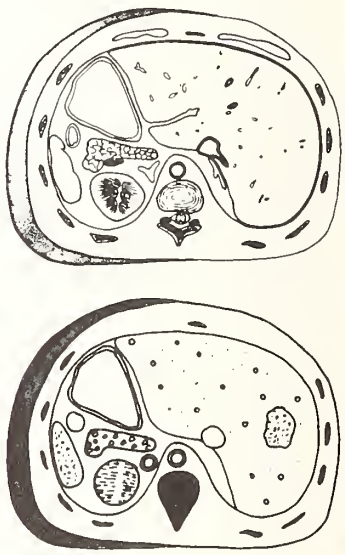

Fig. 12. Simulation of a cross-sectional slice of the human torso which can be scanned with an ultrasonic transducer. The resulting echograms exhibit a 1:1 correspondence to the same section through the human body. The training device would be constructed to show both "normal" anatomy and simulate pathology.

Tissue simulators used to check the performance of ultrasonic diagnostic equipment should include means for examining the sensitivity and resolution (both lateral and longitudinal) of the equipment over the dynamic range of signal intensities encountered in clinical applications (fig. 13). It is desirable that these test objects be stable with respect to time so that instabilities in the diagnostic equipment can be measured. Using the simulator as a standard, equipment adjustments can

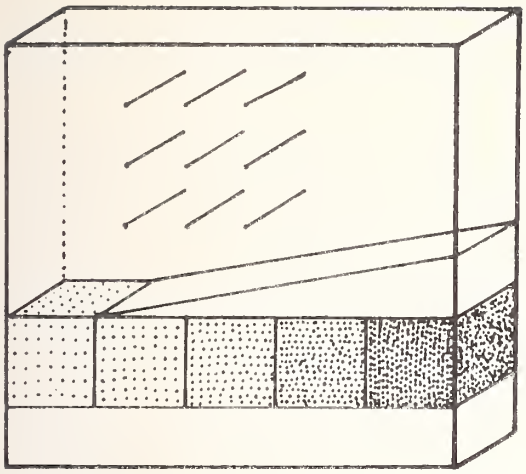

Fig. 13. A test block incorporating low reflectivity specular reflectors, scatterers and wedges for resolution measurements are cast in a plastic block which can be utilized to examine the performance of visualization equipment.

be made to optimize the system performance for displaying certain tissue characteristics, such as was done in optimizing the display of weak scattering interfaces in figure 4, panel E.

Tissue simulators used for basic studies will vary widely in their design as dictated by the experimental conditions under study. We have been using simple disc-shaped test objects of uniform thickness with known scattering densities and impedance characteristics to examine the angular and frequency dependence of scattering in tissue. It is important to control the size of the scatterer. For scatterers which are very small compared to the wavelength of sound, scattering is of the Rayleigh type and has a fourth power cross section. In the range of Bragg scattering, there is a power of two dependence of frequency on the scattering cross section (fig. 14). This plot is an extension of data presented by Freese et al. [15] and nicely illustrates the regions of Rayleigh and Bragg scattering for oil droplets in gelatin and lipid filled cells in fish muscle.

4. Conclusion

Tissue simulators are necessary to meet various requirements with respect to the application of ultrasound to medicine which are not fulfilled by test targets such as the AIUM 100 mm test object. Recently there has been an interest in developing tissue equivalent targets from several sources and this interest stems from both a requirement to provide more quantitative diagnostic methods as well as an interest in reducing unnecessary exposure of patients to ultrasound. Although as yet no toxic effects have been documented for visualization systems used in the customary manner, it is prudent to minimize unnecessary exposure whenever possible. Because it is possible to accurately simulate body structures for ultrasonic scanning, construction of such phantoms would appear to be an important current objective.

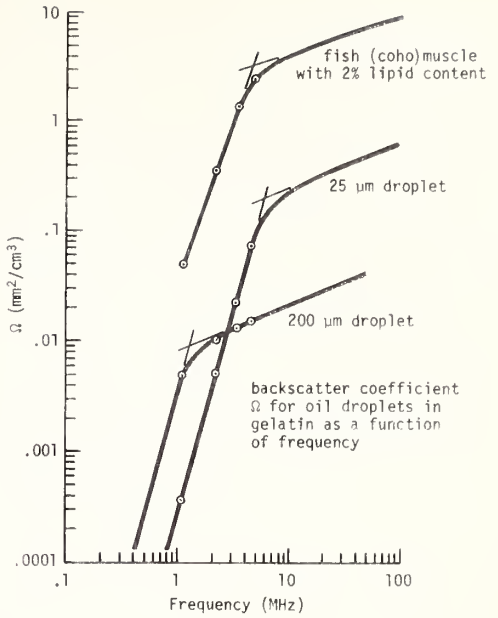

Fig. 14. The plot of the backscatterers' cross section vs. frequency for oil droplets in gelatin and for lipid droplets in muscle display both Rayleigh and Bragg scattering phenomena. The Rayleigh scattering has a fourth power dependence, whereas the Bragg scattering has a second power dependence on frequency.

Acknowledgments

This work was supported in part by NSF Grant APR75-15908, a Smith-Kline Fellowship, and by The Indianapolis Center for Advanced Research. The computer processing technique was developed by Francis J. Fry and Narendra T. Sanghvi.

References

[1] Stanford, E. C. C., J. Soc. Chem. Ind. 5, 218 (1886).

[2] Nelson, W. L. and Cretcher, L. H., J. Amer. Chem. Soc. 51, 1914 (1929).

[3] Atkins, E. D. T., Mackie, W., and Smolko, E. E., Nature 225, 626 (1970).

[4] Atkins, E. D. T., Mackie, W., Parker, K. D., and Smolko, E. E., Polymer Lett. 9, 311 (1971).

[5] Rees, D. A. and Samuel, J. W. B., J. Chem. Soc. C, 2295 (1967).

[6] Larsen, B., Painter, T., Haug, A., and Smidsrød, O., Acta Chem. Scand. 23, 355 (1969).

[7] Painter, T., Smidsrød, O., Larsen, B., and Haug, A., Acta Chem. Scand. 22, 1637 (1968).

[8] McDowell, R. H., J. Soc. Chem. Ind. (London), Monograph No. 24, 19 (1966).

[9] Hirst, E. L., Percival, E., and Wold, J. K., Chem. Ind. (London), 257 (1963).

[10] Smidsrød, O. and Haug, A., Acta Chem. Scand. 19, 329 (1965).

[11] Skinner, E. W. and Phillips, R. W., eds., The Science of Dental Materials, pp. 101-135 (W. B. Saunders Co., Philadelphia, 1967).

[12] Eggleton, R. C., Fabrication of Ultrasonic Test Specimen for Evaluating the Performance of Echo-Ranging Equipment, submitted to AIUM Standards Committee (1970).

[13] Franklin, T. D., Jr., Sanghvi, N. T., Fry, F. J., Egenes, K. M., and Weyman, A. E., Ultrasonic tissue characterization studies of ischemic and infarcted myocardium, presented at 2nd International Symposium on Ultrasonic Tissue Characterization, Session 5; June 13-15, 1977, Gaithersburg, Maryland.

[14] Waag, R. C. et al., personal communication (advanced copy of manuscript).

[15] Freese, M. L. and Hamid, M. A. K., Lipid content determination in whole fish using ultrasonic pulse backscatter, in 1974 Ultrasonics Symposium Proceedings, pp. 69-76, IEEE Cat. No. 74 CH0896-1SU.

Reprinted from *Ultrasonic Tissue Characterization II*, M. Linzer, ed., National Bureau of Standards, Spec. Publ. 525 (U.S. Government Printing Office, Washington, D.C., 1979).

TISSUE EQUIVALENT TEST OBJECTS FOR COMPARISON OF ULTRASOUND TRANSMISSION TOMOGRAPHY BY RECONSTRUCTION WITH PULSE ECHO ULTRASOUND IMAGING

Paul L. Carson and Leonard Shabason

Department of Radiology
University of Colorado Medical Center
Denver, Colorado 80020, U.S.A.

Donald E. Dick

Department of Physical Medicine
University of Colorado Medical Center
Denver, Colorado 80020, U.S.A.

and

William Clayman

Alderson Research Laboratories, Inc.
Stamford, Connecticut 06903, U.S.A.

Tissue equivalent materials have been investigated for evaluation and comparison of pulse echo ultrasound imaging and ultrasound transmission tomography by reconstruction (UTTR). Investigations have centered primarily on various urethane polymers and 3M Reston Brand Flotation Pad material. Attenuation coefficients of the urethane polymers still are somewhat too high, and thus initial test objects or "phantoms" have been constructed from the flotation pad material. One phantom chosen to simulate several characteristics of human breast tissue consists of an annulus of unaltered flotation pad material surrounding a center region in which scattering polystyrene microspheres are embedded. Contrasting material such as polyethylene rods can be inserted between the inner and outer areas of the phantom. The UTTR technique clearly delineates polyethelene rods in the phantom as small as .6 mm in diameter. The scattering at 2.2 to 3.5 MHz nominal frequency exhibits a pulse echo appearance, similar to that of liver tissue, and causes only approximately a 5 percent increase in the attenuation coefficient of the pure flotation pad material.

Key words: Computed tomography-ultrasonic; diagnosis-ultrasonic; tissue equivalent test objects and phantoms; ultrasound imaging; ultrasonic tissue characterization.

1. Introduction

Among the various properties of tissue that can be detected with ultrasound, attenuation and velocity have attracted a great deal of attention. This interest has been intensified by evidence that malignant and benign breast tumors can be distinguished from each other and from normal tissue by significant differences in attenuation of ultrasound by these different tissues [1][1]. The goal of the main project leading to this study has been to develop a system for the quantitative estimation of the spatial distribution of attenuation and velocity coefficients in living tissue. This instrumentation development has been accompanied by the development of various tissue-equivalent test objects or phantoms to help ensure accurate and reliable results.

Simultaneous measurement of velocity and attenuation can be performed with direct approaches to ultrasound computerized tomography (CT), although many questions exist as to the accuracy of these measurements. To study the potential of quantitative and visual diagnosis with the technique, a system for performing ultrasound transmission tomography by reconstruction (UTTR) has been designed and constructed [2]. The attenuation image shown here was obtained with this new instrumentation.

[1]Figures in brackets indicate literature references at the end of this paper.

using principles delineated in reference [3]. Basically, opposed transmitting and receiving transducers are scanned on either side of the imaged object in the translate-rotate motion of early x-ray CT scanners. The amplitude of the rectified and integrated pulse waveform was linearized and used as the input variable in a convolution reconstruction program. The complete UTTR system soon will include the capability for simultaneous generation of pulse-echo images as well as CT scans of velocity, and attenuation. The system has enough flexibility to serve as a general purpose research instrument, but the initial investigations will focus on breast imaging. This emphasis was chosen because of the high incidence of breast cancer in women coupled with the need for more reliable, non-invasive techniques to detect and characterize breast lesions. Another factor is the existence of preliminary encouraging results obtained by others with ultrasound velocity CT images [4].

To provide a controlled comparison of the various imaging approaches, tissue equivalent objects have been developed. This development has followed three approaches which have been pursued concurrently:

1. Development and identification of stable plastics which are equivalent to tissue in terms of physical density, sound propagation velocity, and attenuation as a function of frequency.
2. Simulation of pulse echo scattering using small reflectors embedded in available plastics.
3. Molding the available tissue equivalent plastics and scattering materials into phantoms to allow evaluation and comparison of alternative imaging approaches.

2. Developments

To date, most of the investigation on tissue equivalent plastic has been directed to various urethane polymers such as TDI polyether urethane prepolymer with high molecular weight polyol chain-extenders, and to the 3M Company material used in Reston Flotation Pads. The urethane polymers can be made with densities and ultrasound propagation velocities in the soft tissue range. Shown in figure 1a is an example of attenuation measurements on one of these polymers, which has a density and ultrasound propagation velocity at 27 °C of 1.1 x 10^3 kg/m^3 and 1544 m/s, respectively. Work is progressing on reducing the ultrasound attenuation coefficient in these materials to that of various soft tissues. Advantages of this class of polymer are that the materials are rigid enough to support test objects in known locations, properties can be varied, and the materials are stable in time. The 3M Flotation Pad material exhibits ultrasound interaction characteristics similar to that of fat except for a somewhat higher attenuation coefficient as shown in figure 1b. The amplitude attenuation coefficient in SI units is related to the attenuation coefficient in dB/cm by $\mu(m^{-1}) = 11.513 \cdot \alpha(dB/cm)$. Also, μ/f (s/m) = $1.1513 \times 10^{-5} \cdot \alpha/f$ (dB/cm-MHz). The speed of ultrasound propagation in the flotation pad material at 27 °C is 1461 m/s and its density is 9 x 10^2 kg/m^3. Figure 1 was obtained using broadband transmitters with working frequencies of 2.2 and 4 MHz with diameters of 19 and 13 mm, respectively. A 0.25 mm diameter miniature hydrophone was employed as a receiver in the far field of the transmitter, and attenuation of gated sine waves was measured by interposing and removing samples of the materials under study.

Polystyrene microspheres in the range of 15 to 300 μm in diameter have been embedded in various plastics, and their pulse echo imaging characteristics have been studied in densities of 0.2 to 2.0 spheres per μm^3. At these densities, 80 μm diameter polystyrene microspheres scatter more weakly than normal liver, as determined with commercially available pulse echo imaging systems at 2.2 - 5 MHz. Consequently, polystyrene microspheres of 175 μm diameter, in densities of approximately 0.3 spheres per mm^3, have been chosen for initial simulation of soft tissue scattering.

The phantom designed for comparisons of the various ultrasound imaging techniques is dia-

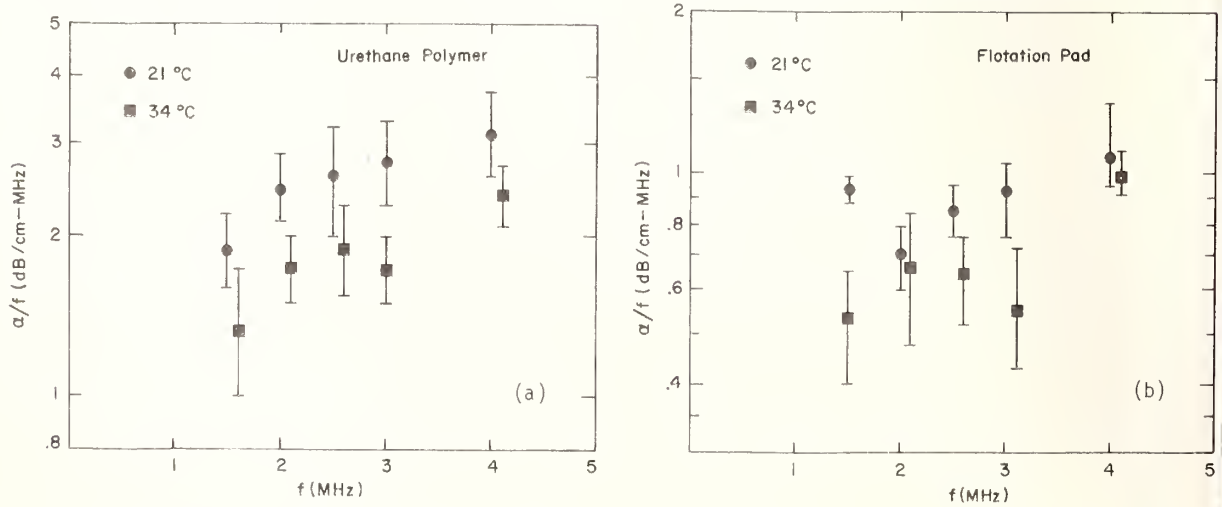

Fig. 1. Semilogarithmic plots of attenuation coefficient as a function of frequency at two temperatures (a) urethane polymer; (b) 3M flotation pad material.

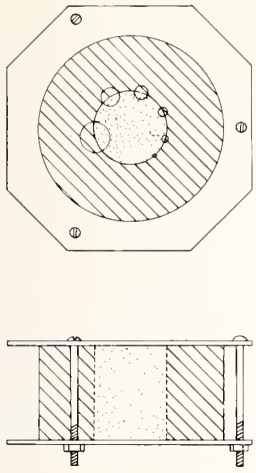

Fig. 2. Top view and side view of the Tissue Equivalent Test Object. The central cylinder contains isotropic scatterers. Rods and tubes may be inserted between the central cylinder and the outer annulus. The three nylon bolts shown in the drawing have been replaced by 0.13 mm diameter nylon monofilament.

grammed in figure 2. An annulus of 10 cm outside diameter consisting of unaltered flotation pad material surrounds a 4 cm diameter of cylinder of the flotation pad material containing the scattering microspheres. This 5 cm thick cylinder is sandwiched between two acrylic plates for geometrical stability. Holes in the acrylic plate located conveniently at the interface between the outer annulus and the central cylinder allow rods and liquid-filled cylinders of various attenuating materials to be inserted between the scattering and nonscattering materials.

3. Examples of Use

Pulse echo images of the phantom obtained with a commercial ultrasound scanner are shown in figure 3. Polyethylene rods of 1.9, 2.7 and 3.3 mm diameter are displayed from left to right at the edge of the inner cylinder. In this image, the polyethylene rods are in the focal zone of the 3.5 MHz transducer and the shadowing of the scattering material by the rods is visualized easily. Figure 4 is an UTTR image of attenuation in the same phantom with rods of 3.3, 2.7, 1.9 and 0.6 mm diameter. As may be seen, each of the four rods was delineated clearly. Phase cancellation at the receiver due to the increased speed of sound in the rods may have contributed to their detectability in both the attenuation image and the pulse echo shadowing of discrete scatterers. The same effect should contribute to the detection of highly attenuating lesions in the body.

Attenuation coefficients for the flotation pad material obtained in this reconstruction are $\alpha = 2.88 \pm 0.01$ dB/cm or $\mu = 33.2 \pm 0.2$ m^{-1}. The quoted errors are the standard error of the mean of several hundred pixels in the reconstructed image. These attenuation coefficients correspond to $\alpha/f = 0.82$ dB/cm-MHz at the 3.5 MHz working frequency employed for the reconstruction. If the frequency averaged attenuation coefficient of $\alpha/f = 0.9$ dB/cm-MHz at 21 °C is accepted from figure 1b as the true value for the flotation pad material, then the effective frequency of the

Fig. 3. Pulse echo image of the tissue equivalent phantom using a conventional scanner with a 3.5 MHz transducer focused at the top side of the central cylinder containing scattering particles. Shadowing of the scatterers by 3.3, 2.7, and 1.9 mm polyethylene rods is apparent.

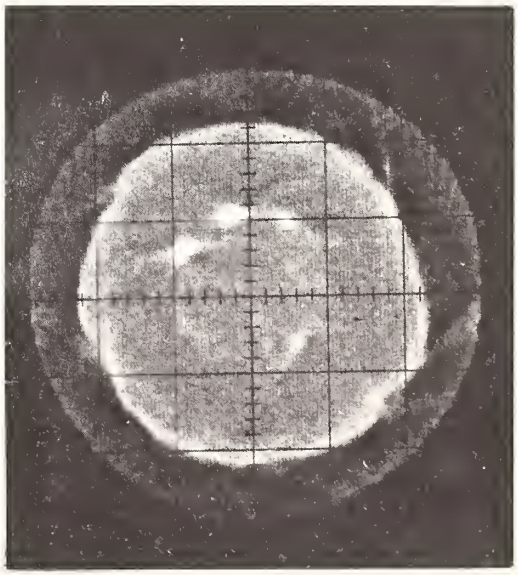

Fig. 4. Attenuation image of the phantom by ultrasound transmission tomography by reconstruction. The polyethylene rods visible in the image range in diameter from 0.6 to 3.3 mm.

broadband ultrasound pulses used to create the UTTR image may be taken to be 3.2 MHz. By comparison, the mean attenuation coefficient of the flotation pad material containing scatterers is 3.02 ± 0.02 dB/cm. This measured value in the central scattering region may be slightly low due to beam hardening effects. Nevertheless, the measured difference in the attenuation coefficient of the material with and without scatterers is only 5 percent, and the real difference probably is not much greater. The greater attenuation in the scattering material is visualized easily in UTTR images displayed at high contrast.

The maximum reconstructed attenuation coefficients at the centers of the 3.3, 2.7, 1.9 and 0.6 mm diameter polyethylene rods are 20, 12, 12 and 6 dB/cm, respectively. Clearly, these apparent attenuation coefficients for the smaller rods are reduced by resolution effects. Bulk measurements of attenuation coefficients of the polyethylene rods were not obtained, because the rods were made by heating and stretching larger, low density polyethylene rods. This process probably would affect the density of the polyethylene, and consequently the ultrasound attenuation coefficient.

Pulse echo imaging of large samples of the flotation pad material containing polystyrene microspheres has indicated that the flotation pad material at 21 °C attenuates ultrasound somewhat more rapidly than normal liver tissue in vivo. It was assumed, therefore, that the flotation pad phantom would be a rigorous test of UTTR and pulse echo systems for breast imaging. Initial measurements on the female breast in vivo, indicate that there are relatively large quantities of tissues in many young, female breasts which are much more attenuating than anticipated. These materials, presumably dense, fibrous tissues, often may be aligned parallel to the skin surface and thus provide a long, attenuating path for transmission imaging in coronal sections of the breast. Attenuation coefficients averaging 15 dB/cm in these highly attenuating tissues have been measured with the 3.5 MHz pulses. It should be noted, however, that much of the attenuation obtained in the UTTR system is due to phase cancellation and refraction at the interface between tissues or phantom materials with relatively low and relatively high speeds of ultrasound propagation.

The breast phantom developed to date will be useful for comparing UTTR and pulse echo imaging under the best conditions, but much more complex phantoms will be required to simulate many important features of normal and abnormal breasts.

Acknowledgments

This investigation was supported in part by grants APR 76-05944 from the National Science Foundation and 5T32 CA 9073 awarded by the National Cancer Institute, Department of Health, Education, and Welfare.

We gratefully acknowledge the contributions of the University of Colorado Medical Center personnel: Will Carter, Tom Oughton, Mary Dick, Elliott Bayly, Gary Thieme, and William R. Hendee, as well as the contributions of Paul E. Hansen, of the 3M Company, who provided sample materials and useful information.

References

[1] Calderon, C., Vilkomerson, D., Mezrich, R., Etzold, K. F., Kingsley, B., and Haskin, M., Differences in the attenuation of ultrasound by normal, benign and malignant breast tissue, J. Clin. Ultras. 4, 249-254 (1976).

[2] Dick, D. E., Bay, H. P., and Carson, P. L., Hardware Design of an Ultrasound CT Scanner, Proceedings, Rocky Mountain Biomedical Engineering Symposium, published April 1977 by the Instrument Society of America.

[3] Carson, P. L., Oughton, T. V., Hendee, W. R., and Ahuja, A. S., Imaging soft tissue through bone with ultrasound transmission tomography by reconstruction, Medical Physics 4, 302-309 (1977).

[4] Greenleaf, J. F., Johnson, S. A., Samayoa, W. F., Duck, F. A., and Wood, E. H., Algebraic Reconstruction of Spatial Distributions of Acoustic Velocities in Tissue from their Time of Flight Profiles, in Acoustical Holography, N. Booth, ed., Vol. 6, pp. 71-90 (Plenum Press, New York, 1975).

APPENDIX

Reprinted from *Ultrasonic Tissue Characterization II*, M. Linzer, ed., National Bureau of Standards, Spec. Publ. 525 (U.S. Government Printing Office, Washington, D.C., 1979).

APPENDIX

DATA OF THE VELOCITY AND ATTENUATION OF ULTRASOUND IN MAMMALIAN TISSUES - A SURVEY

R. J. Parry and R. C. Chivers

Physics Department
University of Surrey
Guildford, England

A compilation of the reported values of velocity and attenuation of ultrasound in mammalian tissues is presented to give a clear picture of the state of knowledge and enable it to be assessed. In the twenty years since the last such compilation, the progress in estimating the relative contributions of the animal species, tissue condition, temperature and frequency at which measurements were made and the method of measurement to the observed variation has been small. It is hoped that this compilation will both be of practical use and also encourage the establishment of a stronger body of fundamental information for the application of ultrasound in medicine and biology.

Key words: Attenuation; mammalian tissues; ultrasound; velocity.

1. Introduction

With the increasingly recognized importance of fundamental work on the interaction of ultrasound with tissue there is a need for ready access to currently available data of the acoustic parameters of mammalian tissues. There are summaries of velocity and attenuation data [1-3][1] but all lack some of the information needed to make a critical assessment of the present state of knowledge. In view of this we have attempted here to produce a survey which is both accurate - not always a feature of previous surveys - and useful in providing such information.

The grouping of the data is primarily by type of tissue and mammalian species and subsequently by tissue condition and temperature. Tissue condition in vitro is categorized as fresh, fixed or refrigerated (though for comparisons to be properly valid more precise details of the history of the tissues must be known).

It is assumed that the measurements were made at sufficiently low intensity such that non-linear effects were not significant. However, only Dussik et al. [4] and Fry and Fry [5] report values for ultrasonic intensity. This may arise from the present state of the literature on the measurement of intensity [6].

The quoted attention coefficient, α, is defined by $A = A_0 e^{-\alpha x}$, where A is the amplitude of a plane wave of initial amplitude A_0 after travelling a distance x in the tissue. Assuming a realistic plane wave, or that any geometrical effect on the amplitude has been removed, this represents the sum of the energy absorbed within the tissue and the energy scattered by inhomogeneities in the tissue [7]. It must also be assumed that the intensities used were low enough for there to be no irreversible changes caused in the tissue and thus that α is not dependent on the intensity. To convert the values quoted to decibels they should be multiplied by 8.686.

The tables include the number of measurements, N, and some indication of the spread of values about the quoted mean: where possible the standard deviation (SD) or standard error (SE) of the set of measurements, otherwise the range of values or some unspecified "variation".

As a guide to what may be expected of the measurements reported, it was thought useful to indicate the measurement technique used. For the velocity measurements these have been divided into pulse transmission or reflection (pulse), interferometric and sing-around techniques and for attenuation into broadband, using pulses containing only a few cycles of vibration, or narrow band, with 20 or more cycles. Results obtained with broadband pulses [10-12] are usually quoted as being at one particular frequency without any detail of how this frequency was selected. For preference the frequency specified should be that of the maximum amplitude in the frequency spectrum of the pulse. Recently the whole frequency spectrum of a broadband pulse has been used to measure attenuation [7,13] and there is the possibility of using swept frequency techniques [60]. Further consideration of measurement methods is out of place in the present context and the reader is referred to the review article by McSkimin [8] and the work of Wehr [9,14] for discussion of the various techniques and the relative errors involved.

[1] Figures in brackets indicate literature references at the end of this paper.

The information collected in the tables below is that relating to whole tissues only. Thus much data on blood is excluded as it is concerned with the constituents rather than whole blood (see Hussey [3] for a summary), and in other reports the "whole blood" is a dilution with plasma of centrifuged red blood cells [57,59]. Nor was it felt appropriate to include all the data from isolated references on the variation of parameters with other features of the tissues, for example the variation of velocity in fat with water content [15,16] and the work on liver homogenates [17,18]. For such information the reader is referred to the original literature.

Summary

The result of a survey such as this should perhaps be some set of values of parameters or curves that may be taken to be characteristic of the various tissues considered. However, considering the data presented here, all that may be concluded is that at the present time it is virtually impossible to separate any variation between different types of tissue from those variations due to the many other factors involved, such as the measurement technique, temperature, condition and treatment of the tissue, the species from which the tissue came and its pathological condition. To produce any "characteristic" values many assumptions would have to be made, the validity of which cannot be assessed from the information available. Thus all that the present authors have set out to do is to present the data with the relevant information, where possible, in order that each worker may draw his own conclusions about average values and their limitations.

The table A, for velocity data and B, for attenuation data contain this information; blank (--) indicates that the appropriate information is not stated in the original paper. To examine the frequency and temperature dependence of velocity, the (a priori unwarranted) assumption is made that the results for different species and conditions may be directly compared and the measurements for two temperature ranges are then represented in figures 1 and 2. The ranges chosen were 23 ± 3 °C and 36 ± 1 °C, the former being rather wide in order to encompass the large body of measurements made at 20 °C and 26 °C. It is left to the reader to opine about the existence of velocity dispersion or to assess temperature dependence of velocity from significant differences between figures 1 and 2 - a task made difficult by the lack of data at 36 ± 1 °C (although some data in the tables does not appear in these figures as it was averaged over a wide frequency range [10]). The remaining figures (3-9) show plots of α/f against f for various tissues - no account being taken of species, condition or temperature. This presentation was chosen as it readily permits assessment of the oft-quoted linear relation between α and f. Comments on the temperature dependence of α are limited by the consistent disinclination of authors to specify this parameter when reporting their results and their tendency to average over wide temperature ranges.

In conclusion, it is only possible to echo Goldman and Hueter's statement of 20 years ago, "No critical discussion is indicated at this time, but it is anticipated that the accumulation of further data on the basis of more precise and extensive measurements should permit important generalizations on the acoustic characteristics of living matter." [1], and in doing so express the hope that future reports in the literature will include sufficient information about tissue condition and measurement technique to enable valid conclusions about their contribution to the spread of parameter values to be assessed and thus permit the "important generalizations on the acoustic characteristics of living matter."

Table. Compilation of (A) velocity and (B) attenuation of various tissues under various conditions.

A. Velocity of ultrasound in various tissues under various conditions.

Species	Condition	Temp. (°C)	f (MHz)	c (m/s)	Variation (m/s)	N	Technique	Precision (%)	Source
				Normal Blood					
man	heparinised	22.4	2	1565	125	12	sing-around	.1	19
		22.6		1570	24	10			
		23.2		1549.6	10.8	10			
		24.2		1556.4	4.7	11			
				Normal Fat					
man, orbit	fresh	20	6 → 14	1582	SD = 20.4	65	pulse	1.5	10
		37		1462	SD = 23.7	16			
man, breast	fresh/dry	25	2.0	1470	--	--	pulse	0.2	20
man, breast	refrigerated	24	1.8	1465	SE = 2	--	interferometric	0.5	16
man	--	24	1.8	1476	SE = 2	2752	interferometric	0.5	16
pig	fresh	24	1.8	1444	SE = 2	58	interferometric	0.5	16
pig	fresh	37	.5 → 7	1440	--	--	--	--	21
cow	fresh	24	1.8	1465	SE = 3	21	interferometric	0.5	16
horse	fresh	24	1.8	1443	SE = 4	56	interferometric	0.5	16

Species	Condition	Temp. (°C)	f (MHz)	c (m/s)	Variation (m/s)	N	Technique	Precision (%)	Source
				Normal Liver					
man	--	24	1.8	1585	SE = 2	--	interferometric	0.5	16
pig	fresh	24	1.8	1587	SE = 3	--	interferometric	0.5	16
pig	fresh	25	2.5	1553	SD = 15.5	7	sing-around	0.5	22
cow	fresh	24	1.8	1590	SE = 2	--	interferometric	0.5	16
cow	fresh	24	1.8	1578	SE = 3	--	interferometric	0.5	16
horse	fresh	24	1.8	1580	SE = 2	--	interferometric	0.5	16
dog	fresh	26	4 & 12	1581	SD = 16.8	8	interferometric	0.2	23
rabbit	fresh	24	1.8	1599	SE = 1	--	interferometric	0.5	16
rabbit	fresh	26	4 & 12	1575	SD = 9.4	13	interferometric	0.2	23
guinea pig	fresh	24	1.8	1575	SE = 3	--	interferometric	0.5	16
				Abnormal Liver					
man, healthy + diseased	refrigerated	24	1.8	1570	SE = 4	18	interferometric	0.5	16
rabbit, bled	fresh	24	1.8	1607	SE = 2	--	interferometric	0.5	16
guinea pig, bled	fresh	24	1.8	1589	SE = 2	--	interferometric	0.5	16
				Normal Kidney					
pig	fresh	24	1.8	1560	SE = 4	--	interferometric	0.5	16
pig	fresh	25	2.5	1558	SD = 15.6	5	sing-around	0.5	22
cow	fresh	24	1.8	1568	SE = 3	--	interferometric	0.5	16
cow	fresh	24	1.8	1572	SE = 3	--	interferometric	0.5	16
horse	fresh	24	1.8	1558	SE = 3	--	interferometric	0.5	16
dog	fresh	26	4 & 12	1559	--	2	interferometric	0.2	23
rabbit	--	--	5	1566	1560 - 1571	2	--	--	24
				Normal Spleen					
pig	fresh	24	1.8	1578	SE = 3	--	interferometric	0.5	16
pig	fresh	25	2.5	1515	SD = 15.2	4	sing-around	0.5	22
cow	fresh	24	1.8	1577	SE = 2	--	interferometric	0.5	16
cow	fresh	24	1.8	1578	SE = 3	--	interferometric	0.5	16
horse	fresh	24	1.8	1595	SE = 3	--	interferometric	0.5	16
dog	fresh	26	4 & 12	1570	--	2	interferometric	0.2	23
				Normal Lung					
dog	fresh	35.0 ± .5	0.98	650	0	2	reflection coefficient[a]	--	25
dog	fresh	35.0 ± .5	1 2.25 5	658 812 1180	--	--	reflection coefficient[a]	less than 10 ms^{-1}	52
dog	--	--	0.39 1	300 580	--	--	pulse	--	55
				Abnormal Lung					
dog, pneumonitic	fresh	35	0.98	340	0	1	reflection coefficient[a]	--	25
				Normal Connective Tissue					
man, breast	fresh/dry	25	2.0	1545	--	--	pulse	0.2	20
				Normal Muscle					
Skeletal muscle: parallel to muscle fibres									
dog	fresh	26	4 & 12	1592	SD = 5.0	7	interferometric	0.2	23
rabbit	fresh	26	4 & 12	1603	SD = 7.9	13	interferometric	0.2	23

Species	Condition	Temp. (°C)	f (MHz)	c (m/s)	Variation (m/s)	N	Technique	Precision (%)	Source
Skeletal muscle: perpendicular to muscle fibres									
man, external eye	fresh	20 37	6 → 14	1612 1631	SD = 12.5 SD = 15.3	83 13	pulse	1.5	10
man, breast	fresh/dry	25	2.0	1545	--	--	pulse	0.2	20
dog	fresh	26	4 & 12	1576	SD = 9.6	8	interferometric	0.2	23
rabbit	fresh	26	4 & 12	1587	SD = 5.5	18	interferometric	0.2	23
Skeletal muscle: direction unspecified									
man, pectoral	refrigerated	24	1.8	1568	SE = 5.5	--	interferometric	0.5	16
man	--	24	1.8	1585	SE = 6	--	interferometric	0.5	16
pig	fresh	24	1.8	1580	SE = 3	--	interferometric	0.5	16
cow	fresh	24	1.8	1581	SE = 4	--	interferometric	0.5	16
cow	fresh	24	1.8	1580	SE = 4	--	interferometric	0.5	16
cow	refrigerated	25	2.5	1580	SD = 16	12	sing-around	0.5	22
horse	fresh	24	1.8	1598	SE = 4	--	interferometric	0.5	16
Cardiac muscle									
pig	fresh	24	1.8	1587	SE = 3	--	interferometric	0.5	16
cow	fresh	24	1.8	1584	SE = 3	--	interferometric	0.5	16
cow	fresh	24	1.8	1570	SE = 2	--	interferometric	0.5	16
horse	fresh	24	1.8	1584	SE = 3	--	interferometric	0.5	16
dog	fresh	26	4 & 12	1572	--	3	interferometric	0.2	23
Normal Nervous Tissues									
man, brain (term foetus)	fresh	24 24 37	5	1524 1521 1540	--	--	pulse	0.1	26[u]
man, brain (foetus)	--	--	--	1525	--	--	--	--	27
man, brain	--	24	1.8	1564	SE = 4	--	interferometric	0.5	16
pig, brain	fresh	24	1.8	1565	SE = 2	--	interferometric	0.5	16
pig, brain	fresh	25	2.5	1506	SD = 15	7	interferometric	0.5	22
cow, brain	fresh	24	1.8	1560	SE = 2	--	interferometric	0.5	16
cow, brain	fresh	24	1.8	1569	SE = 3	--	interferometric	0.5	16
horse, brain	fresh	24	1.8	1560	SE = 2	--	interferometric	0.5	16
dog, brain	fresh	25	2.5	1515	SD = 15	5	sing-around	0.5	22
cat, brain	living/fresh	24 37 60	4.2	1557 1570 1574	--	--	pulse	--	11
rabbit, brain	--	--	5	1508	1380 - 1570	3	--	--	24
man, optic nerve	fresh	20 37	6 → 14	1644 1615	SD = 25.4 SD = 3.1	30 13	pulse	1.5	10
man, cerebro-spinal fluid	fresh	21.8 24.4 25.0	2	1499 1515 1509.5	30 45 7.5	11 9 11	sing-around	0.1	19
Abnormal Nervous Tissues									
man, meningioma	fixed 3 h 48 h	19.0 19.8	2	1524.2 1524.5	6.1 7.5	20 20	sing-around	0.1	19
man, meningioma (5 sections of 1 tumor)	--	19.7	2	1557 1546 1569 1548 1569	31 15 31 31 39	20 20 21 14 14	sing-around	0.1	19
man, glioma	fresh	22.2	2	1529.1	9.1	20	sing-around	0.1	19
man, glioma	fixed	22.3	2	1500	45	17	sing-around	0.1	19

Species	Condition	Temp. (°C)	f (MHz)	c (m/s)	Variation (m/s)	N	Technique	Precision (%)	Source
man, astrocytoma	fresh	27.5	2	1545.4	6.2	41	sing-around	0.1	19
man, astrocytoma	fixed	24.9	2	1517	121	27	sing-around	0.1	19
man, ependymoma	fixed	20.0	2	1501	45	18	sing-around	0.1	19
Normal Ophthalmic Tissues									
man, lens	in vivo	body	--	1585	± 74[b]	53	--	--	28
man, lens	fresh	34.1 (mean)	4	1641	SD = 16[c]	7	interferometric	--	29
man, lens	fresh	37	4				interferometric	0.6	30[d]
(autopsy)				1641.0	SD = 1.3	35			
(operative)				1638.4	SD = 3.0	12			
(autopsy + operative)				1640.5	SD = 1.2	47			
pig, lens	fresh	23	4	1665	SD = 6[e]	10	interferometric	--	29
		30		1673	SD = 5[e]	10			
		35		1677	SD = 3[e]	10			
cow, lens	fresh	22	4	1650	--	--	interferometric	0.5	31
cow, lens	refrigerated	26-31	5	1616	1500 - 1680[f]	--	interferometric	1	12
rabbit lens	--	--	5	1540	SD = 66	5	--	--	24
man, vitreous	in vivo	body	7	1544	± 37[b]	53	--	--	28
man, vitreous	fresh	35.2 (mean)	4	1530	SD = 5[c]	10	interferometric	--	29
man, vitreous	fresh	37	4				interferometric	0.6	30[d]
(autopsy)				1532	SD = 0.6	35			
(operative)				1531.7	SD = 0.9	14			
(autopsy + operative)				1532.4	SD = 0.5	49			
pig, vitreous	fresh	23	4	1510	SD = 3[e]	10	interferometric	--	29
		30		1522	SD = 3[e]	9			
		35		1531	SD = 3[e]	10			
cow, vitreous	fresh	22	4	1495	--	--	interferometric	0.5	31
cow, vitreous	refrigerated	26-31	5	1516	1490 - 1544[f]	--	interferometric	1	12
rabbit, vitreous	--	--	5	1472	SD = 16	6	--	--	24
vitreous + hyaluronidase				1494	SD = 11	6			
cow, aqueous	fresh	22	4	1495	--	--	interferometric	0.5	31
cow, aqueous	refrigerated	26-31	5	1497	1481 - 1525[f]	--	interferometric	--	12
man, cornea/ aqueous	in vivo	body	--	1502	± 45[b]	53	--	--	28
cow, cornea	fresh	22	4	1550	--	--	interferometric	0.5	31
cow, sclera	fresh	22	4	1630	--	--	interferometric	0.5	31
Abnormal Ophthalmic Tissues									
man, lens-cataractous	fresh	35.8	4	1643	--	1	interferometric	--	29
				1688	--	1			
Normal Bone									
Long bones: along axis									
cow, phalanx	fresh	--	5	4030	SD = 110	252	pulse	SD ∿ 3	32
cow, phalanx	dried	--	5	4360	SD = 170	120	pulse	SD ∿ 3	32
cow, femur	dried	--	5	4060	SD = 40	144	pulse	SD ∿ 3	32
guinea pig, femur	--	--	.1	3158	2870 - 3541[g]	40	pulse	--	33
Long bones: across axis									
cow, phalanx	fresh	--	5	3160	SD = 170	252	pulse	SD ∿ 3	32
cow, phalanx	dried	--	5	3270	SD = 160	120	pulse	SD ∿ 3	32
cow, femur	dried	--	5	3420	SD = 340	144	pulse	SD ∿ 3	32

Species	Condition	Temp. (°C)	f (MHz)	c (m/s)	Variation (m/s)	N	Technique	Precision (%)	Source
Long bones: direction unspecified									
man, cortical bone	in vivo	body	5.0	3406	SD = 126	18	pulse	∿ 6	34
dog, tibia	refrigerated	22	3 & 5	--	3210 - 3620[g]	--	pulse	--	35
horse	--	--	--	3700	--	--	pulse	--	36
Skull bone									
man	fresh	body	0.8	3360	--	--	continuous wave reflection	--	37
man	fixed	--	--[h]			23	pulse	4	38[i]
outer layer				2920	SD = 160	9			
diploe layer				3198	SD = 93	5			
inner layer				3098	SD = 220	6			
Abnormal Bone									
guinea pig, completely healed broken femur	fresh	--	0.1	2968	2788 - 3371[g]	15	pulse	--	33
partially healed broken femur				2551	2442 - 2724[g]	16			
Normal Breast Tissue									
man, pre-menopause	in vivo	body	2.0	1510	1450 - 1570[j]	∿ 110	pulse	0.2	20[k]
post-menopause				1468	1430 - 1520[j]	∿ 40			
Abnormal Breast Tissue									
man, carcinoma	refrigerated	24	1.8	1573	SE = 7	--	interferometric	0.5	16
man, carcinoma	in vivo	body	2.0	1478	SD = 28	17	pulse	0.2	20[l]
man, fibro-cystic	in vivo	body	2.0	1531	SD = 23	28	pulse	0.2	20[l]
man, fibro-adenosis	in vivo	body	2.0	1529	SD = 30	6	pulse	0.2	20[l]
man, fibro adenoma	in vivo	body	2.0	1529	SD = 21	6	pulse	0.2	20[l]
Obstetric Tissues									
man, cervix-pregnant	in vivo	body	5	1625	SD = 1.63	108	pulse	.006	39
nonpregnant				1633	SD = 2.86	29			
man, amniotic fluid	--	25	5	1510	--	--	--	--	40
man, milk	--	30	2	1540	--	--	pulse	0.2	20
man, foetal brain	fresh		5		--	--	pulse	0.1	26[u]
17 weeks		24		1490					
(2 samples)		24		1495					
		37		1520					
		37		1523					
28 weeks		24		1498					
(2 samples)		24		1502					
		37		1528					
		37		1529					
40 weeks		24		1521					
(2 samples)		24		1524					
		37		1540					
		37		1540					

B. Attenuation of ultrasound in various tissues under various conditions.

Species	Condition	Temp. (°C)	f (MHz)	α (m^{-1})	Variation (m^{-1})	N	Technique	Precision	Source
				Normal Blood					
dog (citrated)	fresh	30	.58	1.09	--	--	--	--	41
			1.0	1.73					
			1.8	3.22					
			3.0	6.33					
			4.8	12.1					
		40	.58	1.15					
			1.0	1.78					
			1.8	3.45					
			3.0	6.91					
			4.8	12.7					
				Normal Fat					
man, orbit	fresh	37	5.9[m]	230	SD = 22	9 - 13	broadband	--	10
			6.2	220	SD = 15				
			7.5	330	SD = 24				
			7.7	250	SD = 18				
			8.4	320	SD = 26				
			8.8	360	SD = 15				
			9.8	430	SD = 20				
			9.8	450	SD = 24				
			10.46	500	SD = 30				
			13.9	670	SD = 28				
man, orbit	in vivo	--	6	180[p]	--	--	spectrum analysis of a broadband pulse[n]	--	61
			↓	↓					
			12	360					
man	fixed	18 ± 2	1	10	typically SD = 3	at least 6 per point: 1 point per 100 kHz	spectrum analysis of a broadband pulse[n]	$5m^{-1}$	7
			2	22					
			3	35					
			4	47					
			5	63					
			6	84					
			7	115					
man	--	--	.8	5	--	--	--	--	42
man/cow	fresh	--	1	6.9	SD = 2.3	--	narrow band	0.25 dB	4
			3	18	SD = 2.3				
			5	26	SD = 8.1				
pig	fresh	37	1.6	6.9	--	--	--	--	21
			2.8	21					
			4	40					
			6	56					
			7	75					
cow	-- (melted)	20 - 35	.87	4.6	--	--	--	10%	43
			1.7	8.7					
			3.4	16					
				Normal Liver					
man	in vivo	body	1.67	20.3	--	900	broadband	--	44
man	fixed	18 ± 2	1	13.8	typically SD = 6	at least 6 per point: 1 point per 100 kHz	spectrum analysis of a broadband pulse[n]	$5m^{-1}$	7
			2	27.6					
			3	43					
			4	56					
			5	69					
			6	81					
			7	93					
cow	fresh	20 - 35	1.5	16	--	--	--	--	45
			2.4	18					
			4.5	40					
cow	fresh	--	1.5	15	--	--	--	--	46
			2.4	18					
			4.5	38					

Species	Condition	Temp. (°C)	f (MHz)	α (m^{-1})	Variation (m^{-1})	N	Technique	Precision	Source
cow	fresh	25	1	7.7	--	--	--	± 10%	17
	ground (± ∿ 0.5)		1.5	13					
	refrigerated		2	20					
			3	29					
			5	54					
			7	71					
			9.4	104					
cow	fixed	--	.35	4	--	--	--	--	47
			.575	6					
			.6	10					
			.7	9					
cow	--	20 - 35	.3	11	--	--	--	10%	43
			.87	9.5					
			1.7	14					
			3.4	27					
cow	--	--	2	12	--	--	--[r]	--	54
				12	--	--	narrow band[s]	--	
				Normal Kidney					
man/mouse	fresh/frozen/ fixed	22 - 31	96	1000	SD = 86	7	--	± 25%	48
			222	5000	SD = 760	4			
cow	fresh	20 - 35	1.5	19	--	--	--	--	45
			2.4	26					
			4.5	51					
cow	fresh	--	1.5	18	--	--	--	--	46
			2.4	25					
			4.5	53					
cow	fixed	--	.25	5	--	--	--	--	47
			.3	4					
			.35	5					
			.4	6					
			.5	7					
			.6	5					
			.7	9					
			.8	7					
pig	--	--	2	18	--	--	--[r]	--	54
				16	--	--	narrow band[s]	--	
				Normal Spleen					
man	fixed	18 ± 2	1	3.5	typically	at least	spectrum	$5m^{-1}$	7
			2	13	SD = 4.6	6 per	analysis		
			3	26		point:	of a broadband		
			4	40		1 point	pulse[n]		
			5	56		per 100			
			6	74		kHz			
			7	96					
				Normal Lung					
man	fresh	--	1	350	--	--	narrow band	0.25 dB	4
dog	fresh	35.0 ± .5	.98	470.0	10.0	2	--	--	25
dog	fresh	35.0 ± .5	1	430	410 - 470[j]	--	--	--	52
			2.25	590	560 - 640[j]	--			
			5	1160	1040 - 1210[j]	--			
dog	fresh	27 ± 2	2.4	440	SE = 160	--	broadband	0.1 dB	56[t]
			5.0	900	SE = 140	--			
			7.4	1000	SE = 130	--			
				Abnormal Lung					
dog, pneumonitic	fresh	35.0 ± .5	.98	350	--	1	--	--	25

Species	Condition	Temp. (°C)	f (MHz)	α (m^{-1})	Variation (m^{-1})	N	Technique	Precision	Source
				Normal Connective Tissues					
man, skin	fresh	--	1	40	SD = 14	--	narrow band	0.25 dB	4
			3	85	SD = 14				
			5	106	SD = 25				
man/cow, tendon across grain	fresh	--	1	54	SD = 12				
			3	125	SD = 23				
			5	195	SD = 28				
along grain			1	58	SD = 21				
man/cow articular capsule	fresh	--	1	38	SD = 10				
			3	81	SD = 9				
			5	130	SD = 62				
man/cow cartilage	fresh	--	1	58	SD = 17				
			3	144	SD = 23				
			5	220	SD = 62				
cow, elastic tendon, across grain	fresh	--	1	73	SD = 2				
			3	188	SD = 2				
			5	286	SD = 53				
along grain			1	41	SD = 8				
			3	137	SD = 3				
			5	235	SD = 66				
cow, rectum wall	fresh	--	1	6.9	SD = 1.7				
			3	18	SD = 2				
			5	28	SD = 5				
				Normal Muscle					
Skeletal muscle: parallel to muscle fibres									
man	fresh	37	5.9[m]	180	SD = 18	9-13	broadband	--	10
			6.2	210	SD = 18				
			7.5	240	SD = 15				
			7.7	220	SD = 16				
			8.4	310	SD = 24				
			8.8	320	SD = 25				
			9.8	410	SD = 22				
			9.8	400	SD = 24				
			10.46	440	SD = 20				
			13.9	590	SD = 17				
man/cow	fresh	--	1	16	SD = 3	--	narrow band	0.25 dB	4
			3	48	SD = 9				
			5	71	SD = 17				
cow	--	20 - 35	.3	9.0	--	--	--	10%	43
			.87	18.0					
			1.7	25.4					
			3.4	62.1					
Skeletal muscle: perpendicular to muscle fibres									
man	fresh	37	5.9[m]	120	SD = 16	9-13	broadband	--	10
			6.2	170	SD = 21				
			7.5	200	SD = 22				
			7.7	130	SD = 18				
			8.4	220	SD = 33				
			8.8	280	SD = 35				
			9.8	290	SD = 20				
			9.8	300	SD = 23				
			10.46	370	SD = 24				
			13.9	480	SD = 18				
man/cow	fresh	--	1	8	SD = 1	--	narrow band	0.25 dB	4
			3	30	SD = 6				
			5	40	SD = 1				
cow	--	20 - 35	.3	7.5	--	--	--	10%	43
			.87	5.5					
			3.4	26.5					

Species	Condition	Temp. (°C)	f (MHz)	α (m^{-1})	Variation (m^{-1})	N	Technique	Precision	Source
Skeletal muscle: direction unspecified									
man	--	--	.8	9.5	--	--	--	--	42
cow	--	--	2	-- --	21 - 115[g] 21 - 249	--	--[r] narrow band[s]	--	54
Cardiac muscle									
cow	fresh	20 - 35	1.5 2.4 4.5	30 45 80	--	--	--	--	45
cow	fresh	--	1.5 2.4 4.5	30 45 80	--	--	--	--	46
cow	fixed	--	.3 .35 .4 .575 .6 .7 .8	6 5 8 10 10 14 14	--	--	--	--	47
dog	fresh	--	2 4 6 8 10	20 32 50 66 92	SD = 10 SD = 14 SD = 14 SD = 14 SD = 20	12 per point: 1 point per 500 kHz	spectrum analysis of a broadband pulse[n]	--	62
Tongue: parallel to fibres									
cow	fresh	20 - 35	1.5 2.4 4.5	23 32 65	--	--	--	--	45
Tongue: perpendicular to fibres									
cow	fresh	20 - 35	1.5 2.4	45 65	--	--	--	--	45
Tongue: direction unspecified									
cow	fresh	--	1.5 2.4 4.5	20 32 62	--	--	--	--	46
Abnormal Muscle									
dog, infarcted cardiac muscle	fresh	--	2 4 6 8 10	0 20 60 115 190	SE = 10 SE = 10 SE = 15 SE = 15 SE = 10	7 per point: 1 point per 500 kHz	spectrum analysis of a broadband pulse[n]	--	62
Nerve Tissues									
man, brain	fixed	20 - 35	.3 .87 1.7 3.4	8.5 14.0 18.0 36.5	--	--	--	10%	43
man, brain	--	--	1	17	--	--	--	--	49
pig, (whole brain)	fresh	--	2.5	40	36 - 51	12	--	--	50
(white matter)	fresh	--	2.5	18	16 - 21	6			
pig, brain	fixed	--	.35 .6 .8	3 4 5	--	--	--	--	47
cow, brain	fresh	20 - 35	.87 1.7 3.4	8.5 14.0 33.5	--	--	--	10%	43

Species	Condition	Temp. (°C)	f (MHz)	α (m^{-1})	Variation (m^{-1})	N	Technique	Precision	Source
dog, brain	in vivo	body	.97	5.4	--	--	--	1%	41
cat, brain	in vivo	37	4.2	--	28 - 50	--	broadband	--	11
rat, spinal cord	in vivo	30-31.5	.98	10	8 - 12	7	narrow band	--	5
mouse, spinal cord	in vivo	2 ± .1 10 ± .1 28 ± .1	1	1.7 5.0 9.5	--	--	--	--	53
Parallel to nerve fibres									
man, optic nerve	fresh	37	5.9[m] 6.2 7.5 7.7 8.4 8.8 9.8 9.8 10.46 13.9	290 280 430 400 600 500 620 670 600 740	SD = 14 SD = 16 SD = 22 SD = 47 SD = 38 SD = 38 SD = 38 SD = 36 SD = 21 SD = 28	9 - 13	broadband	--	10
man, medulla oblongata	--	20-35	1.7 3.4	14 34	--	--	--	10%	43
cow, sciatic nerve	--	20-35	3.4	35	--	--	--	10%	43
Perpendicular to nerve fibres									
man, optic nerve	fresh	37	5.9[m] 6.2 7.5 7.7 8.4 8.8 9.8 9.8 10.46 13.9	210 240 310 230 370 350 320 410 500 630	SD = 20 SD = 20 SD = 28 SD = 22 SD = 43 SD = 29 SD = 32 SD = 33 SD = 29 SD = 33	9 - 13	broadband	--	10
man, medulla oblongata	--	20-35	1.7 3.4	21 46	--	--	--	10%	43
cow, sciatic nerve	--	20-35	3.4	55	--	--	--	10%	43
Normal Ophthalmic Tissues									
man, lens	--	--	10[o] ↓ 17	92[p] ↓ 156	--	--	spectrum analysis of a broadband pulse[n]	--	13
cow, lens	fresh	28	3.25	64	6	4	--	--	12
cow, lens	--	22	10 13.5	230 310	--	--	--	--	58
cow, vitreous	--	22	6 10 18 30	6 12 20 29	--	--	--	--	58
cow, aqueous/ vitreous	fresh	25-28	30	33	9	large	broadband	15%	12
Normal Bone									
man, skull	fresh	--	.3 .6 .8 1.2 1.6 1.8	23 52 92 170 320 430	7 16 28 51 96 130	--	broadband	--	51

Species	Condition	Temp. (°C)	f (MHz)	α (m^{-1})	Variation (m^{-1})	N	Technique	Precision	Source
			2.25	530	160				
			3.5	780	230				
man, skull	fresh/fixed	--	.8	150	--	--	--	--	37
man, skull	fixed	--	--[h]			24	--	25%	38[i]
outer				1919	SD = 474	9			
diploe				1616	SD = 293	5			
inner				2460	SD = 1250	6			
man, skull	--	--	1	150	--	--	--	--	49
man/cow	fresh	--	1	144	--	--	narrow band	0.25 dB	4
dog, tibia	refrigerated	22	3	150	--	--	--	--	35
			5	220					
horse	--	--[q]	1.43	250	--	--	--	--	36
			2.86	--	460 - 580	--			
			4.5	920	--	--			
				Obstetric Tissues					
cow, uterus	fresh	--	1	19.6	SD = 2	--	narrow band	0.25 dB	4

[a] The velocity was calculated from measurements of the reflection coefficient made with a thermocouple probe in a standing wave field.

[b] The authors do not indicate what this figure represents.

[c] Measurements were made on samples from eyes with a variety of tumors although no pathological condition was seen in the components of the eye.

[d] Reference 30 contains information on the variation of velocity with time after death.

[e] Data for the calculation of the standard deviation were taken from the graphs in the reference.

[f] Calculation of the standard deviation was not possible since each figure quoted by the author is a mean of 16 to 25 measurements.

[g] The authors do not give individual measurements but only quote this range.

[h] The authors do not specify the frequency used, except that the pulse used "contained substantial components in the range 3 to 4 MHz."

[i] The "average value" for bone quoted by these authors must be disregarded because of the manner in which it was obtained.

[j] Only the range can be obtained from the data which are represented graphically.

[k] This includes data from U.S.A. and Australia, and a study comparing measurements with radiographic findings.

[l] Data used to calculate the mean and standard deviation were those marked "a" in tables II to V of reference 20 (i.e. those breasts diagnosed by pathology studies of excised tissue).

[m] These figures refer to the dominant frequency in the acoustic pulse from a reflector in water, but the authors comment that this may change by as much as 12 percent.

[n] This method gives the attenuation as a continuous function of frequency, but the authors did not include diffraction corrections necessary for accurate results.

[o] Frequency resolution 300 kHz.

[p] The attenuation coefficient was assumed to be linear with frequency.

[q] This author also gives some indication of the temperature variation of the attenuation coefficient.

[r] Pulse technique using piezoelectric receiver.

[s] Continuous wave technique using radiation balance receiver.

[t] These authors also give information on the variation of the attenuation coefficient with the degree of inflation of the lung.

[u] Reference 26 contains further information on the variation of velocity in foetal brain with the gestational age of the foetus.

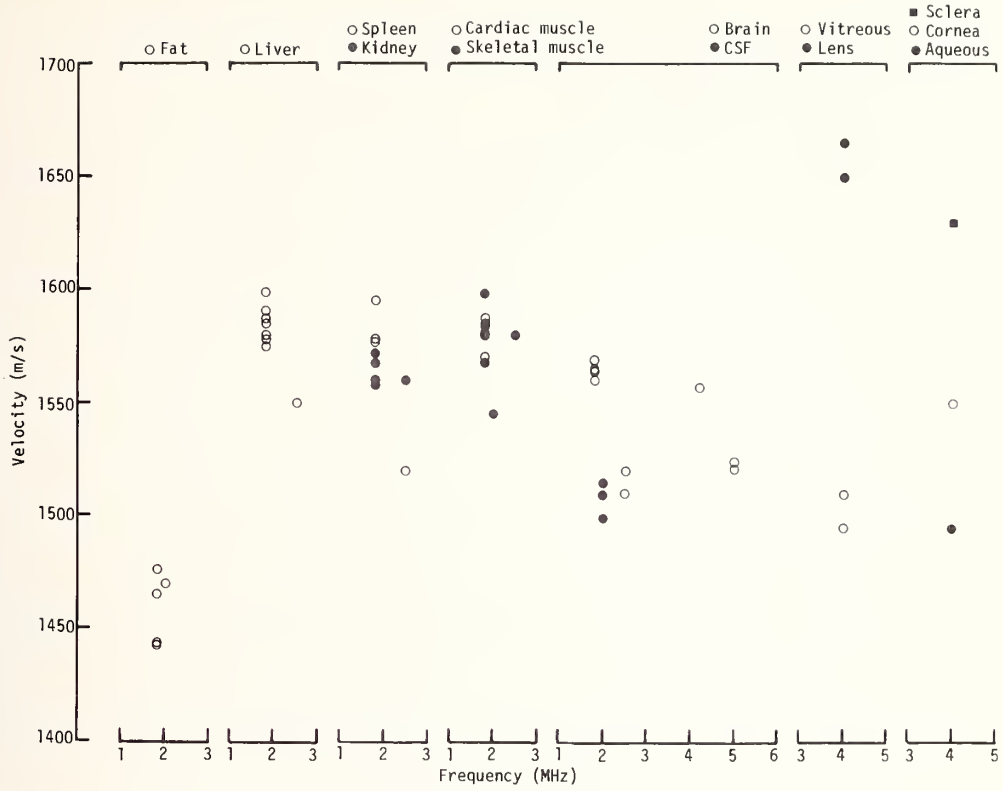

Fig. 1. Frequency dependence of the velocity of ultrasound in various normal tissues at 23 ± 3 °C.

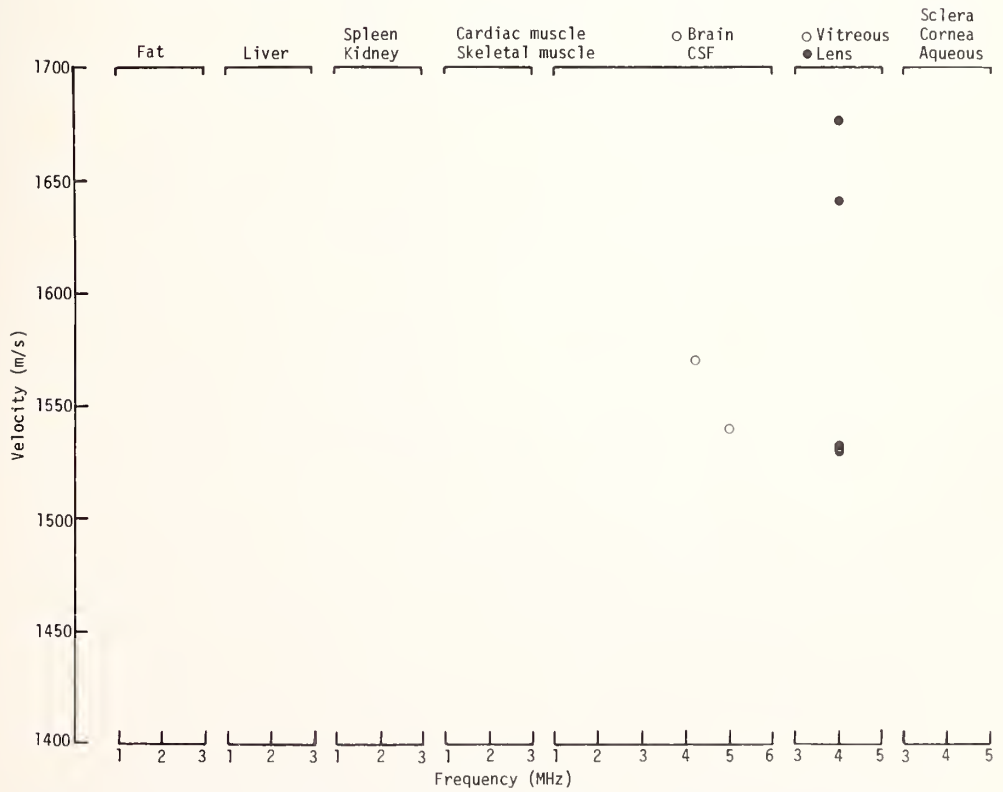

Fig. 2. Frequency dependence of the velocity of ultrasound in various normal tissues at 36 ± 1 °C.

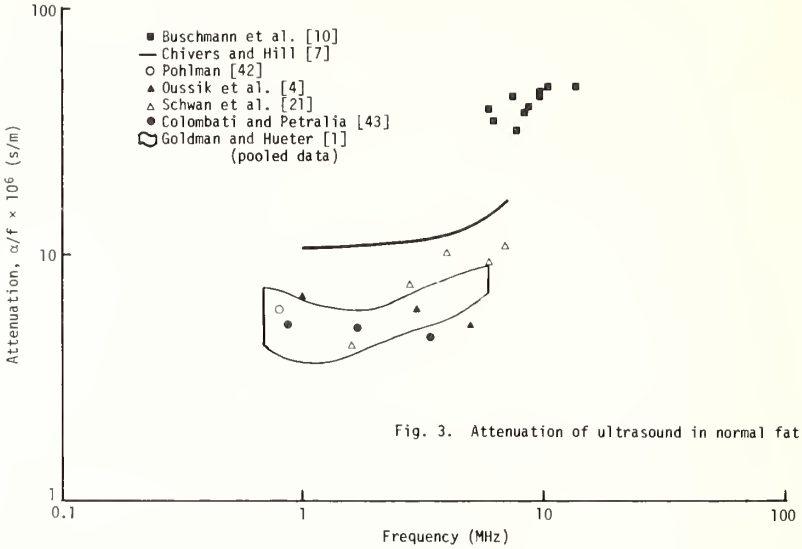

Fig. 3. Attenuation of ultrasound in normal fat.

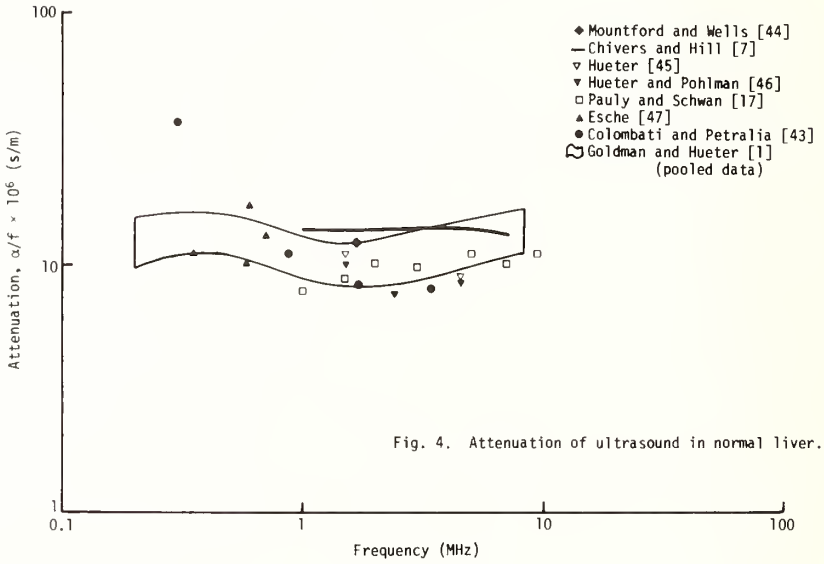

Fig. 4. Attenuation of ultrasound in normal liver.

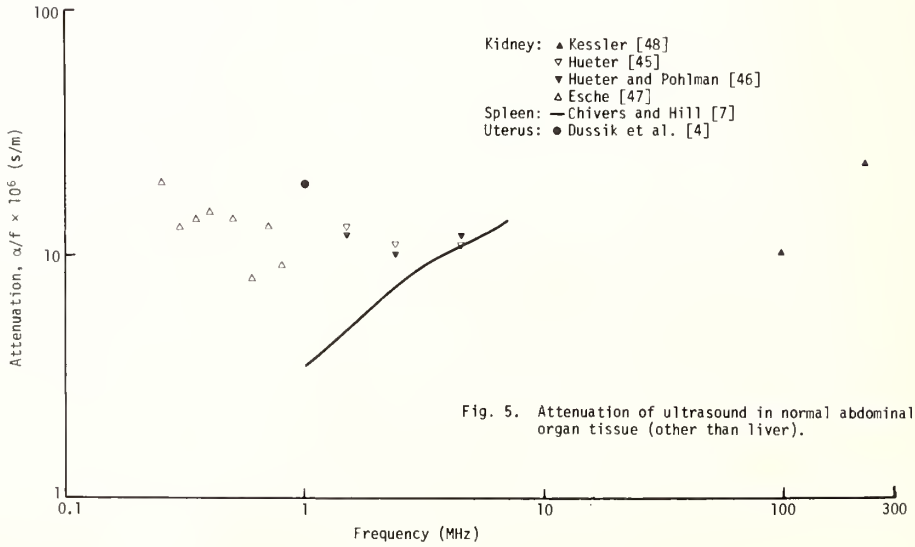

Fig. 5. Attenuation of ultrasound in normal abdominal organ tissue (other than liver).

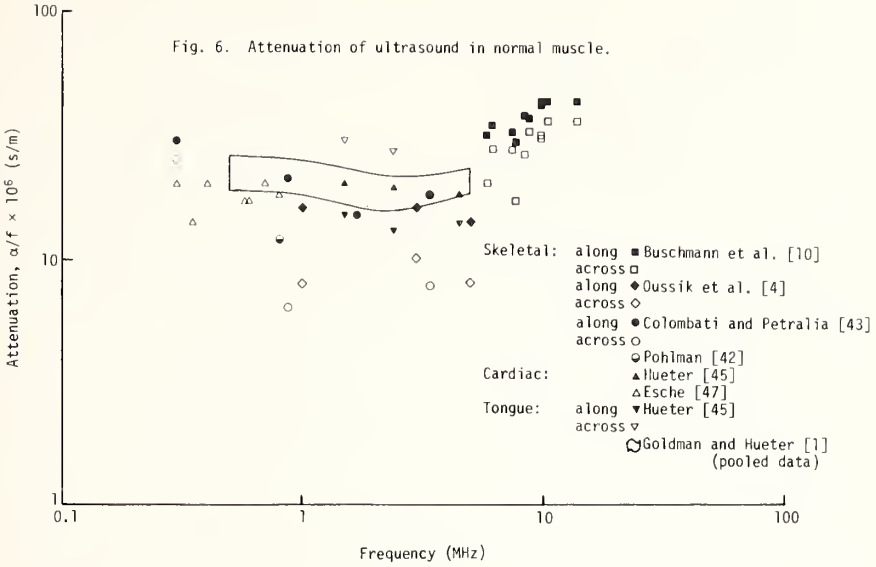

Fig. 6. Attenuation of ultrasound in normal muscle.

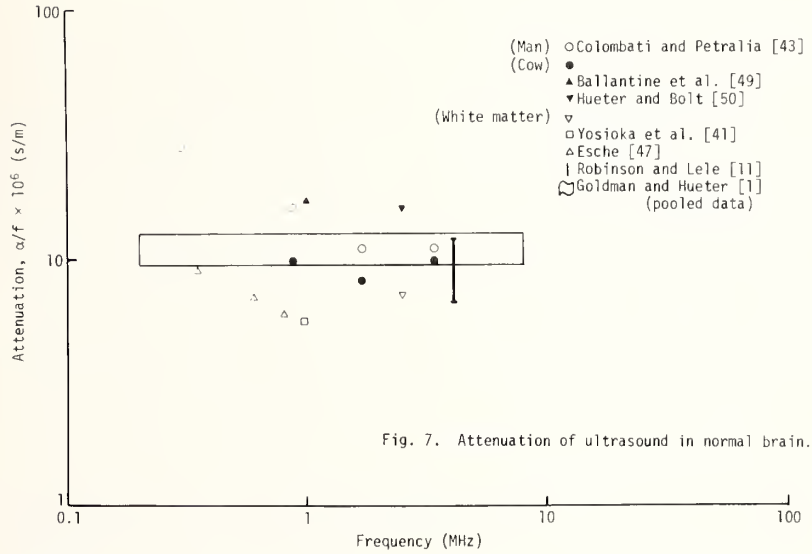

Fig. 7. Attenuation of ultrasound in normal brain.

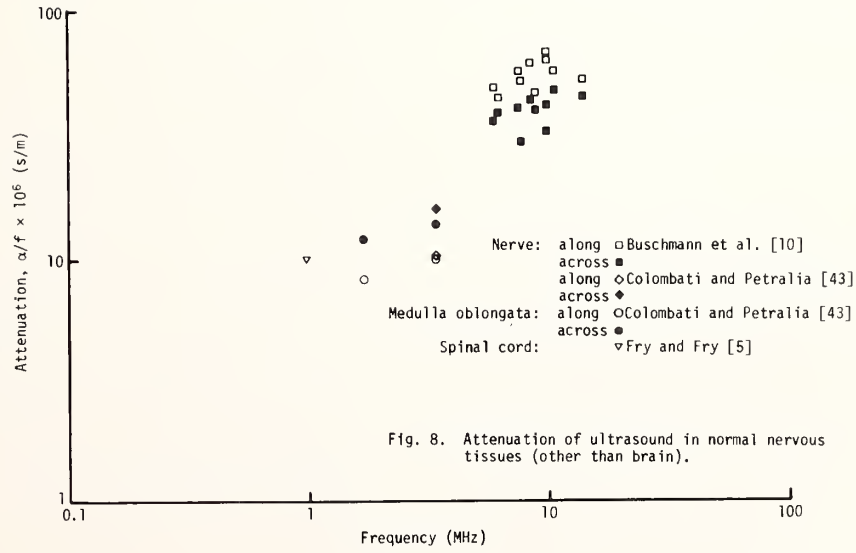

Fig. 8. Attenuation of ultrasound in normal nervous tissues (other than brain).

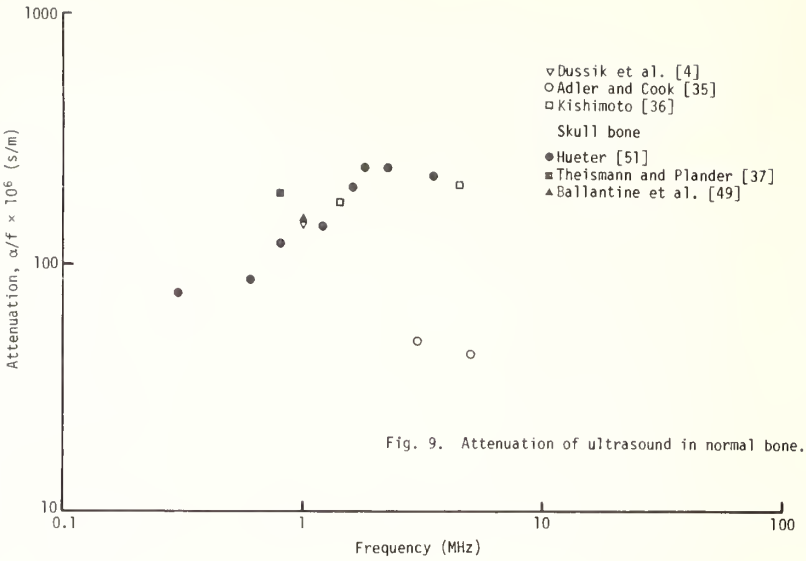

Fig. 9. Attenuation of ultrasound in normal bone.

References

[1] Goldman, D. E. and Hueter, T. F., Tabular data of the velocity and absorption of high-frequency sound in mammalian tissues, J. Acoust. Soc. Am. 28, 35-37 (1956). Errata: J. Acoust. Soc. Am. 29, 655 (1957).

[2] Wells, P. N. T., Absorption and dispersion of ultrasound in biological tissue, Ultrasound in Med. Biol. 1, 369-376 (1975).

[3] Hussey, M., Diagnostic ultrasound (Blackie, Glasgow, 1975).

[4] Dussik, K. T., Fritch, D. J., Kyriazidou, M., and Sears, R. S., Measurements of articular tissues with ultrasound, Am. J. Phys. Med. 37, 160-165 (1958).

[5] Fry, W. J. and Fry, R. B., Temperature changes produced in tissue during ultrasonic irradiation, J. Acoust. Soc. Am. 25, 6-11 (1953).

[6] Zieniuk, J. and Chivers, R. C., Measurement of ultrasonic exposure with radiation force and thermal methods, Ultrasonics 14, 161-172 (1976).

[7] Chivers, R. C. and Hill, C. R., Ultrasonic attenuation in human tissue, Ultrasound in Med. Biol. 2, 25-29 (1975).

[8] McSkimin, H. J., Ultrasonic Methods for Measuring the Mechanical Properties of Liquids and Solids in Physical Acoustics, W. P. Mason, ed., Vol. 1, Part A, pp. 271-334 (Academic Press, New York, 1964).

[9] Wehr, J. S., Classification and discussion of interference methods for measuring the propagation velocity of ultrasonic waves, in Proceedings of the Fourth International Conference on Acoustics, Copenhagen, Paper K15 (1962).

[10] Buschmann, W., Voss, M., and Kemmerling, S., Acoustic properties of normal human orbit tissues, Ophthal. Res. 1, 354-364 (1970).

[11] Robinson, T. C. and Lele, P. P., An analysis of lesion development in the brain and in plastics by high-intensity focussed ultrasound at low-megahertz frequencies, J. Acoust. Soc. Am. 51, 1333-1351 (1972).

[12] Begui, Z. E., Acoustic properties of the refractive media of the eye, J. Acoust. Soc. Am. 26, 365-368 (1954).

[13] Lizzi, F., Katz, L., St. Louis, L., and Coleman, D. J., Applications of spectral analysis in medical ultrasonography, Ultrasonics 14, 77-80 (1976).

[14] Wehr, J. S., Error analysis as a factor in the choice of the proper method of measuring the attenuation and the reflection coefficient of ultrasonic waves in solids, in Proceedings of the Conference on Acoustics of Solid Media (PWN Warsaw, 1964), pp. 239-245.

[15] Frucht, A. H., Die Geschwindigkeit des Ultraschalls in menschlichen und tierischen Geweben, Naturwissenschaften 39, 491-492 (1952).

[16] Frucht, A. H., Die Schallgeschwindigkeit in menschlichen und tierischen Geweben, Zeit. Ges. Exptl. Med. 120, 526-557 (1953).

[17] Pauly, H. and Schwan, H. P., Mechanism of absorption of ultrasound in liver tissue, J. Acoust. Soc. Am. 50, 692-699 (1971).

[18] Danckwerts, H. J., Discrete relaxation processes as a model of the absorption of ultrasound in liver homogenate, J. Acoust. Soc. Am. 55, 1098-1099 (1974).

[19] Van Venrooij, G. E. P. M., Measurement of ultrasound velocity in human tissue, Ultrasonics 9, 240-242 (1971).

[20] Kossoff, G., Fry, E. K., and Jellins, J., Average velocity of ultrasound in the human female breast, J. Acoust. Soc. Am. 53, 1730-1736 (1973).

[21] Schwan, H. P., Carstensen, E. L., and Li, K., Heating of fat-muscle layers by electromagnetic and ultrasonic diathermy, Trans. Am. Inst. Elec. Engrs. I, 72, 483-488 (1953).

[22] Ludwig, G. D., The velocity of sound through tissues and the acoustic impedance of tissues, J. Acoust. Soc. Am. 22, 862-866 (1950).

[23] Goldman, D. E. and Richards, J. R., The measurement of high frequency sound velocity in mammalian soft tissue, J. Acoust. Soc. Am. 26, 981-984 (1954).

[24] Nakajima, A., Nishi, S., Amano, K., Uesugi, T., and Wakai, T., Measurement of the axial length of the eye by ultrasonic device, (in Japanese), J. Clin. Ophth. 14, 1594-1599 (1960).

[25] Dunn, F. and Fry, W. J., Ultrasonic absorption and reflexion by lung tissue, Phys. Med. Biol. 5, 401-410 (1961).

[26] Wladimiroff, J. W., Craft, I. L., and Talbert, D. G., In vitro measurements of sound velocity in human fetal brain tissue, Ultrasound in Med. Biol. 1, 377-382 (1975).

[27] Willocks, J., Donald, I., Duggan, T. C., and Day, N., Foetal cephalometry by ultrasound. J. Obstet. Gynaec. Brit. Cwlth. 71, 11-20 (1964).

[28] Nakajima, A., Kimura, T., and Yamazaki, M., Applications of Ultrasound in Biometry of the Eye in Ultrasonics in Ophthalmology, R. E. Goldberg and L. K. Sarin, eds., pp. 124-144 (W. B. Saunders, London and New York, 1967).

[29] Jansson, F. and Sundmark, E., Determination of the velocity of ultrasound in ocular tissues at different temperatures, Acta Ophthal. 39, 899-910 (1961).

[30] Jansson, F. and Kock, E., Determination of the velocity of ultrasound in the human lens and vitreous, Acta Ophtal. 40, 420-433 (1962).

[31] Oksala, A. and Lehtinen, A., Measurement of the velocity of sound in some parts of the eye, Acta Ophtal. 36, 633-639 (1958).

[32] Lang, S. B., Ultrasonic method for measuring elastic coefficients of bone and results on fresh and dried bovine bones, I.E.E.E. Trans. Bio-Med. Eng. BME-17, 101-105 (1970).

[33] Floriani, L. P., Debevoise, N. T., and Hyatt, G. W., Mechanical properties of healing bone by the use of ultrasound, Surg. Forum 18, 468-470 (1967).

[34] Craven, D. A., Constantini, M. A., Greenfield, M. A., and Stern, R., Measurement of the velocity of ultrasound in human cortical bone and its potential clinical importance. An in vivo preliminary study, Invest. Radiol. 8, 72-77 (1973).

[35] Adler, L. and Cook, K. V., Ultrasonic parameters of freshly frozen dog tibia, J. Acoust. Soc. Am. 58, 1107-1108 (1975).

[36] Kishimoto, T., Ultrasonic absorption in bones, Acustica 8, 179-180 (1958).

[37] Theismann, H. and Pfander, F., Über die Durchlässigkeit des Knochens für Ultraschall, Strahlentherapie 80, 607-610 (1949).

[38] Martin, B. and McElhaney, J. H., The acoustic properties of human skull bone, J. Biomed. Mater. Res. 5, 325-333 (1971).

[39] Bakke, T. and Gytre, T., Ultrasonic measurement of the sound velocity in the pregnant and the non-pregnant cervix uteri, Scand. J. Clin. Lab. Invest 33, 341-346 (1974).

[40] Zana, R. and Lang, J., Interaction of ultrasound with amniotic liquid, J. Acoust. Soc. Am. 55, 391 (1974).

[41] Yosioka, K., Ohmura, A., Hasegawa, T., and Oka, M., Absorption coefficient of ultrasound in soft tissues and their biological conditions, in Proceedings of the 6th International Congress on Acoustics, Tokyo, 1968, pp. M5-M8.

[42] Pohlman, R., Über die Absorption des Ultraschalls im menschlichen Gewebe und ihre Abhängigkeit von der Frequenz, Physikalische Zeit. 40, 159-161 (1939).

[43] Colombati, S. and Petralia S., Assorbimento di ultrasuoni in tessuti animali, La Ricerca Scientifica 20, 71-78 (1950).

[44] Mountford, R. A. and Wells, P. N. T., Ultrasonic liver scanning: the quantitative analysis of the normal A-scan, Phys. Med. Biol. 17, 14-25 (1972).

[45] Hueter, T. F., Messung der Ultraschallabsorption in tierischen Geweben und ihre Abhängigkeit von der Frequenz, Naturwissenschaften 35, 285-287 (1948).

[46] Hueter, T. F. and Pohlman, R., Eine optische Methode zur Bestimmung der Ultraschallabsorption in undurchsichtigen, schallweichen Medien, Z. Angew. Phys. 1, 405-411 (1949).

[47] Esche, R., Untersuchungen zur Ultraschallabsorption in tierischen Geweben und Kunststoffen, Akust. Beih. 2, 71-74 (1952).

[48] Kessler, L. W., VHF ultrasonic attenuation in mammalian tissue, J. Acoust. Soc. Am. 53, 1759-1760 (1973).

[49] Ballantine, H. T., Hueter, T. F., and Bolt, R. H., On the use of ultrasound for tumour

detection, J. Acoust. Soc. Am. 26, 581 (1954).

[50] Hueter, T. F. and Bolt, R. H., An ultrasonic method for outlining the cerebral ventricles, J. Acoust. Soc. Am. 23, 160-167 (1951).

[51] Hueter, T. F., Messung der Ultraschallabsorption im menschlichen Schädelknochen und ihre Abhängigkeit von der Frequenz, Naturwissenschaften 39, 21-22 (1952).

[52] Dunn, F., Attenuation and speed of ultrasound in lung, J. Acoust. Soc. Am. 56, 1638-1639 (1974).

[53] Dunn, F., Temperature and amplitude dependence of acoustic absorption in tissue, J. Acoust. Soc. Am. 34, 1545-1547 (1962).

[54] Marcus, P. W. and Carstensen, E. L., Problems with absorption measurements of inhomogeneous solids, J. Acoust. Soc. Am. 58, 1334-1335 (1975).

[55] Reid, J. M., (1965), reported in F. Dunn, P. D. Edwards and W. J. Fry, Absorption and Dispersion of Ultrasound in Biological Media, H. P. Schwan ed., pp. 205-332 (McGraw-Hill Book Co., New York, 1969).

[56] Bauld, T. J. and Schwan, H. P., Attenuation and reflection of ultrasound in canine lung tissue, J. Acoust. Soc. Am. 56, 1630-1637 (1974).

[57] Carstensen, E. L., Li, K., and Schwan, H. P., Determination of the acoustic properties of blood and its components, J. Acoust. Soc. Am. 25, 286-289 (1953).

[58] Filipczynski, L., Etienne, J., Lypacewicz, G., and Salkowski, J., Visualizing internal structures of the eye by means of ultrasonics, Proc. Vibration Problems 8, 357-368 (1967).

[59] Urick, R. J., A sound velocity measurement for determining the compressibility of finely divided substances, J. Appl. Phys. 18, 983-987 (1947).

[60] Heyser, R. C. and Le Croissette, D. H., A new ultrasonic imaging technique using time delay spectrometry, Ultrasound in Med. Biol. 1, 119-131 (1975).

[61] Lizzi, F. L. and Laviola, M. A., Power spectra measurements of ultrasonic backscatter from ocular tissues, in Proceedings of 1975 I.E.E.E. Ultrasonics Symposium, pp. 29-32 (1975).

[62] Yuhas, D. E., Mimbs, J. W., Miller, J. G., Weiss, A. N., and Sobel, B. E., Changes in ultrasonic attenuation indicative of regional myocardial infarction, in Proceedings of World Federation of Ultrasound in Medicine and Biology, San Francisco, 1976, pp. 1883-1894 (1976).

NBS-114A (REV. 9-78)

U.S. DEPT. OF COMM. BIBLIOGRAPHIC DATA SHEET	1. PUBLICATION OR REPORT NO. NBS SP 525	2. Gov't Accession No.	3. Recipient's Accession No.

4. TITLE AND SUBTITLE

Ultrasonic Tissue Characterization II

5. Publication Date
April 1979

6. Performing Organization Code

7. AUTHOR(S)
Edited by Melvin Linzer

8. Performing Organ. Report No.

9. PERFORMING ORGANIZATION NAME AND ADDRESS

NATIONAL BUREAU OF STANDARDS
DEPARTMENT OF COMMERCE
WASHINGTON, DC 20234

10. Project/Task/Work Unit No.

11. Contract/Grant No.

12. SPONSORING ORGANIZATION NAME AND COMPLETE ADDRESS *(Street, City, State, ZIP)*
National Science Foundation
Washington, D.C.
and National Institutes of Health
Bethesda, Maryland

13. Type of Report & Period Covered

14. Sponsoring Agency Code

15. SUPPLEMENTARY NOTES

Library of Congress Catalog Card Number: 79-600026

☐ Document describes a computer program; SF-185, FIPS Software Summary, is attached.

16. ABSTRACT *(A 200-word or less factual summary of most significant information. If document includes a significant bibliography or literature survey, mention it here.)*

The Second International Symposium on Ultrasonic Imaging and Tissue Characterization was held at the National Bureau of Standards on June 13-15, 1977. The meeting was cosponsored by the National Bureau of Standards, the National Science Foundation, and the National Institutes of Health. This volume contains extended and reviewed papers based on 43 of the 53 talks presented at the Symposium. Topics covered include techniques for measurement of ultrasonic tissue parameters, the dependence of tissue properties on physical and biological variables (e.g., ultrasonic frequency, temperature), mechanisms of ultrasonic tissue interactions, propagation through bone and skull, tumpr Doppler signatures, computerized tomography, signal processing and pattern recognition, and tissue phantoms. A survey of velocity and attenuation data in mammalian tissue is included in an appendix.

17. KEY WORDS *(six to twelve entries; alphabetical order; capitalize only the first letter of the first key word unless a proper name; separated by semicolons)*

Absorption; attenuation; computerized tomography; Doppler; impedance; medical diagnosis; microscopy; pattern recognition; scattering; signal processing; tissue characterization; tissue parameters; ultrasound; velocity.

18. AVAILABILITY

☒ Unlimited

☐ For Official Distribution. Do Not Release to NTIS

☒ Order From Sup. of Doc., Government Printing Office, Washington, DC 20402, SD Stock No. SN003-003-0258-3

☐ Order From National Technical Information Service (NTIS), Springfield, VA. 22161

19. SECURITY CLASS (THIS REPORT)	21. NO. OF PRINTED PAGES
UNCLASSIFIED	339
20. SECURITY CLASS (THIS PAGE)	**22. Price**
UNCLASSIFIED	$5.50

☆ U.S. GOVERNMENT PRINTING OFFICE: 1979 O—291-026

NBS TECHNICAL PUBLICATIONS

PERIODICALS

JOURNAL OF RESEARCH—The Journal of Research of the National Bureau of Standards reports NBS research and development in those disciplines of the physical and engineering sciences in which the Bureau is active. These include physics, chemistry, engineering, mathematics, and computer sciences. Papers cover a broad range of subjects, with major emphasis on measurement methodology, and the basic technology underlying standardization. Also included from time to time are survey articles on topics closely related to the Bureau's technical and scientific programs. As a special service to subscribers each issue contains complete citations to all recent NBS publications in NBS and non-NBS media. Issued six times a year. Annual subscription: domestic $17.00; foreign $21.25. Single copy, $3.00 domestic; $3.75 foreign.

Note: The Journal was formerly published in two sections: Section A "Physics and Chemistry" and Section B "Mathematical Sciences."

DIMENSIONS/NBS

This monthly magazine is published to inform scientists, engineers, businessmen, industry, teachers, students, and consumers of the latest advances in science and technology, with primary emphasis on the work at NBS. The magazine highlights and reviews such issues as energy research, fire protection, building technology, metric conversion, pollution abatement, health and safety, and consumer product performance. In addition, it reports the results of Bureau programs in measurement standards and techniques, properties of matter and materials, engineering standards and services, instrumentation, and automatic data processing.

Annual subscription: Domestic, $11.00; Foreign $13.75

NONPERIODICALS

Monographs—Major contributions to the technical literature on various subjects related to the Bureau's scientific and technical activities.

Handbooks—Recommended codes of engineering and industrial practice (including safety codes) developed in cooperation with interested industries, professional organizations, and regulatory bodies.

Special Publications—Include proceedings of conferences sponsored by NBS, NBS annual reports, and other special publications appropriate to this grouping such as wall charts, pocket cards, and bibliographies.

Applied Mathematics Series—Mathematical tables, manuals, and studies of special interest to physicists, engineers, chemists, biologists, mathematicians, computer programmers, and others engaged in scientific and technical work.

National Standard Reference Data Series—Provides quantitative data on the physical and chemical properties of materials, compiled from the world's literature and critically evaluated. Developed under a world-wide program coordinated by NBS. Program under authority of National Standard Data Act (Public Law 90-396).

NOTE: At present the principal publication outlet for these data is the Journal of Physical and Chemical Reference Data (JPCRD) published quarterly for NBS by the American Chemical Society (ACS) and the American Institute of Physics (AIP). Subscriptions, reprints, and supplements available from ACS, 1155 Sixteenth St. N.W., Wash., D.C. 20056.

Building Science Series—Disseminates technical information developed at the Bureau on building materials, components, systems, and whole structures. The series presents research results, test methods, and performance criteria related to the structural and environmental functions and the durability and safety characteristics of building elements and systems.

Technical Notes—Studies or reports which are complete in themselves but restrictive in their treatment of a subject. Analogous to monographs but not so comprehensive in scope or definitive in treatment of the subject area. Often serve as a vehicle for final reports of work performed at NBS under the sponsorship of other government agencies.

Voluntary Product Standards—Developed under procedures published by the Department of Commerce in Part 10, Title 15, of the Code of Federal Regulations. The purpose of the standards is to establish nationally recognized requirements for products, and to provide all concerned interests with a basis for common understanding of the characteristics of the products. NBS administers this program as a supplement to the activities of the private sector standardizing organizations.

Consumer Information Series—Practical information, based on NBS research and experience, covering areas of interest to the consumer. Easily understandable language and illustrations provide useful background knowledge for shopping in today's technological marketplace.

Order **above** *NBS publications from: Superintendent of Documents, Government Printing Office, Washington, D.C. 20402.*

Order **following** *NBS publications—NBSIR's and FIPS from the National Technical Information Services, Springfield, Va. 22161.*

Federal Information Processing Standards Publications (FIPS PUB)—Publications in this series collectively constitute the Federal Information Processing Standards Register. Register serves as the official source of information in the Federal Government regarding standards issued by NBS pursuant to the Federal Property and Administrative Services Act of 1949 as amended, Public Law 89-306 (79 Stat. 1127), and as implemented by Executive Order 11717 (38 FR 12315, dated May 11, 1973) and Part 6 of Title 15 CFR (Code of Federal Regulations).

NBS Interagency Reports (NBSIR)—A special series of interim or final reports on work performed by NBS for outside sponsors (both government and non-government). In general, initial distribution is handled by the sponsor; public distribution is by the National Technical Information Services (Springfield, Va. 22161) in paper copy or microfiche form.

BIBLIOGRAPHIC SUBSCRIPTION SERVICES

The following current-awareness and literature-survey bibliographies are issued periodically by the Bureau:

Cryogenic Data Center Current Awareness Service. A literature survey issued biweekly. Annual subscription: Domestic, $25.00; Foreign, $30.00.

Liquified Natural Gas. A literature survey issued quarterly. Annual subscription: $20.00.

Superconducting Devices and Materials. A literature survey issued quarterly. Annual subscription: $30.00. Send subscription orders and remittances for the preceding bibliographic services to National Bureau of Standards, Cryogenic Data Center (275.02) Boulder, Colorado 80302.

U.S. DEPARTMENT OF COMMERCE
National Bureau of Standards
Washington, D.C. 20234

OFFICIAL BUSINESS

Penalty for Private Use, $300

POSTAGE AND FEES PAID
U.S. DEPARTMENT OF COMMERCE
COM-215

SPECIAL FOURTH-CLASS RATE
BOOK